



# Development of exploration tools for porphyry-breccia-hosted mineral deposits

Submitted by Callum Scott to the University of Exeter as a thesis for the degree of Doctor of Philosophy in Geology, August 2020.

This thesis is available for Library use on the understanding that it is copyright material and that no quotation from the thesis may be published without proper acknowledgement.

I certify that all material in this thesis which is not my own work has been identified and that no material has been previously submitted and approved for the award of a degree by this or any other University.

## **Abstract**

Porphyry Cu systems often host tourmaline breccias, some, or a part of which, may be economically mineralised. Assessing which are significantly endowed, and at what depth, is problematic as there are relatively few models and exploration tools available for these systems. To address this, breccias from El Teniente in central Chile, one of the world's largest Cu-Mo deposits, were studied.

Three mechanisms have previously been suggested for the formation of the breccias at El Teniente: 1) by replacement of rock flour breccias; 2) as magmatic-hydrothermal intrusion-collapse breccias; and 3) diatreme breccias.

All tourmaline breccia types at Teniente show cyclical dissolution and precipitation textures indicating interaction with multiple fluids, and contain at least two generations of tourmaline in the cement. The generation of permeability and porosity through re-brecciation and/or widespread dissolution of the cement produced favourable conditions for high-grade Cu-Mo mineralisation, frequently around breccia margins. Significant fluid-wall-rock interaction caused substantial fluid contamination resulting in vertical and horizontal changes in tourmaline composition within the breccia pipes.

Explosive devolatilisation and fragmentation of the dacite porphyry underlying the Braden Diatreme generated semi-solidified vermiform clasts that were entrained into the upwardly rising fluidised breccia column. On crystallisation, these exsolved fluids which precipitated molybdenite-quartz ( $\pm$ Cu-Pb-Zn) around the clasts. Magmatic quartz within the dacite clasts, rock flour matrix and the underlying dacite all contain similar internal grain characteristics, CL emission and Ti concentrations, suggesting that the matrix is a highly fragmented derivative of the dacite.

Despite the composition of tourmaline being strongly influenced by its mode of formation (clast- vs. cement-hosted) and proximity to wall rocks, it could not be used to discriminate well- from poorly-endowed breccias, which limits its use as an exploration indicator.

## Acknowledgements

First and foremost, I would like to thank Codelco for supporting this research and permitting it to be published. From División El Teniente I especially wish to express my gratitude to Andrés Brzovic for organising, approving and facilitating this project, and for his continued support and enthusiasm. Ricardo Floody and José Seguel are thanked for their enormously helpful insights and discussions. Perhaps the two most instrumental people on a day-to-day basis were Iván Rojas and Violeta Ríos whom I cannot thank enough for their kindness and generosity. Huge thanks go to René Padillá for his continued patience during my stays in Rancagua. Others at Codelco who I would like to recognise include Paulina Schachter and Romina Osorio.

At CSM there are many people who have helped along this relentless journey. The most influential has been my principal supervisor, Prof. Ben Williamson for providing continued guidance, feedback, support and encouragement throughout the period of study. Huge thanks go to the rest of the supervisory team including Prof. Jens Andersen, Prof. Tom Blenkinsop, Prof. Axel Müller and Prof. José Piquer. Many thanks also go to the School's laboratory staff for their assistance, particularly Steve Pendray for sample preparation, Dr. Joe Pickles for EPMA, SEM and LA-ICP-MS, Sharon Uren for ICP-MS and Malcolm Spence for XRF and XRD support. Finally I'd like to thank Dr. Gavyn Rollinson not only for his QEMSCAN<sup>®</sup> expertise but also for his frequent advice and encouragement.

Outside of the academic world there are countless people who have helped during this long process, firstly and foremost my family, who I can't thank enough. Thanks also to Deirdre and everyone at The Pitt, who are family in all but name, for lending an ear and offering support and advice where possible. Thank you to Rumpus for showing how to enjoy life's simple pleasures and Galit for deep thoughts and discussion. Also thanks to John, I enjoyed our conversations on valley news, gossip and tales from a bygone era over 'bate'.

A big thanks has to go to all those who regularly made it out on parade at the Nags before Covid-19 stopped play. From this, I have learned and heard many life lessons, received some great, and not so great advice, along with much needed reality checks from academia. Finally on the social circle front, and by no means least, I'd like to mention my learned friend Geoff 'Sox'. You have provided regular annoyance and entertainment over the years, delivered many words of encouragement to finish this work, and provided an education on life outside of university. Your use of the English language and humour are unique. In some respects you're an inspiration to many of us, by proving on countless occasions that you can't keep a good man down, apart from on Monday's. Hopefully once 'coronacation' is over we can all reconvene as usual.

This project was supported by a NERC GW4+ Doctoral Training Partnership studentship from the Natural Environment Research Council [NE/L002434/1].

# Contents

1	Introduction .....	1
1.1	Project rationale .....	1
1.2	Breccia architecture.....	2
1.3	Breccia genesis .....	3
1.4	Porphyry indicator minerals .....	4
1.4.1	Tourmaline .....	5
1.5	Chile: Geographical setting and country snapshot.....	6
1.6	Porphyry Cu deposits of Chile and El Teniente.....	7
1.6.1	El Teniente .....	7
1.7	Research aims and objectives.....	9
1.7.1	Research hypotheses .....	9
1.8	Thesis structure.....	10
1.9	Terminology and abbreviations.....	11
2	Literature review .....	12
2.1	Porphyry Cu deposits .....	12
2.1.1	Global distribution, tectonic settings and formation .....	13
2.1.2	Porphyry-style mineralisation and alteration .....	17
2.2	Breccia description and classification .....	20
2.3	Porphyry-breccias.....	21
2.3.1	Formation .....	21
2.3.2	Porphyry-breccia classification .....	22
2.3.3	Magmatic-hydrothermal breccias .....	24
2.3.4	Phreatomagmatic breccias (diatremes).....	25
2.3.5	Phreatic breccias and pebble dykes .....	28
2.4	El Teniente overview .....	29
2.4.1	Location, history and mining .....	29
2.4.2	District Exploration.....	30
2.4.3	Tectonic setting of Chile .....	32
2.4.4	Regional geology: Teniente district.....	35
2.5	El Teniente porphyry system: lithologies, geochronology and genesis.....	38
2.5.1	Lithologies .....	38
2.5.2	Geochronology .....	40
2.5.3	El Teniente porphyry system - genesis .....	44
2.5.4	Teniente Mafic Complex (TMC) .....	47
2.5.5	Teniente Intrusive Complex .....	48
2.5.6	Veins .....	51
2.6	Breccias .....	52

2.6.1	Igneous Breccias .....	54
2.6.2	Biotite Breccias.....	55
2.6.3	Anhydrite Breccias.....	57
2.6.4	Tourmaline Breccias .....	59
2.6.5	Braden Breccia Complex .....	61
2.7	Closing Statements .....	76
3	Sample collection and analytical methodologies .....	77
3.1	Drill core logging and sample collection.....	77
3.2	Sample preparation for optical petrography, SEM ( $\pm$ CL), cold-CL, EPMA and LA-ICP-MS.....	77
3.3	Sample preparation for whole-rock XRF, XRD and ICP-OES and ICP-MS analysis.....	77
3.4	XRF.....	78
3.4.1	XRF QA/AC .....	78
3.5	XRD .....	79
3.6	ICP-MS.....	79
3.6.1	ICP-MS QA/QC .....	80
3.7	ICP-OES .....	88
3.8	SEM ( $\pm$ CL).....	91
3.9	EPMA of tourmaline.....	91
3.9.1	EPMA limitations .....	92
3.9.2	EPMA tourmaline QA/AC.....	92
3.9.3	Artifacts in the EPMA data .....	92
3.10	EPMA Ti-in-quartz .....	95
3.10.1	EPMA Ti-in-quartz QA/QC.....	95
3.11	Quartz LA-ICP-MS.....	98
3.12	Tourmaline LA-ICP-MS .....	98
3.12.1	Tourmaline LA-ICP-MS method development.....	98
3.12.2	Tourmaline LA-ICP-MS QA/QC .....	99
3.13	Automated mineralogical analysis: QEMSCAN <sup>®</sup> .....	101
3.13.1	Data Processing .....	102
3.13.2	QEMSCAN <sup>®</sup> QA/QC .....	102
4	Results: Breccia petrography and geochemistry .....	104
4.1	Braden Diatreme: petrography and links to Mo-Cu mineralisation .....	104
4.1.1	Braden Sericite Breccia .....	104
4.1.2	Fine Sericite Braden Breccia .....	107
4.1.3	Blocky Braden Sericite Breccia (pebble dykes).....	108
4.1.4	Braden Sulphide Breccia .....	109

4.1.5	Juvenile dacite clasts.....	111
4.1.6	Cross-cutting veins within the Braden Diatreme Breccias .....	121
4.2	Braden Diatreme quartz CL response and Ti temperature estimates.....	127
4.2.1	Underlying dacite quartz .....	127
4.2.2	Juvenile dacite clast-hosted quartz .....	129
4.2.3	Rock flour matrix quartz .....	131
4.2.4	Quartz associated with molybdenite (in rock flour matrix at/near dacite clast margins) .....	134
4.2.5	Diablo Breccia hydrothermal cement quartz .....	137
4.2.6	Ti-in-quartz temperature estimates .....	138
4.3	Tourmaline breccia textural classification .....	141
4.3.1	Textural varieties .....	141
4.4	Tourmaline breccia petrography and paragenesis .....	143
4.4.1	Early Tourmaline Breccias .....	143
4.4.2	Marginal Tourmaline Breccia .....	149
4.4.3	Braden Tourmaline Breccia .....	156
4.4.4	Diablo Tourmaline Breccias .....	162
4.4.5	La Huifa Tourmaline Breccia.....	173
4.4.6	Summary .....	185
4.5	Compositional variation of tourmaline .....	187
4.5.1	Major and minor elements .....	187
4.5.2	Trace elements.....	206
4.5.3	Tourmaline rare earth element contents .....	217
4.6	Intra-crystalline tourmaline compositional variations .....	228
4.6.1	Early Tourmaline Breccia.....	228
4.6.2	Marginal Tourmaline Breccia (MTB) .....	236
4.6.3	Braden Tourmaline Breccia (BTB) .....	239
4.6.4	Diablo .....	244
4.6.5	La Huifa .....	252
4.6.6	Summary .....	256
5	Discussion .....	257
5.1	Architecture of El Teniente breccia complexes .....	257
5.2	Models for tourmaline breccia formation at El Teniente .....	262
5.2.1	Magmatic-hydrothermal intrusion breccias.....	262
5.2.2	Hydrothermal replacement model for the Braden Tourmaline Breccia ...	282
5.3	Tourmaline geochemistry and use as an exploration indicator.....	292
5.3.1	Major and minor element data .....	292
5.3.2	Tourmaline trace and REE composition.....	295

5.3.3	Intra-pipe tourmaline compositional variations: Diablo Breccias.....	299
5.3.4	Implications for exploration .....	307
5.4	Braden Diatreme .....	308
5.4.1	Juvenile dacite clasts and alternative interpretations .....	308
5.4.2	Braden Diatreme formation model .....	319
5.4.3	Use of diatreme facies as an exploration indicator .....	333
6	Conclusions .....	334
7	Future work.....	336
7.1	La Huifa.....	336
7.2	Tourmaline .....	336
7.3	Braden Diatreme .....	337
	References .....	338
	Appendices.....	366
	i) Drill hole intercepts and locations	
	ii) Sample descriptions (Excel)	
	iii) QEMSCAN® data (Excel)	
	iv) XRD data (Excel)	
	v) Tourmaline EPMA and LA-ICP-MS data (Excel)	
	vi) Ti-in-quartz EPMA and LA-ICP-MS data (Excel)	
	vii) Whole-rock XRF, ICP-MS and ICP-OES data (Excel)	

## List of Figures

Fig. 1.1 Global map showing the location of Chile along the western edge of South America, bordering the Pacific Ocean (from Un.org, 2010) .....	6
Fig. 1.2 Location of El Teniente in relation to other major porphyry Cu-Mo systems in the northern and central Chilean Cu districts .....	7
Fig. 2.1 Global map of porphyry Cu systems showing principal deposit type(s), contained metals, and age.....	14
Fig. 2.2 Schematics from Sillitoe (2010) of telescoped porphyry Cu systems highlighting mineralisation and alteration relationships described by Lowell and Guilbert (1970) .....	19
Fig. 2.3 Ternary diagrams ( <b>a</b> , <b>b</b> ) from Woodcock and Mort (2008) showing the two alternative methods of breccia classification .....	20
Fig. 2.4 Schematic depiction of a magmatic-hydrothermal breccia genetically linked to the apex of an underlying intermineral porphyry intrusion. Modified after Sillitoe (2010) .....	24
Fig. 2.5 Field photographs of El Teniente (September 2017) .....	30
Fig. 2.6 <b>a</b> ) Alteration map of the Teniente district showing prospective areas for further exploration. From Pardo and Villarroel, (n.d.); <b>b</b> ) Relative location of La Huifa and Mantacillas Alto breccias to the Teniente mine. From Vidakovic (2013).....	31
Fig. 2.7 Regional geology of central Chile and adjoining Argentina, with corresponding geological cross section (north of El Teniente) from Farías et al. (2008) .....	33
Fig. 2.8 Schematic diagram showing the Central Andes and modern flat-slab segment. Reproduced after Parada et al. (2007).....	34
Fig. 2.9 <b>a</b> ) Regional geological map of Chile adapted after Serrano et al. (1996). <b>b</b> ) Lithological map of the Teniente district within the Principal Cordillera. From Vry (2010).....	35
Fig. 2.10 Geology of the Teniente district, showing the spatial association between the Teniente deposit and intersection between the NE-trending Teniente Fault Zone and NW-orientated Codegua Fault: <b>a</b> ) Reproduced after Cannell et al. (2005); <b>b</b> ) Reproduced after Garrido (1995).....	37
Fig. 2.11 Geological map of level 2085 at El Teniente, March 2017. Courtesy of Codelco División El Teniente. ....	39
Fig. 2.12 <b>a</b> ) Time vs. depth plot depicting the magmatic-hydrothermal evolution of El Teniente adapted after Spencer et al. (2015) to include La Huifa.....	43

Fig. 2.13 Photographs of the Braden Diatreme at El Teniente from Cannell et al. (2007) taken in the sublevel 6 mine, 2,210 masl .....	44
Fig. 2.14 Schematic model reproduced after Cannell et al. (2005), showing the three stage structural evolution of El Teniente .....	47
Fig. 2.15 Photographs of underground exposure of the stockwork in TMC .....	48
Fig. 2.16 Summary of the existing vein classification schemes for El Teniente .....	52
Fig. 2.17 Drill core photographs of igneous breccias at El Teniente .....	54
Fig. 2.18 Hand specimens and photomicrograph of El Teniente biotite breccias.....	56
Fig. 2.19 Photographs of El Teniente anhydrite-cemented breccias.....	58
Fig. 2.20 Series of maps showing the Diablo Breccias at different mine levels around level 6 (~2,165 masl). Maps courtesy of Codelco División El Teniente.....	60
Fig. 2.21 Early geological map of the Braden Diatreme and surrounding orebody by the Braden Copper Company (courtesy of Codelco), largely based on mapping by Lindgren and Bastin (1922).....	62
Fig. 2.22 Photographs of the Marginal Breccias.....	68
Fig. 2.23 Outcrop photographs showing syngenetic and subsidence-related structures in the Braden Diatreme, from Floody (2000) .....	71
Fig. 2.24 Braden Diatreme crystal caverns and mineral specimens .....	72
Fig. 2.25 Formation of the Braden Diatreme, reproduced after Floody (2000).....	75
Fig. 3.1 Thompson-Howarth plot illustrating the precision of duplicate analyses of breccias by semi-quantitative XRF.....	79
Fig. 3.2 <b>a)</b> Major and minor element concentrations in acid blanks determined by ICP-MS at CSM; <b>b)</b> Rare earth element concentrations in acid blanks run at CSM.....	82
Fig. 3.3 Thompson-Howarth plot illustrating the precision of duplicate analyses of breccias by ICP-MS .....	87
Fig. 3.4 Thompson-Howarth plot illustrating the precision of breccia sample solution duplicates by ICP-OES .....	90
Fig. 3.5 Twenty-minute wavescans on the quartz standard to model the background and peak (solid vertical black line) of Ti on the PETJ (a) and PETH (b) crystals. ....	96
Fig. 3.6 SEM-BSE, 1 $\mu$ m QEMSCAN <sup>®</sup> mineral map and SEM-CL images of the homogenous quartz core (Qtz1) repeatedly analysed.....	97
Fig. 4.1 XRD pattern for the rock flour matrix from drill hole 1196-172.71 m .....	105

Fig. 4.2 Photographs of hand specimens with corresponding images of 30 µm thin sections below (a-c), and SEM-BSE images (d-g) and SEM-EDS maps (h-i) of the matrix-supported Braden Sericite Breccia with variable chlorite overprints.....	106
Fig. 4.3 Drill core photographs of the Fine Sericite Braden Breccia.....	107
Fig. 4.4 Drill core photographs of Blocky Braden Sericite Breccia.....	108
Fig. 4.5 Series of drill core photos of Braden Sulphide Breccia with distance from annular Marginal Breccias (MBX).....	110
Fig. 4.6 Overlaid XRD patterns for juvenile dacite clasts and rock flour matrix from sample 1196_27 (220.88 m; ~75 m from Marginal Breccias, 0.79 wt.% Cu and 0.21 wt.% Mo).....	112
Fig. 4.7 Photographs of drill core showing juvenile dacite clasts which were apparently viscous when incorporated in the Braden Diatreme facies .....	113
Fig. 4.8 Photos of core containing juvenile dacite clasts from the Braden Diatreme, with transmitted light photomicrographs (XPL) and accompanying QEMSCAN® mineral maps (10 µm pixel spacing) .....	115
Fig. 4.9 SEM-BSE images showing varying concentrations of molybdenite in the rock flour matrix immediately adjacent to juvenile dacite clasts (a-c), within ~2 cm (d-f) and greater than ~2 cm of the dacite clasts (g-h) .....	117
Fig. 4.10 SEM-BSE images and EDS elemental maps (g, j) showing that Cu-Mo±Pb-Zn mineralisation is spatially associated with the contact between the juvenile dacite and rock flour matrix, from DDH1196-172.71 m.....	119
Fig. 4.11 Drill core photos of late-stage veins cross-cutting the Braden Diatreme matrix and clasts .....	121
Fig. 4.12 Images of cross-cutting vein generations in the Braden Diatreme rock flour matrix and juvenile dacite clasts ( <b>a-f</b> : DDH1196-242.04 m and <b>g-m</b> : DDH1196-172.93 m) .....	123
Fig. 4.13 Cold-CL and transmitted light (PPL) images (e, g) of magmatic quartz from the dacite body underlying the Braden Diatreme (DDH1068-1,012.8 m) .....	128
Fig. 4.14 Texture of quartz in dacite clasts in the Braden Sericite Breccia. EPMA point locations (yellow) with matching Ti concentrations (ppm) are also shown for reference .....	130
Fig. 4.15 Quartz from the rock flour matrix in the Braden Diatreme. EPMA point locations (yellow) with Ti concentrations (ppm) are also shown for reference .....	132

Fig. 4.16 Images a-f are SEM-BSE (left) with corresponding SEM-CL (right) and g-n are transmitted light photomicrographs (PPL) (left) with matching cold-CL images (right) of quartz associated with molybdenite mineralisation in the Braden Diatreme 134	
Fig. 4.17 Hydrothermal cement-phase quartz from the Diablo Breccia (DDH2677-118 m) .....	137
Fig. 4.18 Ti, Al and Fe in quartz from different rock types (separated by vertical lines) and generations (ppm) from El Teniente, determined by EPMA.....	139
Fig. 4.19 Textural classification of tourmaline breccias at El Teniente from drill core observations in this study. Each breccia has a variety of textures, largely reflecting the sample location.....	142
Fig. 4.20 Drill core photographs of crackle tourmaline breccias from DDH1754.....	144
Fig. 4.21 SEM-BSE images from the Early Tourmaline Breccia east of the Braden Diatreme from DDH1754-317.5 m (sample shown in Fig. 4.20e) .....	146
Fig. 4.22 Tourmaline breccias from the Marginal Breccia.....	149
Fig. 4.23 Flatbed scans of polished sections of Marginal Tourmaline Breccia samples (all polished sections are 150 $\mu\text{m}$ thick except c which is 30 $\mu\text{m}$ ) with corresponding QEMSCAN <sup>®</sup> (10 $\mu\text{m}$ pixel) mineral maps below .....	151
Fig. 4.24 Photomicrographs in transmitted light of Marginal Tourmaline Breccia in PPL and XPL.....	154
Fig. 4.25 Drill core photographs of the cement-supported BTB (a-d), cut thin section tablet (e), corresponding transmitted light image (XPL) (f) and QEMSCAN <sup>®</sup> mineral maps (g) .....	157
Fig. 4.26 Transmitted light (XPL) (a-c), SEM-BSE photomicrographs (d-h) and thin section scans with corresponding QEMSCAN <sup>®</sup> (10 $\mu\text{m}$ pixel) mineral maps (i-j) of the Braden Tourmaline Breccia.....	160
Fig. 4.27 Photographs of drill core from the Diablo Breccias.....	164
Fig. 4.28 Diablo Breccias - QEMSCAN <sup>®</sup> all-mineral maps (10 $\mu\text{m}$ pixel) filtered (in maps below) for different minerals.....	168
Fig. 4.29 Transmitted light photomicrographs (PPL and XPL) (a-f) and SEM-EDS elemental maps (g-n) of tourmaline in the Diablo Breccia .....	171
Fig. 4.30 Drill core photos of the La Huifa host rocks (Farellones Formation) .....	173
Fig. 4.31 La Huifa alteration-mineralisation events.....	176

Fig. 4.32 Transmitted light (PPL) and cold-CL images showing coarse tourmaline-quartz cement phases and textures present in them from the La Huifa breccias.....	177
Fig. 4.33 Transmitted light photomicrographs (PPL) (a-d), SEM-BSE images (e-f) and WDS/EDS element maps (g-j) showing La Huifa tourmaline textures, relationships and generations.....	181
Fig. 4.34 Tourmaline classification diagrams of data (apfu) from El Teniente.....	188
Fig. 4.35 Major element data (wt.% oxides) for tourmaline from the tourmaline breccias at El Teniente .....	194
Fig. 4.36 List of Diablo drill holes and sample details with corresponding cross sections showing relative drill hole locations. Intercepts of tourmaline breccia, from which the samples were obtained, are also provided. Sections are courtesy of Codelco .....	199
Fig. 4.37 Plots (wt.%) of Diablo Tourmaline Breccia analyses, with groupings, where present, delineated on the graphs. Tourmaline data have been split into their relative depths and positions in the breccia: <b>a)</b> SiO <sub>2</sub> vs. FeO; <b>b)</b> SiO <sub>2</sub> vs. MgO; <b>c)</b> SiO <sub>2</sub> vs. Al <sub>2</sub> O <sub>3</sub> ; <b>d-l)</b> Overleaf. ....	202
Fig. 4.38 Tourmaline minor and trace element LA-ICP-MS data from the five El Teniente tourmaline breccias selected in this study .....	214
Fig. 4.39 Rare earth LA-ICP-MS tourmaline data from all five breccias selected.....	219
Fig. 4.40 Chondrite-normalised (values from Sun and McDonough, 1989) tourmaline REE patterns .....	225
Fig. 4.41 ETB cement-hosted tourmaline and LA-ICP-MS data .....	230
Fig. 4.42 ETB cement-hosted tourmaline and LA-ICP-MS data .....	231
Fig. 4.43 ETB clast-hosted tourmaline and LA-ICP-MS data.....	234
Fig. 4.44 ETB clast-hosted tourmaline and LA-ICP-MS data.....	235
Fig. 4.45 MTB cement-hosted tourmaline and LA-ICP-MS data.....	237
Fig. 4.46 MTB cement-hosted tourmaline and LA-ICP-MS data.....	238
Fig. 4.47 BTB cement-hosted tourmaline and LA-ICP-MS data .....	241
Fig. 4.48 BTB cement-hosted tourmaline and LA-ICP-MS data .....	242
Fig. 4.49 BTB cement-hosted tourmaline and LA-ICP-MS data .....	243
Fig. 4.50 Diablo cement-hosted tourmaline (DDH1974_1; 131.07 m; deep inner) EPMA and LA-ICP-MS data.....	245

Fig. 4.51 Diablo cement-hosted tourmaline (DDH2136_1; 0.96 m; deep inner) EPMA and LA-ICP-MS data.....	246
Fig. 4.52 Diablo cement-hosted tourmaline (DDH2677_3; 118 m; middle inner) EPMA and LA-ICP-MS data.....	248
Fig. 4.53 Diablo cement-hosted tourmaline (DDH2677_3; 118 m; middle inner) EPMA and LA-ICP-MS data.....	249
Fig. 4.54 Diablo cement-hosted tourmaline (DDH2672_9; 166.66 m; shallow inner) EPMA and LA-ICP-MS data.....	251
Fig. 4.55 La Huifa cement-hosted tourmaline (ES026_6; 191.74 m) EPMA and LA-ICP-MS data .....	253
Fig. 4.56 La Huifa cement-hosted tourmaline (ES026_6; 191.74 m) EPMA and LA-ICP-MS data .....	254
Fig. 4.57 La Huifa cement-hosted tourmaline (ES026_6; 191.74 m) EPMA and LA-ICP-MS data .....	255
Fig. 5.1 Schematic of vertically zoned magmatic-hydrothermal breccia complexes at El Teniente genetically linked to the apex and/or flanks of intermineral porphyry intrusions such as the Teniente Dacite Porphyry. Also included on the right is a tourmaline breccia independent of these zoned complexes. Figure adapted from Sillitoe (2010) with observations from the current study added.....	260
Fig. 5.2 Drill core photograph illustrating complex clast morphologies of the TMC wall-rocks in the MTB from corrosive wear. From DDH1213-95.5 m .....	265
Fig. 5.3 Coarse (a-c) and microcrystalline (d-k) breccias from the Diablo sector .....	268
Fig. 5.4 Schematic diagram illustrating the development of coarse tourmaline-cemented breccias.....	271
Fig. 5.5 Formation of microcrystalline tourmaline-quartz-cemented breccias .....	272
Fig. 5.6 <b>Option a:</b> This model illustrates less permeability in the central portions compared with the margins for later Cu-Mo-rich fluids to access. Multiple breccias have been ignored; instead just well- and poorly-mineralised portions are shown. The breccia margins are comparatively less fluidised than the central portions of the breccia column and therefore have increased permeability through lower portions of smaller (<2 mm) fragments, rock flour and more angular clasts .....	277
Fig. 5.7 Interval of drill core from hole 2672 (location shown in Fig. 5.6 and Fig. 5.8) which transects from the TMC host rocks into the Diablo Breccias .....	278

Fig. 5.8 **Option b**: Based on Fig. 5.7, this model considers that all parts of the Diablo Breccias were more or less equally fluidised and takes into account the presence of what have been inferred to represent coarser breccias superimposed on one another and the earlier microcrystalline breccias (parts 1 and 2 overleaf explaining the emplacement of microcrystalline breccias (part 1), subsequent emplacement of coarser breccias containing clasts of earlier breccias (part 2)). Later-stage Cu-Mo-rich fluids infiltrate the most permeable areas of the Diablo Breccias such as fractured margins, microcrystalline breccias, or in areas particularly amenable to dissolution, such as coarse breccia cements. Varying degrees of dissolution creates new porosity and permeability late in the paragenetic sequence (part 3 overleaf) ..... 279

Fig. 5.9 **a**) Textural classification of the Braden Tourmaline and Braden Sericite Breccias at El Teniente from drill core observations in this study. Diagram adapted from Woodcock and Mort (2008); **b-d**) Banding in the BTB cement from DDH1754-9.7 m ..... 284

Fig. 5.10 Gresens' isocon analysis for 'unaltered' (actually 'least altered') (Braden Sericite Breccia) vs. altered (Braden Tourmaline Breccia) samples of the Braden Diatreme ..... 288

Fig. 5.11 Schematic model for a hydrothermal replacement origin for the Braden Diatreme-hosted Braden Tourmaline Breccia ..... 291

Fig. 5.12 Ternary plots for tourmaline major element data from El Salvador, El Teniente and Río Blanco-Los Bronces porphyry Cu deposits ..... 294

Fig. 5.13 Covariation plots (a-f) for some tourmaline trace elements from El Teniente breccias ..... 297

Fig. 5.14 Depth correlation of FeO and MgO from Dill et al. (2012) ..... 300

Fig. 5.15 FeO and MgO as a function of depth (generally deep to shallow from diagram a to h) in the Diablo Breccias ..... 301

Fig. 5.16 FeO vs. MgO (wt.%) cross plots for tourmaline from Skewes et al. (2003) and Frikken (2004) as a function of depth ..... 305

Fig. 5.17 Magmatic and hydrothermal quartz textures in the Braden Diatreme ..... 311

Fig. 5.18 Schematic model illustrating the development of the Braden Diatreme rock flour matrix with exaggerated wall-rock and other lithology components ..... 313

Fig. 5.19 Cross polarised photomicrograph (a) and 1 µm pixel QEMSCAN® maps (b-f) from DDH1196-172.71 m transecting the vermiform dacite:matrix boundaries ..... 314

Fig. 5.20 Images (a-c) of type 9 and 10 veins from Spencer et al. (2015) and other late-stage veins cross-cutting the Braden Diatreme .....	319
Fig. 5.21. Eight stage model of the formation of the Braden Diatreme .....	324

## List of Tables

Table 1.1 Tourmaline end-members and site occupancies .....	5
Table 1.2 Mineral abbreviations within this report follow the guidelines set out by Whitney and Evans (2010) except quartz, which will be abbreviated as 'qtz' .....	11
Table 2.1 Three principal types of breccias found in porphyry systems, from Sillitoe (2010) .....	23
Table 2.2 Different terminology for igneous rock units used in the current study compared to terms used by previous authors .....	38
Table 2.3 Characteristics of the main lithologies comprising the Braden Diatreme. From internal SGL-I-123/03 (2003) report.....	65
Table 2.4 Characteristics of the minor lithological comprising the Braden Diatreme. Reproduced after internal SGL-I-123/03 (2003) report with additional details added...	66
Table 2.5 Main features of the Marginal Breccias. From internal SGL-I-123/03 (2003) report, with additional details added.....	69
Table 3.1 Detection limits for different analytes determined by ICP-MS .....	81
Table 3.2 Accuracy of ICP-MS analyses of certified reference materials.....	83
Table 3.3 Accuracy of ICP-OES analyses of certified reference materials .....	88
Table 3.4 The original EPMA analyses from the Teniente Tourmaline Breccias with all Fe as FeO are presented in the orange columns. Alongside these values are different proportions of FeO and Fe <sub>2</sub> O <sub>3</sub> demonstrating the effect on Si.....	93
Table 3.5 LA-ICP-MS analyses of BCR-2G (n= 14) with measured element masses and corresponding detection limits and uncertainty beneath.....	100
Table 4.1 Paragenetic sequence of the Braden Diatreme .....	126
Table 4.2 Paragenetic sequence for the Early Tourmaline Breccia .....	148
Table 4.3 Paragenetic sequence of the Marginal Tourmaline Breccia.....	153
Table 4.4 Paragenetic sequence for the Braden Tourmaline Breccia.....	162
Table 4.5 Paragenetic sequence for the Diablo Breccias .....	170

Table 4.6 Summary of alteration events and mineralogy/veins associated with them at La Huifa, based on drill core observations .....	175
Table 4.7 Paragenetic sequence of alteration and mineralisation, in particular for hydrothermal cementing phases in the La Huifa Breccia.....	184
Table 4.8 EPMA data (wt.% and apfu) for tourmaline from the five breccias analysed at El Teniente .....	190
Table 4.9 LA-ICP-MS data for tourmaline from the five breccias analysed at El Teniente.....	207
Table 5.1 Comparative concentrations (in wt.%) of major elements from Andean porphyry tourmaline breccia pipes .....	293

# 1 Introduction

## 1.1 Project rationale

Porphyry Cu deposits account for nearly three quarters of global Cu supply, half of all Mo and a significant portion of Au and other important metals (Sillitoe, 2010). Some of the largest known Cu (e.g., Río Blanco-Los Bronces and El Teniente, Chile) and Au (e.g., Grasberg, Papua Province) deposits are also associated with such systems (Wilkinson, 2013).

Formed at a depth of several kilometres in the upper crust, porphyry-type deposits are generally associated with magmatic stocks or clusters of dykes which were emplaced upwards from an underlying magma chamber (Wilkinson, 2013). Porphyry Cu-style mineralisation occurs as a distinctive set of quartz-bearing veinlets within porphyry apophyses (e.g., Gustafson and Hunt 1975; Sillitoe, 2010) and as disseminations and veins throughout the surrounding altered rock (Bogie et al., 2005; Sillitoe, 2010). Many porphyry Cu deposits also contain variable volumes of high crustal level steep, pipe-like phreatic-phreatomagmatic, igneous or magmatic-hydrothermal breccias (e.g., Warnars et al., 1985; Irrarrazaval et al., 2010).

The development of breccias within different porphyry systems is variable, with some major examples, such as Chuquicamata (e.g., Ossandón et al., 2001), being breccia free. In comparison, El Teniente and Río Blanco-Los Bronces (e.g., Warnars et al., 1985; Skewes et al., 2002, 2005; Irrarrazaval et al., 2010; Toro et al., 2012), the world's largest single Cu deposit and the most highly endowed porphyry Cu cluster in the world, respectively, contain large volumes of Cu-Mo-mineralised magmatic-hydrothermal biotite-, anhydrite- and tourmaline-cemented breccias. These often overprint pre-existing porphyry-style alteration-mineralisation and can contain higher-grade ore than the porphyry deposit (Sillitoe, 2010). High-level phreatomagmatic breccias are also commonly associated with deeper porphyry Cu deposits (e.g., Skewes et al., 2002) and may provide vectors towards them (e.g., Rottier et al., 2018), often having large footprints (e.g., Sillitoe, 1985). Porphyry-related breccia pipes are therefore considered an attractive exploration target. The main questions of interest to mineral exploration companies are:

- a) Why are some tourmaline breccias heavily mineralised whilst others are 'barren' or subeconomic? The term 'barren' is used here to describe breccias which are currently not, and have never been economic to mine.
- b) Whether any chemical or textural aspects of outcropping breccias can be used to predict the presence of nearby concealed mineralisation.

Existing descriptive and genetic porphyry Cu ( $\pm$ breccia) deposit models have so far and continue to serve as an effective guide for the exploration industry, particularly where deposits are found near surface. There is growing evidence however that most exposed surface deposits have already been found through extensive global surface mapping (e.g., Richards, 2016; Singer, 2017). For example, despite mineralised porphyry-breccia deposits being relatively common throughout Chile and Peru, they are more often than not 'barren' (Skewes et al., 2002). This is thought to reflect the fact that in general, the vast majority of parent calc-alkaline magmatic systems are 'barren' (Richards, 2016). Hence the discovery rates of world-class deposits is declining, and exploration is becoming increasingly difficult, risky, and costly for companies in terms of time and resources (Gandhi and Sarkar, 2016; Singer, 2017).

To improve the chances of exploration success, industry and academia are increasingly looking to develop new geochemical fertility indicators to: a) identify surface signals of concealed deposits (e.g., Bouzari et al., 2011; Wilkinson et al., 2015; Mao et al., 2016); and b) to help rule out igneous suites of low deposit potential at a district scale (McCuaig and Hronsky, 2014; Richards, 2016; Williamson et al., 2016). This has resulted in research into creating more comprehensive whole-rock and mineral-chemical proxies that are efficient, easily quantifiable, and repeatable to support existing whole-sample litho-geochemical methods (e.g., Loucks, 2014). Although such indicators can be assessed relatively quickly and cheaply, and have been used to differentiate between poorly- and well-mineralised systems, they cannot currently indicate the magnitude of mineralisation in a particular system and can produce a large number of false positives and negatives (e.g., Chiaradia and Caricchi, 2017).

## **1.2 Breccia architecture**

Breccia pipes are roughly circular to ovoid in cross section with vertical heights several times greater than their maximum horizontal dimensions (Sillitoe, 1985). Upper terminations of breccias are rarely preserved, but where they are (e.g., San Pedro de Cachiyuyo District (Chile); Sillitoe and Sawkins, 1971), abrupt terminations are observed. Lateral wall-rock contacts are usually sharp and are characterised by sheeted zones comprising angular to subrounded fragments ranging from several m to less than a cm (Sillitoe, 1985).

Magmatic-hydrothermal breccias typically form in the deeper parts of porphyry Cu systems (>1 km) extending hundreds of metres horizontally and several hundred metres in vertical extent, as near vertical pipe-like bodies along the upper peripheries or atop the adjacent porphyry intrusive (Sillitoe, 1985, 2010). Diatremes on the other hand, are commonly found in the upper regions of porphyry Cu systems (Sillitoe,

1985), being intimately related to high-level magmatic porphyry intrusions, feeder dykes or apophyses (Tâmaş and Milési, 2002; Ross et al., 2017). They are generally the largest of the breccia bodies and often reach the volcanic palaeosurface. Near surface they are regularly  $\geq 1$  km in diameter and  $> 2$  km in vertical extent (Lorenz, 1975, 1986; Sillitoe, 1985; Davies et al., 2008). If root zones and feeder dykes are included then vertical extents may well be several kilometres (Lorenz, 1986; Lorenz and Kurszlaukis, 2007).

### **1.3 Breccia genesis**

A range of mechanisms capable of producing substantial void space across a relatively short geological time period have been proposed to generate the variety of breccias possible within porphyry environments (e.g., igneous, magmatic-hydrothermal, diatremes). The following main processes are involved in brecciation: a) downward movement of magma by either shrinkage, withdrawal, or decompression (e.g., Burnham, 1985), causing mechanical disruption of wall rocks; b) chemical reactions due to localised dissolution and upward removal of rock material by fluids released from cooling magma followed by collapse (e.g., Sillitoe, 1985); c) the explosive release of magmatic-hydrothermal fluids from high-level, water-rich magma chambers during second boiling will lead to the accumulation of fluids and build-up of fluid pressure around the carapace (e.g., Burnham, 1985). Once fluid pressure exceeds lithostatic pressure hydraulic fracturing occurs (Sillitoe, 1985; Tosdal and Richards, 2001). Resulting rapid fluid discharge and decompression will cause expansion and upwelling which are thought to be capable of reopening and further widening existing fractures and faults (e.g., Sillitoe, 1985; Halls, 1994); d) rupturing of a pressure seal at the brittle-ductile transition (Fournier, 1999); e) local or remote seismic activity (Tosdal and Richards, 2001) and f) phreatomagmatism involving external waters and require the “vaporization and expansion of water as steam with rapid cooling and/or quenching of the magma” (White and Valentine, 2016), or magmatic fragmentation through the violent exsolution of contained volatile phases without external intervention (Cashman and Scheu, 2015; White and Valentine, 2016).

Magmatic-hydrothermal breccias are formed through the violent release of over-pressured magmatic fluids and volatiles from the apophyses of an underlying pluton, which likely results from boiling processes during the emplacement and solidification of hydrous magmas (e.g., Burnham and Ohmoto, 1980; Burnham, 1979, 1985; Sillitoe, 1985). In comparison magmatic or phreatomagmatic fragmentation mechanisms can cause explosive magma fragmentation and the generation of maar-diatreme breccias (White and Valentine, 2016).

## 1.4 Porphyry indicator minerals

Many mineral-chemical proxies being developed for porphyry exploration are based on minerals which are ubiquitous in porphyry alteration-mineralisation areas and/or are resistate phases. Some of the most widely studied and potentially useful of these are apatite (Bouzari et al., 2016; Mao et al., 2016; Rukhlov et al., 2016), titanite (Che et al., 2013; Celis et al., 2014; Celis, 2015; Kobylinski et al., 2016), zircon (Ballard et al., 2002; Lee et al., 2017; Hattori et al., 2017; Zhang et al., 2017; Pizarro et al., in press), monazite, garnet, magnetite (Canil et al., 2016; Pisiak et al., 2017), jarosite and tourmaline (Hawthorne and Dirlam, 2011; Baksheev et al., 2012; McClenaghan et al., 2017, 2018). Recent review papers on current and ongoing research into porphyry indicator minerals have been provided by Wilkinson et al. (2017) and Cooke et al. (2020).

These resistant phases are of particular interest because in tropical and arid terrains, where intense chemical and physical weathering, erosion and significant mass transport are commonplace, they may be the only suitable phases to collect during the early stages of an exploration campaign.

Before resistate minerals can be used effectively in an integrated exploration program, pilot studies need to be carefully undertaken to establish how chemical signatures between well-mineralised and 'barren' systems differ (Celis et al., 2014). Such assessments should be based on a range of well-studied mineralised and barren comparators and must take into account petrographic and paragenetic relations for the chosen minerals. For example, the relationship between tourmaline composition and Cu-Mo-Au mineralisation, textural habit and viability for easy quantitative analysis (e.g., some crystals are too narrow to analyse) are all vital information for its use by industry. The final data needs to be validated by cross-checking it with other fertility indicators.

### 1.4.1 Tourmaline

Tourmaline is a complex borosilicate mineral group capable of accommodating a wide range of major, minor and trace elements in its crystal lattice (Marks et al., 2013). It is common in porphyry- and related breccia-type deposits where it is usually the main host of boron. It has a general structural formula of  $XY_3Z_6[T_6O_{18}][BO_3]_3V_3W$ , where common site occupancies include X= □ (vacancy), Na<sup>1+</sup>, K<sup>1+</sup>, Ca<sup>2+</sup>, Pb<sup>2+</sup>; Y= Li<sup>1+</sup>, Mg<sup>2+</sup>, Fe<sup>2+</sup>, Mn<sup>2+</sup>, Al<sup>3+</sup>, V<sup>3+</sup>, Cr<sup>3+</sup>, Fe<sup>3+</sup>, Mn<sup>3+</sup>, Ti<sup>4+</sup>, Zn<sup>2+</sup>; Z= Mg<sup>2+</sup>, Fe<sup>2+</sup>, Al<sup>3+</sup>, V<sup>3+</sup>, Cr<sup>3+</sup>, Fe<sup>3+</sup>; T= Si<sup>4+</sup>, Al<sup>3+</sup>, B<sup>3+</sup>; B= B<sup>3+</sup>, □; V= OH<sup>1-</sup>, O<sup>2-</sup>, and W= OH<sup>1-</sup>, F<sup>1-</sup>, O<sup>2-</sup>. There are fourteen recognised end-members between which a large number of solid-solutions are possible (Hawthorne and Henry, 1999).

The use of tourmaline as a geochemical tool for ore deposit research and in mineral exploration has been demonstrated in a number of previous studies (Power, 1968; Boyle, 1974; Taylor and Slack, 1984; Clarke et al., 1989; Slack, 1996; Williamson et al., 2000; Baksheev et al., 2012; Galbraith et al., 2009). It is particularly effective as it is stable in a wide range of geological environments, suffers negligible intra-crystalline diffusion and can incorporate numerous elements (e.g., Marschall and Jiang, 2011; Slack and Trumbull, 2011; van Hinsberg et al., 2011; Marks et al., 2013). Examples of its use include a study by Pirajno and Smithies (1992) who used FeO/FeO+MgO in tourmaline to map spatial geochemical variations in granite-related hydrothermal mineral deposits, and Baksheev et al. (2012) who suggested that Fe-Al-Mg ratios and concentrations can be used to differentiate porphyry-style Cu, Au and Sn mineralisation. Despite this, there is still limited trace and REE data available for tourmaline (e.g., Jiang et al., 1999, 2002, 2004; Galbraith et al., 2009; Klemme et al., 2011; Yavuz et al., 2011; Marks et al., 2013; Kalliomäki et al., 2017; Harlaux et al., 2019; Trumbull et al., 2020), especially from porphyry Cu deposits.

Table 1.1 Tourmaline end-members and site occupancies.

	<b>X</b>	<b>Y<sub>3</sub></b>	<b>Z<sub>6</sub></b>	<b>V<sub>3</sub></b>	<b>W</b>
Elbaite	Na <sup>+</sup>	Al <sub>1.5</sub> <sup>+</sup> Al <sub>1.5</sub> <sup>3+</sup>	Al <sub>6</sub> <sup>3+</sup>	(OH) <sub>3</sub>	(OH)
Schorl	Na <sup>+</sup>	Fe <sub>3</sub> <sup>2+</sup>	Al <sub>6</sub> <sup>3+</sup>	(OH) <sub>3</sub>	(OH)
Dravite	Na <sup>+</sup>	Mg <sub>3</sub> <sup>2+</sup>	Al <sub>6</sub> <sup>3+</sup>	(OH) <sub>3</sub>	(OH)
Olenite	Na <sup>+</sup>	Al <sub>3</sub> <sup>3+</sup>	Al <sub>6</sub> <sup>3+</sup>	(O) <sub>3</sub>	(OH)
Buergerite	Na <sup>+</sup>	Fe <sub>3</sub> <sup>3+</sup>	Al <sub>6</sub> <sup>3+</sup>	(O) <sub>3</sub>	(F)
Povondraite	Na <sup>+</sup>	Fe <sub>3</sub> <sup>3+</sup>	Fe <sub>4</sub> <sup>3+</sup> Mg <sub>2</sub> <sup>2+</sup>	(OH) <sub>3</sub>	(O)
Rossmannite	[ ]	Li <sup>+</sup> Al <sub>2</sub> <sup>3+</sup>	Al <sub>6</sub> <sup>3+</sup>	(OH) <sub>3</sub>	(OH)
Foitite	[ ]	Fe <sub>2</sub> <sup>2+</sup> Al <sub>6</sub> <sup>3+</sup>	Al <sub>6</sub> <sup>3+</sup>	(OH) <sub>3</sub>	(OH)
Magnesio-foitite	[ ]	Mg <sub>2</sub> <sup>2+</sup> Al <sub>3</sub> <sup>3+</sup>	Al <sub>6</sub> <sup>3+</sup>	(OH) <sub>3</sub>	(OH)

## 1.5 Chile: Geographical setting and country snapshot

The Republic of Chile (Chile) is located on the Pacific coast of South America, bordering Peru to its north, Bolivia to the NE, Argentina to the east and the Drake Passage to the south (Fig. 1.1). With the Andes to the east, the Pacific Ocean to the west and from its extremely long N-S axis, extending across 39° of latitude, the climate is Chile is highly varied (CIA, 2017). In the south, the climate is mostly cool and damp, in the central region it is Mediterranean-like, and in the north it is mainly temperate-desert (KPMG, 2014). It is the 38<sup>th</sup> largest country globally with roughly 90% of its population located within the middle third of the country, around the capital Santiago (CIA, 2017). Chile has an established mining industry supported by a “well-functioning market economy and well-defined mining and environmental regulations” (KPMG, 2014). The most important metals to the Chilean economy are Cu and Au, for which it is the world’s number one and two producer, respectively (KPMG, 2014).

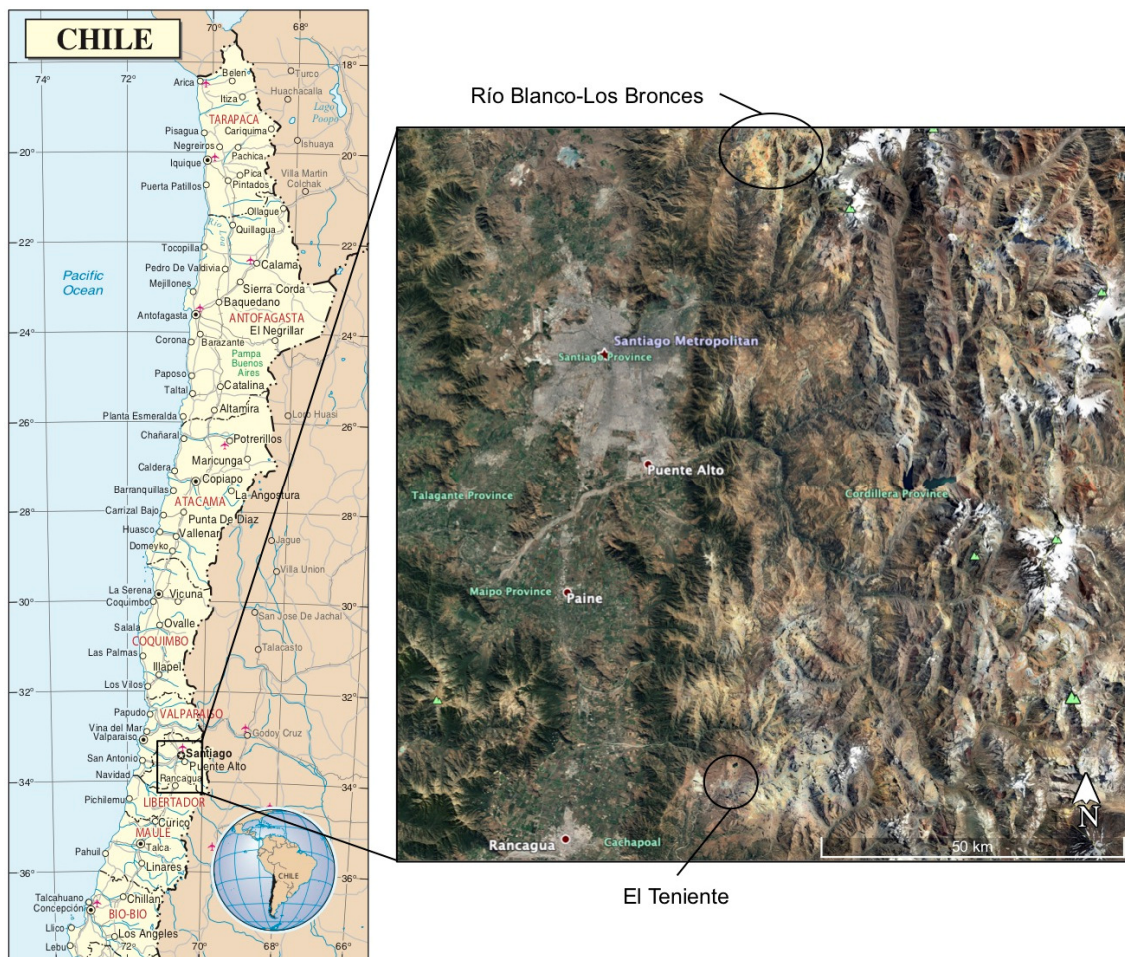


Fig. 1.1 Global map showing the location of Chile along the western edge of South America, bordering the Pacific Ocean (from Un.org, 2010). Inset shows the regional location of the Teniente porphyry Cu-Mo case study system which is roughly 75 to 80 km SSE of the capital Santiago (34°05'S, 70°21'W). The Río Blanco-Los Bronces porphyry-breccia cluster to the NE of Santiago is also shown. Image is from Google Earth (2020).

## 1.6 Porphyry Cu deposits of Chile and El Teniente

The Andes, which extends ~6,000 km from west-central Colombia to central Chile and



Fig. 1.2 Location of El Teniente in relation to other major porphyry Cu-Mo systems in the northern and central Chilean Cu districts. The rough location of the flat slab segment (28 to 33°), separating the Northern Volcanic Zone (NVZ) to the north from the Southern Volcanic Zone (SVZ) in the south is shown. Palaeocene and Early Cretaceous porphyry Cu deposits are omitted.

### 1.6.1 El Teniente

El Teniente is currently one of the world's most important sources of Cu and is the largest known resource of Mo (Sillitoe, 2010). It is situated on the western margin of the Andean Cordillera, within the central Chilean porphyry Cu belt; one of five metallogenic belts in the country (Vry et al., 2010; Spencer et al., 2015). El Teniente is considered to represent a classic example of a porphyry deposit where Cu-Mo

western-central Argentina, is one of the largest and most highly endowed metallogenic belts globally, containing world-class porphyry- and epithermal-type deposits (Irrarrazaval et al., 2010). Chile hosts six of largest porphyry Cu ( $\pm$ breccia) deposits in the world (Fig. 1.2): Río Blanco-Los Bronces, Chuquicamata, Escondida, Collahuasi, Andina, Radomiro Tomic, and El Teniente (Mining Technology, 2013). A number of these contain large, sometimes superimposed, Cu-Mo mineralised and barren magmatic-hydrothermal, and/or phreatomagmatic breccias. In general, such breccias are thought to have formed due to exsolution of high-temperature magmatic fluids from cooling plutons and subsequent interaction with external fluids, over a period of 1 to 3 million years (Warnaars et al., 1985; Skewes and Stern, 1994, 1995; Skewes et al., 2002; Stern et al., 2010). The Andes has considerable potential for future porphyry Cu exploration; it has been divided into twenty 'tracts'/regions where the geology is favourable for porphyry Cu formation (Cunningham et al., 2007).

mineralisation is concentrically zoned around a series of felsic-intermediate intrusives, albeit with a large volume of breccias also present (Skewes et al., 2002; Makshev et al., 2004; Cannell et al., 2005; Klemm et al., 2007; Spencer et al., 2015).

Breccias at El Teniente are typically peripheral to, or on the apices of the various felsic intrusions and often form what are called breccia complexes, which consist of multiple overlapping breccia facies (e.g., Vry et al., 2010; this study). The five main facies at El Teniente are igneous, biotite, anhydrite, tourmaline and rock flour (diatreme) breccias. Tourmaline-cemented breccias were some of the last breccias to form and are variably mineralised across the deposit and district. They are characterised by tourmaline being a major component of the cement, which is typically dark blue-black.

The largest breccia at El Teniente is the Braden Diatreme which is situated in the centre of the deposit, and was one of the last features to form (Makshev et al., 2004). It has been classified as a diatreme having a phreatomagmatic origin (e.g., Sillitoe, 1985; Makshev et al., 2004; Cannell et al., 2007), based on its spatial extent and facies characteristics resembling those of diatremes observed elsewhere. It is surrounded by the Cu-Mo-mineralised 'Marginal Breccia(s)' (Cannell et al., 2005, 2007). Being largely sub-economic, it has been relatively little studied and is therefore poorly understood.

Satellite porphyry-breccias around El Teniente include Diablo, located a few hundred metres SW of the Braden Diatreme, which is a series of tourmaline-anhydrite-( $\pm$ Cu-Mo sulphide) cemented breccias with particularly high-grades (Floody R, 2017., personal communication). In addition to this is the La Huifa prospect which is a recent discovery located 2 km north of the El Teniente mine. This is being progressively recognised as a mineralised cluster of breccia orebodies and associated porphyries (Codelco, 2015).

El Teniente deposit was selected for this study because it is a geologically young system which has been little affected by supergene alteration, exhumation or erosion and is therefore well preserved. The tectonic setting, regional geology, and magmatic-hydrothermal evolution of El Teniente have also been the focus of a large number of studies over the last 90 years, internally by Codelco División El Teniente geologists and then in at least four PhD studies, and a number of unpublished and published academic works (e.g., Lindgren and Bastin, 1922; Howell and Molloy, 1960; Camus, 1975; Skewes et al., 2002, 2005; Cannell et al., 2005, 2007; Skewes and Stern, 2007; Rabbia et al., 2009; Astudillo et al., 2010; Muñoz et al., 2012; Vry et al., 2010; Spencer et al., 2015; Skewes et al., 2020). These have generated a comprehensive dataset for lithological characteristics (e.g., Cannell, 2004; Cannell et al., 2005; Stern et al., 2010), fluid inclusions (Cannell, 2004; Klemm et al., 2006, 2007; Vry et al., 2010) and the ages of magmatic and hydrothermal events (Cannell, 2004; Makshev et al., 2004; Spencer et al., 2015).

## **1.7 Research aims and objectives**

The primary aims of this project were to expand the understanding of the 3D nature (vertical and horizontal zonation of mineralisation) and formation mechanisms of the Braden Diatreme and other breccia bodies at El Teniente in order to develop an architectural-exploration model. An important aspect of the genetic studies was to explore the sometimes close spatial relationship between Mo-Cu mineralisation, and juvenile, apparently magmatic spatters in the Braden Diatreme breccias, which resemble the underlying, and potentially brecciation-causative, 'late' dacite porphyry intrusion. An additional aim was to assess the viability of using tourmaline as a geochemical fertility indicator for porphyry-breccias. A prerequisite for this was to distinguish Cu-Mo-mineralised from 'barren' (weakly mineralised) breccias by undertaking detailed textural descriptions and paragenetic studies on tourmaline-bearing breccias. It was particularly important to determine the relative timing of tourmaline crystallisation and Cu-Mo mineralisation, i.e. whether these were contemporaneous with brecciation (same fluids) or the breccias provided a conduit for later fluids and open-space for tourmaline precipitation and mineralisation.

### **1.7.1 Research hypotheses**

The following hypotheses were tested:

1. The Braden and other breccias at El Teniente are vertically and horizontally zoned in terms of structures, clast characteristics (e.g., rounding), and alteration and mineralisation, which can be used to determine the level of current exposure within the system, and therefore whether Cu-Mo mineralisation may be present at depth, or has been eroded off.
2. The Braden Diatreme is phreatomagmatic (formed by interaction of magmas with meteoric-derived waters at depth (as suggested by Sillitoe, 1985), whereas some breccias within the Braden (Braden Tourmaline and Braden Sulphide) are replacive or alteration overprints (Braden Chlorite Breccia) and the Marginal, Diablo and La Huifa breccias are magmatic-hydrothermal intrusion ( $\pm$ collapse) breccias, which formed from explosive brecciation initiated through volatile-rich porphyry magmas interacting with relatively oxidising groundwaters, causing the rapid precipitation of an early tourmaline-quartz cement.
3. The 'late' dacite porphyry, present as a stock below the Braden Diatreme (and as late concentric dykes around the Braden), which is also observed as vermiform, apparently once 'plastic' clasts in the Braden Sericite ('rock flour') Breccia, was the source of the fluids which caused brecciation, alteration and Cu-Mo mineralisation. Explosive exsolution of volatiles from the porphyry magmas initiated brecciation (e.g., Cashman and Scheu, 2015), as opposed to brecciation being phreatomagmatic (e.g., White and Valentine, 2016).

4. Poorly- and well-mineralised (Cu-Mo) tourmaline breccias in the Teniente district show differences in tourmaline composition, which may provide an exploration indicator.
5. The compositions of hydrothermal tourmaline from different depths in the variably mineralised Diablo tourmaline breccias reflect upward changes in fluid characteristics.
6. The composition of tourmaline in the Diablo Breccias was influenced by interaction with wall rocks of the Teniente Mafic Complex (volcanoplutonic complex of basalts, diabase, andesite and gabbro).

## 1.8 Thesis structure

The thesis is split into seven chapters which includes the following:

**Chapter 1:** Introduction - provides the rationale for the thesis, a basic introduction to the case study, and the research aims and objectives, and hypotheses to test.

**Chapter 2:** Literature review - on porphyry Cu deposits, breccias and the Teniente porphyry Cu-Mo deposit.

**Chapter 3:** Methodologies - discusses the various techniques used to address the hypotheses in this investigation. This includes details of the field and sampling campaigns, sample preparation, analytical techniques and QA/QC procedures.

**Chapter 4:** Results - presents the observational and measured data from this investigation, including textural characteristics, paragenetic relations and qualitative and quantitative tourmaline data.

**Chapter 5:** Discussion - considers whether the architecture and mode of formation of breccias at El Teniente, together with the chemical composition of hydrothermal tourmaline, can be used as exploration indicators, i.e. to predict the extent and location of mineralisation.

**Chapter 6:** Conclusions - provides a summary of the main outcomes of the work and recommendations for future studies.

**Chapter 7:** Future work - a brief list of recommendations for additional work to further this study.

### References.

**Appendices:** A series of appendices and referrals to electronic appendices are included as follows: i) drill hole locations and intercepts studied (this document); ii) sample descriptions (Excel); iii) QEMSCAN<sup>®</sup> data (Excel); iv) XRD data (Excel); v) Tourmaline EPMA and LA-ICP-MS (Excel); vi) Ti-in-Quartz EPMA and LA-ICP-MS (Excel) and vii) Whole-rock XRF, ICP-MS and ICP-OES data (Excel).

## 1.9 Terminology and abbreviations

Mineral abbreviations within this report follow the guidelines set out by Whitney and Evans (2010). Some of the most common minerals encountered at El Teniente are shown in Table 1.2. General abbreviations and definitions relating to this study are also provided below.

Barren	Currently not, and have never been economic to mine
CL	Cathodoluminescence
Codelco	Corporación Nacional del Cobre de Chile
DDH	Diamond Drill Hole
EDS	Energy Dispersive Spectroscopy
EPMA	Electron probe micro-analysis
Fragmentation	A process where 'a continuous liquid or solid phase is transformed to a continuous gas phase with suspended particles (liquid and/or solid)' (Cashman and Scheu, 2015)
Juvenile material	Clasts within the breccia derived from the underlying parental magma. They have distinctive 'wispy', 'cusped', 'vermiform' or 'spatter' shapes
LA-ICP-MS	Laser Ablation-Inductively Coupled Plasma-Mass Spectrometry
Ma	Millions of years before present
MASH	Melting, Assimilation, Storage and Homogenisation zone
MASL	Metres Above Sea Level
MORB	Mid-Ocean Ridge Basalt, primitive melts
PPL	Plane Polarised Light microscopy
QEMSCAN <sup>®</sup>	Quantitative Evaluation of Minerals by Automated Scanning Electron Microscope
RL	Reflected Light microscopy
SEM	Scanning Electron Microscope
SQD	Sewell Quartz Diorite
TMC	Teniente Mafic Complex
TFZ	Teniente Fault Zone
XPL	Cross polarised light microscopy

Table 1.2 Mineral abbreviations within this report follow the guidelines set out by Whitney and Evans (2010) except quartz, which will be abbreviated as 'qtz'.

Abbreviation	Mineral name or group	Abbreviation	Mineral name or group
Ab	Albite	Ill	Illite
Act	Actinolite	Kfs	K-feldspar
Ank	Ankerite	Mag	Magnetite
Ap	Apatite	Mol	Molybdenite
Bt	Biotite	Ms	Muscovite
Bn	Bornite	Opa	Opaque mineral
Cal	Calcite	Pl	Plagioclase
Ccp	Chalcopyrite	Py	Pyrite
Chl	Chlorite	Qtz	Quartz
Drv	Dravite	Rt	Rutile
Ep	Epidote	Ser	Sericite
Gth	Goethite	Srl	Schorl
Gn	Galena	Sp	Sphalerite
Gp	Gypsum	Tur	Tourmaline
Hbl	Hornblende	Ttn	Titanite

## 2 Literature review

Prior to describing the geology of the Teniente district and deposit, a brief overview is given of porphyry-breccia-type Cu deposits including their formation, brecciation processes, breccia classification and alteration and mineralisation.

### 2.1 Porphyry Cu deposits

There have been numerous publications since the mid-late 20<sup>th</sup> Century describing the magmatic-hydrothermal processes that form porphyry Cu-Mo and Cu-Au deposits (e.g., Lowell and Guilbert, 1970; Corbett and Leach, 1998; Cooke et al., 2005; Seedorff et al., 2005; Sillitoe, 2010; Richards, 2013). Early literature mainly attempted to develop genetic models for porphyry-epithermal systems, and to advance geochemical and geophysical exploration techniques (e.g., Lovering et al., 1948, 1950; Almond and Morris, 1951; Clarke, 1953; Moxham et al., 1965; Davis and Guilbert, 1973; Abrams et al., 1983). Recent developments in mineral exploration, building upon these earlier studies are summarised in several papers such as Thompson et al. (1999), Behn et al. (2001), Berger et al. (2003), Cameron et al. (2005), Kelley et al. (2009), Chang et al. (2011), Bouzari et al. (2011), Wilkinson et al. (2017) and Cooke et al. (2020).

Porphyry-type systems are described as “large volumes (10–>100 km<sup>3</sup>) of hydrothermally altered rock centered on porphyry copper stocks that may also contain skarn, carbonate-replacement, sediment-hosted, and high- and intermediate-sulfidation epithermal base and precious metal mineralization” (Sillitoe, 2010). These large systems and their underlying plutons have magmatic-hydrothermal histories spanning millions of years, but ore formation typically only occurred during one or more, commonly multiple, short-lived events with durations of a few hundred thousand years or less (Seedorff et al., 2005; Sillitoe, 2010; Richards, 2016). Porphyry Cu-type deposits can range in size from tens of millions to billions of tonnes but typically contain hundreds of millions of tonnes of low-grade (0.5 to 1.5% Cu) ore (Sinclair, 2007; Sillitoe, 2010; Richards, 2016). Cu is predominantly concentrated within sulphide minerals that are either disseminated or veinlet-hosted and in some cases breccia bodies may host significant ore. Mo, Au and REE may also be important by-products.

Economic Cu-Mo porphyries have a strong association with relatively oxidised and water-, Cu-Mo- and sulphur-rich magmas (Ballard et al., 2002; Sillitoe, 2010). The igneous intrusions related to Cu porphyry-type systems are said to be “exclusively of I-type and magnetite-series affiliation (Ishihara, 1981), typically metaluminous and medium-K calc-alkaline”, but on occasions may fall into the high-K calc-alkaline (shoshonitic) or alkaline fields (Sillitoe, 2010). The source magma types have been constrained to calc-alkaline and adakitic compositions (Cline and Bodnar, 1991; Richards, 2003).

Although a connection between adakitic magmatism and giant porphyry deposits in Chile has been demonstrated in studies by Oyarzun et al. (2001), Reich et al. (2003), Wang et al. (2006) and Chiaradia et al. (2012), the formation of adakitic magmas remains debatable with little direct evidence for slab melting (Richards and Kerrich, 2007; Richards, 2011a, b; Sun et al., 2014). High Sr/Y values, often used to define adakites, can be produced by other mechanisms including the fractionation of amphibole and/or garnet, and delayed plagioclase crystallisation, in especially high H<sub>2</sub>O but otherwise normal calc-alkaline magmas (Chiaradia et al., 2012; Richards, 2011b; Wilkinson, 2013). Consequently considerable debate remains around the formation processes of giant ore deposits; whether they have a unique mode of formation, or just an “optimum coincidence of common geological processes” (Richards, 2013). Nonetheless, at some point these magmas are transformed, and become capable of generating porphyry ore deposits (Wilkinson, 2013).

### **2.1.1 Global distribution, tectonic settings and formation**

Porphyry-epithermal systems display a strong spatial association with tectonic plate boundaries forming orogen-parallel metallogenic belts on the Earth's surface up to hundreds of kilometres long, such as the Andes in South America (Corbett and Leach, 1998; Richards and Tosdal, 2001; Seedorff et al., 2005; Sillitoe, 2010). At a district scale, porphyry Cu systems tend to occur as clusters, in equidimensional groupings, or in alignments oriented either parallel or transverse to magmatic arcs that may be 5 and 30 km across and in length, respectively (Sillitoe, 2010). They are genetically and spatially associated with larger granitic intrusions (Blundy et al., 2015; Richards, 2016) and especially with high-level cupolas and dyke complexes.

The young geological ages of many porphyry deposits (e.g., Fig. 2.1) is largely a result of their shallow formation depths, older deposits being mostly removed by erosion (Berger et al., 2008). Over half of the world's twenty-five largest known porphyry deposits, in terms of contained metals, are therefore Palaeocene-Eocene, Eocene-Oligocene and mid Miocene-Pliocene in age (Cooke et al., 2005). Fifteen of these are associated with tectonic regions where “low-angle subduction of aseismic ridges, seamount chains, or oceanic plateaus have been synchronous with ore formation, resulting in crustal thickening, rapid uplift, and exhumation” (Cooke et al., 2005).

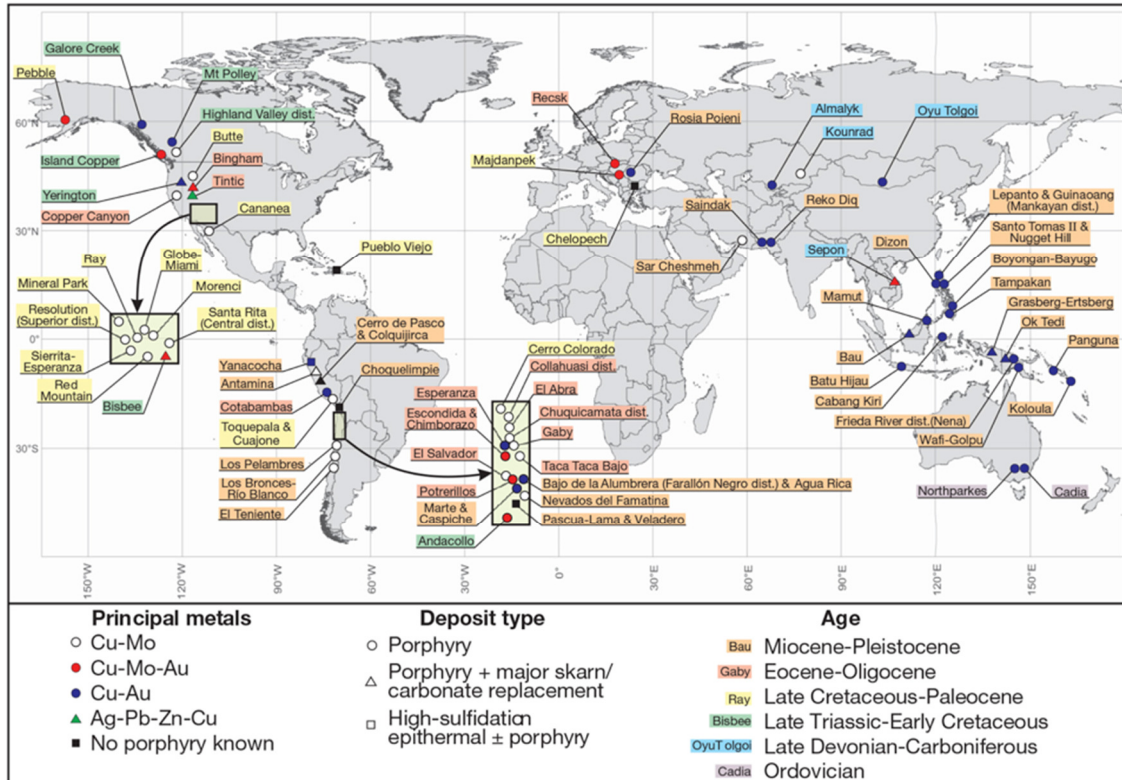


Fig. 2.1 Global map of porphyry Cu systems showing principal deposit type(s), contained metals, and age. The majority of known worldwide deposits are predominantly from the Mesozoic and Cenozoic eras. From Sillitoe (2010).

Plate tectonics and slab dynamics (e.g., trench advance or rollback, degree of obliquity and regional stress fields) within subduction-related environments strongly influence the development of porphyry-type systems (e.g., Kerrich et al., 2000; Richards and Tosdal, 2001; Cooke et al., 2005; Rosenbaum et al., 2005; Sillitoe, 1985, 2010; Bertrand et al., 2014). Compressional regimes with rapid uplift and exhumation, 'alongside reactivation of basement structures (and overriding plate sutures), coupled with a hiatus in volcanism and associated crustal thickening are all favourable conditions' (Cooke et al., 2005). Restricted magma ascent in compressional conditions also increases the chance of developing large shallow magma chambers and promoting fractionation whilst limiting volcanism and fluid escape (Sillitoe, 1985). If magma ascent continued to the palaeosurface to produce active volcanism then the ore-forming potential of the system may be lost (e.g., Ernst, 2000).

As plate subduction proceeds, the down-going oceanic crust, and associated volatile/metal-rich sediments and/or pre-existing features (e.g., Richards, 2003; Cooke et al., 2005), dehydrate and release volatiles (mainly H<sub>2</sub>O and CO<sub>2</sub>) into the overlying mantle wedge (Wilkinson, 2013). This will likely initiate partial melting, and, as the fluids may be largely seawater-derived, the production of relatively oxidised melts which are capable of transporting Cu, Au and sulphur into the upper crust (Hedenquist

and Lowenstern, 1994; Sillitoe, 1997; Cooke et al., 2005). This process was invoked by Skewes et al. (2002) for the formation of the Teniente Cu-Mo porphyry deposit, where, based on mantle-like Pb-Os isotope ratios, magmas were derived from and formed “in the sub-Andean mantle contaminated by the subduction of a small amount of pelagic and terrigenous sediment, and continental crust tectonically eroded off the continental margin”.

Buoyancy contrasts between the newly formed, relatively oxidising primitive melts in the mantle wedge and surrounding material cause the metal- and volatile-rich melts to rise into the lithosphere along deep-seated broad deformation zones (e.g., Richards and Tosdal, 2001). At the mantle lithosphere-lower crust boundary, further upward migration of the once primitive melts ceases due to neutral buoyancy and/or because compressive stresses in the upper plate may close structures (Richards, 2003). This region is termed the MASH zone, which stands for Melting, Assimilation, Storage and Homogenisation (Richards, 2003; Gil-Rodríguez, 2010; Bertrand et al., 2014). Within this, the magmas become progressively enriched in H<sub>2</sub>O and S along with metals (Richards, 2003). Once sufficiently buoyant, these rise through the crust and pond to form mid- to high-level (4 to 10 km) multiphase crustal magma chambers and both mineralised and barren porphyry apophyses (e.g., Wilkinson, 2013). The rate of ascent, and at which point a large magma chamber will begin to form, is thought to be governed by the degree of volatile degassing and fractionation, and as such the viscosity of the magma, during ascent (Annen et al., 2006).

Studies of large porphyry Cu deposits indicate that through a variety of processes, magma chambers evolve over protracted periods of >100,000 to several million years (e.g., Maksaev et al., 2004; Sillitoe, 2010). These processes include fractionation, assimilation, thermal stratification and convection, bubble formation, volatile transfer and concentration in the upper parts of the chamber (Stern et al., 2010), melt-volatile exsolution and magma mixing/chamber recharge by mantle-derived mafic magmas (Maughan et al., 2002; Richards, 2003; Wilkinson, 2013; Richards, 2016).

Deep-seated, lower-crustal recharge for example has been proposed as a factor for the development of El Teniente because the deposit itself contains more metal and sulphur than can be derived from a single isolated magma chamber (Stern et al., 2010). These episodic influxes of hotter mafic intrusions into the magma chamber not only cause volatile enrichment but will also induce pressure/temperature fluctuations and buoyancy contrasts (Sparks and Marshall, 1986; Hattori and Keith, 2001; Edmonds, 2008; Blundy et al., 2015 and references therein; Tapster et al., 2016).

The solubility of Cu and Mo in melts and fluids, and their relative partitioning between the melt, silicates, sulphides and magmatic volatile phases (MVPs) during melt ascent will affect the mineralising potential of a developing porphyry system (e.g., Candela and Holland, 1984; Štemprok, 1990; O'Neill and Eggins, 2002). Maximising metal contents of the resultant aqueous phase is achieved through the parental magmas being water-rich (~4 wt.%) and relatively oxidised (Sillitoe, 2010). Fluid exsolution from the melt and formation of a MVP takes place during first- and second-type boiling (Candela, 1989). First-type boiling is the result of upward movement and depressurisation of the magma or fracturing (Candela, 1989), whilst second-type boiling is initiated from the melt crystallising causing volatile species to reach saturation and escape (Vigneresse et al., 2019). Due to high fluid-melt partition coefficients, most S and ore-forming metals will partition into the MVP (Vigneresse et al., 2019).

The main components of the MVP, which are typically liquid or in the gaseous phase under surface conditions, are HCl, H<sub>2</sub>S, SO<sub>2</sub>, CO<sub>2</sub> and H<sub>2</sub>O (Heinrich et al., 2004; Heinrich, 2005). As the MVP migrates upward and outwards, depressurisation causes it to undergo phase separation into coexisting hypersaline brine and vapours containing Cl and S ligands (Richards and Tosdal, 2001; Wilkinson, 2013). These gradually cool, react with wall rocks and may mix with groundwaters, leading to the precipitation of metal sulphides, mostly within veins or disseminations in the parent intrusion and surrounding wall rocks (Wilkinson, 2013; Richards, 2016).

Richards (2016) summarised the recent research which suggests that porphyry-style ore bodies 'may form by a combination of different processes during specific fluid-release events such as Cu-rich brines mixing with S-rich gases to precipitate Cu-sulphides (Blundy et al., 2015); precipitation of Cu-sulphides through SO<sub>2</sub> reacting with plagioclase (Henley et al., 2015); vapour bubbles with attached sulphide melt globules floating to the top of magma chambers (Mungall et al., 2015); and Cu-rich sulphide liquids being left deep in the crust (Lee et al., 2012; Wilkinson, 2013)'.

It is clear that none of these individual properties and mechanisms are unique to the formation of giant porphyry orebodies, instead it is believed that a favourable combination of multiple factors from crustal to deposit scale result in the formation of giant deposits (Richards, 2016). Although the total metal endowment may relate to large-scale tectonic processes, the ore grades relate 'mainly to the hypogene processes at the trap site, the structure (permeability architecture) of the district (leaky versus focused hydrothermal fluid-flow regimes)', and therefore even with the most favourable geodynamic processes, and crustal architecture, without efficient mineralising processes, systems may only produce giant low-grade geochemical anomalies (Cooke et al., 2005).

## 2.1.2 Porphyry-style mineralisation and alteration

**Cu-Mo-Au mineralisation** - Characteristic alteration-mineralisation shells begin to form as fluids progressively circulate throughout surrounding rock units (e.g., Lowell and Guilbert, 1970). Cu-Mo mineralisation can be significantly controlled by lithologies such as reduced shale or large mafic complexes where these Fe-rich units may not only provide a physical barrier but also important chemical traps capable of initiating Cu-Mo precipitation (Sillitoe, 2010).

Porphyry-style Cu mineralisation usually occurs within large-scale low-grade (<1% Cu) stockworks, and as disseminations throughout the deposit (Bogie et al., 2005; Sillitoe, 2000, 2010). Veins often host the majority of the ore (Seedorff et al., 2005) and have therefore received the greatest attention (e.g., Meyer, 1965; Gustafson and Quiroga, 1995; Pollard and Taylor, 2002; Cannell et al., 2005). The most widely cited and used vein classification scheme was proposed by Gustafson and Hunt (1975), based on their detailed work at El Salvador. Veins are classified using descriptive criteria including mineralogy, texture and nature of the alteration envelopes. Sillitoe (2010) divided vein sequences into the three groups below largely based on Gustafson and Hunt (1975). Repetitions of groups 1 and 2 veinlets may occur where a time gap between porphyry phases are significantly large, and repeated veinlet reopening during subsequent veining events may further complicate classification.

1. Early, quartz- and sulphide-free veinlets containing one or more of actinolite, magnetite (M-type), (early) biotite (EB-type), and K-feldspar, typically lack alteration selvages. These veinlets are mostly emplaced during potassic alteration.
2. Sulphide-bearing, granular quartz-dominated veinlets with either narrow or no readily recognisable alteration selvages (A- and B-types). A-type veinlets are abundant in many deposits, composed of granular quartz-copper sulphides-K-feldspar-anhydrite±biotite±magnetite, and range from stockworks to subparallel, sheeted arrays. The earliest A-type veinlets may be sinuous and have nonmatching margins, features attributed to formation under high-temperature, ductile conditions, whereas later veinlets are more planar (Sillitoe, 2010). B-type veins are frequently planar and composed of quartz-molybdenite ±chalcopyrite±pyrite with central sutures observed (Fig. 2.2c). They often cross-cut A-type veinlets and are largely absent from Au-rich porphyry Cu stockworks. Given both A- and B-type are intimately associated with the core zones of porphyry Cu deposits, background alteration is mainly potassic.
3. Late, crystalline quartz-sulphide veins and veinlets with prominent, feldspar-destructive alteration selvages (including D-type). This category also includes uncommon, but economically important coarse chalcopyrite±bornite±chalcocite veinlets at some deposits such as Grasberg (Pollard and Taylor, 2002). These veins accompany the chlorite-sericite, sericitic, and deep advanced argillic overprints.

A strong correlation exists between quartz veinlet intensity and metal contents; with considerable amounts of Cu contained in quartz-dominated group 2 (A and B) veinlets, and most molybdenite in many porphyry Cu-Mo deposits is found in B-type veinlets (Sillitoe, 2010). Whether the Cu-sulphides are “coprecipitated with veinlet quartz or, as generally seems to be the case, introduced paragenetically later” still remains enigmatic (Sillitoe, 2010) although recent studies (e.g., Driesner and Heinrich, 2019) support the latter.

**Alteration** - Depending on levels of erosion, porphyry-type deposits have large (up to 10 km wide) hydrothermal alteration halos (Fig. 2.2), displaying characteristic mineralogical and chemical zoning patterns (Lowell and Guilbert, 1970). The alteration-mineralisation in porphyry Cu deposits is described by Sillitoe (2010) as being “zoned upward from barren, early sodic-calcic through potentially ore-grade potassic, chlorite-sericite, and sericitic, to advanced argillic, the last of these constituting the lithocaps, which may be >1 km in thickness if unaffected by significant erosion”. These alteration facies provide useful exploration targets and vectors towards economic mineralisation (Seedorff et al., 2005; Sillitoe, 2010; Wilkinson et al., 2017). Often, to the frustration of mineral exploration companies, these magmatic-hydrothermally-derived porphyry alteration assemblages are present in both well-mineralised and ‘barren’ hydrothermal systems, and similar mineralogical assemblages can be produced by completely unrelated processes such as regional metamorphism (Wilkinson et al., 2015). For brevity, five of the most common alteration assemblages are described below.

1. Potassic alteration is pervasive in the ore zone of chalcopyrite ± bornite, and is the result of metasomatic addition of potassium (Sillitoe, 2010). Characteristic gangue minerals include K-feldspar, magnetite, secondary biotite, quartz, and rutile among others (Taylor, 2009; Sillitoe, 2010).
2. Propylitic alteration is ubiquitous and extensively developed distal to, and for up to seven km from porphyry deposits, mostly at deeper levels (Sillitoe, 2010). It is primarily comprised of an assemblage of epidote, chlorite and calcite with other minerals including iron oxides, apatite and sericite (Beane and Bodnar, 1995; Taylor, 2009).
3. Phyllic alteration assemblages are characterised by sericite-quartz and pyrite that typically forms over a wide range of temperatures. It is frequently formed late in the development of the hydrothermal system and often overprints earlier potassic and chlorite-sericite alteration zones (Parry et al., 2002). Hand specimens appear bleached and frequently lack texture.
4. Sodic-calcic alteration is typically deep below porphyry Cu mineralisation and has a characteristic mineral assemblage of albite/oligoclase, actinolite, and magnetite with lesser diopside, epidote and garnet. This zone is normally weakly-mineralised, but may be locally ore-bearing (Sillitoe, 2010).
5. Argillic to advanced argillic alteration is mainly found in the lithocap

environment, where the latter may overprint the sericitic alteration within the upper parts of porphyry Cu deposits (Sillitoe, 2010). Lithological units with low acid buffering capacities like felsic-intrusives are preferentially affected by advanced argillic alteration opposed to high acid-buffering units like mafic igneous rocks (Sillitoe, 2010).

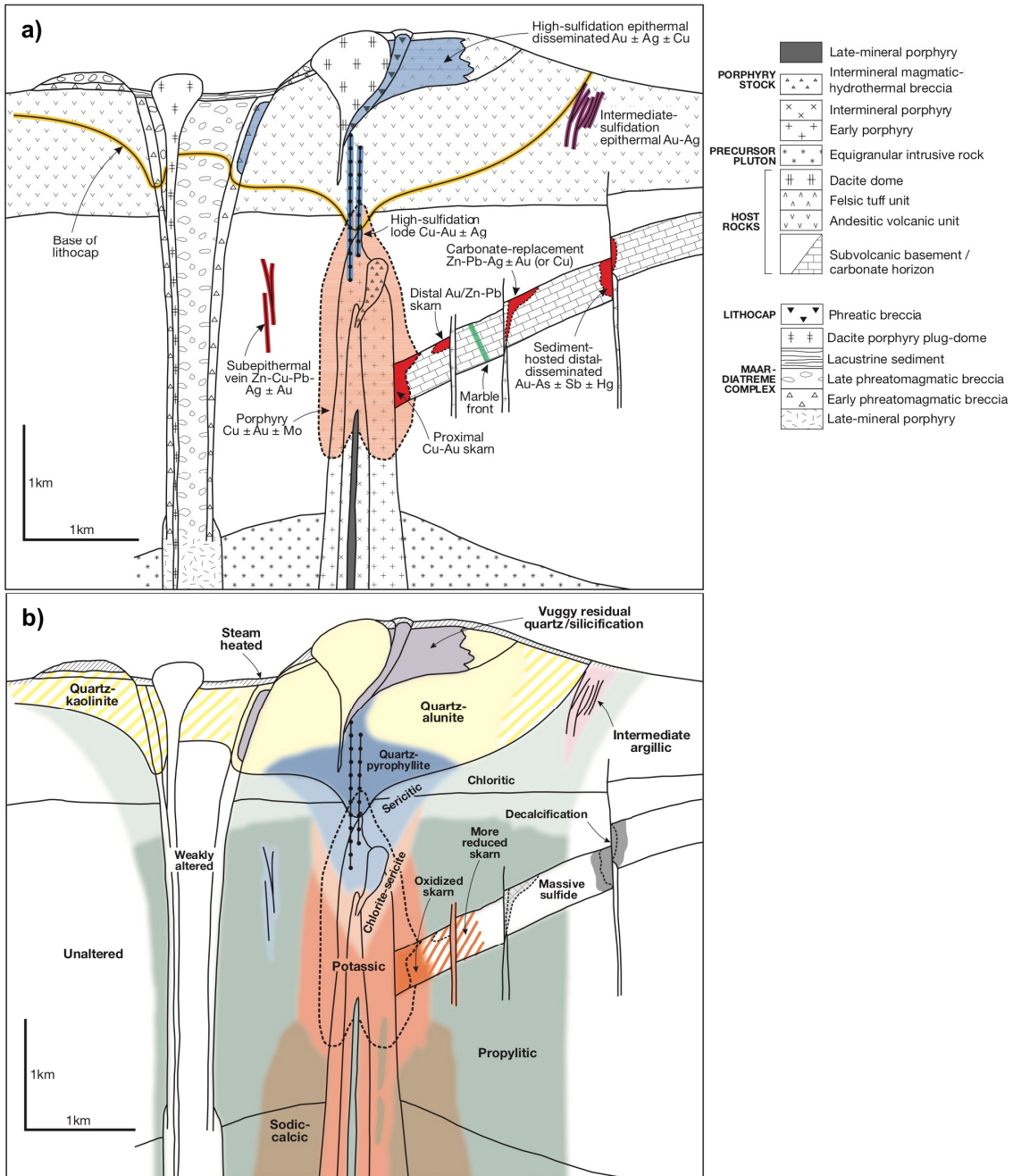


Fig. 2.2 Schematics from Sillitoe (2010) of telescoped porphyry Cu systems highlighting mineralisation and alteration relationships described by Lowell and Guilbert (1970): **a)** Anatomy of telescoped porphyry Cu system, showing the spatial relationship of a multiphase porphyry stock to the surrounding host rocks. A centrally located porphyry Cu±Au deposit and lithocap environment are shown, as is the potential for proximal and distal skarns. The three main types of breccias are shown; magmatic-hydrothermal, phreatomagmatic and phreatic. Magmatic-hydrothermal breccias form at relatively great depth and do not reach the palaeosurface; **b)** Generalised alteration-mineralisation zoning pattern based on the geological and deposit template shown in a.

## 2.2 Breccia description and classification

Breccias can be described as having rounded to angular fragments within a matrix of locally derived rock material, or, a cement comprised of hydrothermal minerals variably infilling cavities (Taylor and Pollard, 1993; Taylor, 2003a, b). This study used the methodology for describing and classifying breccias developed by Woodcock and Mort (2008), where: matrix is defined as ‘any fine-grained clastic particulate material produced by local fragmentation of larger particles or through the introduction of more exotic sediment’. Cement is defined as “crystalline material grown in place, either as infill of void space or as a replacement of clasts or matrix”. Two main types of cement exist: minerals crystallised from a magma which produce a crystalline igneous rock (e.g., igneous breccias) or minerals precipitated from aqueous fluids (water and/ or vapours).

Breccias were classified based on the relative proportions of the three main breccia components: clasts, matrix (small clasts) and infill, and the discrimination of crackle (<10° average rotation), mosaic (10 to 20°) and chaotic (>20° rotation) (Fig. 2.3). Worth noting is that although in 2D this approach is simple, in 3D it is complicated by the possibility of clast movement in/out of the plane of measurement.

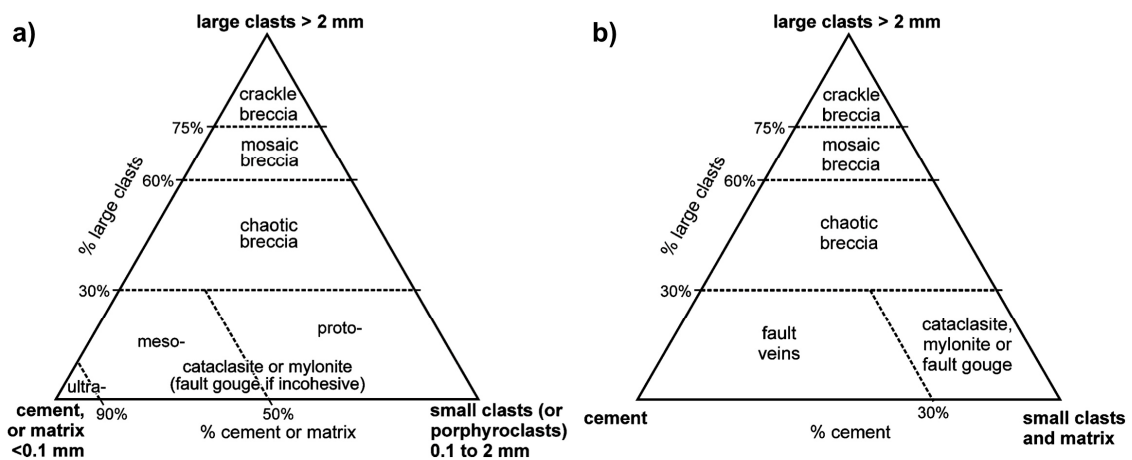


Fig. 2.3 Ternary diagrams (a, b) from Woodcock and Mort (2008) showing the two alternative methods of breccia classification. The 2 mm limit is in agreement with sedimentology usage and with an earlier suggestion by Laznicka (1988): **a)** Proposed classification schemes of breccias where cataclasites and mylonites are subdivided according to % matrix; **b)** Ternary diagram combining matrix with small clasts rather than cement allowing breccias with crystalline cement to be distinguished from fine-grained matrix. The 30% large clasts line was arbitrarily chosen and is open to debate.

## 2.3 Porphyry-breccias

Breccias are common features of porphyry Cu-Mo-Au deposits worldwide (e.g., Farmin, 1934; Gates, 1959; Johnston and Lowell, 1961; Kents, 1961; Mills, 1972; Sillitoe, 1973; Mitcham, 1974; Landtwing et al., 2002; Ross et al., 2002; Frikken et al., 2005; Johnson and Thompson, 2006; Sillitoe, 2010; Dill et al., 2012; Simmons et al., 2013; Byrne and Tosdal, 2014). Owing to their high ore potential, breccias have long attracted the interest of mining companies, and swarms or clusters of intrusive breccias have been taken to indicate a buried pluton which may potentially host a large porphyry system (e.g., Perry, 1961; Simons, 1964; Gilmour, 1977).

They are particularly frequent in the Miocene central porphyry Cu belt of Chile (e.g., Sillitoe and Sawkins, 1971; Sillitoe, 1985; Skewes and Stern, 1994, 1995; Frikken et al., 2005) and in some instances, they constitute the highest-grade parts of orebodies. For example Cu-Mo mineralisation at Los Sulfatos (Río Blanco-Los Bronces district) is related to 'a large, multiphase, igneous to magmatic-hydrothermal breccia complex, and at least two separate centers of porphyry Cu-style mineralisation extending over an area of  $\sim 3 \times 1.5$  km' (Irrarrazaval et al., 2010). Overall, however, "<50% of breccias in any cluster of pipes are ore bearing, a characteristic that has often frustrated the explorationist" (Sillitoe, 1985).

### 2.3.1 Formation

A range of mechanisms have been proposed to generate the variety of breccias possible within porphyry environments, which are largely applicable to breccias elsewhere. Perhaps some of the most influential modeling papers that discussed fragmentation, transport and consolidation processes include Norton and Cathles (1973), McCallum (1985), Burnham (1985) and Halls (1994). All mechanisms must be capable of producing substantial void space across a relatively short geological time period. Individual mechanisms may be mutually exclusive to varying degrees, and brecciation occurs over short time intervals. The following summarises the main processes involved in brecciation.

- Chemical reactions due to localised dissolution and upward removal of rock material by fluids released from cooling magma followed by collapse (e.g., Sillitoe, 1985).
- Downward movement of magma by either shrinkage, withdrawal, or decompression (e.g., Burnham, 1985), causing mechanical disruption of wall rocks. Withdrawal of magma is however considered to be unlikely (Sillitoe, 1985), although it can pre-weaken areas making them more susceptible/better for brecciation through the generation of ring faults or fractured zones.
- The explosive release of magmatic-hydrothermal fluids from high-level, water-

rich magma chambers during second boiling will lead to the accumulation of fluids and build-up of fluid pressure around the carapace (e.g., Burnham, 1985). Once fluid pressure exceeds lithostatic pressure hydraulic fracturing will occur (Sillitoe, 1985; Tosdal and Richards, 2001). Resulting rapid fluid discharge and decompression will cause expansion and upwelling, which are thought to be capable of reopening and further widening existing fractures and faults, through hydraulic fracturing of host rocks (e.g., Sillitoe, 1985; Halls, 1994).

- Local or remote seismic activity (Tosdal and Richards, 2001).
- Rupturing of a pressure seal at the brittle-ductile transition (Fournier, 1999).
- Phreatomagmatism involving external waters, or magmatic fragmentation through the violent exsolution of contained volatile phases (White and Valentine, 2016).
- An intriguing possibility for the formation of breccia pips, suggested by Richards (2011b), is that “the cylindrical shapes of many porphyry stocks may have arisen first as breccia pipes or diatremes with associated high permeability fracture zones later bored out by rapidly escaping volatiles, only later to be back-filled with porphyritic magma”.

### **2.3.2 Porphyry-breccia classification**

A clear practical classification for porphyry-ore-related breccias, in the context of a broad genetic framework, was not presented until the review paper by Sillitoe (1985), which remains one of the most logical and internally consistent schemes available. This scheme was somewhat updated in Sillitoe (2010), shown in Table 2.1. It was later complimented by Corbett and Leach (1995, 1998), who in agreement with Sillitoe (1985), found magmatic-hydrothermal breccias generally form at relatively deep levels and need not vent to the surface, whereas phreatomagmatic and phreatic breccias are higher in the porphyry system and “may vent as diatreme/maar volcanoes or remain as milled matrix fluidized breccias, commonly as dikes which exploit pre-existing structures at varying depths” (Corbett and Leach, 1998). Porphyry-breccias can be further classified on the basis of the composition and abundance of the cement/matrix, size and shape of clasts, clast cement/matrix ratio and position in the system.

Table 2.1 Three principal types of breccias found in porphyry systems, from Sillitoe (2010), which largely follows the earlier proposed scheme in Sillitoe (1985). Breccias are classified by formation process, relative timing and their position in the mineralising system. Phreatic breccias have been further subdivided into porphyry and epithermal varieties.

Type	Position in system and form	Relative timing and alteration	Clast and matrix/cement features	Clast/matrix	Cu phases/ economic potential
Magmatic-hydrothermal	Within and around porphyry Cu deposits.	Typical intermineral, potassic±chlorite-sericite.	Commonly monomict and polymictic, angular-subrounded clasts. Quartz, magnetite, biotite, sulphides, anhydrite, igneous, tourmaline, sulphide cement.	Clast- or cement-supported.	May contain high-grade ore, mostly chalcopyrite or bornite.
Phreatic (porphyry Cu level)	Within and around porphyry Cu deposits.	Late. Sericitic and advanced argillic alteration.	Polymictic, rounded to subrounded in a muddy rock flour matrix.	Matrix-supported.	Barren unless rich in pre-existing Cu/Mo/Au.
Phreatic (epithermal level)	Within lithocap, local surface expressions as eruption breccias. Irregular bodies 10s-100s m in diameter.	Typically intermineral relative to lithocap development. Advanced argillic.	Commonly polymictic, silicified angular to rounded clasts in rock flour, chalcedony, quartz, alunite±barite, sulphides matrix.	Clast- or matrix-supported.	May contain high sulphidation Cu/Au/Ag.
Phreatomagmatic	Span porphyry Cu and epithermal environments. Surface manifestations are maar volcanoes (present in ~20% of systems). Km scale downward narrowing conduits rooted in intrusions.	Commonly late but early examples noted. Sericite and advanced argillic alteration. Early examples often have overprinting alteration dependent on level.	Polymictic, rounded to angular clasts in rock flour matrix. Contains cm sized juvenile material derived from causative intrusion. Early examples cut by porphyry mineralisation.	Matrix-supported, juvenile material and tuff present.	Commonly uneconomic. May host porphyry Cu mineralisation in clasts or high sulphidation ore types. Can be ore-destructive.

### 2.3.3 Magmatic-hydrothermal breccias

**Geometry and timing** - Many porphyry Cu deposits encompass “minor volumes (5 to 10%) of magmatic-hydrothermal breccia” (Sillitoe, 2010), that are characterised by a distinct magmatic fluid component. They typically form in the deeper parts of porphyry Cu systems (>1 km) extending hundreds of metres horizontally and several hundred metres in vertical extent, as near vertical pipe-like bodies along the upper peripheries (e.g., Fig. 2.4) or atop the adjacent porphyry intrusive (Sillitoe, 1985, 2010, 2019). Field relations and spatial positioning of many magmatic-hydrothermal breccias, located towards the apices of the causative intermineral porphyry intrusions, suggests that magmatic-hydrothermal porphyry Cu-related breccias are largely syn- or post-porphyry Cu formation, and often contain altered and mineralised clasts (Sillitoe, 2010; Vry et al., 2010; Perelló et al., 2012).

**Formation** - Magmatic-hydrothermal breccias are formed by the violent release of over-pressured magmatic fluids and volatiles from the apophyses of an underlying

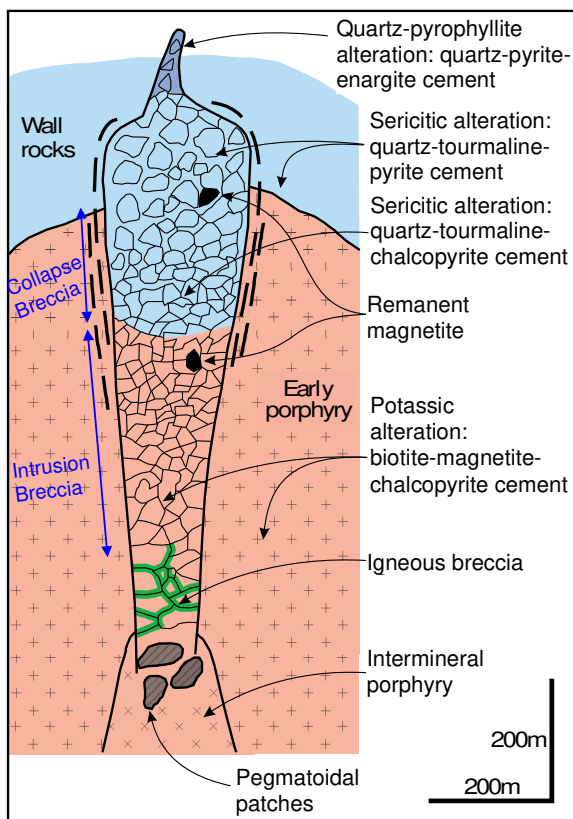


Fig. 2.4 Schematic depiction of a magmatic-hydrothermal breccia genetically linked to the apex of an underlying intermineral porphyry intrusion. The entire breccia body originally underwent potassic alteration which was partially overprinted by sericitic and, subsequently, advanced argillic assemblages. Modified after Sillitoe (2010).

pluton, which likely results from boiling processes during the emplacement and solidification of hydrous magmas (e.g., Burnham and Ohmoto, 1980; Burnham, 1979, 1985; Sillitoe, 1985). From depth of formation and field relations (e.g., San Pedro District, Chile; Sillitoe and Sawkins, 1971), these breccias are blind and did not extend far above the parental porphyry intrusion or penetrate the overlying epithermal environment (Corbett and Leach, 1998). They were therefore not likely connected to subaerial volcanism thereby preserving the mineralising potential of a system (Oyarzun et al., 2001). Some of the larger breccias such as those at Río Blanco-Los Bronces do however extend several hundred metres above the intrusions (e.g., Irarrazaval et al., 2010; Toro et al., 2012). Upper terminations of pipes are rarely preserved, however in

the San Pedro de Cachiyuyo District (Chile), Sillitoe and Sawkins (1971) observed an abrupt termination 'against a dome-shaped roof overlain by hydrothermally altered un-brecciated rock'.

**Magmatic-hydrothermal textural sub-classifications** - Two sub-facies within magmatic-hydrothermal breccia pipes, termed 'intrusion' and 'collapse' (Fig. 2.4), were proposed by Corbett and Leach (1998). Intrusion breccias describe facies that developed from the expulsion of volatiles from an underlying pluton into overlying host rocks (e.g., Sillitoe, 1985). Collapse breccias, on the other hand, "formed during relaxation following the initial explosive intrusion breccia event, and are typically best exposed about the outer, particularly the upper, portions of breccia pipes" (Corbett and Leach, 1998). Significant downward movement within magmatic-hydrothermal breccia pipes has been observed in the Los Bronces pipe, where "scarce fragments of overlying andesitic volcanics, which once formed a roof over the granodiorite pluton, are found up to 200 metres below the uppermost outcrop of the breccia pipe" (Sillitoe and Sawkins, 1971).

**Magmatic-hydrothermal mineralogical sub-classifications** - Breccia clasts may be set in a combination of fine-grained igneous material or hydrothermal cement. Igneous cements (e.g., Fig. 2.4) tend to be more common at depth near the magmatic source (Gustafson and Hunt, 1975; Sillitoe, 2010). Hydrothermal cements are a mixture of varying portions of biotite, anhydrite, quartz, tourmaline and Cu-sulphides. Where breccias extend for several hundred metres downwards, alteration assemblages change with depth (Fig. 2.4) mimicking the adjacent porphyry intrusion. Deeper portions commonly display potassic alteration, which grades upwards into sericitic and then (rarely) advanced argillic alteration (Río Blanco-Los Bronces; Irrazaval et al., 2010; Toro et al., 2012). The lack of tuffaceous material, subangular to angular, usually monomictic clast populations, and the common observation that magmatic-hydrothermal breccias are normally blind, allows these breccias to be distinguished from higher-level phreatomagmatic and phreatic breccias (Sillitoe, 2010).

#### **2.3.4 Phreatomagmatic breccias (diatremes)**

Diatreme is a term used to describe downward-tapering, subsurface volcanic conduits filled with a mixture of brecciated volcanoclastic deposits and wall-rock (Ross et al., 2017). They are commonly found in the upper regions of porphyry Cu systems (Sillitoe, 1985), being intimately related to high-level magmatic porphyry intrusions, feeder dykes or apophyses (Tâmaş and Milési, 2002; Ross et al., 2017). Documented examples in porphyry Cu deposits include the Braden Diatreme at El Teniente (Sillitoe, 1985; Cannell et al., 2005), Agua Rica in Argentina (Landtwing et al., 2002) and Cerro De Pasco in Peru (Rottier et al., 2018). They are also found in epithermal

environments, often hosting significant ore (e.g., Roşia Montană, Romania; Wallier et al., 2006 and Cerro Maricunga, northern Chile; Lohmeier et al., 2019).

**Size** - Diatremes are generally the largest of the breccia bodies. Near surface they are regularly  $\geq 1$  km in diameter and  $>2$  km in vertical extent (Lorenz, 1975, 1986; Sillitoe, 1985; Davies et al., 2008). If root zones and feeder dykes are included then vertical extents may well be several kilometres (Lorenz, 1986; Lorenz and Kurszlaukis, 2007). The largest documented example is the Guinaoang breccia pipe in the Philippines which is 8.5 deep  $\times$  3.5 km wide (Tâmaş and Milési, 2002; Ross et al., 2017). Other sizable examples include Montana Tunnels (USA): 2.1 km deep  $\times$  0.6 km wide (Sillitoe et al., 1985) and Wau (Papua New Guinea):  $\sim 1.4$  km deep  $\times$  1.4 km wide (Sillitoe et al., 1984).

**Diatreme and host rock contacts** - The contact between phreatomagmatic breccias and their host rocks is sharp, and the emplacement is commonly associated with ring faults (Sillitoe, 1985; Sillitoe et al., 1985; Baker et al., 1986). Violent interaction between the breccia body and the host rocks causes large sections of the host rocks, ranging from a few cm up to several hundred m, to be incorporated into the breccia body (Davies et al., 2008). This can sometimes generate a distinct breccia facies often termed annuli breccia or 'marginal breccias' which are typically enriched in clasts that are more angular in nature due to not being fluidised and transported.

**Matrix and clasts** - The matrix-supported breccias are heterolithic with widely separated cm-sized clasts set within a rock flour matrix "containing an andesitic to dacitic tuffaceous component, the latter commonly difficult to recognize where alteration is intense" (Sillitoe, 2010). Where the tuffaceous component is relatively high it has been previously termed 'tuffisite' (Cloos, 1941; Sillitoe, 1985). Matrix typically accounts for  $>50$  vol.% of the rock (Sillitoe, 1985) and reflects the rock fragments from which it is derived except external/exotic fragments such as surficial sediments. Fine-grained rock flour is formed from the attrition and abrasion of fragments during horizontal and vertical displacement during intense fluidisation, likely as slurries (Sillitoe, 1985). Additional brecciation events and subsidence contributes to the final intermingled relationships between the breccia body and the host rocks (Tâmaş and Milési, 2002).

A defining feature unique to diatremes is the presence of entrained juvenile igneous material derived from the parental magma. This is characterised by distinctive ragged-shaped/plastically deformed ("wispy", "cusped" or "vermiform") margins (e.g., Fig. 8, Richards, 2011a). Their presence is important, as it is direct evidence of a magmatic contribution to brecciation and emplacement whilst semi-solidified. Evidence to suggest that many diatremes reached surface as maar volcanoes includes carbonised

wood, accretionary lapilli, lacustrine sedimentary deposits and blocks of base surge (e.g., Montana Tunnels; Sillitoe et al., 1985).

**Nature and relative timing of mineralisation** - Diatremes are predominantly late-stage and post-date porphyry Cu mineralisation (Sillitoe, 2010). As a result, many emplaced within the mineralised envelope can be porphyry Cu destructive such as the Braden Diatreme at El Teniente (Cannell et al., 2005; Vry et al., 2010). Diatremes do however rarely pre-date porphyry mineralisation (e.g., Caspiche, Chile; Sillitoe et al., 2013; Boyongan, Philippines; Braxton et al., 2008, 2018 and Tanjung Jahe, Southeast Java; Harrison et al., 2018). They are often subeconomic although Cu-Mo mineralisation is often found replacing clasts and/or matrix (e.g., Braden Diatreme, El Teniente; Sillitoe, 1985; Cannell et al., 2005; this study), and/or wall rocks (e.g., Grasberg).

Cu-Au mineralisation is often concentrated around fracture zones associated with diatremes (Baker et al., 1986; e.g., Caspiche, Chile; Sillitoe et al., 2013). Whether the parental intrusive of the diatreme is the source of these mineralising fluids remains enigmatic and poorly understood. In the lithocap environment, the breccias may be overprinted by late-stage epithermal mineralisation (e.g., Wafi diatreme, Papua New Guinea; Rinne et al., 2018).

**Alteration** - Diatreme breccias generally show pervasive clay alteration and pyrite impregnation of their matrix and clasts, mainly due to interaction with hot gases associated with their formation (Corbett and Leach, 1998). A vertical and lateral zonation in alteration is also frequently observed (e.g., Roşia Montană; Mârza et al., 1997). Higher temperature clays and micas such as sericite will be dominant at depth, which progressively grade into lower temperature clays (illite and smectite) at higher levels (Corbett and Leach, 1998). Advanced argillic alteration is sometimes present at the lithocap level.

**Formation** - Diatremes typically emanate from irregularly shaped root zones (see Figs. 1 and 2 from Lorenz and Kurszlaukis, 2007) at a depth of at least 1 km (Tâmaş and Milési, 2002). These are the sites of explosive magma fragmentation; most known exposures are from diamond mining of kimberlite pipes, where the diatremes often constrict towards a feeder dyke (Lorenz and Kurszlaukis, 2007).

Two mechanisms causing explosive magma fragmentation are considered for maar-diatreme formation: magmatic or phreatomagmatic. Magmatic fragmentation, which was recently outlined and discussed by Cashman and Scheu (2015), involves the expansion of juvenile volatile phases from the magma without external intervention. Phreatomagmatic eruptions, on the other hand, require “vaporization and expansion of water as steam with rapid cooling and/or quenching of the magma” (White and

Valentine, 2016). Lorenz and Kurszlaukis (2007) distinguished that some authors who advocate a magmatic origin do accept the potential involvement of groundwaters but, however, do not provide any details on the mechanism. Zimanowski et al. (2015), and references therein, consider phreatomagmatic explosions to be the result of “complex interactions of four components which are independent and often internally heterogeneous (magma, magmatic volatiles, external water, and wall rock)”.

The difficulty in distinguishing between products derived from phreatomagmatic processes and those from explosive magmatic eruptions are discussed by White and Valentine (2016). They propose that traditional methods of determining whether magmatic or phreatomagmatic processes were involved (e.g., based on assessments of particle vesicularity, shape of particles, and degree of quenching) are not entirely diagnostic. In particular, many studies “have typically tested for phreatomagmatism using the above, and if the fingerprint is lacking, magmatic fragmentation is considered proven”. Further complicating matters, White and Valentine (2016) showed that “features commonly linked to some types of purely magmatic fragmentation can also form by purely phreatomagmatic fragmentation, or by fragmentation that combines both”.

### **2.3.5 Phreatic breccias and pebble dykes**

Phreatic breccias, which can often be found within the porphyry and lithocap environment, are usually emplaced following potassic alteration (e.g., Sillitoe, 2010). Several categories of phreatic breccia are widely observed in porphyry Cu systems. These are “subdivided into pebble dikes and, uncommonly, larger bodies resulting from flashing of relatively cool groundwater on approach to magma, typically late-mineral porphyry dikes; and steep, tabular to irregular bodies triggered by vapour-pressure buildup beneath impermeable layers, commonly resulting from self-sealing by silicification” (Sillitoe, 2010).

Pebble dykes typically formed by the explosive venting of depressurised volatiles along joints or faults and their emplacement is commonly lithologically controlled. They are fragment-supported with clasts commonly well-rounded/milled and are usually subeconomic. Given the late timing of phreatic breccias, porphyry Cu mineralised clasts (disseminated and/or veined) are commonly overprinted by later sericite alteration at porphyry Cu level or advanced argillic at shallower levels (Sillitoe, 2010).

## 2.4 El Teniente overview

### 2.4.1 Location, history and mining

El Teniente is the world's largest underground mine (daily production of 140,000 tonnes of ore/day; Brzovic et al., 2008), the sixth largest Cu mine by reserve (Mining Technology, 2015) and the world's largest resource of Mo (Sillitoe, 2010). Located 75 to 80 km south of Santiago (34°05'S, 70°21'W), it lies 2,000 to 3,200 masl in the Libertador General Bernardo O'Higgins region of the Andes (Fig. 2.5). Access within the Teniente district is difficult due to the rugged mountainous terrain, with some peaks reaching >4,000 m. Heavy snowfall is common in the winter month's further hindering access. The nearest city to El Teniente is Rancagua, ~67 km west of the mine and linked by the Carretera de Cobre ("Copper Highway"). Until the early 1970's the mineworkers inhabited Sewell, a small town built on the steep ridgeline west of El Teniente. Sewell, also known as the Ciudad de las Escaleras (City of Stairs), is now a UNESCO heritage site owned by Codelco.

A review of the history of El Teniente was presented by Hustrulid and Bullock (2001), on which the following description is based. As the legend goes, a fugitive Spanish-official discovered El Teniente in the 1800s, with exploitation beginning in 1819 (Baros, 1995). In 1904, W. Braden and E.W. Nash founded the Braden Copper Co. (later the Kennecott Corporation in 1915) at El Teniente, calling it the Braden Mine and in doing so built a concentration plant capable of processing 250 t/day. In April 1967, the Government of Chile bought 51% of the Teniente property from Braden Copper, renamed it El Teniente and undertook a major mine expansion program to increase daily production to 63,000 tonnes. Constitutional reform in 1971 meant that El Teniente become part of a state-owned company, which was named Codelco.

Initial mining reportedly focused on high-grade (~30% Cu) chalcopyrite-bornite-cemented Marginal Tourmaline Breccias (Floody R., personal communication, 2017). Today, block caving is used to extract ore underground from a number of blocks/'mines' around the Braden Diatreme. Since operations began, an estimated >2,400 km of underground drifts and in excess of 1,500 km of underground roads have been developed (Mining Technology, 2015). This vast amount of exposure probably makes El Teniente one of the most mapped deposits globally, particularly the eastern side (Seguel J., personal communication, 2017). As a testament to the world-class nature of the deposit, El Teniente is undergoing an extensive \$3.4bn expansion project called El Teniente New Mine Level, which will extend the production life by 50 years. The New Mine Level project will access approximately 2.02 billion tonnes of ore reserves (grading 0.86% Cu), lying ~350 m below the existing undercut level of the mine (Mining Technology, 2015).

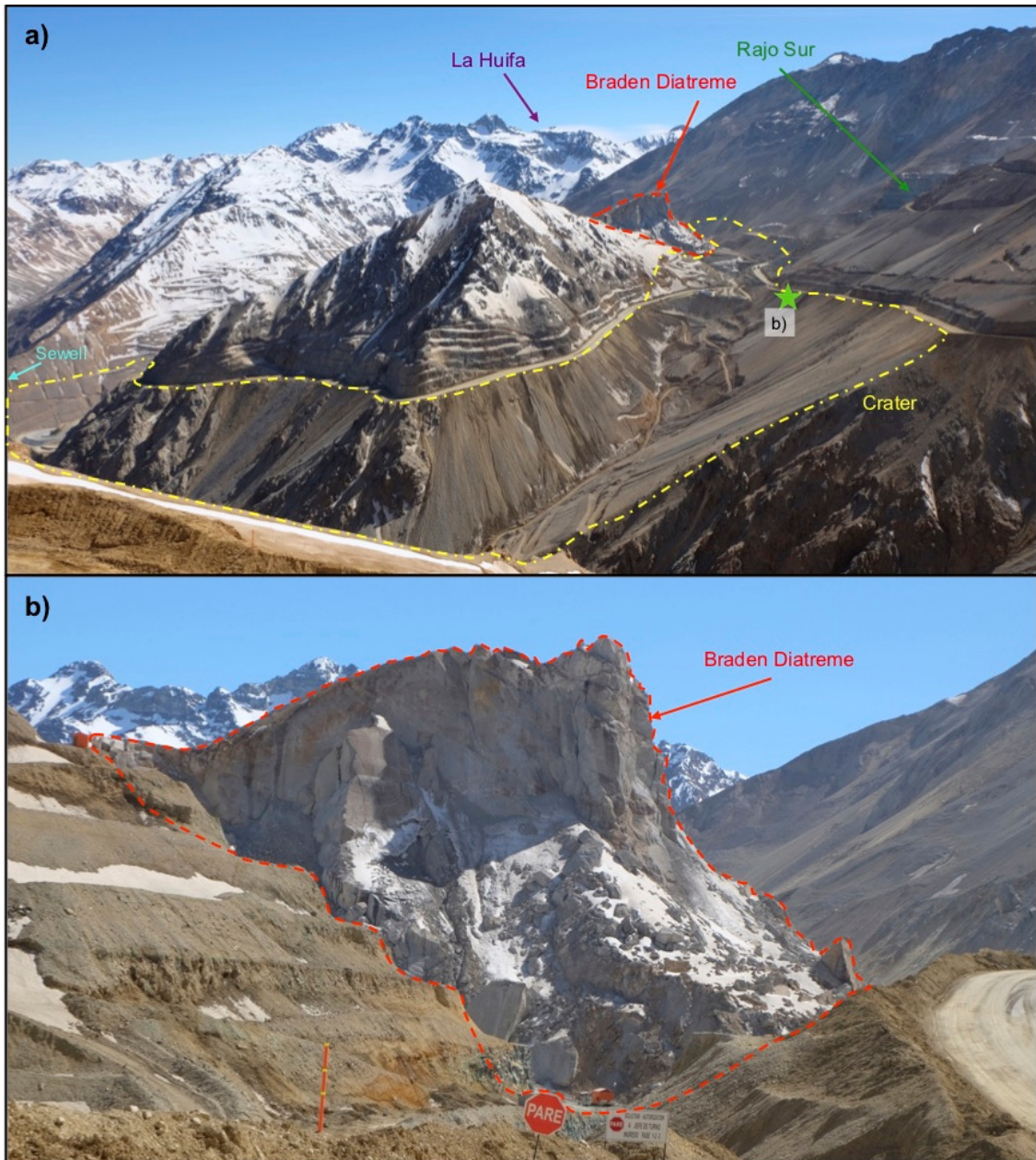


Fig. 2.5 Field photographs of El Teniente (September 2017): **a)** Wide angle photo ( $34^{\circ} 6'19.58''S$ ,  $70^{\circ}22'6.83''W$ ) looking northwards towards the Braden Diatreme (red). Underground caving operations centred around the Braden Diatreme has resulted in significant surface subsidence forming an extensive crater (yellow). Consequently access to the Braden Diatreme and surrounding areas is strictly prohibited. Green star indicates the location where photo b) was taken; **b)** Close up of the Braden Diatreme taken from the haul road. Approximate outcrop is delineated in red.

## 2.4.2 District Exploration

Aside from El Teniente itself, Codelco are undertaking brownfields exploration within the Teniente district. Regional hydrothermal alteration, visible from Landsat data, has been historically mapped throughout the district and a number of prospects identified including Agua Amarga, Olla Blanca, Quebrada Coya, Los Puquios, Codegua, La Juanita and La Huifa-La Negra; only the outcropping Extravío stock/breccia and a diorite stock at Los Puquios show potassic alteration (Cannell, 2004).

Through the continued reevaluation of old datasets, application of 3D predictive models and geochronology, Codelco have identified two prospective mineralised ‘corridors/strips’ in the district which are outlined below based on the review by (Pardo and Villarroel, n.d.).

- 1) **‘Porphyry Cu-Au and intermediate to high sulphidation epithermal strip’ (14 to 7 Ma)**: Located on the western-central area of the Teniente district extending for 40×15 km, it is the most promising area for discoveries. It is characterised by various areas of advanced argillic alteration aligned NW-SE and NE-SW (Fig. 2.6) with exposed levels of lithocap and silica ‘ledges’. ‘Pre-mineral phreatic breccias and post-mineral diatremes are also present’. The Agua Amarga sector represents one of the largest altered areas in the district. The epithermal system is characterised by zoning of silica-alunite-pyrophyllite and sericite-chlorite-hematite that grades to magnetite and biotite at depth. D-type quartz veins at depth could indicate the transition to a porphyry system.
- 2) **‘Cu-Mo porphyry strip’ (6.5 to 4.5 Ma)**: This incorporates the felsic-intermediate intrusives (aligned NNW-SSE) and breccias at the Teniente deposit. This enormous system is variably exposed, with some mineralised centres outcropping and others remaining blind (Pardo, 2015). The development of numerous high-grade magmatic-hydrothermal breccias continues to form new areas of exploration interest.

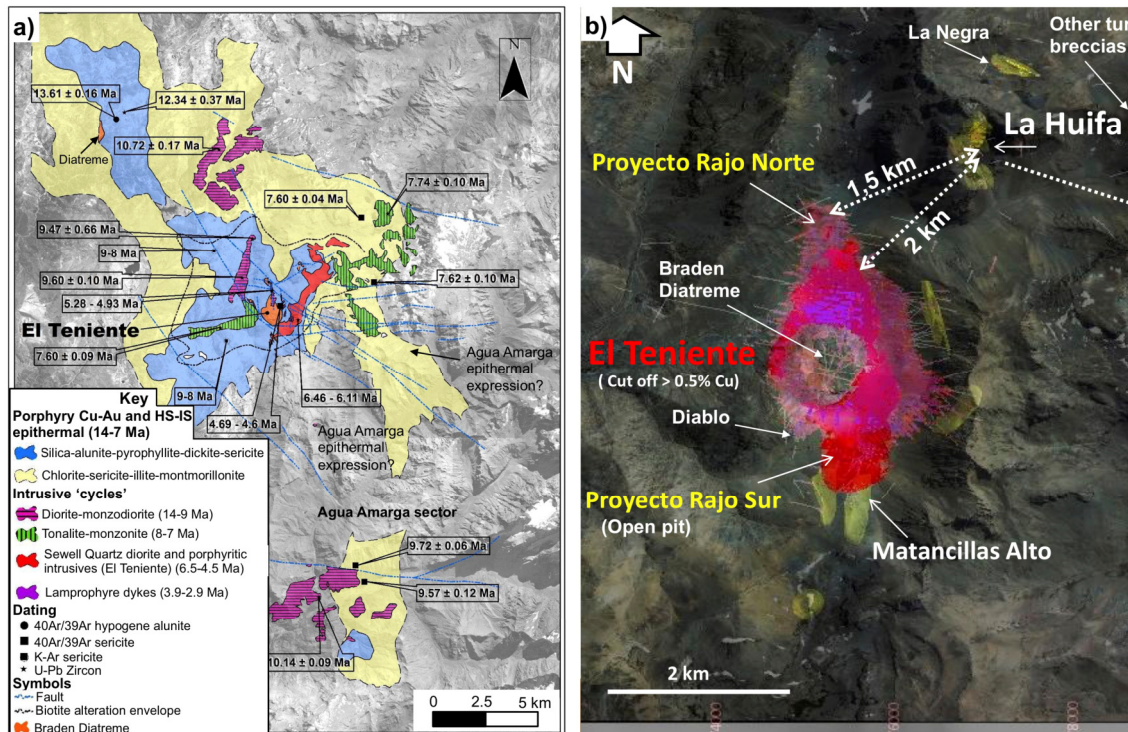


Fig. 2.6 **a)** Alteration map of the Teniente district showing prospective areas for further exploration. Other smaller diatremes have been identified several km north of El Teniente mine and other breccia complexes are present (see Fig. 2 of Stern et al., 2010). From Pardo and Villarroel, (n.d.); **b)** Relative location of La Huifa and Mantacillas Alto breccias to the Teniente mine. From Vidakovic (2013).

### 2.4.3 Tectonic setting of Chile

The tectonic evolution of the Mio-Pliocene porphyry Cu belt of central Chile and geologic setting has been subject to a number of studies, and is reviewed by Skewes and Stern (1994), Charrier et al. (2002), Camus (2003, 2005), Sillitoe and Perelló (2005), Hollings et al. (2005), Stern and Skewes (2005), Sillitoe (2010) and Piquer et al. (2016; 2019; Stern, 2020) among others, on which the following brief regional summary is mainly based.

Andean porphyry-type deposits are linked to the near-continuous subduction of the oceanic Nazca plate beneath the South American plate in an approximately easterly direction since the early Cretaceous (Camus, 2002, 2003; Cooke et al., 2005). Chile can be subdivided into three parallel, north trending structural provinces (Fig. 2.7) from oldest to youngest: 'Coastal Cordillera', 'Central Depression' and the 'Principal/Main Cordillera', with the latter being host to three giant Andean Cu deposits: Los Pelambres, Río Blanco-Los Bronces and El Teniente (Frikken, 2004; Hollings et al., 2005; Moreno and Gibbons, 2007). The Coastal Cordillera is composed of highly deformed late Palaeozoic to Triassic metamorphic and igneous 'basement' rocks of the Andes, overlain by Mesozoic sedimentary and volcanic units that define the Mesozoic magmatic arc (Piquer et al., 2016, 2017).

Separating the Coastal Cordillera on the east from the Principal Cordillera in the west, is the Central Depression; a >1,000 km long valley infilled with up to 500 m of Oligocene-Holocene unconsolidated sedimentary and pyroclastic units derived from volcanic centres (Piquer et al., 2017), alongside minor Oligocene-Miocene magmatic intrusives (Parada et al., 2007). The majority of rocks within the Central Depression can be included within the Coya Machalí (also known as the Abanico Formation; Charrier et al., 2002) and Farellones Formations (Rivano et al., 1990; Parada et al., 2007).

The Principal Cordillera (21°30' to 34°30'S) can be subdivided into eastern (Quaternary magmatic arc), central and western (Tertiary magmatic arc) sections (Fig. 2.7). The Eastern section (the current position of the active Quaternary magmatic arc) is comprised of Mesozoic sedimentary packages deposited in a back-arc basin whilst the Western Principal Cordillera is dominated by Tertiary volcanic and volcanoclastic packages (Piquer et al., 2016).

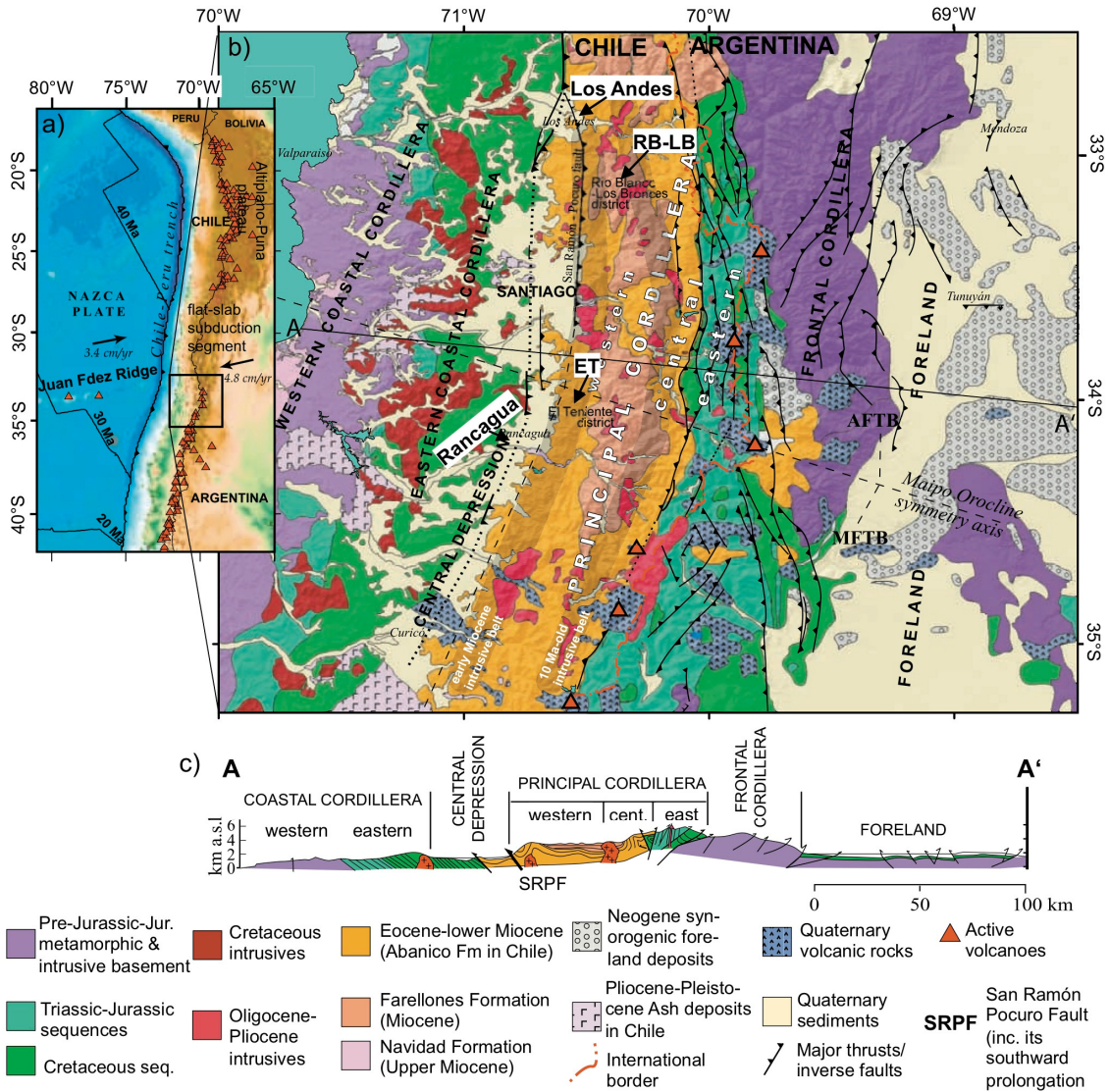


Fig. 2.7 Regional geology of central Chile and adjoining Argentina, with corresponding geological cross section (north of El Teniente) modified after Farías et al. (2008), also showing major thrusts active during the Neogene. The three major tectonic domains of Chile are outlined, along with the active volcanic front to the east. Abbreviations: AFTB: Aconagua fold-and-thrust belt; MFTB: Malargüe fold-and-thrust belt. Locations of the Río Blanco-Los Bronces ('RB-LB;') and Teniente ('ET') districts in the western Principal Cordillera are labeled.

The three Miocene-Early Pliocene giant porphyry deposits are situated near the boundary (Fig. 2.8) between the now volcanically inactive flat slab segment and the presently active SVZ (Vry et al., 2010). The crust within the SVZ is 35 to 40 km thick with subduction of the oceanic crust at an angle of approximately 30°, compared with a shallower 5° to 10° angle and a thicker crust of 55 to 65 km within the flat slab segment (Vry et al., 2010). Following the formation of the Los Pelambres, Farellones, and Coya Machalí Formations, according to Irrazaval et al. (2010), there were two stages of Mio-Pliocene magmatic activity on the southern margin of the central Chile- west-central Argentina belt, between latitudes 31° and 35°:

1. During the early to late Miocene (~18 to <15, perhaps 6 Ma), tholeiitic to calc-alkaline magmas erupted from stratovolcanoes and dome complexes generating the Farellones Formation. Slightly later, between ~12 and 8 Ma, granodiorite plutons and porphyry Cu-bearing stocks were emplaced.
2. Throughout the late Miocene to early Pliocene (~7.5 to 4.5 Ma), there were major mineralising events at Río Blanco-Los Bronces and El Teniente, which were followed by post mineral lamprophyre dyke intrusions (4 to 3 Ma) at El Teniente (Maksaev et al., 2004). Late- to post-mineral diatreme breccias at Teniente and Río Blanco-Los Bronces appear to have destroyed variable volumes of pre-existing porphyry-style mineralisation.

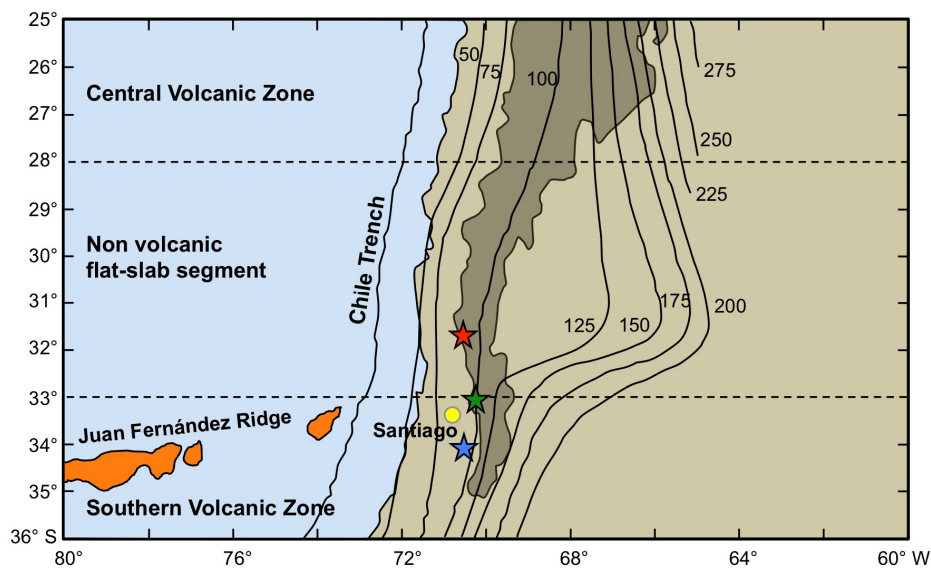


Fig. 2.8 Schematic diagram showing the Central Andes and modern flat-slab segment. Depth contours (in km) of the Wadati-Benioff zone and regions >3 km in elevation (dark brown) are shown. Stars illustrate the locations from north to south of the Los Pelambres-El Pachón (red), Río Blanco-Los Bronces (green) and El Teniente (blue) deposits. Reproduced after Parada et al. (2007).

At the end of stage one, and during much of stage 2, there was a ~40 km eastward migration of the arc front to the site of modern volcanic activity (Stern, 1989; Skewes and Stern, 1995; Irarrazaval et al., 2010). Increasing convergence and shallowing of the angle of subduction caused crustal thickening up to ~50 to 60 km and initial deformation in the Coya-Machalí Formation (Kay and Kurtz, 1995; Godoy et al., 1999; Kay et al., 1999). This, combined with high rates of uplift and exhumation of the fault-bound block, aided in the generation of oxidised melts and major mineralising events (Skewes and Stern, 1995; Kay et al., 1999; Camus, 2003; Irarrazaval et al., 2010). The subduction of the Juan Fernández Ridge is also thought to have had an important role in the genesis of central Chilean porphyry deposits (e.g., Skewes and Stern, 1995; Hollings et al., 2005) by encouraging crustal-scale faulting, slab segmentation (Garrido et al., 2002) and even acting as a source of metals (Stern, 1989, 1991; Skewes et al., 2002; Cooke et al., 2005; Skewes and Stern, 2005).

## 2.4.4 Regional geology: Teniente district

The Teniente district is characterised by two main regional lithologies (Fig. 2.9): the Coya-Machalí and Farellones Formations. Both were intruded by a series of calc-alkaline felsic-intermediate intrusives (Cannell et al., 2005). Other less prominent lithologies in the district include the Pliocene Colón-Coya Formation, which is mainly composed of unconsolidated rock debris with localised andesitic lavas, volcanic ash flows and conglomerate, unconformably overlain on the Coya-Machalí and Farellones Formations (Encinas et al., 2006). The valleys of the Teniente district are infilled with unconsolidated Quaternary glacial material (Cannell, 2004).

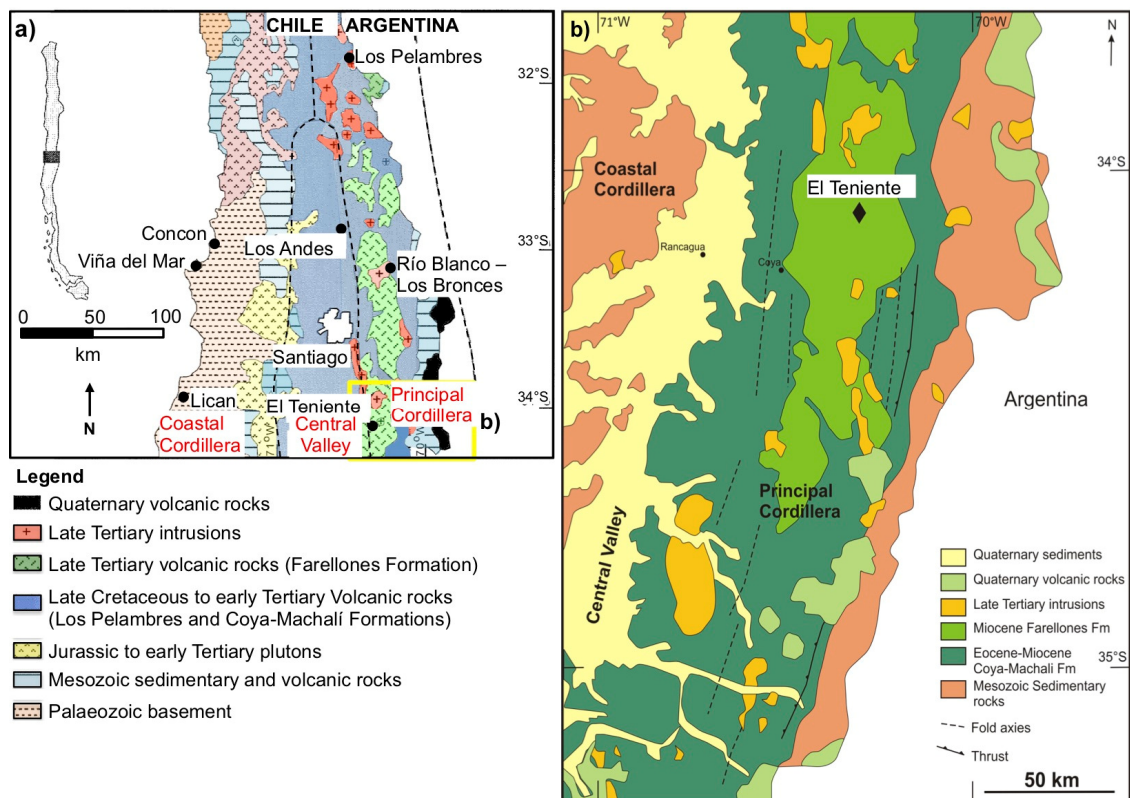


Fig. 2.9 **a**) Regional geological map of Chile adapted after Serrano et al. (1996). Approximate location of **b** is outlined in yellow. **b**) Lithological map of the Teniente district within the Principal Cordillera. Regional stratigraphy is dominated by the Farellones and Coya Machalí Formations and a series of intrusive complexes. From Vry (2010).

**The Coya-Machalí Formation** - The oldest unit to outcrop in the Teniente region is the Coya-Machalí Formation (26 to 16 Ma). This is a 3,500 m thick Oligocene to early Miocene sequence composed of low to medium-K basalts, andesitic, dacitic lava flows and associated volcanoclastic units which formed overlying relatively thin continental crust (Cannell, 2004; Cannell et al., 2005; Vry, 2010). The Formation is thought to be derived from a series of regional volcanic centres close to lacustrine and fluvial systems (Rivera and Falcón, 1998), with deposition related to crustal extension and an increase in convergence rates between the Nazca and South American plates

(Charrier et al., 2002). In the Teniente district the formation changes from calc-alkaline in the north to a more tholeiitic composition in the south (Hollings et al., 2005) and was initially deformed in the early Miocene and then again in the late Miocene-Pliocene (Kurtz et al., 1997).

**The Farellones Formation** - The dominant unit immediately surrounding El Teniente is the ~2,500 m thick mid to late Miocene (15 to 6 Ma) Farellones Formation (Kay and Kurtz, 1995; Godoy et al., 1999). It unconformably overlies the Coya-Machalí Formation (Moreno and Gibbons, 2007), although concordant, discordant and faulted contacts have been reported (Godoy et al., 1999; Charrier et al., 2002). The Farellones Formation is understood to have been deposited within extensional basins that were controlled by NW to W-trending transverse faults, with material derived from erupting and collapsing stratovolcanoes overlying a relatively thin crust (Kay and Kurtz, 1995; Vry, 2010). The Formation consists of a flat lying to gently dipping sequence of interbedded ash and lava flows intruded by dykes, sills and stocks ranging from medium- to high-K basaltic to rhyolitic in composition (Skewes et al., 2002; Parada et al., 2007). In the vicinity of the Teniente deposit, Howell and Molloy (1960) subdivided the Farellones Formation into three stratigraphic sub-members, which was summarised in Table 2.1 of Cannell (2004). For brevity, these sub-members include 'upper', 'middle' and 'lower' sections of the Farellones Formation. They were identified using a combination of satellite images, aerial photos, field and underground mapping and radiometric ages through the work of Howell and Molloy (1960), Rivano et al. (1990), Koeppen and Godoy (1994), Kay and Kurtz (1995) and Rivera and Falcón (1998).

**El Teniente district structural geology** - El Teniente has a close spatial association with large-scale crustal lineaments and fault splays (Cuadra, 1986). Overlapping close to the Braden Diatreme are the NE-trending Teniente Fault Zone (TFZ), also locally termed the Agua Amarga Fault, and the NW-trending Codegua Fault (Fig. 2.10). Surface expressions of the Codegua fault are difficult to find despite the structure clearly defined by the local-regional aeromagnetic surveys and by the alignment of four relict volcanic centres (11 to 9 Ma; Rivera and Falcón, 1998; Cannell et al., 2005). The Codegua Fault has been interpreted as a 'basin-bounding structure, having undergone appreciable vertical movement' (Cannell et al., 2005). The near parallel alignments of the Diorite Porphyries and the Teniente Dacite Porphyry to the Codegua Fault suggest it likely had an influencing factor in their emplacement (Floody R., 2017 personal communication).

The TFZ comprises of multiple anastomosing strike-slip faults in a deformation zone ~14 km long and 3 km wide, oriented ~65° E (Garrido et al., 1994). The anastomosing faults are ‘associated with well-developed poorly mineralised argillic alteration’ that extends over 14 km (Camus, 1975; Cuadra, 1986; Garrido et al., 1994; Skewes et al., 2002; Cannell et al., 2005). Codelco División El Teniente have recognised a number of ENE trending faults that follow the trace of the TFZ along with a number of tourmaline±anhydrite breccia complexes and lamprophyre dykes suggesting that their formation and emplacement is linked to the TFZ (Garrido et al., 1994).

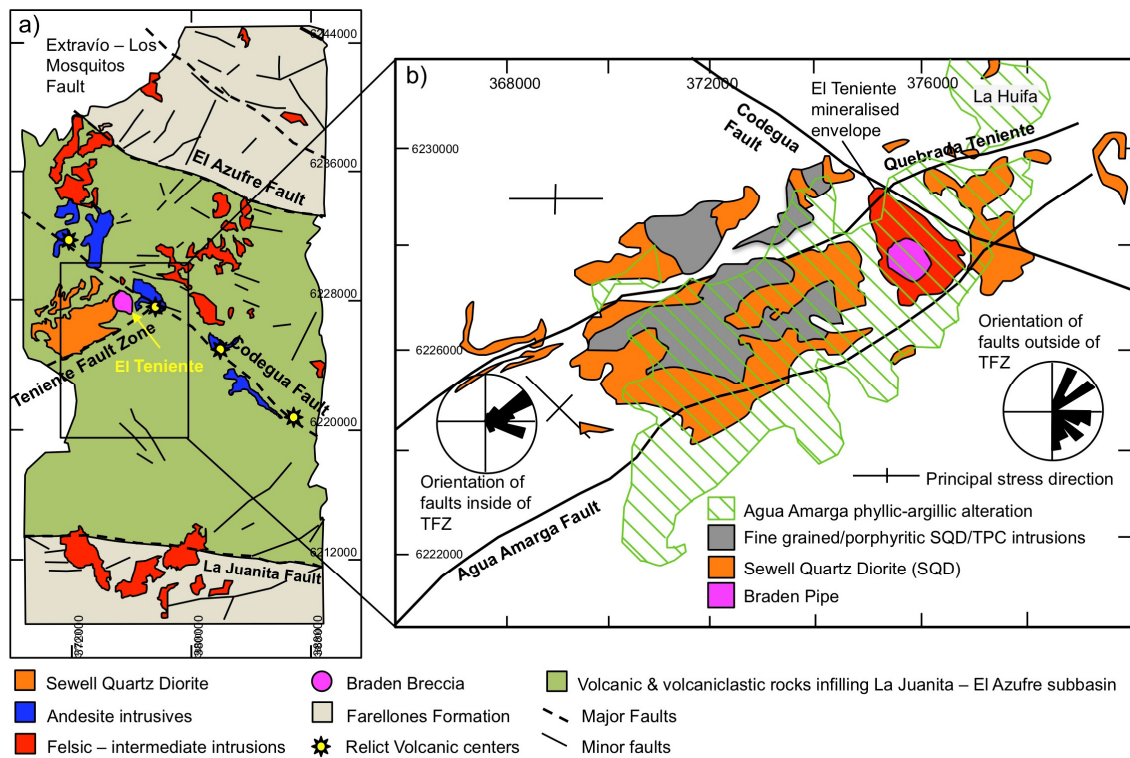


Fig. 2.10 Geology of the Teniente district, showing the spatial association between the Teniente deposit and intersection between the NE-trending Teniente Fault Zone and NW-oriented Codegua Fault: **a)** Reproduced after Cannell et al. (2005); **b)** Reproduced after Garrido (1995).

## 2.5 El Teniente porphyry system: lithologies, geochronology and genesis

### 2.5.1 Lithologies

El Teniente mine is hosted within the Teniente Mafic Complex a late-Miocene volcanoplutonic complex emplaced within the middle to late Miocene Farellones Formation (Skewes et al., 2002; Cannell et al., 2005, 2007; Vry et al., 2010; Spencer et al., 2015; Wilkinson et al., 2020). Following the emplacement of the TMC, a series of late Miocene-Pliocene felsic-intermediate plutons were emplaced, alongside multiple uneconomic and well-mineralised breccia complexes, of igneous, magmatic-hydrothermal and phreatomagmatic origin (Skewes et al., 2002; Stern et al., 2010; Vry et al., 2010; Spencer et al., 2015). Over time, a variety of names have been given for the intrusive units (Table 2.2; Fig. 2.11) which has led to some confusion, and therefore this study will follow the same terminology as the mine classification, Vry et al. (2010) and Spencer et al. (2015) scheme below.

Table 2.2 Different terminology for igneous rock units used in the current study compared to terms used by previous authors.

<b>This study</b> ; Mine Classification; Vry et al. (2010); Spencer et al. (2015)	Cannell et al. (2005)	Skewes and Stern (2007)
Teniente Mafic Complex (TMC)	Teniente Host Sequence	Teniente Mafic Complex
Sewell Quartz Diorite (SQD)	Sewell Tonalite	Sewell Tonalite
A-Porphyry	Gray Porphyry	A porphyry igneous breccia
Diorite Porphyries	Dacite Pipes	Quartz diorite porphyries
Grueso Porphyry	Marginal Porphyry	Not mentioned
Teniente Dacite Porphyry (TDP)	Dacite porphyry dike	Teniente Dacite Porphyry
Latite dykes or 'dacite dykes' (Maksaev et al., 2004)	Latite dykes	Dacite ring dyke

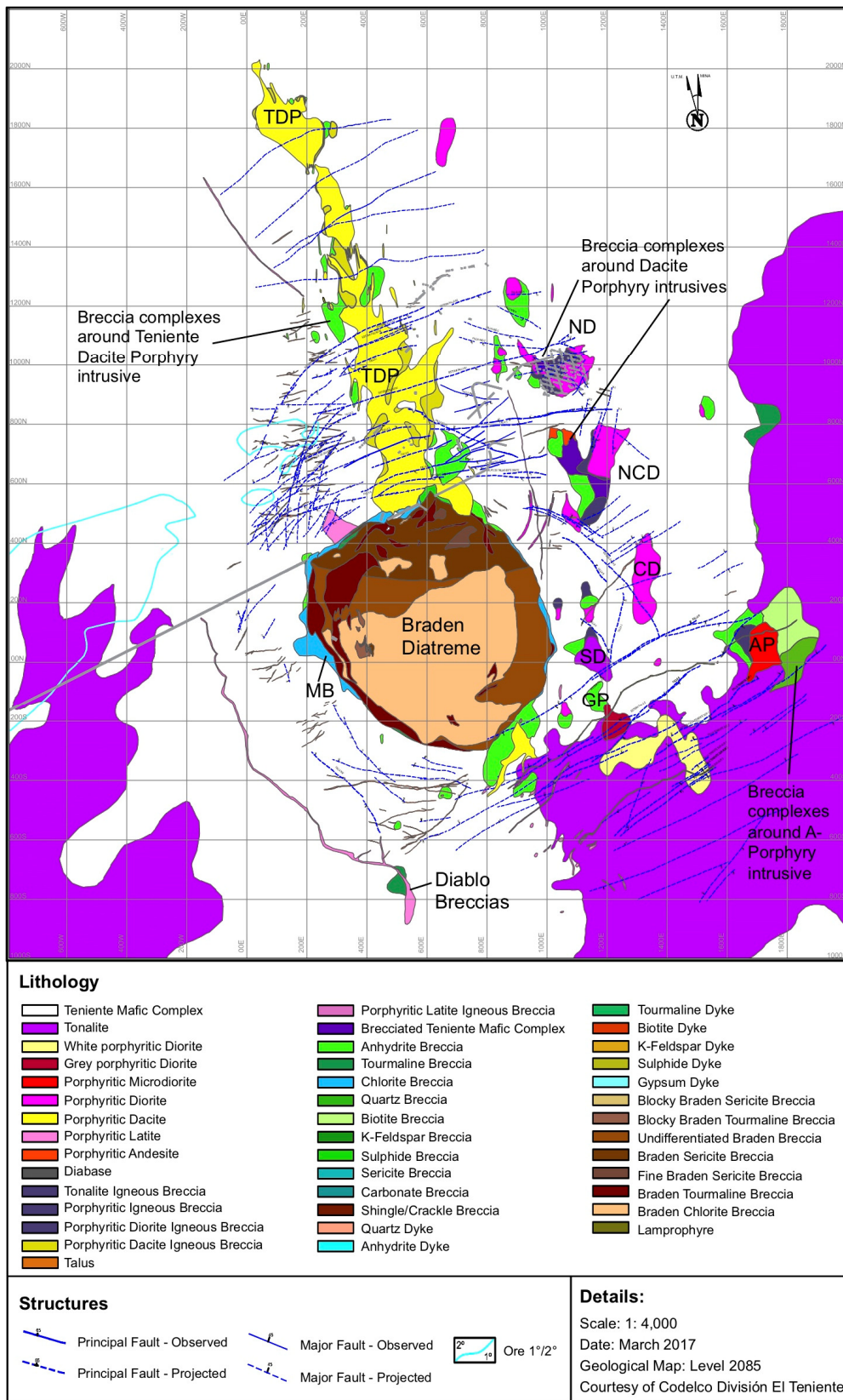


Fig. 2.11 Geological map of level 2085 at El Teniente, March 2017. Of particular note are the facies variations in the Braden Diatreme and the Diorite Porphyries to the east of the Braden Diatreme and the Teniente Dacite Porphyry. Note the concentric faults around the Braden Diatreme, and the breccia bodies adjacent to felsic intrusives. Abbreviations: TDP= Teniente Dacite Porphyry, ND= Northern Diorite, NCD= Northern Central Diorite, CD= Central Diorite, SD= Southern Diorite, AP= A-Porphyry, GP= Grueso Porphyry, Diablo= Diablo Breccias, MB= Marginal Breccias, BP= Braden Diatreme. Local mine grid is oriented 14.5° east of geographic north. Courtesy of Codelco División El Teniente.

## 2.5.2 Geochronology

During the 20<sup>th</sup> Century, the geochronology of El Teniente was based on whole-rock K-Ar dating from felsic intrusions and K-Ar age determinations for biotite and sericite presented by Quirt (1972), Clark et al. (1983) and Cuadra (1986, 1992). The most comprehensive geochronological datasets for El Teniente were presented by Cannell (2004) and Makshev et al. (2004), which included  $^{40}\text{Ar}/^{39}\text{Ar}$  dates on whole-rock samples, biotite and sericite from the various intrusions and some breccias at El Teniente. In addition to these, they presented U-Pb SHRIMP zircon analyses from the Teniente Intrusive Complex, molybdenite Re-Os dating from vein and breccia samples and apatite fission track dates. Spencer et al. (2015) presented molybdenite Re-Os dating of main and late mineralisation-stage samples proximal to the Central, Southern Diorite and North-Central Diorite Porphyries, Marginal Tourmaline Breccia, a type 6b vein associated with the southern tip of the TDP, and from an anastomosing NW-trending fault zone that coincides with a significant Mo anomaly east of the Braden Diatreme.

From combined isotopic dating, Makshev et al. (2004) recognised five episodes of felsic intrusive activity within the Teniente orebody listed below and illustrated in Fig. 2.12. A minimum of five superimposing mineralisation events “at  $6.30\pm 0.03$ ,  $5.60\pm 0.02$ ,  $5.01$  to  $4.96$ ,  $4.89\pm 0.08$  to  $4.78\pm 0.03$ , and  $4.42\pm 0.02$  Ma” are concurrent with the five intrusive episodes (molybdenite Re-Os; Makshev et al., 2004). In order of emplacement (Fig. 2.12), the main intrusive events at El Teniente are the TMC, SQD, La Huifa, A-Porphyry, Diorite Porphyries ( $\pm$ breccias), TDP (final major igneous intrusion associated with significant mineralisation), Marginal Breccias, Braden Diatreme and post mineralisation hornblende dykes (Makshev et al., 2004; Vry et al., 2010). These were emplaced in late Miocene country rocks yielding a ‘apatite fission-track age of  $8.9 (\pm 2.8)$  Ma for a mafic sill, in accord with previous K-Ar ages of  $12.0 (\pm 0.7)$  to  $6.6 (\pm 0.4)$  Ma for volcanic rocks from the district’. To date no crystallisation ages have been obtained for the North-Central Diorite and no emplacement ages currently exist for the Southern Diorite (Spencer et al., 2015).

- 1) ‘Sewell Quartz Diorite and other quartz diorite-tonalite intrusions of the eastern part of El Teniente crystallised from  $6.46 (\pm 0.11)$  to  $6.11 (\pm 0.13)$  Ma (zircon U-Pb)’;
- 2) ‘Quartz diorite-tonalite SE of the orebody, with biotite  $^{40}\text{Ar}/^{39}\text{Ar}$  plateau ages of  $5.63 (\pm 0.12)$  and  $5.47 (\pm 0.12)$  Ma. These ages agree with a hydrothermal overprint on zircons from the intrusions of the previous episode at  $5.67 (\pm 0.19)$  to  $5.48 (\pm 0.19)$  Ma (U-Pb)’;
- 3) ‘Teniente Dacite Porphyry crystallised at  $5.28 (\pm 0.10)$  Ma (zircon U-Pb)’;

- 4) 'Dacite ring dyke encircling the Braden Diatreme crystallised at 4.82 ( $\pm 0.09$ ) Ma (zircon U-Pb)' and;
- 5) 'Minor dacite intrusions and dykes yielded a biotite  $^{40}\text{Ar}/^{39}\text{Ar}$  plateau age of 4.58 ( $\pm 0.10$ ) Ma, and sericite  $^{40}\text{Ar}/^{39}\text{Ar}$  plateau ages of 4.56 ( $\pm 0.12$ ) to 4.46 ( $\pm 0.10$ ) Ma'.

**Breccia geochronology** - For the purpose of this study, Teniente tourmaline breccias have been subdivided into five different breccias on the basis of age in relation to the defined mineralising events at El Teniente, or location. These are:

1. Early poorly mineralised tourmaline breccias commonly found on the eastern side of the deposit (no age data available).
2. The Marginal Breccia records a whole-rock sericite K-Ar age of 4.7 Ma (Cuadra, 1986), and a  $^{40}\text{Ar}/^{39}\text{Ar}$  step heating age of 4.67 ( $\pm 0.11$ ) Ma (Maksaev et al., 2004). Spencer et al. (2015) undertook Re-Os dating on the Marginal Breccia, on both the western ( $4.59 \pm 0.029$  Ma) and eastern ( $4.584 \pm 0.020$  Ma) sides of the Braden Diatreme.
3. The youngest molybdenite Re-Os ages from Cannell (2004) were obtained from the tourmaline-anhydrite-sulphide-cemented Diablo Breccias, located in the far south of the deposit, adjacent to a sericitised late dacite dyke. It returned Re-Os ages of 4.705 ( $\pm 0.076$ ) Ma and 4.691 ( $\pm 0.015$ ) Ma (replicate). Although the late dacite dyke has not been dated, the close spatial association suggests a genetic association (Cannell, 2004). The ages of this breccia are similar to the 'late mineralisation (type 10) veins from the western edge of the Central ( $4.613 \pm 0.020$  Ma) and Southern Diorites ( $4.698 \pm 0.023$  Ma and  $4.666 \pm 0.023$  Ma replicate)' (Spencer et al., 2015).
4. Late 'post-main mineralisation' weakly Cu-Mo mineralised Braden Tourmaline Breccia. High precision geochronological data is not available for this breccia but it formed after the Braden Diatreme. Two ages of hydrothermal breccias from within the Braden Diatreme were presented by Maksaev et al. (2004; Table 2) for a "tourmalinized breccia from Braden Diatreme" (sample TT-135) and a "hydrothermal breccia within Braden Diatreme" (sample TT-134) that yielded  $^{40}\text{Ar}/^{39}\text{Ar}$  whole-rock sericite ages of 4.68 ( $\pm 0.12$ ) Ma and 4.49 ( $\pm 0.10$ ) Ma respectively.
5. La Huifa refers to a series of quartz diorite to dacitic porphyries dated at ~8 Ma (Charrier and Munizaga, 1979; Cannell, 2004) to 7 Ma (Laguna La Huifa quartz diorite porphyry; Skewes et al., 2002). Hydrothermal biotite from a sample of porphyry from the La Huifa breccia recorded a K-Ar age of 7.0 ( $\pm 0.4$ ) Ma (Cuadra, 1986). Later reanalysis yielded a  $^{40}\text{Ar}/^{39}\text{Ar}$  plateau age of  $6.97 \pm 0.10$  Ma (Maksaev et al., 2004). Molybdenite Re-Os dating has placed the mineralising event at La Huifa between 6.64 and 6.51 Ma (Pardo, 2015); coeval to the early stages of El Teniente (Floody R., personal communication, 2017).

One of the youngest features at El Teniente is the Braden Diatreme which is surrounded by the Cu-Mo-rich pre-Braden 'Marginal Breccia(s)'. The age of the central rock-flour part of the Braden Diatreme has been "dated by K-Ar at 4.5 Ma (Cuadra, 1986), and at 4.75 Ma by  $^{40}\text{Ar}/^{39}\text{Ar}$  (Figure 7; Makshev et al., 2002), both in sericite from altered rock fragments within the pipe" (Skewes et al., 2002). Further sericite  $^{40}\text{Ar}/^{39}\text{Ar}$  ages from 4.81 ( $\pm 0.12$ ) to 4.49 ( $\pm 0.10$ ) Ma were obtained by Makshev et al. (2004). It is clear from this data that the Marginal Breccias and Braden Diatreme formed roughly together, within less than a few hundred thousand years of each other, between 4.8 and 4.5 Ma (e.g., Cannell et al., 2005). Emplacement of the diatreme was followed by quartz-sericite alteration (sericite  $^{40}\text{Ar}/^{39}\text{Ar}$ ) "within and peripheral to the pipe from 4.81 $\pm$ 0.12 to 4.37 $\pm$ 0.10 Ma" (Makshev et al., 2004).

Limitations in the K-Ar and Ar-Ar geochronometers, primarily used to date the Braden Diatreme, however, were identified by Cannell (2004), Makshev et al. (2004) and Cannell et al. (2007). Unlike the molybdenite Re-Os system which was unaffected by the multiple hydrothermal episodes at El Teniente, 'the  $^{40}\text{Ar}/^{39}\text{Ar}$  system of micas is thought to have been reset by high-temperature ( $>350^\circ\text{C}$ ) fluid circulation and therefore only provide a record of the latest history of this supergiant ore-forming system' (Makshev et al., 2004). For example Ar-Ar and K-Ar data around the Braden Diatreme show a systematic zoning where the youngest ages were obtained from samples closest to the Braden Diatreme and the oldest from shallow levels on the margins of the Teniente deposit was interpreted to represent the final cooling history of El Teniente.

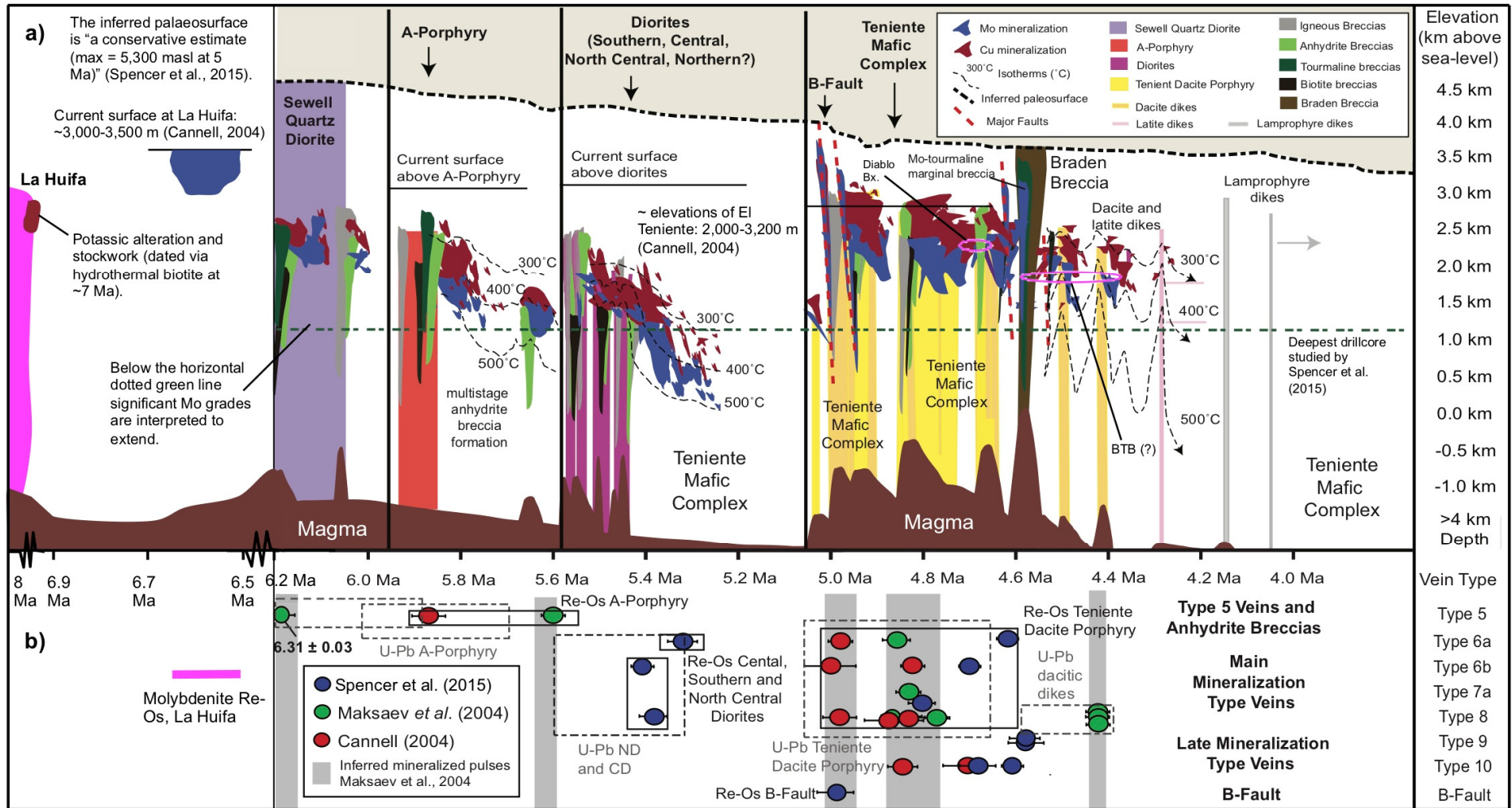


Fig. 2.12 **a)** Time vs. depth plot depicting the magmatic-hydrothermal evolution of El Teniente adapted after Spencer et al. (2015) to include La Huifa (ages discussed earlier). Depth indication for La Huifa does not correlate with the remainder of the diagram. Timing of the Diablo Breccias are highlighted (pink) based on Re-Os age obtained from Cannell (2004). Braden Tourmaline Breccia age range (pink) is based  $^{40}\text{Ar}/^{39}\text{Ar}$  whole-rock sericite for a "Hydrothermal breccia within Braden Diatreme" (sample TT-134) from Maksaeve et al. (2004). "The positions of Mo and Cu mineralization relate to enriched ore zones ( $>0.03\%$  Mo,  $>1.5\%$  Cu) surrounding each intrusion and are based on grade distributions, vein cross-cutting relationships" (Spencer et al., 2015). **b)** Re-Os dates with "dotted boxes represent the youngest reliable overlapping U-Pb zircon dates previously obtained for each intrusion" (Spencer et al., 2015). Re-Os dates from La Huifa are from Pardo (2015) and no crystallisation ages are currently available for the North Central and Southern Diorites.

Despite limitations in geochronological data, cross-cutting relations allow the relative timing of the TDP, Marginal Breccias, the Braden Diatreme and the Braden Tourmaline Breccia to be constrained. The Braden Diatreme cross-cuts the TDP and therefore formed after its intrusion (U-Pb:  $5.28 \pm 0.10$  Ma) thereby providing an upper age limit (Maksaev et al., 2004). Fragments of Marginal Breccias (Fig. 2.13a) and clasts containing late magmatic-hydrothermal alteration are found within the Braden Diatreme (Cannell et al., 2007; Spencer et al., 2015; this study), which further supports that the Braden Diatreme is younger than these stages. The Braden Tourmaline Breccia cross-cuts the Braden Diatreme matrix (Fig. 2.13) and therefore post-dates the formation of the Braden Diatreme.

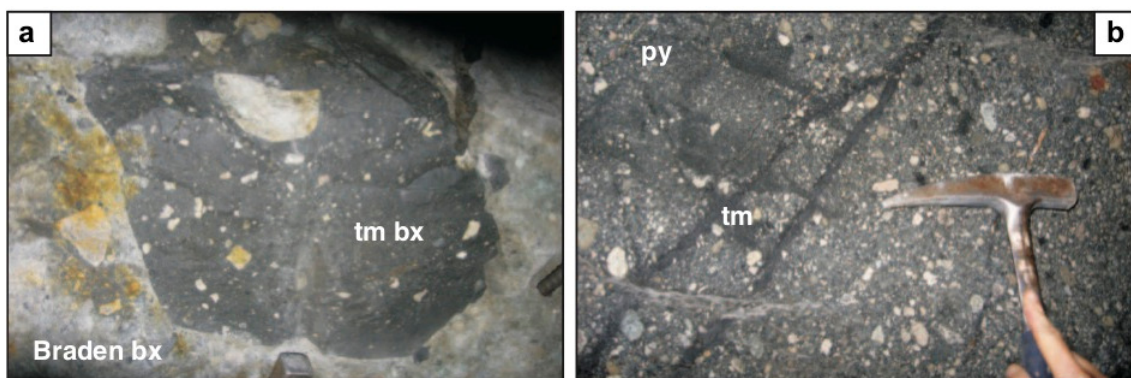


Fig. 2.13 Photographs of the Braden Diatreme at El Teniente from Cannell et al. (2007) and taken in the sublevel 6 mine, 2,210 masl: **a)** Clast of Marginal Tourmaline Breccia hosted in the sericite-altered, rock four Braden Sericite Breccia. Tip of sledgehammer at bottom for scale; **b)** Diffuse tourmaline veins with irregular tourmaline halos cutting the Braden Diatreme. Minor magmatic-hydrothermal activity after the formation of the Braden Diatreme is evidenced by the thin pyrite vein in the upper left corner that cross-cuts the breccia.

### 2.5.3 El Teniente porphyry system - genesis

Since its discovery, El Teniente has been subject to a number of unpublished and published studies by mine geologists and academics to help constrain its magmatic evolution and the nature of Cu-Mo mineralisation. Lindgren and Bastin (1922) presented the first comprehensive geological description of the deposit in which they recognised that it had been affected by multiple hydrothermal events associated with a sequence of igneous intrusions. They suggested that it represents an ‘andesitic sill-hosted’ deposit. Later, Howell and Molloy (1960) established El Teniente as a classic example of a porphyry Cu deposit. This was overturned by Skewes et al. (2002, 2005), Skewes and Stern (2005; 2007), Stern et al. (2007), and more recently Stern et al. (2019), who suggested that it should be classified as a “megabreccia, or breccia” deposit, rather than a porphyry Cu-Mo deposit.

The two models primarily differ in the relative importance of brecciation versus stockwork, and the “timing relationships between felsic intrusion, brecciation, stockwork development, and mineralization” (Cannell et al., 2007). This was largely by analogy with the models for neighbouring Miocene-Pliocene breccia-dominated deposits within Central Chile (e.g., Los Pelambres and Río Blanco-Los Bronces). Skewes, Stern and coworkers argued that Cu-Mo mineralisation at El Teniente is associated with multiple igneous and hydrothermal breccias that formed prior to, and independently of the felsic plutons which played little or no role in the Cu-Mo mineralisation. They also suggested that the TDP is a late- to post-mineralisation intrusive which either removed pre-existing Cu mineralisation or remobilised it into a stockwork (Cannell et al., 2005; Vry, 2010). More recently Stern et al. (2019) suggest that “the breccias formed first and the porphyries intruded into the zone of weakness created by the breccias, since some of these porphyry bodies, such as Porphyry A contain clasts of the breccias they intrude, and others of these small porphyries have no associated breccias surrounding them”.

This megabreccia model is contradictory to earlier and recent geochronological, structural and fluid studies (e.g., Maksaeve et al., 2004; Cannell et al., 2005, 2007; Klemm et al., 2007; Rabbia et al., 2009; Astudillo et al., 2010) that again interpret El Teniente as a porphyry Cu deposit. They provide evidence that the felsic porphyries are temporally and genetically related to Cu-Mo mineralisation. Cannell et al. (2007) argue that “if as Skewes and Stern (2007) suggest the post-mineralisation dacite porphyries intruded mineralised breccia complexes there should be an abrupt decrease in Cu-Mo grades at the contacts”. Instead they noted that moderately mineralised intrusions at El Teniente occur adjacent to high-grade breccias and the grade boundaries are diffuse. The term “megabreccia” is also confusing as by definition it has been used to describe breccias with clasts ranging from 1 to 400 m in diameter (e.g., Landes, 1945; Longwell, 1951). The mineralised biotite-, anhydrite- and tourmaline-cemented hydrothermal breccias at El Teniente have clast populations smaller than 1 m (Cannell et al., 2007) and are therefore, by definition, not megabreccias.

In agreement with Cannell et al. (2007), the author of this study believes it is unsuitable and confusing to use the term megabreccia to describe a large-scale hydrothermal system with a significant breccia component. The deposit at El Teniente will therefore be referred to as a porphyry Cu deposit with a notable breccia component (a porphyry-breccia system) in the remainder of this thesis. A simplified three stage structural model (Fig. 2.14) has been proposed by Cannell et al. (2005) for the formation of the Teniente deposit, in particular of the Braden Diatreme:

1. Emplacement of a deep-seated pluton which led to doming and the formation of inwardly dipping late magmatic and principal hydrothermal vein stockwork, centred on the middle of the deposit. The formation of dense vein halos is interpreted to be the result of multiple overlapping porphyry±breccia intrusions acting as efficient conduits for fluid pulses, where local fluid pressures exceeded stresses induced by the intruding magma (e.g., Burnham, 1979). Vry et al. (2010) later noted that these veins correspond to the main mineralisation stage.
2. An inferred period of magma withdrawal causing relaxation and subsidence during the late hydrothermal stage. This led to the development of steeply dipping, concentric fractures, veins and faults now observed surrounding the Braden Diatreme.
3. During the late hydrothermal stage, a major magmatic resurgence associated with uplift and reactivation of the concentric faults, led to the emplacement of dacite (locally termed latite) dykes, the Marginal Breccias, and pebble dykes into dilatational cone sheets above the magma chamber. Once lithostatic pressure was exceeded by late-stage fluids and/or magmatic pressure, explosive breccia formation and fluidisation took place leading to the formation of the Braden Diatreme, which exploited the concentric fractures and resulted in the characteristic funnel-shaped pipe which is bordered by the Marginal Breccias. There is uncertainty, however, as to whether the Marginal Breccia always had an annular shape or once took up the entire volume of the pipe, with the central portion later obliterated by the Braden Diatreme. In either case, the emplacement of the Braden Diatreme is thought to have depressurised the system and terminated any further significant mineralisation (Floody R., personal communication, 2017). The final stages in the development of the Teniente system involved late northeast-trending faults and lamprophyre dykes (3.8 Ma), formed in response to renewed movement along the TFZ as the system waned.

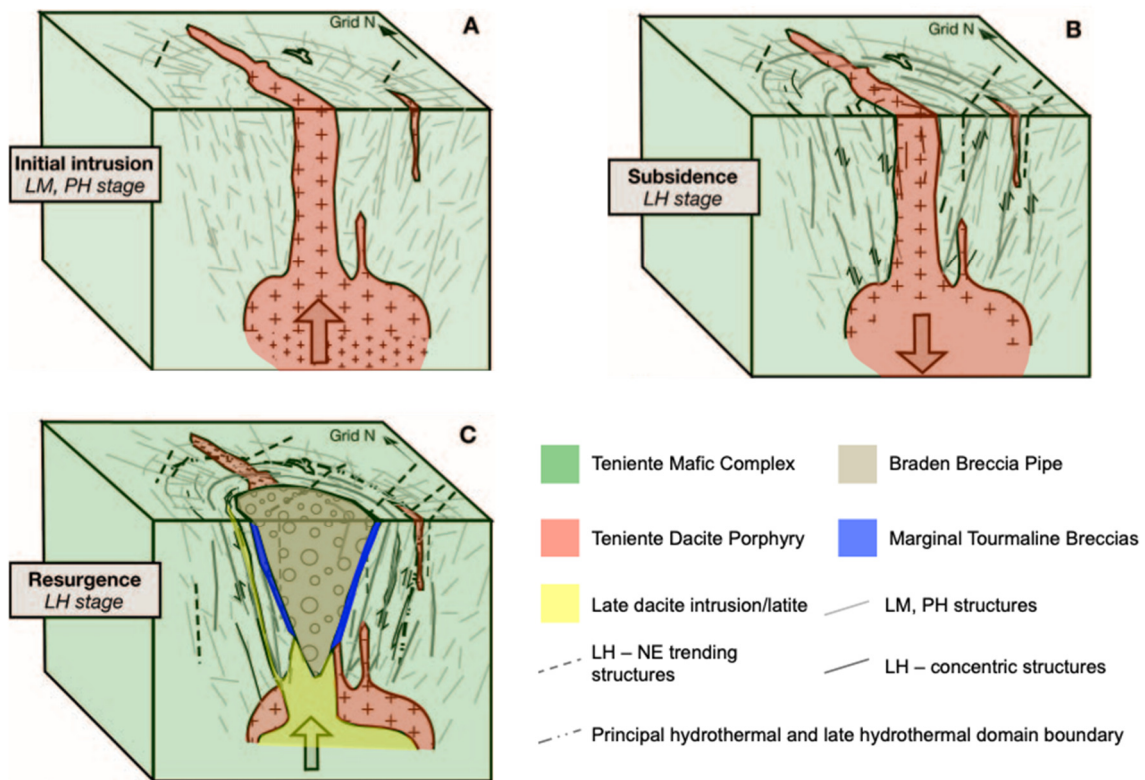


Fig. 2.14 Schematic model reproduced after Cannell et al. (2005), showing the three stage structural evolution of El Teniente: **a)** Doming related to the emplacement of a magma chamber; **b)** Magma expulsion and subsequent subsidence generating steeply dipping concentric fractures; **c)** Magma resurgence, uplift, reactivation of concentric faults, and emplacement of latite dykes, the Marginal Breccias and finally the Braden Diatreme.

### 2.5.4 Teniente Mafic Complex (TMC)

The TMC, which consists of the oldest rocks at El Teniente mine ( $8.9 \pm 1.4$  Ma), intruded the Farellones Formation and hosts the mineralised felsic-intermediate intrusions and breccias which form the Teniente deposit (e.g., Lindgren and Bastin, 1922; Howell and Molloy, 1960; Skewes and Arévalo, 2000; Skewes et al., 2002, 2005; Cannell et al., 2005; Vry et al., 2010; Wilkinson et al., 2020). It is estimated that the TMC laccolith has a minimum volume of  $\sim 50 \text{ km}^3$ , a vertical extent  $> 2,000 \text{ m}$  and a thickness of  $\sim 1 \text{ km}$  (Stern et al., 2010). Most of the stockwork is hosted in the biotite-altered units of the TMC which is estimated to contain in up to 80% of the Cu-Mo at El Teniente (Skewes et al., 2002; Cannell, 2004). The stockwork (e.g., Fig. 2.15) represents “at least a kilometre of vertical development, occupying an estimated volume of more than  $4.5 \text{ km}^3$  of altered rock”, with vein abundances commonly exceeding “50 veins plus veinlets per meter of core”, and “veins typically comprise 5 to 20% of the overall rock volume” (Cannell et al., 2007).

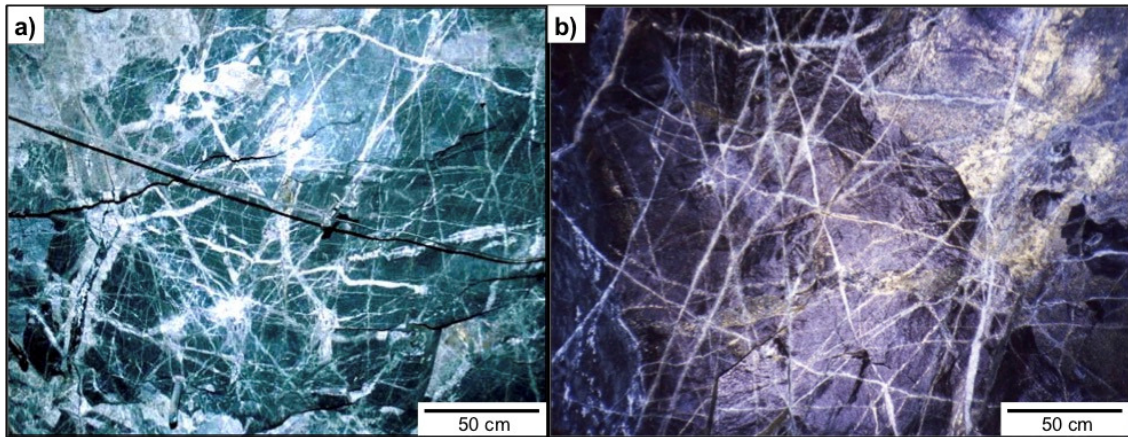


Fig. 2.15 Photographs of underground exposure of the stockwork in TMC: **a)** Intense quartz-anhydrite-sulphide vein stockwork in the biotite-altered Teniente Mafic Complex. Later veins have a white phyllic alteration halo compared to the darker grey-brown-black biotite alteration halo from earlier veins. Exposure is from the Esmeralda Mine, sublevel 6 (2,210 masl). From Cannell et al. (2005); **b)** Underground exposure of stock work veining in the biotite-altered TMC. Image courtesy of Codelco División El Teniente.

Prior to Cannell et al. (2005), detailed lithological descriptions of the TMC had not been published because of poor drill core quality, which was complicated by 'the lack of textural or colour contrast between the predominantly basaltic to andesitic units' (Vry et al., 2010). In addition, many original textures within the TMC have been obscured due to pervasive alteration-mineralisation and brecciation (Howell and Molloy, 1960; Skewes et al., 2002; Cannell, 2004; Stern et al., 2010; Vry et al., 2010).

In general, the TMC comprises dark green/black rocks with aphanitic to porphyritic appearance (Skewes et al., 2002; Cannell et al., 2005; Stern et al., 2010). They have been divided into nine subdivisions including volcano-sedimentary lithofacies (coherent andesite, volcanoclastic siltstones and breccias), and intrusive lithofacies (fine and coarse-grained andesite porphyry, diorite porphyry, gabbro, andesite dykes). The predominant intrusive facies however was interpreted as andesite porphyry with lesser diorite porphyry, andesite dykes and minor gabbro, shown in more detail in internal SGL-I-123/03 (2003) report. The principal phenocrysts in the TMC include labradorite-bytownite, which in places, display flow alignment textures (Lindgren and Bastin, 1922; Howell and Molloy, 1960; Cannell, 2004; Vry et al., 2010).

### 2.5.5 Teniente Intrusive Complex

Over a period of approximately 1.5 million years in the late Miocene-Pliocene, a series of intermediate-felsic intrusions (SQD, A-porphyry, TDP, Diorite Porphyries, Grueso porphyry, late dacite intrusions/dykes and lamprophyres) were emplaced into the TMC (Maksaev et al., 2004; Cannell et al., 2005; Vry et al., 2010), which are collectively termed the Teniente Intrusive Complex. Brief outlines are provided below.

**Sewell Quartz Diorite (SQD)** - This is the oldest felsic to intermediate unit, thought to have been emplaced between 12.4 to 7 Ma (Cuadra, 1986, 1992; Kay and Kurtz, 1995; Rivera and Falcón, 1998; Skewes et al., 2002). Younger ages between 6.7 and  $5.5 \pm 0.6$  Ma have also been suggested by Cannell et al. (2005). It is regarded to have been emplaced pre-mineralisation at El Teniente (Lindgren and Bastin, 1922; Howell and Molloy, 1960; Makshev et al., 2004; Vry et al., 2010). The SQD is a large stock on the southeast side of the deposit (Fig. 2.14), outcropping over an area roughly half as large as the TMC with an estimated volume of  $\sim 30 \text{ km}^3$  (Stern et al., 2010). Previous studies (e.g., Skewes et al., 2002; Cannell, 2004; Cannell et al., 2005; Vry et al., 2010) have shown that this unit is texturally heterogeneous, comprising an inner equigranular portion and an outer porphyritic zone.

**The A-Porphyry** - This is a relatively small " $<1 \text{ km}^3$  granitoid stock" (Stern et al., 2010). It intruded along the western margin of the SQD directly adjacent to the TMC and is associated with a copper-rich (1 to 2 wt.% Cu) magmatic-hydrothermal anhydrite breccia and microdiorite igneous breccias (Cannell, 2004; Vry et al., 2010; Stern et al., 2007, 2010; Spencer et al., 2015). The A-Porphyry was emplaced between 6.9 and 5.7 Ma (zircon U-Pb), implying that the unit may have formed from multiple intrusion and brecciation pulses, or that it contains inherited zircons from the adjacent SQD (Makshev et al., 2004).

**Diorite Porphyries (Diorite Pipes)** - East of the Braden Diatreme, and NW of the SQD, are four relatively small  $\sim 200$  m wide, equally sized intrusive diorite porphyries, termed the 'Northern', 'North-Central', 'Central' and 'Southern' Diorites; that all intruded the TMC (Cannell et al., 2005, 2007; Vry et al., 2010; Spencer et al., 2015). These porphyries are thought to be responsible for most of the mineralisation at El Teniente and are associated with high-grade hydrothermal anhydrite and tourmaline breccia complexes (Floody R., personal communication, 2017).

The Diorite Porphyries consist of  $\sim 30$  to 50% plagioclase phenocrysts with lesser proportions (5 to 15%) of amphibole and biotite phenocrysts, within an aplitic groundmass of plagioclase, K-feldspar, quartz and minor Cu-Fe sulphides (Cannell, 2004; Vry et al., 2010; Spencer et al., 2015). The Na-rich plagioclase phenocrysts are often altered to sericite, chlorite and quartz (Cannell, 2004; Vry et al., 2010). Whole-rock geochemistry has shown the Diorite Porphyries are enriched in K linked to strong potassic alteration (e.g., Vry et al., 2010). SHRIMP U-Pb zircon ages for both the Northern and Central Diorite Porphyries are very similar (average 5.6 Ma) ranging from 7.0 to 4.8 Ma, suggesting they formed synchronously and soon after the intrusion of the A-Porphyry (Spencer, 2015).

**The Teniente Dacite Porphyry (TDP)** - The TDP ( $5.28 \pm 0.10$  Ma) is a north-south trending elongate, subvertical dyke-like body (Maksaev et al., 2004). It has a maximum width of 300 m and extends ~1.5 km north of the Braden Diatreme, beyond the limit of the 0.5% Cu grade envelope (Stern et al., 2010; Vry, 2010). It outcrops unaltered and barren on the northern side of the Teniente river valley (Cannell, 2004). A series of igneous, biotite and anhydrite breccia complexes are associated to this unit, and are often located around the margins. Mineralogically and texturally the TDP is similar to the Diorite Porphyries, although it displays a degree of heterogeneity with distinct textural boundaries implying it formed from multiple intrusive events, reflected by the large range of zircon ages (Skewes et al., 2002; Maksaev et al., 2004; Cannell et al., 2005). The two dominant intrusive subtypes include:

1. The younger “euhedral phase” which occurs in the northernmost parts and the eastern edge of the intrusive body (Vry, 2010). Mineralogically, this phase contains euhedral plagioclase phenocrysts within a fine-grained aplitic groundmass (Cannell et al., 2005). It contains xenoliths of the subhedral phase, but typically has lower Cu grades. The northern limits are considered barren (Cannell, 2004).
2. The older “subhedral phase” forms the majority of the southern part of the intrusion, and contains plagioclase phenocrysts which display resorbed crystal edges within a coarse groundmass (Cannell et al., 2005; Vry et al., 2010).

**Grueso Porphyry** - Located SE of the Braden Diatreme along the margin of the SQD and the TMC, the Grueso Porphyry ( $4.89 \pm 0.08$  Re-Os; Maksaev et al., 2004) is geochemically and mineralogically similar to the Diorite Porphyries and the TDP. It is composed of albite-oligoclase feldspar, biotite and quartz phenocrysts within an aplitic groundmass of feldspar and quartz.

**Late dacite (‘latite’) intrusions and dykes** - Late dacite dykes and stocks are porphyritic with mainly biotite, sericitised albite, amphibole and quartz phenocrysts (20 to 40 vol.%) within an aplitic groundmass of feldspar and quartz (Skewes et al., 2002; Cannell et al., 2005; Vry et al., 2010). The late dacite intrusions show “moderate to strong quartz-sericite-calcite and only minor biotite-quartz-chlorite alteration at deep levels” (Maksaev et al., 2004). Chemically, they are similar to the TDP and other felsic intrusives at El Teniente (Skewes et al., 2002). A more detailed description and discussion of their major, minor and trace element compositions is presented in Stern et al. (2010), and references therein.

Intrusive dykes (2 to 15 m wide; Maksaev et al., 2004), often termed 'ring dykes', form discontinuous concentric bodies around the Braden Diatreme. Emplaced during the latter stages of the development of the Teniente system, they are believed to represent magmatic injections of over-pressurised volatile-rich felsic magma along the pre-existing cone fractures. The presence of dacite/latite blocks in the Braden Diatreme, and a K-Ar age between 5.3 to 4.8 Ma suggests "at least some latite porphyry intruded prior to the formation of the Braden Diatreme and may have played a role in the formation of the pipe" (Floody, 2000). Immediately north of the Braden Diatreme is a barren dacite stock that is brecciated at its contact with the Braden Diatreme which is "irregularly rooted within a barren dacite at a depth of ~2,000 m" (Maksaev et al., 2004).

**Lamprophyre Dykes** - The youngest intrusions ( $3.85 \pm 0.18$  to  $2.9 \pm 0.60$  Ma; Cuadra, 1986; Maksaev et al., 2004) at El Teniente are post-mineralisation lamprophyre dykes which cross cut all other units (Skewes et al., 2002; Rabbia et al., 2009; Stern et al., 2010; Vry et al., 2010). They are composed of amphibole and plagioclase phenocrysts within a fine groundmass of plagioclase, amphibole and biotite (Camus, 1975; Skewes et al., 2002; Vry et al., 2010). Their intrusion is believed to have been in part lithologically controlled, often emplaced "through fractures located along zones of weakness associated with lithological contacts which control dip" (Camus, 1975).

### 2.5.6 Veins

Although not a primary focus of this study, a summary of the vein classifications and terminology used at El Teniente is briefly provided. Broadly speaking, the Teniente vein stockwork is typical of porphyry Cu deposits globally (e.g., Gustafson and Hunt, 1975). Early magnetite veins are cut by a stockwork of "quartz- anhydrite-sulfide veins that have Na-K feldspar-, biotite- and chlorite-bearing alteration assemblages" which are termed 'late magmatic' at El Teniente (Cannell et al., 2007). The biotite veins "are cut by well-mineralized, sulfide-rich veins with distinctive phyllic alteration halos" (principal hydrothermal) that are in turn cut by "mineralized veins with a diverse gangue and sulfide mineralogy and associated with a second generation of phyllic alteration (late hydrothermal stage)" (Cannell et al., 2007).

To date, three vein classification schemes (El Teniente Mine Classification, 2003; Cannell et al., 2005; Vry et al., 2010) have been developed (Fig. 2.16). Despite these schemes being similar, inconsistencies in the relative timing and mineral assemblages remain. This may be due to intense alteration overprints and/or repetitive veinlet reactivation making some veins difficult to assign to a particular stage, or a lack of cross-cutting relationships. The Mine Classification identifies fifteen distinctive vein generations over three separate mineralisation stages termed 'Late Magmatic' stage

(associated with potassic alteration), 'Principal Hydrothermal' stage (related to quartz-sericite alteration) and the 'Late Hydrothermal' stage. Approximately 60%, 30% and 10% of the total Cu at El Teniente is suggested to have been introduced during these stages, respectively. Vry et al. (2010) also classified veins into the three paragenetic stages they termed 'the pre-mineralisation stage', 'the main mineralisation stage' and 'the late mineralisation stage' and correlates these to the development of the deposit.

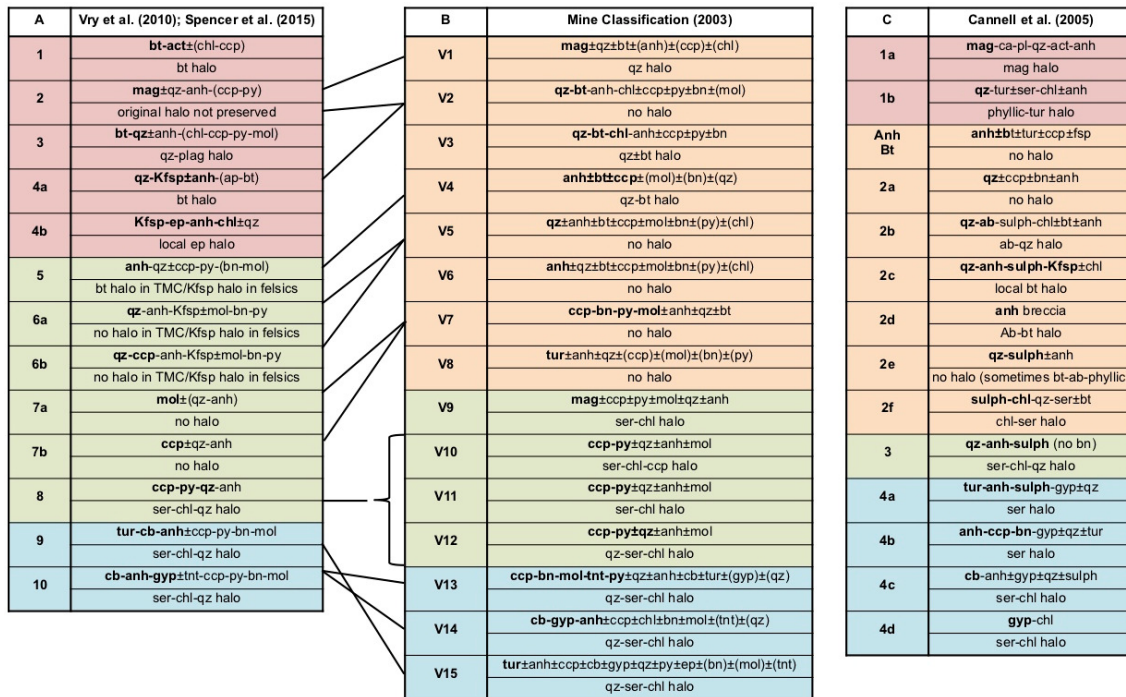


Fig. 2.16 Summary of the existing vein classification schemes for El Teniente: **a**) Scheme developed by Vry et al. (2010), the same scheme used in this study and that by Spencer et al. (2015); **b**) Mine geologists scheme; **c**) Alternative scheme proposed by Cannell et al. (2005). The paragenetic stages are shown in the following colours: Red= Pre-mineralisation; Orange= Late Magmatic as defined by the mine geologists and Cannell et al. (2005); Green= Principal Hydrothermal; Blue= Late Hydrothermal. Reproduced after Spencer et al. (2015).

## 2.6 Breccias

Pipe-like mineralised igneous, magmatic-hydrothermal breccias have been emplaced into the TMC during the same time period as the felsic-intermediate porphyry intrusions (Stern et al., 2010). Extensive mapping and logging by mine geologists has shown that each of the felsic-intermediate intrusions at El Teniente has its own breccia complex. Breccias are often the highest-grade parts of the orebody and are therefore where underground mining is often centred on (Cannell et al., 2007). These breccia complexes are typically peripheral to, or on the apices of the felsic intrusions (Vry et al., 2010). Unusually shaped dacite clasts with vermiform morphologies (e.g., Fig. 4d of Cannell et al., 2007) are documented in some anhydrite breccias, and are believed to be juvenile magmatic clasts proving a genetic association between breccias and felsic

intrusives. Most dacite clasts, however, are rounded to angular and lack “distinctive wispy or fluidal textures” (Cannell et al., 2007). The roots to these mineralised breccia pipes are below the current deepest level of mining and exploration drilling, and are thought to be derived from the same magma chamber as the felsic porphyries, >4 km below the palaeosurface (Stern et al., 2010).

Codelco División El Teniente have identified five main breccia facies at El Teniente: igneous, biotite, anhydrite, tourmaline and rock flour. A brief description of these are provided below. The largest breccia is the Braden Diatreme, which is surrounded by the mineralised ‘Marginal Breccia(s)’. Other less common breccias include actinolite-, magnetite-, K-feldspar-, quartz-, chlorite-, sulphide- and gypsum-cemented facies (Skewes et al., 2002; Cannell et al., 2005; Vry et al., 2010). Cross-cutting relations show that igneous breccias were the initial facies to form, later followed by K-feldspar, biotite, anhydrite, and tourmaline breccias, which are some of the last breccias to form (Vry et al., 2010).

Breccias are mapped based on their matrix/cement composition, colour, and texture. Contacts between the breccia margins and host rocks can be gradational or sharp. Many breccia bodies cutting the biotite-altered TMC are difficult to recognise because of the lack of any differentiable colour, mineralogical or textural contrast with clasts, and/or they are obscured by subsequent brecciation, intrusive events and alteration (Skewes et al., 2002). Despite these problems, matrix/cement composition is an important classification method because breccias at the deposit are both monolithic and/or heterolithic, with clast nature dependent on the temporal stage in which they were emplaced and the location (Skewes et al., 2002). It is important that these bodies be understood given they not only reflect a complex sequence of events, they also host to a large quantity of high-grade hypogene ore. For example in the Esmeralda sector there is ~3.5 Mt of fine Cu in just one group of igneous breccias, and there are more than ten breccia complexes at the deposit (Skewes et al., 2002).

### 2.6.1 Igneous Breccias

All felsic-intermediate intrusions at El Teniente are associated to some degree with igneous breccias (Fig. 2.17), which are mainly found as vertically elongate shells along the peripheries of these intrusions (Cannell et al., 2005, 2007; Vry et al., 2010). They are observed in the deeper portions of breccia complexes and it is thought these breccia bodies are related to the emplacement of their parent porphyry intrusions, having “probably formed by forceful intrusion-and possible subsequent retraction-of magmas with resulting entrainment and/or collapse of country-rock fragments and reworking of crystallised carapace material” (Vry et al., 2010).

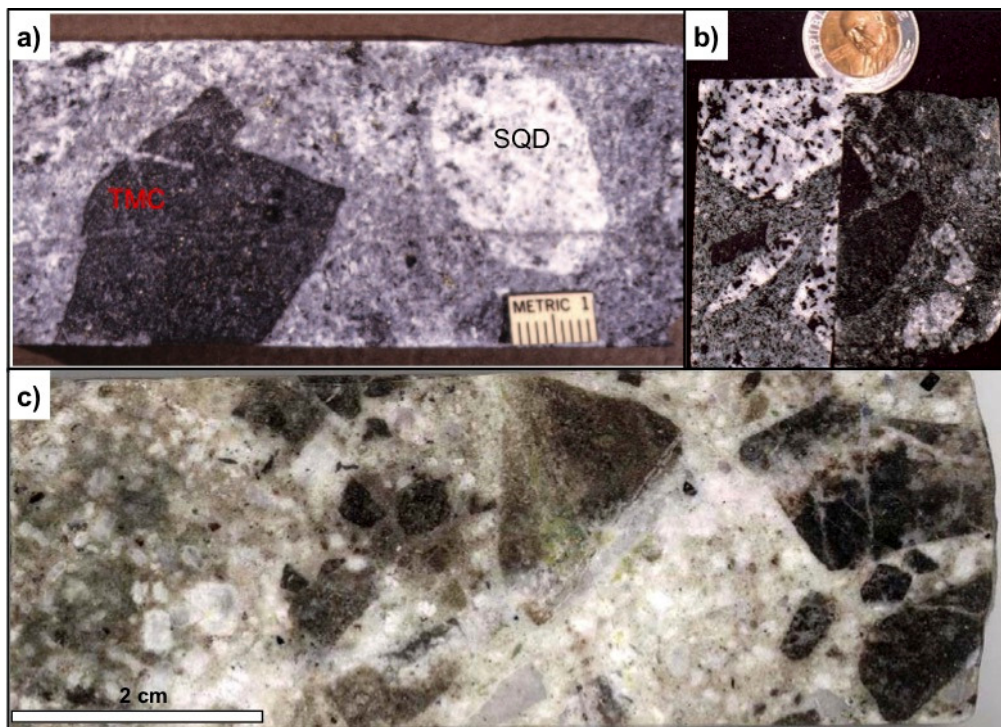


Fig. 2.17 Drill core photographs of igneous breccias at El Teniente: **a)** Microdiorite-cemented igneous breccia from the A-Porphyry with clasts of SQD and TMC rocks. From Skewes and Stern (2007); **b)** Heterolithic igneous breccias with higher portions of felsic (left: DDH1337-106.38 m) and biotite-altered mafic clasts (right: DDH1034-30.48 m). “The lack of secondary biotite in the felsic clasts suggests that the mafic clasts were altered prior to their incorporation in these breccias” (Skewes et al., 2002). From Skewes et al. (2002); **c)** Dacitic igneous cement (plagioclase-quartz-phyric) with veined and biotite-altered TMC wall-rock clasts. Cannell (2004) interpreted a degree of assimilation of the wall-rock clasts took place resulting in the biotite-enriched domains in the igneous cement. Sample is from a dacitic intrusion that has intruded along the margin of the SQD (DDH1676-395.6 m). From Cannell (2004).

The term igneous breccia is applied to fine-grained, equigranular, holocrystalline “igneous”-looking cements containing biotite, quartz, feldspars, anhydrite, chalcopryrite and iron oxides (e.g., Skewes et al., 2002; Skewes and Stern, 2007; Stern et al., 2007). When the cements are dark coloured they are difficult to identify from similar looking mafic clasts and the TMC wall rocks within drill core or underground exposures. Consequently, these breccias are problematic to map and their extent may be

underestimated at present (Vry, 2010). In some areas igneous breccias appear to grade into biotite breccias (Skewes et al., 2002).

Igneous breccias are typically chaotic, cement-supported and consist of subangular to subrounded polymictic mafic and porphyritic felsic clasts that are locally derived from adjacent units between which the breccias were emplaced. This indicates that the breccias post-date the crystallisation of the parent porphyry intrusions and the subrounded nature of some clasts indicates a degree of transport and/or chemical abrasion (Vry et al., 2010). In some areas of the mine, igneous breccias are associated with high-grade Cu mineralisation such as in the Esmeralda sector, where an igneous breccia >60 m wide contains rounded tonalite and TMC clasts in a chalcopyrite-rich “igneous” matrix. Grades are in excess of 1.5% Cu, and the roots have yet to be intersected (Skewes et al., 2002).

### **2.6.2 Biotite Breccias**

Biotite breccias at El Teniente are similar to those at Los Pelambres (e.g., Skewes and Atkinson, 1985; Atkinson et al., 1996) and Río Blanco-Los Bronces (Serrano et al., 1996). Although studies have noted that the TMC has been cut by biotite-cemented breccias (e.g., Cannell et al., 2005), it is particularly difficult to distinguish the breccias from the pervasively biotite-altered fine-grained TMC (e.g., Fig 4a: Cannell et al., 2007). Due to this, these breccias were only documented underground and in drill core at the turn of the century and may therefore have greater extents in the deposit than is currently recognised (e.g., Skewes, 1999; Skewes et al., 2002; Cannell et al., 2005).

At El Teniente, biotite breccias formed relatively early in the development of the deposit, with fragments of biotite breccias found within anhydrite, tourmaline, and rock flour breccias (Skewes et al., 2002; this study). Almost all veining stages have cut the biotite breccias also supporting their early formation. They post-date magnetite-actinolite alteration (containing early magnetite-altered clasts) and their intrusive timing overlaps with the late magmatic stage stockwork-forming event (Skewes et al., 2002; Cannell, 2004). Later events associated with the intrusion of breccias and felsic plutons have often altered the biotite to chlorite, further complicating recognition (Skewes et al., 2002). Potassic alteration and relatively high Cu grades are commonly associated with these breccias. Some biotite breccias around the Braden Diatreme, for example, grade 1 to 3% Cu and 0.03 to 0.06% Mo.

The breccias are believed to have a sub-vertical to vertical orientation close to the contacts of felsic intrusives, in particular the Diorite Porphyries (Cannell, 2004). Biotite breccias are usually monolithic, with intensely biotite-altered clasts of the TMC and in minor cases clasts of felsic intrusives (Skewes et al., 2002; Cannell et al., 2005). Brown biotite is the dominant cementing mineral, with crystals typically only a few mm but they can be up to a few cm (Fig. 2.18). Biotite crystals typically grow from clast margins into open-space, with the remainder of the cavity variably filled with a mixture of sulphides, anhydrite, tourmaline, quartz and feldspar. Where potassic alteration is intense, K-feldspar can become a significant cementing component, and can be replacive in many clasts.

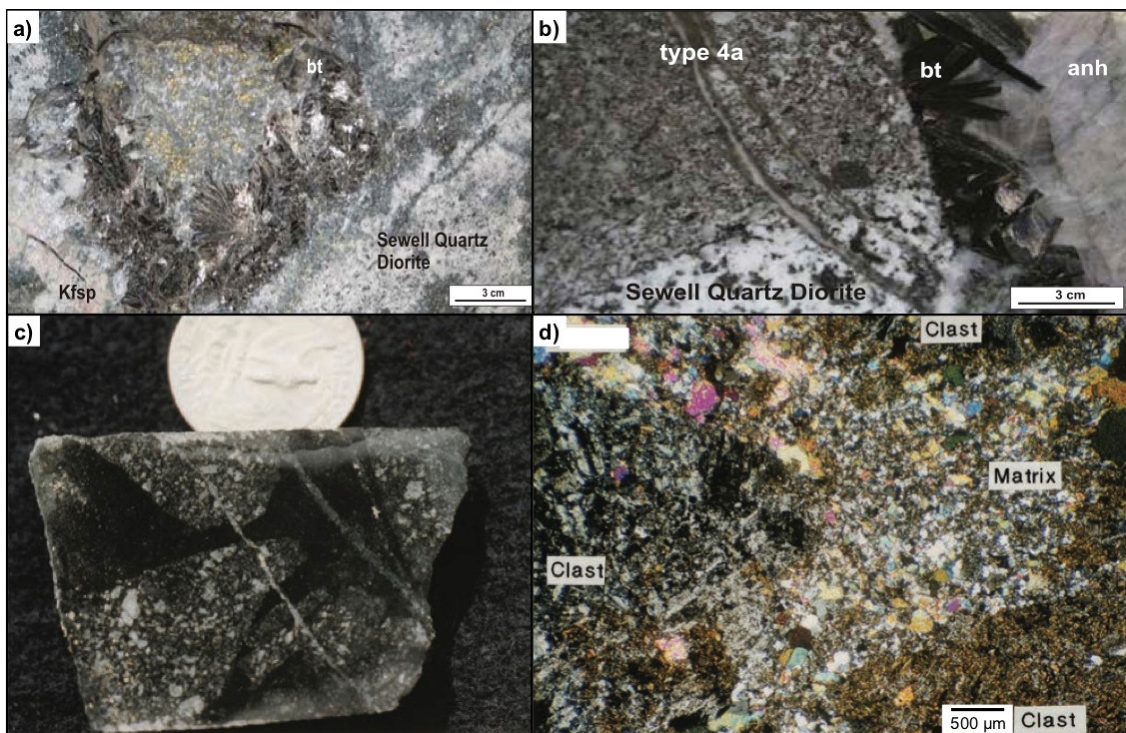


Fig. 2.18 Hand specimens (a-c) and photomicrograph (d) of El Teniente biotite breccias: **a)** Biotite-cemented breccia from the A-Porphyry complex with SQD clasts. From Vry et al. (2010); **b)** Coarse biotite-anhydrite-cemented breccia from the A-Porphyry with clasts of the “Sewell Quartz Diorite in an igneous matrix (A-Porphyry) cut by type 4a veins”. From Vry et al. (2010); **c)** Biotite-altered clasts and Cumineralised porphyritic basalt (TMC) cemented by fine-grained biotite. Clasts and cement are cross-cut by ‘late magmatic’ quartz-anhydrite veins with lesser portions of chlorite (after biotite), chalcopyrite, and pyrite. From Skewes et al. (2002); **d)** XPL photomicrograph showing biotite-rich cement with variable portions of “anhydrite, quartz, feldspar, and chalcopyrite, and biotite-altered gabbro clasts”. From Skewes et al. (2002).

### 2.6.3 Anhydrite Breccias

Anhydrite breccias commonly occur in the upper portions of intrusions above areas that have been previously brecciated by biotite and igneous breccias (Skewes et al., 2002; Cannell, 2004; Cannell et al., 2007; Vry et al., 2010). In contrast to biotite breccias, they are widely distributed across the deposit and are easily recognised and mapped (Skewes et al., 2002). They are, however, absent from the SQD with the exception of those adjacent to the A-Porphyry-breccia complex. Observations in this complex have shown a transition from biotite-dominated breccias at depth to more anhydrite-rich varieties at shallower levels (e.g., DDH1974, this study). Where gradational contacts are present, mapping a well-defined boundary is also difficult. Some believe in fact that they are probably the most common breccia facies at El Teniente (Seguel J., personal communication, 2017).

Anhydrite breccias (Fig. 2.19) are described as being polymictic, ranging from clast- to cement-supported and, depending on their location, contain mm to tens of cm subrounded to subangular clasts of SQD, TDP, TMC, dacite or igneous breccia (Vry, 2010). Clasts are cemented by anhydrite and lesser biotite, tourmaline, quartz, gypsum, carbonate, apatite, chalcopyrite, pyrite, bornite and rutile (Skewes et al., 2002). Cement can account for up to 20 to 30 vol.% of the breccia, depending on spatial location relative to earlier or later breccia bodies. For example, later stage anhydrite breccia cements are dominated by anhydrite±quartz-tourmaline (often grading into tourmaline breccias) which differ from earlier cements that are mostly comprised of anhydrite-biotite (grading from biotite breccias).

Anhydrite-cemented breccias are typically well-mineralised and are usually enriched in Mo, which is focused around clast margins. Cu-sulphide mineralisation sometimes occurs alongside significant molybdenite in the breccia cement “suggesting that late-stage Cu was introduced together with Mo” (Spencer, 2015). Anhydrite-quartz-feldspar-biotite-sulphide veining is also common in the vicinity to these breccia bodies (Skewes et al., 2002; Cannell et al., 2007).

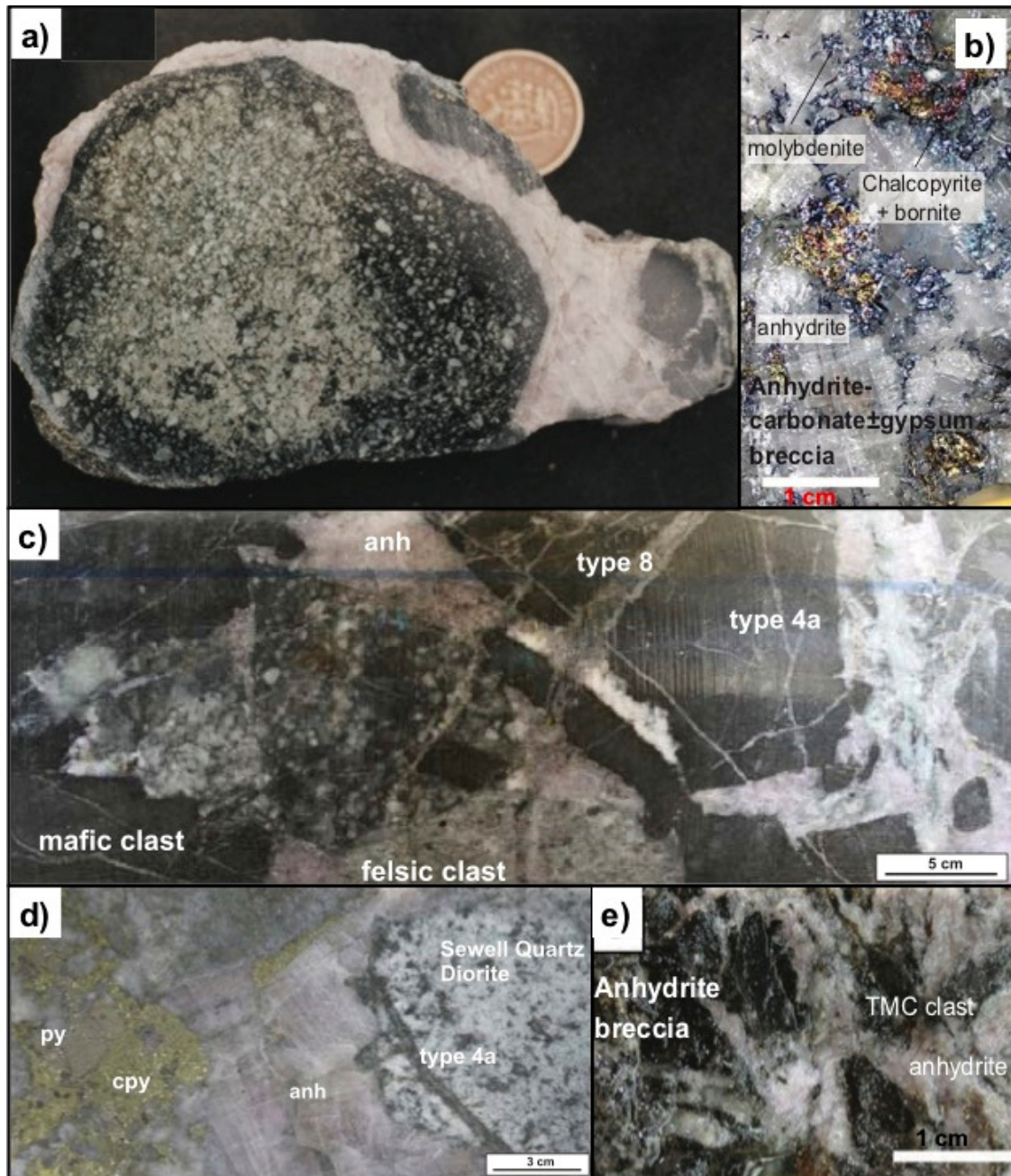


Fig. 2.19 Photographs of El Teniente anhydrite-cemented breccias: **a)** Anhydrite breccia containing a large rounded clast of dacite porphyry altered to biotite around its margins, a clast of dark anhydrite in front of the coin with “numerous inclusions of co-precipitated biotite and chalcopyrite” and a small clast on the right of biotitised mafic rock (Skewes et al., 2002). Sample from a tunnel in the Esmeralda project NE of the Braden Diatreme. From Skewes et al. (2002); **b)** Anhydrite-carbonate- (±gypsum) cemented breccia with bornite-chalcopyrite-molybdenite. From Spencer et al. (2015); **c)** Anhydrite-cemented breccia containing clasts of the TMC encompassing type 4a veins truncated by cement, clasts of igneous breccia and dacite. Type 8 veins cut clasts and cement. Sample is adjacent to the North-Central Diorite Porphyry, from Vry et al. (2010); **d)** SQD clasts containing truncated type 4a veins cemented by anhydrite-chalcopyrite (±pyrite) “with sulfides partly cutting and/or replacing anhydrite” (Vry et al., 2010); **e)** “Anhydrite breccia associated with the carapace of the Southern Diorite” from Spencer et al. (2015).

#### 2.6.4 Tourmaline Breccias

Tourmaline breccias are a common feature of the Teniente district and resemble those from Río Blanco-Los Bronces (Warnaars et al., 1985; Serrano et al., 1996; Vargas et al., 1999; Skewes et al., 2002). They are reported to have vertical extensions of over 1 km; their roots have not yet been intercepted (Skewes et al., 2002). They appear to have formed above or independent of other breccia facies (Vry et al., 2010; this study). Fluid inclusion and stable isotope studies indicate that cementing minerals in these breccias were precipitated from high-temperature magmatic fluids (Skewes et al., 2002; Spencer, 2015) and the subangular nature of the clasts implies relatively little transport. Tourmaline breccias can be monolithic or heterolithic, and clasts are commonly silicified and/or sericitised or bleached. To date, no comprehensive quantitative dataset for tourmaline chemistry from El Teniente, including paragenetic relationships, has been presented. The Marginal Tourmaline and Braden Tourmaline Breccias are described in Section 2.6.5 with the other Braden Diatreme facies.

**Early Tourmaline Breccias** - The early, pre-main mineralisation, crackle tourmaline breccias are small (<1 m drill core intervals) and have been mostly mapped on the eastern side of the deposit, at shallow mine levels. They are spatially situated along the upper margin of the SQD having formed at a similar time to the biotite and anhydrite breccias (Spencer, 2015). However, truly non-mineralised tourmaline breccias, i.e. not Cu-Mo mineralised at any observed depth, have not been identified at El Teniente (Piquer J., personal communication, 2017).

**Diablo Breccias** - The Diablo Breccias are hosted in the TMC, and are situated south of the Braden Diatreme adjacent to a NW-trending porphyritic latite dyke (Fig. 2.20). Some of the highest Mo grades at El Teniente are associated with this breccia (Spencer et al., 2015). It is primarily a tourmaline-cemented breccia although there are areas with more tourmaline-anhydrite, anhydrite and sulphide-cemented portions (Fig. 2.20).

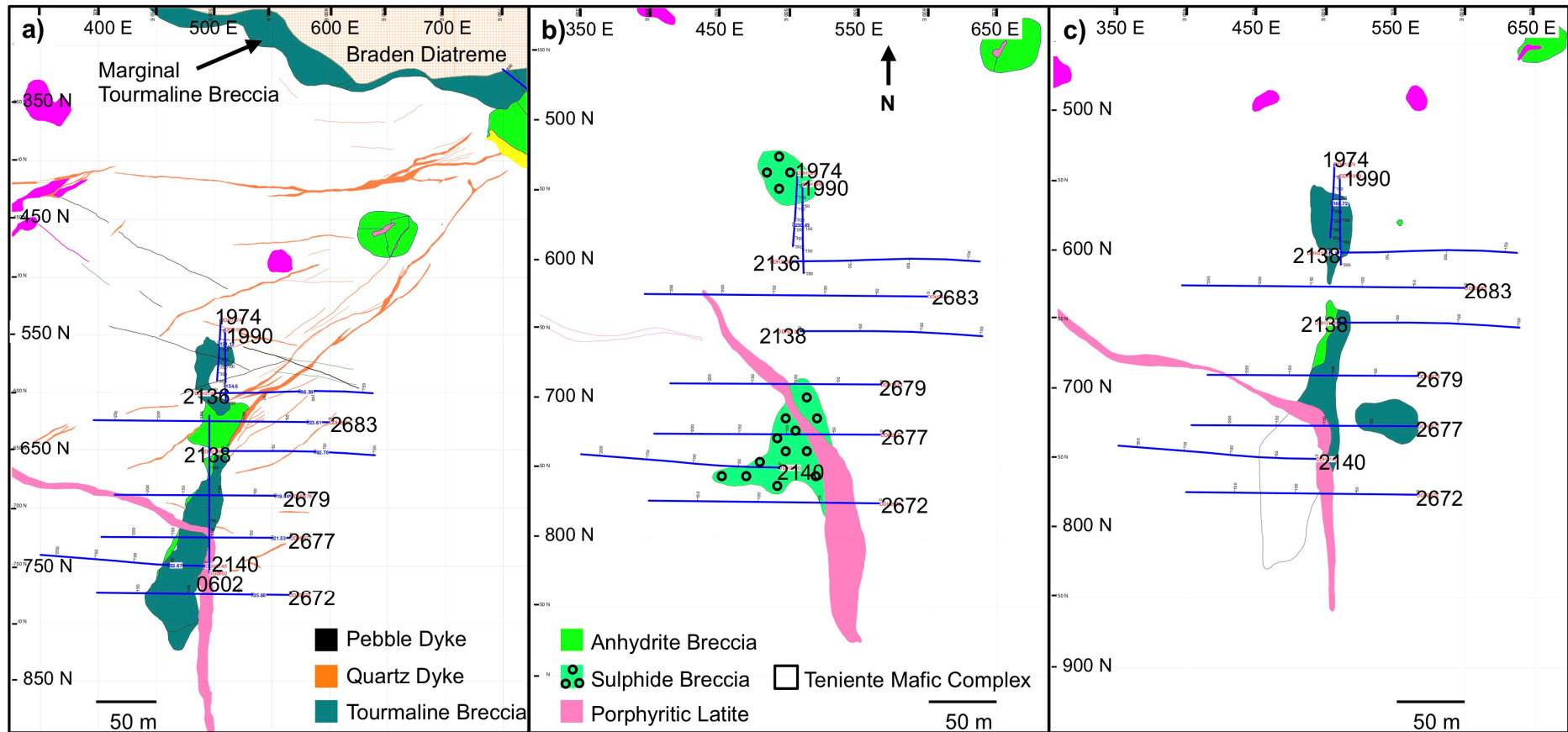


Fig. 2.20 Series of maps showing the Diablo Breccias at different mine levels around level 6 (~2,165 masl): Map a) is the shallowest and map c) the deepest of the three. The maps illustrate that the breccias flare inwards and outwards and are cross-cut by a number of “quartz dykes” (thick quartz veins that are often >30 cm thick, and can be up to >1 m thick (this study)), porphyritic latite and pebble dykes: **a)** Map of caving level (‘TTE6\_Hundimiento’); which shows mainly tourmaline-cemented breccia with minor anhydrite-cemented portions; **b)** Level Teniente Sub-6 where sulphide-cemented portions are dominant. With increasing depth the porphyritic latite also increases in width; **c)** Map from Teniente 6 transport level (‘TTE6\_Accareo’) - mixture of tourmaline- and anhydrite-cemented portions. Drill holes used in this study are shown as blue lines. Maps are plotted on the local mine grid which is oriented 14.5°E of geographic north. Maps courtesy of Codelco División El Teniente.

**La Huifa-La Negra (including outcropping Extravío Breccia)** - Re-drilling at La Huifa, between 2012 and 2014, led to the discovery of a series of steeply dipping north trending porphyry dykes and hydrothermal breccia pipes larger than previously thought (Floody R., personal communication, 2017). These porphyry-breccias have intruded into propylitically-altered volcanic packages of the Farellones Formation ~1.5 to 2 km NE of El Teniente and 1.5 km east of the Recursos Norte project (Cannell, 2004; Codelco, 2013, 2014; Pardo, 2015). These are structurally located at the intersection of the NE trending 'S fault' and the WNW trending 'La Huifa Fault' (Seguel J., personal communication, 2017).

Advanced drilling has shown that this area is evolving into a hypothesised mineralised cluster comprised of breccia orebodies and associated porphyries called the Cerro Extravío Cluster (Codelco, 2015). The full size of the La Huifa orebody is currently unknown, however it has been suggested to have the potential of 200 Mt at 0.8 to 1% Cu (Codelco, 2013). The Extravío tourmaline breccia pipe, has already been shown to contain 11.1 Mt (resource) @1% Cu and 0.039% Mo (Floody and Huete, 1998; Cannell, 2004). Higher concentrations of Cu-Mo are associated with hydrothermal tourmaline-anhydrite-quartz breccias at La Huifa. These contain variable chalcopryrite-bornite±molybdenite and sodic-calcic alteration (albite-actinolite) which is strongly associated with chalcopryrite-bornite mineralisation (Pardo, 2015). Aside from the La Huifa porphyry-breccia cluster, another porphyry-breccia project currently being evaluated, near Rajo Sur open pit, SE of the Braden Diatreme, is Matancillas Alto which has a "divisional target of 40 Mt @0.6% Cu" (Vidakovic, 2013).

### **2.6.5 Braden Breccia Complex**

By far the largest feature at El Teniente is the late to post-mineralisation Braden Diatreme. Lying at the centre of the Teniente deposit, this hosts the underground infrastructure of the mine, with mining taking place around its peripheries (Floody, 2000). In the description of this unit, the following terminology will be used: Braden Diatreme refers to the structure and the Braden Breccia Complex to the breccia facies/brecciated material which fills the structure.

Due to the Braden Diatreme being subeconomic, some of the most detailed published work was by Lindgren and Bastin (1922), Howell and Molloy (1960) and Camus (1975). Lindgren and Bastin (1922) first recognised the Braden Diatreme on surface and within the upper levels of the mine. They termed it the "Braden Explosive Vent" that was infilled by 'Braden Tuff'. These authors were also the first to describe the presence of stratification in the body and they also identified that the breccia was not a favourable site for Cu-Mo mineralisation. Howell and Molloy (1960) re-named the structure the

“Braden Breccia” and the brecciated/fragmented material that infilled it as the “Braden Formation”.

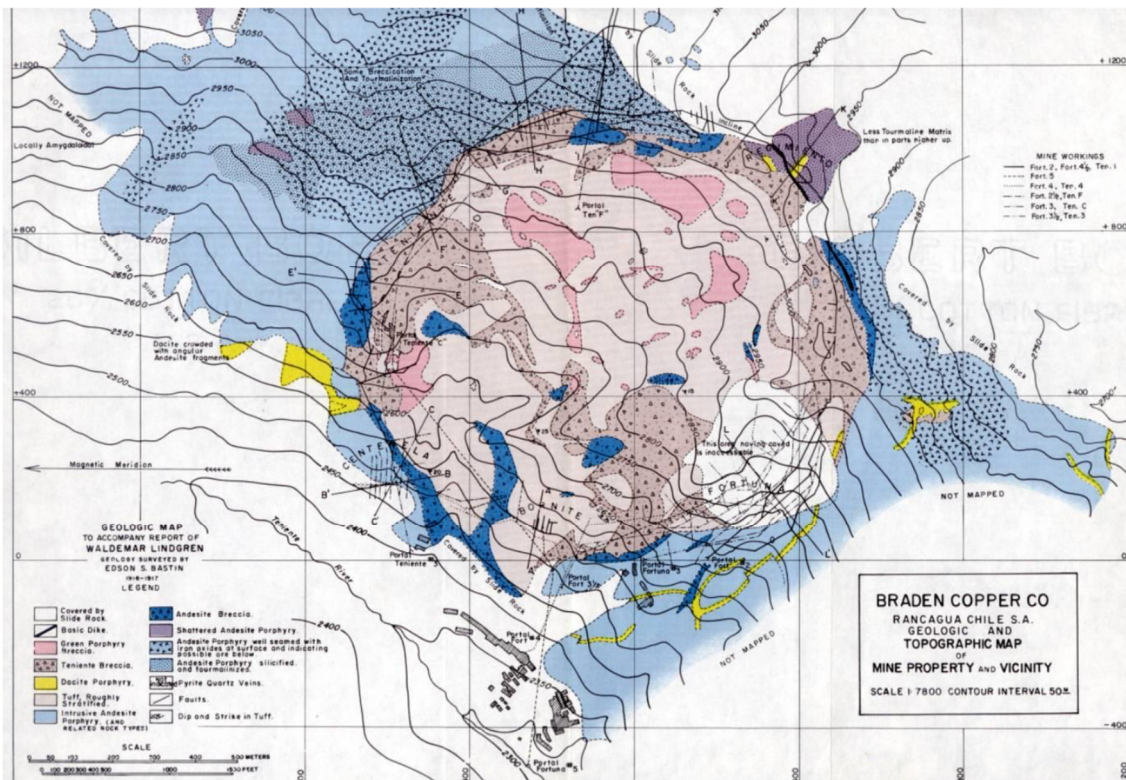


Fig. 2.21 Early geological map of the Braden Diatreme and surrounding orebody by the Braden Copper Company (courtesy of Codelco), largely based on mapping by Lindgren and Bastin (1922). The individual facies within the heterogeneous Braden Diatreme were recognised at this early stage but have been mapped since as a single unit, most likely due to its limited economic significance.

Despite the early recognition of multiple breccia facies in the Braden Diatreme (e.g., Lindgren and Bastin, 1922), for several decades most work was focussed on recognising the high-grade areas found on its margins (Cuadra, 1986; Floody, 2000). Only two units were therefore distinguished and mapped until the 1990’s, these being the “Marginal Breccia” (1 to >2% Cu) and the “Braden Breccia” (0.2 to <1% Cu), the latter representing >95 vol.% of the Braden Diatreme (Floody R., personal communication, 2017).

As a result of continued development and expansion at El Teniente, particularly adjacent to the Braden Diatreme, there have been a number of internal Codelco geological studies aimed at lithologically, structurally and geotechnically characterising the Braden Breccia Complex. This was to help predict how the Braden Diatreme as a whole, and how individual lithologies will respond to future expansion projects and help to predict and mitigate detrimental effects (e.g., Uribe, 2000; Uribe and Floody, 2000). This involved a compilation of historical maps, ~2,763 m of new diamond drill holes and the development of a preliminary geological model between the years 1999 to 2000, presented in an internal report by Floody (2000).

Using macro and microscopic features of the breccia facies (e.g., Laznicka, 1988), including the dominant composition of matrix/cement and textural characteristics /fabrics (shape, size and composition of clasts, clast: matrix ratio etc.), up to ten breccia facies were described and mapped (Uribe, 2000; Floody, 2000). These have been divided into 'Major', 'Minor' and the Marginal Breccias below.

Major facies (Table 2.3):

- Braden Sericite Breccia (BBS)
- Braden Chlorite Breccia (BCB)
- Braden Tourmaline Breccia (BTB)

Minor facies (Table 2.4):

- Fine Sericite Braden Breccia (FSBB)
- Blocky Braden Sericite Breccia (BBSB)
- Blocky Braden Tourmaline Breccia (BBTB)
- Braden Sulphide Breccia (BSB)

Marginal Breccias (Table 2.5):

- Marginal Tourmaline Breccia (MBXTU)
- Marginal Chlorite Breccia (MBXCL)
- Marginal Anhydrite Breccia (MBXANH)

### **Major Lithologies**

The major lithologies of the Braden Diatreme account for approximately 80 to 90 vol.% of its total volume (Floody R., personal communication, 2017). The “matrix” or “rock flour matrix” is largely composed of finely ground/comminuted rock fragments, with a composition reflecting the brecciated fragments±host rocks.

**Braden Sericite Breccia (BSB)** - This is one of the most common units in the Braden Diatreme. It is matrix-supported with a chaotic texture. The matrix is largely composed of sericite±quartz, a high portion of fine clasts/particles <1 mm, micas (muscovite/Fe illite-illite), and minor more variable amounts of chlorite (clinochlore), anhydrite, gypsum, and a variety of clays, thought to have formed from the physical attrition of fragmented rock during explosive brecciation (Floody, 2000). Clasts include TMC, dacites, and earlier hydrothermal breccias (Vega and Maksaev, 2003), which range from rounded to subrounded and are mostly <30 cm in diameter. Large clasts can be in excess of 1 m. Varying degrees of texturally destructive quartz-sericite-pyrite and argillic alteration has overprinted all clasts. The unit has sharp contacts with all other units in the Braden Breccia Complex, apart from with the Braden Tourmaline, Sulphide

and Chlorite Breccias where more transitional contacts are observed (Floody R., personal communication, 2017). Stratification has been observed in this unit from present-day surface to a depth of 1,100 m (Vega and Maksaev, 2003).

**Braden Chlorite Breccia (BCB)** - The Braden Chlorite Breccia is a later hydrothermal overprint of the Braden Sericite Breccia. Combined, they comprise >80 vol.% of the Braden Diatreme. The BCB is mainly situated in the southern part of the Braden Diatreme and at deeper levels in the pipe (Floody, 2000).

**Braden Tourmaline Breccia (BTB)** - The BTB occurs as irregular tabular bodies at all levels throughout the Braden Diatreme. It has a generally concentric distribution largely sub-parallel to the pipe margins (Floody, 2000). It is a chaotic, cement-supported breccia. Dark grey to black microcrystalline tourmaline is intergrown with quartz, anhydrite and lesser chlorite-sericite-chalcopyrite cement (Table 2.3). The clast population is the same as in the Braden Sericite and Chlorite Breccia, except clasts have undergone comparatively more silicification and minor tourmalinisation (Table 2.3).

Higher Cu grades compared to other Braden Diatreme facies (except the Braden Sulphide Breccia) are found within the BTB. Some of these higher-grade areas may at some point become economically mineable, provided they are accessible and it is possible to extract the ore around support infrastructure (Floody R., personal communication, 2017). The exact formation mechanism of this breccia facies is still unknown although it could be due to the following:

- a) Physical brecciation event re-brecciating existing material (e.g., Floody, 2000).
- b) Chemical brecciation/replacement originating from percolating fluids that 'partially replaced the rock flour matrix of these pre-existing breccias by small tourmaline crystals' (Lindgren and Bastin, 1922; Floody, 2000). Lindgren and Bastin (1922) also highlighted that selectively replacing the rock flour matrix with sub-mm-sized tourmaline produces the characteristic grey to black tourmaline cement that is distinctive of many tourmaline breccias associated with porphyry deposits. It should be noted that no direct evidence supporting this replacement process has so far been presented.

Table 2.3 Characteristics of the main lithologies comprising the Braden Diatreme. From internal SGL-I-123/03 (2003) report.

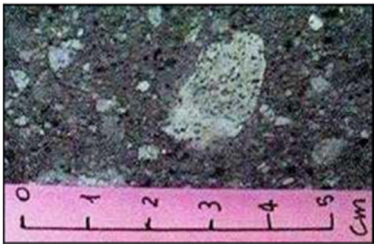
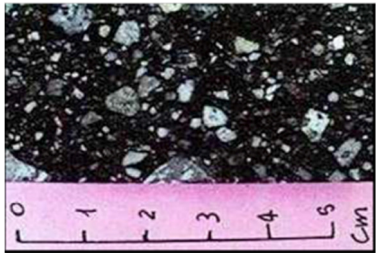
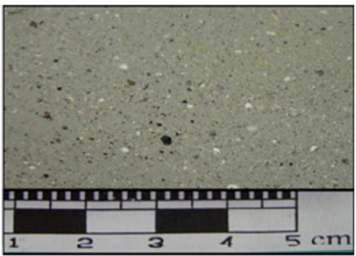
Major lithologies		Braden Sericite Breccia	Braden Chlorite Breccia	Braden Tourmaline Breccia
General Fabric		Clast- and matrix-supported. Variable, similar to concrete in appearance.	Clast- and matrix-supported. Variable, similar to greenish concrete in appearance.	Cement-supported. Speckled, sharply altered fragments.
Macroscopic appearance				
Matrix or cement	Rock vol.%	60-80	20-60	50-80
	Colour	Light grey to brownish	Grey-brown-green	Black-grey
	Comp.	Sericite, quartz±tourmaline-chlorite	Sericite, chlorite, quartz±tourmaline	Tourmaline, quartz, chlorite, sulphides
	Fine particles	High proportion	High proportion	High proportion
	Alteration	Sericite/argillic	Sericite/argillic	Argillic/sericite
Clasts	Rock. Vol.%	20-40	40-80	20-50
	Size	2-5 mm	0.5-5 cm	2-5 mm
	Comp.	Polymictic	Polymictic	Polymictic
	Shape	Rounded to subangular	Rounded to subangular	Rounded to subangular
	Alteration	Sericitic/argillic, tourmalinisation and chloritisation	Sericitic, sometimes intense argillic, chloritisation and tourmalinisation	Argillic and silicification
	Occurrence	Occupies most of the Braden Breccia Complex, predominantly in the northern half and upper levels.	Widely distributed, irregular bodies, mainly in the southern part and towards deeper levels of the complex. Also observed as thin dykes.	Irregular, tabular, widely distributed bodies to an extent in annular fractures and towards the margin of the Braden Complex. Fuzzy and transitional contacts with the Braden Sericite Breccia.

Table 2.4 Characteristics of the minor lithologies comprising the Braden Diatreme. Reproduced after internal SGL-I-123/03 (2003) report with additional details added.

Major lithologies		Blocky Braden Tourmaline Breccia	Blocky Braden Sericite Breccia (aka pebble dykes)	Fine Sericite Braden Breccia	Braden Sulphide Breccia
General Fabric		Clast-supported. Blocky clasts. Cu-Mo mineralisation can be important.	Clast-supported.	Matrix-supported. Fine, homogenous, similar to a tuff.	Clast- and matrix-supported. Speckled with metallic lustre.
Macroscopic appearance					
Matrix or cement	Rock vol.%	10-60	10-60	>90	20-50
	Colour	Dark grey/black	Light brown to grey	Light brown to cream/grey	Grey to metallic, iridescent
	Comp.	Tourmaline, quartz±sericite, chlorite, pyrite, chalcocopyrite	Sericite, quartz ±tourmaline-sulphides	Sericite, quartz ±tourmaline-sulphides	Cu-sulphides (tennantite, tetrahedrite, chalcocopyrite, bornite), pyrite, anhydrite, tourmaline, quartz, sericite, gypsum, chlorite
	Fine particles	Variable	Variable	High proportion	Low proportion
	Alteration	Argillic/sericitic	Sericite/argillic	Sericite/argillic	Quartz-sericite (silicification)
Clasts	Rock. Vol.%	40-90	40-90	<10	50-80
	Size	2-10 mm, 1>10 cm	2-10 mm, 1>10 cm	2-10 mm	2-5 mm, 0.5- >10 cm
	Comp.	Polymictic	Polymictic	Polymictic	Polymictic
	Shape	Subrounded to subangular	Subrounded to subangular	Subrounded to subangular	Subrounded to subangular
	Alteration	Sericite/argillic	Sericite/argillic	Sericite/argillic/tourmalinisation	Sericite/argillic±silicification
	Occurrence	Irregular and tabular bodies, sharp contacts or transitional towards finer breccias. Found as a series of subvertical dyke-like bodies of variable thickness. Due to the large size of the clasts, they are very difficult to identify in drill core.	Dykes of little thickness with sharp contacts. Spatially, these are only found on some levels of the mine and represent ~5 vol.% of the Braden Diatreme (Vega and Maksaev, 2003).	Generally thin bodies, tabular injections. Looks like it may have formed as a result of injections of fine material (Floody, 2000; this study). One of the largest bodies recognised covers an area of 350×150 m and has a vertical extension of >120 m.	Body of cylindrical shape, subvertical, recognised in the central part of the complex, between levels Ten Sub 6 (~2,165 masl) and Ten 4 (2,346 masl). Located in different parts of the Braden Diatreme, estimated to comprise 2 to 3 vol.% of the Braden Diatreme (Vega and Maksaev, 2003).

## **Marginal Breccias**

Surrounding the rock flour matrix-dominated breccias are the Marginal Breccia(s), which was previously termed “pre-pipe-breccia” by Howell and Molloy (1960). It is frequently referred to as the ‘Marginal Tourmaline Breccia’ (Fig. 2.22) given that it is the most common marginal facies and the cement is usually dominated by tourmaline. Spatially, it ranges from 1 to 60 m thick and tapers down to 5 to 10 m at greater depths (Maksaev et al., 2004). Clasts of the Marginal Breccias have been found within the Braden Sericite Breccia, indicating that it was emplaced prior to the formation of the Braden Diatreme (Howell and Molloy, 1960; Floody, 2000). The exact spatial extent of the Marginal Breccias, however, before the emplacement of the Braden Diatreme will never be truly known. Given that emplacement was likely structurally controlled, Cannell (2004) suggested that it was “probably similar to its present day distribution” having been emplaced into ring fractures.

Fluid inclusions from quartz within the Marginal Breccias are highly saline, homogenise at temperatures of ~400°C, which when combined with stable isotope analysis of cement-hosted anhydrite and tourmaline suggests the breccia formed from magmatic fluids (Skewes et al., 2002). The main difference between this and other Braden Diatreme units is that the Marginal Breccias are generally comprised of angular clasts from the adjacent TMC, which are commonly silicified and bleached. The Marginal Breccia is subdivided into tourmaline, chlorite and anhydrite facies discussed below. All of these breccias are mineable, and are often high-grade.

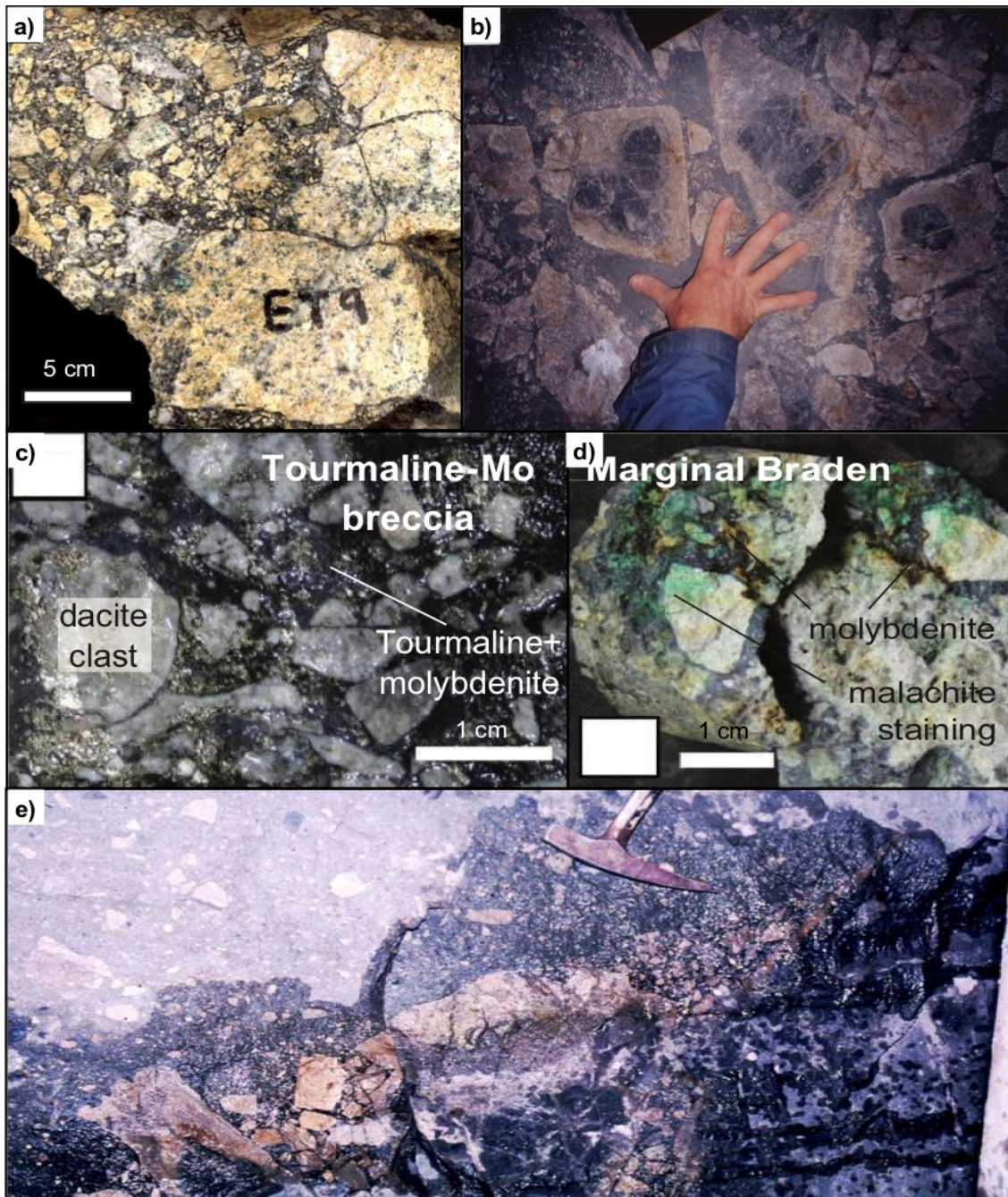
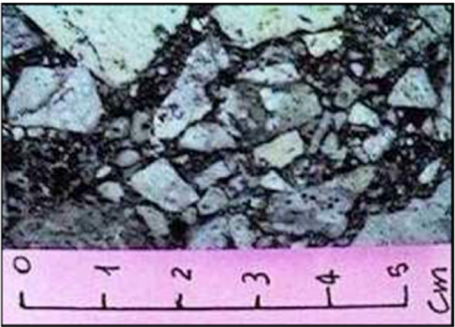
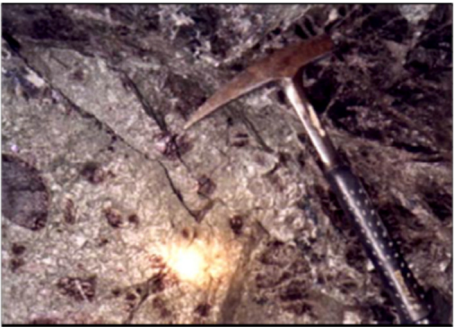


Fig. 2.22 Photographs of the Marginal Breccias: **a)** Monolithic Marginal Tourmaline Breccia with angular sericite-altered clasts cemented by tourmaline, anhydrite, quartz and Cu-sulphides. From Cannell (2004); **b)** MBXTU with clasts of biotite-altered TMC “that have developed strongly bleached borders consisting almost completely of sericite and quartz, along with minor carbonates and clay” (Skewes et al., 2002). Photo taken on the NE margin of the Braden Diatreme. From Skewes et al. (2002); **c)** Black tourmaline-molybdenite cement, from the Marginal Breccia on the western rim of the Braden Diatreme. From Spencer et al. (2015); **d)** Mo-rich oxidised and altered Marginal Breccia from the western rim of the Braden Diatreme. From Spencer et al. (2015); **e)** Contact between the monomictic, clast-supported Marginal Breccia (bottom), and a ‘cross-cutting clast-poor, rock flour matrix-supported Braden breccia (top)’. From Cannell (2004).

Table 2.5 Main features of the Marginal Breccias. From internal SGL-I-123/03 (2003) report, with additional details added.

Major lithologies		Marginal Tourmaline Breccia	Marginal Chlorite Breccia	Marginal Anhydrite Breccia
General Fabric		Clast- and cement-supported. Mottled and dark black-grey.	Clast-supported.	Clast-supported.
Macroscopic appearance				
Matrix or cement	Rock vol.%	20-50	20-40	20-30
	Colour	Grey-black	Varying shades of grey	White-grey
	Comp.	Tourmaline, quartz ( $\pm$ chlorite, anhydrite, chalcopyrite)	Sericite, quartz, chlorite ( $\pm$ tourmaline, anhydrite, chalcopyrite, bornite)	Sericite, quartz ( $\pm$ tourmaline, anhydrite, chalcopyrite, bornite)
	Fine particles	Moderate	Low	Moderate
	Alteration	Quartz-sericite	Argillic	Argillic
Clasts	Rock. Vol.%	50-80	40-90	70-80
	Size	2->20 mm	2-10 mm, 1>10 cm	2->20 mm
	Comp.	Dacite-andesite	Mostly andesite $\pm$ dacite	Dacite-andesite
	Shape	Subrounded to subangular	Subrounded to subangular	Subrounded to subangular
	Alteration	Silicification/argillic	Chlorite-sericite and minor silicification	Silicification/argillic
	Occurrence	Marginal zone of the Braden Complex; forming a ring of breccias. It hosts high-grade Cu mineralisation which has been intensely exploited, and during the early days of the discovery of El Teniente areas reportedly contained up to 30% Cu due to the bornite-chalcopyrite-rich cement (Floody R., personal communication, 2017).	Marginal zone of the Braden Breccia Complex. Easily identified from its characteristic green (chloritised) clasts. This facies is typically smaller, with thicknesses ranging from 10 to 15 m (Floody, 2000).	The least common Marginal facies (Floody, 2000). Mainly in the peripheral zone of the northern part of the Braden Breccia Complex. Commonly in contact with the "dacitic porphyry".

## **Braden Diatreme size and structures**

**Size** - The Braden Diatreme is shaped like an inverted cone which, on surface, has a diameter of ~1,200 m, which progressively decreases to ~700 m at ~1,900 masl (Floody, 2000). Surface topography is sloping, with the eastern margin at ~3,300 masl, whilst the western margin is at ~2,300 masl. The pipe itself is asymmetric, with the eastern margin almost vertical whilst the remainder of the pipe dips concentrically inwards at approximately 60 to 80° (Howell and Molloy, 1960; Camus, 1975). One of the deepest drill holes at El Teniente has intersected the Braden Diatreme at 1,400 m below surface where it is still in excess of 600 m in diameter (Cannell et al., 2005). Based on estimates of local exhumation rates (e.g., Skewes and Holmgren, 1993; Kurtz et al., 1997), morphological reconstructions of nearby volcanic centers (Rivera and Falcón, 1998), and evidence from fluid inclusions from the Braden Diatreme (Cannell, 2004), it is believed that ~2,000 m of erosion has taken place at El Teniente since 5 Ma. The Braden Diatreme is therefore likely to have had an initial vertical extent in excess of 3.5 km (Skewes and Holmgren, 1993; Stern et al., 2010).

Based on spatial relations, the Braden Diatreme is estimated to contain ~3 Bt of fragmented and milled rock (Maksaev et al., 2004). From an economic perspective, although it is been considered largely uneconomic (Cannell et al., 2005), Skewes and Stern (2007) highlight that it contains “over 1 Mt of fine Cu at grades of >0.7% Cu, and a total of >5 Mt of Cu at an average grade of 0.4%, with an additional >1 Mt of high-grade (>1%) Cu in the Marginal Breccia rim to this pipe”. Admittedly, this is low by El Teniente standards, but it still represents a significant resource.

**Structures** - The structures in the diatreme are either associated with syngenetic to late-stage fluid pulses or related to the subsidence via the surrounding active caving operations. The most common structures are minor faults and late veinlets which are often superimposed on one another. The veinlets are composed of gypsum with lesser pyrite, quartz, ankerite, tourmaline, haematite, Cu-sulphides and sericite (Howell and Molloy, 1960), and are associated with a phase of late ‘Póstuma’ hydrothermal alteration in the formation of the deposit.

The syngenetic structures are related to the consolidation processes immediately after the formation of the diatreme. The two most common features encountered are stratification sporadic cavities. The stratification, which is easily seen on surface (Fig. 2.23), and in the upper levels of the Braden Diatreme, shows “graded or cross-bedded” structures and in some of the upper levels there are ‘channels filled with tuffaceous material that cut the coarser zones of the pipe’ (Camus, 1975). Horizontal bedding (Fig. 2.23) was once thought to be consistent across the pipe, but it is now known to

dip inwards towards the centre where it is at its flattest as a result of subsidence (Howell and Molloy, 1960).

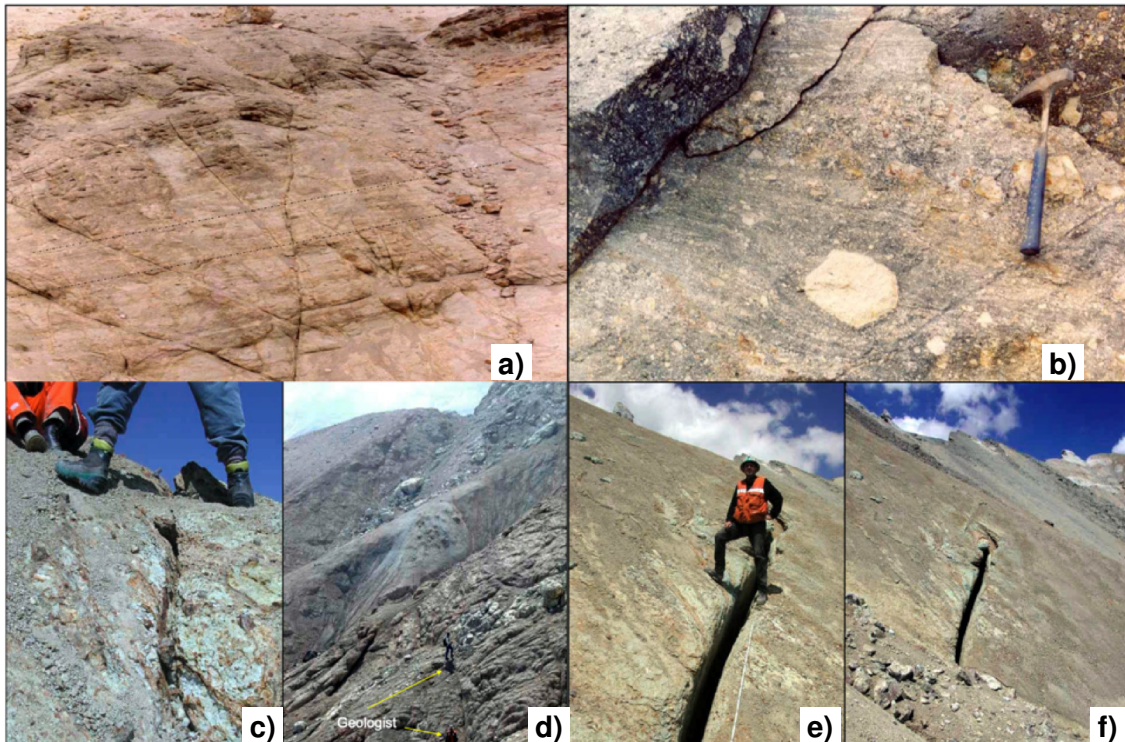


Fig. 2.23 Outcrop photographs showing syngenetic and subsidence-related structures in the Braden Diatreme, from Floody (2000): **a)** General appearance of the Braden Sericite Breccia unit with faint stratification outlined by dotted line; **b)** Braden Tourmaline Breccia showing banding around a fragment; **c)** Looking south with the 'F1 Fracture' where the opening is ~10 cm; **d)** Looking to the north showing the extension of the F1 Fracture; **e)** Partial view to the south of the 'F3 Fracture', located on the eastern edge of the Teniente cavity; **f)** Photograph looking south of the F3 fracture. These fractures are the result of active deformation of the Braden Diatreme.

The number and size of cavities/caverns developed in different breccia units inside the Braden Diatreme seems to be dependent on their location. Cannell (2004) described some as having volumes "up to 300 cubic metres". Those located largely at the edge are smaller than those towards the centre. At the time of discovery, some of these cavities still contained saline waters, the largest being on Teniente-6 (2,165 masl) which is several m<sup>3</sup> in size (Fig. 2.24b). Inside these are euhedral crystals of gypsum up to 6×1 m (length × breadth) whilst the walls are covered in euhedral and subhedral crystals of sulphides (pyrite, chalcopyrite, bornite), tennantite-tetrahedrite, sphalerite, gypsum, barite, quartz, anhydrite, apatite and calcite (Floody, 2000). The large gypsum crystals also often contain fluid inclusions several cm long. The caverns were/are only discovered when they were intercepted during mining development, so, the exact extent or distribution of all caverns in the Braden Diatreme is unknown. Features resembling fumaroles were also documented on surface during the initial stages of mining at El Teniente (Floody R., personal communication, 2017).



Fig. 2.24 Braden Diatreme crystal caverns and mineral specimens: **a)** View of one of the caverns from one of the development drives in the Braden Diatreme on level 6 (2,165 masl). This side of the cavern has been blocked up and the inside is shown to the right; **b)** Crystal cavern on level 6, with large gypsum crystals growing inwards and the walls coated in a mixture of coarse tetrahedrite and Cu-sulphides shown in d, e and f; **c)** Gypsum crystal from one of the caverns with a cm sized pocket of fluid inside it; **d)** Euhedral pyrite-quartz specimen from one of the level 6 crystal caverns in the Braden Diatreme on public display in the Sewell Museum; **e)** Chalcopyrite with minor tetrahedrite from the level 6 crystal cavern; **f)** Museum sample at Sewell showing tetrahedrite, calcite, pyrite and chalcopyrite crystals.

### Formation of the Braden Diatreme

Lindgren and Bastin (1922) were the first to propose a volcanic origin for the Braden Diatreme, suggesting the violent interaction of magma with meteoric waters. The occurrences of obsidian and tuffaceous material also lead Camus (1975) to propose an explosive origin and the formation of a volcanic vent. Sillitoe (1985) was the first to classify the Braden Pipe as a diatreme, believing it to be generated in a manner “that complies with Daubrée’s (1891) original definition of a diatreme as a vent produced by volcanic explosion”.

This classification was based on its geometry and facies characteristics (e.g., poorly sorted, fine-grained rock flour matrix-supported breccia with well-rounded heterolithic rock fragments and a tuffaceous component). Sillitoe (1985) suggested that the Braden Diatreme may have formed as the result of interaction between magma and external water (phreatomagmatism), the latter from what is “believed to have been an aquifer charged with groundwater at depths of 1 to 2 km, or even more, beneath the palaeosurface”. The presence of large fault zones nearby may have also facilitated

groundwater ingress. There has, however, been no direct evidence published for a direct involvement of meteoric waters in the formation of the Braden Diatreme.

Additional studies supporting a diatreme origin include Floody (2000), Vega and Maksaev (2003), Maksaev et al. (2004) and Cannell et al. (2007). All noted that the spatial extent, relative timing and facies characteristics, particularly 'extraneous accidental fragments of atypical porphyry, jasper, and aphanitic lithic clasts, that were probably carried from depth are typical of a diatreme vent generated by cataclysmic phreatomagmatic explosions' (Maksaev et al., 2004).

Geochronological dating of the nearby intrusives and the Braden Diatreme (sericite  $^{40}\text{Ar}/^{39}\text{Ar}$  age of 4.75 Ma) lead Maksaev et al. (2004) to temporally link the formation of the Braden Diatreme to a period of intrusive activity which includes the injection of concentric late dacite ring dykes (U-Pb 4.82 Ma) and a barren dacite stock (biotite and sericite  $^{40}\text{Ar}/^{39}\text{Ar}$  plateau ages between 4.58 and 4.46 Ma) beneath the Braden Diatreme. The underlying dacite is termed 'latite porphyry' by mine geologists and hundreds of metres of late dacite facies were intersected by drill holes DDH1068 and DDH1079 (Cannell, 2004). It was these long intercepts that lead to interpretations that a large dacite stock at depth is present. Both of these holes however were not surveyed so deviation is possible and therefore their exact locations cannot be confirmed.

The presence of late dacite megablocks (>100 m) in the Braden Diatreme (Howell and Molloy, 1960; Skewes et al., 2002) also suggests that the late underlying dacite intruded prior to the formation of the Braden Diatreme and may have played a role in its formation (Skewes et al., 2002). These megablocks could alternatively have been wall-rock transported downwards or a brecciated intra-pipe intrusion (Cannell, 2004).

Interestingly, small 20 to 30 cm dacite dykes have been encountered during development work, where in one instance a late dyke hosted in the Braden Sericite Breccia started on the floor of the tunnel, and progressively up the side wall began to disrupt, break down into fragments and then near the ceiling formed into a breccia resembling a small version of the Braden Diatreme (Floody R., personal communication, 2017). Unfortunately this exposure is now shotcreted over. Direct evidence for phreatomagmatism, or magmatic fragmentation not involving externally derived waters (e.g., emplacement, decompression and explosive devolatilisation), and linking these mechanisms to the Braden Diatreme and/or a causative intrusion through features such as wispy juvenile clasts is lacking due to the "pervasive alteration to various associations of sericite, chlorite, smectite, calcite, and siderite with subordinate dravite" (Maksaev et al., 2004).

The effect of diatreme formation is thought to have been the sudden depressurisation of the porphyry system and further, albeit minor, ore deposition and magma degassing (Maksaev et al., 2004). In terms of the wider El Teniente mineralising system, several studies (e.g., Camus, 1975; Vry et al., 2010; Spencer et al., 2015) have implied that the Braden Diatreme largely marked the end of significant economic Cu-Mo mineralisation and is therefore mostly 'barren' regarding sulphide mineralisation. The exception to this is "minor mineralization associated with small dacitic dikes at ~4.42 Ma" (Spencer et al., 2015). This is part of wider "hydrothermal circulation within and peripheral to the breccia between  $4.81 \pm 0.12$  and  $4.37 \pm 0.10$  Ma" (sericite  $^{40}\text{Ar}/^{39}\text{Ar}$ ) described by (Maksaev et al., 2004) who suggested fluid circulation was particularly focused along the shattered Braden Diatreme margins. In contrast, Vega and Maksaev (2003) proposed that the Braden Diatreme formed during, and not post-mineralisation, as suggested by Sillitoe (1985). Cannell et al. (2007) also suggested 'the Braden Diatreme marks the culmination of hydrothermal activity'.

One of the final stages in the genesis of the pipe was the development of crystal caverns on various mine levels containing cm-sized Cu-Fe-sulphides that line the walls and coarse gypsum crystals (Cannell, 2004), the latter 'possibly generated by the ingress of circulating groundwater into the breccia pipe' (Spencer et al., 2015).

The generation of the Braden Diatreme through a single process is difficult to explain and was more likely the result of several distinct but roughly simultaneous processes (Fig. 2.25). These included the emplacement of an underlying felsic (dacite) body, a change in temperature and pressure, and perhaps mixing with groundwaters which lead to a sudden, violent conversion of water to steam to drive a phreatomagmatic eruption. This caused explosive fragmentation of existing rock units, formation of the main conduit, transport and fluidisation processes, subsidence and reconsolidation. Given the presence of the large cavities in the pipe, some of the gases involved must have remained trapped in the fluidised/granulated breccia column during consolidation. The Pipe was later infiltrated by fluids resulting in further Mo-Cu mineralisation, the formation of the Braden Chlorite, Braden Tourmaline and Braden Sulphide Breccias and infill of fractures and caverns. Finally the emplacement of hornblende and pebble dykes took place as per the model of Floody (2000) and Maksaev et al. (2004).

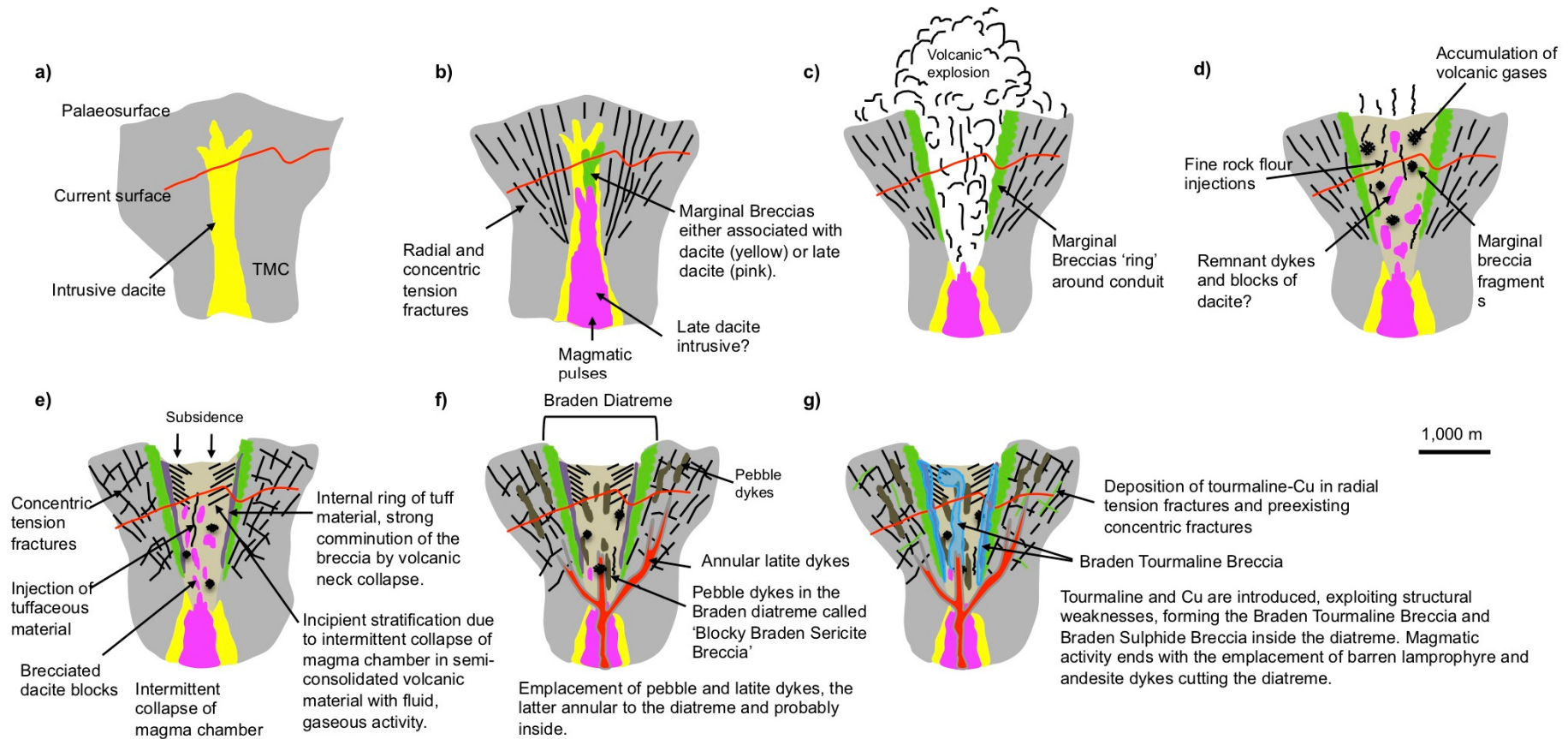


Fig. 2.25 Formation of the Braden Diatreme, reproduced after Floody (2000): **a)** Intrusion of a dacite body into the TMC; **b)** Intrusion of 'late dacite' (locally termed latite). The Marginal Breccias formed pre-Braden, although the causative intrusion of these breccias is unknown; **c)** Explosive brecciation and formation of main conduit and annular Marginal Breccias; **d)** Infill of conduit with brecciated material, continued venting (?), and fine rock flour injections; **e)** Subsidence, formation of stratification; **f)** Late-stage reactivation (Póstuma alteration-mineralisation) of the magmatic chamber causing emplacement pebble and latite dykes, the latter annular to the diatreme and probably inside; **g)** Late activity includes the introduction of tourmaline and copper to the system taking advantage of structural weaknesses. These form the Braden Tourmaline Breccia and Braden Sulphide Breccia inside the diatreme. The Braden Tourmaline Breccia may or may not introduce further tourmaline to the Marginal Tourmaline Breccia. Magmatic activity ends with the placement of barren lamprophyre and andesite dykes which cut the diatreme (not shown).

## 2.7 Closing Statements

As is clear from this chapter, the evolution of porphyry-breccia systems has been the subject of numerous studies, however there is still uncertainty regarding their formation and how to determine if they are significantly mineralised. With regards to El Teniente, the main knowledge gaps and uncertainties addressed in this thesis are:

1. There has been no detailed petrological study comparing the textural characteristics, number and composition of tourmaline generations and wider paragenetic relationships (e.g., relative timing to Cu-Mo mineralisation) between the different breccia facies at El Teniente.
2. There has been no previous assessment of variations in chemical composition of tourmaline as a function of depth and proximity to wall rocks.
3. The La Huifa breccias have not yet been described in the published literature.
4. Although the poorly studied Braden Diatreme is thought to mark the end of the system, there is still considerable debate as to if it terminated mineralisation, or if instead it marked the peak of the system as suggested by Cannell et al. (2007). In relation to this, the role of the underlying dacite porphyry in the formation of the Braden Diatreme is as yet unclear.
5. Large areas around the outer margins of the Braden Diatreme (not including the Marginal Breccias) are Mo-Cu mineralised, including the 'Braden Sulphide Breccia'. The relationship between this and late Mo-Cu mineralisation in the Braden Diatreme rock flour matrix remains enigmatic. For example, the Braden Sulphide Breccia could have formed due to ingress of fluids from the underlying dacite intrusives.
6. The origin of the weakly mineralised Braden Tourmaline Breccia inside the Braden Diatreme remains uncertain. For example, did it result from re-brecciation of the existing rock flour facies, or did hydrothermal fluids progressively replace the rock flour matrix with tourmaline, and is this how some of these matrix/cement-supported breccias in porphyry-breccia systems were formed?

### **3 Sample collection and analytical methodologies**

#### **3.1 Drill core logging and sample collection**

Two visits to El Teniente were carried out within the allotted six-month Codelco student agreement, the first between September and November 2017, and the second during January 2018. A number of drill cores from El Teniente and La Huifa were studied and sampled during this period and brief visits made to surface exposures and underground workings. Details of these activities are presented in Appendix i along with location maps.

Drill cores were selected based on their location within and around the Braden Diatreme so that breccias from different levels could be compared. Three hundred and twenty-eight samples from twenty-three drill holes (Appendix ii) were collected and 3,138 m of drill core studied. The La Huifa breccia, which is separate to El Teniente, was also sampled at different depths and locations. The second field season (January 2018) largely focused on the Diablo Breccias, which were systematically studied and sampled at different depths, mainly from 36 mm (BQ) or 47 mm (NQ) diameter drill core, and with a few samples from 62 mm diameter (HQ) geotechnical drill core.

#### **3.2 Sample preparation for optical petrography, SEM ( $\pm$ CL), cold-CL, EPMA and LA-ICP-MS**

Scanning electron microscopy (SEM), electron probe micro-analyser (EPMA), cathodoluminescence (CL) and laser ablation inductively coupled plasma mass spectrometry (LA-ICP-MS) analyses were performed on polished thin sections. For SEM and CL, these were prepared at CSM by cutting the core samples into  $\sim 20 \times 40 \times 5$  mm blocks which were bonded onto glass slides and then progressively ground and lapped to a thickness of  $\sim 30$   $\mu$ m and then polished. Sections 150  $\mu$ m thick were separately prepared for EPMA and LA-ICP-MS analysis. All sections for EPMA and SEM analyses were carbon coated to a thickness of  $\sim 25$  nm. Cold-CL studies used a CITL Mk5-2 electron source mounted on a Nikon Eclipse LV100 microscope with  $\times 2.5$ ,  $\times 5$ ,  $\times 10$  and  $\times 20$  objectives, coupled to a DS-Ri2 camera.

#### **3.3 Sample preparation for whole-rock XRF, XRD and ICP-OES and ICP-MS analysis**

Twenty-four samples were selected for whole-rock analysis from drill cores which intersected the Braden Sericite Breccia, the Braden Tourmaline Breccia and Braden Sulphide Breccia, as well as samples of the separate Marginal Tourmaline Breccia for comparison.

The core samples, each weighing around 150 g, were first jaw crushed to 5 to 10 mm. The crusher was thoroughly cleaned with methylated spirits between samples and new sample bags were used after each step of the preparation procedure to reduce cross-contamination. Crushed samples were riffled (Jones Type) to obtain between 25 to 50 g of representative material for milling. A tungsten-carbide TEMA pot was used to mill the samples down to a fine powder, of flour-like consistency. To reduce cross-contamination, quartz sand was milled between the grinding of each sample, and the mill then brushed out and wiped clean with methylated spirits. All work areas were also thoroughly cleaned between operations. A tungsten-carbide mill was used in preference to a steel or agate mill due to interest in Fe, Cr, Mn and Si which may have been introduced using steel (Hickson and Juras, 1986) or agate mills. Using a tungsten-carbide mill, however, will have introduced W, Co, Ta and Nb (Hickson and Juras, 1986; Yamazaki, 2011) whilst agate mills can introduce Ag, Cs, W and U (Takamasa and Nakai, 2009).

### **3.4 XRF**

Semi-quantitative XRF analysis was carried out to determine approximate major element compositions as a guide for ICP-OES calibration and analysis. This was carried out on pressed powder pellets which were produced by mixing 5 g of sample powder with elvacite binder, placing the mixture into a steel cylinder platen to form a circular disc, covering this with 40 g of lithium tetraborate and then compressing the material in a 10 tonne press to form a circular disc with sample powder on one surface. The pressed powder pellets were analysed in a Bruker S4 Pioneer XRF. Raw data were output and processed using EVAL software. In order to determine loss/gains in mass (i.e. water and other volatile species) on ignition, a separate aliquot of powder was weighed, fused at 1,030°C for 60 minutes and then reweighed to calculate the change in mass.

#### **3.4.1 XRF QA/AC**

To determine precision of the XRF analyses, powder duplicates were prepared every ten samples. Precision was calculated from duplicate analyses of regularly inserted sample powders into the batch runs, using the Thompson and Howarth method. It was found to be better than 2% for all elements except for a few analyses of Fe<sub>2</sub>O<sub>3</sub>, Al<sub>2</sub>O<sub>3</sub>, SiO<sub>2</sub>, CaO and K<sub>2</sub>O (Fig. 3.1).

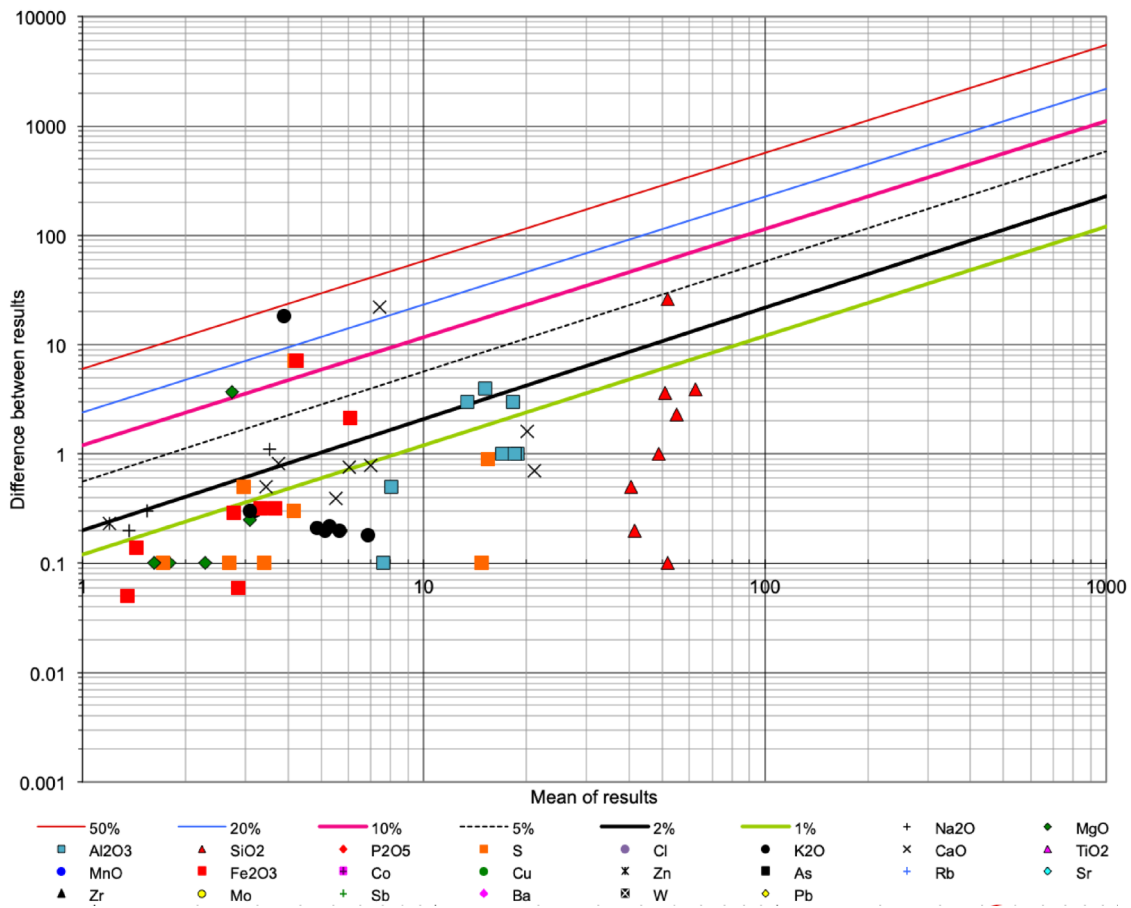


Fig. 3.1 Thompson-Howarth plot illustrating the precision of duplicate analyses of breccias by semi-quantitative XRF. Precision contour lines as follows: red= 50%, blue= 20%, pink= 10%, dotted line= 5%, black= 2% and green= 1%

### 3.5 XRD

Qualitative XRD analyses were undertaken at CSM using a Siemens D5000 X-ray Diffractometer set up in Bragg-Brentano configuration and to use monochromatic  $K\alpha$  radiation. A 1.5 kW Cu anode filament was operated at 40 kV and 30 mA. Data were collected using a scintillation point detector, with a scan range between 2 and 70° 2 $\theta$ , a step size of 0.02° 2 $\theta$  and a scan time of 1 second per step. Data were interpreted using EVA v.18.0.0.0. software and the JCPDS PDF-2 (2004) database.

### 3.6 ICP-MS

Whole-rock powders were first prepared as sample solutions using a four acid (HF, HCl, HNO<sub>3</sub>, HClO<sub>4</sub>) digestion procedure. For this, 100 mg of dried (50°C overnight) sample powder was weighed into a 50 ml Teflon® digestion vessel which was wetted with deionised H<sub>2</sub>O. Next, 4 ml of HF acid (47 to 51% Fisher Tracemetal Grade) was carefully added to the vessel. After any reaction had subsided, 4 ml of aqua regia was added and the vessel then sealed and placed in a DigiPrep digestion block, pre-set at 160°C and left overnight, or for at least 8 hours. Upon removal and cooling, 1 ml HClO<sub>4</sub>

(VWR Normatom 65%) was added to the vessel which was then returned to the digestion block and taken to incipient dryness at 180°C. All HF and perchloric acid had fumed off by this stage. Once dry and cool, a further 1 ml of HNO<sub>3</sub> was placed into the vessel and this returned to the digestion block to evaporate to dryness at 180°C. When dry, the vessel was once again removed, allowed to cool and a further 1 ml of concentrated HNO<sub>3</sub> and 5 ml of deionised H<sub>2</sub>O added. This mixture was warmed gently in the digestion block for 30 minutes at 100°C. On cooling, 44 ml of deionised H<sub>2</sub>O was added, mixed in and the solution then transferred to a 50 ml polypropylene sample container. Five mL of the sample solution was then diluted with 45 mL of 5% HNO<sub>3</sub> that was then placed in a sealed polypropylene sample tube (QMx Digiprep) prior to analysis. Sample solutions were analysed at CSM in an Agilent 7700 with a quadruple mass spectrometer.

Although an effective dissolution procedure for multi-element analysis, there are the potential for issues relating to incomplete digestion of resistant phases (e.g., zirconium minerals, rutile and tourmaline) that need to be considered when using a four acid attack. For example the partial digestion of refractory minerals, such as zircon, can result in low values of Zr (e.g., Webb et al., 2012; Potts et al., 2015). However no residues were detected or suspected and therefore a subsidiary fusion/sintering approach was not undertaken.

### **3.6.1 ICP-MS QA/QC**

Suitable certified reference materials and reagent blanks were included in the workflow to validate the procedure. Pairs of certified reference materials (AGV-2 'andesite', DNC-1 'dolerite', GSP-2 'granodiorite' and 73305 'rock; blended'), selected to best cover the breccias at El Teniente (clasts of diorite, dacite and Teniente Mafic Complex (diabase, gabbro, andesite and basalts), hydrothermal cement and/or rock flour matrix) were analysed at the beginning and end of batches to determine drift whilst one in ten analyses was a duplicate (i.e. the same sample solution was analysed twice). Detection limits, assessed by analysing acid blanks every ten samples, were calculated as:  $3 \times \text{standard deviation of blanks} \times \text{dilution factor/mass of sample taken for digestion}$ . Detection limits (Table 3.1) were <1 ppm for all elements except for B (4.2 ppm), Mo (<0.0007 wt.%), K (<0.0006 wt.%), Ti (<0.001 wt.%), Fe is (<0.0011 wt.%) and Zn (<0.0033 wt.%). Concentrations of elements in the blanks are shown in Fig. 3.2.

Table 3.1 Detection limits for different analytes determined by ICP-MS, calculated using 3 standard deviations of the mean analyte value from each blank. The limits for Sm, Eu, Gd, Tb, Dy, Ho, Er, Tm, Yb and Lu were calculated from the samples based on original counts for the blanks.

<b>Analyte</b>	<b>Detection limit</b>	<b>Unit</b>	<b>Analyte</b>	<b>Detection limit</b>	<b>Unit</b>
Li	0.01	ppm	La	0.07	ppm
B	4.2	ppm	Ce	0.1	ppm
K	0.0006	wt.%	Pr	0.01	ppm
Sc	0.76	ppb	Nd	0.02	ppm
Ti	0.001	wt.%	Sm	0.0015	ppm
Mn	0.48	ppm	Eu	0.6	ppb
Fe	0.0011	wt.%	Gd	0.0011	ppm
Co	0.02	ppm	Tb	0.0411	ppm
Cu	0.13	ppm	Dy	0.001	ppm
Zn	0.0033	wt.%	Ho	0.2	ppm
Ga	0.001	ppm	Er	0.5	ppb
As	0.01	ppm	Tm	0.1	ppb
Rb	0.04	ppm	Yb	0.4	ppb
Sr	0.57	ppm	Lu	0.3	ppb
Y	0.67	ppb	Hf	0.62	ppb
Nb	0.73	ppb	Ta	0.36	ppb
Mo	0.0007	wt.%	W	0.05	ppm
Sb	0.80	ppb	Pb	0.06	ppm
Cs	0.56	ppb	Th	0.65	ppb
Ba	0.14	ppm	U	0.64	ppb

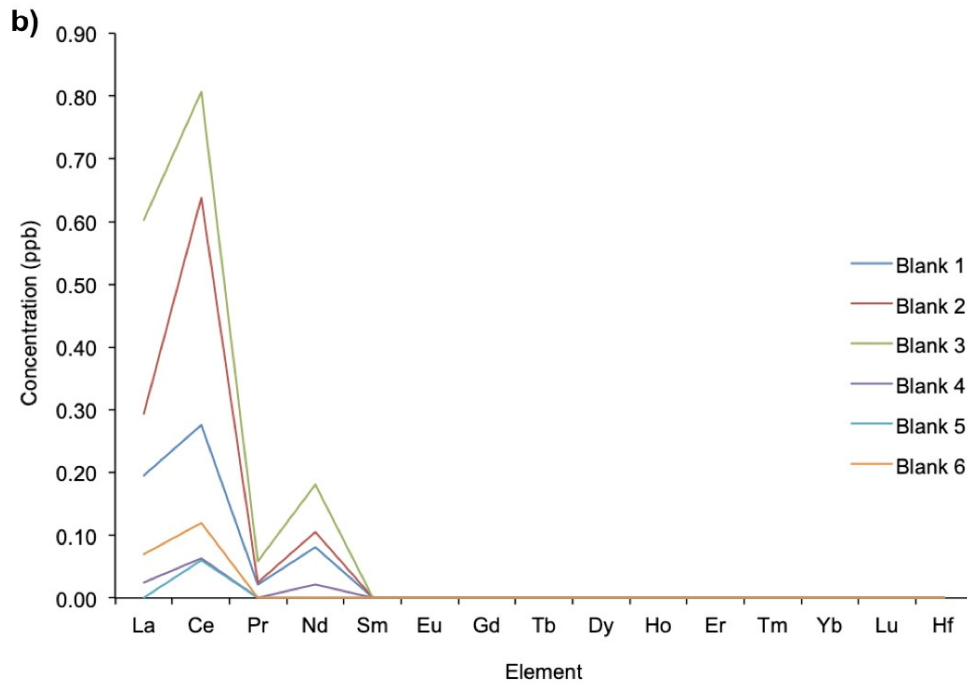
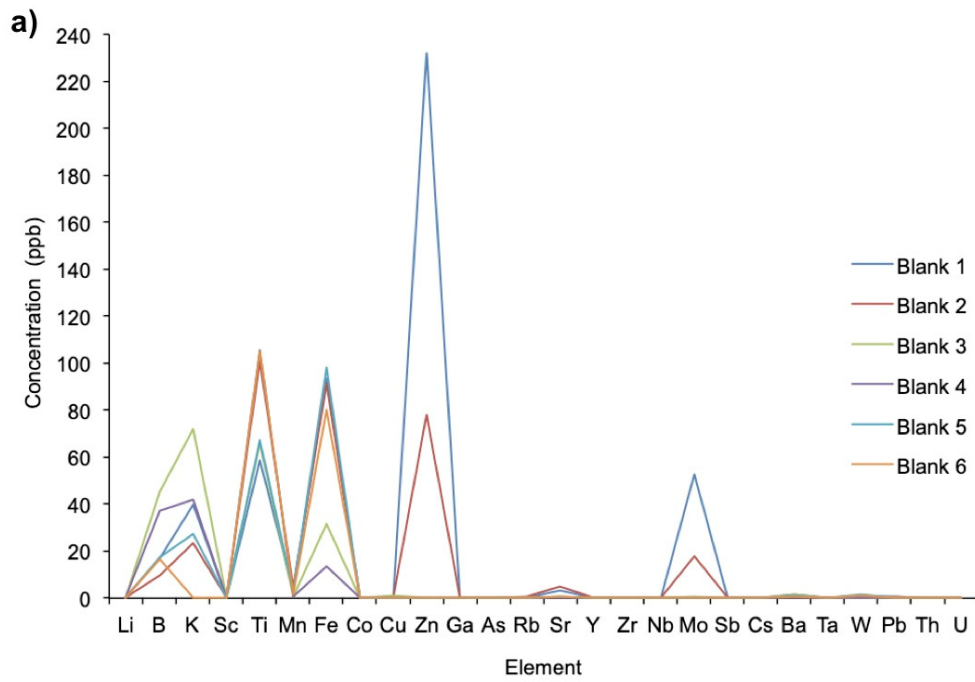


Fig. 3.2 **a)** Major and minor element concentrations in acid blanks determined by ICP-MS at CSM; **b)** Rare earth element concentrations in acid blanks run at CSM.

**Accuracy** - Accuracy was calculated as the percentage difference between the values obtained for the reference materials in this study and the certified values (Table 3.2).

Table 3.2 Accuracy of ICP-MS analyses of certified reference materials. Shown overleaf as a continuation, are the certified values and the average of the obtained values for the reference materials in this study.

<b>CRM: AGV-2, andesite (no B, As, Mo, W)</b>	
Better than:	
5%	Fe, Co, Rb, Sr, Y, Nb, La, Ce, Pr, Sm, Gd, Dy, Ho, Tm, Lu, Th, U
10%	Sc, Ti, Zr, Sb, Cs, Nd, Eu, Er, Yb, Hf, Pb
15%	K, Mn, Cu, Ba
20%	
25%	Ga
Worse than 25%	Li, Zn, Tb, Ta
<b>CRM: DNC-1, dolerite (no Mo, Cs, Ce, Tb, Hf, Ta, W, Th, U)</b>	
Better than:	
5%	Sc, Ga, Y, Zr, Ba, Pr, Sm, Dy, Er, Tm, Lu, Pb
10%	Li, K, Ti, Fe, Rb, Nd, Eu, Ho, Yb
15%	Co, Sr, Sb, La, Gd
20%	Mn, Cu
25%	
Worse than 25%	B, Zn, As, Nb
<b>CRM: GSP-2, granodiorite (no B, As, Sb, Tb, Ta, W)</b>	
Better than:	
5%	Sc, Fe, Co, Rb, Sr, Y, Nb, Sm, Dy, Ho, Yb
10%	Li, Ti, Mn, Cs, La, Eu, Er, Pb, Th, U
15%	K, Cu, Ba, Ce, Nd, Gd, Tm
20%	Pr
25%	Lu
Worse than 25%	Zn, Ga, Zr, Mo, Hf
<b>CRM: 73305, rock</b>	
Better than:	
5%	Li, Sc, Y, Zr, Ba, Ce, Pr, Nd, Sm, Eu, Gd, Dy, Ho, Er, Th, U
10%	Ti, Fe, Co, Rb, Sr, Nb, La, Yb, Hf
15%	K, Mn, Sb, Cs, Pb
20%	Cu, Tm, Lu
25%	Ga, Ta
Worse than 25%	B, Zn, As, Mo, Tb, W

Table 3.2 cont. Below are the mean ( $\bar{X}$ ) of obtained values (n= 6) for the certified reference materials, official certified value, and accuracy for ICP-MS.

CRM	AGV-2 $\bar{X}$ (ppb)	Certified Value (ppb)	Accuracy	DNC-2 $\bar{X}$ (ppb)	Certified Value (ppb)	Accuracy	GSP-2 $\bar{X}$ (ppb)	Certified Value (ppb)	Accuracy	73305 $\bar{X}$ (ppb)	Certified Value (ppb)	Accuracy
Li (ppb)	10,280	110,000	0.9%	4,874	5,200	6.3%	33,017	36,000	8.3%	43,230	44,000	1.7%
B (ppb)	17,978		N/A	9,562	900	90.6%	10,511		N/A	18,609	154,000	87.9%
K (ppb)	26,802,383	23,900,000	10.8%	2,168,718	1,940,000	10.5%	50,855,251	44,800,000	11.9%	40,120,980	34,522,821	14.0%
Sc (ppb)	14,063	13,000	7.6%	32,591	31,000	4.9%	6,577	6,300	4.2%	18,400	18,500	0.5%
Ti (ppb)	6,731,894	6,300,000	6.4%	3,145,673	2,843,601	9.6%	4,272,416	4,000,000	6.4%	4,206,727	3,950,000	6.1%
Mn (ppb)	860,416	770,000	10.5%	1,416,715	1,161,890	18.0%	352,621	320,000	9.3%	201,234	173,000	14.0%
Fe (ppb)	48,725,805	46,800,000	4.0%	74,768,665	69,720,279	6.8%	35,401,052	34,300,000	3.1%	55,977,850	53,146,853	5.1%
Co (ppb)	16,837	16,000	5.0%	63,921	57,000	10.8%	7,531	7,300	3.1%	22,384	21,000	6.2%
Cu (ppb)	61,465	53,000	13.8%	118,303	100,000	15.5%	49,054	43,000	12.3%	50,036	42,000	16.1%
Zn (ppb)	120,281	86,000	28.5%	94,043	70,000	25.6%	174,216	120,000	31.1%	81,226	55,000	32.3%
Ga (ppb)	25,523	20,000	21.6%	15,163	15,000	1.1%	54,817	22,000	59.9%	33,088	26,000	21.4%
As (ppb)	2,265		N/A	572	120	79.0%	9,846		N/A	3,559	1,400	60.7%
Rb (ppb)	66,090	68,600	3.7%	4,169	4,500	7.4%	248,044	245,000	1.2%	218,008	205,000	6.0%
Sr (ppb)	681,310	658,000	3.4%	164,893	144,000	12.7%	235,703	240,000	1.8%	98,853	90,000	9.0%

CRM	AGV-2 $\bar{X}$ (ppb)	Certified Value (ppb)	Accuracy	DNC-2 $\bar{X}$ (ppb)	Certified Value (ppb)	Accuracy	GSP-2 $\bar{X}$ (ppb)	Certified Value (ppb)	Accuracy	73305 $\bar{X}$ (ppb)	Certified Value (ppb)	Accuracy
Y (ppb)	19,339	20,000	3.3%	17,975	18,000	0.1%	26,888	28,000	4.0%	25,433	26,000	2.2%
Zn (ppb)	250,537	230,000	8.2%	38,650	38,000	1.7%	127,846	550,000	76.8%	96,427	96,000	0.4%
Nb (ppb)	14,394	15,000	4.0%	1,614	3,000	46.2%	27,122	27,000	0.4%	13,577	14,300	5.1%
Mo (ppb)	4,703		N/A	1,557		N/A	3,233	2,100	35.0%	1,122	350	68.8%
Sb (ppb)	559	600	6.8%	846	960	11.9%	355		N/A	159	180	11.7%
Cs (ppb)	1,255	1,160	7.6%	208		N/A	1,277	1,200	6.0%	15,638	14,000	10.5%
Ba (ppb)	1,282,801	1,140,000	11.1%	119,920	118,000	1.6%	1,535,969	1,340,000	12.8%	463,133	450,000	2.8%
La (ppb)	39,582	38,000	4.0%	4,143	3,600	13.1%	198,609	180,000	9.4%	57,540	62,000	7.2%
Ce (ppb)	69,575	68,000	2.3%	9,272		N/A	469,100	410,000	12.6%	109,592	109,000	0.5%
Pr (ppb)	8,674	8,300	4.3%	1,218	1,200	1.5%	60,261	51,000	15.4%	13,062	13,600	4.0%
Nd (ppb)	32,578	30,000	7.9%	5,559	5,200	6.5%	222,995	200,000	10.3%	47,778	48,000	0.5%
Sm (ppb)	5,849	5,700	2.6%	1,543	1,500	2.8%	27,887	27,000	3.2%	8,056	8,400	4.1%
Eu (ppb)	1,667	1,540	7.6%	639	590	7.6%	2,430	2,300	5.4%	1,683	1,700	1.0%
Gd (ppb)	4,930	4,690	4.9%	2,266	2,000	11.7%	13,850	12,000	13.4%	6,466	6,700	3.5%
Tb (ppb)	472	640	26.2%	245		N/A	1,166		N/A	678	1,050	35.4%

CRM	AGV-2 $\bar{X}$ (ppb)	Certified Value (ppb)	Accuracy	DNC-2 $\bar{X}$ (ppb)	Certified Value (ppb)	Accuracy	GSP-2 $\bar{X}$ (ppb)	Certified Value (ppb)	Accuracy	73305 $\bar{X}$ (ppb)	Certified Value (ppb)	Accuracy
Dy (ppb)	3,723	3,600	3.3%	3,017	3,000	0.6%	6,169	6,100	1.1%	4,974	5,100	2.5%
Ho (ppb)	685	710	3.5%	661	620	6.2%	973	1,000	2.7%	936	980	4.4%
Er (ppb)	1,940	1,790	7.7%	2,109	2,100	0.4%	2,420	2,200	9.1%	2,642	2,700	2.2%
Tm (ppb)	249	260	4.1%	295	300	1.7%	256	290	11.6%	352	430	18.0%
Yb (ppb)	1,743	1,600	8.2%	2,151	2,000	7.0%	1,547	1,600	3.3%	2,426	2,600	6.7%
Lu (ppb)	242	250	3.2%	307	300	2.3%	175	230	24.1%	337	410	17.7%
Hf (ppb)	5,630	5,080	9.8%	1,062		N/A	3,249	1,400	56.9%	2,647	2,900	8.7%
Ta (ppb)	2,292	890	61.2%	887		N/A	1,112		N/A	1,177	900	23.5%
W (ppb)				1,422		N/A	1,071		N/A	1,578	790	50.0%
Pb (ppb)	14,018	13,000	7.3%	6,402	6,300	1.6%	45,895	42,000	8.5%	7,556	8,700	13.2%
Th (ppb)	6,247	6,100	2.4%	241		N/A	113,343	105,000	7.4%	12,650	12,800	1.2%
U (ppb)	1,931	1,880	2.6%	40		N/A	2,244	2,400	6.5%	1,567	1,500	4.3%

**Precision** - Precision, determined from duplicate analyses of sample powders inserted at regular intervals (one in ten) into the batch runs, was calculated using the Thompson and Howarth (1973, 1978) method (e.g., Fletcher, 1981; Stanley, 2003b, 2006; Stanley and Lawie, 2007; Abzalov, 2008, 2011). It was found to be better than 10% for all elements except B, Li and (for a few analyses) Hf, Ta, Sb, As, Ce, Zr and Cu (Fig. 3.3). Precision for K, Fe, Rb, Ti, Ba, La, Sm and Mn (all but one analysis) was better than 5%.

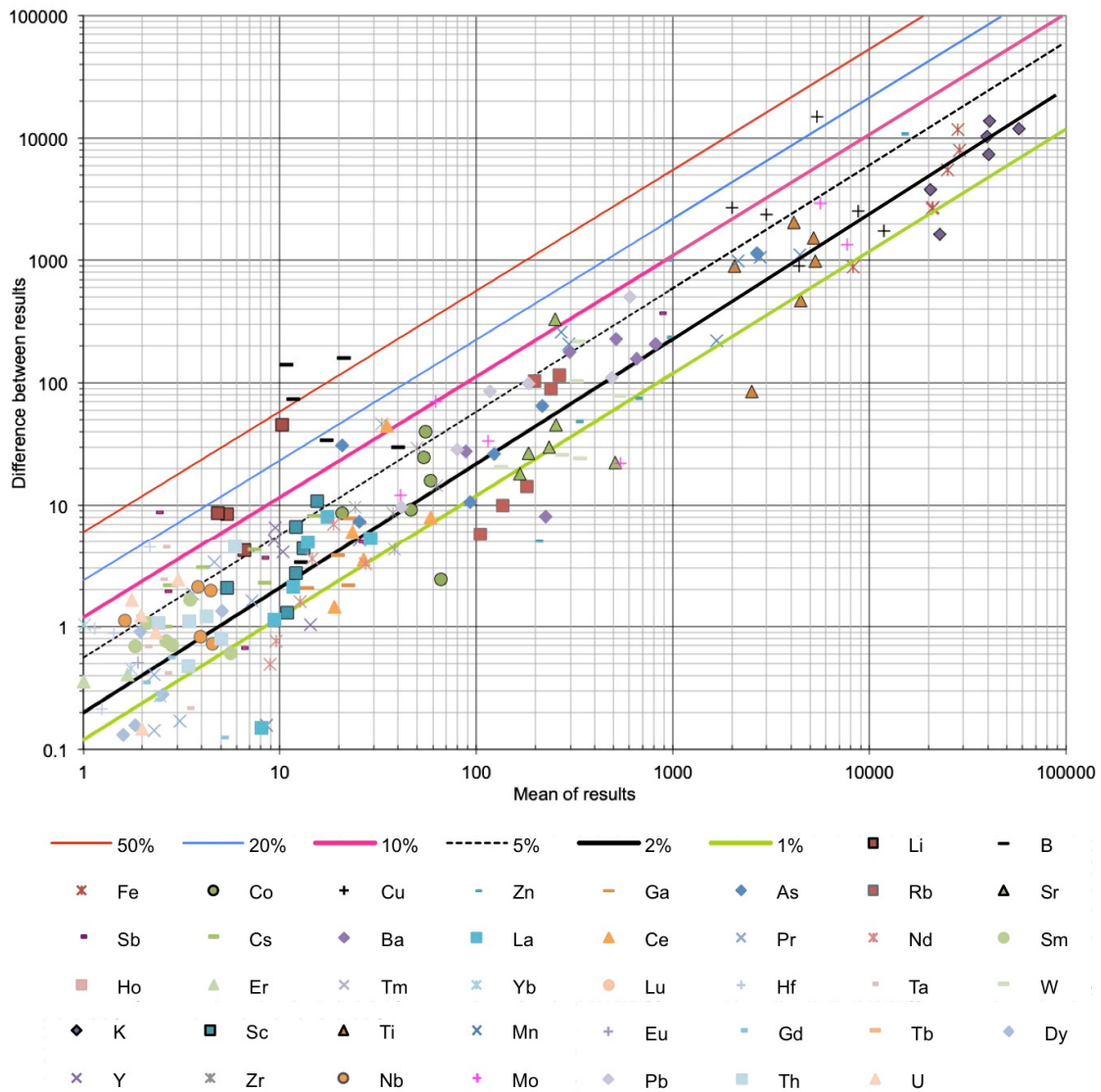


Fig. 3.3 Thompson-Howarth plot illustrating the precision of duplicate analyses of breccias by ICP-MS. Precision contour lines as follows: red= 50%, blue= 20%, pink= 10%, dotted line= 5%, black= 2% and green= 1%

### 3.7 ICP-OES

Unfortunately, there was no fully tested preparation procedure at CSM for quantitative XRF of samples with high sulphide contents, and major element determinations (together with some trace elements) were therefore carried out by ICP-OES. The following elements were determined: Fe, Al, Mg, Ca, Na, K, Cu, Ti, Mn, S, and P. The same sample and CRM solutions used for ICP-MS were analysed. These were diluted by a further 10× to give a sample solution to 5% HNO<sub>3</sub> ratio of 1:500. Due to the wide range of elemental concentrations in the solutions, polynomial regression lines were applied to fix most of the matrix effects. Quantification limits (Appendix vii) were 0.002 wt.% for Fe<sub>2</sub>O<sub>3</sub>, 0.012 wt.% for Al<sub>2</sub>O<sub>3</sub>, 0.022 wt.% for MgO, 0.004 wt.% for CaO, 0.001 wt.% for Na<sub>2</sub>O, 0.002 wt.% for K<sub>2</sub>O, 0.001 wt.% for CuO, 0.002 wt.% for TiO<sub>2</sub>, 0.0001 wt.% for MnO, 0.021 wt.% for S, 0.095 wt.% for P<sub>2</sub>O<sub>5</sub>. The sample solutions were analysed in an Agilent 5110 ICP-OES instrument at CSM.

**Accuracy** - Analytical accuracy, expressed as the percentage difference between measured and accepted values for an internal standard solution, were all within 1% except for K (5.17%), and Ca (1.49%). Accuracy based on the reference materials in this study and the certified values of these materials is presented in Table 3.3.

Table 3.3 Accuracy of ICP-OES analyses of certified reference materials. Shown overleaf as a continuation, are the certified values and the average of the obtained values for the reference materials in this study.

<b>CRM: AGV-2, andesite (no S)</b>	
Better than:	
5%	Fe <sub>2</sub> O <sub>3</sub> , Na <sub>2</sub> O, TiO <sub>2</sub>
10%	CaO, K <sub>2</sub> O, MnO
15%	Al <sub>2</sub> O <sub>3</sub> , MgO, P <sub>2</sub> O <sub>5</sub>
20%	
25%	
Worse than 25%	Cu
<b>CRM: DNC-1, dolerite (no S)</b>	
Better than:	
5%	Fe <sub>2</sub> O <sub>3</sub> , Al <sub>2</sub> O <sub>3</sub> , MgO, CaO, TiO <sub>2</sub> , MnO,
10%	Na <sub>2</sub> O
15%	
20%	P <sub>2</sub> O <sub>5</sub>
25%	K <sub>2</sub> O
Worse than 25%	CuO
<b>CRM: GSP-2, granodiorite (no S)</b>	
Better than:	
5%	CaO, Na <sub>2</sub> O, K <sub>2</sub> O, TiO <sub>2</sub> , MnO
10%	Fe <sub>2</sub> O <sub>3</sub> , Al <sub>2</sub> O <sub>3</sub> , MgO, P <sub>2</sub> O <sub>5</sub>
15%	
20%	
25%	
Worse than 25%	Cu

Table 3.3 cont. Below are the mean ( $\bar{X}$ ) of obtained values (n= 3 for AGV-2, DNC-1, 73305 and n= 5 for GSP-2) for the certified reference materials, official certified value, and accuracy for ICP-OES.

	AGV-2 $\bar{X}$ (ppb)	Certified Value AGV- 2	Accur- acy	DNC-2 $\bar{X}$ (ppb)	Certified Value DNC-2	Accur- acy	GSP-2 $\bar{X}$ (ppb)	Certified Value GSP-2	Accur- acy	73305 $\bar{X}$ (ppb)	Certified Value 73305	Accur- acy
Fe <sub>2</sub> O <sub>3</sub>	44,430,976	46,800,000	5.0%	70,451,096	69,720,279	1.0%	32,273,005	34,300,000	5.9%	52,209,248	53,146,853	1.8%
Al <sub>2</sub> O <sub>3</sub>	87,398,544	100,447,480	13.0%	108,099,425	107,857,540	0.2%	79,155,914	87,920,950	10.0%	106,216,520		N/A
MgO	9,554,561	10,734,112	11.0%	59,881,588	61,087,952	2.0%	5,333,132	5,909,792	9.8%	11,635,618		N/A
CaO	35,304,701	37,378,600	5.5%	78,663,962	82,118,570	4.4%	14,792,107	15,008,616	1.4%	4,270,960		N/A
Na <sub>2</sub> O	29,678,930	30,787,190	3.6%	15,260,196	13,991,480	8.3%	20,588,872	20,252,778	1.7%	2,725,266		N/A
K <sub>2</sub> O	25,130,658	23,900,000	5.1%	2,475,530	1,940,000	21.6%	43,633,937	44,800,000	2.6%	35,269,743	34,522,821	2.2%
CuO	22,973	53,000	56.7%	70,612	100,000	41.6%	14,774	43,000	65.6%	18,619	42,000	55.7%
TiO <sub>2</sub>	6,374,129	6,300,000	1.2%	2,989,097	2,843,601	4.9%	4,014,734	4,000,000	0.4%	4,068,190	3,950,000	3.0%
MnO	725,146	770,000	5.8%	1,199,976	1,161,890	3.2%	322,513	320,000	0.9%	216,658	173,000	25.2%
S	68,865		N/A	572,359		N/A	503,742		N/A	82,559		N/A
P <sub>2</sub> O <sub>5</sub>	2,152,827	1,920,160	12.1%	258,072	305,480	18.4%	1,249,032	1,134,640	10.0%	636,535		N/A

**Precision** - All sample solutions (including CRMs) were analysed in duplicate. Precision of the analytical solution duplicates (all original ICP-MS solutions were duplicated), representing analytical uncertainty of the instrument, was always better than 1%, whilst precision of duplicate breccia samples (field/drill core duplicates, as per ICP-MS) for each element varies from better than 1% to worse than 20% (Fig. 3.4).

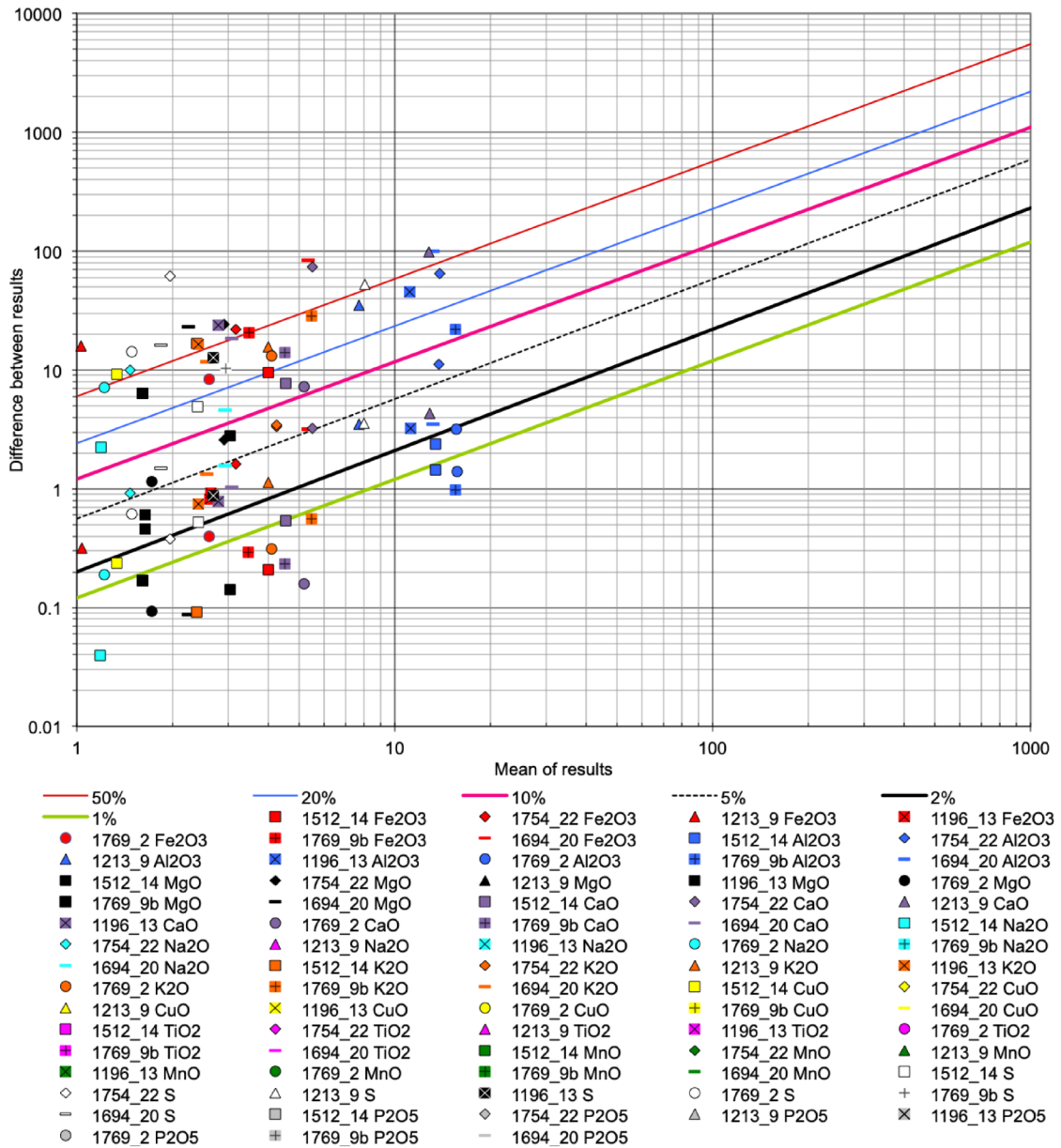


Fig. 3.4 Thompson-Howarth plot illustrating the precision of breccia sample solution duplicates by ICP-OES. Precision contour lines as follows: red= 50%, blue= 20%, pink= 10%, dotted line= 5%, black= 2% and green= better than 1%

### 3.8 SEM ( $\pm$ CL)

Two SEMs at CSM were used during the study, a TESCAN VEGA3 equipped with a secondary- and backscattered electron (BSE) detector and an X-ray energy dispersive detector (EDS), and a Quanta 650F FEG SEM equipped with two Bruker EDS and one CL detector. Images acquired using the BSE detector show the distribution of minerals/phases with different average atomic number. The VEGA3 SEM instrument used an accelerating voltage of 20 kV, a beam current of 17 nA and a working distance of 15 to 20 mm. The Quanta 650F FEG SEM was operated at a working distance of 15 mm for CL imaging and 13 mm for SEM-BSE imaging. CL and SEM-BSE images were collected on the FEG SEM using an accelerating voltage of 15 kV and a spot size of 4.5  $\mu\text{m}$ .

### 3.9 EPMA of tourmaline

Quantitative tourmaline analysis was carried out using a JOEL JXA-8200 with one EDS and four wavelength (WDS) dispersive X-ray detectors, using an accelerating voltage of 20 kV, a beam current of 25 nA and a spot size of 5  $\mu\text{m}$ ; the same conditions used by London and Manning (1995) and Williamson et al. (2000). Suitable crystals and points for analysis were first selected from BSE images of the sample surface, mainly to avoid grain boundaries, fractures and inclusions. Microprobe analyses were performed as traverses parallel to the *c*-axis and perpendicular to it across basal sections where available.

The following standards were used: jadeite for  $\text{Na}_2\text{O}$ , fluorite for F, orthoclase for  $\text{K}_2\text{O}$ , almandine for FeO, periclase for MgO, MK2- $\text{Al}_2\text{O}_3$  for  $\text{Al}_2\text{O}_3$ , MK2- $\text{CaSiO}_3$  for CaO and  $\text{SiO}_2$ , bustamite for MnO, rutile for  $\text{TiO}_2$  and cuprite for CuO. Raw data were reduced by means of the Armstrong PRZ correction. Detection limits ( $3\sigma$  of single point backgrounds) were 0.043 wt.% for  $\text{Na}_2\text{O}$ , 0.096 wt.% for F, 0.014 wt.% for  $\text{K}_2\text{O}$ , 0.038 wt.% for FeO, 0.076 wt.% for  $\text{SiO}_2$ , 0.080 wt.% for  $\text{Al}_2\text{O}_3$ , 0.030 wt.% for CaO, 0.031 wt.% for MnO, 0.041 wt.% for MgO, 0.043 wt.% for  $\text{TiO}_2$  and 0.036 wt.% for CuO.

The data for tourmaline (wt.%) were recalculated to atoms per formula unit (apfu) based on 24.5 O. To achieve this required a number of assumptions, mainly that B is fixed at 3 apfu, OH+F at 4 apfu (e.g., Hawthorne, 1996; Marks et al., 2013), and that total iron ( $\text{Fe}_{\text{tot}}$ ) is contained as  $\text{Fe}^{2+}$  (i.e. as FeO, see section 3.9.2). Li was calculated from three minus the sum of the Y-site cations which was then added back to the equivalent wt.%  $\text{Li}_2\text{O}$  and the process repeated (e.g., Henry and Dutrow, 1996). The spreadsheet used for calculating tourmaline formulae was that developed by Julie Selway and Jian Xiong.

### 3.9.1 EPMA limitations

Containing Li, B and OH groups, alongside the potential for variable Fe states ( $\text{Fe}^{2+}/\text{Fe}^{3+}$ ), undertaking elemental analysis of tourmaline using an electron microprobe can be challenging. A number of issues arise from the inability of EPMA to detect, or quantify light elements with an atomic number of  $<6$  including H, Li, Be and B. This is somewhat challenging with the tourmaline group ( $\text{XY}_3\text{Z}_6[\text{T}_6\text{O}_{18}][\text{BO}_3]_3\text{V}_3\text{W}$ ), beryl ( $\text{Be}_3\text{Al}_2(\text{Si}_6\text{O}_{18})$ ) and spodumene ( $\text{LiAlSi}_2\text{O}_6$ ). Problematic site occupancies in tourmaline include: Y=  $\text{Li}^{1+}$ ,  $\text{Fe}^{2+}$ ,  $\text{Fe}^{3+}$ ; Z=  $\text{Fe}^{2+}$ ,  $\text{Fe}^{3+}$ ; T=  $\text{B}^{3+}$ ; B=  $\text{B}^{3+}$ ; V=  $\text{OH}^{1-}$ ,  $\text{O}^{2-}$ ; and W=  $\text{OH}^{1-}$ ,  $\text{F}^{1-}$ ,  $\text{O}^{2-}$ . This results in tourmaline analyses differing by  $\sim 15\%$  from 100% totals due to the presence of water, omission of non-analysed elements (e.g., fluorine) and the inability to measure B and Li. Although the incapacity to determine the oxidation state of Fe in tourmaline is not strictly a problem for elemental analysis, it is important when determining site occupancies, and due to stoichiometry and a number of assumptions used (discussed above), during the raw data processing, a number of artifacts in the data can be introduced (discussed below).

### 3.9.2 EPMA tourmaline QA/AC

To determine accuracy and precision, a secondary tourmaline standard was analysed, for which data, for exactly the same crystal, had been obtained previously by Müller et al. (2005) (Fig. 3f in Müller et al., 2005). Accuracy, calculated as the percentage difference between the obtained and published values, was as follows:  $\text{SiO}_2$  1.2%, F 12.5%, FeO 4.6%,  $\text{K}_2\text{O}$  24.6%, MgO 6.6%,  $\text{Na}_2\text{O}$  3.3%, MnO 9.5%, CaO 2.9%,  $\text{Al}_2\text{O}_3$  2.8% and  $\text{TiO}_2$  7.7%. Precision, expressed as percent relative standard deviation ( $(\text{standard deviation}/\text{mean}) \times 100$ ,  $n = 7$ ) was:  $\text{SiO}_2$  1.5%, F 9.3%, FeO 2%,  $\text{K}_2\text{O}$  35.1%, MgO 22%,  $\text{Na}_2\text{O}$  4.5%, MnO 12%, CaO 26.8%,  $\text{Al}_2\text{O}_3$  1.3% and  $\text{TiO}_2$  21.5%.

### 3.9.3 Artifacts in the EPMA data

In the analysis of tourmaline, Fe was assumed to be in form of FeO (rather than  $\text{Fe}_2\text{O}_3$ ) as there was no micro-spot method available to determine  $\text{Fe}^{2+}/\text{Fe}^{3+}$ . This is, however, believed to have introduced artifacts in the calculation of apfu for all tourmaline generations in the breccias, including fine fibrous overgrowths and coarser crystals, mainly high Si ( $> 6.0$  apfu) and high  $\Sigma Y$  site occupancy ( $>3$  apfu). This is demonstrated in Table 3.4 where inputting example values for  $\text{Fe}_2\text{O}_3$  into the unedited EPMA analyses (retaining the same  $\text{Fe}_{\text{tot}}$ ) decreases Si and the  $\Sigma Y$  site occupancy (apfu). Values for Si  $<6.1$  are considered within error ( $<2\%$ ) of the maximum theoretical site occupancy of 6 apfu. Similar values of  $<6.1$  Si were also reported by Zhang et al. (2019). Reductions in  $\Sigma Y$  are the result of decreases in Mg (compensated for by increases in Mg in the Z site) and variable changes in  $\text{Fe}^{2+}/\text{Fe}^{3+}$ .

Table 3.4 The original EPMA analyses from the Teniente Tourmaline Breccias with all Fe as FeO are presented in the orange columns. Alongside these values are different proportions of FeO and Fe<sub>2</sub>O<sub>3</sub> demonstrating the effect on Si. Samples are from: 1754\_31= Early Tourmaline Breccia; ES26\_6= La Huifa; 1754\_13= Braden Tourmaline Breccia; 2677\_3= Diablo and 1694\_20= Marginal Tourmaline Breccia. Assumptions include: B<sub>2</sub>O<sub>3</sub>, H<sub>2</sub>O and Li<sub>2</sub>O= calculated by stoichiometry, B= 3 apfu, OH+F= 4 apfu and Li= 15-total (T+Z+Y).

	Point 9, T1	Point 9, T1	Point 9, T1	Point 9, T1	Point_1 ES26_6	Pt_1 ES26_6	Point_1 ES26_6	Point_1 ES26_6	Point_1 1754_13	Point_1 1754_13	Point_1 1754_13	Point_1 1754_13
SiO <sub>2</sub>	34.37	34.37	34.37	34.37	35.69	35.69	35.69	35.69	35.66	35.66	35.66	35.66
TiO <sub>2</sub>	0.72	0.72	0.72	0.72	1.57	1.57	1.57	1.57	1.99	1.99	1.99	1.99
Al <sub>2</sub> O <sub>3</sub>	26.97	26.97	26.97	26.97	20.54	20.54	20.54	20.54	21.73	21.73	21.73	21.73
Fe <sub>2</sub> O <sub>3</sub>	0.00	3.00	6.00	9.00	0.00	4.00	8.00	9.00	0.00	4.00	6.00	8.00
FeO	12.56	9.56	6.56	3.56	18.54	14.54	10.54	8.54	16.62	12.62	10.62	8.62
MgO	7.64	7.64	7.64	7.64	7.36	7.36	7.36	7.36	7.55	7.55	7.55	7.55
CaO	0.50	0.50	0.50	0.50	1.45	1.45	1.45	1.45	0.85	0.85	0.85	0.85
MnO	0.00	0.00	0.00	0.00	0.00	0.00	0.00	0.00	0.00	0.00	0.00	0.00
Na <sub>2</sub> O	2.54	2.54	2.54	2.54	2.19	2.19	2.19	2.19	2.54	2.54	2.54	2.54
K <sub>2</sub> O	0.01	0.01	0.01	0.01	0.02	0.02	0.02	0.02	0.00	0.00	0.00	0.00
F	0.00	0.00	0.00	0.00	0.00	0.00	0.00	0.00	0.00	0.00	0.00	0.00
H <sub>2</sub> O*	3.49	3.51	3.53	3.57	3.43	3.47	3.51	3.52	3.46	3.49	3.51	3.53
Li <sub>2</sub> O*	0.00	0.00	0.06	0.34	0.00	0.12	0.36	0.42	0.00	0.12	0.24	0.35
Total:	98.89	98.98	99.13	99.55	100.73	100.99	101.38	101.48	100.42	100.68	100.87	101.07
T: Si	5.914	5.877	5.837	5.779	6.236	6.174	6.103	6.086	6.185	6.124	6.089	6.054
Al	0.086	0.123	0.163	0.221	0.00	0.00	0.00	0.00	0.00	0.00	0.00	0.00
Z: Al	5.383	5.313	5.235	5.123	4.230	4.188	4.140	4.128	4.442	4.398	4.373	4.348
Mg	0.617	0.687	0.765	0.877	1.770	1.812	1.860	1.871	1.558	1.602	1.627	1.652
Fe <sup>3+</sup>	0.00	0.00	0.00	0.00	0.00	0.00	0.00	0.001	0.00	0.00	0.00	0.00
Y: Al	0.00	0.00	0.00	0.00	0.00	0.00	0.00	0.00	0.00	0.00	0.00	0.00
Ti	0.093	0.092	0.091	0.091	0.206	0.204	0.201	0.201	0.260	0.257	0.256	0.254
Fe <sup>3+</sup>	0.00	0.386	0.767	1.139	0.00	0.521	1.029	1.154	0.00	0.517	0.771	1.022
Mg	1.342	1.261	1.169	1.038	0.147	0.086	0.016	0.00	0.0394	0.331	0.294	0.259
Fe <sup>2+</sup>	1.807	1.367	0.932	0.501	2.709	2.103	1.507	1.360	2.411	1.812	1.516	1.2240
Li*	0.00	0.00	0.041	0.232	0.00	0.087	0.246	0.285	0.00	0.083	0.163	0.241
Σ Y	3.242	3.106	3.00	3.00	3.062	3.00	3.00	3.00	3.064	3.00	3.00	3.00
X: Ca	0.092	0.091	0.091	0.090	0.271	0.269	0.266	0.265	0.159	0.157	0.156	0.155
Na	0.847	9.842	0.836	0.828	0.742	0.735	0.726	0.724	0.854	0.846	0.841	0.836
K	0.003	0.003	0.003	0.003	0.004	0.004	0.004	0.004	0.00	0.00	0.00	0.00
Min.:	Schorl	Schorl	Schorl	Buergerite	Schorl	Schorl	Schorl	Schorl	Schorl	Schorl	Schorl	Schorl

	Point 1 2677_3	Point 1 2677_3	Point 1 2677_3	Point 1 2677_3	Point 1 T2 1694_20	Point 1 T2 1694_20	Point 1 T2 1694_20	Point 1 T2 1694_20
SiO <sub>2</sub>	36.34	36.34	36.34	36.34	35.55	35.55	35.55	35.55
TiO <sub>2</sub>	0.55	0.55	0.55	0.55	2.61	2.61	2.61	2.61
Al <sub>2</sub> O <sub>3</sub>	28.01	28.01	28.01	28.01	19.73	19.73	19.73	19.73
Fe <sub>2</sub> O <sub>3</sub>	0.00	1.00	3.00	5.00	0.00	1.00	2.00	3.00
FeO	10.67	9.67	7.67	5.67	18.56	16.56	16.56	15.56
MgO	7.78	7.78	7.78	7.78	7.54	7.54	7.54	7.54
CaO	0.74	0.74	0.74	0.74	1.20	1.20	1.20	1.20
MnO	0.00	0.00	0.00	0.00	0.00	0.00	0.00	0.00
Na <sub>2</sub> O	2.73	2.73	2.73	2.73	2.62	2.62	2.62	2.62
K <sub>2</sub> O	0.02	0.02	0.02	0.02	0.06	0.06	0.06	0.06
F	0.00	0.00	0.00	0.00	0.00	0.00	0.00	0.00
H <sub>2</sub> O*	3.60	3.61	3.63	3.65	3.44	3.45	3.45	3.46
Li <sub>2</sub> O*	0.02	0.07	0.19	0.00	0.00	0.00	0.01	0.07
Total:	100.88	100.98	101.18	101.44	101.28	101.31	101.35	101.45
T: Si	6.056	6.039	6.005	5.967	6.198	6.185	6.171	6.153
Al	0.00	0.00	0.00	0.00	0.00	0.00	0.00	0.00
Z: Al	5.501	5.486	5.455	5.388	4.054	4.045	4.037	4.025
Mg	0.499	0.514	0.545	0.612	1.946	1.955	1.951	1.946
Fe <sup>3+</sup>	0.00	0.00	0.00	0.00	0.00	0.00	0.012	0.030
Y: Al	0.00	0.00	0.00	0.00	0.00	0.00	0.00	0.00
Ti	0.069	0.068	0.068	0.068	0.342	0.341	0.341	0.340
Fe <sup>3+</sup>	0.00	0.125	0.373	0.618	0.00	0.131	0.249	0.361
Mg	1.434	1.413	1.372	1.293	0.013	0.001	0.00	0.00
Fe <sup>2+</sup>	1.487	1.344	1.060	0.779	2.706	2.555	2.404	2.252
Li*	0.011	0.050	0.127	0.243	0.00	0.00	0.006	0.047
Σ Y	3.00	3.00	3.00	3.00	3.062	3.028	3.00	3.00
X: Ca	0.132	0.131	0.131	0.130	0.225	0.224	0.224	0.223
Na	0.882	0.880	0.875	0.869	0.886	0.884	0.882	0.879
K	0.005	0.005	0.005	0.005	0.014	0.014	0.014	0.014
Mineral	Schorl	Schorl	Schorl	Schorl	Schorl	Schorl	Schorl	Schorl

### **3.10 EPMA Ti-in-quartz**

This was a pilot study to compliment cold-CL observations. Quantitative quartz analysis was carried out at CSM using the same EMPA instrument set up as described above. Conditions used were an accelerating voltage of 20 kV, a beam current of 70 nA and a spot size of 15  $\mu\text{m}$  (to aid beam stability). Measurements were done for 200 seconds on the Ti peak and 200 seconds on the adjacent background. The following standards were used: MK2- $\text{Al}_2\text{O}_3$  for  $\text{Al}_2\text{O}_3$ , rutile for  $\text{TiO}_2$  and haematite for Fe. Al was placed on both TAP and TAPH crystals, Fe on LIFH and Ti on PETJ. Detection limits ( $3\sigma$  background) were 70 ppm Ti, 73 ppm Fe and 152 ppm Al. Raw data were reduced by means of the Armstrong PRZ correction with an added assumption that analyses contain 100% Si (Si was not analysed for due to dead time affects). No glass standards or blanks were available at CSM.

For the Ti-in-quartz geothermometer to be valid, however, rutile must be established as an equilibrium phase within the mineral assemblage. This was verified from petrographic and QEMSCAN<sup>®</sup> analysis where a number of quartz phenocrysts and matrix-hosted xenocrysts were found to contain rutile inclusions. This did however cause issues because elevated Ti signals attributed to secondary fluorescence of Ti (Bremsstrahlung radiation) was caused by rutile crystals on and below the surface. This required pre-screening and careful checking before and afterwards to mitigate this issue.

#### **3.10.1 EPMA Ti-in-quartz QA/QC**

Due to the known instability of quartz under commonly used beam conditions (e.g., Kronz et al., 2012), preliminary work was undertaken to ensure the optimum conditions were used for the El Teniente samples and the instrument setup at CSM. As such, a series of exposure experiments were undertaken for different beam currents and spot sizes. To begin with, 100 nA, 20 kV and a 5  $\mu\text{m}$  spot size was trialed over 12 minutes, the same conditions used by Kronz et al. (2012). Under these conditions, the signal intensity rapidly decreased after a few minutes. The spot size was therefore incrementally increased from 5 to 10 and then 15  $\mu\text{m}$ . Despite this, the signal still degraded after a few minutes. The beam current was then progressively decreased from 100 nA until an optimum set of conditions was obtained, which was 70 nA and a 10  $\mu\text{m}$  spot size.

The Ti peak and background curvature were modeled to help mitigate the effects of a high background related to Bremsstrahlung, i.e. to improve the detection limits for Ti. To achieve this, the Ti  $\text{K}\alpha$  peak and background were measured for 20 minutes using a beam current of 160 nA. Ti was initially measured on the PETJ and PETH crystals. The range and crystal D-spacing of the PETH crystal however only allowed for one Ti

K $\alpha$  background to be modelled (Fig. 3.5). Since the software on the CSM electron probe is only capable of applying a linear background interpolation model, this resulted in an artificially low background and therefore systematically higher reported Ti concentrations. It was therefore decided not to analyse for Ti on the PETH crystal.

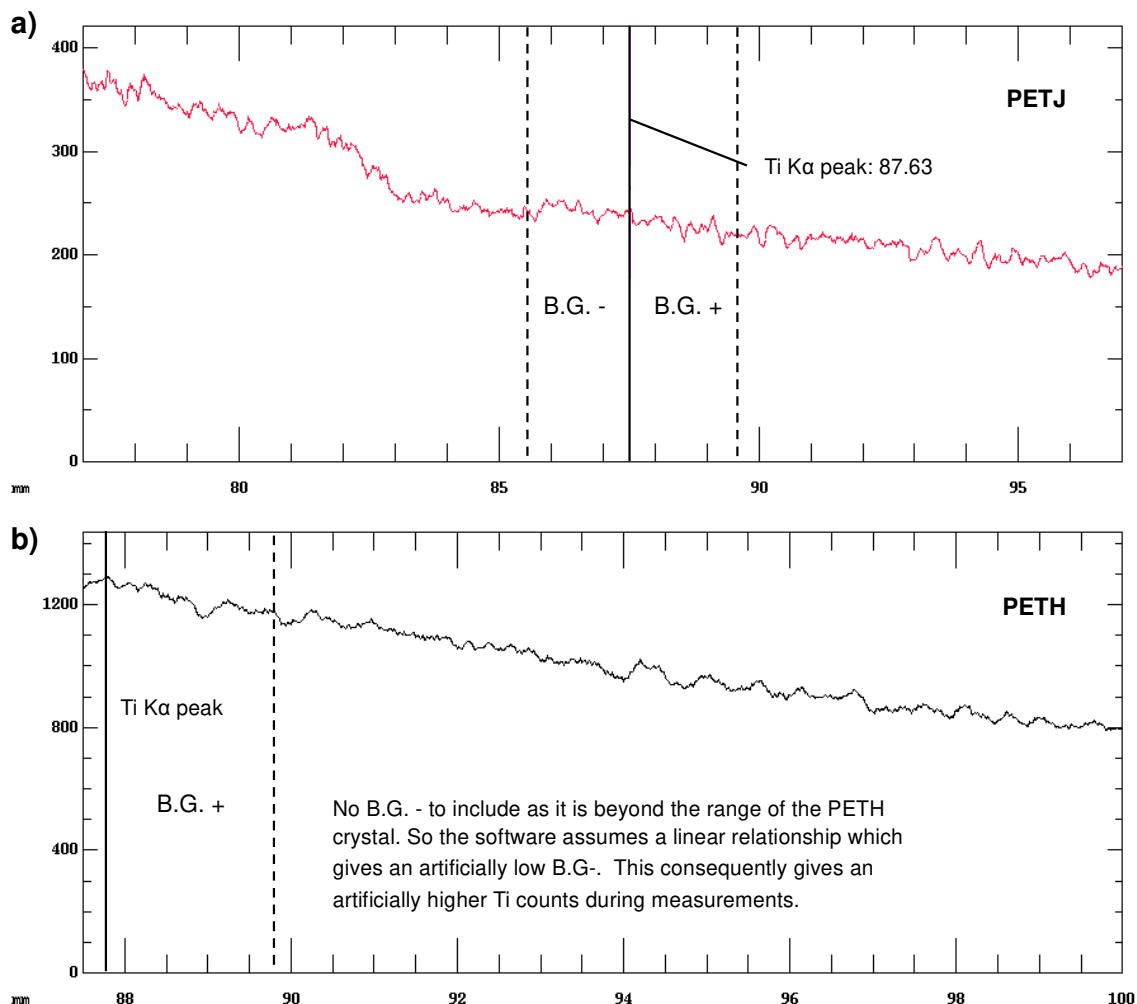


Fig. 3.5 Twenty-minute wavescans on the quartz standard to model the background and peak (solid vertical black line) of Ti on the PETJ (a) and PETH (b) crystals.

**Internal quartz EPMA ‘standard’** - A homogenous quartz grain (Fig. 3.6) was analysed repeatedly by EPMA at the start, during and at the end of each sample run to help monitor any potential drift and to assess the repeatability. No other suitably large, homogenous, Ti-phase-free crystal was available or identified in the El Teniente samples. The Ti concentrations in the repeatedly analysed quartz grain (Fig. 3.6) ranged from 73 ppm ( $\pm 21.15\%$  error based on the standard deviation in X-ray counting) to 127 ppm ( $\pm 12.8\%$ ). Using  $T (^{\circ}\text{C}) = (-3765 / (\log \text{Ti} - 5.69)) - 273$  from Wark and Watson (2006) gives a temperature range between 714 $^{\circ}\text{C}$  and 776 $^{\circ}\text{C}$ .



### 3.11 Quartz LA-ICP-MS

Four analyses of quartz by LA-ICP-MS were conducted at CSM using a New Wave NWR 213 ESI laser (Nd:YAG 213 nm) coupled to an Agilent ICP-MS 7700 Quadrupole mass spectrometer. The analyses were performed using a laser repetition rate of 10 Hz, a fluence of  $6 \text{ jcm}^{-2}$ , a  $50 \text{ }\mu\text{m}$  spot size and an ablation time of 40 seconds. The element isotopes determined were  $^{49}\text{Ti}$ ,  $^{27}\text{Al}$ , and  $^{57}\text{Fe}$ . NIST SRM 610 certified reference material was used to externally calibrate the instrument and to verify the quality of the analyses. This was analysed three times at the beginning and three times at the end of each set samples. Only the Diablo cement quartz produced reliable data. Quartz in the Braden Diatreme (clast- or matrix-hosted) ablated poorly and nearly always instantaneously fractured which resulted in contamination from adjacent phases.

### 3.12 Tourmaline LA-ICP-MS

LA-ICP-MS analyses of 170 points were carried out on  $150 \text{ }\mu\text{m}$  thick polished thin sections, each of which had been previously characterised by EPMA. Prior to ablation, areas were carefully examined by SEM to avoid any inclusions such as quartz or rutile. Ablation was carried out in an He-Ar atmosphere with flow rates of 700 ml/min He and 0.8 L/min Ar.

Data were collected using a  $40 \text{ }\mu\text{m}$  spot, 30 seconds of gas blank followed by 5 pre-ablation pulses, a dwell time of 60 seconds, a laser repetition rate of 10 Hz and a fluence of  $5 \text{ jcm}^{-2}$ . The minor and trace element isotopes measured included:  $^7\text{Li}$ ,  $^{23}\text{Na}$ ,  $^{39}\text{K}$ ,  $^{44}\text{Ca}$ ,  $^{45}\text{Sc}$ ,  $^{49}\text{Ti}$ ,  $^{51}\text{V}$ ,  $^{52}\text{Cr}$ ,  $^{55}\text{Mn}$ ,  $^{59}\text{Co}$ ,  $^{60}\text{Ni}$ ,  $^{65}\text{Cu}$ ,  $^{66}\text{Zn}$ ,  $^{75}\text{As}$ ,  $^{85}\text{Rb}$ ,  $^{88}\text{Sr}$ ,  $^{89}\text{Y}$ ,  $^{93}\text{Nb}$ ,  $^{95}\text{Mo}$ ,  $^{118}\text{Sn}$ ,  $^{139}\text{La}$ ,  $^{140}\text{Ce}$ ,  $^{141}\text{Pr}$ ,  $^{146}\text{Nd}$ ,  $^{147}\text{Sm}$ ,  $^{151}\text{Eu}$ ,  $^{157}\text{Gd}$ ,  $^{159}\text{Tb}$ ,  $^{163}\text{Dy}$ ,  $^{165}\text{Ho}$ ,  $^{166}\text{Er}$ ,  $^{169}\text{Tm}$ ,  $^{172}\text{Yb}$ ,  $^{175}\text{Lu}$  and  $^{208}\text{Pb}$ . Data processing and reduction was carried out using the Iolite software package within Igor Pro (Paton et al., 2011). Analytical uncertainty and limits of detection (LOD) are shown in Table 3.5. LOD, which were calculated using the  $3\sigma$  criterion (e.g., Longerich et al., 1996), were better than: 1 ppm for REE, Y, Nb and Co; 5 ppm for Li, Ti, V, Cr, Ni, As, Rb, and Sn; 6.3 ppm for Sc and Mn; and 7.5 ppm for Cu and Zn.

#### 3.12.1 Tourmaline LA-ICP-MS method development

To assess the affects of spot size on detection limits, a tourmaline crystal was repeatedly analysed using different spot sizes and ablation times. Firstly, a  $40 \text{ }\mu\text{m}$  spot and an ablation time of 40 s were used, with the ablation time then increased to 60 s. Tourmaline was then ablated for 60 seconds but with increased spot sizes of  $50 \text{ }\mu\text{m}$  and  $100 \text{ }\mu\text{m}$ . The best detection limits (several ppm to  $\sim 1$  ppm and below for many elements) were achieved by increasing the ablation time to 60 s and increasing the

spot size to 100 µm. Due to the needle-like nature of many tourmaline crystals and fine scale of zonation, however, using a spot size of 100 µm was not practical. Final settings were a 40 µm spot with a dwell time of 60 seconds.

### **3.12.2 Tourmaline LA-ICP-MS QA/QC**

Trace element concentrations were externally calibrated using the certified reference material NIST SRM 610, which was analysed three times at the beginning and at the end of each sample run. For each LA-ICP-MS analysis, the Si content previously determined by EMPA was used as an internal standard.

The possibility of mixed ablation signals, particularly when analysing later feathery tourmaline crystal overgrowths was taken into account and care was taken to best mitigate and prevent this as best as possible. Careful petrography identified particularly intergrown tips at the sample surface and these were ignored. The surrounding phases intergrown with quartz were also identified and during data processing the signals were monitored to prevent the signal from these unwanted phases being incorporated.

**Accuracy and precision** - Accuracy and precision were determined from the analysis of certified reference material BCR-2G (reference values are from GeoReM and Jochum et al., 2016). Accuracy, which was calculated as the percentage difference between certified values and obtained values (Table 3.5), was better than: 10% for Li, Sc, V, Eu and Gd; 15% for Zn, Rb, La, Pr, Sm, Er and Tm; 20% for Ti, Mn, Co, Ni, Y, Mo, Ce, Nd, Tb, Dy, Ho, Yb and Lu; and 25% for Cr, Nb, and Pb. Cu and Sn were 50% and 40%, respectively.

Precision, based on repeated analyses of BCR-2G, is expressed as the percent relative standard deviation '%RSD' ( $(\text{standard deviation}/\text{mean average}) \times 100$ , where  $n=14$ ) for each analyte shown in Table 3.5. The %RSD was mostly within 5 to 10% of the certified values except for Ni, Zn, Rb, Tm, Yb and Pb which were between 10 and 15%. Cu and Zn had an RSD of 26.8 and 17.5%, respectively, whilst Ti was <5%. Precision was also calculated for repeated analyses ( $n=5$ ) of a relatively homogenous coarse tourmaline grain from La Huifa (Appendix v). This gave values better than: 5% for V, Mn, Co, Ni, Na and Ca; 10% for Sc, Ti, Zn and K; 15% for Sn and Pb; and 20% for Y, Nb, La, Ho, Er, Tm and Lu. All other analytes had a precision worse than 20% except Li, Cu, Rb, Mo and Sm which were below detection.

Table 3.5 LA-ICP-MS analyses of BCR-2G (n= 14) with measured element masses and corresponding detection limits and uncertainty beneath. Analytical uncertainty includes precision ('%RSD') and accuracy ('% diff'). Certified values from GeoReM are in ppm and ' $\bar{X}$  (meas.)', i.e. the mean average of the analyses. No arsenic values were given for BCR-2G so accuracy is unavailable.

Measured masses:		<sup>7</sup> Li	<sup>45</sup> Sc	<sup>49</sup> Ti	<sup>51</sup> V	<sup>52</sup> Cr	<sup>55</sup> Mn	<sup>59</sup> Co	<sup>60</sup> Ni
D.L (ppm)	Min.	0.68	2.00	0.80	1.50	1.70	2.00	0.16	0.71
	Max.	3.20	14.00	4.30	6.80	11.00	14.00	1.90	7.50
	Mean	1.39	6.30	1.70	3.12	4.21	6.30	0.56	2.63
Analytical uncertainty	$\bar{X}$ (meas.)	8.64	32.52	12,133.47	387.88	14.05	1,325.34	33.01	10.87
	Certified value	9.13	33.53	13,575.25	417.60	15.85	1,522.59	37.33	12.57
	RSD%	5.14	5.46	4.44	5.10	8.86	6.47	6.42	11.54
	% diff.	4.22	1.48	16.21	9.57	20.97	16.94	15.10	19.55
Measured masses:		<sup>65</sup> Cu	<sup>66</sup> Zn	<sup>75</sup> As	<sup>85</sup> Rb	<sup>89</sup> Y	<sup>93</sup> Nb	<sup>95</sup> Mo	<sup>118</sup> Sn
D.L (ppm)	Min.	1.90	2.00	1.20	1.20	0.05	0.06	0.35	0.28
	Max.	18.00	17.00	8.50	8.50	0.55	0.52	5.10	3.20
	Mean	7.09	7.28	2.97	2.97	0.20	0.20	1.38	1.17
Analytical uncertainty	$\bar{X}$ (meas.)	14.02	140.83	N/A	42.35	29.83	10.38	226.21	1.86
	Certified value	19.66	129.50	N/A	46.02	36.07	12.44	250.66	2.28
	RSD%	26.83	10.93	N/A	11.47	7.08	6.40	7.76	17.54
	% diff.	49.76	11.24	N/A	10.98	17.31	20.47	19.36	40.06
Measured masses:		<sup>139</sup> La	<sup>140</sup> Ce	<sup>141</sup> Pr	<sup>146</sup> Nd	<sup>147</sup> Sm	<sup>151</sup> Eu	<sup>157</sup> Gd	<sup>159</sup> Tb
D.L (ppm)	Min.	0.04	0.04	0.04	0.22	0.29	0.07	0.24	0.03
	Max.	0.52	0.43	0.47	2.10	2.60	0.99	2.30	0.39
	Mean	0.17	0.16	0.13	0.79	0.94	0.29	0.85	0.12
Analytical uncertainty	$\bar{X}$ (meas.)	21.83	45.85	5.97	24.77	5.90	1.80	6.28	0.89
	Certified value	25.08	53.12	6.83	28.26	6.55	1.99	6.81	1.08
	RSD%	7.73	6.89	5.92	7.96	8.26	7.25	7.09	8.77
	% diff.	13.16	16.25	12.26	16.66	11.63	9.56	6.88	15.05
Measured masses:		<sup>163</sup> Dy	<sup>165</sup> Ho	<sup>166</sup> Er	<sup>169</sup> Tm	<sup>172</sup> Yb	<sup>175</sup> Lu	<sup>208</sup> Pb	<sup>23</sup> Na
D.L (ppm)	Min.	0.15	0.03	0.11	0.04	0.16	0.03	0.11	19.00
	Max.	1.70	0.31	1.60	0.40	1.60	0.37	1.20	130.00
	Mean	0.49	0.14	0.41	0.12	0.58	0.13	0.43	49.80
Analytical uncertainty	$\bar{X}$ (meas.)	5.56	1.07	3.34	0.44	2.89	0.42	9.08	2,3280
	Certified value	6.42	1.31	3.67	0.53	3.39	0.50	10.59	2,3146
	RSD%	7.83	9.14	7.66	11.67	14.44	8.99	12.98	3.60
	% diff.	15.89	18.51	10.89	14.75	17.46	19.29	21.13	2.93

### **3.13 Automated mineralogical analysis: QEMSCAN®**

QEMSCAN® (Quantitative Evaluation of Minerals by Automated Scanning Electron Microscope) was initially designed to support mineral-processing applications but is now also used in a wide range of geological studies (e.g., Pirrie and Rollinson, 2011). Data outputs can include but are not limited to false colour images of sections (mineral maps) and data for mineral associations and quantitative modal mineralogy (Pirrie and Rollinson, 2011). Further details of the technique are provided by Gottlieb et al. (2000), Pirrie et al. (2004), Goodall and Scales (2007) and Pirrie and Rollinson (2011).

Depending on the desired outcome and nature of the samples, QEMSCAN® offers four modes of measurement: PMA (Particle Mineral Analysis), BMA (Bulk Mineral Analysis), TMS/SMS (Trace/Specific Mineral Search) and Fieldscan; the automated equivalent of a traditional point count of a thin section (Pirrie and Rollinson, 2011). For this study, Fieldscan was the most applicable as it allows mineral quantification and the identification of textures and fabrics by providing both false colour mineral maps and quantitative data for mineral proportions. Samples were introduced into the QEMSCAN® SEM as polished sections which were carbon coated to a thickness of ~25 nm.

The area of the polished section to be analysed was divided into pre-defined square fields determined by the user. A BSE image was then automatically acquired for each field to aid in the delineation of different 'particles' (minerals, phases or background (resin or glass)). The fields were then subdivided into a grid of pixels, using a specified spacing, whereupon each pixel area was subject to X-ray elemental point analysis (Pirrie and Rollinson, 2011). These spectra were compared with a database (Species Identification Protocol - SIP) of over 750 known minerals and compounds and then assigned to the most appropriate mineral category (Pirrie and Rollinson, 2011). Areas of resin and glass were disregarded due to being below a predefined BSE threshold (epoxy resin) or filtered out using a database entry (glass). A single sample can be characterised by in excess of six million data points, with the identification of most minerals/phases taking place in approximately 10 milliseconds per point (Rollinson G., personal communication, 2018).

The QEMSCAN® 4300 system at CSM is based on a Zeiss EVO 50 SEM platform which uses a tungsten filament, and has a backscattered electron detector and four light-element Bruker SDD (Silicon Drift Droplet) Energy Dispersive X-ray Spectrometers (EDS). Analyses were undertaken at an accelerating voltage of 25 kV and a low beam current of 5 nA. One thousand counts were collected per X-ray spectra, i.e. per pixel. Pixel spacing was either 10 or 1 µm depending on the detail desired.

### **3.13.1 Data Processing**

Data collection and data processing used iMeasure 4.2 and iDiscover 4.2 SR1 and 4.3 software, respectively, according to instrument and programme settings outlined in Rollinson et al. (2011). The internally developed 'ODG6' SIP was used in this study and modified specifically for each batch of samples. The raw data (compressed EDS spectra and accompanying BSE signal), recorded into a 'datastore', required significant processing before final output. This included checking and validating a large number of mineral compositional groupings and sub-groupings in a robust, and tested database, which was then tailored for the project as required (Pirrie and Rollinson, 2011). To help in correctly identifying the phases present, a good knowledge of the samples, including their modal mineralogy, alteration phases present and an experienced operator/researcher was required (Pirrie and Rollinson, 2011).

### **3.13.2 QEMSCAN® QA/QC**

To ensure reliable and repeatable data, a number of in-house QA/QC procedures were followed. This included the operator initially optimising the beam by checking the filament saturation, tilt, shift, wobble and astigmatism. The grey scale of the BSE image was calibrated using gold and quartz which have known values. The beam was calibrated on the faraday cup, prior to the start of measurements and during data acquisition, then self-calibrated every thirty minutes.

Given mineral/phase classification mainly relies on chemical differences (less so BSE contrast), the system cannot separate polymorphs. It also struggles where minerals or phases have overlapping chemical compositions, mainly due to the limitation of 1,000 counts per spectra which means that each are relatively noisy and there are inherent poor detection limits. The main problematic mineral identifications in the breccias were chlorite vs. tourmaline, anhydrite vs. gypsum and molybdenite vs. celestine. Chlorite and tourmaline, which are the main phases that occur together, have very similar concentrations of Fe, Mg and Si; tourmaline also contains boron (which chlorite does not) but this could not be used as it was invisible to the X-ray detector. Separating these two phases therefore required specific database development, with validation using a chlorite standard that was cross validated using other techniques including optical petrography. It required very precise filtering of the data according to the ratios of Fe, Mg and Si. This gave an estimated accuracy of ~90 to 95%.

Gypsum and anhydrite presented a similar problem, which was overcome by using differences in BSE signal intensity. This was not 100% accurate though as the BSE dips at grain boundaries, which can lead to minor misclassification; this was largely dealt with by using a boundary phase removal process. The correct identification of tourmaline, chlorite, gypsum and anhydrite was manually checked using a much larger number of counts.

For molybdenite (Mo, S) and celestine (Sr, S, O), initially celestine was reported in the molybdenite category because Sr cannot be seen directly in the 4.2 SR1 version software as it is assumed to overlap with Si, and to a lesser extent P. There are also overlaps between Mo ( $L\alpha$  and  $L\beta$ ) and S ( $K\alpha$ ) peaks (the  $K\alpha$  and  $K\beta$  Mo peaks are typically too weak to be detected at 1,000 counts), so QEMSCAN<sup>®</sup> uses a BSE threshold of >100 to identify molybdenite from other S-bearing phases (molybdenum has a higher atomic number than S). Molybdenite vs. celestine identifications were done manually in the same SEM-EDS system using a much larger number of counts.

Very finely intergrown minerals, such as mixed clays (clusters of nano- to micro-crystals), were difficult or impossible to identify separately due to the relatively large excitation volume of the electron beam, which is likely to have been between 3 and 5  $\mu\text{m}$  in diameter, depending on the nature of the material. This often leads to boundary effects and mixed signals, known as 'mixels'. These artifacts were particularly prevalent in the rock flour breccias when mapped using a 10  $\mu\text{m}$  pixel spacing, and where molybdenite was often present as sub-micron crystals. To attempt to overcome this issue, a number of finer, 1  $\mu\text{m}$  pixel interval, maps (1 $\times$ 1 mm) were created, however this made very little difference as many of the intergrown crystals were still less than 1  $\mu\text{m}$  in size.

Determining grain size was also sometimes an issue as the system cannot differentiate "touching grains of the same mineral" as "the technique is not able to determine the boundary thus identifies the grain as one". The opposite is also true where an 'inclusion or rogue pixel in a grain can cause a large grain to be divided and then identified as more than one' (Scott and Rollinson, 2016). Finally, data for determined porosity (including from grain plucking and fractures) may not be wholly accurate as it includes the 'background' category, but only when this is constrained (Rollinson G., personal communication, 2018).

## 4 Results: Breccia petrography and geochemistry

In this chapter, textural descriptions and classifications of the Braden Diatreme and tourmaline breccia bodies at El Teniente are presented, along with major, minor and trace element compositions for tourmaline from each unit.

### 4.1 Braden Diatreme: petrography and links to Mo-Cu mineralisation

The Braden Diatreme breccia facies are characterised by the common occurrence of varying volumes of fine-grained K-feldspar, Fe-illite/illite, sericite and quartz±chlorite 'rock flour' matrix (Fig. 4.1). The following sub-units are described in this chapter: Braden Sericite Breccia, Fine Braden Sericite Breccia, Blocky Braden Sericite Breccia and the Braden Sulphide Breccia, including their paragenetic relations with Mo-Cu mineralisation. The Braden Tourmaline Breccia is described separately in Section 4.4.3 with the other tourmaline breccias.

#### 4.1.1 Braden Sericite Breccia

**Clasts** - This polymictic matrix-supported breccia is poorly sorted with >20° of clast rotation creating a chaotic texture (Fig. 4.2). Large and small clasts are rounded to subrounded and less commonly subangular. Clasts are derived from all units at El Teniente including the TMC wall rocks, dacite-diorite intrusives and previously emplaced hydrothermal tourmaline (±biotite) breccias. The most common clasts are from the TMC and dacite-diorite, with relative clast proportions varying with location in the pipe. For example, dacite becomes the dominant clast type towards the contact with the underlying dacite intrusive. No fragments resembling fluviolacustrine sediments, organic-rich material, or accretionary lapilli were observed in this study as expected by Tămaş and Milési (2002) for diatremes which reached palaeosurface.

The most common size range of large (>2 mm) clasts is 2 mm to 10 cm, although there are significantly larger, >20 m, 'mega' dacite and ~5 m blocks of Marginal Tourmaline Breccia (e.g., DDH1694: 88.4 to 92 m). There is no link between clast size or composition and the degree of rounding. Less common fragments include earlier hydrothermal biotite (now altered to chlorite; Fig. 4.2i) and tourmaline breccias (Fig. 4.2h), which account for <10% of the total clast population. They are subrounded to rounded and are usually <10 cm across. Clasts of earlier hydrothermal tourmaline breccias, depending on size, contain angular fragments of the TMC, and the tourmalines show patchy zoning in Al-Fe (Fig. 4.2h). End-stage space-fill in the breccia clasts is made up of anhydrite, quartz and chalcopyrite.

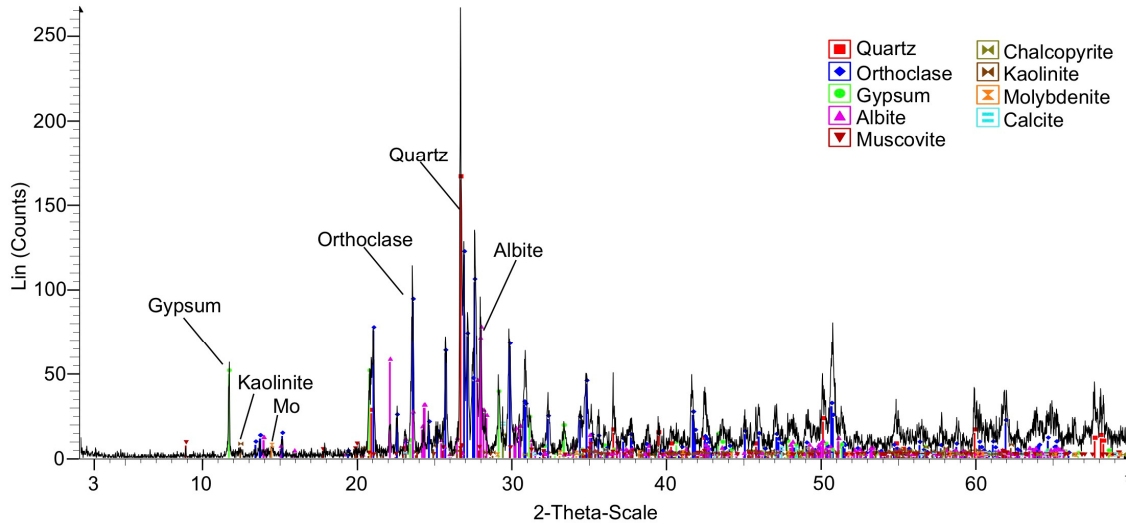


Fig. 4.1 XRD pattern for the rock flour matrix from drill hole 1196-172.71 m indicating the presence of quartz, orthoclase, gypsum, albite, muscovite, chalcopyrite, kaolinite, molybdenite and calcite. Molybdenite and chalcopyrite are associated with a later overprint associated with the formation of the Braden Sulphide Breccia, and are not normally found at such concentrations within the Braden Sericite Breccia.

**Matrix** - The rock flour matrix comprises between 50 and 75 vol.% of the rock and is composed of a mixture of fine particles (<0.2 mm), mostly consisting of fine-grained <5  $\mu\text{m}$  K-feldspar intergrown with a combination of fine clays (Fe-illite/illite), sericite, quartz and variable chlorite (Fig. 4.1 and Fig. 4.2). It is highly porous on a micron-scale (Fig. 4.2f) with <50  $\mu\text{m}$  vugs common. Infilling this porosity is a mixture of anhydrite-gypsum, ankerite and quartz $\pm$ pyrite. Molybdenite and chalcopyrite fill some pore spaces but only where close (~10's m) to the Braden Sulphide and Braden Tourmaline Breccias, respectively. A number of infilling quartz patches have distinct zones, showing cores with  $\leq 10 \mu\text{m}$  iron oxide inclusions and inclusion-free overgrowths (see Fig. 4.2f).

**Alteration** - Texturally destructive sericite-pyrite alteration has overprinted both the clasts and matrix (Fig. 4.2c). Replacement of ferromagnesian-rich phenocrysts and matrix-hosted xenocrysts by coarse (<1 cm) pyrite has resulted in euhedral relict textures (Fig. 4.2e). Coarser pyrite often has quartz and anhydrite inclusions along with remnants of the sericite-Fe-illite/illite-altered clasts (e.g., Fig. 4.2d, e). Overprinting much of this sericite-pyrite-altered facies are a number of distinct alteration zones which resulted from either the formation of the Braden Sulphide Breccia (Section 4.1.4), the Braden Chlorite Breccia, or the Braden Tourmaline Breccia (Section 4.4.3). The chlorite overprint affects both matrix and clasts (e.g., Fig. 4.2a, b). Ferromagnesian-rich clasts from the TMC have undergone more intense alteration than those from the felsic units.

**Cu-Mo mineralisation** - The Braden Sericite Breccia is considered uneconomic by Codelco geologists, although pre-brecciation porphyry-style Cu±Mo mineralisation is present within some clasts, such as those from the TMC. The main sulphide in the Braden Sericite Breccia is pyrite (~1 to 2%) which is hosted within both the clasts (Fig. 4.2b, c) and matrix (Fig. 4.2a). The exception to this is surrounding the Braden Tourmaline Breccia and within the Braden Sulphide Breccia where chalcopyrite and chalcopyrite-molybdenite are the main sulphide phases, respectively. Later discontinuous gypsum veinlets±chalcopyrite, bornite, tennantite-tetrahedrite, probably related to Póstuma alteration, cross-cut these facies, discussed later.

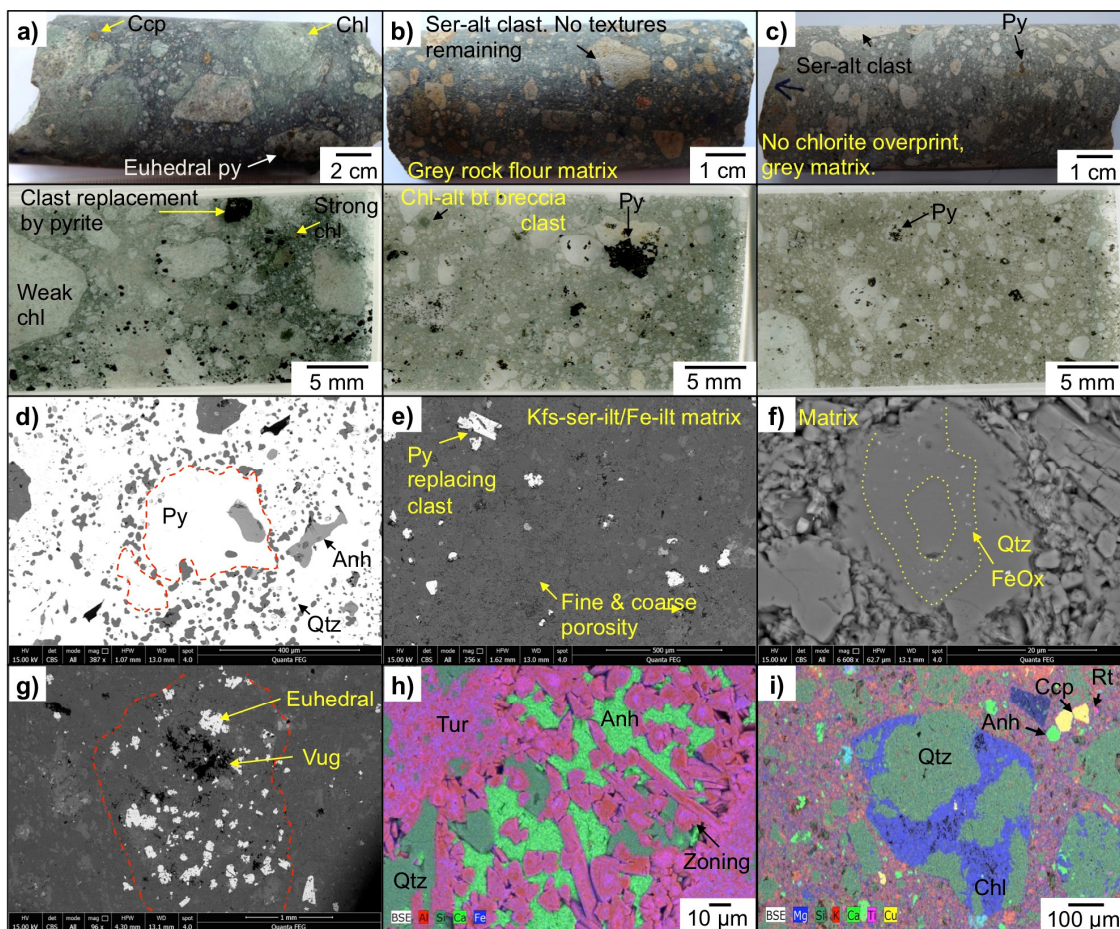


Fig. 4.2 Photographs of hand specimens with corresponding images of 30  $\mu$ m thin sections below (a-c), and SEM-BSE images (d-g) and SEM-EDS maps (h-i) of the matrix-supported Braden Sericite Breccia with variable chlorite overprints: **a)** Strongly chlorite-altered matrix with less altered clasts. Pyrite is pervasive throughout the sample. From DDH1068-429.5 m; **b)** Weak chloritisation of the matrix with comparatively less chlorite-altered clasts, and replacement of clasts by pyrite. From DDH1079-363.7 m; **c)** Light grey to cream clasts and matrix, lacking chlorite alteration. From DDH1694-92.5 m. (**d-h** from DDH1068-429.5 m and **i-k** from DDH1079-363.7 m); **d)** Quartz-anhydrite inclusions within pyrite; **e)** Euhedral pyrite replacing clasts and infilling voids in matrix; **f)** Matrix-hosted quartz with a zone rich in FeOx inclusions shown in yellow; **g)** Sericitised clast partially replaced by euhedral pyrite; **h)** Clast of tourmaline breccia in the Braden Sericite Breccia. Tourmaline has patchy or rare concentric zoning. Quartz and anhydrite infill void space; **i)** Rounded clast of chlorite-altered biotite breccia in the Braden Sericite Breccia matrix. Chlorite is coarse and cements the silicified fragments in the clast.

#### 4.1.2 Fine Sericite Braden Breccia

The Fine Sericite Braden Breccia occurs as irregular zones, <50 m wide (e.g., DDH1769), in the Braden Diatreme, with either sharp or gradational (e.g., Fig. 4.3c) contacts. It cross-cuts the Braden Sericite and Blocky Braden Sericite Breccias with the matrix infiltrating the latter (see Fig. 4.3c) for several cm. It is texturally distinct from other breccia facies in the Braden Diatreme by having a higher ratio of matrix:clasts and a clast population that is generally much finer (<10 mm) than in the Braden Sericite Breccia. Where large clasts (>2 mm) are present, their sizes vary from ~1 cm to several cm (e.g., Fig. 4.3b). Clast roundness is varied, with some being subangular/angular (Fig. 4.3c) and others well-rounded (Fig. 4.3a). The matrix comprises >85 vol.% of the rock, and in places >97 vol.% (Fig. 4.3) and is composed of K-feldspar, Fe-illite/illite, sericite, quartz and variable chlorite.

Moderate to intense, texturally destructive sericite alteration has coloured clasts cream-white and destroyed all primary textures. Clasts are now composed of a fine-grained mix of muscovite/illite, K-feldspar, rutile, plagioclase and minor tourmaline-titanite. No juvenile clasts were observed in this unit. It contains little sulphides including pyrite, which is only present within larger altered clasts (e.g., Fig. 4.3b). A mixture of discontinuous gypsum-chalcopyrite-tennantite-tetrahedrite veinlets related to Póstuma alteration cross-cut the unit. Ankerite locally infills remaining space.

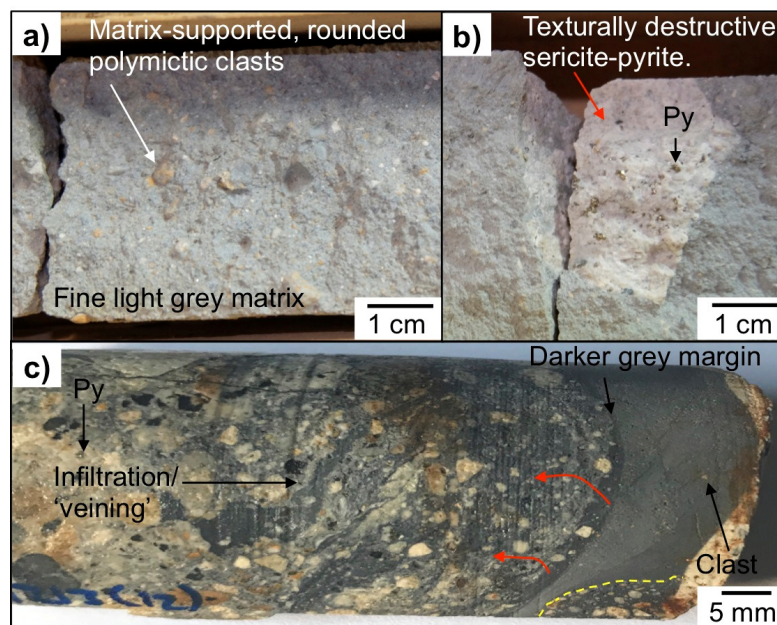


Fig. 4.3 Drill core photographs of the Fine Sericite Braden Breccia: **a)** Fine-grained blue-grey matrix with <1 cm well-rounded clasts. The breccia contains a higher portion of fine clasts (0.1 to 2 mm) than larger clasts (>2 mm). From DDH1775-128.90 m; **b)** Texturally destructive pyrite-sericite alteration of clasts. From DDH1775-136.25 m; **c)** Narrow interval (<2 cm) of Fine Sericite Braden Breccia cross-cutting the Braden Sericite Breccia/Blocky Braden Sericite Breccia. The narrow interval is near entirely composed of matrix, which permeates outwards (red arrows) into the surrounding rock. From DDH1213-212.97 m.

### 4.1.3 Blocky Braden Sericite Breccia (pebble dykes)

The Blocky Braden Sericite Breccia occurs as tabular bodies cross-cutting the Braden Sericite Breccia. It is dark to light grey, clast-supported and with  $>20^\circ$  clast rotation. It was distinguished from the Braden Sericite Breccia by having a coarser ( $<20\%$  fine  $<2$  mm clasts) clast population that comprises  $>70$  vol.% of the rock. Most large and small clasts are rounded to subrounded and are  $<5$  cm, although they can exceed several m. Clasts include the TMC, felsic-intermediate intrusives and pre-existing hydrothermal tourmaline breccias (e.g., Fig. 4.4b). The matrix is composed of sericite-quartz with lesser illite/Fe-illite and pyrite. No juvenile clast component was identified in this unit. In places it has been weakly to moderately overprinted by chlorite. It shows variable grading between clast-rich (Fig. 4.4a-d) and clast-poor areas (Fig. 4.4e, f).

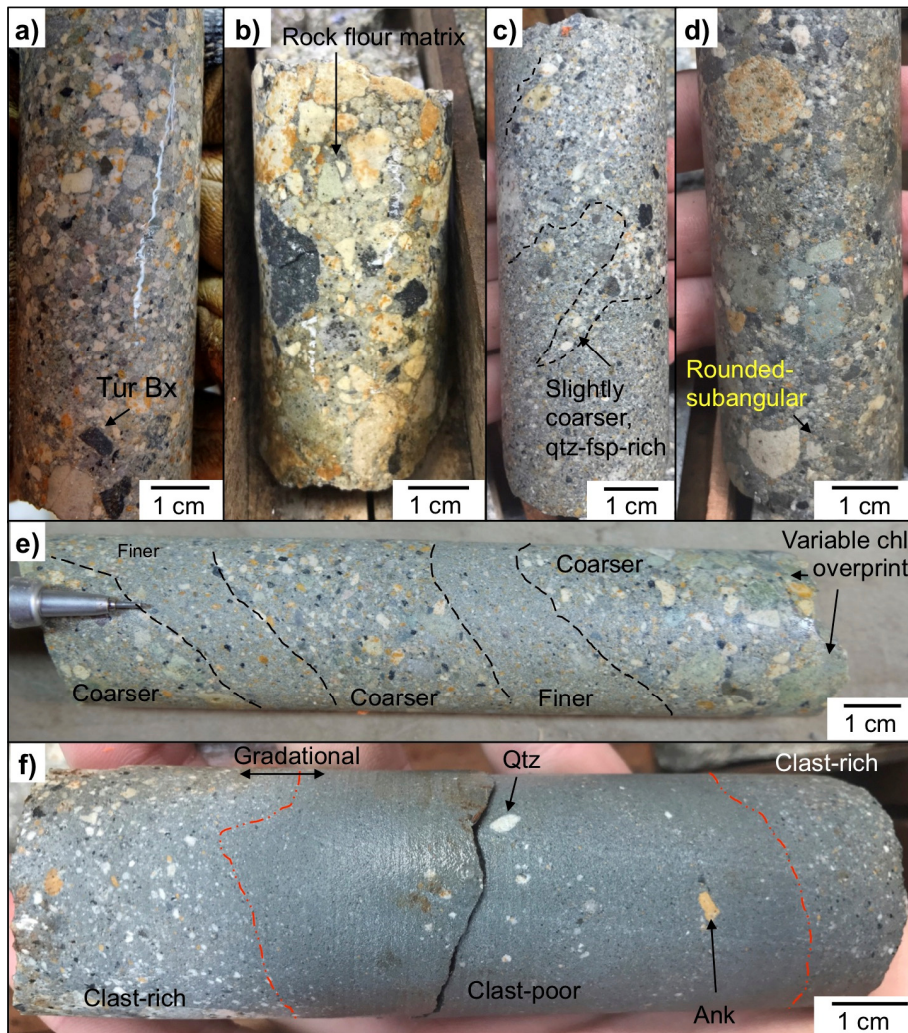


Fig. 4.4 Drill core photographs of Blocky Braden Sericite Breccia: **a-b)** Rounded to sub-rounded clasts in a sericite-quartz matrix. From DDH1694-251.00 m and DDH1213-108.94 m respectively; **c)** Fine and coarser areas outlined in black. From DDH1694-250.85 m; **d)** Larger (~1 cm) and smaller ( $<500 \mu\text{m}$ ) rounded-subrounded clasts with a grey sericite-quartz matrix. From DDH694-249.04 m; **e)** Finer ( $<2$  mm) and coarser ( $>2$  mm) intervals outlined in black. From DDH1694-252.07 m; **f)** Blocky Sericite Breccia is present either side of the drill core photo with an inner portion of Fine Sericite Braden Breccia. From DDH1694-258.20 m.

#### 4.1.4 Braden Sulphide Breccia

The Braden Sericite Breccia has been subject to fluid- and/or vapour-induced overprints resulting in higher Mo (up to 0.55 wt.%) and Cu (up to 1.79 wt.%). These enriched areas are termed the 'Braden Sulphide Breccia', which are largely situated within a couple of hundred metres of the Braden Diatreme margin. Intersections of the Braden Sulphide Breccia in drill core range from tens of cm to tens of metres, and can be up to ~60 m in length (e.g., DDH1213: 145.70 to 205.42 m). Clast population characteristics are the same as in the Braden Sericite Breccia in terms of composition, size distribution, degree of rounding and sorting. Clasts contain a mixture of K-feldspar, quartz, muscovite/illite, biotite/Fe-illite, rutile, titanite, anhydrite-gypsum and chalcopyrite-pyrite.

The rock flour matrix is the same as in the Braden Sericite Breccia (largely composed of K-feldspar with varying amounts of illite/Fe-illite, kaolinite and chlorite) with the key distinction that it is variably impregnated with molybdenite. Coarse chalcopyrite veinlets, irregular sphalerite and added gypsum-anhydrite are also present. A number of mineralising events have been identified which, in varying proportions, contributed to their elevated Mo and Cu concentrations. These have been grouped based on relative timing, mineral assemblages and style of mineralisation into the following approximate time sequence (oldest to youngest), as illustrated in Fig. 4.5:

1. Pre-brecciation porphyry-style disseminated and veinlet Cu-Mo mineralisation, as shown in a number of clasts (e.g., Fig. 4.5c);
2. On a scale of <10 cm, increased molybdenite with euhedral quartz±gypsum-anhydrite-barite-apatite-chalcopyrite-sphalerite-galena are spatially associated with the margins, and within a few cm, of what have been interpreted as juvenile dacite clasts (discussed in more detail in Section 4.1.5). Molybdenite decreases with increasing distance from these dacite clasts becoming negligible >2 cm from the clast margins. Euhedral quartz (with molybdenite-sphalerite-barite inclusions) and coarse (>200 µm) sphalerite-galena are largely restricted to within <10 mm of the dacite clasts;
- 2b. Wider-scale pervasive impregnation of the porous rock flour matrix with <20 µm long acicular molybdenite and coarser chalcopyrite (Fig. 4.5g). Depending on the concentration of molybdenite, the grey rock flour matrix is darkened to shades of blue and a metallic luster where molybdenite is >0.1% (e.g., Fig. 4.5f). Although pervasive, molybdenite does not completely infill the rock flour matrix porosity and the sericite-pyrite-altered clasts in the matrix do not have the molybdenite overprint. Other coeval phases include quartz, gypsum-anhydrite;
3. Veining of gypsum-ankerite-anhydrite-chalcopyrite-sphalerite-galena (±tourmaline) cutting clasts and causing minor brecciation of clasts;
4. Partial replacement of the molybdenite-bearing rock flour matrix by late

anhydrite-gypsum-ankerite ( $\pm$ chalcopyrite-tennantite-tetrahedrite-sphalerite-galena) assemblages (Fig. 4.5h, i).

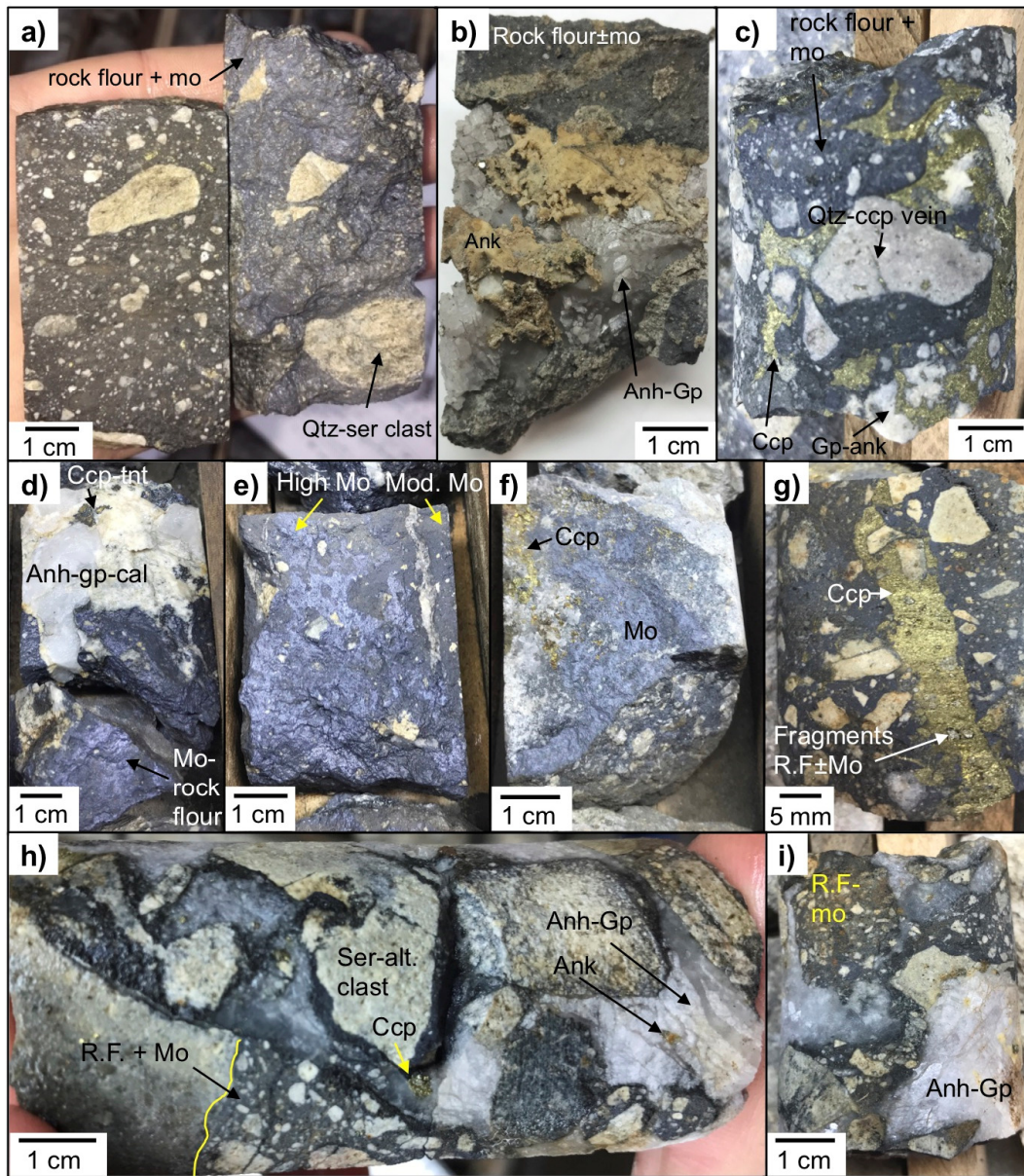


Fig. 4.5 Series of drill core photos of Braden Sulphide Breccia with distance from annular Marginal Breccias (MBX): **a**) Braden Sericite Breccia with moderate replacement of the rock flour matrix by tourmaline - no molybdenite overprint (left) and pervasive molybdenite overprint of the Sericite Breccia (right). Samples from DDH1196; **b**) Anhydrite-gypsum-ankerite re-brecciating weakly molybdenised rock flour (0.34% Cu, 0.085% Mo and ~86 m from MBX). From DDH1196-231.34 m; **c**) Chalcopyrite-gypsum-ankerite re-brecciation of the molybdenite-bearing rock flour matrix (1.79% Cu, 0.38% Mo and ~71 m from MBX). From DDH1196-216.68 m; **d**) Coarse anhydrite-gypsum ( $\pm$ chalcopyrite-tetrahedrite) brecciation of the molybdenised rock flour (0.83% Cu, 0.4% Mo and ~55 m from MBX). From DDH1213-155.51 m; **e**) Strong molybdenite overprint with associated metallic luster (0.83% Cu, 0.4% Mo and ~73 m from MBX). From DDH1213-155.73 m; **f**) Weakly molybdenised rock flour (1.34% Cu, 0.15% Mo and ~31 m from MBX). From DDH1213-131.30 m; **g**) Coarse chalcopyrite alongside molybdenised rock flour (1.79% Cu, 0.38% Mo and ~72 m from MBX). From DDH1196-216.87 m; **h-i**) Coarse anhydrite-gypsum-chalcopyrite cement in the re-brecciated molybdenite-bearing rock flour. h is from DDH1196-200.25 m and i is from DDH1196-200.50 m. Both have grades of ~0.43% Cu, 0.17% Mo and are ~55 m from MBX. 'R.F.'= rock flour. Assay data provided by Codelco.

#### 4.1.5 Juvenile dacite clasts

Newly identified in this study are dacite clasts interpreted as originating from the intrusion which has been shown to underlie the Braden Diatreme (Floody, 2000; Cannell, 2004). Material of this type, characterised by what appear to be ductile textures (having wispy or vermiform shapes and/or blocky to ragged margins, Fig. 4.7), probably indicating that they were viscous when incorporated into the breccia, is frequently referred to as 'juvenile' in the literature (Lorenz and Kurszlaukis, 2007, and references therein).

**Composition** - Distinguishing between the mineralogical compositions of the juvenile dacite clasts and the enclosing rock flour matrix was difficult from whole-rock XRD (Fig. 4.6) and QEMSCAN<sup>®</sup> (discussed later) due to moderate to intense sericite-pyrite-chlorite-argillic alteration which affects both clasts and matrix (e.g., Fig. 4.7c). Selective drilling, sampling and XRD analysis of dacite clasts and rock flour matrix (see Fig. 4.6 for locations and data) shows that both are primarily composed of quartz, orthoclase (mapped as K-feldspar in QEMSCAN<sup>®</sup>), albite, gypsum, muscovite, kaolinite and calcite. The main distinguishing feature is that the rock flour matrix adjacent to juvenile clasts contains very fine (<20 µm) molybdenite and/or an assemblage of molybdenite-quartz-sphalerite(±galena)-chalcocopyrite. Dacite clasts are weakly Mo-Cu mineralised except where later Cu±Mo-bearing veins cross-cut them. In addition, the clasts have not been affected by potassic (K-feldspar/biotite) alteration.

**Textures and distribution** - Juvenile dacite clasts are distributed throughout the Braden Diatreme in the Braden Sericite-, Braden Tourmaline- and Braden Sulphide Breccias (e.g., Fig. 4.7). Juvenile dacite clasts are more common at greater depths in the Braden Diatreme, mainly occurring within ~500 m of the underlying dacite and within 100 m of the rock flour breccia margin - defined by the position of the annular Marginal Breccias. The most common size range of these texturally distinctive clasts is between 1 and 5 cm although they do range from 0.2 to 10 cm. Juvenile clasts <1 cm are difficult to identify from other small rock clasts. They comprise <10% of the total clast population in the Braden Diatreme. Rock flour inclusions (<2 cm) within the juvenile dacite are rarely observed (Fig. 4.7i).

Strong sericite-pyrite-argillic (±clay, carbonate) alteration has destroyed many of the primary magmatic textures (e.g., Fig. 4.7e) in the dacite clasts although feldspar phenocrysts (sometimes showing Carlsbad twinning) and resorbed quartz phenocrysts are still to varying extents visible (e.g., Fig. 4.7g, h). No biotite phenocrysts are present. Compared with the TMC wall rocks, and other earlier felsic intrusives, the juvenile dacite clasts contain fewer well-developed quartz-anhydrite-sulphide veins. A small number of clasts do however contain discontinuous <5 mm thick quartz-

chalcopyrite veinlets (Fig. 4.7b, g, h). Many of the cream coloured regions sometimes also host miarolitic cavities (<1 cm) at their centres (e.g., Fig. 4.8b).

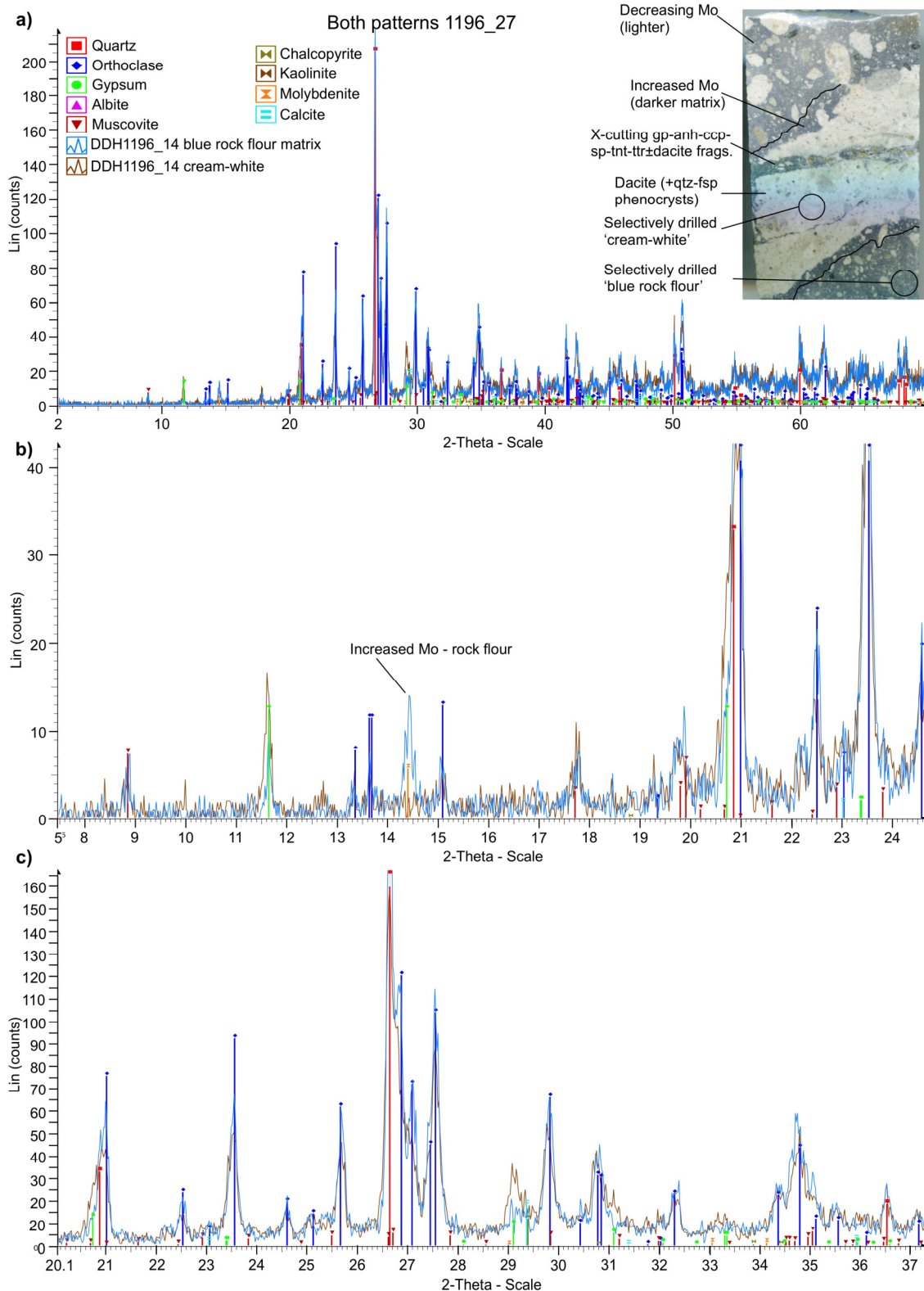


Fig. 4.6 Overlaid XRD patterns for juvenile dacite clasts and rock flour matrix from sample 1196\_27 (220.88 m; ~75 m from Marginal Breccias, 0.79 wt.% Cu and 0.21 wt.% Mo). Sample and drill locations used for XRD analysis are shown in the image - top right: **a)** 2 to 70° 2 $\theta$ ; **b)** 7.5 to 24.5° 2 $\theta$ ; **c)** 20.1 to 37.2° 2 $\theta$ .

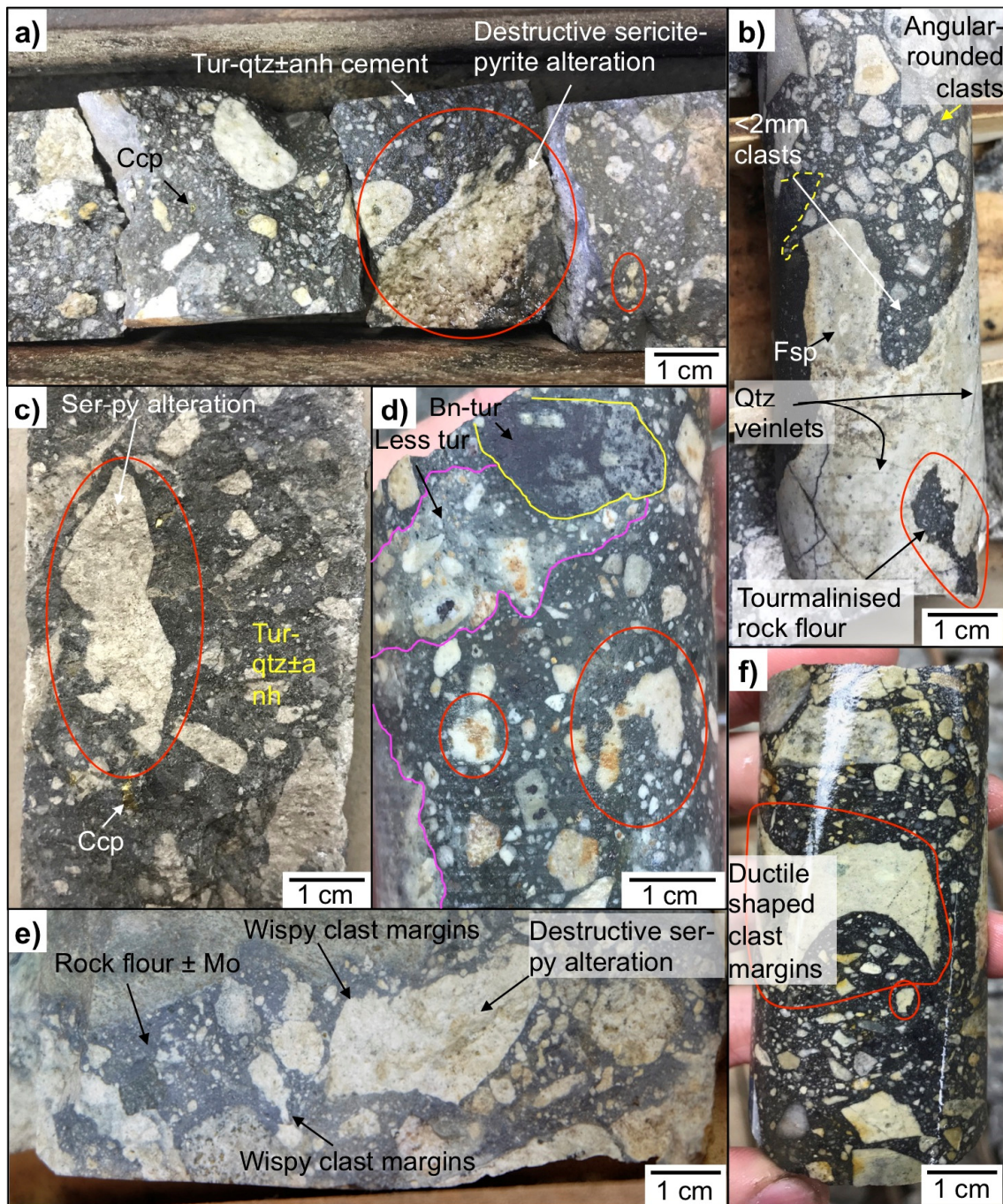


Fig. 4.7 Photographs of drill core showing juvenile dacite clasts which were apparently viscous when incorporated in the Braden Diatreme facies: **a)** Sericite-altered dacite clasts within tourmaline-altered rock flour matrix from the Braden Sericite Breccia. Clasts show varying degrees of rounding with wispy margins illustrated in red. From DDH1213-112.62 m (~13.5 m from MBX, 0.81% Cu and 0.021% Mo); **b)** Large >5 cm dacite clast containing sericitised feldspar phenocrysts and discontinuous quartz veins. From the Braden Tourmaline Breccia (BTB): DDH1769-87.48 m (~79 m from MBX, 0.61% Cu and 0.021% Mo); **c)** Sericite-altered dacite clast with blocky margins (red) within the BTB. From DDH1196-162.22 m (~17 m from MBX, 1.79% Cu and 0.18% Mo); **d)** Ductile dacite clast within the BTB. From DDH1694-87.69 m (~7.8 m from MBX, 0.72% Cu and 0.024% Mo); **e)** <1 cm dacite blebs alongside larger dacite clasts within the BSB, both with molybdenite overprint. From DDH1196-232.87 m (~87 m from MBX, 0.34% Cu and 0.085% Mo); **f)** Small <0.5 mm juvenile dacite clasts showing texturally destructive sericite alteration. From DDH1754-5.06 m (~87 m from MBX, 0.34% Cu and 0.085% Mo). MBX= Marginal Breccias. Assay data from Codelco.

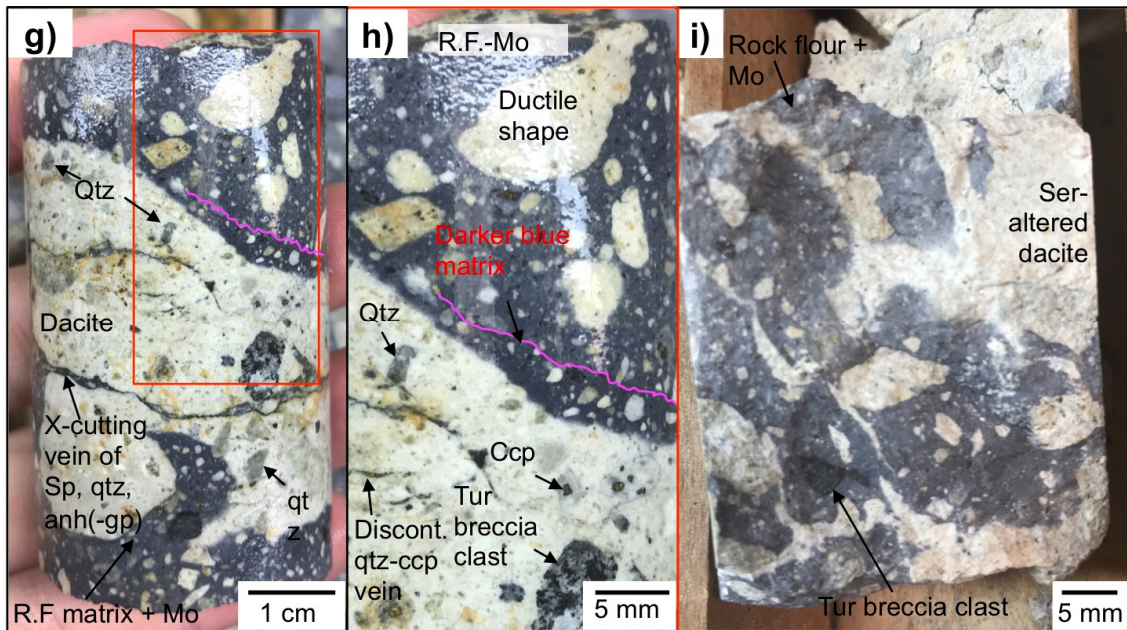


Fig. 4.7 cont. Juvenile dacite clasts within the BSB and BTB which have undergone varying degrees of destructive sericite alteration: **g-h**) Porphyritic dacite with feldspar and quartz phenocrysts and discontinuous quartz-chalcopyrite veins. Immediately adjacent is heavily molybdenised, darker blue rock flour (pink lines). From DDH1196-172.93 m (~28 m from MBX, 1.12% Cu and 0.55% Mo); **i**) Vermiform irregular stringers of juvenile dacite in rock flour matrix with strong texturally destructive sericitic alteration. From DDH1196-232.87 m (~88 m from MBX, 0.34% Cu and 0.085% Mo). MBX= Marginal Breccias.

**Juvenile dacite and Mo-Cu mineralisation** - Many juvenile dacite clasts are bordered by dark <2 cm zones of rock flour matrix which is enriched in molybdenite (Fig. 4.8a-b). Although the sharp colour contrast between clasts and rock flour matrix is identifiable in hand specimens and with a transmitted light microscope (e.g., Fig. 4.8a, b, d), it is indistinct in SEM-BSE images (e.g., Fig. 4.8g) and QEMSCAN® mineral maps (e.g., Fig. 4.8c). The latter show that both the juvenile dacite clasts and rock flour matrix are composed primarily of K-feldspar. The dacite-rock flour matrix contact is however identifiable from individual molybdenite mineral maps (e.g., Fig. 4.8h), where juvenile dacite clasts contain very little to no fine-grained (<20 µm) disseminated/pervasive molybdenite or Cu mineralisation except when associated to late-stage veinlets of gypsum-anhydrite-ankerite-quartz-tourmaline±chalcopyrite-pyrite-tennantite-tetrahedrite.

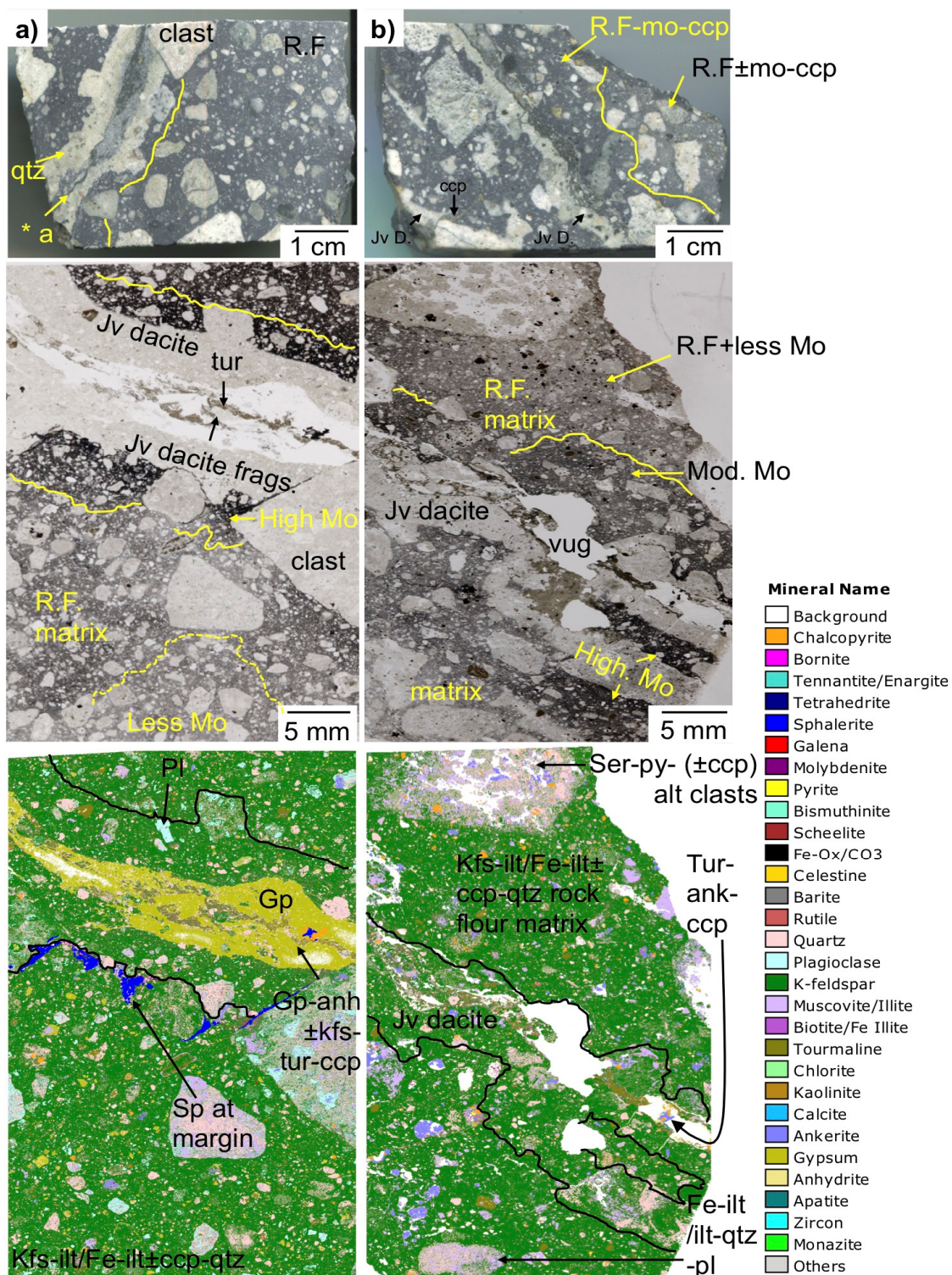


Fig. 4.8 Photos of core containing juvenile dacite clasts from the Braden Diatreme, with transmitted light photomicrographs (XPL) and accompanying QEMSCAN<sup>®</sup> mineral maps (10  $\mu$ m pixel spacing) below. Yellow lines indicate changing molybdenite content in the rock flour matrix. Black lines represent the margin between the juvenile dacite and the rock flour matrix: **a)** High molybdenite at and within a few mm of the dacite margin has caused intense blackening of the rock flour (XPL image). Sphalerite is also largely only found at the margin and as an inclusion in later chalcopyrite. Later anhydrite-gypsum $\pm$ chalcopyrite-sphalerite-galena vein with dacite fragments (\*a) cross-cuts the dacite. From DDH1196-172.71 m (~27 m from MBX, 1.12% Cu and 0.55% Mo); **b)** Juvenile dacite with cavities in the centre infilled by minor tourmaline and later ankerite-chalcopyrite. Clasts are highly altered and can contain appreciable porosity. From DDH1196-220.88 m (~76 m from MBX, 0.79% Cu and 0.21% Mo). Assay data is from Codelco.

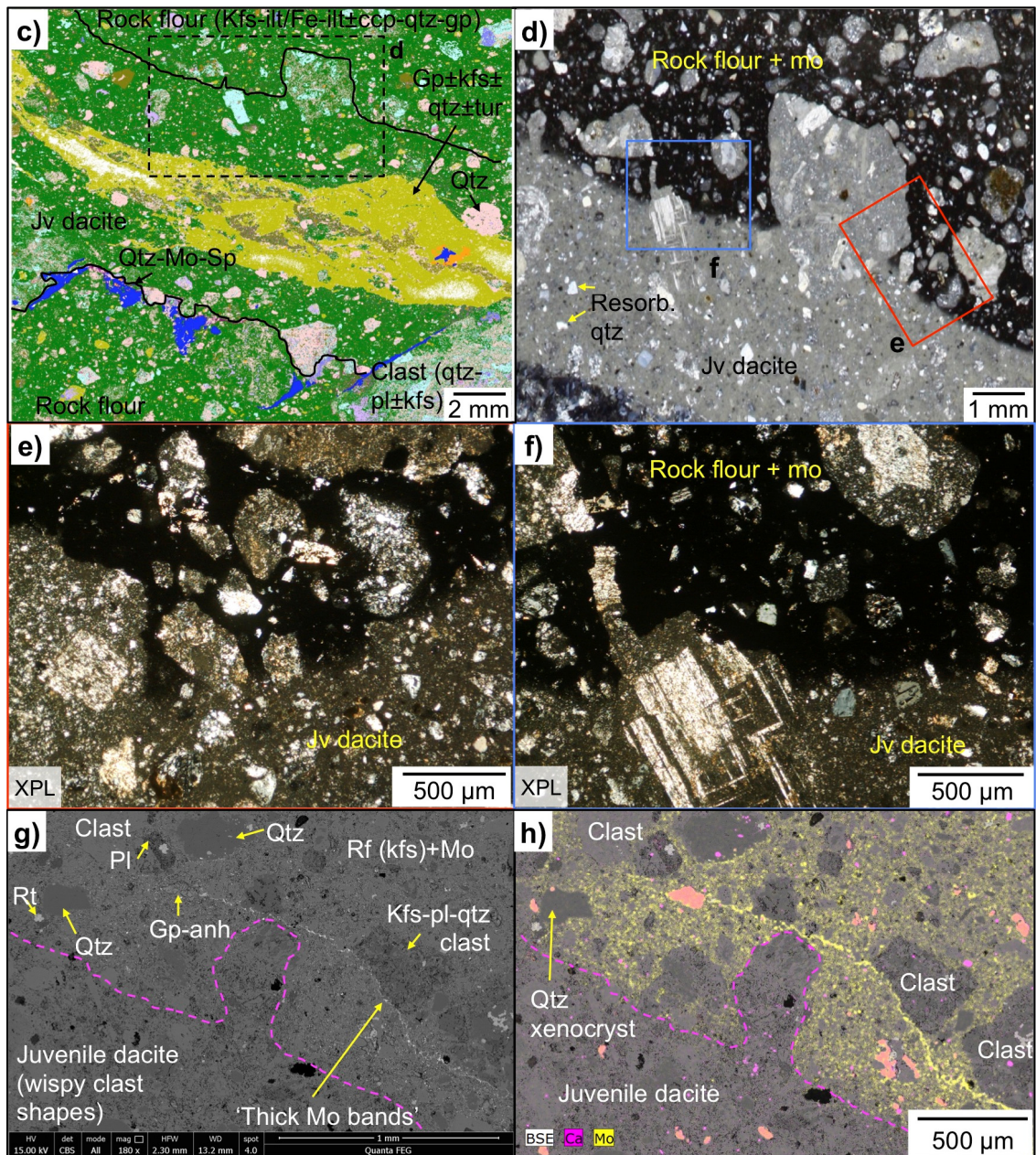


Fig. 4.8 cont. Juvenile dacite in rock flour matrix, from DDH1196-172.71 m: **c)** 10 µm pixel QEMSCAN® mineral map showing indistinct contact between juvenile dacite and rock flour matrix - most easily marked by the presence of molybdenite-quartz±sphalerite on the rock flour matrix side of the contact; **d)** Transmitted light photomicrograph (PPL - location shown in c) of juvenile dacite containing a variety of mainly euhedral plagioclase phenocrysts (confirming a magmatic origin for the dacite), which are absent in the rock flour matrix; **e-f)** Transmitted light photomicrographs (PPL - location shown in c) of dark black finer-grained rock flour and euhedral plagioclase phenocrysts in the dacite; **g-h)** SEM-BSE images with Mo and Ca elemental maps overlaid in h. Molybdenite is spatially restricted to the rock flour matrix. Like the juvenile dacite, clasts within the rock flour matrix do not contain molybdenite.

The decrease in molybdenite (and to a lesser extent quartz) with increasing distance from the dacite clasts is illustrated in Fig. 4.9. The rock flour matrix adjacent to the clasts, where increased molybdenite with lesser variable sphalerite-chalcopyrite-galena-quartz are present, still contain moderate porosity (Fig. 4.9a-c). This porosity is characterised by interconnecting <math><50\ \mu\text{m}</math> vugs that are variably infilled with the aforementioned mineral phases (Fig. 4.9c) with larger cavities (50 to 400  $\mu\text{m}</math>) unevenly infilled by gypsum $\pm$ quartz (Fig. 4.9b). At or within a few cm of the dacite-rock flour matrix margins, 20  $\mu\text{m}</math> wide 'bands' of interlocking <math><10\ \mu\text{m}</math> long molybdenite blades are present in the matrix (e.g., Fig. 4.9d). These are not spatially associated with distinct changes in rock flour mineralogy nor are they restricted to clast margins. Like molybdenite, the concentration of quartz in the rock flour matrix decreases (Fig. 4.9e-f) until there is little to no molybdenite or quartz in the matrix unless it is within the Braden Sulphide Breccia where molybdenite still remains pervasive throughout (Fig. 4.9g-h).$$

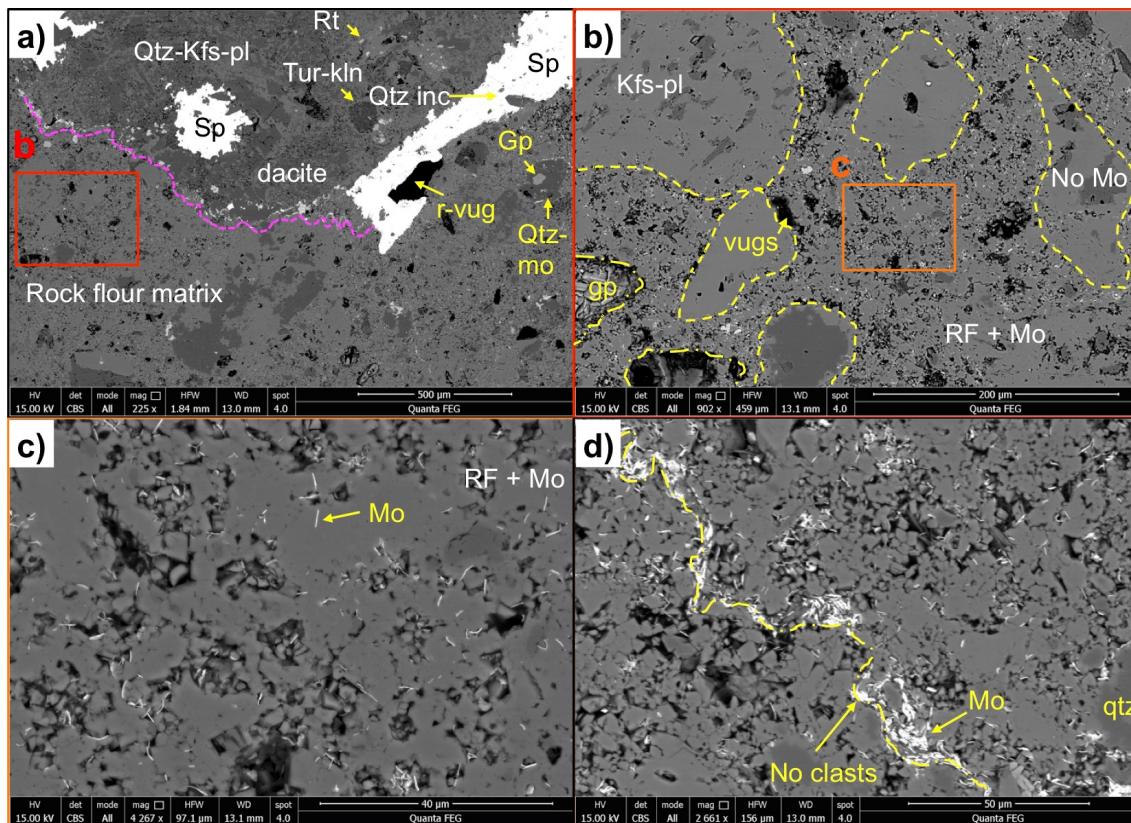


Fig. 4.9 SEM-BSE images showing varying concentrations of molybdenite in the rock flour matrix immediately adjacent to juvenile dacite clasts (a-c), within  $\sim 2$  cm (d-f) and greater than  $\sim 2$  cm of the dacite clasts (g-h): **a)** Dacite-rock flour margin with coarse ( $>500\ \mu\text{m}$ ) sphalerite ( $\pm$ quartz inclusions). Finer molybdenite is present throughout the matrix. From DDH1196-172.71 m; **b)** Porous rock flour containing fine-grained  $<20\ \mu\text{m}$  molybdenite blades. Clasts (outlined in yellow) do not contain molybdenite. Larger vugs are to varying degrees infilled by gypsum (bottom left). From DDH1196-172.71 m. c-h overleaf. **c)** Molybdenite blades ( $<10\ \mu\text{m}$  long) partially infilling porosity in the rock flour matrix. Sample is  $\sim 250\ \mu\text{m}$  from dacite margin. From DDH1196-172.71 m; **d)** 10 to 30  $\mu\text{m}$  thick bands of finer interlocking molybdenite blades. Image is  $<200\ \mu\text{m}$  from the dacite clasts. From DDH1196-220.88 m; **e-h)** Overleaf.

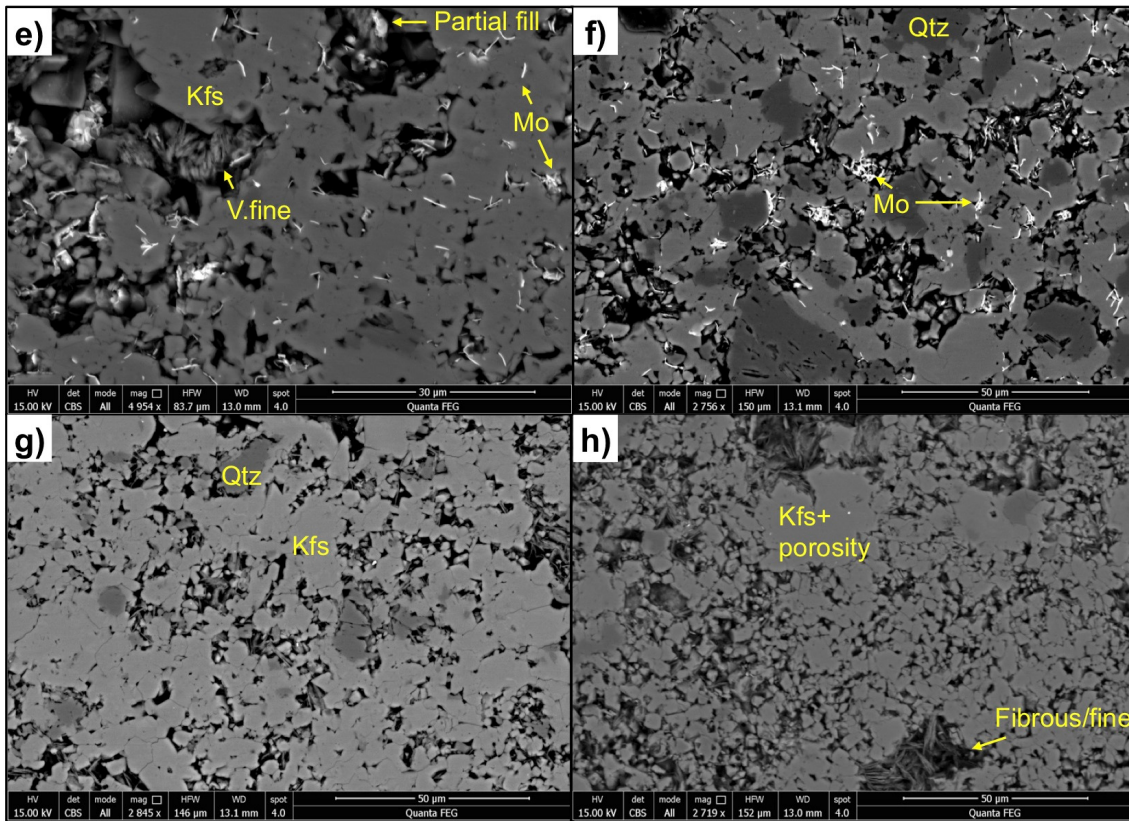


Fig. 4.9 cont. **e-f**) Molybdenite partially infilling cavities in K-feldspar-quartz-dominated rock flour matrix. From DDH1196-172.71 m and 232.98 m, respectively; **g-h**) Rock flour matrix with no molybdenite overprint and little associated quartz. From DDH1196-232.98 m and DDH1196-220.88 m, respectively.

Intense molybdenite±sphalerite-galena mineralisation (e.g., Fig. 4.10) occurs immediately adjacent to many of the dacite clasts or within 5 mm of the dacite clast margins. Such mineralisation is not seen elsewhere in the rock flour. The molybdenite is usually finely intergrown with sphalerite, galena and euhedral quartz (Fig. 4.10a-d). Sphalerite is coarse (>200 μm) and contains anhedral galena (<50 μm), acicular molybdenite (<20 μm) and quartz (<20 to 100 μm) inclusions. Smaller <20 μm acicular molybdenite commonly forms larger aggregates exceeding 50 μm across. At the margins of the dacite clasts molybdenite directly often forms rims on quartz (e.g., Fig. 4.10c) or <10 μm inclusions (e.g., Fig. 4.10c-e). The quartz also often contains anhydrite-gypsum and apatite inclusions (Fig. 4.10i-l).

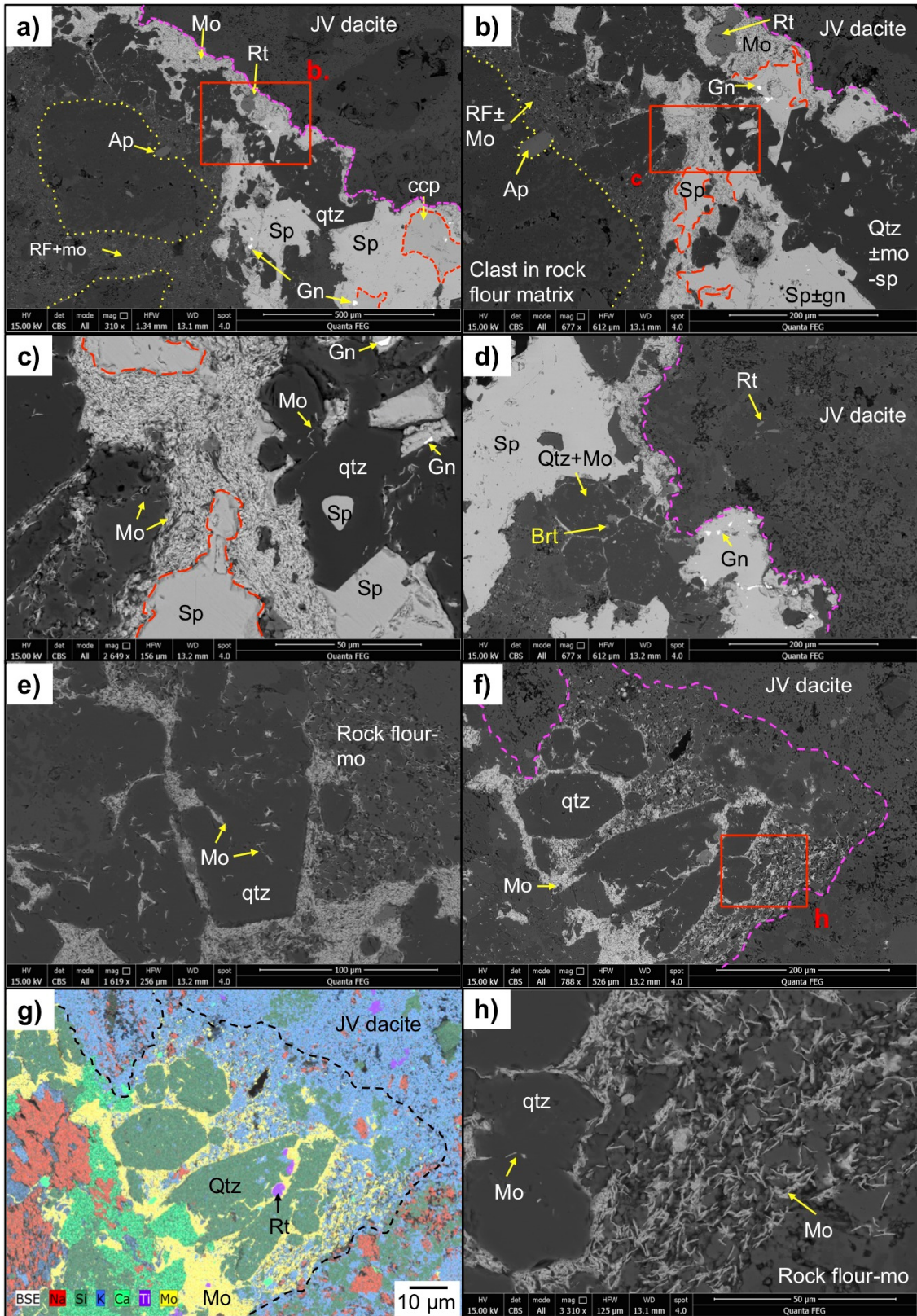


Fig. 4.10 SEM-BSE images and EDS elemental maps (g, j) showing that Cu-Mo±Pb-Zn mineralisation is spatially associated with the contact between the juvenile dacite and rock flour matrix, from DDH1196-172.71 m: **a-d**) <20 μm molybdenite intergrown with euhedral quartz, sphalerite, chalcopyrite and lesser galena, rutile, apatite and anhydrite at the dacite-rock flour contact (pink). Quartz contains molybdenite, sphalerite (c), barite and rutile inclusions. Sphalerite contains galena and quartz inclusions (d); **e**) <20 μm long acicular molybdenite inclusions in coarser (~100 μm) euhedral quartz; **f-g**) Little to no molybdenite is present in the dacite. Euhedral quartz are intergrown with molybdenite at the margin; **h**) <20 μm molybdenite blades partially infill rock flour matrix.

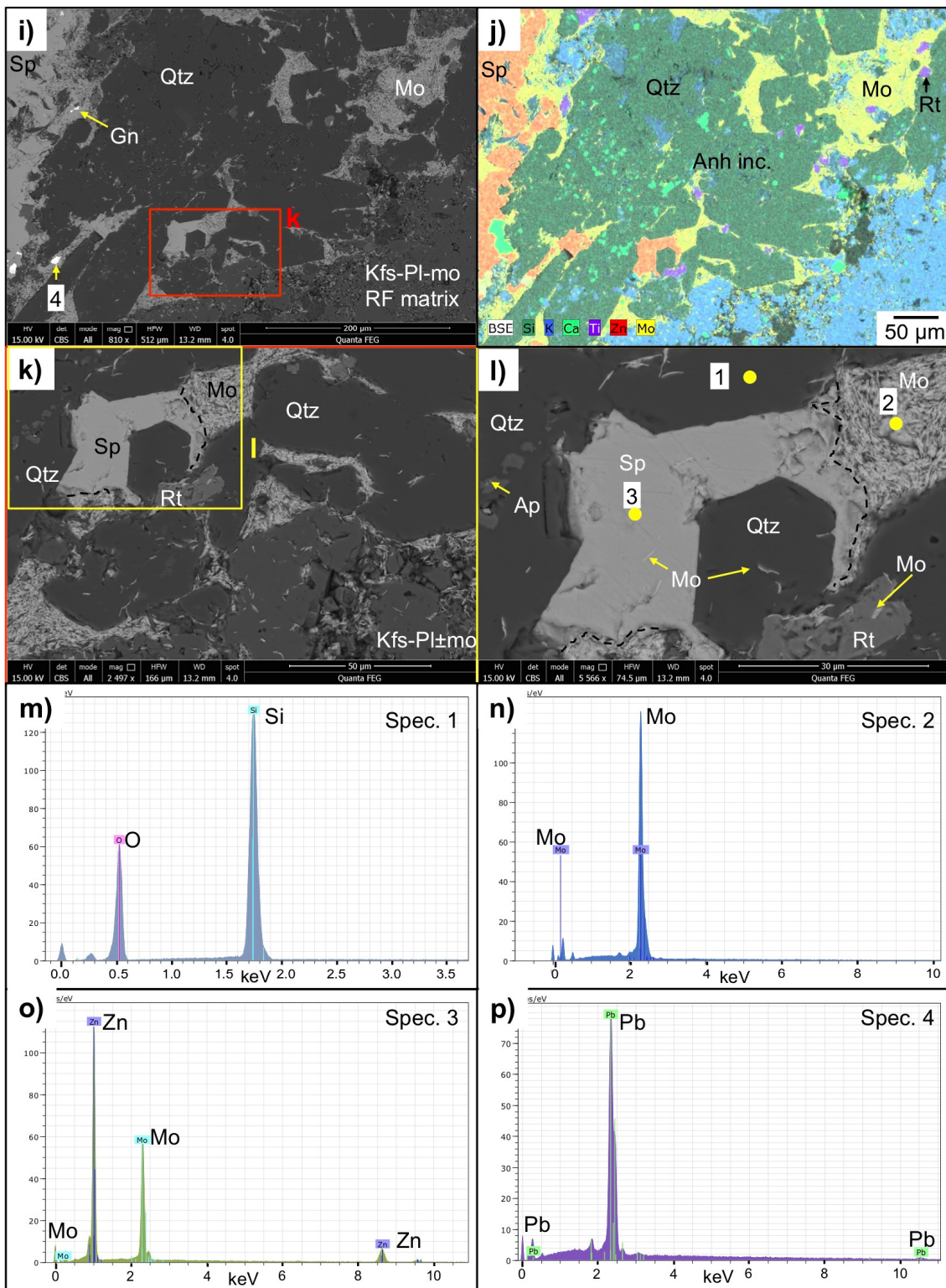


Fig. 4.10 cont. **i-j)** SEM-BSE image (left) and EDS elemental map (right) of euhedral quartz with molybdenite and anhydrite inclusions, with a later surrounding infill of molybdenite, sphalerite and rutile. Sphalerite has <20 μm inclusions of galena; **k-l)** SEM-BSE images of quartz containing molybdenite and apatite inclusions at the dacite-rock flour contact. EDS spectra locations for m-p are shown; **m)** Quartz; **n)** Molybdenite (Mo and S peaks); **o)** Sphalerite with <5 μm molybdenite inclusions (see part l) creating mixed signal. However, the Mo peak may also partially be a sulphur peak for sphalerite; **p)** Galena inclusion within sphalerite.

#### 4.1.6 Cross-cutting veins within the Braden Diatreme Breccias

A number of vein generations cross-cut the Braden Diatreme which are mainly composed of gypsum and ankerite with lesser Cu-sulphides/sulfosalts±sphalerite and galena (e.g., Fig. 4.11a, d, e, f). They are mostly <1 cm thick, can extend for >30 cm, vary from widely spaced veinlets, metres apart, to closely spaced vein arrays. Rock flour breccia inclusions (<1 mm) are sometimes present in the gypsum veins (e.g., Fig. 4.11c). Where juvenile dacite clasts are cross-cut, <1 mm angular dacite fragments are found within the veins (see Fig. 4.11f). The later veins lack alteration halos and cross-cut areas of the Braden Diatreme with (Fig. 4.11f) and without pervasive molybdenite in the matrix (e.g., Fig. 4.11a-e).

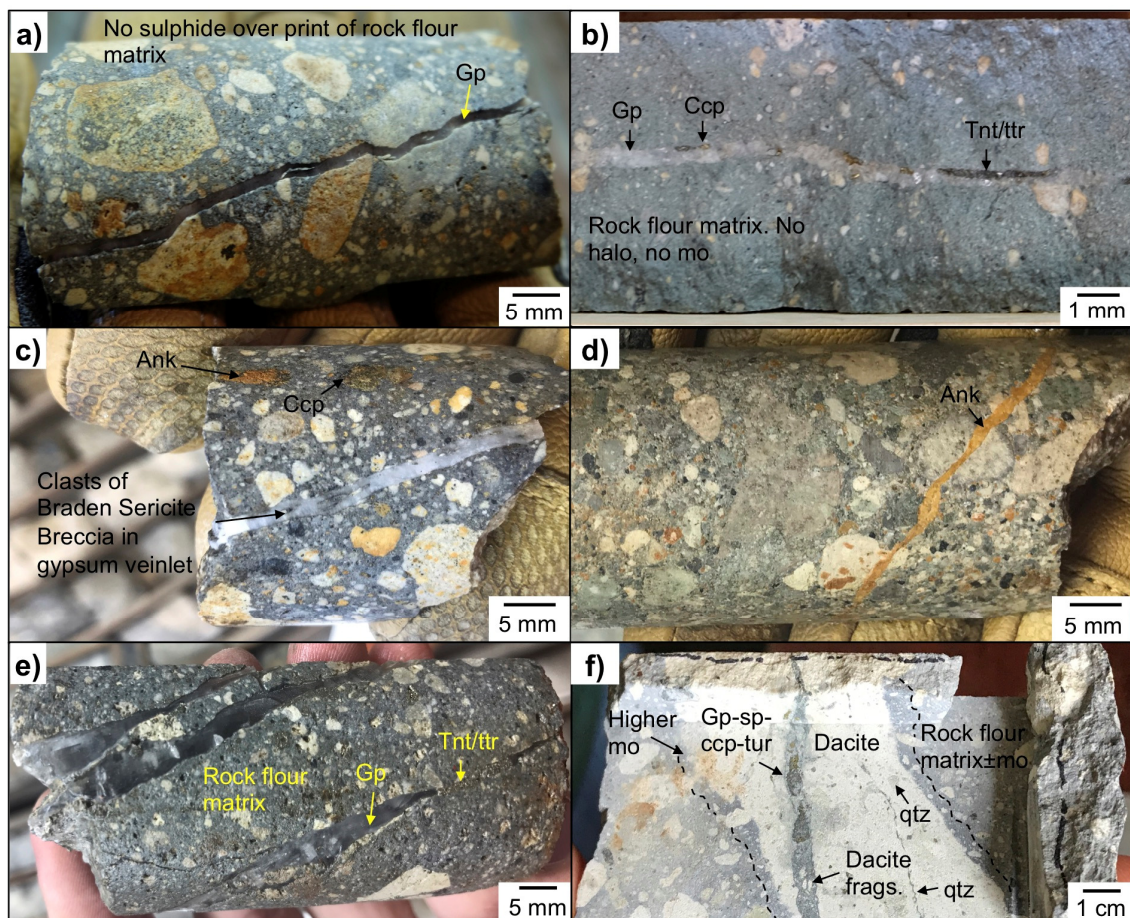


Fig. 4.11 Drill core photos of late-stage veins cross-cutting the Braden Diatreme matrix and clasts: **a)** Gypsum veinlet cutting across the rock flour matrix and fractured clasts. No Cu or Mo are present in the vein. From DDH1213-114.45 m; **b)** Gypsum veinlet with tennantite-tetrahedrite-chalcopyrite cross-cutting the Fine Braden Sericite Breccia. From DDH1775-135.64 m; **c)** Small <2 mm fragments of rock flour within a gypsum vein. From DDH1213-113.39 m; **d)** Ankerite vein cutting across coarse Braden Sericite Breccia. From 1694-246.74 m; **e)** Gypsum veinlet array containing variable tennantite-tetrahedrite cutting the rock flour matrix. From DDH1079-368.56 m; **f)** Juvenile dacite clast cross-cut by a gypsum vein containing sphalerite, chalcopyrite, tourmaline and <5 mm fragments of dacite. Rock flour adjacent to dacite contains variable molybdenite. From DDH1196-220.88 m.

Mineralogically distinct domains are present in these veins that cross-cut the matrix and dacite clasts, particularly in areas of pervasive molybdenite. For example the main mineralogy of the gypsum/anhydrite-ankerite veins abruptly changes between ankerite-calcite-quartz ( $\pm$ Cu-sulphide) in the molybdenite-bearing rock flour matrix (Fig. 4.12a, b, e) to anhydrite-gypsum-quartz ( $\pm$ Cu-sulphide) in the juvenile dacite clasts (Fig. 4.12e-f). A similar change is observed in the top right of the section in Fig. 4.12a-b where the quartz-tourmaline-altered clast is cross-cut by a quartz-tourmaline-ankerite vein that changes to gypsum-ankerite on contact with the rock flour matrix containing molybdenite.

The centre of these veins are characterised by ankerite with end-stage space-fill by Cu-Zn-Pb sulphides (Fig. 4.12a, g). Chalcopyrite and sphalerite are intergrown and contain small  $<150 \mu\text{m}$  anhedral galena inclusions with convolute/lobate margins (Fig. 4.12i-j). Cu-sulfosalts are also sometimes present (Fig. 4.12a). Surrounding the ankerite-sulphide cores are ankerite with tourmaline and molybdenite inclusions towards the margins. For example, in Fig. 4.12g, a tourmaline-rich 'band/zone' surrounding the ankerite-sulphide-rich core is present. This observation is not however consistently observed in all late-stage ankerite-gypsum veins.

Tourmaline and molybdenite are usually only found within 1 mm of the vein margins. Molybdenite at these margins is very fine-grained ( $<30 \mu\text{m}$ ) and is not always spatially associated with tourmaline (Fig. 4.12d). Tourmaline is present in varying quantities in the veins, is acicular, and up to  $200 \mu\text{m}$  long (Fig. 4.12g, i, m). Tourmaline sometimes contains molybdenite inclusions with molybdenite also space-filling around tourmaline (Fig. 4.12l, m). Other inclusions towards the margins include quartz-rutile ( $<200 \mu\text{m}$ ) and rock flour matrix (Fig. 4.12c, d).

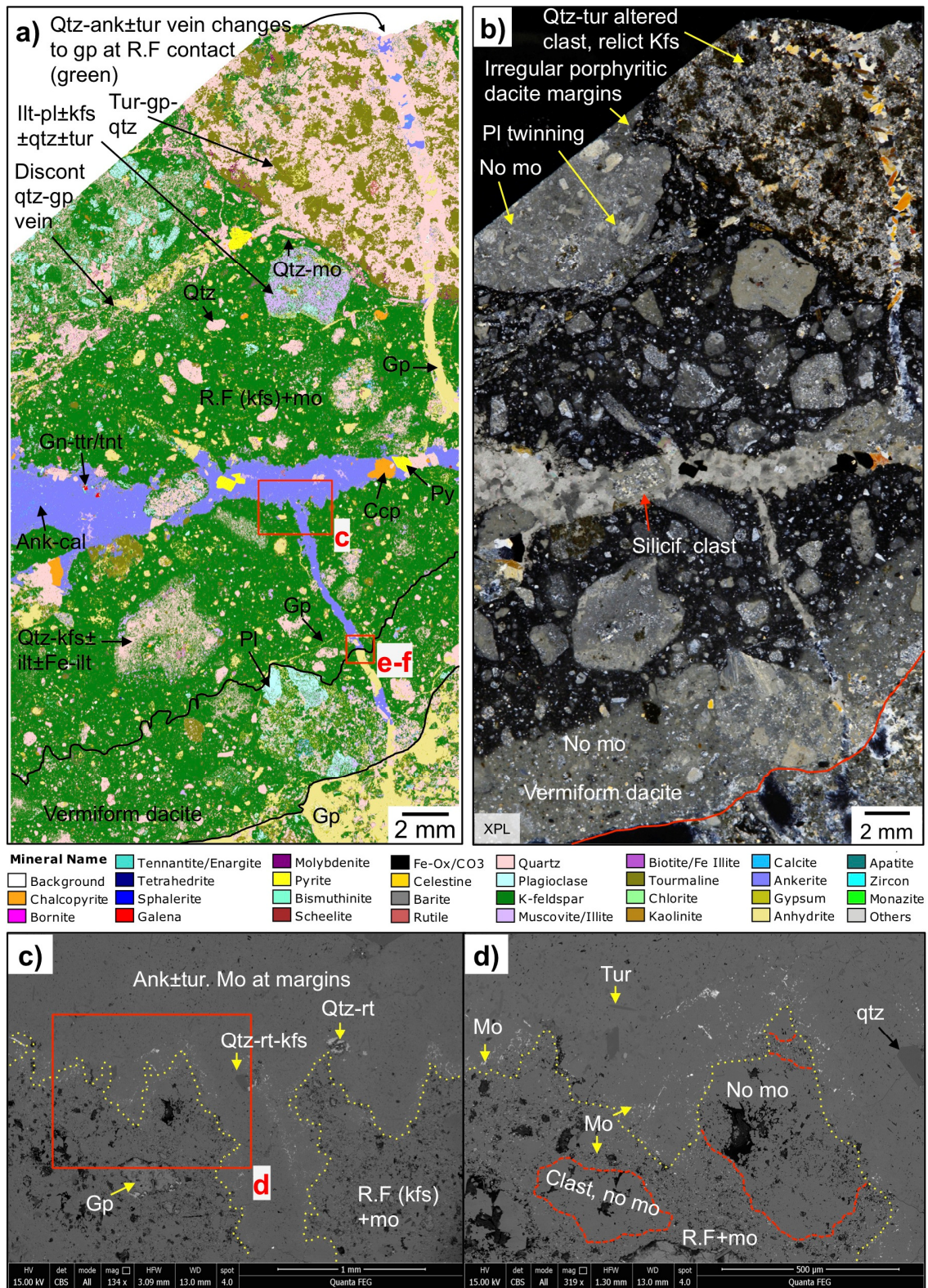


Fig. 4.12 Images of cross-cutting vein generations in the Braden Diatreme rock flow matrix and juvenile dacite clasts (**a-f**: DDH1196-242.04 m and **g-m**: DDH1196-172.93 m); **a-b**) 10  $\mu$ m pixel spacing QEMSCAN<sup>®</sup> mineral map (left) and corresponding transmitted light photograph (XPL) (right) showing dark black rock flow matrix (dominated by K-feldspar) with molybdenite overprint (responsible for the black colour in hand specimen) that is strongest adjacent to dacite. Cross-cutting the dacite and rock flow matrix is ankerite-calcite±sulphide vein; **c-d**) SEM-BSE images of ankerite vein-rock flow matrix contact (yellow) with ankerite-hosted molybdenite largely within 250  $\mu$ m of the margin, with locations shown in a.

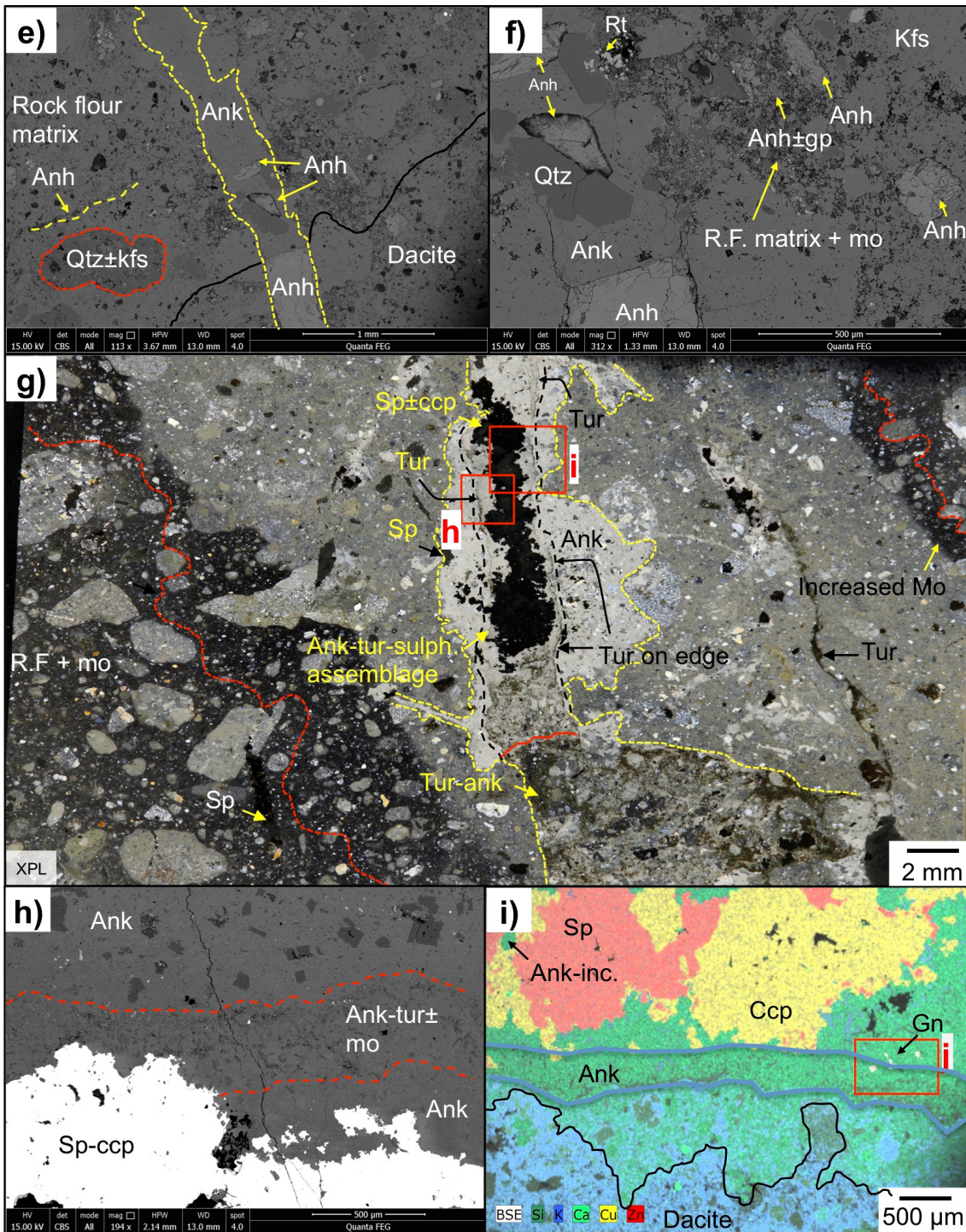


Fig. 4.12 cont. **e-f)** SEM-BSE images of rock flow matrix - dacite contact (black line). The vein mineralogy changes from ankerite in the rock flow matrix to anhydrite in the dacite; **g)** Transmitted light photograph (XPL) illustrating dacite hosted in the variably molybdenite-bearing rock flow matrix. The dacite is cross-cut by an ankerite vein containing sphalerite-chalcopyrite±galena towards the centre with tourmaline-molybdenite found towards the outer portions, marked by the red line. Central portion likely represents a miarolitic cavity infilled by later molybdenite-ankerite-tourmaline-Cu-Pb-Zn assemblages. From DDH1196-172.93 m; **h)** SEM-BSE image of the central portion of the vein dominated by sphalerite and chalcopyrite with a surrounding zone (red outline) of tourmaline and molybdenite in ankerite; **i)** SEM-BSE with EDS map overlaid showing intergrown sphalerite-chalcopyrite in the centre of the vein surrounded by tourmaline-molybdenite-ankerite and an ankerite outer. Black line illustrates edge of vein/cavity.

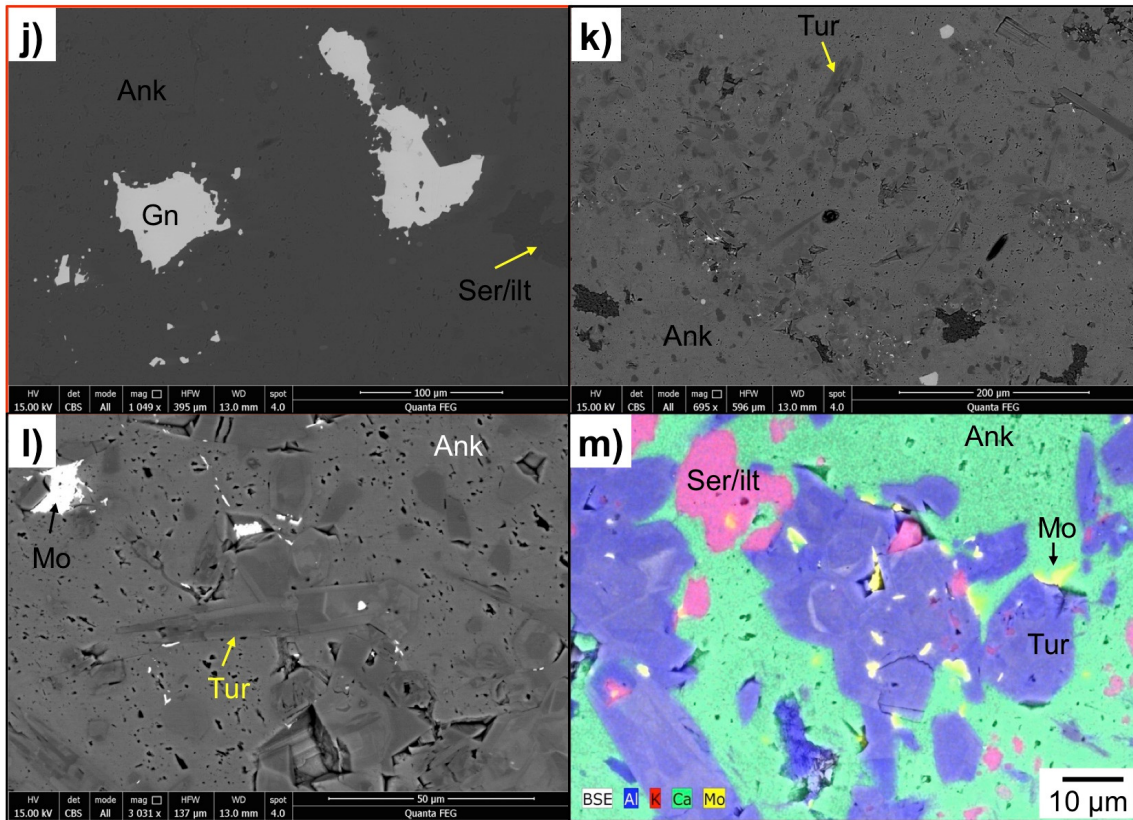
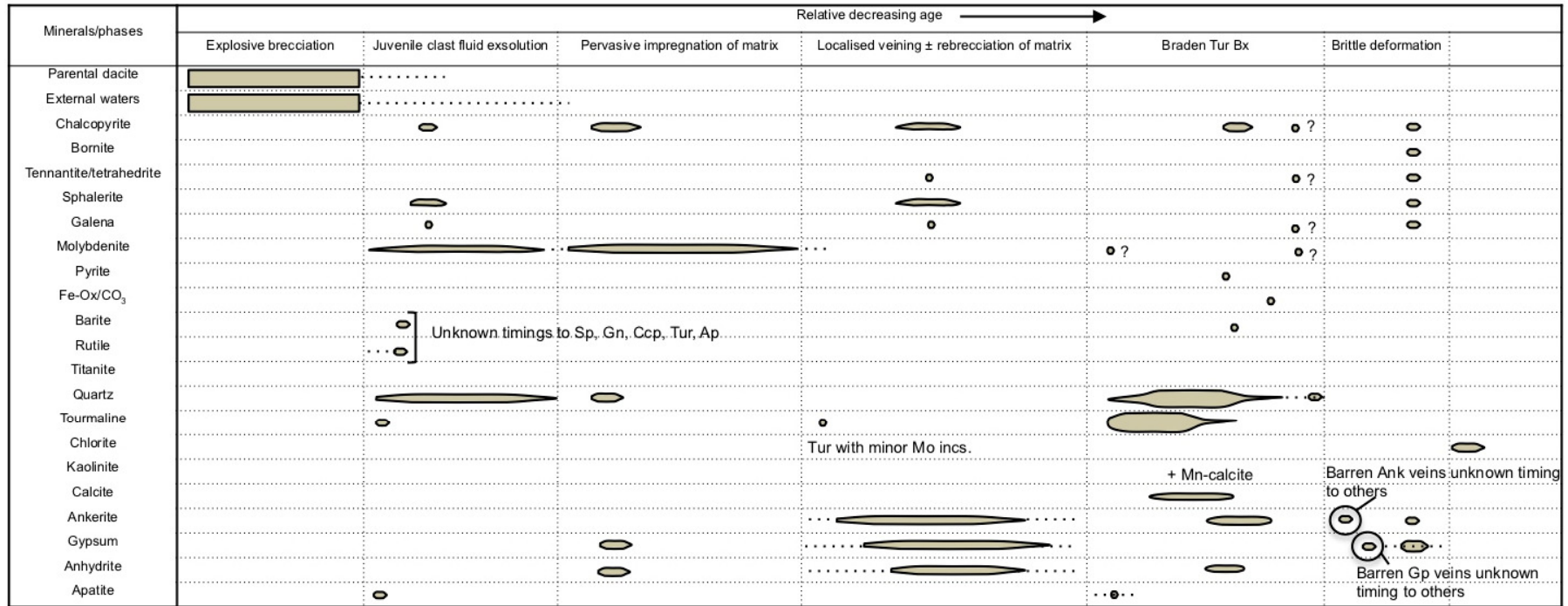
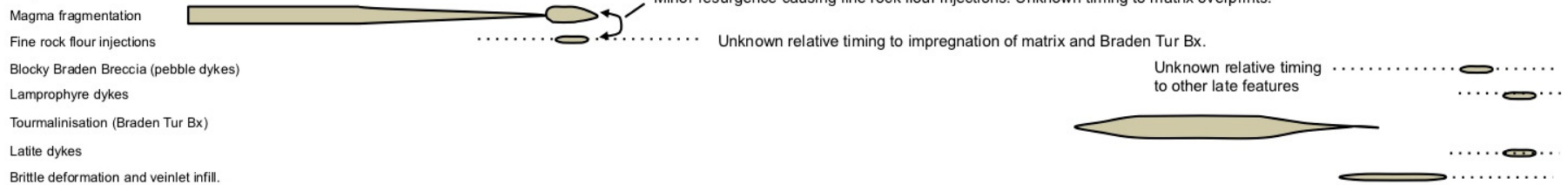


Fig. 4.12 cont. **j)** SEM-BSE image of ankerite with galena inclusions displaying irregular, convolute/lobate margins. Sericite inclusions are also present; **k-m)** SEM-BSE images and SEM-BSE with EDS map overlaid (**m**) illustrating acicular tourmaline inclusions with patchy zoning within an ankerite vein cross-cutting a juvenile dacite clast. Images are taken from the outer portion of the vein. Molybdenite is also found adjacent to tourmaline and as inclusions in tourmaline.

Table 4.1 Paragenetic sequence of the Braden Diatreme. Shown below the paragenesis are key stages including explosive magma fragmentation, resurgence in fragmentation linked with injection of fine rock flour (Fine Sericite Braden Breccia). Other key stages include fluid overprints of the rock flour and tourmalinisation forming the Braden Tourmaline Breccia. Towards the end of the sequence, pebble, lamprophyre dykes and latite dykes form. Mineral abundances or stage intensity are reflected by relative thickness of lines.



**Stage:**



## 4.2 Braden Diatreme quartz CL response and Ti temperature estimates

The mineralogically pervasive and texturally destructive sericite alteration of clasts and matrix in the Braden Diatreme frustrated the interpretation of the juvenile dacite clasts as either magmatic in origin, representing viscous magma emplaced into the rock flour during breccia formation, or as solid fragments of older felsic magmatic wall-rock entrained during emplacement of the breccia, or as complex-shaped patches of rock flour breccia which, for some unknown reason, had resisted tourmalinisation or impregnation by Mo±Cu-Zn-Pb-rich fluids. These possibilities were tested by comparing the CL response (from cold-cathode- and SEM-CL) and elemental characteristics (EPMA) of quartz from the juvenile dacite clasts and rock flour matrix. For ease of analysis, the quartz was grouped and described based on its occurrence and paragenetic associations as being from:

- Dacite underlying the Braden Diatreme (i.e. magmatic quartz entrained as xenocrysts or in xenoliths, or from other rock clasts);
- In bleb-shaped, cream-white juvenile dacite clasts, i.e. in frozen viscous dacitic magma globules entrained within the upwards-emplacing Braden Diatreme (magmatic quartz variably overprinted by later hydrothermal quartz, the latter also infilling cavities where present);
- Mo(±Zn-Pb-Cu) mineralisation at dacite clast margins (hydrothermal quartz);
- Non-tourmalinised (pale grey) rock flour matrix, with the rock flour being brecciated dacite ± other materials in the wall rocks;
- Hydrothermal quartz from the Diablo Breccia tourmaline-quartz-anhydrite cement as a comparator.

### 4.2.1 Underlying dacite quartz

Magmatic quartz from the dacite intrusive underlying the Braden Diatreme occurs as euhedral to subhedral grains 100 µm to 2 mm in diameter (Fig. 4.13). Many are partially resorbed and/or fractured. Less than 25% contain euhedral <500 µm inclusions of biotite (Fig. 4.13b) and a rare few host <100 µm anhedral inclusions of the dacite groundmass (Fig. 4.13a). Most quartz is moderately luminescent, showing varying shades of blue (Fig. 4.13) between generally darker and lighter blue zones (Fig. 4.13a, c, h). Some quartz (~25 to 50%) show no variations in CL colour or intensity (Fig. 4.13b). No secondary textures or structures resulting from alteration and no later cross-cutting quartz veins were observed. The intensity and colour of CL in quartz from the underlying dacite is similar to the quartz in the dacite clasts and the xenocrysts in the rock flour matrix.

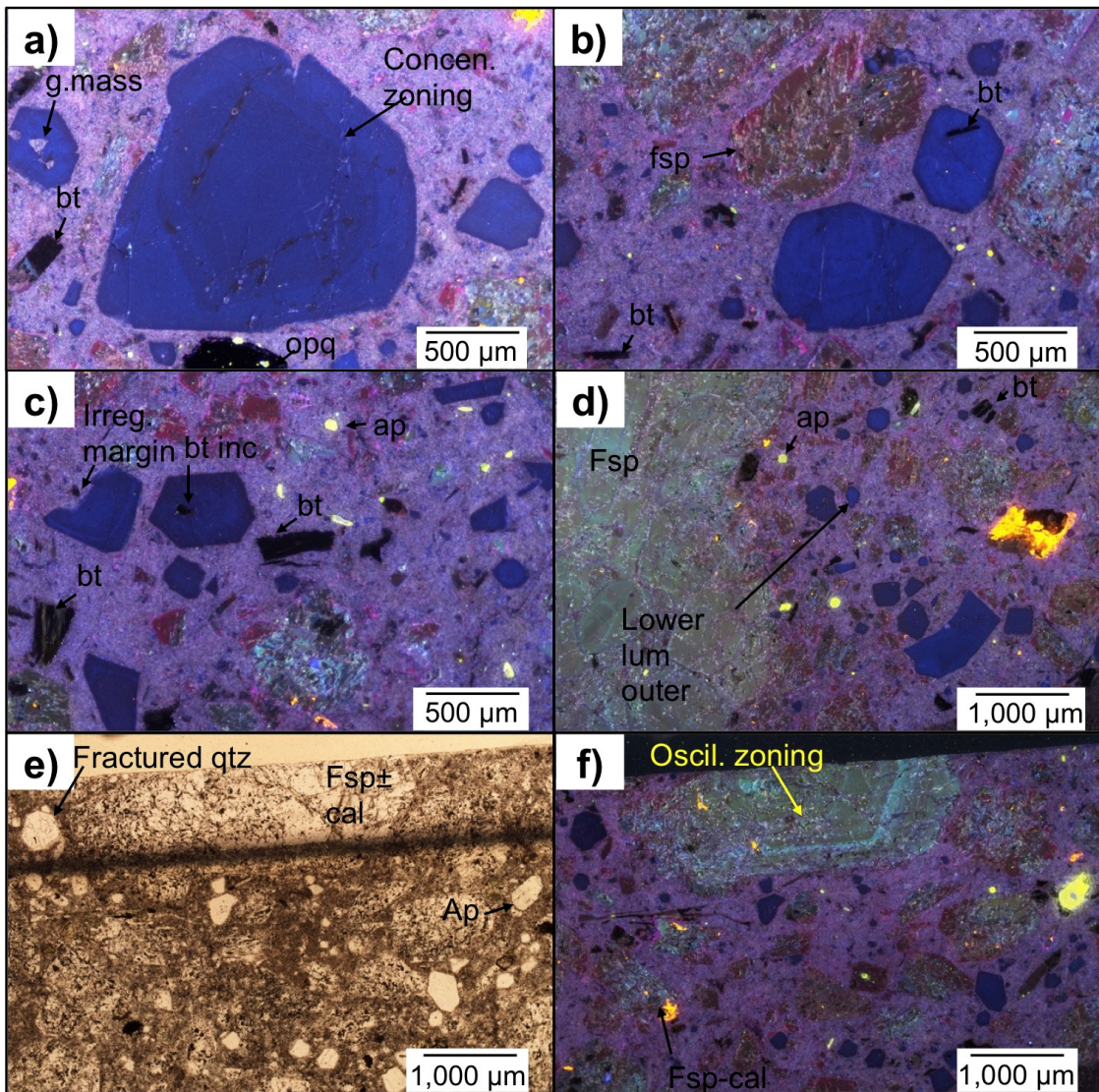


Fig. 4.13 Cold-CL and transmitted light (PPL) images (e, g) of magmatic quartz from the dacite body underlying the Braden Diatreme (DDH1068-1,012.8 m): **a-b**) Quartz phenocrysts with blue CL and varying degrees of concentric zoning. Biotite and rock flour inclusions are common. Some quartz is weakly zoned or shows no CL zoning; **c**) Euhedral quartz phenocrysts alongside feldspar and non-luminescing biotite phenocrysts. Magmatic apatite occurs as homogeneous euhedral grains, 100 to 200  $\mu\text{m}$  in diameter, with bright green luminescence; **d**) Coarse feldspar phenocryst (>1 mm) and quartz phenocrysts showing variable blue luminescence; **e-f**) Transmitted light (PPL) photomicrograph (left) and cold-CL image (right) showing euhedral to subhedral quartz phenocrysts <1,000  $\mu\text{m}$  and larger (>1 mm) oscillatory zoned plagioclase phenocrysts. Feldspar phenocrysts show blue-green luminescence (top of image f). Apatite displays a bright green luminescence and feldspar has oscillatory zoning; **g-h**) Overleaf.

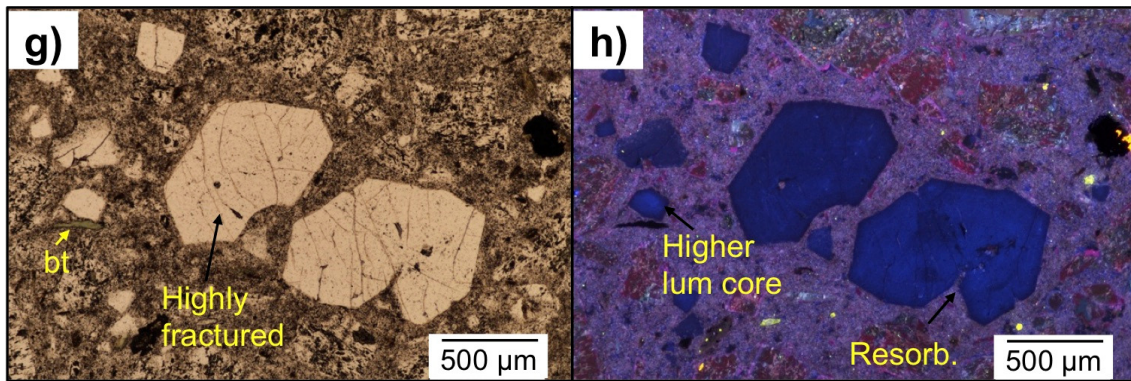


Fig. 4.13 cont. **g-h**) PPL photomicrograph (left) and cold-CL image (right) showing highly fractured quartz phenocrysts alongside slightly smaller, tabular biotite.

#### 4.2.2 Juvenile dacite clast-hosted quartz

Dacite clasts contain a mixture of magmatic and hydrothermal quartz, each displaying different textural characteristics. Magmatic quartz comprises between 40 and 60% of total quartz in the dacite clasts. Texturally, clast-hosted magmatic quartz (e.g., Fig. 4.14a, g) are similar to those described from the underlying dacite, having a blue CL response, varying degrees of growth zonation (Fig. 4.14c) and being between 100 and ~1,000  $\mu\text{m}$  in diameter. Like in the underlying dacite, ~30 to 50% are well zoned (Fig. 4.14a, g) whilst others are comparatively homogenous (Fig. 4.14c). CL reveals that unlike the underlying dacite intrusive, a number of magmatic quartz phenocrysts are cross-cut by darker blue ( $\pm$ pink) luminescing quartz phases <30  $\mu\text{m}$  wide (e.g., Fig. 4.14k) and/or have <50  $\mu\text{m}$  thick discontinuous and even darker rims (e.g., Fig. 4.14b). No biotite inclusions or relics of these were observed.

Subhedral mottled red-pink luminescing grains (e.g., Fig. 4.14b, f, g) between ~200  $\mu\text{m}$  and 500  $\mu\text{m}$  in diameter with non-luminescing, fine (<100  $\mu\text{m}$ ) acicular tourmaline inclusions account for between 15% and 30% of juvenile dacite clast-hosted quartz. They are also present in the rock flour matrix. Pink-red luminescing quartz locally overgrows brighter blue CL quartz similar to magmatic grains (Fig. 4.14g). Remaining quartz is characterised by weakly luminescing blue-purple grains that are euhedral to subhedral, often have irregular to jagged margins and occasionally K-feldspar inclusions (Fig. 4.14h-i).

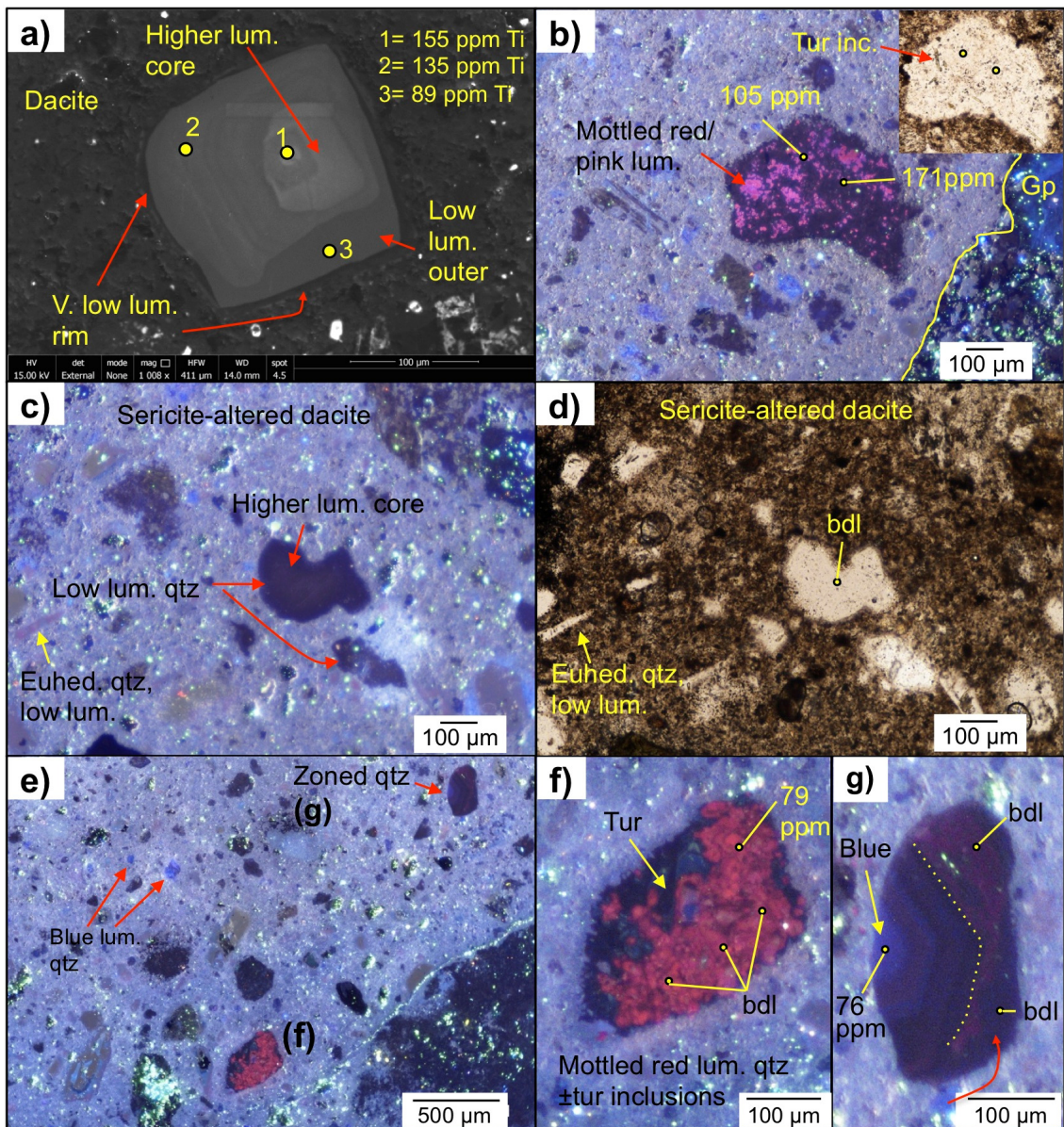


Fig. 4.14 Texture of quartz in dacite clasts in the Braden Sericite Breccia. EPMA point locations (yellow) with matching Ti concentrations (ppm) are also shown for reference: **a)** SEM-CL image showing zoned quartz with a brighter CL core that progressively gets darker towards the rims. From DDH1196-172.71 m; **b)** Cold-CL image and PPL insert of quartz displaying a mottled pink-red CL containing <100  $\mu\text{m}$  acicular tourmaline inclusions. From DDH1196-172.71 m; **c-d)** Cold-CL (left) and PPL photomicrograph (right) of subhedral quartz phenocrysts containing no mineral inclusions and a weak blue luminescence with little zoning. From DDH1196-172.71 m; **e-g)** Cold-CL images of subhedral quartz crystals with blue-purple or mottled pink-red luminescence (f). Pink luminescence contains non-luminescing acicular tourmaline inclusions and overgrows concentrically zoned higher luminescing blue quartz (g). From DDH1196-242.04 m; **h-k)** Overleaf.

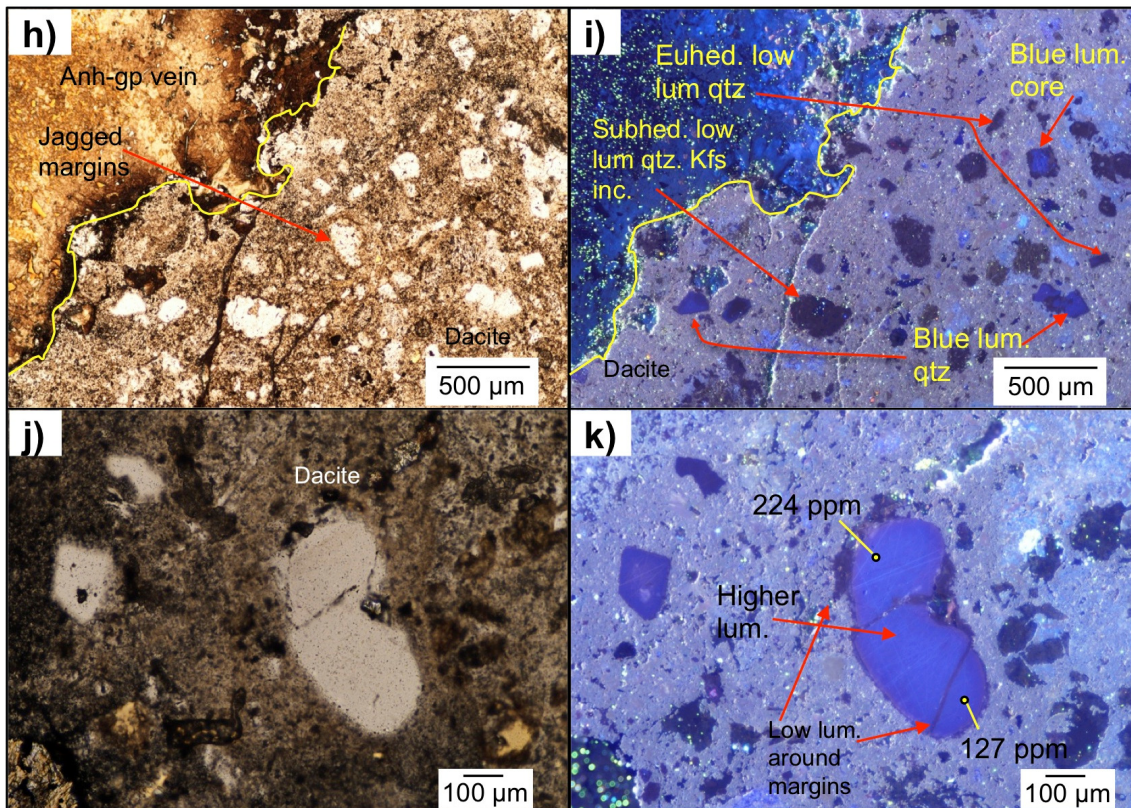


Fig. 4.14 cont. **h-i)** Transmitted light photomicrograph (PPL - left) and cold-CL (right) of an anhydrite-gypsum vein (outlined in yellow) cross-cutting the dacite clast. Dacite contains quartz phenocrysts with bright blue CL cores, and darker blue-purple CL euhedral quartz of a similar size and shape to biotite phenocrysts in the underlying dacite. Quartz associated with later hydrothermal alteration displays a weak blue to purple luminescence and more irregular shapes and margins. From DDH1196-172.71 m; **j-k)** Transmitted light photomicrograph (PPL, left) and cold-CL (right) of resorbed quartz with a darker CL rim and cross-cutting phase. From DDH1196-220.88 m. EPMA point locations (yellow) with matching Ti concentrations (ppm) are also shown for reference.

### 4.2.3 Rock flour matrix quartz

The rock flour matrix contains a number of quartz phases distinguished from their paragenetic relationships, shapes, CL and internal textures; listed and described below. A number of these phases are distinctly similar to quartz in the underlying dacite and/or matrix-hosted dacite clasts. Direct cross-cutting relations between generations are not always apparent.

1. Dacite clasts and quartz xenocrysts, the latter with a similar internal blue luminescence and growth textures to the underlying dacite, account for between 15 and 40% of quartz in the rock flour matrix. They vary from subhedral to euhedral and, being between 100 and 500 μm in diameter, are slightly smaller than quartz in the underlying dacite. In CL, the dacite clasts and quartz xenocrysts vary between relatively bright and dull blue luminescence, and contain a number of imposed alteration structures (Fig. 4.13b-d). No biotite inclusions were observed but darker CL zones, similar to the overgrowths, are present (Fig. 4.15b). Later pink luminescent overgrowths/rims are commonly present.

2. Mottled pink-red luminescent subhedral quartz up to 500  $\mu\text{m}$  in diameter account for <20% of quartz in the rock flour matrix (Fig. 4.15a, i, j). They share the same luminescence textures and properties to the mottled quartz in the dacite clasts described earlier. Acicular 50  $\mu\text{m}$  tourmaline ( $\pm$ rutile) inclusions are common.
3. Weakly blue-purple luminescing euhedral quartz associated with chalcopyrite infill of cavities in the matrix (Fig. 4.15f). Quartz are largely homogenous with weak oscillatory zoning sometimes present. Grain size is dependent on the extent of the cavity and volume of chalcopyrite infill.
4. Dark CL (blue-purple) quartz with jagged margins associated to small (<2 mm) silicified fragments (Fig. 4.15e, h). They account for <30% of quartz in the matrix.
5. Euhedral quartz (with molybdenite inclusions) associated with molybdenite is spatially situated within a few mm of the dacite margin. They commonly overgrow brighter CL quartz, as also seen in the dacites; these are described in more detail in the next section.

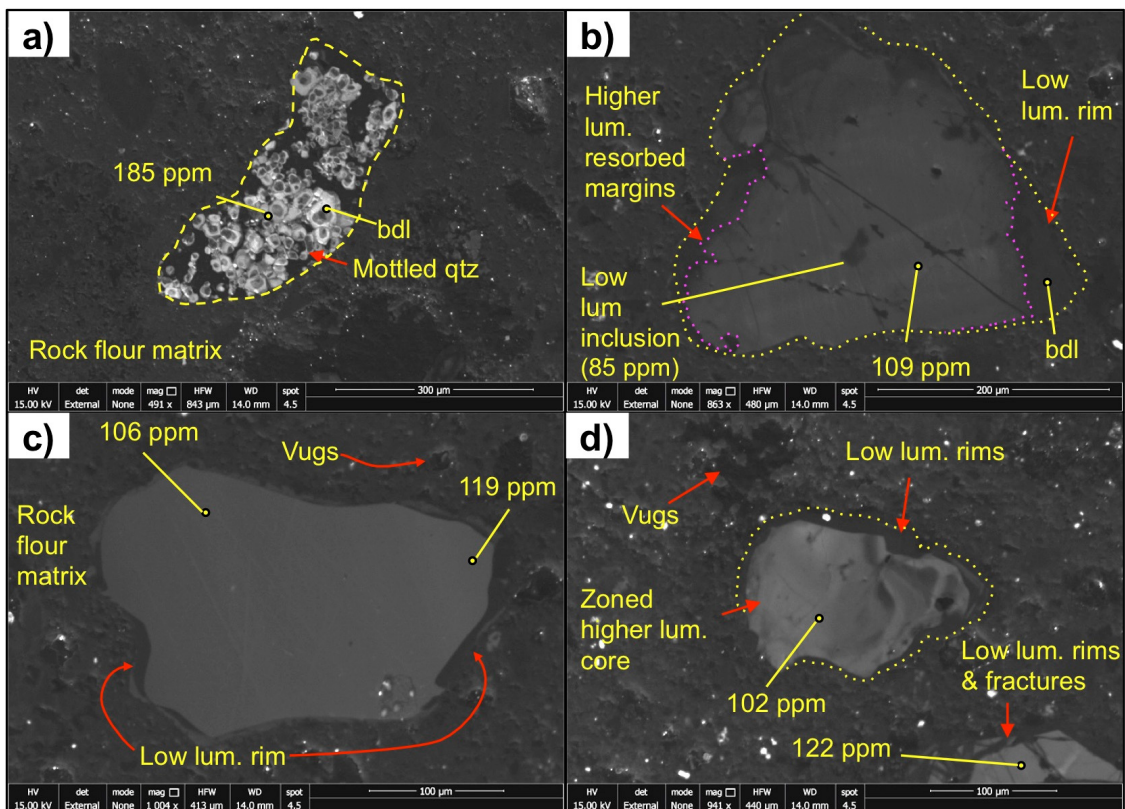


Fig. 4.15 Quartz from the rock flour matrix in the Braden Diatreme. EPMA point locations (yellow) with Ti concentrations (ppm) are also shown for reference: **a)** SEM-CL image of subhedral quartz with a mottled texture. From DDH1196-172.71 m; **b-c)** SEM-CL images of subhedral quartz with brighter CL cores and resorbed margins (pink), and darker CL irregular overgrowths outlined in yellow. Darker CL secondary quartz phases (<30  $\mu\text{m}$  thick) also cross-cut the quartz (b). From DDH1196-172.71 m; **d)** SEM-CL image showing an irregularly zoned brighter CL core with discontinuous darker rims. From DDH1196-220.88 m; **e-j)** Overleaf.

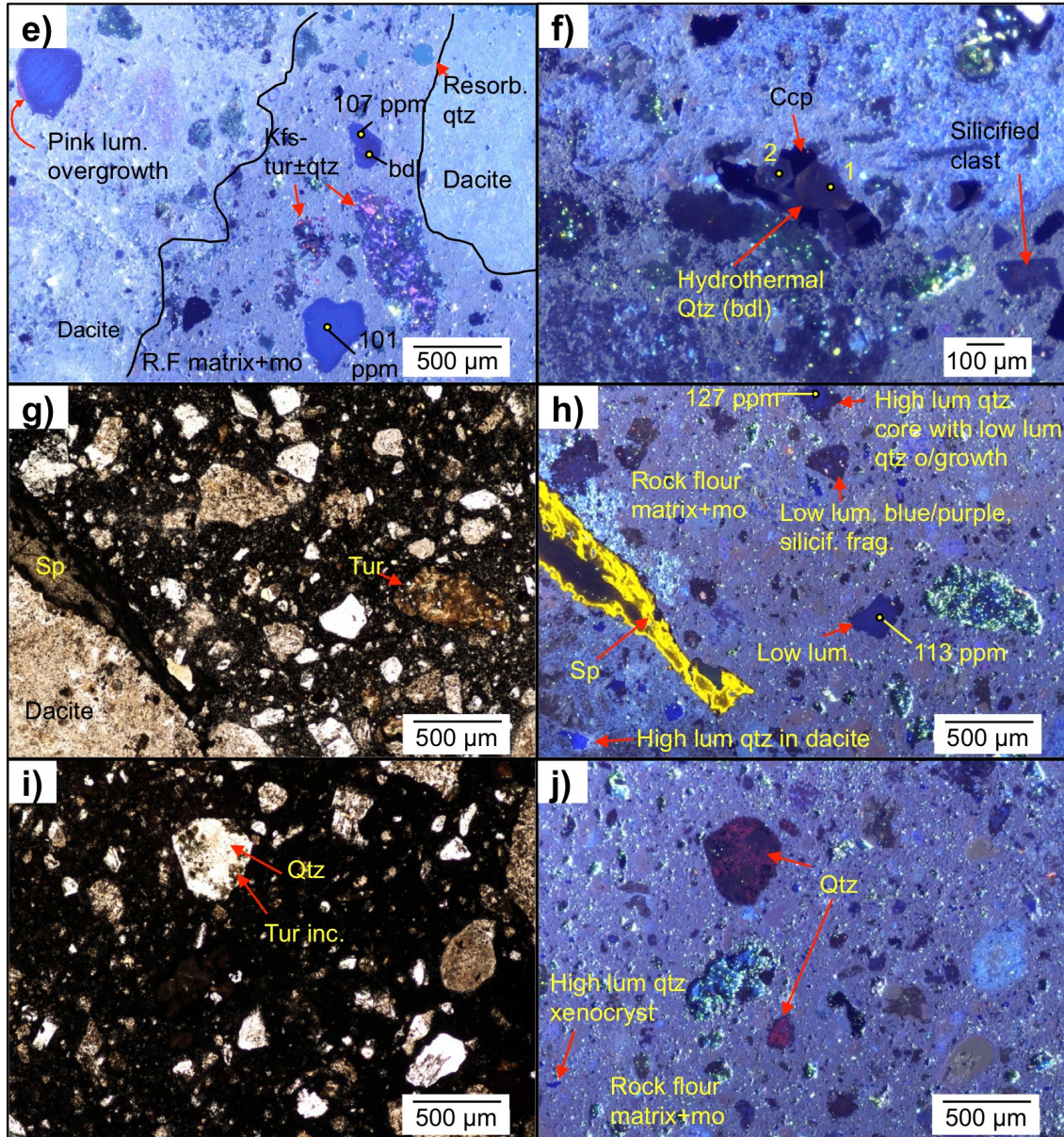


Fig. 4.15 cont. **e)** Cold-CL image of the dacite clasts (black lines) and rock flour matrix. Both contain similarly luminescing quartz grains which are variably resorbed. A small number of quartz crystals in the dacite have lighter pink/brighter luminescing rims. A euhedral/subhedral, dark CL silicified clast is present in the rock flour matrix. From DDH1196-220.88 m; **f)** Cold-CL image showing dark CL euhedral quartz infilling voids alongside chalcopyrite. From DDH1196-220.88 m; **g-h)** Transmitted light (PPL) photomicrograph (left) and cold-CL image (right) of sphalerite at the dacite-molybdenised rock flour matrix contact. Quartz xenocrysts in rock flour matrix have higher luminescing cores similar to quartz in the dacite. From DDH1196-172.71; **i-j)** PPL photomicrograph (left) and cold-CL image (right) illustrating non-luminescing tourmaline inclusions within mottled red-pink luminescing quartz. From DDH1196-172.71 m. EPMA point locations (yellow) with matching Ti concentrations (ppm) are also shown for reference.

#### 4.2.4 Quartz associated with molybdenite (in rock flour matrix at/near dacite clast margins)

Within a few mm, and less commonly up to a few cm, of the dacite-rock flour matrix contact, quartz is often directly associated with molybdenite mineralisation (Fig. 4.16). Compared to other quartz (described earlier), molybdenite-stage quartz grains are generally euhedral, between 10 to >100  $\mu\text{m}$  and show no visible CL response (Fig. 4.16c-f), although they do contain rare remnants of primary magmatic quartz which is irregularly shaped, is brighter in CL and commonly hosts molybdenite inclusions (e.g., Fig. 4.16a-d). The molybdenite inclusions are as <20  $\mu\text{m}$  long blades and also infill around the molybdenite-bearing quartz (Fig. 4.16). Other common inclusions are rutile and K-feldspar (rock flour). Molybdenite-stage quartz usually have a homogeneous texture, i.e. lacking well-developed growth zones or variations in CL intensity, and contain very few fractures or veins.

Primary magmatic quartz, identified from its higher CL response and similar internal grain textures to those in the underlying dacite, displays concentric growth zoning, are cross-cut by a darker CL quartz phases, <50  $\mu\text{m}$  in width, and are overgrown by similarly dark CL quartz (Fig. 4.16b). Cross-cutting the molybdenite-stage quartz and molybdenite are quartz-tourmaline veinlets up to 300  $\mu\text{m}$  thick (Fig. 4.16m, n). Tourmaline, which forms <100  $\mu\text{m}$  wide acicular inclusions (Fig. 4.16m, n), commonly grew inwards from the margins. Despite having the same mineralogy as the mottled pink-red quartz grains in the dacite and rock flour matrix, the quartz has only weak blue-purple in CL.

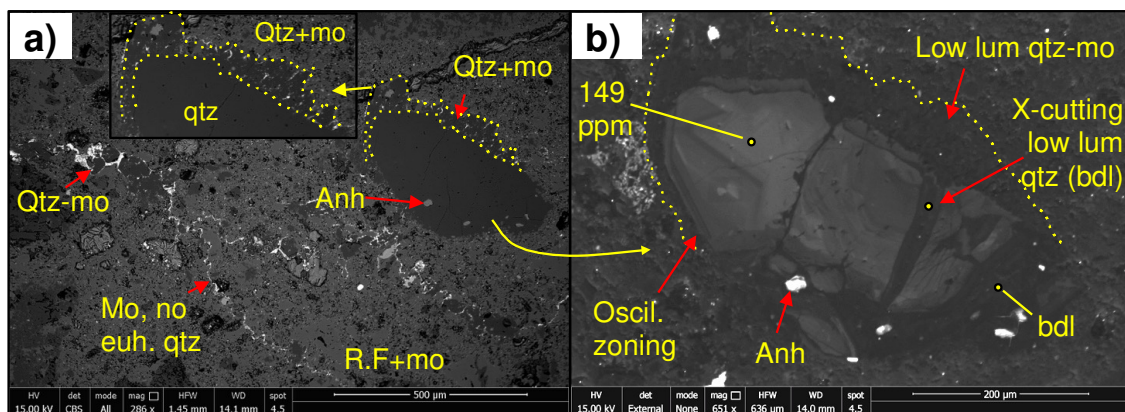


Fig. 4.16 Images a-f are SEM-BSE (left) with corresponding SEM-CL (right) and g-n are transmitted light photomicrographs (PPL) (left) with matching cold-CL images (right) of quartz associated with molybdenite mineralisation in the Braden Diatreme. Images a-h are from DDH1196-172.71 m and i-n are from DDH1196-242.04 m: **a-b)** <40  $\mu\text{m}$  wide bands of interlocking molybdenite blades in the rock flour matrix that are spatially associated with euhedral quartz containing molybdenite inclusions. Larger, brighter CL subhedral quartz xenocrysts in the matrix show growth zonation that is later cross-cut and overgrown by darker CL quartz with molybdenite inclusions. EPMA point locations (yellow) with matching Ti concentrations (ppm) are also shown for reference.

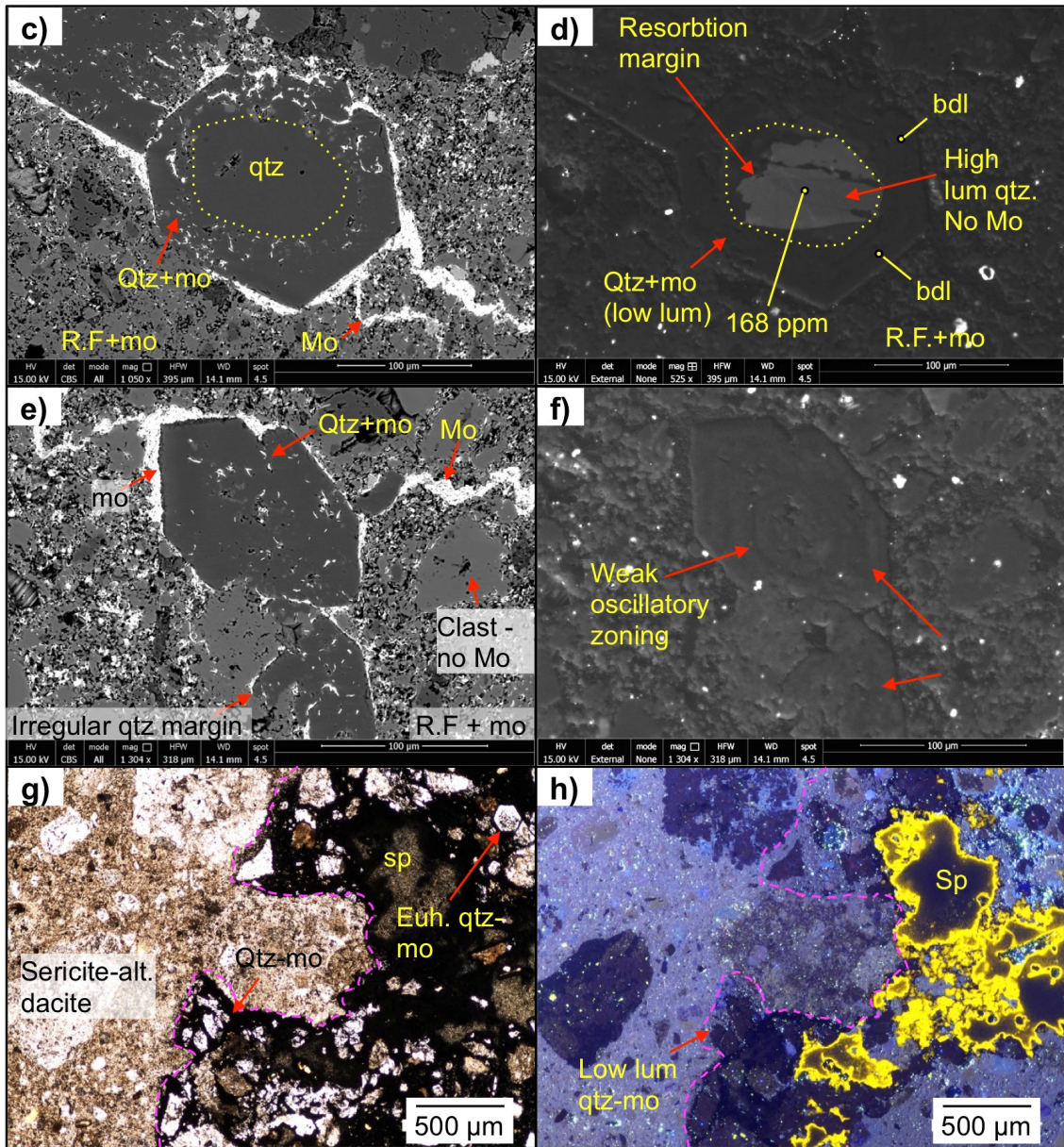


Fig. 4.16 cont. **c-d)** Euhedral quartz in rock flour matrix with a bright CL resorbed core containing no Cu-Mo, overgrown by a non-luminescing molybdenite-bearing quartz phase. Molybdenite also infills surrounding porous rock flour matrix; **e-f)** Weakly luminescing euhedral quartz with faint oscillatory zonation and molybdenite inclusions. Surrounding porous rock flour is impregnated with fine (<20 μm) molybdenite blades; **g-h)** Coarse sphalerite (yellow-CL) precipitated at the dacite clast margin (pink line) intergrown with poorly luminescing euhedral quartz containing molybdenite inclusions. Phenocrysts in dacite have often been partially replaced by darker CL blue-purple quartz. EPMA point locations (yellow) with matching Ti concentrations (ppm) are also shown for reference.

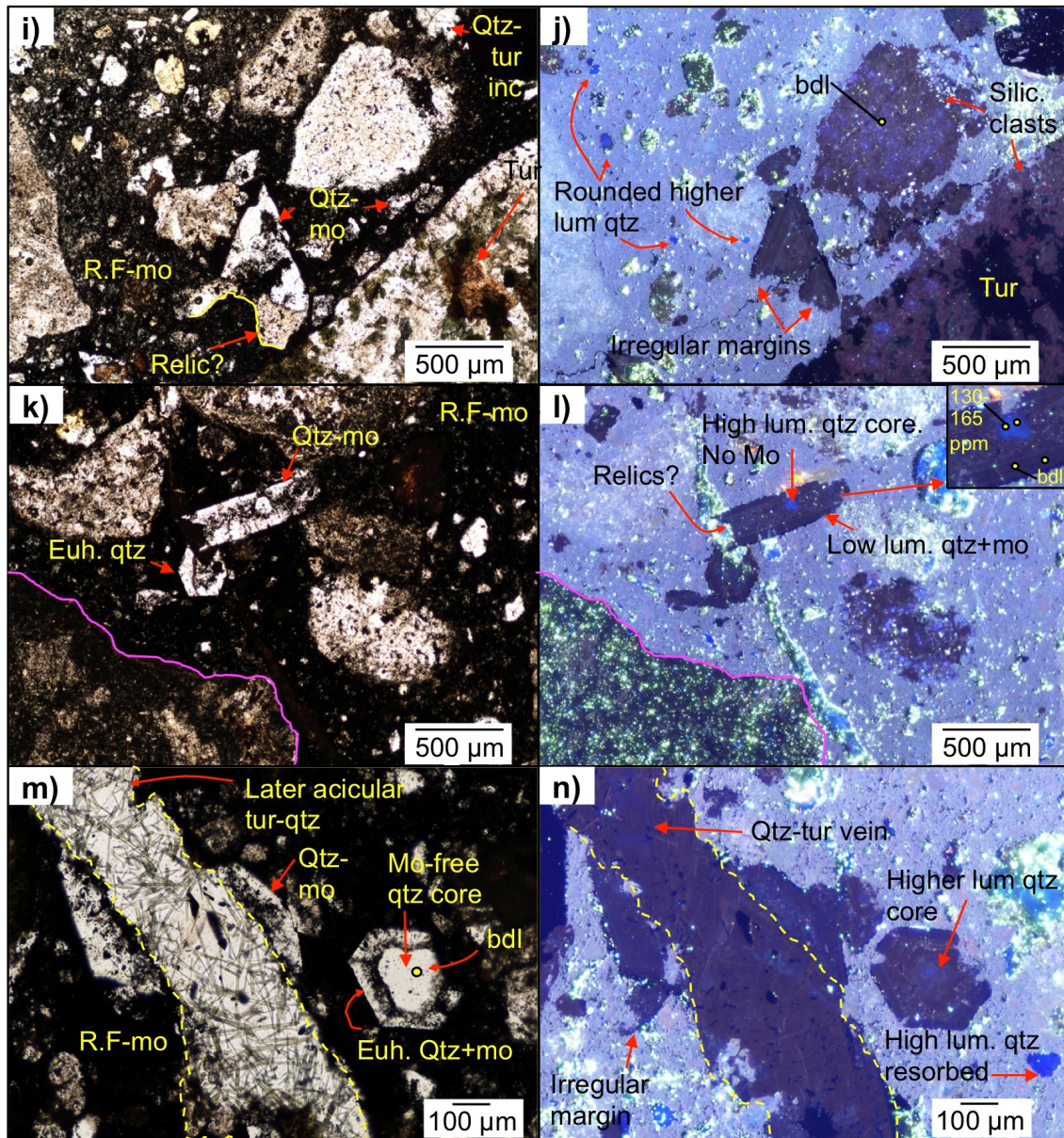


Fig. 4.16 cont. Transmitted light (PPL) photomicrographs (left) and cold-CL images (right) showing quartz associated with molybdenite mineralisation in the Braden Diatreme: **i-j**) Euhedral concentric zoned quartz with molybdenite inclusions and highly irregular margins. Silicified clasts contain minor tourmaline and show no growth zoning. Higher luminescence quartz xenocrysts are rounded and much smaller than in dacite clasts or underlying dacite; **k-l**) Bright CL quartz core containing no Cu-Mo overgrown by euhedral, darker CL quartz with molybdenite inclusions. Quartz is in molybdenite-rich rock flour matrix; **m-n**) Quartz-tourmaline vein cross-cutting quartz with molybdenite inclusions and the molybdenite-rich rock flour matrix. Vein has similar CL to the quartz containing molybdenite. Brighter CL quartz cores have irregular margins and are overgrown by a lower CL phase. EPMA point locations (yellow) with matching Ti concentrations (ppm) are also shown for reference.

#### 4.2.5 Diablo Breccia hydrothermal cement quartz

As a comparator, quartz from the Mo-Cu-mineralised magmatic-hydrothermal Diablo Breccia cement are described below. Quartz is one of the main cementing phases alongside tourmaline-anhydrite-chalcopyrite-pyrite and variably sphalerite (Fig. 4.17a). Quartz is present in the cement as mosaics of roughly equigranular grains up to a few mm in diameter. It shows varying shades of blue in CL that does not significantly change when adjacent to sulphides (Fig. 4.17c). The CL intensity of quartz grains from the Diablo cement is similar to that of the quartz associated with molybdenite in the Braden Diatreme except the latter is often more blue-purple in CL. No pink, red or brown luminescing phases were observed in the sample studied. Primary growth textures include growth zones that are alongside patchy zoning (Fig. 4.17c). No evidence of later quartz overgrowths, ‘healed’ fractures or cross-cutting darker CL phases were observed. Quartz crystals are not highly fractured and do not display resorption margins. Ti concentrations are only a few ppm.

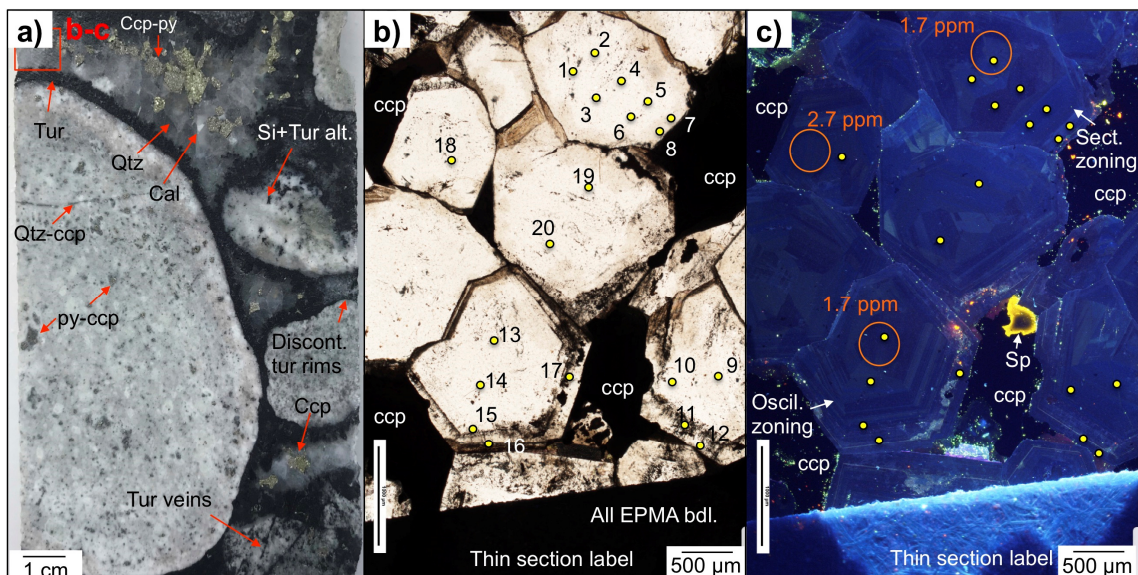


Fig. 4.17 Hydrothermal cement-phase quartz from the Diablo Breccia (DDH2677-118 m): **a)** Drill core photograph of the cement-supported Diablo Breccia with rounded, variably silicified and tourmalinised clasts. Early tourmaline cementing phases form discontinuous rims on clasts. Later stage open-space fill is predominantly quartz and late chalcopyrite-pyrite-sphalerite. Red box indicates location of b and c; **b-c)** Transmitted light (PPL) (b) and cold-CL image (c) of euhedral quartz with oscillatory growth zoning overprinted by patchy zonation. EPMA point locations (yellow) and LA-ICP-MS spots (orange) with corresponding Ti concentrations are also shown for reference. All EPMA data for Ti was below detection.

#### 4.2.6 Ti-in-quartz temperature estimates

The relative concentrations of Ti-in-quartz (Fig. 4.18) show a good general correlation with observed CL response. Both the dacite clasts and rock flour matrix contain a mixture of magmatic and hydrothermal quartz, where Ti ranges up to 300 ppm in relatively bright blue CL magmatic quartz and is below detection limits ('d.l.') in darker CL hydrothermal quartz (d.l.= 70 ppm). These concentrations of Ti equates to a temperature range between 706°C and 899°C respectively for magmatic quartz using the equation ( $T^{\circ}\text{C} = (-3765 / (\log\text{Ti} - 5.69)) - 273$ ) by Wark and Watson (2006). Uncertainties in the temperature estimates (see Fig. 4.18d) for magmatic quartz (based on SD% error) can be up to  $\pm 50^{\circ}\text{C}$  but are mostly  $\pm 20^{\circ}\text{C}$ .

There were a small number of hydrothermal quartz grains which contained detectable Ti, including the mottled pink-red grains containing tourmaline inclusions and some hydrothermal quartz associated with molybdenite. This could be attributed to secondary fluorescence of Ti in rutile but re-examination of these grains found no rutile inclusions on surface. Rutile could however be below the surface. No Ti could be detected in quartz associated with molybdenite mineralisation in the rock flour matrix, or in any of the hydrothermal quartz from the Diablo Breccia. Due to the inclusion-rich nature of many clast- and matrix-hosted hydrothermal phases, LA-ICP-MS proved unsuccessful returning exceedingly high elemental concentrations inferred to be from contamination. LA-ICP-MS was therefore only applied to the coarser Diablo cement, which contained between ~1 and 2 ppm Ti equating to around 400°C (Fig. 4.18d).

Al (Fig. 4.18b) concentrations show a larger range than for Ti and Fe, with most quartz analyses having <6,000 ppm Al. The majority of magmatic phenocrysts/xenocrysts are below detection (<152 ppm). Many hydrothermal quartz grains paragenetically associated to molybdenite regularly contain Al ranging from below detection up to 6,000 ppm. Most magmatic quartz contain no detectable Fe (Fig. 4.18c) (d.l.= 73 ppm) whereas hydrothermal quartz, in particular quartz associated with molybdenite, contains comparatively elevated Fe concentrations, regularly up to 900 ppm.

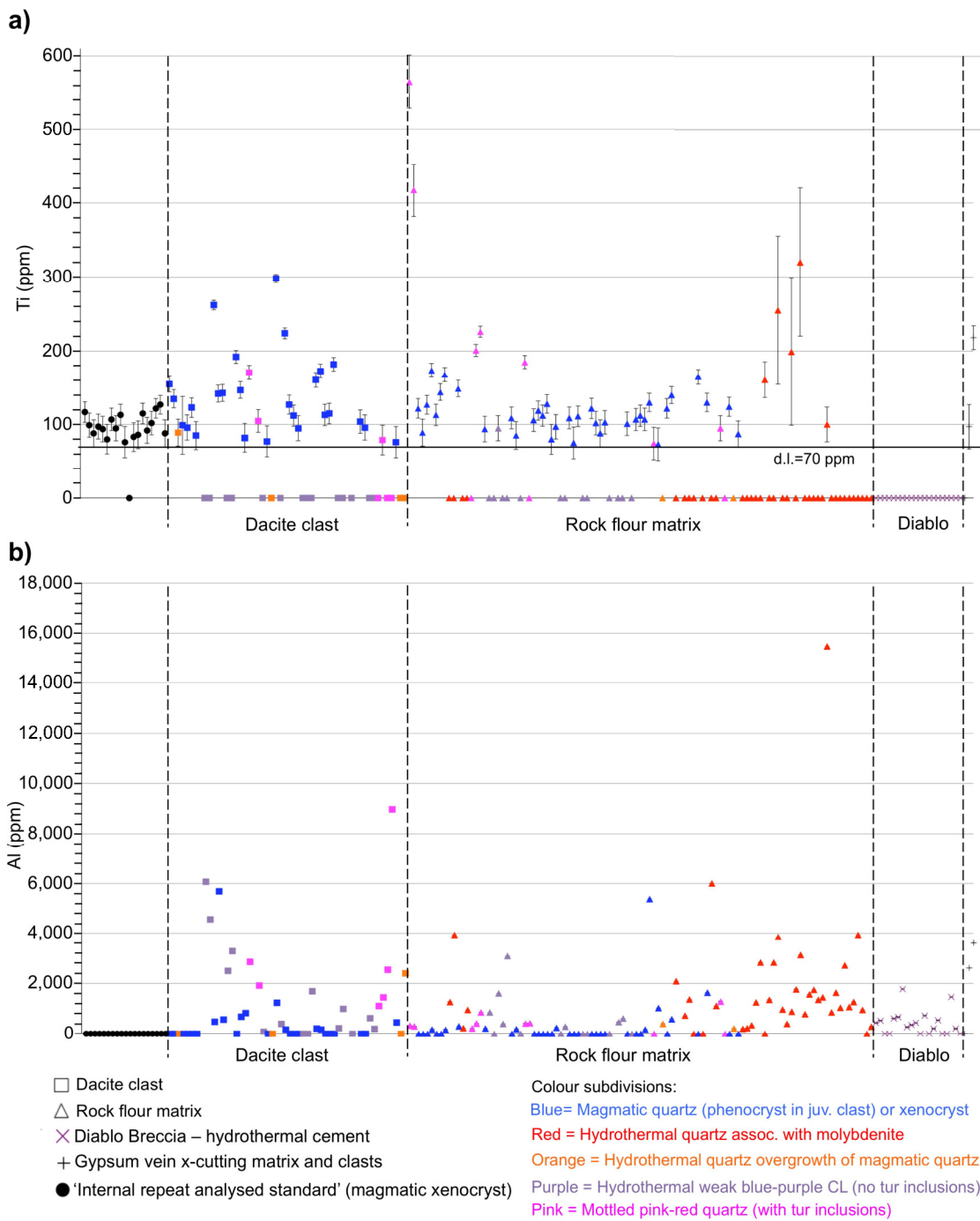
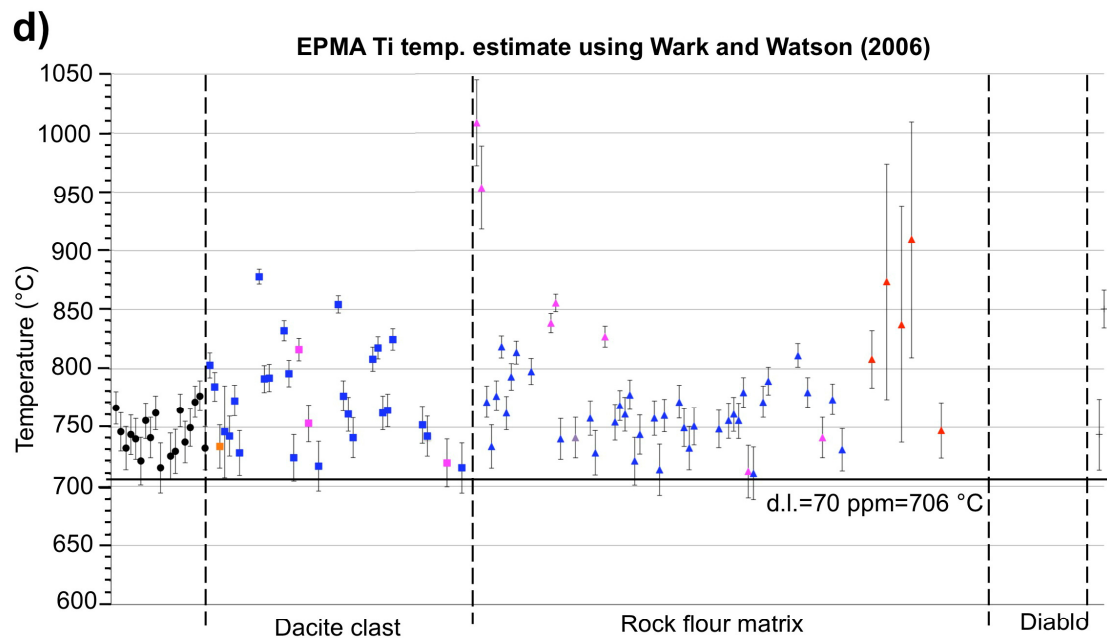
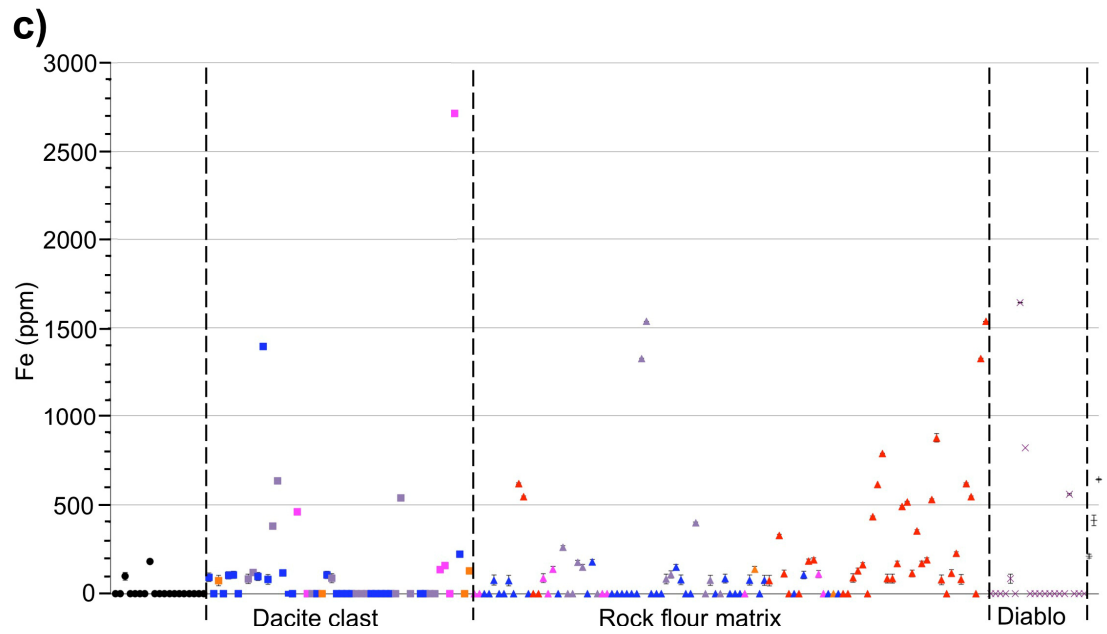


Fig. 4.18 Ti, Al and Fe in quartz from different rock types (separated by vertical lines) and generations (ppm) from El Teniente, determined by EPMA: **a)** Quartz Ti data with no discernable difference between dacite and rock flour matrix-hosted quartz. Hydrothermal cement quartz from the Diablo Breccia are largely below detection limits; **b)** Quartz Al concentrations are variable, with a number from each location below detection limits (152 ppm). Error bars are smaller than the symbol size; **c-d)** Overleaf. Error bars are the standard deviation in X-ray counting. Square shaped analyses are from dacite clasts and triangular from the rock flour matrix with colour coding further dividing samples.



- Dacite clast
  - △ Rock flour matrix
  - × Diablo Breccia – hydrothermal cement
  - + Gypsum vein x-cutting matrix and clasts
  - 'Internal repeat analysed standard' (magmatic xenocryst)
- Colour subdivisions:
- Blue= Magmatic quartz (phenocryst in juv. clast) or xenocryst
  - Red = Hydrothermal quartz assoc. with molybdenite
  - Orange = Hydrothermal quartz overgrowth of magmatic quartz
  - Purple = Hydrothermal weak blue-purple CL (no tur inclusions)
  - Pink = Mottled pink-red quartz (with tur inclusions)

Fig. 4.18 cont. **c)** Most Fe is below detection limits (73 ppm) except for a number of analyses from the rock flour matrix, dacite and cement; **d)** Quartz temperature (on  $T(^{\circ}\text{C}) = (-3765 / (\log \text{Ti} - 5.69)) - 273$ ) estimates for El Teniente Braden Diatreme clasts, rock flour matrix and hydrothermal quartz from the Diablo Breccia, EPMA detection limit shown as black line (70 ppm). Square shaped analyses are from dacite clasts and triangular from the rock flour matrix with colour coding further dividing samples.

### 4.3 Tourmaline breccia textural classification

Textural description and classification of the tourmaline breccias has been carried out using the scheme of Woodcock and Mort (2008), as this has become accepted as the most useful non-genetic scheme. From this, the following definitions have been applied: large clasts: clasts >2 mm; small clasts: clasts 0.1 to 2 mm; matrix: fine-grained particulate material produced by either local fragmentation of larger particles or by introduction of more exotic sediment; and cement: crystalline material grown in place, either as infill of void space or as a replacement of clasts or matrix. Each of the tourmaline breccias at El Teniente have been plotted on the Woodcock and Mort (2008) triangular diagram in Fig. 4.19, which has been modified to also show rounding. Breccias are categorised as either chaotic (30 to 60% clasts >2 mm), mosaic (60 to 75% clasts >2 mm) and crackle breccias (>75% clasts >2 mm). Data observations are from drill core, and therefore may differ from outcrop descriptions.

#### 4.3.1 Textural varieties

Tourmaline breccias in the Teniente district are either monomictic and/or polymictic, i.e. containing one or a variety of different clasts (e.g., TMC, dacite etc.) respectively. Clasts are derived from either surrounding wall rocks or porphyry intrusives. Wall rocks at El Teniente are the TMC except at La Huifa where they are propylitically-altered andesite and tuff from the Farellones Formation.

**Crackle breccias** - Zones of crackle brecciation up to several metres wide are found on the edges/margins of all tourmaline breccia bodies (except the Braden Tourmaline Breccia). These transition inwards into mosaic and then chaotic breccias and outwards into irregular tourmaline ( $\pm$ other cementing phases) veining and weakly tourmalinised wall-rock packages. The crackle breccias are clast-supported, monomictic, with no evidence of clast transportation, and individual clasts show <10° rotation.

Clasts range in size from 2 mm to > several centimetres and are typically cemented by blue-black microcrystalline tourmaline-quartz assemblages with lesser apatite, Cu-sulphides and iron oxides. Small clasts (0.1 to 2 mm) account for <25% of total clasts. Cements are variably Cu-Mo mineralised although this post-dates brecciation and tourmaline cementation. Clasts often show porphyry Cu-type mineralisation (disseminations and A-B-type veins), and any open-space was typically filled with quartz and/or anhydrite. Alteration is the same, although relatively weakly developed, as in the main breccia body, i.e. tourmalinisation and silicification ( $\pm$ argillic alteration).

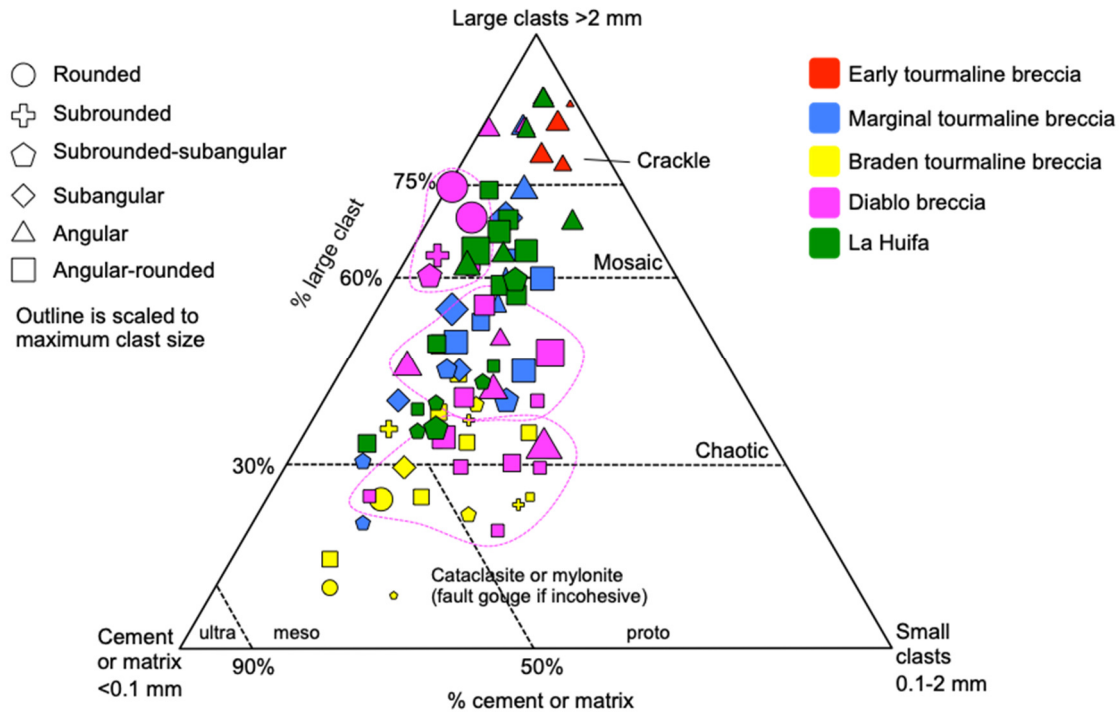


Fig. 4.19 Textural classification of tourmaline breccias at El Teniente from drill core observations in this study. Each breccia has a variety of textures, largely reflecting the sample location. For example crackle breccias are found on the peripheries to the main breccia body and at least three textural groups are present in the Diablo Breccia (pink outlines). Diagram adapted from Woodcock and Mort (2008).

**Mosaic breccias** - All tourmaline breccias, except the Early Tourmaline Breccias, show mosaic textures. These breccias are polymictic and are clast- as well as cement-supported. The cement accounts for ~20 to 60 vol.% of the breccias and is composed of variable proportions of tourmaline, quartz, anhydrite, Cu-Mo-sulphides, Ca-bearing phases, chlorite and smaller abraded material. Cu-Mo mineralisation is mostly late in their paragenesis and is post-tourmaline. Chalcopyrite-quartz veinlets cross-cut the breccia in places (e.g., Diablo) and introduce additional Cu into porous areas of cement. Large clasts are angular to rounded and range from 2 mm up to tens of centimetres. They show evidence of 10 to 20° rotation and smaller clasts (<2 mm) often tend to have distinctively shard-like angular morphologies.

**Chaotic breccias** - The polymictic Braden Tourmaline Breccia is the most chaotic of all tourmaline breccias studied, exhibiting >20° clast rotation, no geometric fit with adjacent clasts and significant transport (evident from well-rounded clasts and higher portions of small <2 mm clasts). Like mosaic breccias, chaotic breccias can be both clast- and cement-supported. Cements are made up of the same combination of minerals as listed above. Large clasts are angular to rounded and range from 2 mm to tens of centimetres. Smaller clasts (0.1 to 2 mm) are angular and subrounded. Chaotic breccias are more frequently observed away from the margins of the breccia body.

## 4.4 Tourmaline breccia petrography and paragenesis

As a precursor to describing the tourmaline geochemical data, the spatial associations between different tourmaline generations and Cu-Mo mineralisation are outlined. A paragenetic sequence for each breccia is presented.

### 4.4.1 Early Tourmaline Breccias

Early Tourmaline Breccias are mostly encountered on the eastern side of the Teniente deposit, at shallow mine levels (R Floody., personal communication, 2017). These breccias have a relatively limited spatial distribution resulting in short drill core intercepts of typically <30 cm (e.g., Fig. 4.20). With little economic significance, they have been largely overlooked and therefore their true extents are still unknown. They are easily identified in drill core based on colour contrasts with their TMC host rocks (Fig. 4.20).

The Early Tourmaline Breccias contain large black to cream-white clasts (>2 mm), making up >85 vol.%, which are silicically-altered porphyritic basalt from the TMC (Fig. 4.20e). They show little tessellation, and <10° average rotation, allowing fragments to be easily matched-up. Clasts are angular and range from 2 to 70 mm. A small number of shard-like small clasts (<2 mm) are present in the cement. There is no evidence of clast transportation or multiple episodes of brecciation.

Clasts contain a number of Cu-Mo-bearing vein generations associated with the main mineralising events at El Teniente, such as type 6a, 6b and 7b (e.g., Vry et al., 2010), which are truncated at clast margins. Chalcopyrite-pyrite disseminations (<1 mm across) occur throughout the clasts and within the cement are fine open-space molybdenite (<50 µm) infills.

The crackle breccia cement (<15 vol.% of the rock) is composed of microcrystalline (<1 mm) dark blue to black (Fig. 4.20) tourmaline (40 to 70 vol.%), quartz (20 to 30 vol.%), manganoan calcite and anhydrite (20 to 30 vol.%). Other components include Cu-Fe-sulphides (<2 vol.%), molybdenite (<1 vol.%), apatite and rutile. Tourmaline varies texturally, depending on location within the crackle breccias, and is grouped as: (1) a mixture of very fine- to fine-grained (<10 to >300 µm) microcrystalline crystals intergrown with quartz, or as coarser ~100 µm acicular or blocky crystals infilling voids in the cement, and; (2) less commonly as fine to coarse (<100 to few mm) crystals within the clasts (Fig. 4.21e). Chalcopyrite is present as inclusions within cement-stage manganoan calcite (Fig. 4.20l) or as end-stage open-space fill; it post-dates the tourmaline.

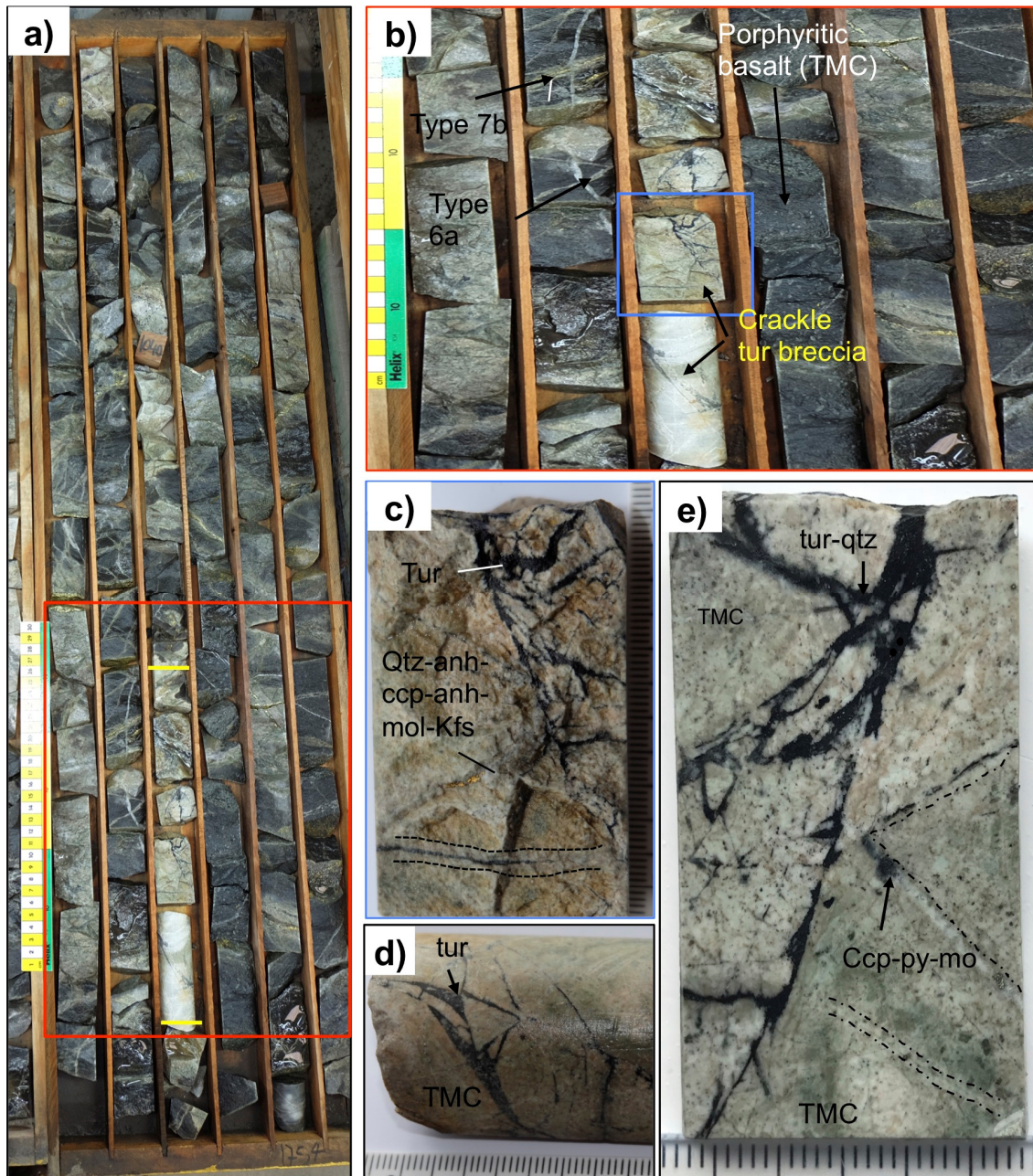


Fig. 4.20 Drill core photographs of crackle tourmaline breccias from DDH1754; **a-b)** Short drill intercepts (yellow limits) of the Early crackle Tourmaline Breccias from the eastern side of the deposit (DDH1754-317.5 m). The TMC is Cu-Mo mineralised, predominantly with a mixture of type 4a, 6a, 6b and 7b veinlets and chalcopyrite disseminations. The zone of crackle breccia is bleached white; **c-d)** Dark blue microcrystalline tourmaline cement; **e)** Strongly veined and bleached porphyritic basalt TMC clasts. Original porphyritic texture is still visible and porphyry-style veins are truncated by the tourmaline-quartz cement.

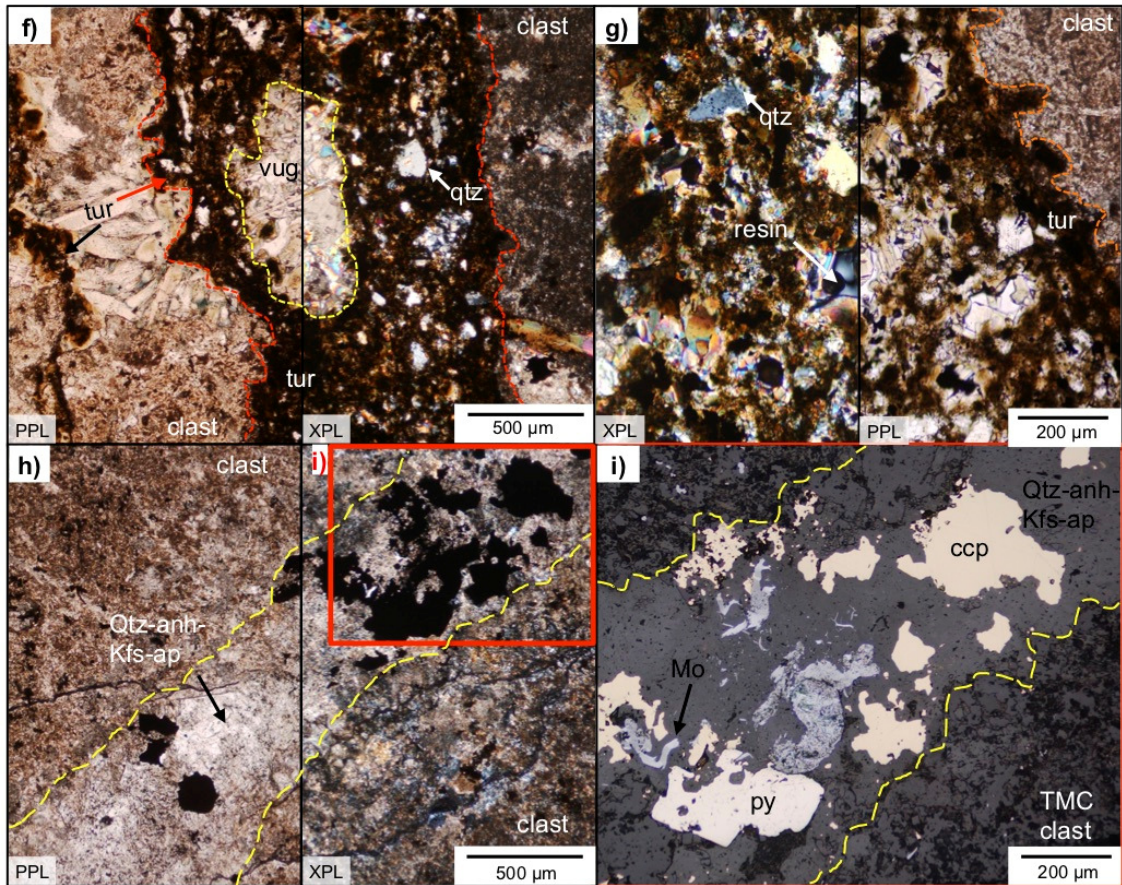


Fig. 4.20 cont. Transmitted (PPL) (f-h) and reflected light (i) photomicrographs of Early crackle Tourmaline Breccia east of the Braden Diatreme from DDH1754-317.5 m; **f)** Dark brown fine-grained ( $\leq 100 \mu\text{m}$ ) microcrystalline tourmaline-manganoan calcite-quartz cement with cavities infilled by slightly coarser-grained ( $\sim 100 \mu\text{m}$ ) acicular tourmaline, quartz and manganoan calcite. Clasts are altered to a mixture of fine sericite-illite intergrown with quartz; **g)** Microcrystalline brown tourmaline-manganoan calcite-quartz cement with coarser tourmaline-quartz within cavities. The cement has sharp, irregular contacts with the clast margins; **h)** PPL (left) and XPL (right) photomicrographs of a type 6b vein within a TMC clast largely quartz-anhydrite-apatite-chalcopyrite-pyrite-Mo truncated by the tourmaline-quartz cement at the clast margin; **i)** Reflected light image of the vein shown to the left.

Tourmaline is optically brown to dark brown in PPL (Fig. 4.20), and in SEM-BSE images shows varying degrees of intercrystalline zonation (Fig. 4.21). The most common zonation observed is patchy (Fig. 4.21d, f, h, j, k) attributed to the substitution  $(\text{Fe}^{2+}, \text{Fe}^{3+})(\text{Mg}, \text{Al})_{-1}$  (Fig. 4.21h,-j). Mineral inclusions within tourmaline include quartz, apatite and less commonly rutile (Fig. 4.21 h-j).

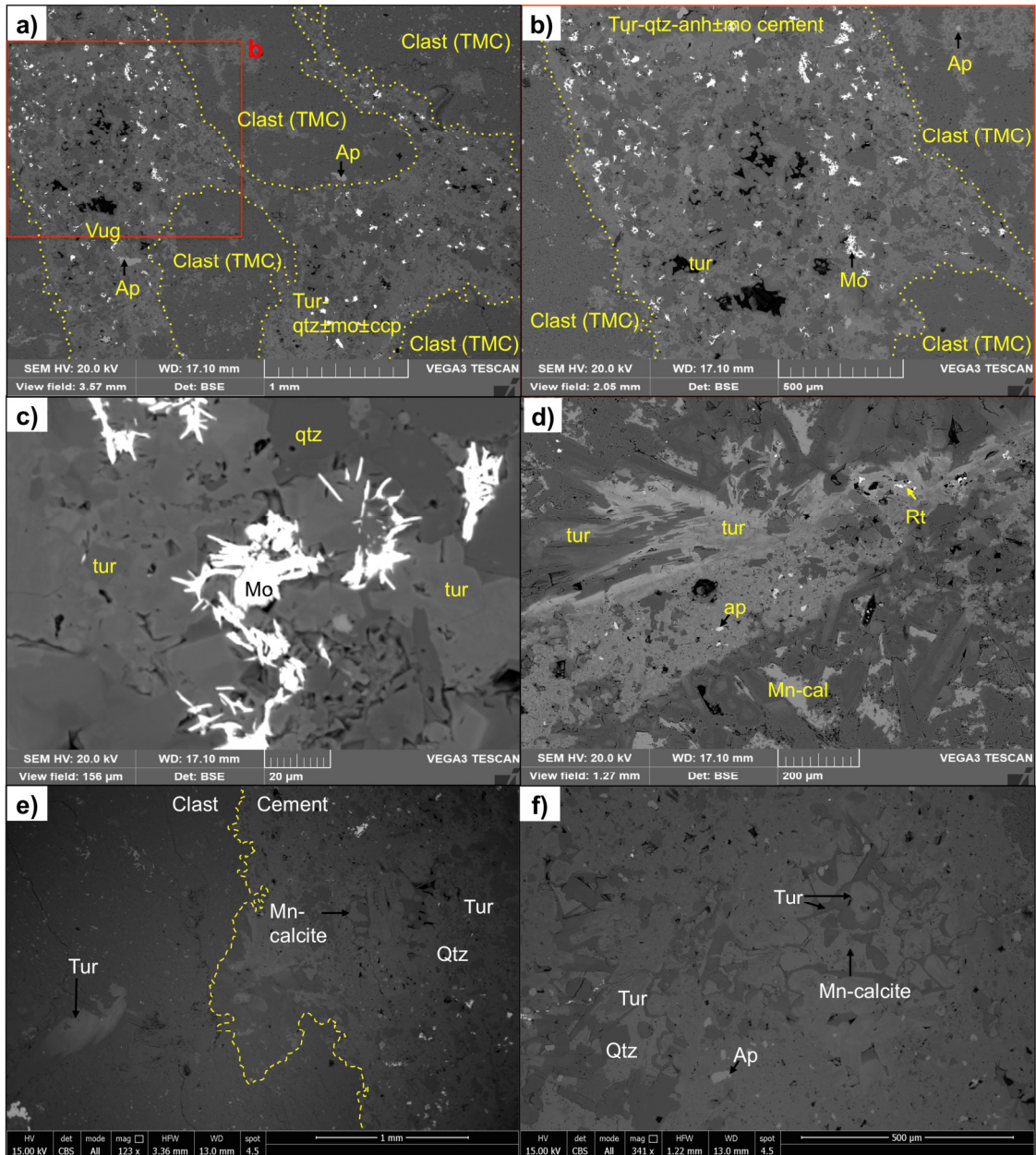


Fig. 4.21 SEM-BSE images from the Early Tourmaline Breccia east of the Braden Diatreme from DDH1754-317.5 m (sample shown in Fig. 4.20e); **a-b**) Clast margins are outlined in yellow with tourmaline-quartz cementing the clasts. Molybdenite is spatially constrained to the relatively porous cement. Location of b is outlined in red. Apatite is within both the clasts and cement; **c**) <30  $\mu\text{m}$  molybdenite blades infilling void space between acicular tourmaline; **d**) Coarse (200 to 300  $\mu\text{m}$ ) tourmaline crystals intergrown with manganian calcite containing rutile and apatite inclusions. The degree/intensity of tourmaline zonation is variable across short distances (<1 mm); **e**) Coarse clast-hosted tourmaline on the left and tourmaline cement on the right; **f**) Mixture of blocky tourmaline crystals with later manganian calcite and quartz infill.

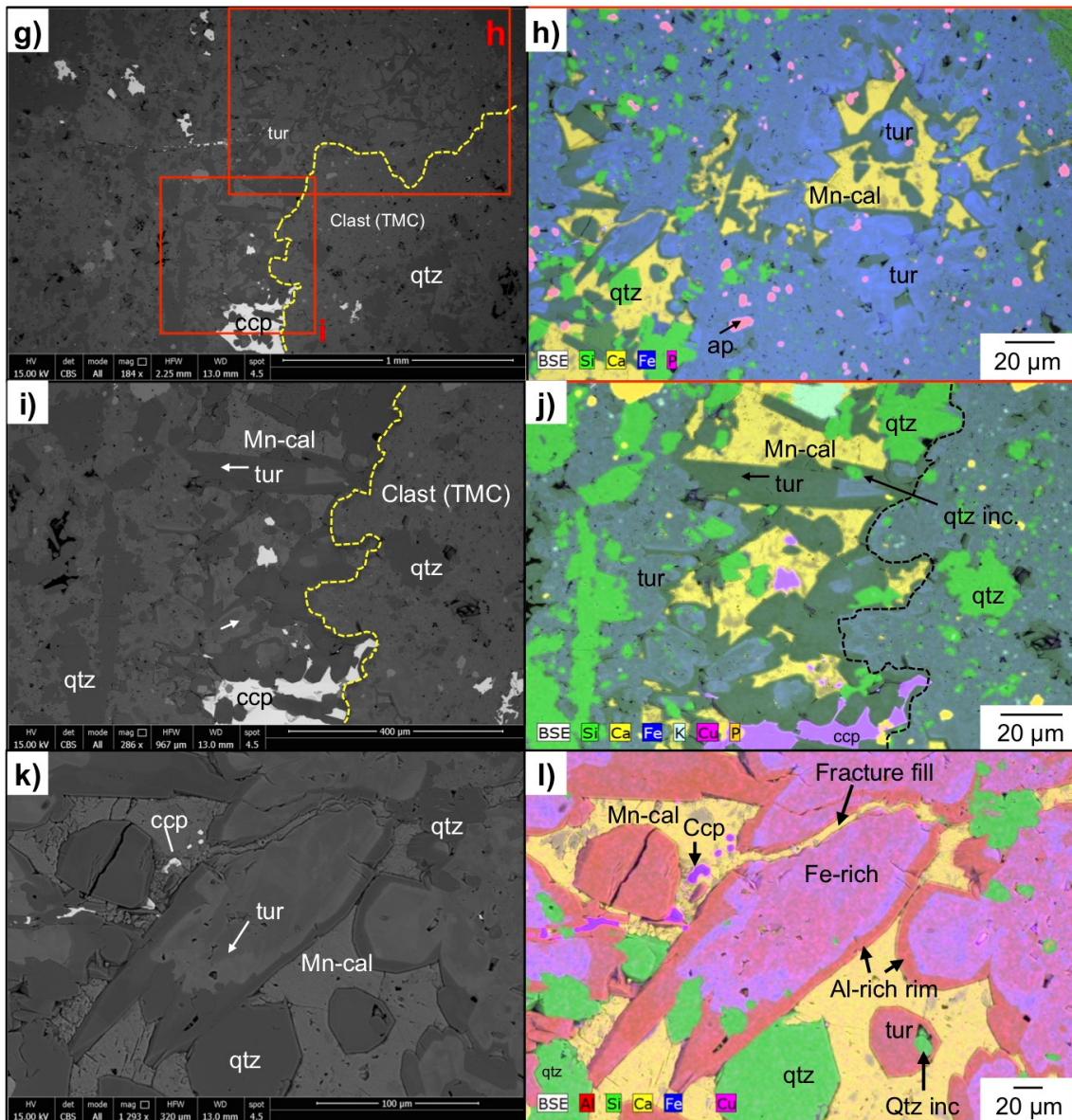
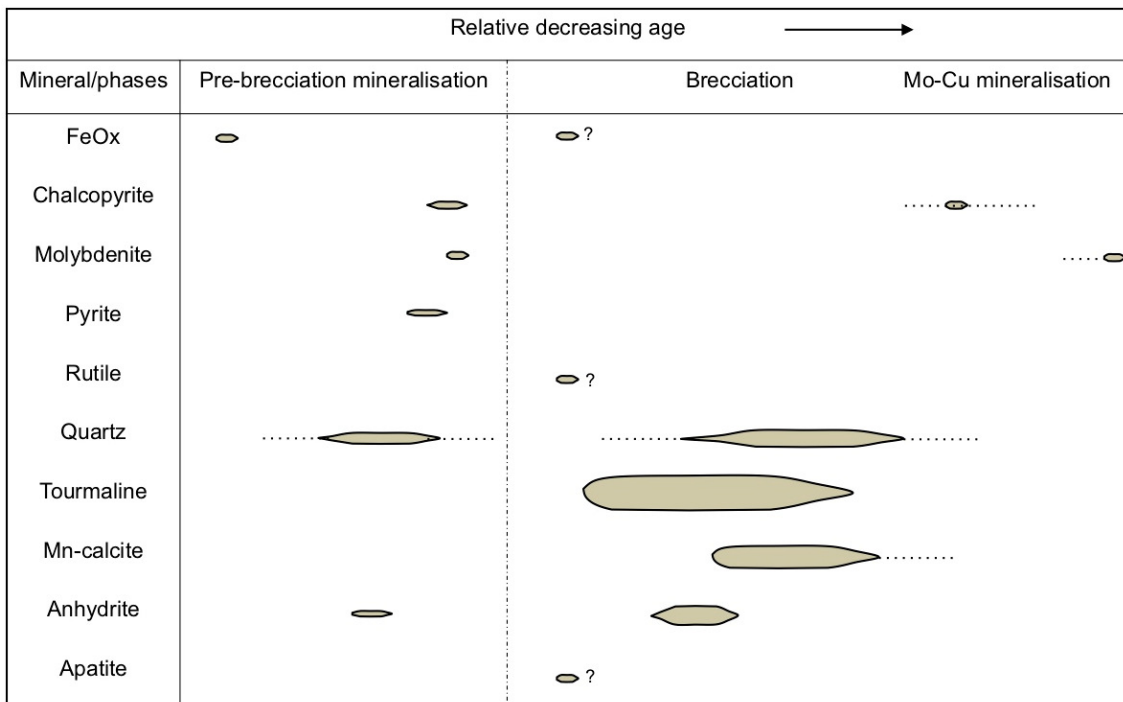


Fig. 4.21 cont. **g-h)** SEM-BSE image (left) and EDS elemental map (right) showing clast-hosted apatite and quartz and a fine tourmaline-manganoc calcite±quartz infill. Tourmaline precedes managnoan calcite±quartz infill. Tourmaline often shows Fe-rich cores and lighter Fe-poor (Al-rich) outer zones; **i-j)** SEM-BSE image (left) and EDS elemental map (right) showing tourmaline with an Fe-rich core and comparatively Fe-poor outer. Tourmaline also has quartz inclusions. Tourmaline is closely followed by a quartz-manganoc calcite-chalcopyrite assemblage, the latter is also disseminated throughout clasts; **k-l)** SEM-BSE image (left) and EDS elemental map (right) of faint complex patchy zonation within the Fe-rich core and a Al-rich rim. The tourmaline has been fractured and then healed/infilled by manganoc calcite containing chalcopyrite. Quartz inclusions are common in tourmaline and quartz also grows euhedrally next to tourmaline.

Given the lack of cross-cutting relationships available, only one generation of tourmaline has been identified within this breccia. Tourmaline has however been divided into clast- and cement-hosted for later quantitative geochemical comparison. Tourmaline ( $\pm$ quartz) is the first cementing phase growing off clast margins into open-space. Infilling around tourmaline is a mixture of quartz, anhydrite and manganoan calcite  $\pm$  chalcocopyrite. The last phase to have crystallised is the late infill of micron-sized molybdenite that is largely restricted to the more porous cement. It is texturally similar to the fine-grained molybdenite in areas of the Braden Diatreme, discussed earlier in Section 4.1. 'Pre-brecciation mineralisation' is related to the clast-hosted porphyry Cu vein stages. The mineralogy of these veins is consistent with the main mineralising stages at El Teniente (e.g., Vry et al., 2010).

Table 4.2 Paragenetic sequence for the Early Tourmaline Breccias. Main cementing phases during brecciation are tourmaline with lesser quartz, anhydrite and manganoan calcite. Later molybdenite infills cavities in the cement and is not associated with any further significant gangue phases. Cu-sulphides and molybdenite post-date tourmaline. Thickness of lines - approximate mineral abundance.



#### 4.4.2 Marginal Tourmaline Breccia

The Marginal Tourmaline Breccia is part of the Marginal Breccias which also include the Marginal Anhydrite and Chlorite facies. A gradual transition from Marginal Anhydrite to Marginal Tourmaline Breccia is commonly observed, as indicated by an increase in the ratio of tourmaline to anhydrite in the cement (e.g., Fig. 4.22b vs. Fig. 4.22a, c).

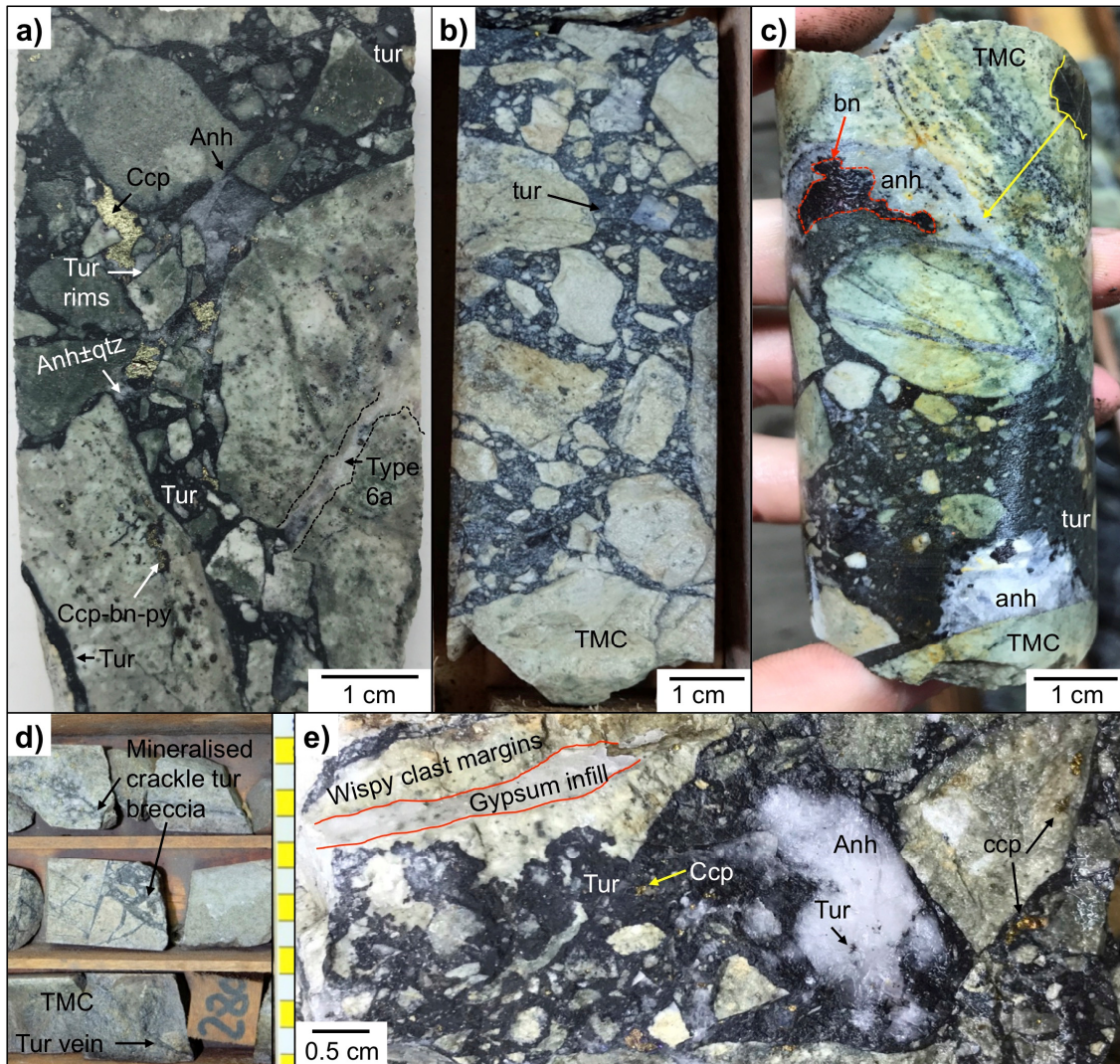


Fig. 4.22 Tourmaline breccias from the Marginal Breccia: **a)** Clasts of the TMC cemented by microcrystalline tourmaline-quartz-anhydrite±chalcopyrite-pyrite. A portion of small fragmented clasts are also present. Clasts are rich in chalcopyrite-bornite porphyry-style mineralisation. From DDH1754-9.14 m; **b)** Monomictic with angular clasts of the TMC cemented by tourmaline±chalcopyrite-pyrite. From DDH1754-9.14 m; **c)** Rounded TMC clasts (corrosive wear and physical attrition) along with an increased anhydrite-bornite cementing component. Black TMC clasts (top right) have been bleached (yellow arrow) and overprinted by chlorite. From DDH1754-45.87 m; **d)** Transitioning in the TMC host rocks, small intervals of tourmaline crackle breccias are present for up to tens of metres from the Marginal Breccias. From DDH1213-84 m; **e)** Microcrystalline dark blue-black tourmaline cement with anhydrite (±tourmaline inclusions) and chalcopyrite. Some TMC clasts have irregular, sinusoidal margins. Fractures have been infilled by gypsum. From DDH1213-95.5 m.

The Marginal Tourmaline Breccia is largely clast-supported, although cement-supported regions are observed. It grades laterally outwards into in-situ crackle breccias near the peripheries or contacts with the TMC host rocks (Fig. 4.22d). Clasts, which are mostly derived from the TMC wall rocks, and less commonly from the dacite, are angular to subangular (locally subrounded) and have undergone  $>20^\circ$  average rotation (sometimes 10 to  $20^\circ$ ) creating a chaotic or mosaic texture. Clast rotation often decreases towards the margins of the Marginal Breccias. Rounding is not related to clast size, with clasts of all sizes being both subrounded and/or angular. A number of wall-rock clasts have sinusoidal/wispy margin textures (Fig. 4.22e) resembling chemical abrasion outlined by Jébrak (1997). A moderate volume of crushed rock (0.1 to 2 mm, mainly quartz and plagioclase), derived from physical fragmentation and abrasion of larger clasts, is present in the cement, accounting for  $<15\%$  of its volume.

Clast-cement proportions vary over short distances (metres) in the breccia, with some areas having relatively lower contents of clasts ( $\sim 20$  to  $25$  vol.% of the rock) and others comparatively higher ( $\sim 50$  to  $80$  vol.% of the rock). Clast sizes range from 2 to 100 mm although the largest observed in this study was  $\sim 40$  cm. Porphyry-style alteration-mineralisation prior to brecciation have added disseminated and veinlet-style (e.g., type 5, 6a, 6b, 7b) chalcopyrite and bornite to the clasts, evidenced from many of the veinlets being truncated at clast margins (Fig. 4.23d). Few veins cross-cut the breccia except minor discontinuous quartz-anhydrite veins and gypsum-dominated veins. Chalcopyrite and bornite are commonly found in the cement as end-stage open-space fills which post-date the crystallisation of tourmaline. The breccias contain little pyrite.

Clasts in the breccia have mostly been affected by silicic, sericitic, chloritic and argillic alteration and therefore contain a complex mixture of quartz, K-feldspar, plagioclase, chlorite, muscovite/illite, biotite/Fe-illite, rutile and tourmaline (Fig. 4.23; QEMSCAN<sup>®</sup> mineral maps). Some clasts have discontinuous plagioclase alteration rims (2 mm thick) whilst clasts  $<1$  cm are now largely composed of plagioclase and/or quartz (e.g., Fig. 4.23d).

Tourmaline is present as scattered ( $<1$  mm) isolated needles in clasts or more commonly as  $<100$   $\mu\text{m}$  intergrown crystals forming the blue-black cement. The cement is comprised of 50 to 70 vol.% of microcrystalline ( $<1$  mm) dark blue/black tourmaline, 10 to 20 vol.% anhydrite (-gypsum), 10 to 30 vol.% quartz,  $<5$  to  $\sim 10$  vol.% chalcopyrite and bornite, and variable amounts of ankerite, calcite, chlorite and sericite (Fig. 4.24). Coarser tourmaline (up to  $\sim 200$   $\mu\text{m}$  in length), usually found in cavities (Fig. 4.24i, j), frequently has green tips/overgrowths that are only present in these larger tourmaline crystals (e.g., Fig. 4.24j). From SEM-BSE imaging, these show complex patchy and

more rarely oscillatory zoning (Fig. 4.24k). No evidence of re-brecciation has been observed.

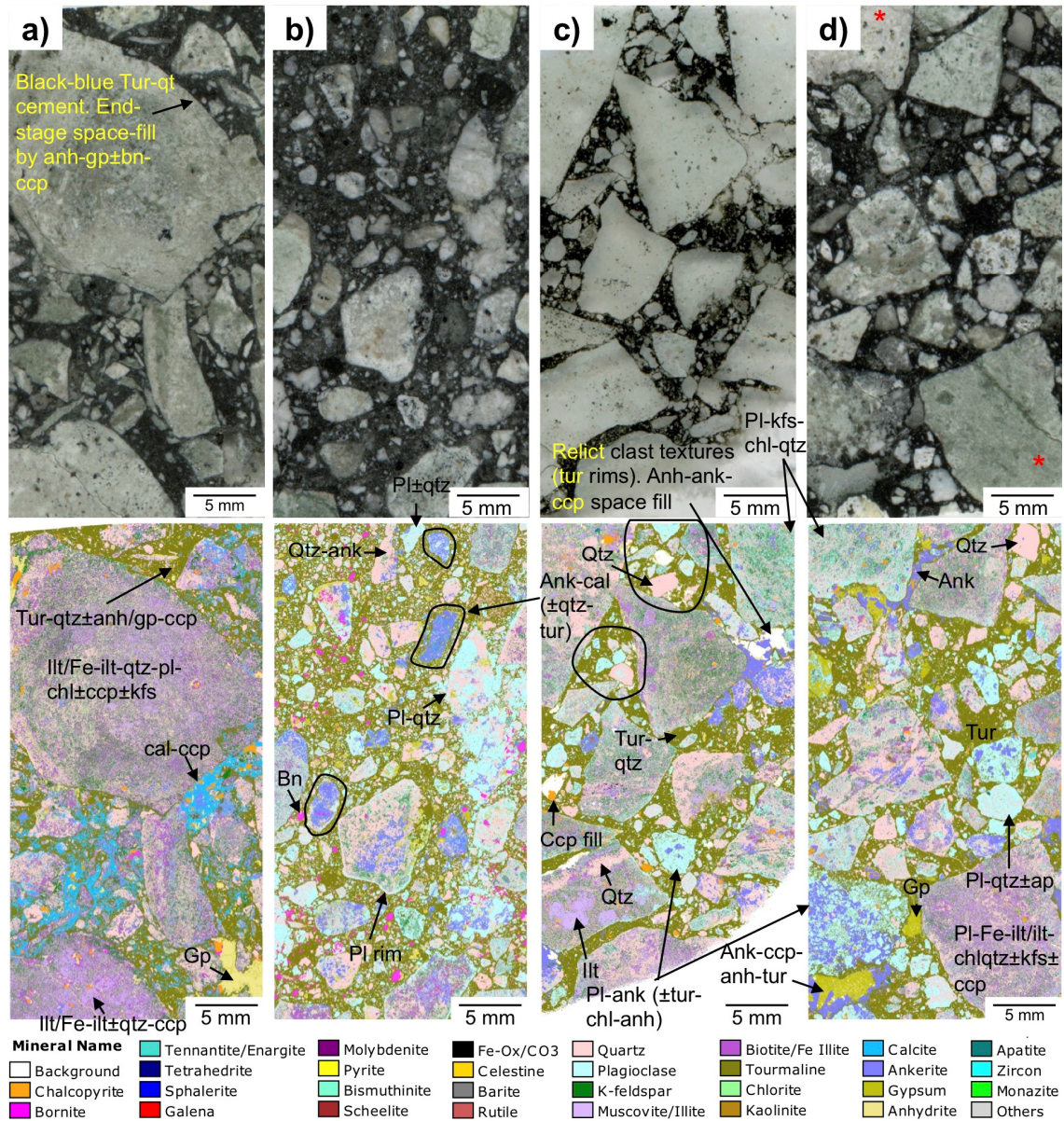
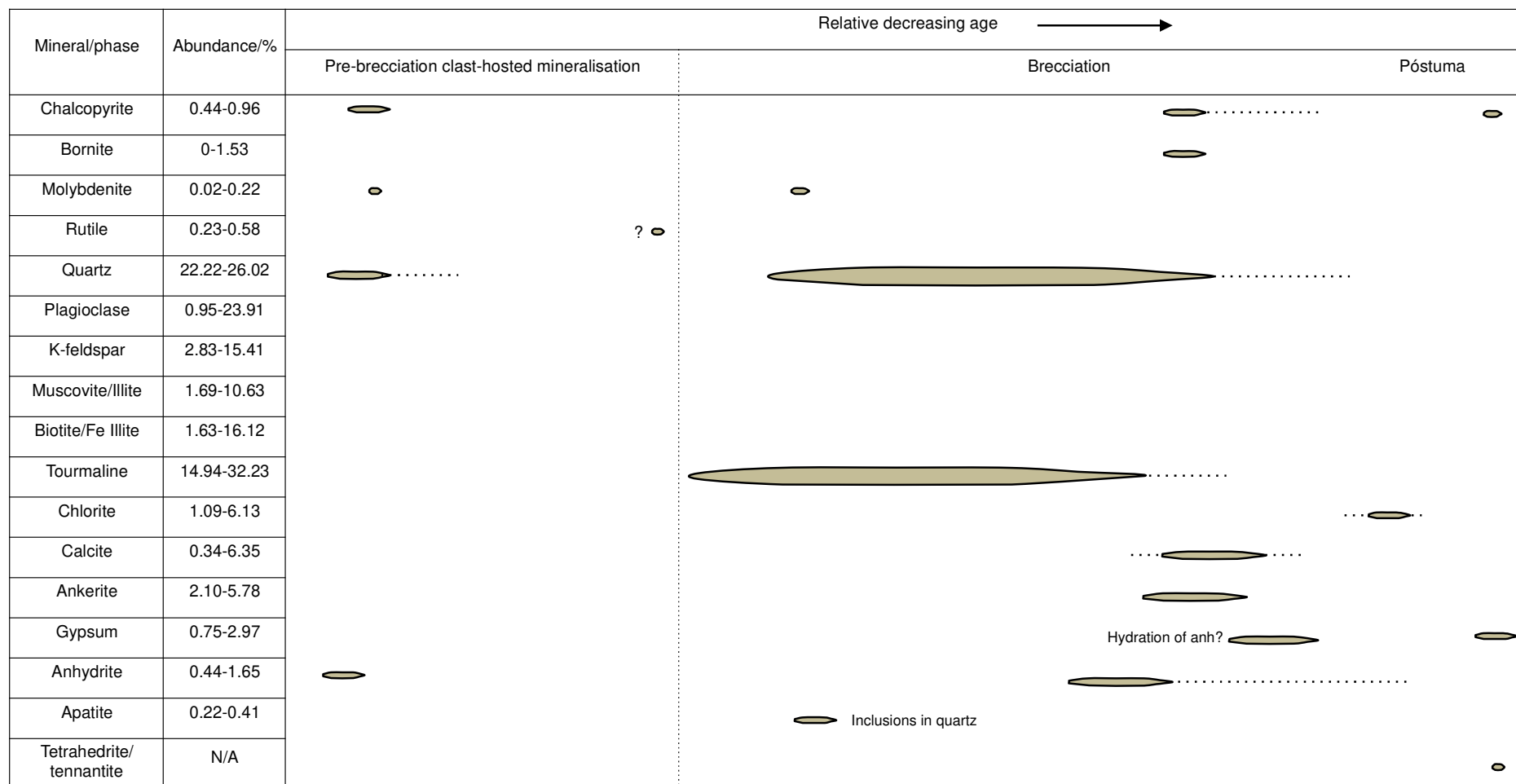


Fig. 4.23 Flatbed scans of polished sections of Marginal Tourmaline Breccia samples (all polished sections are 150  $\mu$ m thick except c which is 30  $\mu$ m) with corresponding QEMSCAN<sup>®</sup> (10  $\mu$ m pixel) mineral maps below. All samples contain microcrystalline tourmaline-quartz cement containing variable proportions of anhydrite-gypsum, calcite and chalcopyrite-bornite: **a)** Larger angular to subangular clasts altered to a mixture of quartz, illite/Fe-illite, chlorite, K-feldspar, and lesser variable tourmaline, gypsum-anhydrite, ankerite and Cu-sulphides. This sample has areas of calcite-rich (blue) cement associated with chalcopyrite-bornite. Coarse gypsum-anhydrite-chalcopyrite (bottom right of mineral map image a) infill of cavities around tourmaline-quartz cement. From DDH1213-95.50 m; **b)** Many clasts <5 mm are composed of quartz, plagioclase with lesser/variable amounts of ankerite, K-feldspar and chalcopyrite-bornite. Some clasts are almost entirely altered to ankerite-calcite (circled). From DDH1694-75 m; **c)** A number of clasts >2 mm, which are angular to subangular, are almost entirely composed of plagioclase and quartz (circled). Open-space has been partially infilled by anhydrite-ankerite-chalcopyrite. From DDH1694-89.90 m; **d)** Note the more felsic clast in the top left (\*) of the section has undergone less biotite $\pm$ chlorite alteration than the clast from the TMC in the bottom right (\*) of the section. The porphyritic felsic clast is now largely comprised of a quartz groundmass and phenocrysts of plagioclase, K-feldspar, ankerite and chalcopyrite. Some fragments are near entirely made up of plagioclase or quartz. From DDH1694-89.90 m.

Due to the fine-grained nature of the tourmaline cement, and lack of clear cross-cutting relationships, optically identifying different generations of tourmaline is difficult (Table 4.3). Fine (<200  $\mu\text{m}$ ) optically green overgrowths (Fig. 4.24j) are rarely observed where tourmaline is infilling large (>1 mm) cavities. Intergrown tourmaline and quartz are the earliest cementing phases and a portion of tourmaline precedes the growth of quartz, which is followed by anhydrite-gypsum (Fig. 4.24a, c) and the deposition of Cu-sulphides. Anhydrite and quartz can be considerably coarser-grained (up to 10 mm in places), often enclosing smaller fibrous to acicular tourmaline (Fig. 4.24a) and contain fluid (Fig. 4.24c) and mineral (tourmaline, quartz, Cu-sulphides) inclusions (Fig. 4.24f). Subhedral to anhedral and variably resorbed quartz crystals in the cement show similar blue CL signatures to a lot of the quartz in the clasts (Fig. 4.24l). They contain no tourmaline or other mineral inclusions and are sometimes overgrown by weaker blue-purple CL quartz phases. Quartz associated to silicification of clasts or breccia-phase cementing quartz has a darker blue-purple CL.

The paragenetic sequence in the Marginal Tourmaline Breccia can be divided into five main stages: 1) Pre-brecciation clast-hosted Cu-Mo mineralisation in the TMC host rocks which is characterised by porphyry-style vein assemblages and disseminations consistent with the main mineralising stages at El Teniente (e.g., Vry, 2010); 2) Brecciation with crystallisation of tourmaline intergrown with quartz; 3) Anhydrite, Cu-sulphides and molybdenite typically infilling around intergrown tourmaline-quartz and calcite; 4) Chlorite alteration of clasts which, where intense, produced the Marginal Chlorite Breccia. Minor quartz-anhydrite are associated with this event; 5) Formation of small discrete gypsum veinlets which contain minor amounts of tetrahydroite and tennantite. This stage is related to Póstuma alteration-mineralisation which infills fractures that cross-cut the breccia clasts and cement.

Table 4.3 Paragenetic sequence of the Marginal Tourmaline Breccia. Mineral abundances are averages of the QEMSCAN® data presented in Appendix iii. Note that samples used in this study are Mo-poor so may not truly be representative of the other more Mo-rich areas in the Marginal Breccias. Thickness of lines= approximate mineral abundance.



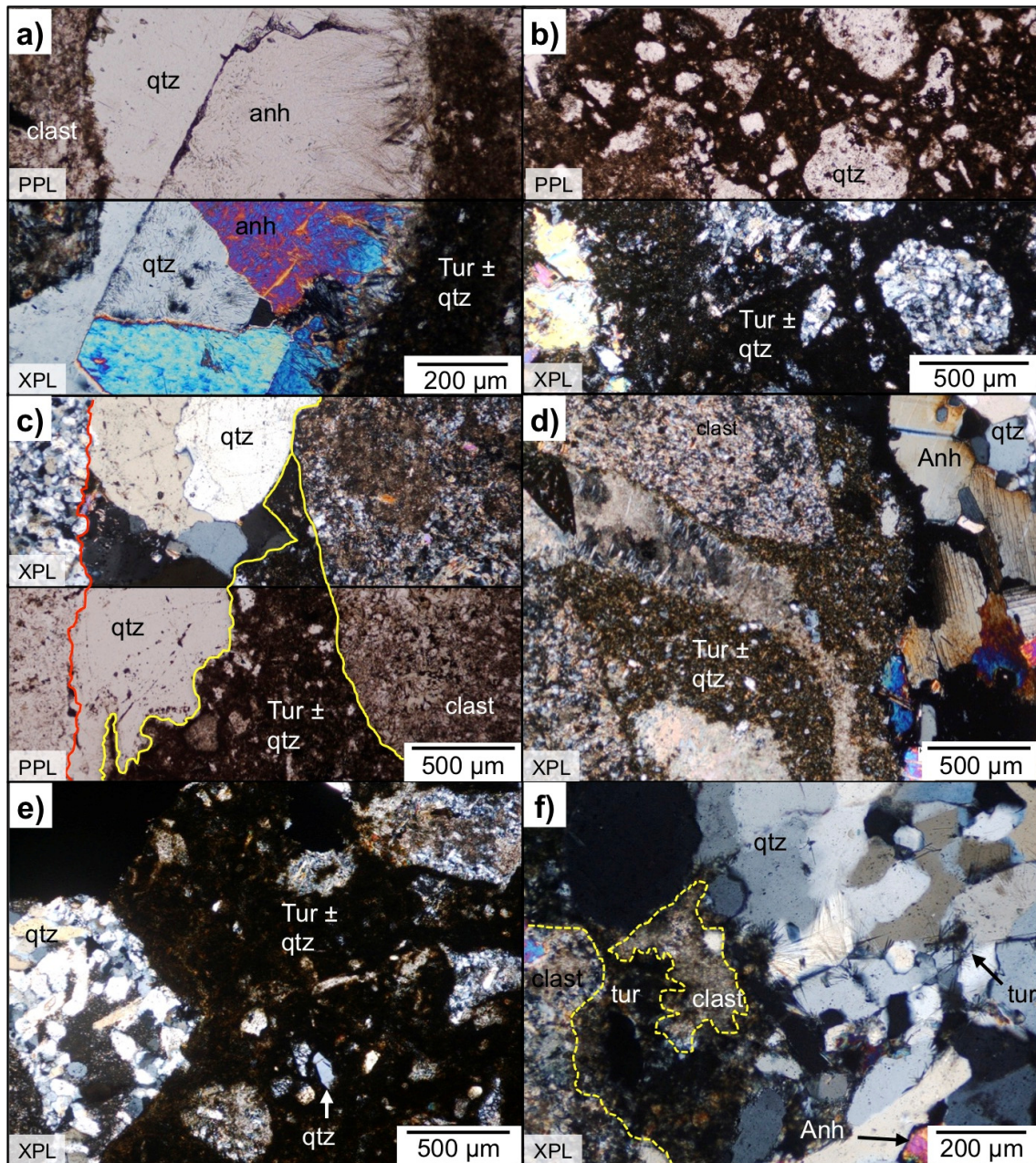


Fig. 4.24 Photomicrographs in transmitted light of Marginal Tourmaline Breccia in PPL and XPL: **a)** Fine-grained <100 μm long and <10 μm wide acicular tourmaline intergrown with quartz, with a later anhydrite-quartz infill. From DDH1754-45.07 m; **b)** Microcrystalline tourmaline-quartz cement with <500 μm angular rock fragments in cement and a later quartz infill. From DDH1754-45.07 m; **c)** Silicic-altered clasts cemented by tourmaline-quartz (yellow) and patches of coarser quartz with fluid inclusion trails. From DDH1754-45.07 m; **d)** Finely intergrown tourmaline-quartz rims on brecciated sericite-silicic-altered clasts and a later anhydrite-quartz infill. From DDH1754-48.20 m; **e)** Pervasively quartz-sericite-altered clasts and <500 μm rock fragments. From DDH1213-95.45 m; **f)** <30 μm acicular tourmaline inclusions in coarse quartz-anhydrite. From DDH1754-39.30 m.

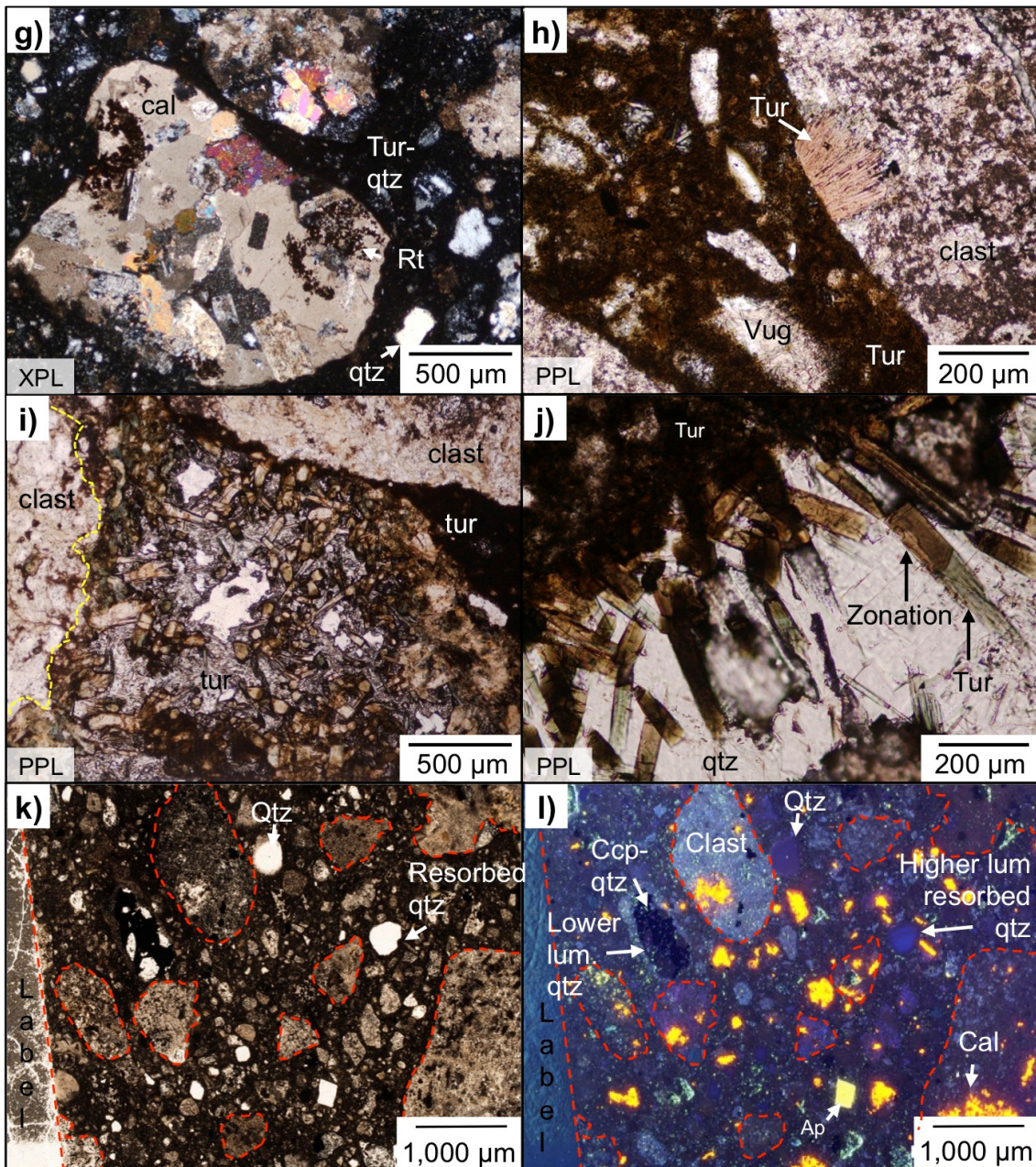


Fig. 4.24 cont. **g)** Pervasive and texturally-destructive calcite, rutile and quartz replacements in some clasts. From DDH1754-39.3 m; **h)** Dark brown microcrystalline tourmaline cement. Coarser tourmaline observed in vugs and clasts. From DDH1754-39.30 m; **i)** Patches of coarser (>100 μm) tourmaline (left) in cavities within the cement. From DDH1213-95.45 m; **j)** Coarse tourmaline with patchy zoning and optically (PPL) green zones towards its tips. From DD1694-89.88 m; **k-l)** Transmitted light (PPL) (left) and cold-CL (right) images of the cement which is largely made up of tourmaline, quartz and crushed rock fragments. Quartz xenocrysts in the cement show higher CL signatures compared to lower luminescing ('lum.') blue-purple CL quartz infilling cement cavities alongside chalcopyrite. From DDH1213-95.45 m. Red dashed lines show clast/fragment margins.

### 4.4.3 Braden Tourmaline Breccia

The Braden Tourmaline Breccia (BTB) is primarily hosted in the Braden Sericite (rock flour) Breccia (BSB) and less commonly the Braden Chlorite Breccia at all levels in the Braden Diatreme. The BTB is poorly sorted, chaotic and cement-supported (Fig. 4.25a, b). It is distinguished from the BSB by the colour difference in the grey rock flour matrix and the darker blue to black tourmaline cement (Fig. 4.25c-e). The cement-supported, chaotic and polymictic BTB has the same breccia framework as the BSB in terms of clast population characteristics (size, shape, rounding, composition etc.).

Contacts between breccia facies are sharp to transitional, and the surrounding rock flour breccia (within <1 to 5 cm) is variably tourmalinised which causes a slight darkening of the grey matrix (Fig. 4.25f). Where the adjacent BSB is stratified, this continues into the BTB. The cement is composed of microcrystalline blue-black tourmaline with lesser quartz, anhydrite, gypsum, chalcopyrite and rock flour, the latter becoming a more common component at or near the breccia margin (Fig. 4.25). The proportion of tourmaline as a cementing component is highly variable, with relatively little tourmaline and higher levels of sericite giving the rock a lighter grey colour (e.g., Fig. 4.25f and Fig. 4.26j). The BTB contains comparatively less porosity than the BSB and there are areas in the BTB that are more tourmaline-rich (see Fig. 4.25f, g and individual QEMSCAN<sup>®</sup> mineral maps beneath).

The clasts range from rounded to subangular, are strongly rotated (>20°) and have lost all apparent geometric fit to adjacent clasts (e.g., Fig. 4.25a, b). Fragments of all rock types at El Teniente are present including porphyritic dacite, TMC, and previous hydrothermal breccias. Total clast volume accounts for between 25 to 60 vol.% of the rock. Of the clast population, 40 to 65% of clasts are >2 mm and 45 to 60% are <2 mm and it therefore has a high volume of fragmented/fine material. Small clasts (0.1 to 2 mm) are rounded to angular and are often incorporated into the tourmaline-quartz-calcite-manganoan calcite cement (Fig. 4.26a, b). Larger clasts (>2 mm) are rounded to angular with no correlation between size and degree of rounding. The largest clasts observed in drill core exceed a few metres, although these account for <15% of the clast population.

Some areas contain a higher volume of smaller clasts (Fig. 4.25a) and an overall lower volume of clasts (Fig. 4.25b). Clasts are moderately to intensely sericite-pyrite-altered and have undergone more intense quartz-tourmaline-sericite alteration compared to the BSB. The most intense alteration is along clast margins, fracture planes and mineral cleavages. Approximately 10 to 25% of clasts contain tourmaline rosettes (<2 mm) which are often intergrown with quartz. These may however predate the BTB.

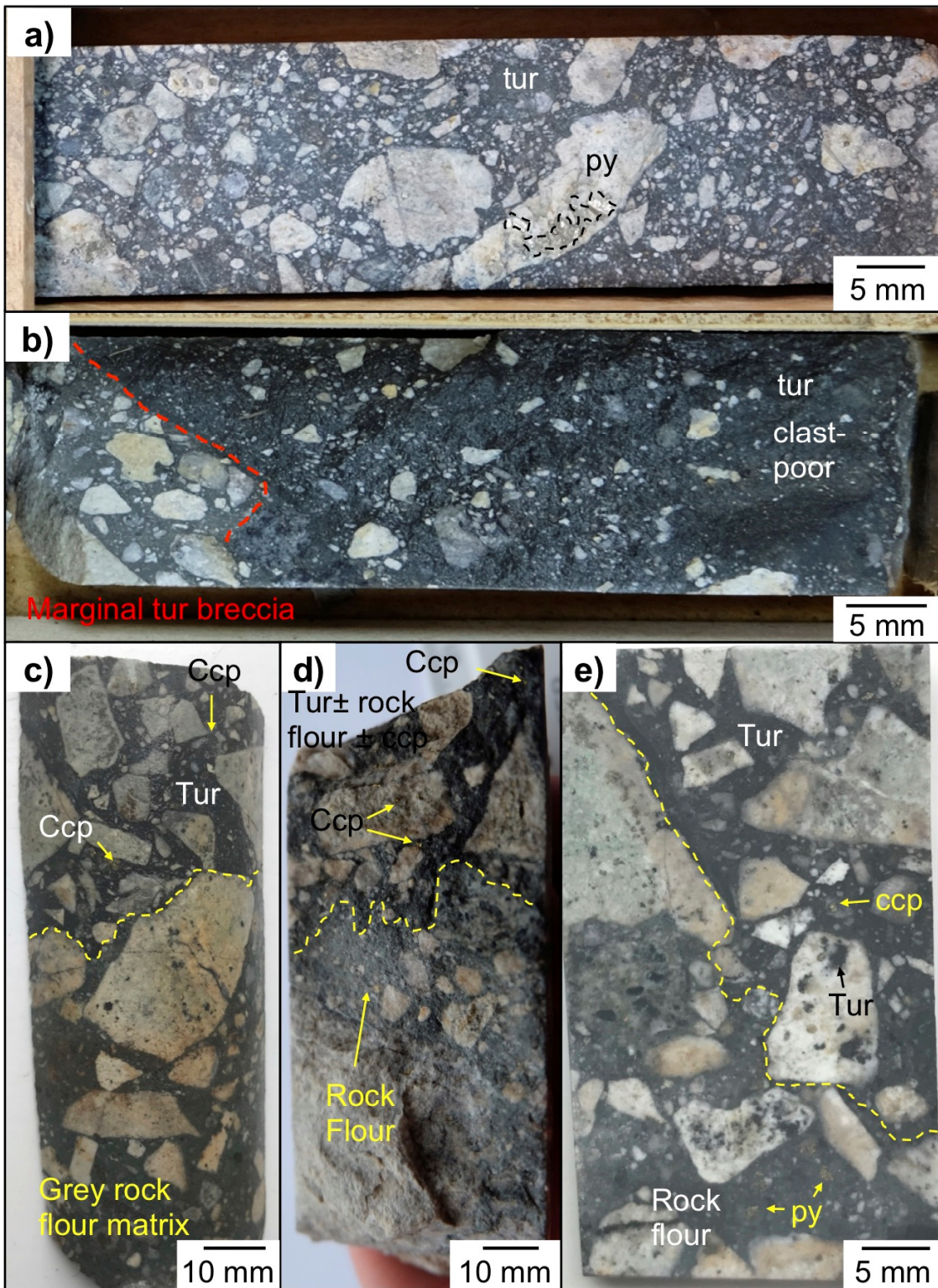


Fig. 4.25 Drill core photographs of the cement-supported BTB (a-d), cut thin section tablet (e), corresponding transmitted light image (XPL) (f) and QEMSCAN® mineral maps (g). Images c-g are from DDH1213-100.07 m: **a)** Well-rounded to angular sericite-pyrite-altered clasts with a chaotic texture. Coarse pyrite is outlined with a black dashed line. From DDH1775-57.91 m; **b)** Comparatively clast-poor core sample which contains a clast of the Marginal Tourmaline Breccia. From DDH1769-88.39 m; **c-e)** BSB and BTB contact with the approximate boundary marked by a dotted yellow line. The BTB has a darker blue-black cement compared with the lighter grey rock flour matrix. Both have the same breccia framework in terms of clast populations and characteristics. Clasts are however tourmaline-quartz altered at and near the contact; **f-g)** Overleaf.

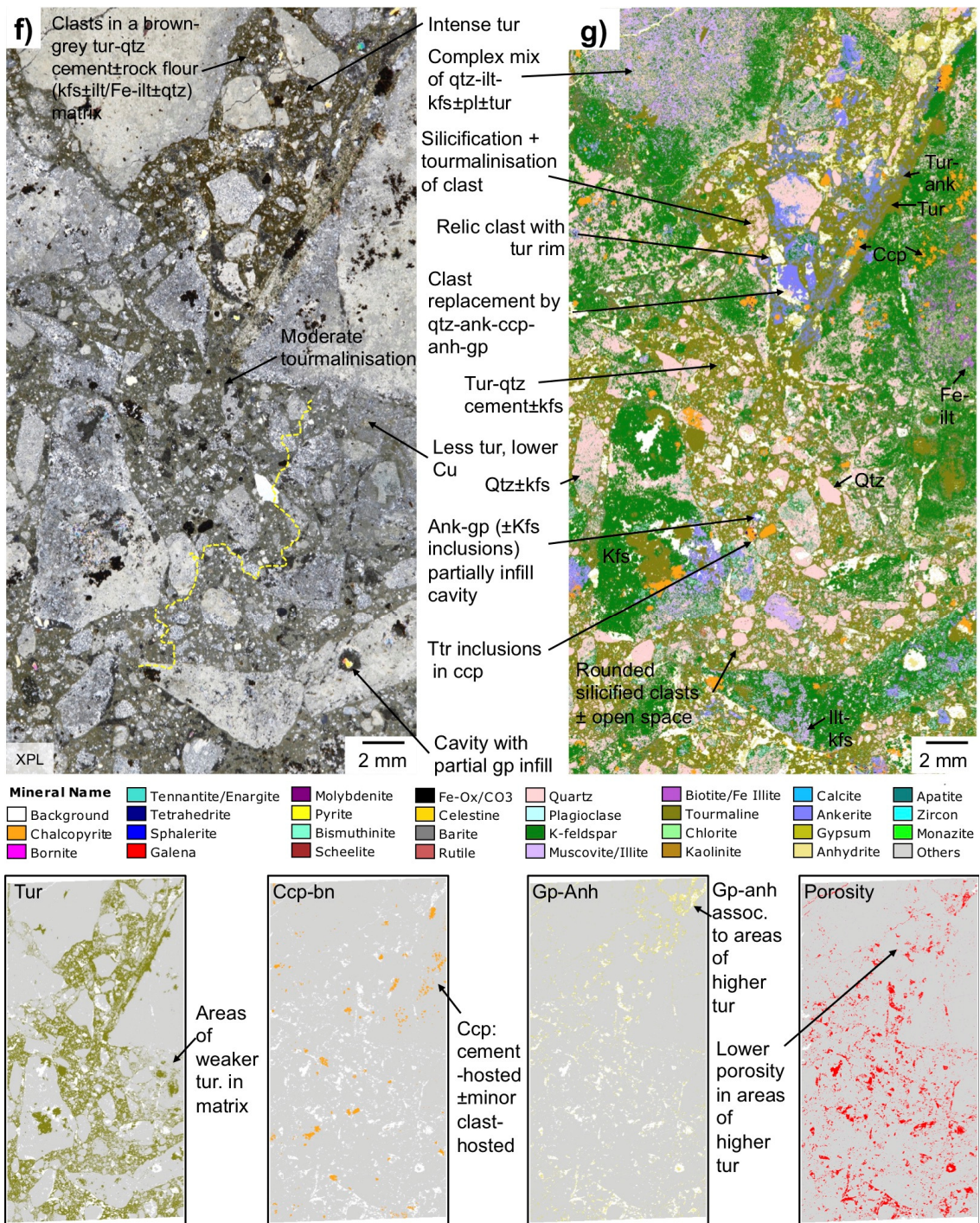


Fig. 4.25 cont. **d)** Transmitted light (XPL) photomicrograph of a Braden Tourmaline and Braden Sericite Breccia contact. Varying degrees of tourmalinisation are reflected by the differing shades of brown-grey throughout the section, with darker brown at the top of the section correlating with increased tourmaline; **e)** QEMSCAN® mineral map (10 µm pixel spacing) with individual mineral and porosity maps beneath. Increased tourmaline is associated with gypsum-anhydrite, quartz and increased porosity.

The blue-grey cement, which is mainly composed of tourmaline and quartz, accounts for between 40 and 75 vol.% of the breccia. Quartz often contains apatite and rutile inclusions and is intimately intergrown with tourmaline. Where tourmaline and quartz concentrations are higher, relict clast textures are common. They are characterised by

a quartz infill rimmed by tourmaline and can be up to a few mm in diameter (e.g., Fig. 4.25g). Other cementing phases include calcite(-manganoan calcite) $\pm$ chlorite-sericite-chalcopyrite and pyrite (Fig. 4.26). Where higher volumes of quartz and calcite (-manganoan calcite) occur, the cement is a lighter grey (Fig. 4.26i, j). The cementing phases have also reactivated some clast-hosted porphyry-style veinlets and introduced manganoan calcite and gypsum (e.g., Fig. 4.26j).

Tourmaline is present in the BTB as either: (1) a mixture of fine (<50  $\mu$ m) micro-crystals intergrown with quartz; (2) as coarser ~50 to 400  $\mu$ m long acicular or blocky crystals infilling larger voids (>1 mm), alongside coarser quartz and calcite/manganoan calcite in the cement; (3) less commonly as ~0.5 to 1 mm crystals within the clasts. An estimated 40 to 70% of the tourmaline is zoned, with homogenous tourmaline frequently observed alongside moderately to strongly zoned crystals. From the SEM-BSE images in Fig. 4.26g, the zonation can be either oscillatory, at a fine scale (<5  $\mu$ m), or patchy and coarser (up to 70  $\mu$ m), both attributed to the substitution ( $\text{Fe}^{2+}$ ,  $\text{Fe}^{3+}$ )(Mg, Al)<sub>-1</sub> (Fig. 4.26g). Coarser acicular to blocky tourmaline in the cement often has fibrous overgrowths towards the crystal tips or on fractured tourmaline grains, often healing the fracture (Fig. 4.26g). These overgrowths extend up to ~200  $\mu$ m parallel to the *c*-axis (Fig. 4.26h) and are optically a paler brown to green. Neither the tourmaline nor overgrowths are pitted or embayed, and there is therefore no evidence of dissolution observed. Likewise, there is no evidence of re-brecciation. The tourmaline is largely inclusion free although it occasionally contains inclusions of quartz (<30  $\mu$ m diameter) and acicular molybdenite (<20  $\mu$ m in length) (e.g., Fig. 4.26f, h).

Although the BTB is considered subeconomic, chalcopyrite $\pm$ bornite and traces of molybdenite are present in the cement. Fine-grained (<1 mm) chalcopyrite and pyrite infill spaces around tourmaline and are present within space-filling quartz-anhydrite-manganoan calcite as inclusions (Fig. 4.26). Molybdenite is relatively uncommon in the BTB except where it is near the margins of the Braden Diatreme. There, it is present as very fine-grained (<20  $\mu$ m) infills in cracks and fractures or voids around tourmaline. Juvenile dacite clasts, which look like they were viscous when entrained within the BTB, are also present (e.g., DDH1754-5.06 m; shown earlier in Section 4.1.5; Fig. 4.7). The fine habit of molybdenite resembles the pervasive molybdenite impregnation of the rock flour matrix in the Braden Diatreme, as discussed in Section 4.1. Surrounding the BTB is a ~15 m wide chalcopyrite halo where this is the main sulphide phase in the rock flour breccia. Infrequent late discontinuous and irregular quartz and gypsum veins, together with Cu-sulfosalts, cross-cut the breccia; because of this late paragenetic timing, these are likely related to Póstuma alteration.

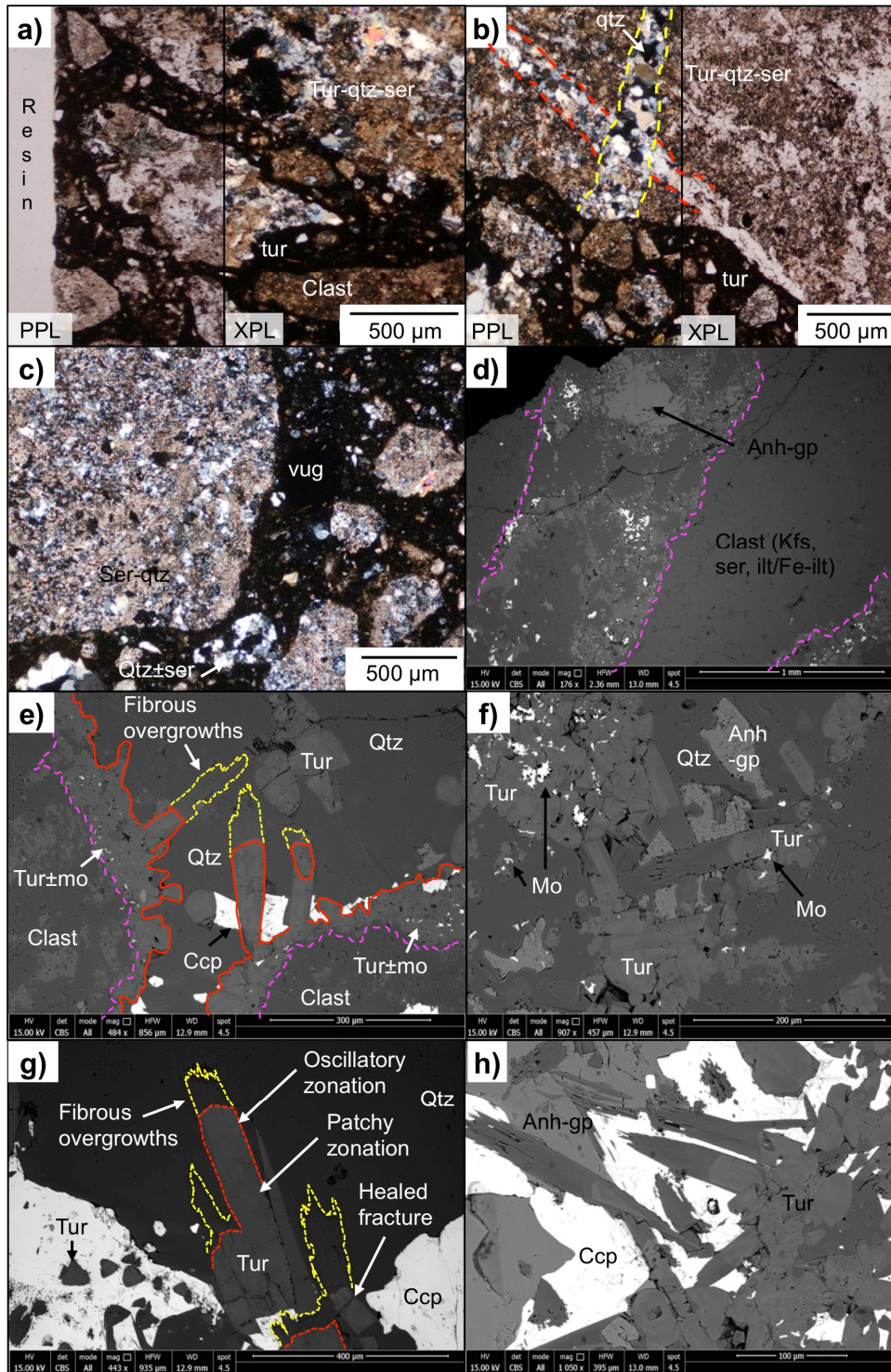


Fig. 4.26 Transmitted light (XPL) (a-c), SEM-BSE photomicrographs (d-h) and thin section scans with corresponding QEMSCAN® (10 µm pixel) mineral maps (i-j) of the Braden Tourmaline Breccia: **a-b)** Microcrystalline <50 µm dark brown-black tourmaline intergrown with quartz and <500 µm sericite-altered rock fragments forming the cement. Early pre-brecciation porphyry-style veins are truncated at clast margins. From DDH1754-7.19 m; **c)** Quartz-sericite-altered clasts cemented by tourmaline-quartz±rock fragments. Clasts are rimmed by tourmaline-molybdenite (red). Voids are to differing degrees infilled by quartz and tourmaline; **d)** End-stage cement fill is anhydrite-gypsum; **e-h)** Tourmaline zonation and later anhydrite (-gypsum) and/or quartz infill (c-h from DDH1754-5.06 m). Coarse tourmaline with fibrous overgrowths (yellow) often has oscillatory and patchy zonation (g). Fractures have been 'healed' by Al-rich tourmaline.

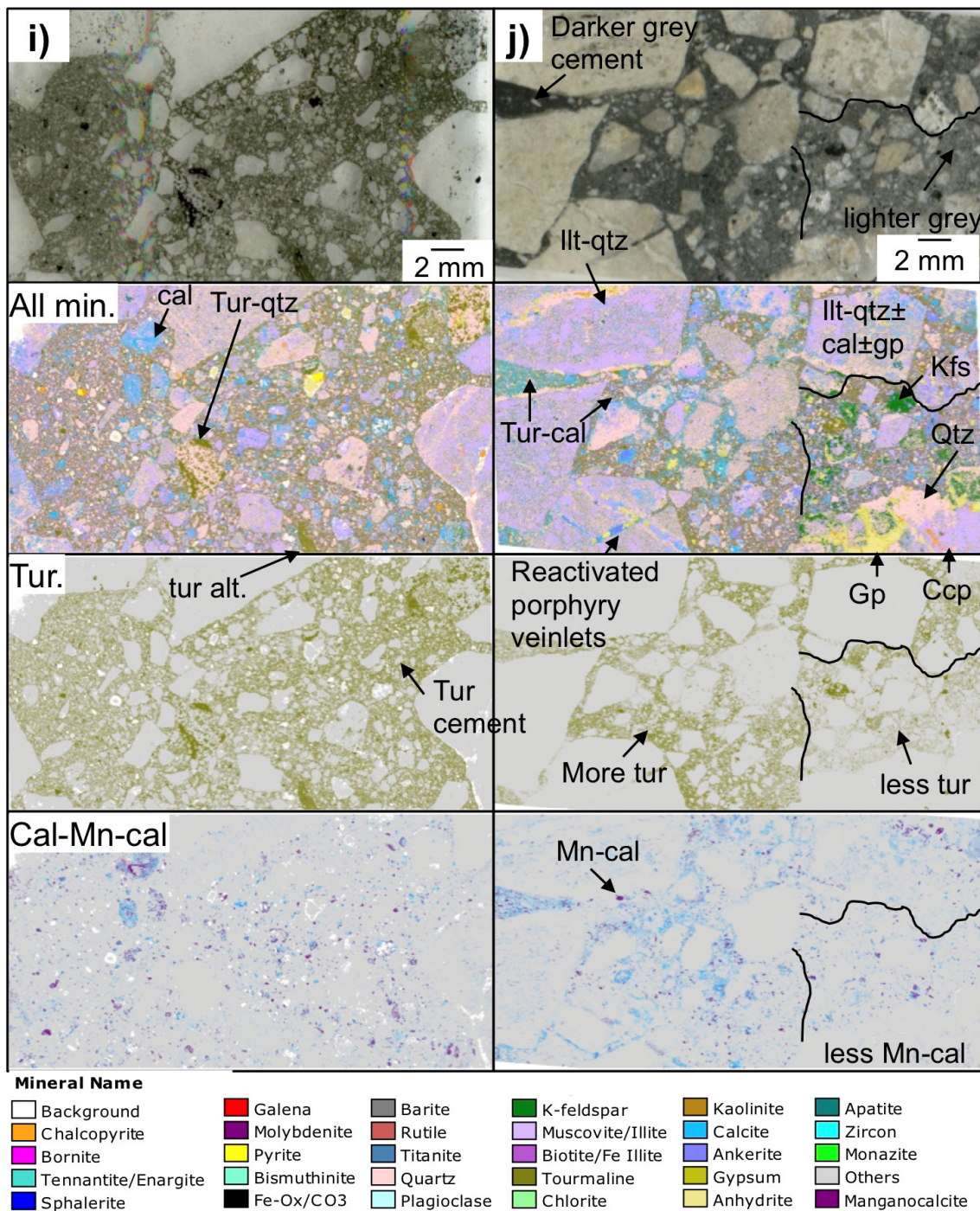


Fig. 4.26 cont. **i-j**) From top to bottom are 30 µm (i) and 150 µm (j) thin section scans, with corresponding QEMSCAN® (10 µm pixel) mineral maps (for all minerals, just tourmaline and then just manganocalcitic). Individual mineral maps show tourmaline is largely restricted to the cement, as is most of the calcite±manganocalcitic. Chalcopyrite is disseminated throughout the clasts and cement, with anhydrite-gypsum as a later cementing phase. Lower amounts of tourmaline produce a lighter grey coloured cement. **i**) From DDH1754-7.19 m; **j**) From DDH1754-11.11 m. Same field of view and scale for each.

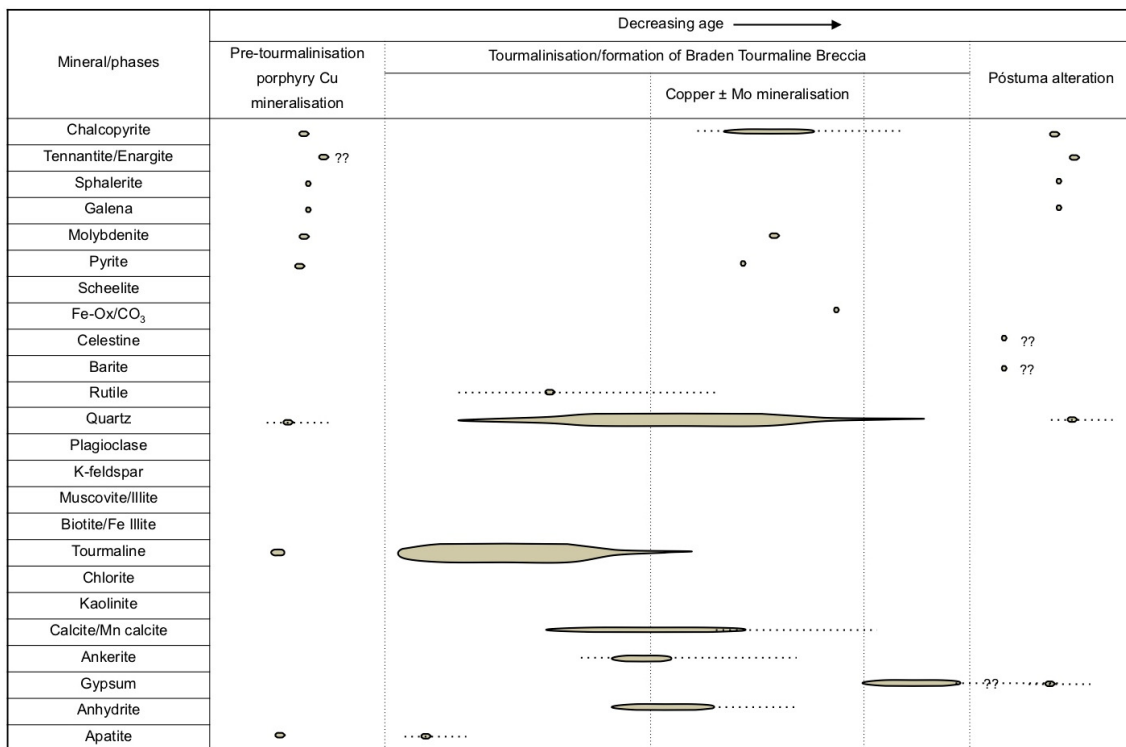
The paragenetic sequence of the Braden Tourmaline Breccia is divided into four main stages

1. Pre-brecciation Cu-Mo porphyry-style mineralisation hosted in brecciated clasts of mineralised felsic-intermediate intrusives, TMC wall rocks and less commonly

previous hydrothermal breccias.

2. Introduction of intergrown tourmaline and quartz which are the first major cementing phases. No embayed or pitted generations of tourmaline were observed nor noticeable textures of dissolution followed by regrowth. The first stage of tourmaline is overgrown by a generation of more Al-rich tourmaline, typically parallel to the *c*-axis.
3. Precipitation of manganoan calcite, anhydrite ( $\pm$ gypsum), quartz and Cu and Mo sulphides $\pm$ pyrite. Cu-Mo mineralisation is typically late, relative to tourmaline crystallisation, in the formation of the Braden Tourmaline Breccia. This mineralisation has reactivated clast-hosted porphyry veinlets.
4. Minor quartz and gypsum veinlets with a variety of Cu-sulfosalts (e.g., tennantite-tetrahedrite) associated with Póstuma alteration.

Table 4.4 Paragenetic sequence for the Braden Tourmaline Breccia. Thickness of lines= approximate mineral abundance. No evidence of the Braden Tourmaline Breccia being re-brecciated was observed.



#### 4.4.4 Diablo Tourmaline Breccias

The Diablo Breccias are a number of variably Cu-Mo mineralised superimposed breccias. They are polymictic and either clast- or cement-supported (Fig. 4.27) ranging from a chaotic to jigsaw-fit. Towards the margins with the Cu-Mo mineralised TMC host rock, they often grade into clast-supported crackle breccias. Within 50 m of the Diablo Breccias there are tourmaline-quartz veins and small (<10 cm) bodies of tourmaline breccia. Cross-cutting the breccias are mineralised (chalcopyrite-bornite)

quartz dykes (>90% quartz) >10 cm wide, weakly Cu-Mo-mineralised porphyritic latite dykes and chalcopyrite veinlets (Fig. 4.27a). The cements are composed of varying proportions of tourmaline, anhydrite, quartz, Cu-sulphides and molybdenite (Fig. 4.27). From drill core studies, the Diablo Breccias have been divided into seven textural sub-classifications depending on the ratio of cement:clasts, cement composition and cement texture (fine vs. coarse) as follows:

1. Crackle breccias on the margins of the breccia body where >85 vol.% of the rock is composed of angular clasts, of which >75% are >2 mm.
2. Fine-grained chaotic, cement-supported microcrystalline tourmaline breccia with high to medium aspect ratio angular clasts and chalcopyrite throughout the cement (e.g., Fig. 4.27b). These have been cross-cut by later coarser-cemented breccias (No. 4).
3. Fine-grained clast-supported mosaic to chaotic tourmaline breccia (Fig. 4.27e, k, l). Microcrystalline tourmaline-quartz zones texturally resemble those in the Marginal and Braden Tourmaline Breccias. Mixture of variably mineralised (porphyry-style disseminations and veinlets) bleached-pale cream angular to subrounded clasts. Cement accounts for 40 to 70 vol.% of the rock and is mostly blue-black microcrystalline tourmaline closely and variably intergrown with quartz, anhydrite and sulphides. Clasts sometimes have a rim of early molybdenite and chalcopyrite, which always post-dates tourmaline. This breccia variety does not appear to cross-cut the coarser breccias.
4. Coarse (>1 mm) tourmaline-quartz-anhydrite-chalcopyrite breccia (Fig. 4.27d, i). Tourmaline forms rims on the brecciated clasts which are bleached a pale cream-white. Chalcopyrite-pyrite, and variable anhydrite, form a significant component of the cement.
5. Coarse anhydrite-quartz-chalcopyrite cement with minor tourmaline (Fig. 4.27f, g). Tourmaline is a minor cementing component mainly forming coarse (~1 mm) inclusions in anhydrite. The proportion of small clasts can be high and the breccia mostly has a mosaic texture. Anhydrite shows well-developed growth zoning.
6. Anhydrite-chalcopyrite-bornite-molybdenite-rich breccia (Fig. 4.27m-o). This is cement-supported (25 to 60 vol.% of the rock), contains clasts of all sizes (large and small) however small clasts (0.1 to 2 mm) account for <10% of the clast population. Aside from the clasts being comparatively more rounded than other Diablo Breccias, it does in places share the same breccia framework as the coarse tourmaline-cemented breccias (number 4). Cu-Mo sulphides, and less so anhydrite, can represent a major cementing phase and sometimes overprint other breccias (e.g., Fig. 4.27a).
7. Not often seen are poorly mineralised areas with a porous tourmaline cement (Fig. 4.27c). The tourmaline is coarse and cavities have been variably infilled with gypsum. Clasts are pervasively bleached a pale cream-white and have

more porosity than clasts elsewhere in the breccia.

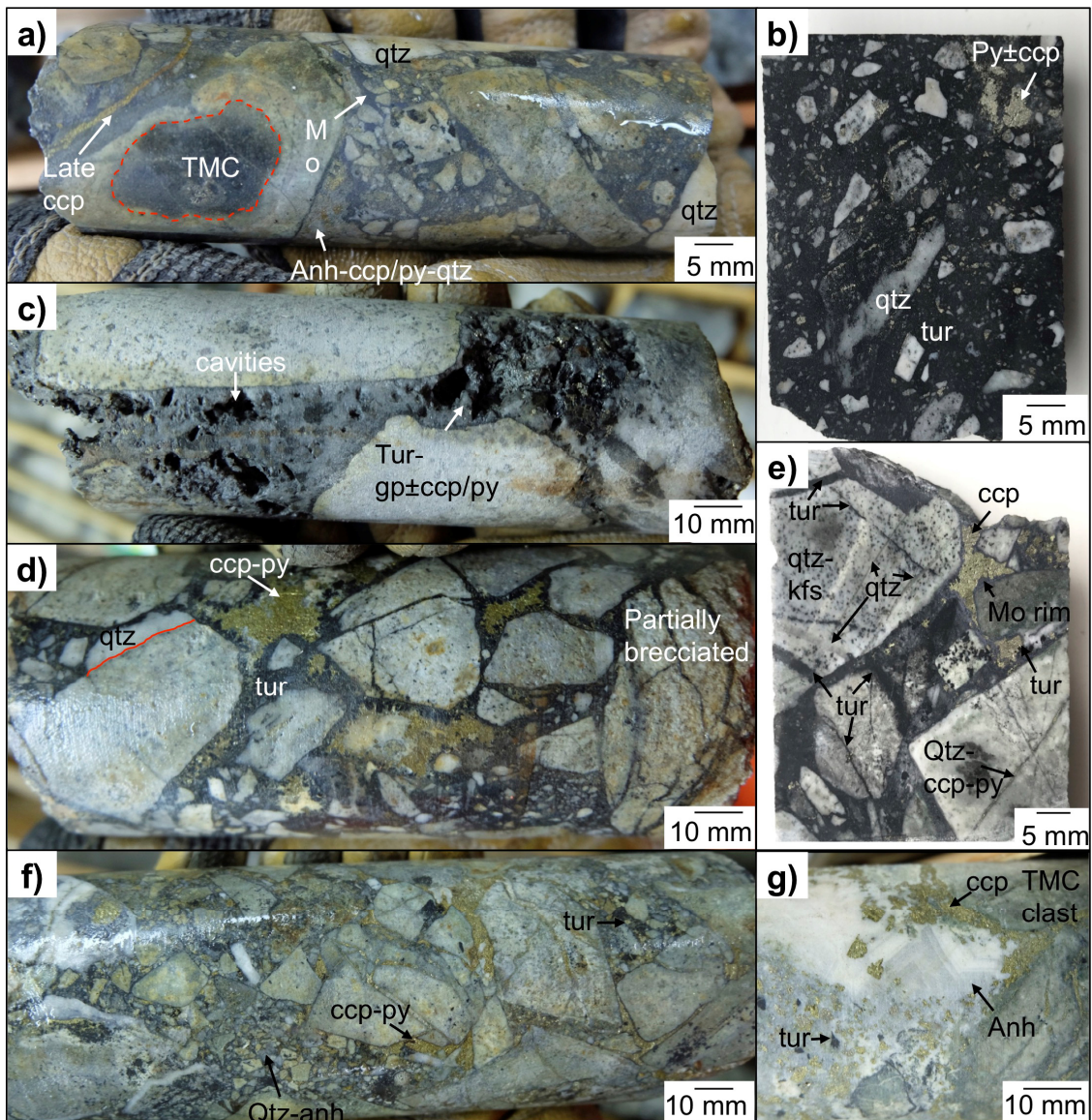


Fig. 4.27 Photographs of drill core from the Diablo Breccias: **a)** Poorly sorted and chaotic clast texture, cemented by a mixture of molybdenite, tourmaline, quartz, anhydrite and chalcopyrite. TMC clasts >2 cm have bleached rims, example outlined in red. From DDH1990-52.10 m; **b)** Microcrystalline dark blue to black tourmaline cement-supported breccia with mostly angular clasts. Disseminated and discontinuous chalcopyrite veinlets are present throughout the cement. From DDH2672-94.93 m; **c)** Porous tourmaline cement from the margin of the breccia pipe with variable gypsum infill. From DDH2677-102.40 m; **d)** Coarse black tourmaline rims on clasts with a later quartz-anhydrite-chalcopyrite infill. Some clasts are partially brecciated with very little tessellation having taken place. From SG0602-53 m; **e)** Fine-grained tourmaline-molybdenite-chalcopyrite cement supporting poorly sorted angular to subrounded clasts. Clasts contain numerous porphyry-style veinlets truncated at clast margins. Molybdenite rims are present on some clasts. From DDH2679-110.28 m; **f)** Tourmaline-anhydrite-Cu-sulphide cement with angular to subrounded and intensely bleached clasts. Sample contains comparatively high volume of clasts <5 mm in diameter. From SG0602-46.10 m; **g)** Comparatively tourmaline-poor cement, with space-fill of coarse zoned anhydrite and calcite which contain chalcopyrite-pyrite-tourmaline inclusions. From DDH2679-139.50 m.

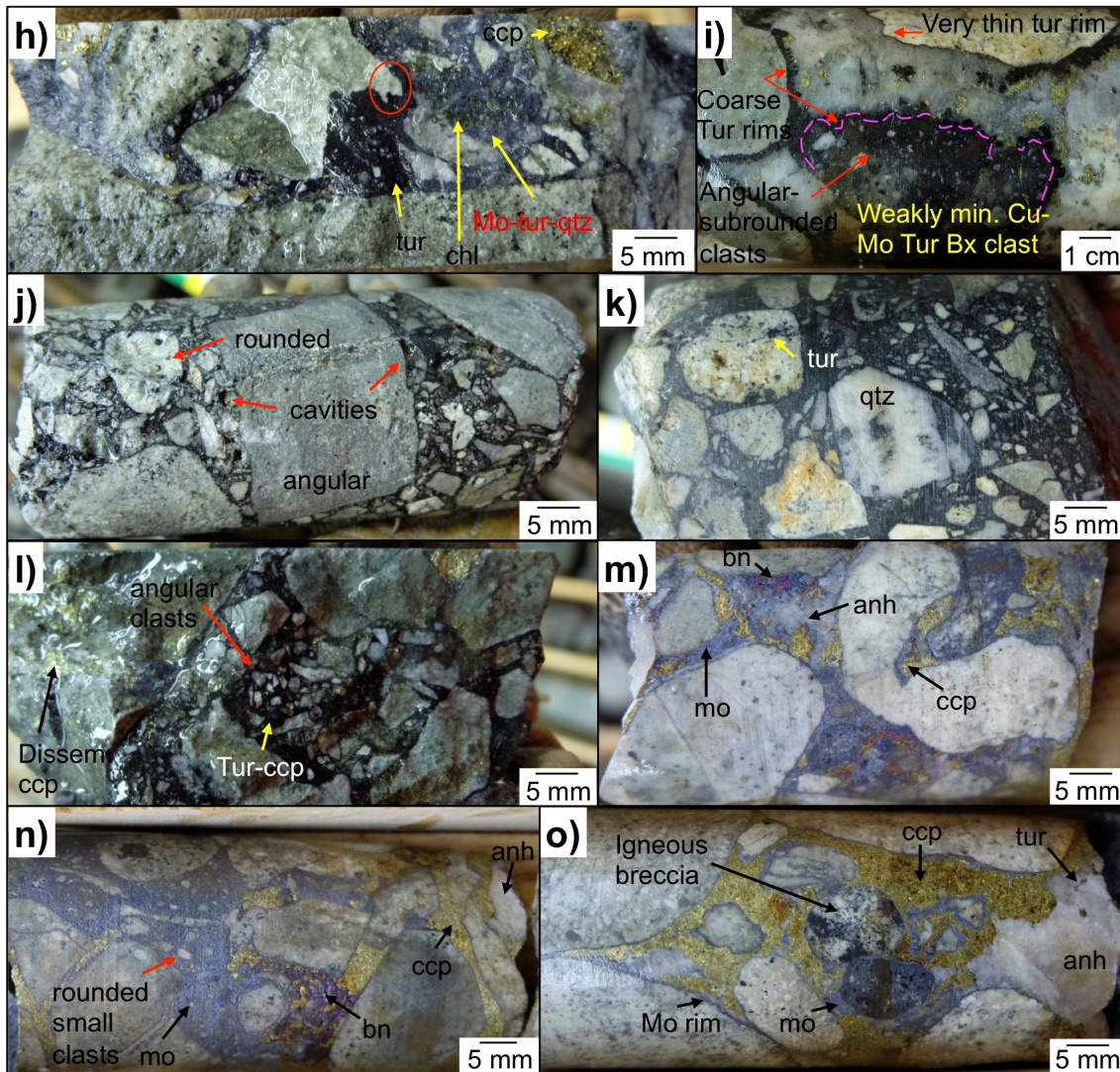


Fig. 4.27 cont. **h)** Microcrystalline tourmaline cement intergrown with quartz-molybdenite and anhydrite. Clasts are angular and some show irregular wispy margins (red), similar to those characterising juvenile material. From DDH2136-0.91 m; **i)** Coarse tourmaline-anhydrite-chalcopyrite cement. Tourmaline forms discontinuous rims on clasts and re-brecciated microcrystalline breccia fragments are also present. From DDH2677-118.4 m; **j)** Comparatively sulphide-poor chaotic tourmaline cement. Clasts and cement contain porosity. From SG0602-52.0 m; **k)** Microcrystalline tourmaline and quartz cementing angular to subrounded clasts of TMC. From SG0602-92.5 m; **l)** Tourmaline cement with minor quartz; high proportion of <15 mm angular clasts. From DDH2677-157.9 m; **m)** Anhydrite-chalcopyrite-bornite-molybdenite-cemented breccia, with a noticeable increase in clast rounding. Clasts are intensely bleached to pale cream-white and have <2 mm thick molybdenite rims. From DDH2672-101.5 m; **n)** Chalcopyrite-bornite-molybdenite-anhydrite-cementing angular to rounded clasts. Small clasts are also well-rounded. From DDH2672-97.8 m; **o)** Anhydrite-chalcopyrite-molybdenite cement with minor tourmaline inclusions in anhydrite. Clasts are rounded and molybdenite rims are common. From DDH2672-100.5 m.

Clasts in the Diablo Breccias are mostly derived from the TMC (30 to 70% of clasts) and porphyritic dacite (10 to 30% of clasts). Rounded clasts of igneous breccia are rarely present (Fig. 4.27o). Clasts represent between 40 to 85 vol.% of the coarser

and finer breccias and clast size does not appear to be linked to the degree of rounding, except in the sulphide-rich portions which contain an increased volume of rounded clasts (50 to 80% rounded and 30 to 50% angular clasts). Small clasts (0.1 to 2 mm) are angular to subrounded (rounded in sulphide-rich portions) whilst large clasts (>2 mm) range from well-rounded to subangular. The most common size of large clasts observed in drill core from the Diablo Breccias range from 2 to 20 cm, with the largest observed in this study being ~50 cm. Clast rotation is mostly >20°, giving a chaotic appearance, although it can be 10 to 20° locally or <10° at the margins of the breccias. There is no lateral or vertical change in clast roundness, with rounded and angular clasts present in both central and marginal portions of the breccia columns.

Clasts of the TMC and felsic intrusives contain tourmaline rosettes and pre-brecciation Cu-Mo mineralisation in chalcopyrite-quartz-anhydrite±molybdenite veins which are truncated at clast margins. Similar textures are present at La Huifa, discussed in Section 4.4.5. Finer and coarser cements also contain a small portion of crushed rock (<0.1 mm) and many small clasts (0.1 to 2 mm) are composed almost entirely of quartz (Fig. 4.28).

The earliest cementing phase to have formed in the coarser breccias is 20 to 100 µm-thick tourmaline rims on brecciated clasts. Molybdenite rims are present in the sulphide-rich and tourmaline-anhydrite-cemented portions. There are no visible to the naked eye molybdenite rims in the microcrystalline tourmaline breccias (Fig. 4.27b). Around the tourmaline rims are coarse anhydrite-quartz-chalcopyrite±calcite±ankerite infills which often have very fine <100 µm and larger (>1 mm) blocky tourmaline inclusions (Fig. 4.27g). Quartz and anhydrite often contain multiple fluid inclusions. Molybdenite, chalcopyrite, pyrite (±galena inclusions), quartz and anhydrite formed synchronously, often present as inclusions in one another. Some of the last cementing phases include anhydrite-gypsum, calcite and quartz which infill remaining cavities. Minor constituents in the cement include apatite, kaolinite, galena and sphalerite.

Although the Diablo Breccias are Cu-Mo-mineralised throughout, higher-grade chalcopyrite-bornite-molybdenite zones are also present (Fig. 4.27m-o). These have been identified frequently at the margins and within inner regions of the breccia and overprint and/or variably replace earlier cement phases. The Cu-Mo-rich cements are coarser (often >2 mm grains) and associated with higher volumes of anhydrite (20 to 40 vol.% of the cement). Molybdenite is present as inclusions within anhydrite, chalcopyrite and bornite. Tourmaline is not a major cementing component but is present as inclusions within anhydrite and quartz. The Cu-Mo sulphide-rich portions share same breccia framework as finer and coarser breccias.

Clasts in the Diablo Breccias are variably sericitic- and silicic-altered giving them a pale cream to white colour. They contain a mixture of K-feldspar, quartz, sericite, plagioclase, chlorite, illite/Fe-illite and apatite (e.g., Fig. 4.28). Clasts >2 cm show well-defined rims in places (<2 mm thick) of mainly plagioclase (albite) with lesser quartz, chlorite and illite (Fig. 4.28b), with a core of mainly K-feldspar, rutile, chlorite, Fe-illite, calcite and minor iron oxides. Subparallel chalcocopyrite ( $\pm$ quartz, sphalerite, galena) veinlet arrays (5 mm) cross-cut the breccias (e.g., Fig. 4.28a) and partially infill surrounding cement cavities (top right of Fig. 4.28a). Intense silicification has resulted in the formation of cm-scale euhedral relics, probably after phenocrysts, composed of quartz which have molybdenite-tourmaline rims (e.g., Fig. 4.28a and Fig. 4.29c).

**Tourmaline** - No embayed or pitted tourmaline were observed, or evidence of tourmaline partial dissolution followed by regrowth in the finer or coarser breccias. Two generations of tourmaline have been identified in the coarser tourmaline cements. The first is composed of crystals ranging from <20  $\mu\text{m}$  up to 2 mm long and between  $\sim$ 20 and 200  $\mu\text{m}$  wide that commonly form continuous or discontinuous rims around brecciated clasts (Fig. 4.29e). Where multiple individual crystals are present they often form larger aggregates or radiating splays (e.g., Fig. 4.29c). They are dark to light brown to green with relatively high order interference colours and are often intergrown with quartz, apatite, anhydrite/gypsum (Fig. 4.29a). Patchy zonation is most common with minor, very fine (<10  $\mu\text{m}$ ) oscillatory growth zoning sometimes present. Small <100  $\mu\text{m}$  rutile and quartz are the most common inclusions (Fig. 4.29h) within this tourmaline generation, although manganoan-calcite, anhydrite-gypsum have also been observed (e.g., Fig. 4.29j).

Overgrowing most of the larger blocky tourmaline crystals are fine needle/acicular overgrowths parallel to the *c*-axis (Fig. 4.29e, f, j). The overgrowths have a combined width similar to the original crystals and are <200  $\mu\text{m}$  long. They are mostly in optical continuity with the larger, earlier tourmaline generation and sometimes show oscillatory zoning. This second generation is commonly intergrown with coarser quartz-anhydrite (Fig. 4.29b, e) and although uncommon, the needles are sometimes slightly deformed (see Fig. 4.29f). Aside from being on the tips of crystals, this second generation is found on fractured tourmaline grains and often in 'healed' fractures (Fig. 4.29i). This second generation is enriched in Al relative to the earlier phase (Fig. 4.29g, i, j). The colour and chemical change between the generations is sharp. The microcrystalline tourmaline cement (Fig. 4.29k) is not seen alongside coarser tourmaline, instead observed as inclusions in the coarser cements. It is intergrown with quartz and anhydrite and has no overgrowths. Considerable porosity remains in the microcrystalline cement.

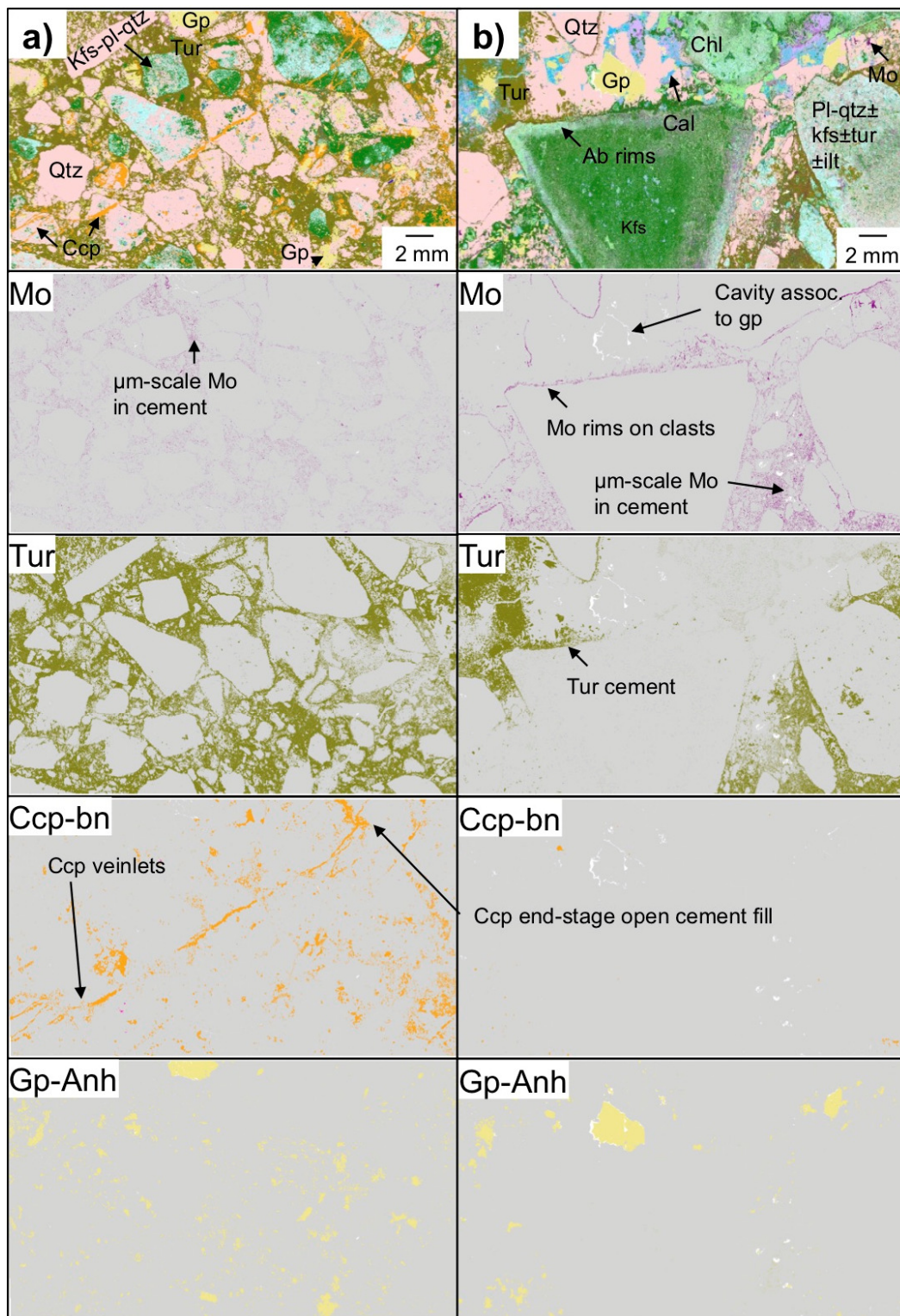
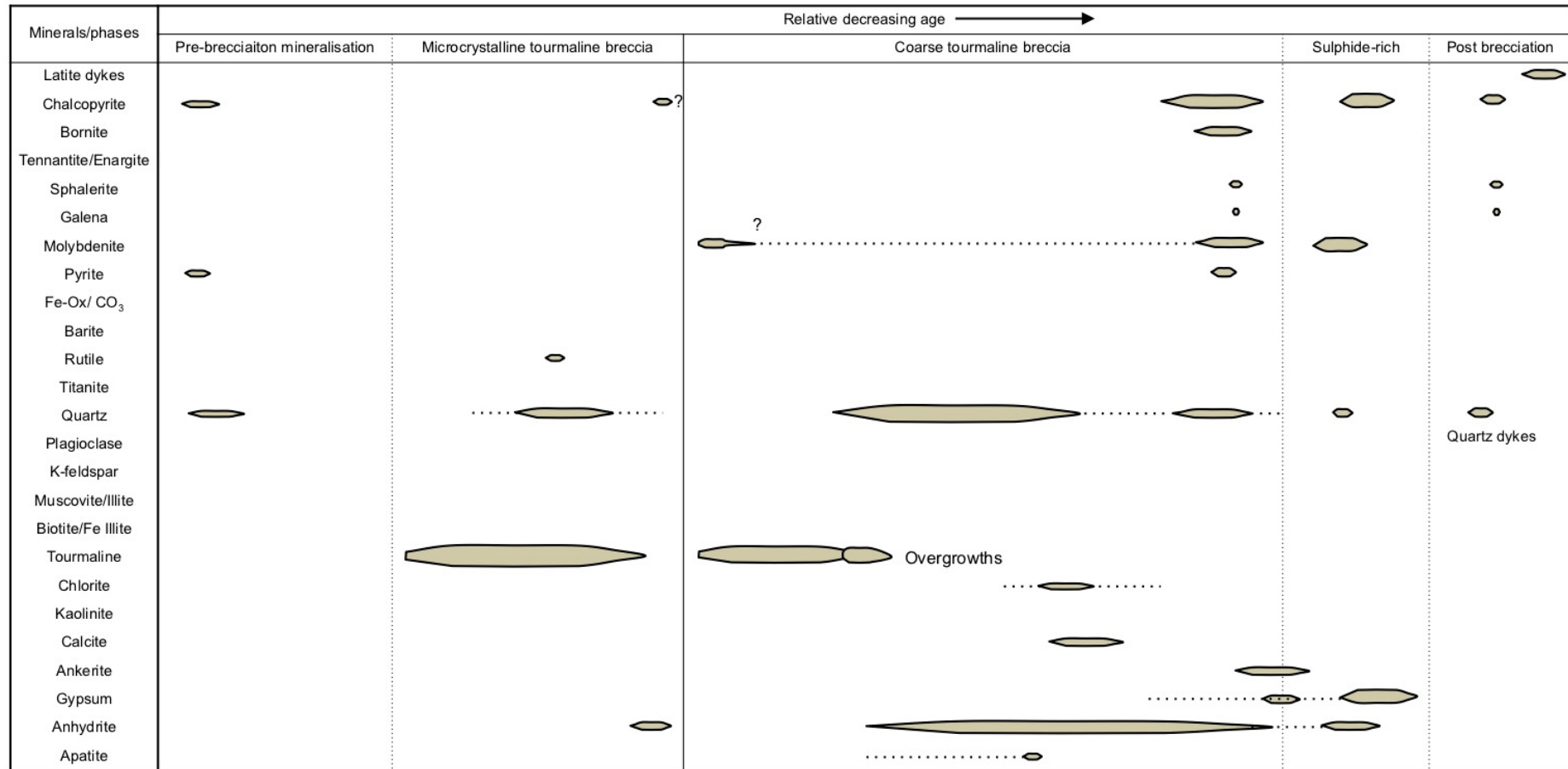


Fig. 4.28 Diablo Breccias - QEMSCAN® all-mineral maps (10  $\mu\text{m}$  pixel) filtered (in maps below) for different minerals: **a)** Poorly sorted, chaotic tourmaline cement-supported breccia with intense silicification of clasts, in particular small clasts. Molybdenite is disseminated throughout the cement and anhydrite-gypsum-quartz filling cavities. Chalcopyrite veins cross-cut the breccia and introduce more chalcopyrite to surrounding cement. From DDH1190-181.25 m; **b)** Albite rims on angular clasts, tourmaline-quartz $\pm$ chlorite cement. Early molybdenite rims on clasts and disseminated/intergrown with tourmaline throughout cement. From DDH2136-0.96 m.

**Paragenesis** - The paragenetic sequence for the Diablo Breccias has been divided into six main stages which are to varying extents likely repeated, as follows:

1. Initial emplacement of weakly mineralised microcrystalline tourmaline breccias. Majority of open-space has been infilled by tourmaline-quartz cement with lesser anhydrite. Rutile inclusions within tourmaline are present and Cu-Mo where present is post-tourmaline.
2. Re-brecciation of these earlier breccias, formation of blocky tourmaline rims on clasts (e.g., Fig. 4.27d) and formation of coarse quartz-anhydrite cements. Molybdenite is in places intergrown with tourmaline (e.g., Fig. 4.28). Clasts of earlier microcrystalline tourmaline breccia are incorporated into these later breccias and are overgrown by coarser tourmaline.
3. End-stage open-space has been variably infilled with anhydrite-quartz-chalcopyrite-bornite-molybdenite (e.g., Fig. 4.28).
4. Later Cu-Mo overprint of coarse and fine breccias associated with differing degrees of dissolution of earlier cement phases, generating sulphide-rich cements. In places significant chemical/corrosive dissolution resulted in the removal of earlier paragenetic cementing sequences (tourmaline-quartz), increased bleaching and rounding of clasts and dissolution of smaller clasts. In this process, dissolution caused the generation of significant porosity and permeability. Alternatively fine Mo overprint of tourmaline cement can preserve earlier cements.
5. Chalcopyrite veinlets cross-cut the breccia clasts and cement infilling remaining porosity (Fig. 4.28a).
6. Post-brecciation well-mineralised (chalcopyrite-bornite) quartz dykes and variably mineralised latite dykes cut the breccias.

Table 4.5 Paragenetic sequence for the Diablo Breccias. Mineral abundances are reflected by relative thickness of lines.



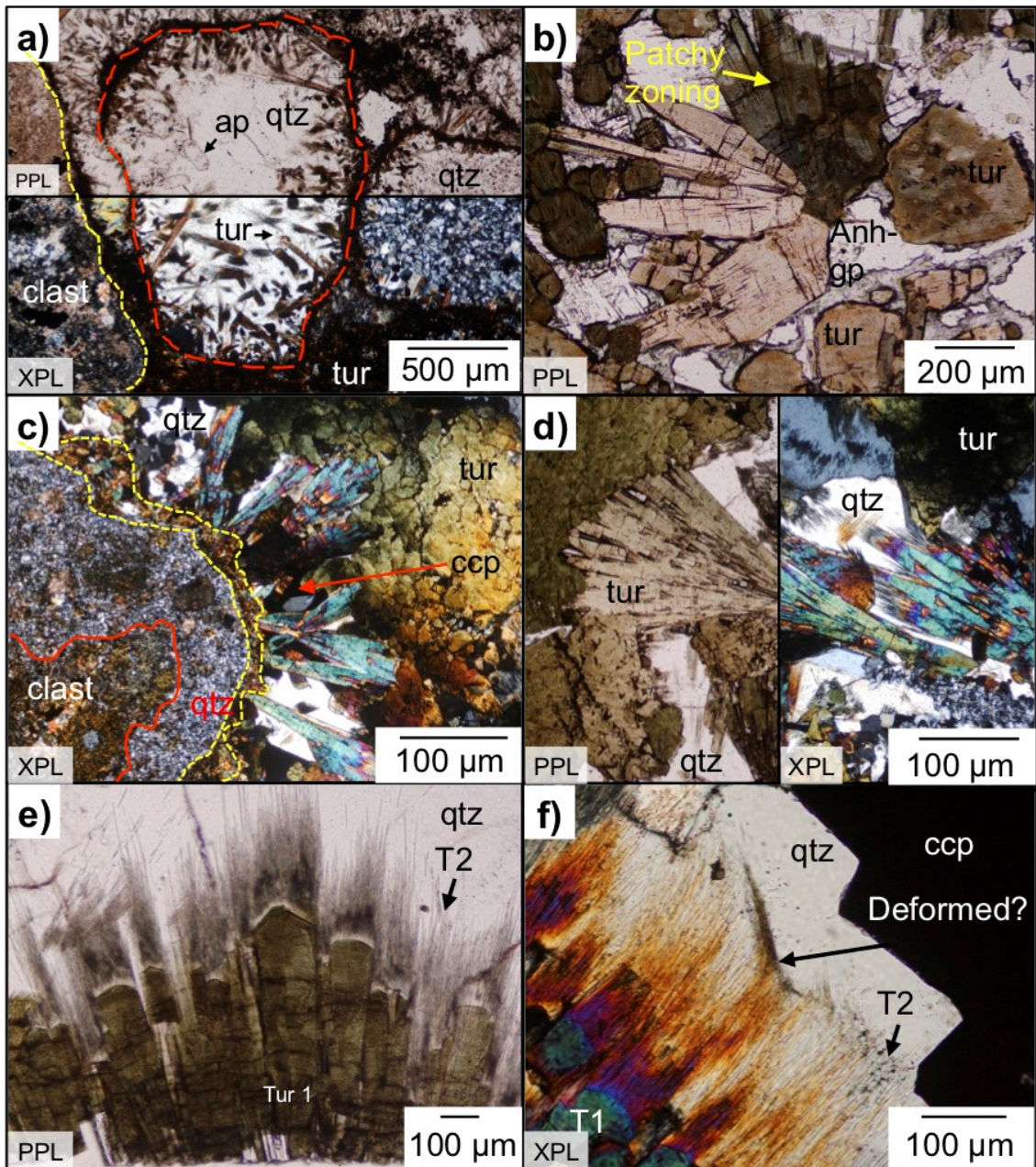


Fig. 4.29 Transmitted light photomicrographs (PPL and XPL) (a-f) and SEM-EDS elemental maps (g-n) of tourmaline in the Diablo Breccia: **a)** Intense silicification of clasts, with cavity infill by a mixture of tourmaline, quartz and apatite. From DDH1974-131 m; **b)** Tourmaline-quartz-anhydrite cement with tourmaline showing patchy zoning. The anhydrite has been partially hydrated to gypsum. From DDH2672-115 m; **c)** Silicified clast margin with a tourmaline rim. Tourmaline growth into open-space with later quartz and chalcopyrite infill. From DDH2677-118 m; **d)** Tourmaline rosettes within tourmaline-quartz cement. Tourmaline has high interference colours and green-light brown pleochroism. From DDH2677-118 m; **e)** Fibrous tourmaline overgrowths parallel to the *c*-axis of acicular-blocky tourmaline. From DDH2677-118 m; **f)** Stunted/deformed tourmaline overgrowths in quartz nearby chalcopyrite. From DDH2677-118 m.

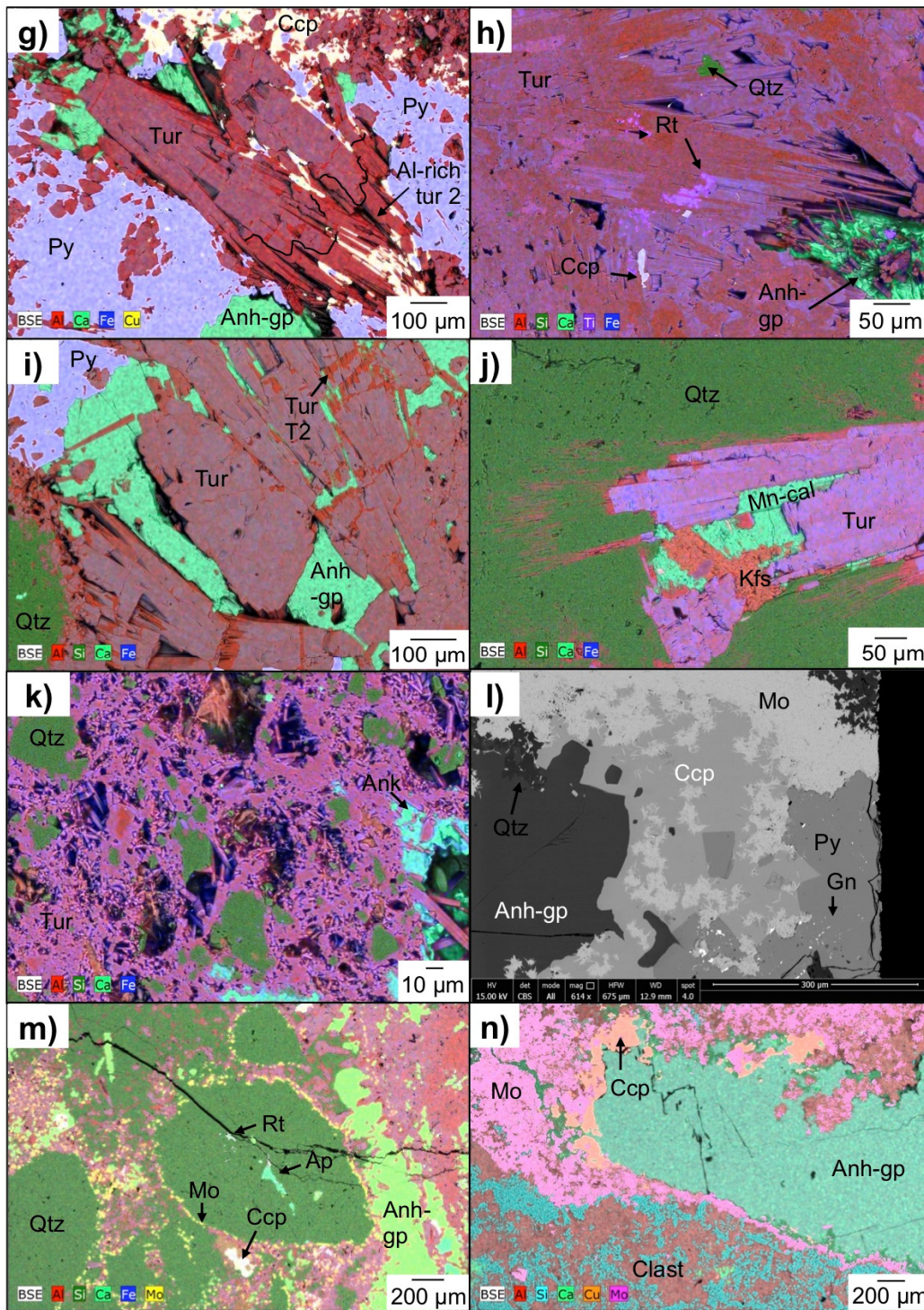


Fig. 4.29 cont. **g)** Relatively Al-rich tourmaline tips ('tur 2') intergrown with pyrite and fine <50 μm chalcopyrite. From DDH2683-151.63 m; **h)** Individual acicular tourmaline crystals combined to form a larger tourmaline aggregate with rutile and quartz inclusions. Patchy zonation reflecting the substitution  $(\text{Fe}^{2+}, \text{Fe}^{3+})(\text{Mg}, \text{Al})_{-1}$ . From DDH2672-94.93 m; **i)** Blocky fractured tourmaline intergrown with anhydrite-gypsum and pyrite. Fractures are 'healed' by relatively Al-rich tourmaline. From DDH2683-151.63 m; **j)** Fine acicular tourmaline overgrowths intergrown with quartz. Manganocian calcite inclusion within tourmaline. From DDH2136-0.96 m; **k)** Microcrystalline tourmaline-quartz-anhydrite cement with significant porosity compared to coarser mineral-rich cement areas. From DDH1990-181.25 m; **l)** Intergrown molybdenite-pyrite and chalcopyrite within the anhydrite-quartz cement. Note galena inclusions in pyrite. From DDH2683-151.63 m; **m)** Intensely silicified relict clasts discernable from the presence of molybdenite-tourmaline rims. Anhydrite infill is later than tourmaline. From 1974-285.65 m; **n)** Molybdenite rim on clast with later anhydrite-chalcopyrite infill. From DDH1974-285.65 m.

#### 4.4.5 La Huifa Tourmaline Breccia

**Wall rocks** - The Farellones Formation wall rocks are propylitically-altered and mostly consist of andesites and tuffs (Fig. 4.30). Within 10 to 15 m of the La Huifa breccia, wall rocks are veined, locally brecciated and are weakly potassic-, sodic-calcic- and chlorite-altered. They contain epidote, actinolite±albite, tourmaline stars (<1 cm) and discontinuous 0.5 to 4 cm thick cross-cutting tourmaline-anhydrite-quartz-chalcopyrite veinlet arrays associated with brecciation. These veins can resemble 'micro breccias' (Fig. 4.30c) and consist of angular fragments (<1 cm) cemented by tourmaline-anhydrite-chalcopyrite.

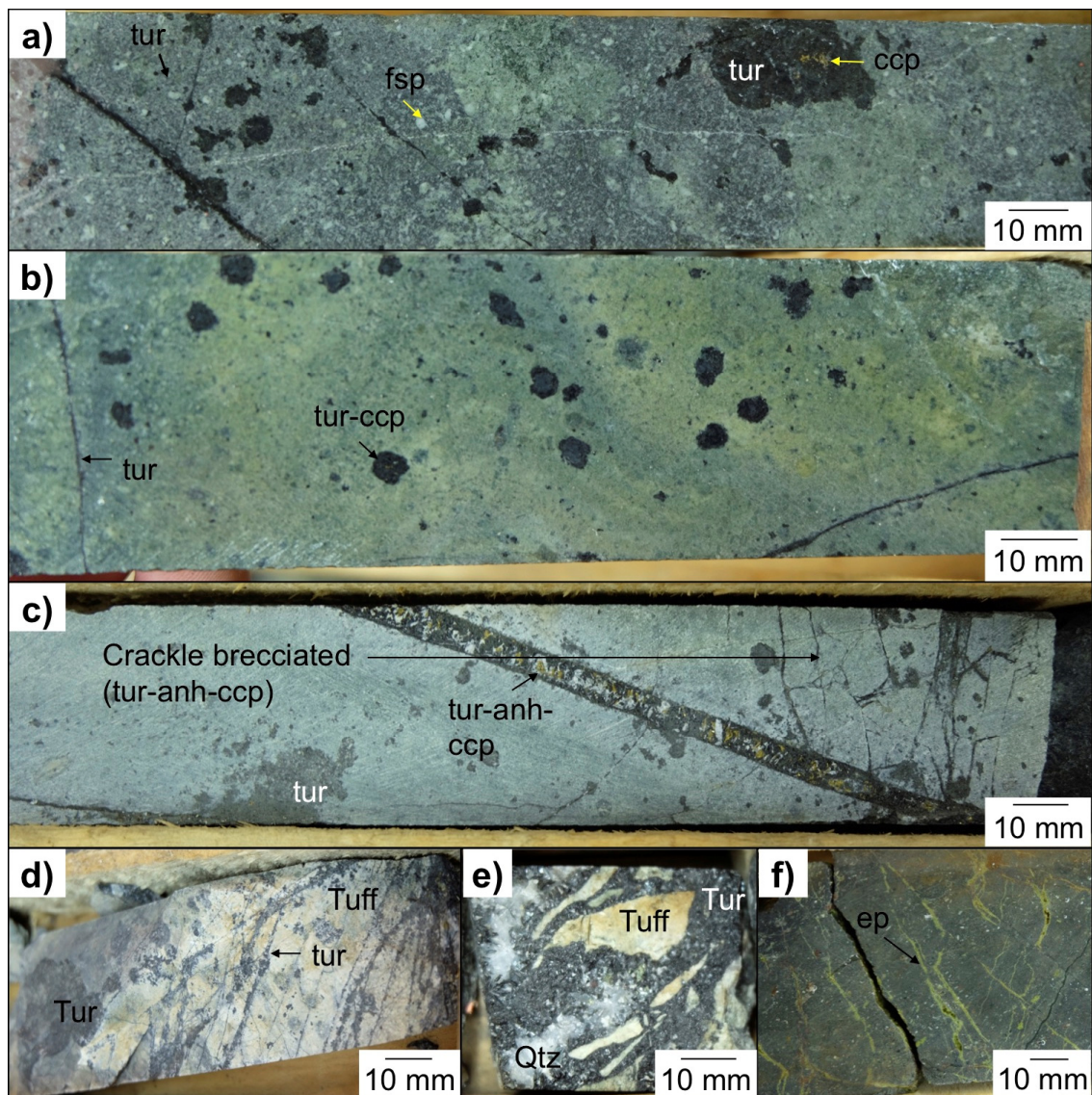


Fig. 4.30 Drill core photos of the La Huifa host rocks (Farellones Formation): **a**) Propylitically-altered porphyritic andesite with cross-cutting tourmaline veins and tourmaline stars ~8 m from the breccia contact From ES026-100.80 m; **b**) Tourmaline stars and flow banding in andesite a few metres from the breccia From ES026-104.80 m; **c**) Tourmaline-anhydrite-chalcopyrite veins and adjacent crackle breccia with the same mineralogy From ES026-104.40 m; **d**) Heavily veined and tourmalinised tuff bleached a light cream From ES026-129 m; **e**) Angular tuff fragments cemented by tourmaline-quartz From ES026~269 m; **f**) Propylitically-altered andesite with irregular epidote veins From ES005-4 m.

**Textural description** - La Huifa breccias are texturally diverse and are mainly polymictic, although monomictic areas (e.g., Fig. 4.30e) are present. They are typically cement-supported, though clast-supported crackle breccias (Fig. 4.30c) are observed towards the margins. The clast population consists of weakly potassic-, sodic-calcic- ( $\pm$ chlorite) altered monzodiorite and propylitically-altered andesites and tuffs. Small (0.1 to 2 mm) and larger clasts are mostly angular to subangular although subrounded clasts are present. Clasts up to few metres have been observed in the exploration tunnel (R Floody., personal communication, 2017) although in drill core the most common size range observed is between 1 and 6 cm.

Compared with other breccias at El Teniente, clasts in the La Huifa breccias contain fewer porphyry-style veinlets. Instead, the economic Cu-Mo sulphide mineralisation is related to initial brecciation, generation of porosity and subsequent space-fill. Clasts are rotated by 10 to 20° and sometimes >20°, creating a mosaic to chaotic appearance, and comprise between 45 and 80 vol.% of the rock. Towards the breccia margins/apices clasts can become aligned and clast-supported (Fig. 4.31e). Sorting is mostly poor although regions are moderately well sorted and some large clasts are not entirely fragmented (e.g., Fig. 4.31b). Relict clast textures are sometimes present in the tourmaline-anhydrite cement (e.g., Fig. 4.31g).

**Alteration events** - Evidence is preserved for a number of overprinting alteration events at La Huifa, slightly different to those at El Teniente, which are summarised in Table 4.6 and shown in Fig. 4.31. These are as follows:

1. Potassic
2. Sodic-calcic
3. Retrograde chlorite-sericite
4. Argillic $\pm$ advanced argillic

Unlike at El Teniente, early potassic alteration is poorly represented at La Huifa and, where observed, the majority of Cu-Mo mineralisation is paragenetically later than this. Evidence for this early potassic alteration is from the presence of biotite-altered hornblende phenocrysts in brecciated porphyry fragments and EB veins (variably altered to chlorite). Primary mafic minerals in wall rocks and brecciated clasts are altered to a mixture of rutile and magnetite-hematite.

Sodic-calcic alteration is the most pervasive alteration event observed. It is characterised by albite, tourmaline, actinolite, magnetite and lesser epidote and apatite. Earlier EB veinlets have often been re-worked (destroying the biotite) forming infrequent, discontinuous narrow (<3 mm) tourmaline-anhydrite-quartz $\pm$ chalcopyrite-bornite-actinolite veinlets with minor albite-quartz halos. Albitisation is more intense on

brecciated clast rims adjacent to the hydrothermal cement compared with inner portions of the clasts (e.g., Fig. 4.31). Mafic minerals within brecciated clasts are altered to a mixture of chlorite-actinolite±calcite and plagioclase is saussuritised to epidote and calcite.

Variably overprinting much of the earlier events is a retrograde chlorite-sericite (little pyrite) event. Chlorite is disseminated throughout wall rocks and brecciated clasts (e.g., Fig. 4.30 and Fig. 4.31g), where primary magmatic and secondary biotite (potassic alteration) has been altered to chlorite. Actinolite, associated with the earlier sodic-calcic event, is also altered to chlorite, although both are intergrown so may have formed together. Sericitic alteration is widespread, mainly at the expense of plagioclase.

Texturally destructive argillic alteration has resulted in significant weakening of clasts, causing them to become friable, except for albitic rims which remain unaffected (Fig. 4.31b, d). The tourmaline cement in areas of intense argillic contains significant porosity, with many cavities lined with limonite and CuOx coatings (Fig. 4.31f). Advanced argillic alteration is observed near what has been inferred to be the upper portions and/or margins of the breccia, based on an alignment of elongate clasts. This is characterised by silicified clasts cemented in a residual, vuggy/porous tourmaline-quartz cement with secondary limonite and CuOx coatings (e.g., Fig. 4.31e).

Table 4.6 Summary of alteration events and mineralogy/veins associated with them at La Huifa, based on drill core observations. The veins do not follow the Teniente classification scheme and have instead been classified using the scheme outlined by Sillitoe (2010), based on work by Gustafson and Hunt (1975).

Alteration event	Veins	Mineralogy	Halo
Potassic	EB	Biotite	Minor K-feldspar
	A	Quartz-chalcopryrite-bornite	Albite (?)
	B	Quartz-chalcopryrite-pyrite±molybdenite±biotite	
Sodic-calcic		Chlorite-actinolite-epidote-tourmaline-albite-calcite-magnetite-chalcopryrite-bornite	
Chlorite-sericite	D	Quartz-pyrite±chalcopryrite	Sericite-quartz
		Chlorite-sericite-haematite-epidote-carbonate	
Argillic		Clays-carbonates-oxides-CuOx-limonite	

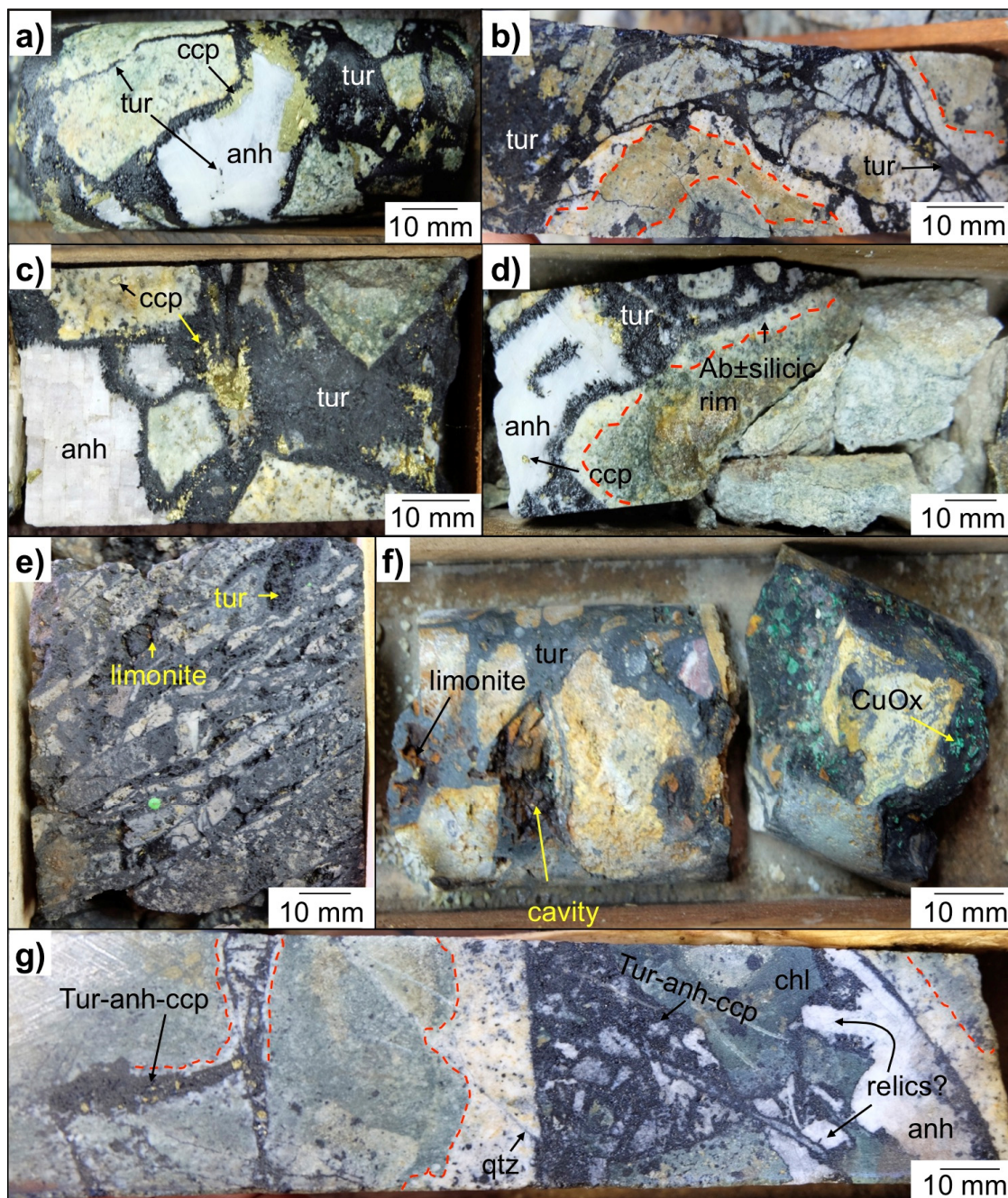


Fig. 4.31 La Huifa alteration-mineralisation events: **a)** Tourmaline-anhydrite-chalcopyrite cement with sodic-calcic-altered clasts overprinted by chlorite. From ES026-232 m; **b)** Mosaic breccia with argillic alteration overprinting sodic-calcic-altered clasts, cemented by tourmaline-chalcopyrite. Red lines indicate progressive bleaching. From ES026-152.6 m; **c)** Coarse tourmaline and blocky anhydrite (having subhedral-clast like shapes in places) cementing sodic-calcic- and chlorite-altered clasts. Chalcopyrite is post-tourmaline. From ES026-210 m; **d)** Cream-white albite rims on argillised clasts which have few original textures remaining. From ES026-207.85 m; **e)** Pervasively leached, silicified aligned clasts (major axis 1 to 5 cm) cemented by porous tourmaline. From ES05-3.1 m; **f)** Argillically-altered tourmaline breccia, with original clast textures pervasively destroyed. Tourmaline cement is leached and now contains cavities with partial limonite and CuOx coatings. From ES03-85.79 m; **g)** Propylitically-altered andesite clasts cemented by tourmaline and anhydrite±chalcopyrite. Andesite contains truncated quartz veins at the cement contact and clasts are often bleached to a pale cream colour adjacent to cement. From ES026-164.25 m.

**Cement** - The cement at La Huifa accounts for between 20 to 50 vol.% of the rock and is coarser (>1 mm) and richer in Ca-bearing phases than the breccias at El Teniente. It is composed of tourmaline, anhydrite, calcite, gypsum, quartz, chalcopyrite, bornite, pyrite, ankerite and minor molybdenite. The main sulphide minerals are chalcopyrite, bornite and pyrite. Relative proportions of sulphides are variable with localised areas more dominated by chalcopyrite-bornite or pyrite-chalcopyrite. Chalcopyrite often has tennantite rims and inclusions of sphalerite, quartz, tourmaline and minor haematite. Tourmaline was the first cementing phase, forming blocky (>1 mm) rims on brecciated clasts, then followed by anhydrite/gypsum (with tourmaline inclusions), calcite, ankerite, quartz and chalcopyrite-bornite infill. Anhydrite was locally replaced by gypsum. Late quartz-sphalerite±galena veins (<2 mm wide) cut across the earlier tourmaline and anhydrite-sulphide cement phases.

Calcite, anhydrite and quartz exhibit a wide variety of complex textures including growth and patchy zoning, dissolution, overgrowth and healed micro-fractures under CL (Fig. 4.32d, f). In transmitted light, these are only visible in places from the presence of faint inclusion trails (e.g., Fig. 4.32c). From CL images, quartz shows varying shades of blue to pink, well-developed concentric zoning and more poorly defined superimposed patchy zoning. Quartz associated with chalcopyrite exhibits blue to pink CL with moderate intensity. There is no change in quartz CL intensity adjacent to sulphides. Oscillatory zoning is typically fine, with individual zones being <50 µm thick, whilst patchy zoning usually exceeds a few hundred microns in width.

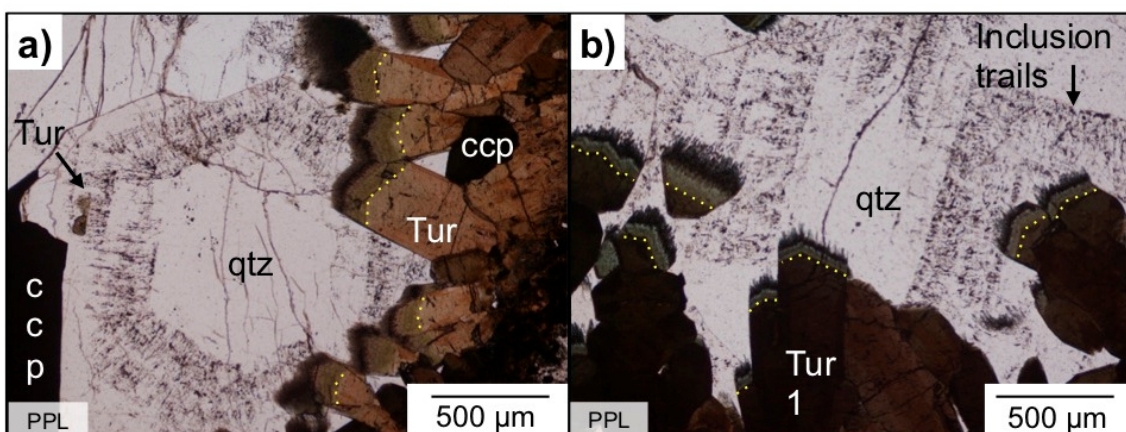


Fig. 4.32 Transmitted light (PPL) and cold-CL images showing coarse tourmaline-quartz cement phases and textures present in them from the La Huifa breccias: **a-b)** Coarse tourmaline with brighter fibrous green-blue tips. Coarse quartz (±chalcopyrite) infills remaining void space and has inclusion-rich zones. From ES026-231.84 m; **c-d)** See overleaf.

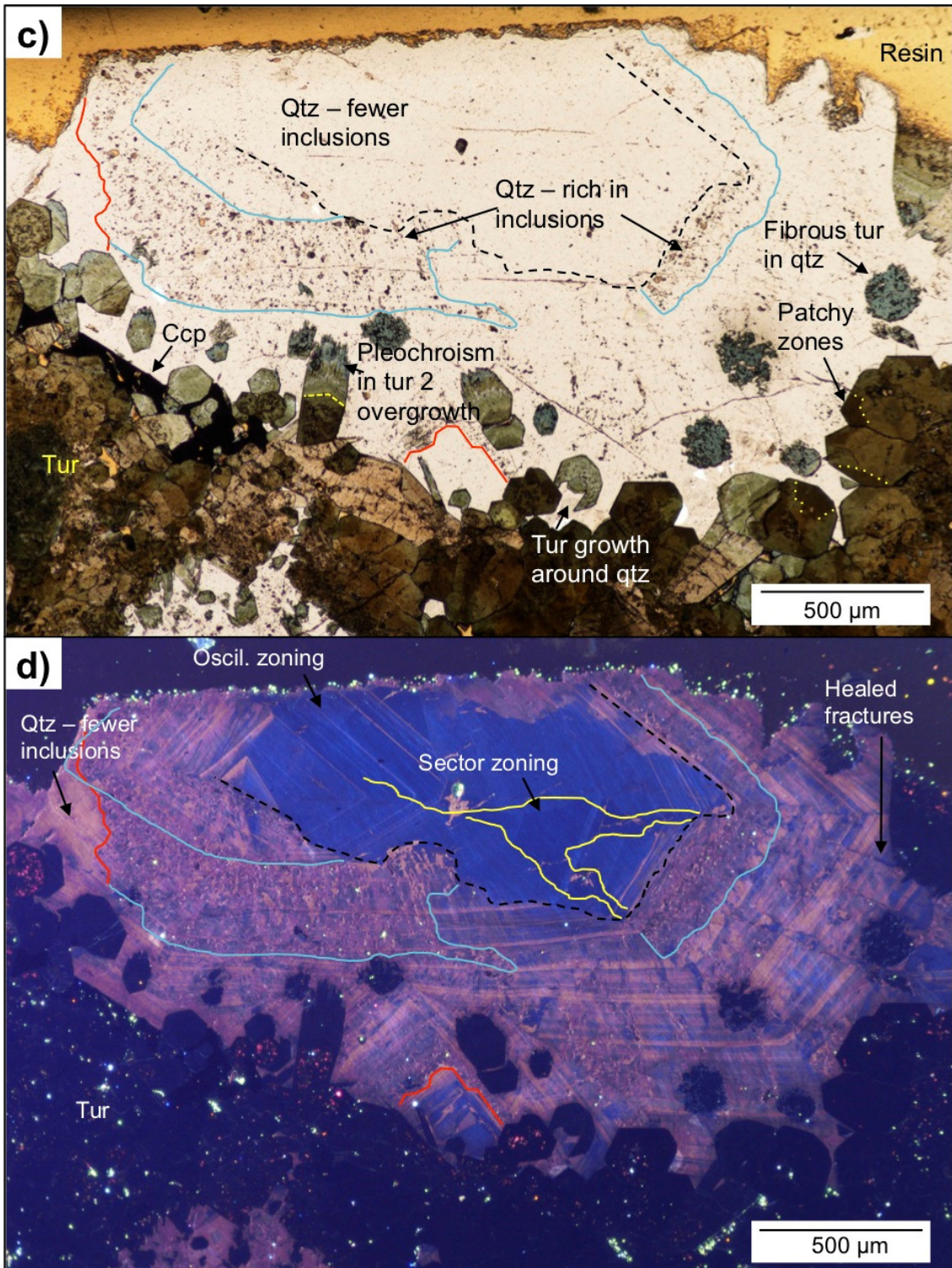


Fig. 4.32 cont. **c-d**) Transmitted light photomicrograph (PPL) (top) and corresponding cold-CL image (below) of quartz infill with complex oscillatory growth zonation variably overprinted by patchy zonation with dissolution fronts. Fluid inclusion-rich zones also present. Brown-green tourmaline, which has patchy zonation (outlined in yellow), clearly crystallised prior to quartz. Bright green CL are remnants of diamond polishing powder. From ES026-231.16 m.

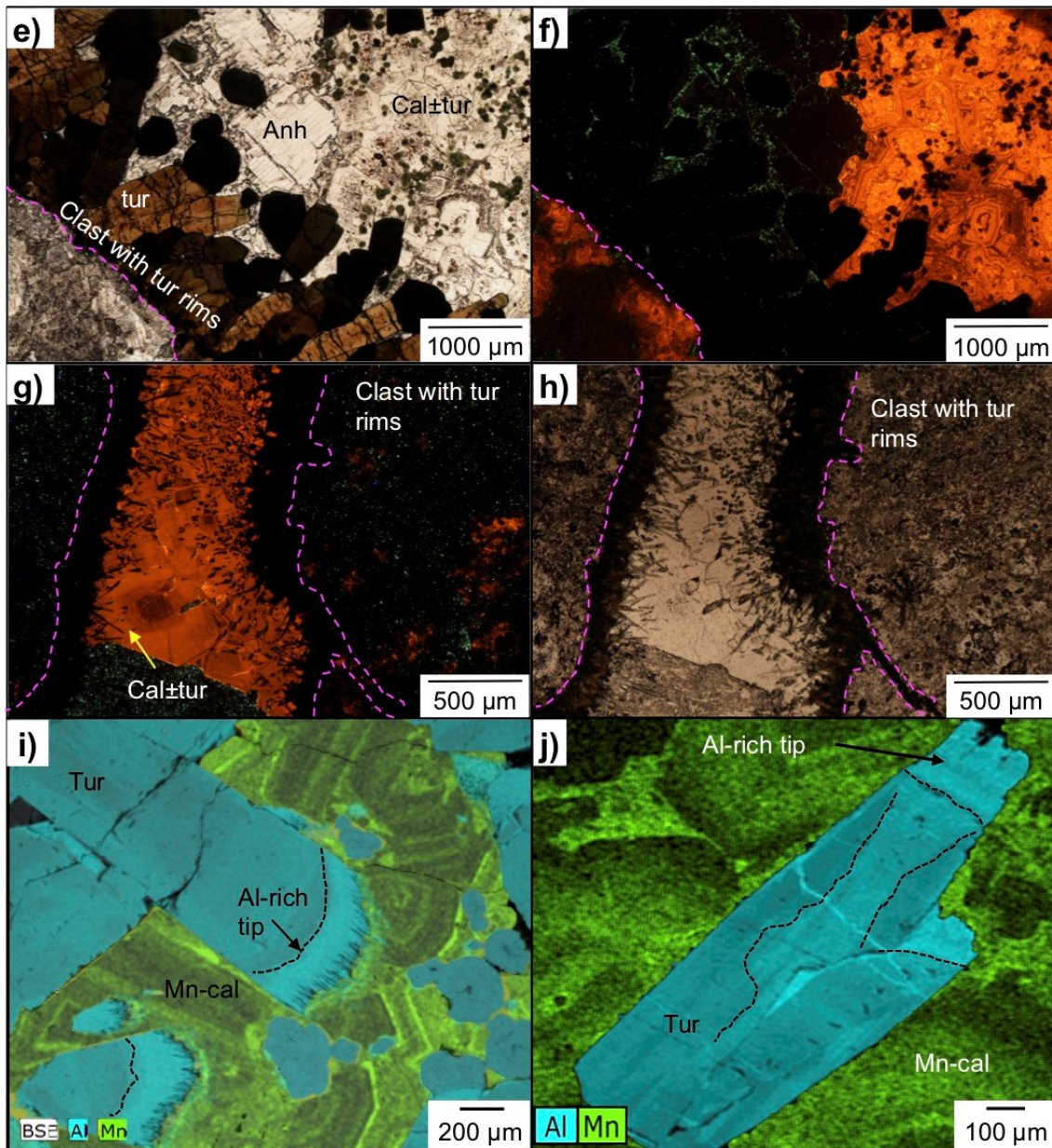


Fig. 4.32 cont. **e-f)** Transmitted light photomicrograph (PPL) (left) and cold-CL (right) images showing coarse tourmaline rim on sodic-calcic-altered clast with anhydrite-calcite infilling remaining void space. Calcite contains tourmaline inclusions and exhibits growth zones. Chalcopyrite is post-tourmaline. From ES026-231.16 m; **g-h)** Cold-CL (left) and transmitted light photomicrograph (PPL) (right) images of finer-grained acicular tourmaline rims on sodic-calcic-altered clasts with moderately zoned calcite infill. From ES026-231.84 m; **i)** SEM-EDS map showing coarse euhedral tourmaline with fibrous Al-rich tips. Strongly zoned (oscillatory growth) manganoc calcite infill. From ES026-233.04 m; **j)** SEM-EDS map of euhedral tourmaline in zoned manganoc calcite. Tourmaline has patchy zonation, a fibrous Al-rich tip and an Al-rich 'healed' fracture. From ES026-233.04 m.

**Tourmaline petrography** - Tourmaline is dark blue/black in hand specimen and is found within the wall rocks, brecciated clasts and hydrothermal cement. It shows a complex mixture of concentric and oscillatory zoning commonly alongside patch zoning (e.g., Fig. 4.33e). Individual oscillatory zones are <50  $\mu\text{m}$  thick (e.g., Fig. 4.33b). Patchy zonation is irregular, typically between 50 to 200  $\mu\text{m}$  in width, and is characteristically more prevalent than oscillatory zoning. Compared to the other El Teniente tourmaline breccias, the cementing tourmaline at La Huifa is comparatively coarse, being 100  $\mu\text{m}$  to >3 mm long and >500  $\mu\text{m}$  to a few mm wide (Fig. 4.33). The main inclusion phases in tourmaline are rutile (<100  $\mu\text{m}$ , Fig. 4.33f) and FeOx. Tourmaline is often intergrown with quartz, anhydrite/gypsum and chalcopyrite that crystallised synchronously to immediately after it infilled remaining space.

Many of the inner cores of larger tourmaline crystals show embayments and are strongly pitted (see Fig. 4.33f, g), showing signs of dissolution, and are overgrown by comb-like fibrous tourmaline. The overgrowths, which are typically the same width as the earlier tourmaline phase, and can be in excess of 50  $\mu\text{m}$  long (Fig. 4.33a, b), are comprised of individual crystals (<10  $\mu\text{m}$  thick), displaying blue-green pleochroism (Fig. 4.33a, b), and are comparatively enriched in Al and/or Mg (Fig. 4.33g, h). Fractured tourmaline crystals are often 'healed' by infills of other cementing phases and later fibrous to comb-like tourmaline overgrowths (see Fig. 4.33c, d). The overgrowths are themselves optically zoned with differing shades of blue-green pleochroism (Fig. 4.33a, b).

Based on the textures and relationships seen, tourmaline has been classified into three groups/generations as follows: 1) pitted and embayed tourmaline; 2) coarse euhedral/blocky to acicular tourmaline; and 3) fibrous overgrowths, shown in Fig. 4.33. All pre-date the bulk precipitation of Cu-sulphides. No microcrystalline tourmaline-cemented areas (like those in the Braden Tourmaline Breccia) were observed at La Huifa.

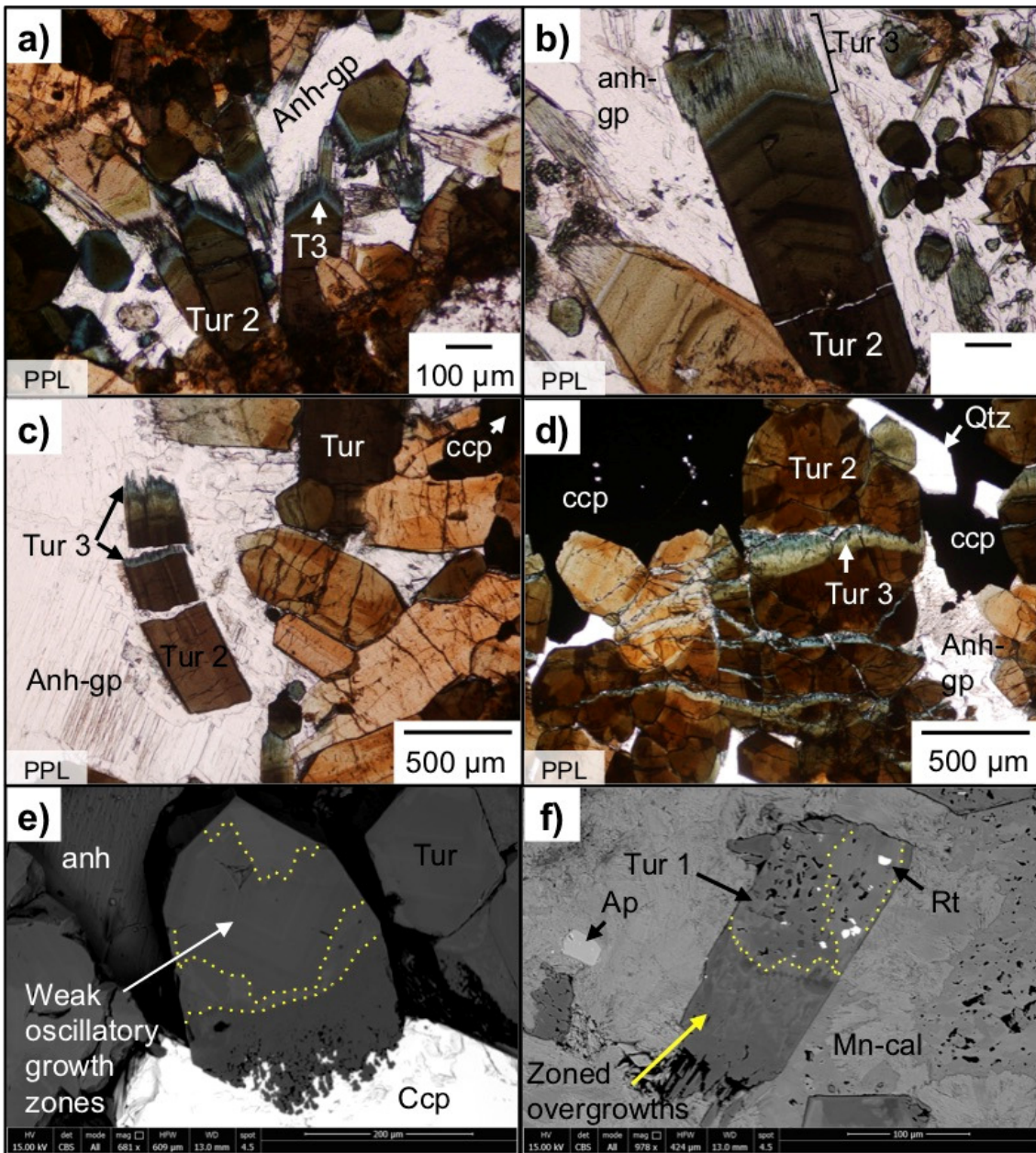


Fig. 4.33 Transmitted light photomicrographs (PPL) (a-d), SEM-BSE images (e-f) and WDS/EDS element maps (g-j) showing La Huifa tourmaline textures, relationships and generations: **a)** Coarse brown-green tourmaline with fibrous tips, which transition from bright blue to green, surrounded by later space-filling anhydrite-gypsum. From ES026-233.04 m; **b)** Euhedral oscillatory zoned tourmaline with fibrous (zoned) overgrowths and later anhydrite. From ES026-137.95 m; **c)** Fractured tourmaline with comb-like overgrowths on fractured surfaces and crystal tips. From ES026-191.74 m; **d)** Brown tourmaline with fractures 'healed' by green-blue tourmaline. Later chalcopyrite-anhydrite and quartz infilled most remaining space. From ES026-191.74 m; **e)** Oscillatory growth zoning and patchy zonation outlined in yellow. Overgrowths partially intergrown with chalcopyrite. From ES026-231.16 m; **f)** Embayed and pitted tourmaline core with rutile inclusions and patch zoning. Overgrowths are non-pitted or embayed but are complexly zoned. From ES026-191.74 m.

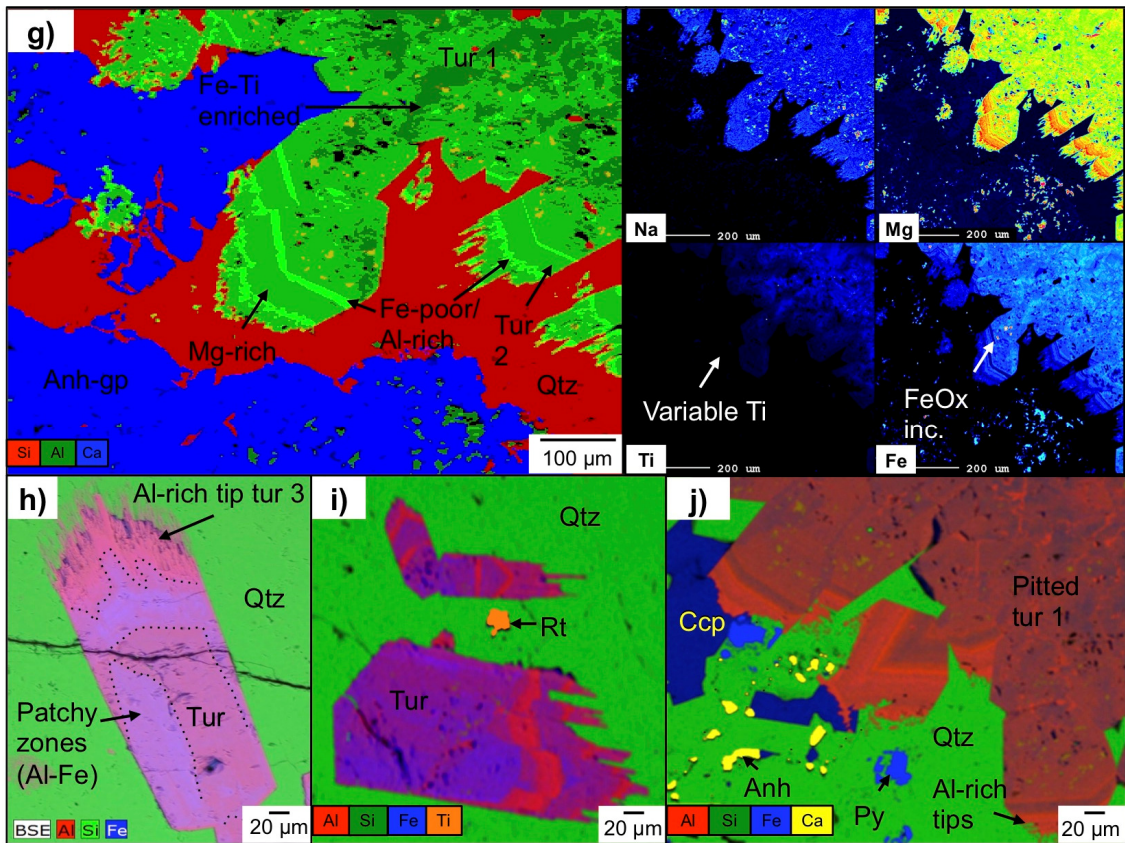
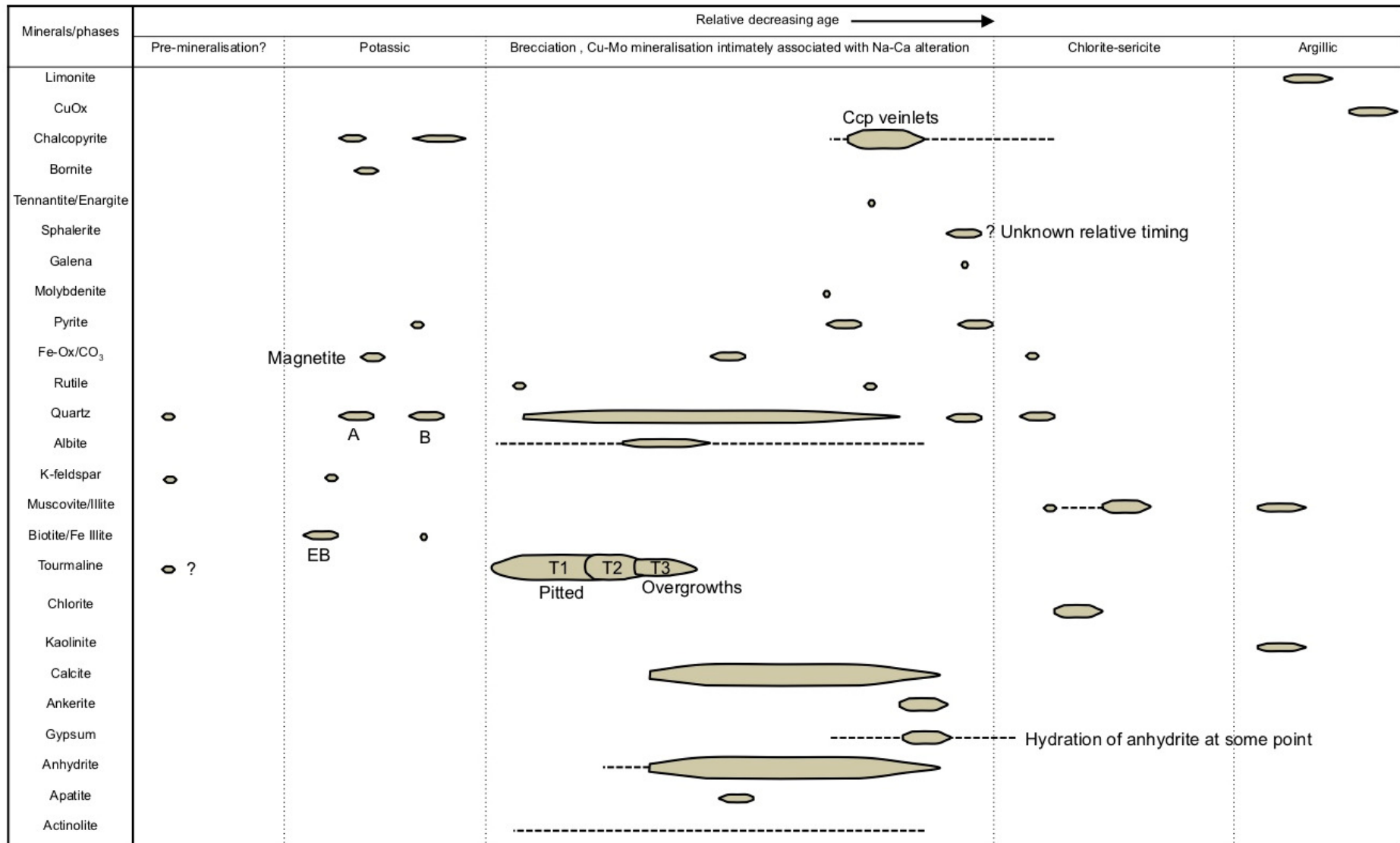


Fig. 4.33 cont. **g)** Combined (left) and individual (right) WDS elemental maps showing pitted tourmaline with FeOx inclusions and cavities filled by later quartz. This tourmaline is overgrown by a relatively fresh variety that has Al-rich/Fe-poor and Mg-rich growth zones. Later coeval quartz and anhydrite infill remaining space. Ti is variable within individual tourmaline crystals, although later tourmaline phases are comparatively Ti-depleted. From ES026-237.93 m; **h)** Euhedral tourmaline within quartz showing Al-Fe patchy zonation and Al-rich tips. From ES026-237.93 m; **i)** Tourmaline and rutile inclusions in quartz. Tourmaline shows Al-Fe zonation. From ES026-233.04 m; **j)** Al-Fe-zoned tourmaline with quartz-anhydrite-chalcopyrite infill. Tourmaline frequently has Al-rich tips. From ES026-231.84 m.

From the textural characteristics described, there were multiple fluid pulses at La Huifa resulting in periods of alteration and mineralisation, and the distinct growth and dissolution of tourmaline. The paragenetic sequence of La Huifa can be divided into six main phases:

1. Potassic alteration;
2. Initial brecciation and formation of coarse tourmaline that is now pitted and embayed;
3. Formation of non-pitted tourmaline and tourmaline overgrowths/healed fractures. The grain boundaries of the second and third generations are not embayed or pitted, showing that they were not destabilised by the later mineralising fluids;
4. Fill of remaining spaces with quartz, various Ca-bearing phases and chalcopyrite-bornite. The precipitation of the bulk of the Cu-sulphides was likely associated with sodic-calcic alteration;
5. Chlorite-sericite overprint;
6. Argillic alteration, leaving porous tourmaline cement and formation of CuOx likely from the replacement of chalcopyrite.

Table 4.7 Paragenetic sequence of alteration and mineralisation, in particular for hydrothermal cementing phases in the La Huifa Breccia. Of the three tourmaline generations, the first is usually pitted and embayed. This is overgrown by fresher tourmaline which is itself overgrown by comb-like needles. Thickness of lines= approximate mineral abundance.



#### 4.4.6 Summary

Listed below are the main findings of this section covering the tourmaline breccias at El Teniente and the Braden Diatreme.

##### **Tourmaline Breccias:**

- All tourmaline breccias follow a similar paragenetic sequence where early cement-phases include tourmaline-quartz and some of the last phases include Cu-Mo sulphides alongside anhydrite and further quartz.
- The presence of and timing of porosity/permeability is a major factor in the mineralising potential of breccias. Open-space generated early on brecciation can become quickly filled with early cement phases reducing permeability available for later Cu-Mo-rich fluids. The preservation of this early porosity and permeability, or the generation of late permeability through re-brecciation and/or dissolution can create extremely favourable sites for mineralisation. This often results in very high-grade breccias and in cases sulphide cements. The timing of this permeability generation is key to the mineralising potential of tourmaline breccias.
- Well-mineralised sulphide-cemented portions share same breccia framework as adjacent breccias albeit showing a stronger affinity to increased clast rounding (well-rounded to sub rounded) and increasing portions of anhydrite.
- Breccia margins are particularly well Cu-Mo mineralised often having sulphide-cement, especially in the Diablo sector.
- Paragenetic sequences are often repeated several times evidenced by tourmaline and quartz cement textures such as multiple generations and dissolution.

##### **Braden Tourmaline Breccia:**

- Shares the same breccia framework as the host Braden Diatreme facies such as a polymictic clast population of rounded to angular clasts.
- Between the clasts is a mixture of rock flour matrix (same composition as that in the Braden Sericite Breccia) and later hydrothermal tourmaline-quartz±ankerite-anhydrite-gypsum-chalcopyrite cement.
- These hydrothermal fluids have to varying degrees replaced the rock flour matrix and relict clast textures are often identified by quartz with tourmaline rims.
- A chalcopyrite halo of a few to tens of metres surrounds the Braden Tourmaline Breccia. In this halo, chalcopyrite is the main sulphide phase in the Braden Diatreme.

- Features such as stratification/crude bedding developed in the Braden Diatreme are also present in the Braden Tourmaline Breccia. These are not truncated at the Braden Tourmaline Breccia margins.
- The Braden Tourmaline Breccia is weakly mineralised and Cu-sulphides are paragenetically late, often being the last phases to form.

#### **Braden Diatreme:**

- An explosive origin (either involving external waters, or explosive exsolution) involving fragmentation of a porphyritic intrusive is supported through the identification of juvenile clasts with viscous-wispy-shaped clast morphologies.
- The juvenile clasts have the same composition as the underlying dacite intrusive and the rock flour matrix. Both of these have experienced varying degrees of sericite (-quartz) alteration and chlorite overprints. The former is often intense and texturally destructive, obscuring many primary features like feldspar phenocrysts.
- Wispy/vermiform textures are best preserved at greater depths and towards the margins of the Braden Diatreme.
- Ti-in-quartz study shows that a large number of fragmented and abraded quartz grains in the matrix are xenocrysts with same internal grain textures as the underlying dacite. These xenocrysts are often more rounded and smaller as a result of brecciation. Quartz grains in the matrix also have similar Ti contents.
- There is a spatial association between the juvenile material and Mo-Cu±Pb-Zn mineralisation in the surrounding matrix. Minor syn- to post-brecciation fluid exsolution from juvenile dacite clasts has resulted in the localised impregnation of surrounding rock flour (few cm) by Mo, quartz and lesser tourmaline, chalcopyrite, sphalerite and galena.
- Post-brecciation, fluids continued to permeate the rock flour on a larger scale than from the juvenile clasts causing a more pervasive mineralogically similar overprint of the rock flour matrix and the development of the 'Braden Sulphide Breccia' through the introduction of more anhydrite-gypsum-ankerite-chalcopyrite-tetrahedrite-tennantite.
- The molybdenised rock flour is locally re-brecciated and re-cemented with anhydrite-gypsum and minor tetrahedrite-tennantite.

## 4.5 Compositional variation of tourmaline

A comprehensive quantitative dataset comprising major and minor EPMA and accompanying trace and REE LA-ICP-MS data from the five tourmaline breccias in the Teniente district is provided.

### 4.5.1 Major and minor elements

Hydrothermal tourmaline from El Teniente plots within the fields for schorl and dravite on the discrimination diagrams in Fig. 4.34a,b with a small number of those from the Marginal Breccias falling in the Mg-foitite (Fig. 4.34a) and Fe-uvite fields (Fig. 4.34b). The substitution mechanisms for the tourmalines at El Teniente are illustrated in Fig. 4.34c-e and include a combination of  $\text{NaFe}^{2+}(\square\text{Al})_{-1}$ ,  $(\text{Fe}^{2+}\text{Fe}^{3+})(\text{MgAl})_{-1}$ ,  $(\text{Fe})(\text{Mg})_{-1}$  and  $(\text{Ca}(\text{Fe}, \text{Mg}))(\text{Al Na})_{-1}$  exchanges.

Major element data for tourmaline from all El Teniente tourmaline breccias overlap to varying degrees (Fig. 4.35). The largest variation is in  $\text{Al}_2\text{O}_3$  (13 to 35 wt.%), FeO (2 to 30 wt.%), MgO (~3 to 10 wt.%) and  $\text{SiO}_2$  (30 to 39 wt.% equating to ~6 apfu).  $\text{Na}_2\text{O}$  (1.5 to 3.0 wt.%), CaO (0 to 2.5 wt.%) and  $\text{TiO}_2$  (0.02 to 3 wt.%) have less variation, whilst  $\text{K}_2\text{O}$  (0.01 to 1.0 wt.%) and MnO (0.03 to 0.15 wt.%) are largely below EPMA detection limits.  $\text{SiO}_2$  vs. FeO (Fig. 4.35a) show a linear negative correlation ( $\text{SiO}_2$  increases with decreasing FeO) due to the closure effect, given that they are major components of tourmaline. A negative linear correlation is also observed for FeO vs.  $\text{Al}_2\text{O}_3$  (Fig. 4.35j), with decreasing  $\text{Al}_2\text{O}_3$  associated with increasing FeO. A weak negative correlation is also present between FeO and MgO (Fig. 4.35i). A positive correlation is observed for  $\text{SiO}_2$  vs.  $\text{Al}_2\text{O}_3$  (Fig. 4.35b) and a weaker positive correlation between  $\text{SiO}_2$  and MgO (Fig. 4.35c). Other elements show no clear linear correlations. Major element tourmaline data from each breccia are described below and shown in Table 4.8.

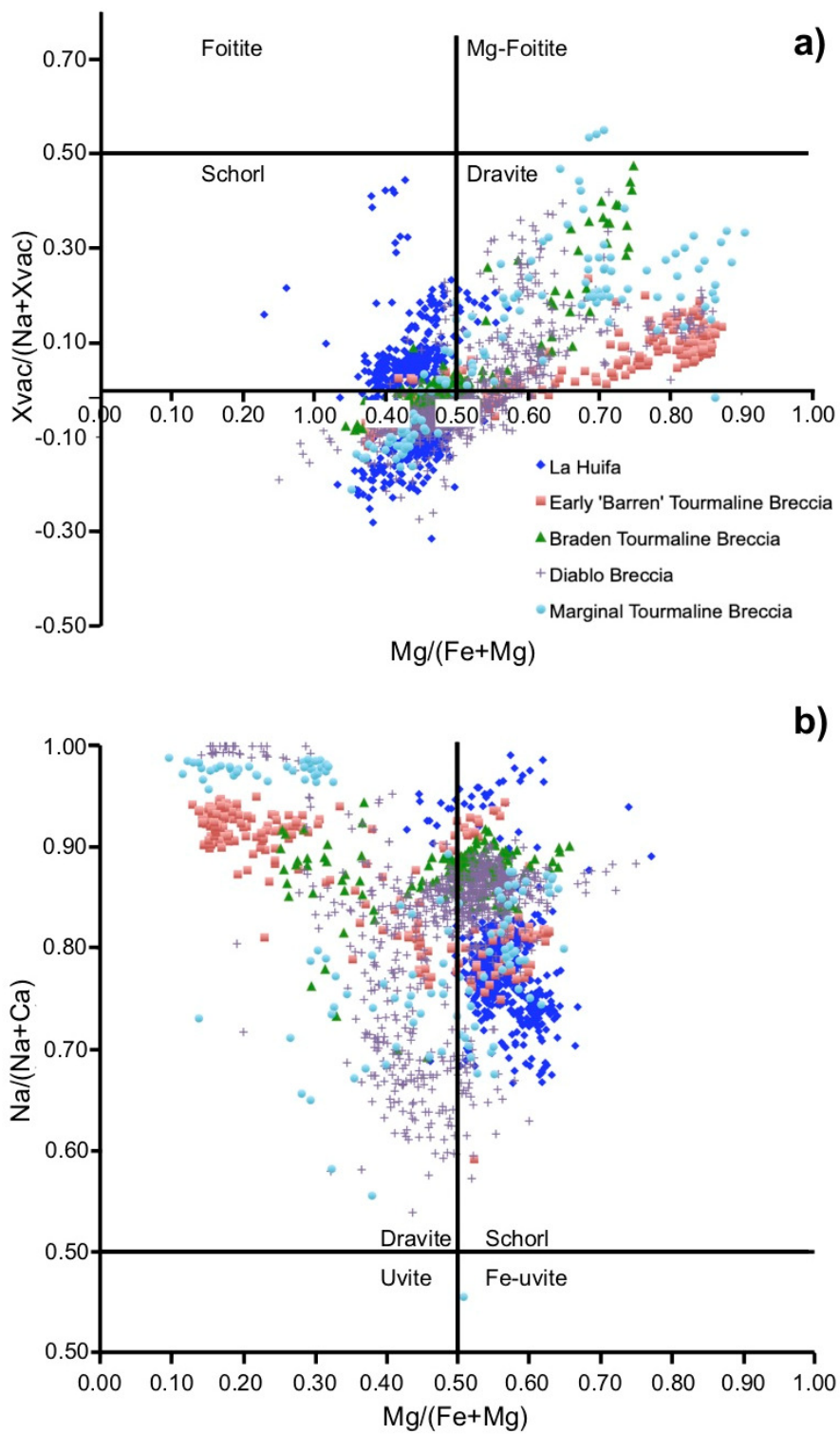


Fig. 4.34 Tourmaline classification diagrams of data (apfu) from El Teniente: **a)**  $Mg/(Fe+Mg)$  vs.  $X_{vac}/(Na+X_{vac})$ ; **b)**  $Fe/(Fe+Mg)$  vs.  $Na/(Na+Ca)$ ; **c)**  $Fe$  vs.  $X_{vac}$ ; **d)**  $Mg$  vs.  $Fe$ ; **e)**  $Al$  vs.  $Fe$ .

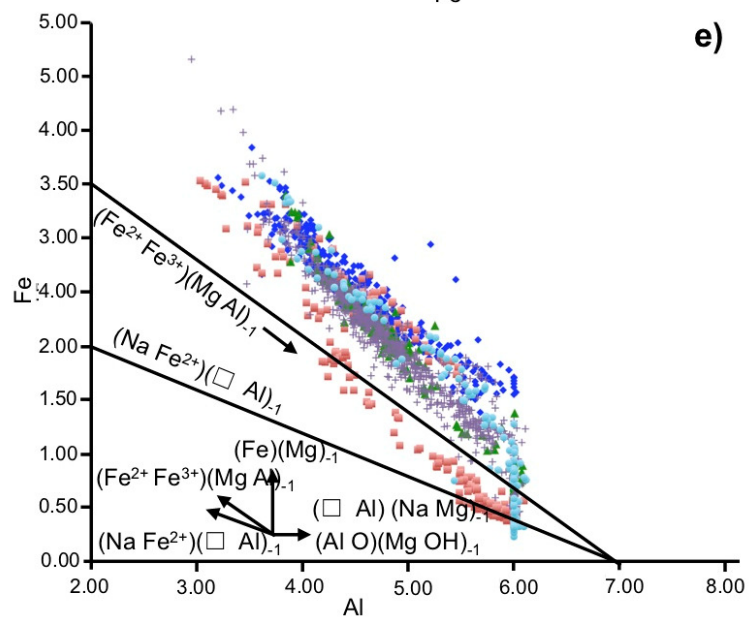
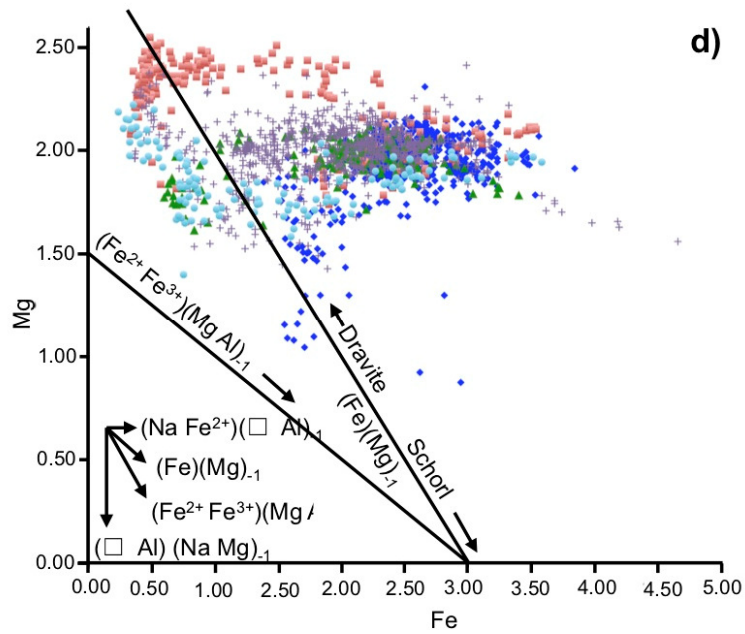
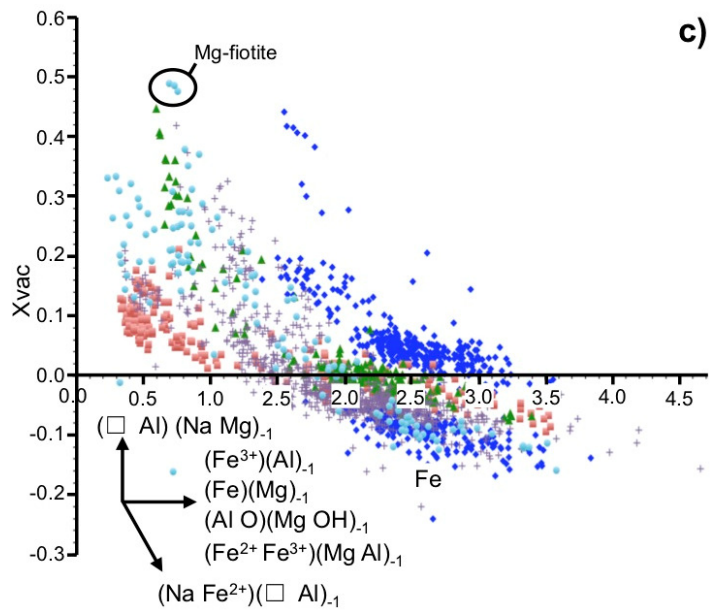


Table 4.8 EPMA data (wt.% and apfu) for tourmaline from the five breccias analysed at El Teniente. Assumptions include: B<sub>2</sub>O<sub>3</sub>, H<sub>2</sub>O and Li<sub>2</sub>O= calculated by stoichiometry; B= 3 apfu, OH+F= 4 apfu and Li= 15-total (T+Z+Y). Abbreviations include: 'Bx'= breccia, 'Tur'= tourmaline,  $\bar{X}$ = mean average of data where n is the number beneath, N/A= not acquired and 'LOD'= limit of detection. Data from the Diablo Breccia have also been divided into sample depths below.

EPMA data																		
Bx:	Early Tur Bx.				Marginal Tur Bx.		Braden Tur Bx				La Huifa						Diablo	
	Cement		Clast		Cement		Cement core		Overgrowths		Pitted		Non-pitted		Overgrowths		Bulk data	
	Range	$\bar{X}$ (122)	Range	$\bar{X}$ (136)	Range	$\bar{X}$ (133)	Range	$\bar{X}$ (142)	Range	$\bar{X}$ (21)	Range	$\bar{X}$	Range	$\bar{X}$ (484)	Range	$\bar{X}$ (72)	Range	$\bar{X}$ (738)
SiO <sub>2</sub>	33.58-37.85	36.22	33.96-37.93	36.65	29.67-38.54	36.46	33.45-37.92	35.94	35.30-37.98	36.74	N/A	N/A	33.69-36.62	35.59	35.00-36.96	35.97	33.33-38.15	35.95
TiO <sub>2</sub>	0.18-4.13	1.19	0.10-5.34	1.84	<LOD-3.41	0.67	0.19-2.89	1.42	<LOD-1.74	0.69	N/A	N/A	<LOD-3.82	1.06	<LOD-1.63	0.53	0.08-3.35	1.33
Al <sub>2</sub> O <sub>3</sub>	16.08-32.19	25.91	13.94-33.77	27.34	17.03-34.79	28.05	18.12-33.83	23.93	22.59-32.47	28.08	N/A	N/A	14.81-30.45	21.49	20.43-32.17	26.75	13.24-34.26	24.68
FeO	3.21-23.11	10.25	2.48-22.95	7.51	1.76-23.82	10.55	4.47-22.61	14.52	5.15-15.21	9.82	N/A	N/A	10.70-25.29	17.71	9.97-18.20	13.60	2.74-29.51	13.57
MgO	6.71-10.13	8.81	6.92-10.57	9.26	5.47-9.39	7.52	6.61-8.48	7.66	6.74-8.35	7.88	N/A	N/A	3.35-8.77	7.58	3.60-8.10	6.62	5.54-10.22	7.88
CaO	0.26-3.26	0.65	0.28-1.33	0.61	0.04-13.71	0.96	0.29-1.16	0.65	0.36-0.90	0.65	N/A	N/A	0.08-1.99	1.21	0.03-1.76	0.75	<LOD-2.51	1.02
MnO	<LOD-0.05	0.04	<LOD-0.04	0.03	<LOD-0.10	0.05	<LOD-0.4	0.03	<LOD-0.04	0.04	N/A	N/A	<LOD-0.09	0.04	<LOD-0.17	0.06	<LOD-0.27	0.05
Na <sub>2</sub> O	2.21-2.89	2.58	2.19-2.85	2.59	1.12-2.79	2.30	1.60-2.84	2.55	2.11-2.69	2.44	N/A	N/A	1.87-2.93	2.31	1.73-2.60	2.24	1.53-3.17	2.46
K <sub>2</sub> O	<LOD-0.03	0.02	<LOD-0.03	0.02	<LOD-0.64	0.05	<LOD-0.03	0.02	<LOD-0.02	0.02	N/A	N/A	<LOD-0.11	0.04	<LOD-0.06	0.03	<LOD-0.18	0.04
F	<LOD-0.15	0.12	<LOD-0.18	0.12	<LOD-0.96	0.15	<LOD-0.15	0.11	<LOD	<LOD	N/A	N/A	<LOD	<LOD	<LOD	<LOD	<LOD-0.16	0.13
Li <sub>2</sub> O*	0.00-0.58	0.15	0.00-0.66	0.23	0.00-3.29	0.20	0.00-0.40	0.04	0.12-0.45	0.19	N/A	N/A	0.00-0.36	<LOD	0.00-0.24	0.02	0.00-0.56	0.05
Si	5.84-6.40	6.11	5.91-6.35	6.07	5.10-6.35	6.07	5.83-6.34	6.15	6.03-6.21	6.10	N/A	N/A	5.90-6.47	6.21	5.94-6.25	6.11	5.83-6.49	6.11
Ti	0.02-0.54	0.15	0.01-0.73	0.23	0.00-0.45	0.09	0.00-0.38	0.18	0.01-0.22	0.09	N/A	N/A	0.00-0.52	0.13	0.00-0.22	0.07	0.00-0.44	0.17
Al <sub>tot</sub>	3.46-6.07	5.13	3.03-6.44	5.29	3.61-6.48	5.47	3.85-6.42	4.88	4.57-6.15	5.48	N/A	N/A	3.20-6.03	4.42	4.24-6.36	5.35	2.95-6.40	4.92
Fe <sub>tot</sub>	0.43-3.52	1.48	0.33-3.54	1.08	0.23-3.58	1.50	0.60-3.40	1.95	0.69-2.19	1.37	N/A	N/A	1.50-3.84	2.59	1.38-2.67	1.93	0.36-4.66	1.95

EPMA data																		
Bx:	Early Tur Bx.				Marginal Tur Bx.		Braden Tur Bx				La Huifa						Diablo	
	Cement		Clast		Cement		Cement core		Overgrowths		Pitted		Non-pitted		Overgrowths		Bulk data	
	Range	$\bar{X}$ (122)	Range	$\bar{X}$ (136)	Range	$\bar{X}$ (133)	Range	$\bar{X}$ (142)	Range	$\bar{X}$ (21)	Range	$\bar{X}$	Range	$\bar{X}$ (484)	Range	$\bar{X}$ (72)	Range	$\bar{X}$ (738)
Mg <sub>tot</sub>	1.74-2.48	2.21	1.66-2.55	2.28	1.40-2.22	1.86	1.62-2.12	2.02	1.65-2.09	1.95	N/A	N/A	0.87-2.31	1.97	0.92-2.06	1.68	1.43-2.47	2.00
Ca	0.05-0.61	0.12	0.05-0.25	0.11	0.01-2.52	0.17	0.05-0.20	0.12	0.06-0.16	0.12	N/A	N/A	0.01-0.38	0.23	0.00-0.33	0.14	0.00-0.45	0.18
Mn	0.00-0.01	0.00	0.00-0.01	0.00	0.00-0.01	0.00	0.00-0.01	0.00	0.00-0.01	0.00	N/A	N/A	0.00-0.01	0.00	0.00-0.02	0.00	0.00-0.04	0.00
Na	0.71-0.95	0.85	0.68-0.92	0.83	0.37-0.96	0.74	0.50-0.96	0.85	0.65-0.89	0.79	N/A	N/A	0.61-1.00	0.78	0.55-0.86	0.74	0.48-1.07	0.81
K	0.00-0.01	0.00	0.00-0.01	0.00	0.00-0.14	0.01	0.00-0.01	0.00	0.00-0.00	0.00	N/A	N/A	0.00-0.03	0.01	0.00-0.01	0.00	0.00-0.04	0.01

EPMA data: Diablo																
	Deep inner				Middle Inner						Middle Margin				Shallow	
	2136_1		1974_1		2677_3		1990_6		2672_1		2683_3		2679_2		2672_9	
	Range	$\bar{X}$ (155)	Range	$\bar{X}$ (104)	Range	$\bar{X}$ (81)	Range	$\bar{X}$ (46)	Range	$\bar{X}$ (207)	Range	$\bar{X}$ (96)	Range	$\bar{X}$ (65)	Range	$\bar{X}$ (25)
SiO <sub>2</sub>	33.33-37.45	35.61	33.51-37.03	35.70	35.18-37.57	36.08	35.63-38.15	37.34	34.45-37.50	36.07	34.25-37.01	35.50	34.17-37.51	35.98	35.76-37.41	36.83
TiO <sub>2</sub>	0.18-2.73	1.93	0.10-3.35	1.73	0.12-2.62	1.01	0.13-0.89	0.25	0.10-2.16	0.76	0.18-3.20	1.83	0.16-2.74	1.77	0.09-0.92	0.45
Al <sub>2</sub> O <sub>3</sub>	13.24-32.27	22.08	18.98-32.37	23.72	20.07-31.92	24.00	27.29-34.26	32.46	17.13-31.87	26.83	16.32-29.88	21.16	19.29-32.51	24.61	25.83-31.09	29.14
FeO	6.17-29.51	16.46	7.05-20.81	14.61	5.73-17.42	14.23	2.74-11.72	4.70	5.72-21.88	11.45	8.54-21.90	17.55	3.81-19.79	12.70	6.80-14.88	9.26
MgO	5.54-8.68	7.58	6.34-8.45	7.58	7.66-8.66	8.17	6.42-10.22	8.51	5.63-9.58	7.91	7.11-8.31	7.70	7.51-9.85	8.28	6.19-8.70	7.77
CaO	0.60-1.26	0.83	0.60-1.77	0.92	0.61-1.07	0.78	0.03-0.48	0.12	0.27-2.51	1.55	0.49-1.74	0.81	0.55-2.27	0.93	0.60-1.31	1.03
MnO	0.03-	0.04	0.03-	0.05	0.03-	0.03	0.03-0.04	0.03	0.03-	0.06	0.03-	0.03	0.03-	0.04	0.03-	0.04

EPMA data: Diablo																
	Deep inner				Middle Inner						Middle Margin				Shallow	
	2136_1		1974_1		2677_3		1990_6		2672_1		2683_3		2679_2		2672_9	
	Range	$\bar{X}$ (155)	Range	$\bar{X}$ (104)	Range	$\bar{X}$ (81)	Range	$\bar{X}$ (46)	Range	$\bar{X}$ (207)	Range	$\bar{X}$ (96)	Range	$\bar{X}$ (65)	Range	$\bar{X}$ (25)
	0.05		0.07		0.04				0.27		0.04		0.04		0.06	
Na <sub>2</sub> O	2.23-3.17	2.64	1.53-2.84	2.55	2.37-2.94	2.68	1.85-2.90	2.61	1.59-2.86	2.07	2.18-2.83	2.65	1.97-2.80	2.59	1.75-2.44	2.16
K <sub>2</sub> O	0.02-0.18	0.05	0.02-0.06	0.04	0.02-0.06	0.04	0.01-0.16	0.03	0.01-0.10	0.02	0.02-0.09	0.05	0.02-0.06	0.04	0.02-0.03	0.02
F	0	0	0	0	0	0	0.09-0.09	0.09	0.11-0.16	0.14	0	0	0	0	0	0
Li <sub>2</sub> O*	0-0.56	0.02	0-0.33	0.03	0-0.47	0.02	0-0.49	0.22	0-0.34	0.06	0-0.28	0.01	0-0.44	0.04	0.00-0.31	0.16
Si	5.98-6.49	6.16	5.88-6.33	6.12	5.96-6.28	6.15	5.92-6.13	6.01	5.83-6.31	6.05	5.99-6.34	6.18	5.93-6.22	6.09	5.96-6.16	6.07
Ti	0.02-0.35	0.16	0.01-0.44	0.22	0.01-0.34	0.13	0.02-0.11	0.03	0.01-0.28	0.10	0.02-0.42	0.24	0.02-0.36	0.23	0-0.11	0.05
Al <sub>tot</sub>	2.95-6.18	4.49	3.94-6.17	4.78	4.11-6.12	4.82	5.49-6.40	6.16	3.66-6.10	5.30	3.48-5.76	4.33	4.06-6.12	4.90	5.17-6.04	5.66
Fe <sub>tot</sub>	0.84-4.66	2.94	0.95-3.06	2.10	0.77-2.54	2.04	0.36-1.67	0.64	0.78-3.32	1.61	1.17-3.33	2.56	0.51-2.95	1.81	0.92-2.11	1.28
Mg <sub>tot</sub>	1.56-2.25	3.22	1.56-2.13	1.94	1.84-2.23	2.08	1.53-2.47	2.04	1.43-2.41	2.00	1.81-2.11	2.00	1.80-2.37	2.09	1.53-2.11	1.91
Ca	0.11-0.24	0.15	0.11-0.32	0.17	0.11-0.20	0.14	0-0.09	0.01	0.05-0.45	0.28	0.09-0.32	0.15	0.10-0.41	0.17	0.10-0.24	0.18
Mn	0-0.01	0	0-0.01	0	0-0.01	0	0-0.01	0	0-0.04	0	0-0.01	0	0-0.01	0	0-0.01	0
Na	0.70-1.07	0.89	0.48-0.97	0.85	0.74-0.98	0.89	0.57-0.91	0.81	0.50-0.90	0.67	0.72-0.98	0.89	0.64-0.94	0.85	0	0
K	0.01-0.04	0.01	0-0.01	0.01	0-0.01	0.01	0-0.03	0	0-0.2	0	0-0.02	0.01	0-0.01	0.01	0.56-0.80	0.69

**La Huifa** - MgO concentrations overlap with the Braden Tourmaline, Diablo and Marginal Breccias ranging between 3.4 and 9 wt.%, with most La Huifa tourmalines containing between 5.8 and 8.5 wt.% MgO. FeO shows a larger range between 11.2 and 26 wt.% although La Huifa tourmalines have a comparatively restricted FeO range compared to the other breccias, which frequently have analyses containing as low as ~2 wt.% FeO (see Fig. 4.35i, j). La Huifa tourmalines also have the most restricted range of SiO<sub>2</sub> between 34 and 37 wt.% whilst other breccias frequently contain SiO<sub>2</sub> concentrations between 33.5 to 38.5 wt.%. CaO shows a bimodal distribution with a Ca-poor group containing <0.6 wt.% and remaining tourmalines containing up to 2 wt.% CaO. No other distinct major element trends are seen in the La Huifa data (Fig. 4.35).

**Early Tourmaline Breccia** - The elemental graphs (Fig. 4.35) show a bimodal distribution is present for many elements such as FeO and SiO<sub>2</sub> (Fig. 4.35a), Al<sub>2</sub>O<sub>3</sub> (Fig. 4.35b) and to a lesser extent CaO (Fig. 4.35h). Two distinct groups of data can be separated based on SiO<sub>2</sub>; one with comparatively lower SiO<sub>2</sub> (34 to 36 wt.%) and higher SiO<sub>2</sub> >36 wt.% which both correspond to higher (10 to 25 wt.%) and lower (<10 wt.%) FeO respectively. The breccia is relatively enriched in MgO (7 to 10 wt.%) compared to other breccias (e.g., Fig. 4.35c, i) which contain between 3 and 9 wt.% MgO.

**Braden Tourmaline Breccia** - Major elemental concentrations of tourmaline from this breccia largely overlap with the other El Teniente breccias. It contains variable TiO<sub>2</sub> (most data are 0.8 to 2.9 wt.%), MgO (6.5 to 8.5 wt.%), Al<sub>2</sub>O<sub>3</sub> (17 to 33 wt.%), Na<sub>2</sub>O (1.6 to 2.8 wt.%) and SiO<sub>2</sub> (33.5 to 38 wt.%). This breccia has the smallest range of CaO (0.25 to 0.95 wt.%) and is relatively depleted in K<sub>2</sub>O (<0.04 wt.%) compared with the other breccias which frequently have up to ~0.8% K<sub>2</sub>O (Fig. 4.35d).

**Marginal Tourmaline Breccia** - Concentrations of MgO (6.3 to 9.3 wt.%), Al<sub>2</sub>O<sub>3</sub> (17 to 34.8 wt.%), CaO (up to 1.8 wt.% although outliers up to 4.34 wt.%), SiO<sub>2</sub> (17.8 to 38.5 wt.%) and FeO (1.8 to 23.8 wt.%) overlap with the other El Teniente breccias. Two groups of tourmaline data are identified based on CaO (Fig. 4.35h) as follows: <0.3 wt.% and >0.6 wt.% CaO. Analyses with lower CaO (<0.3 wt.%) typically have SiO<sub>2</sub> >37 wt.% whereas remaining data containing >0.6 wt.% CaO have more variable SiO<sub>2</sub> values between 34.5 and 37.5 wt.% (Fig. 4.35h).

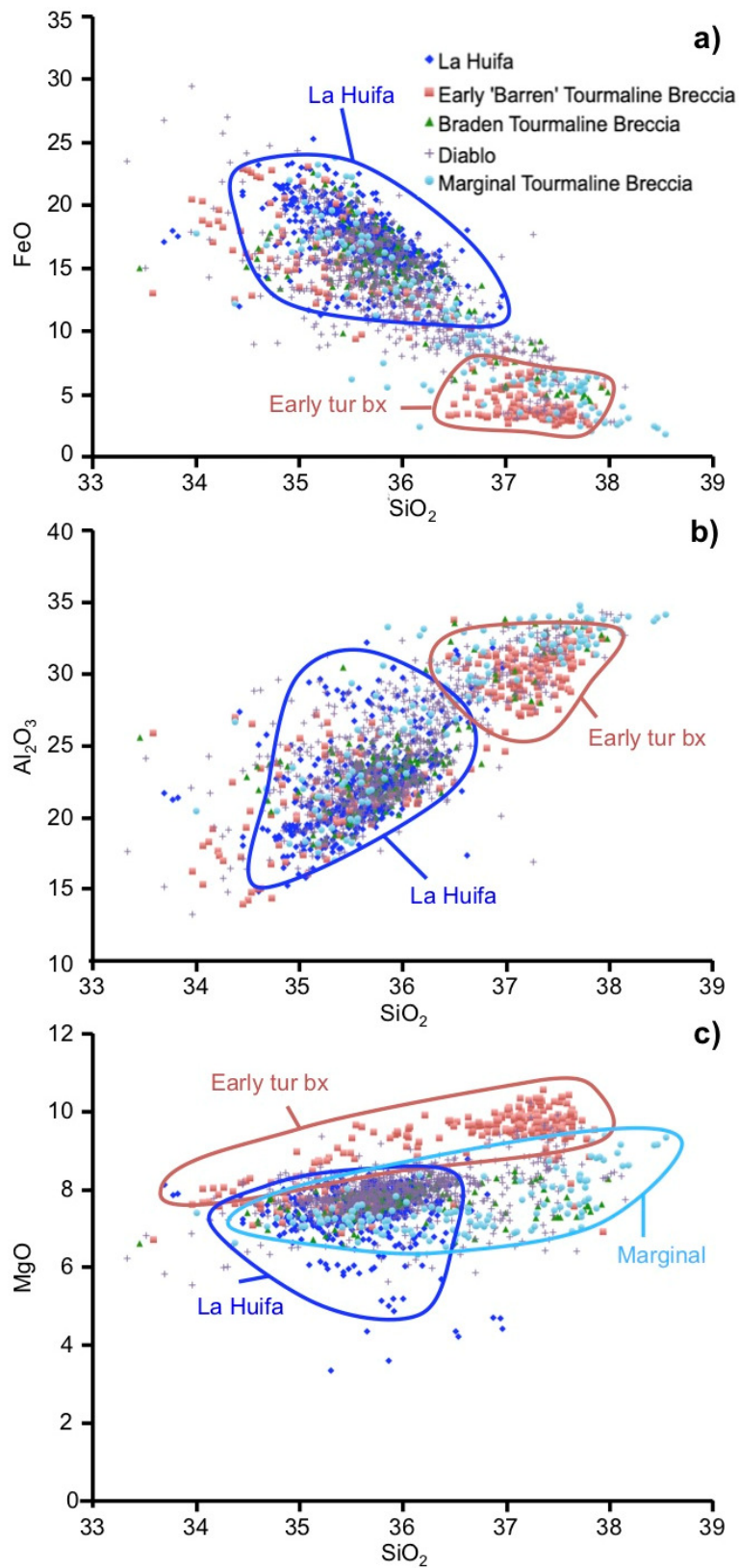


Fig. 4.35 Major element data (wt.% oxides) for tourmaline from the tourmaline breccias at El Teniente: **a)** SiO<sub>2</sub> vs. FeO; **b)** SiO<sub>2</sub> vs. Al<sub>2</sub>O<sub>3</sub>; **c)** SiO<sub>2</sub> vs. MgO; **d-l)** Overleaf.

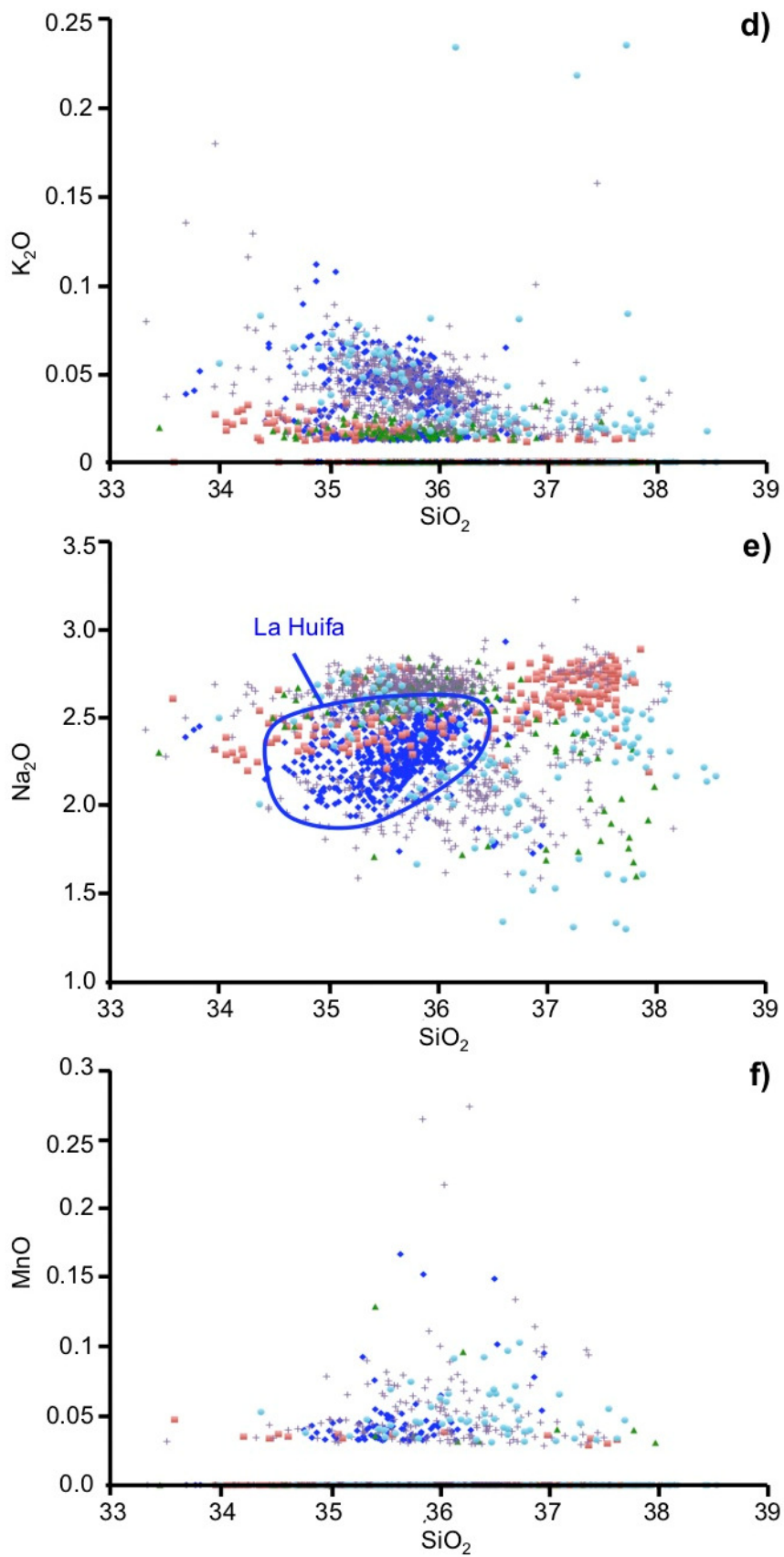


Fig. 4.35 cont. **d)**  $\text{SiO}_2$  vs.  $\text{K}_2\text{O}$ ; **e)**  $\text{Na}_2\text{O}$  vs.  $\text{SiO}_2$ ; **f)**  $\text{SiO}_2$  vs.  $\text{MnO}$ .

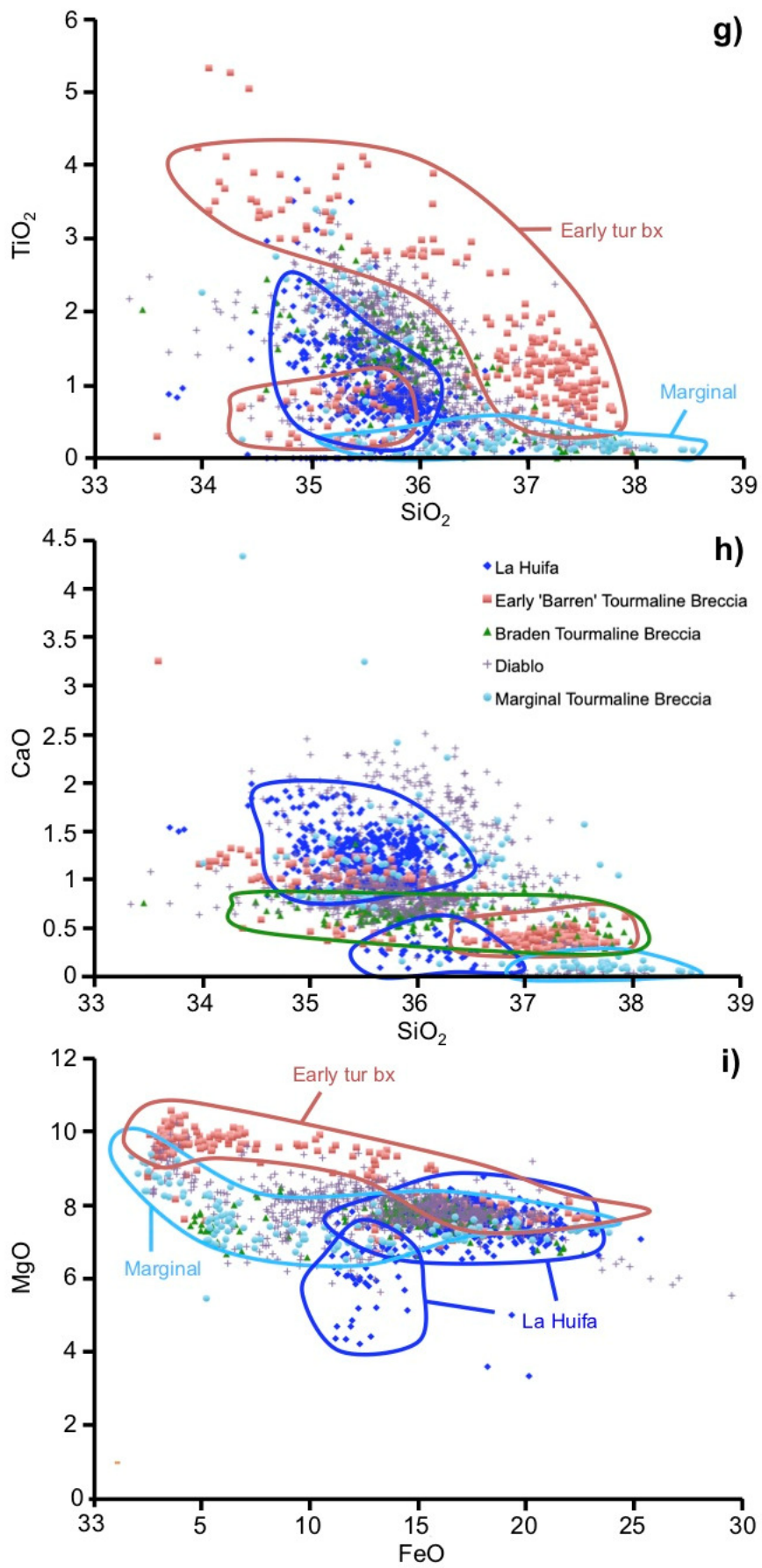


Fig. 4.35 cont. **g)**  $\text{SiO}_2$  vs.  $\text{TiO}_2$ ; **h)**  $\text{SiO}_2$  vs.  $\text{CaO}$ ; **i)**  $\text{FeO}$  vs.  $\text{MgO}$ .

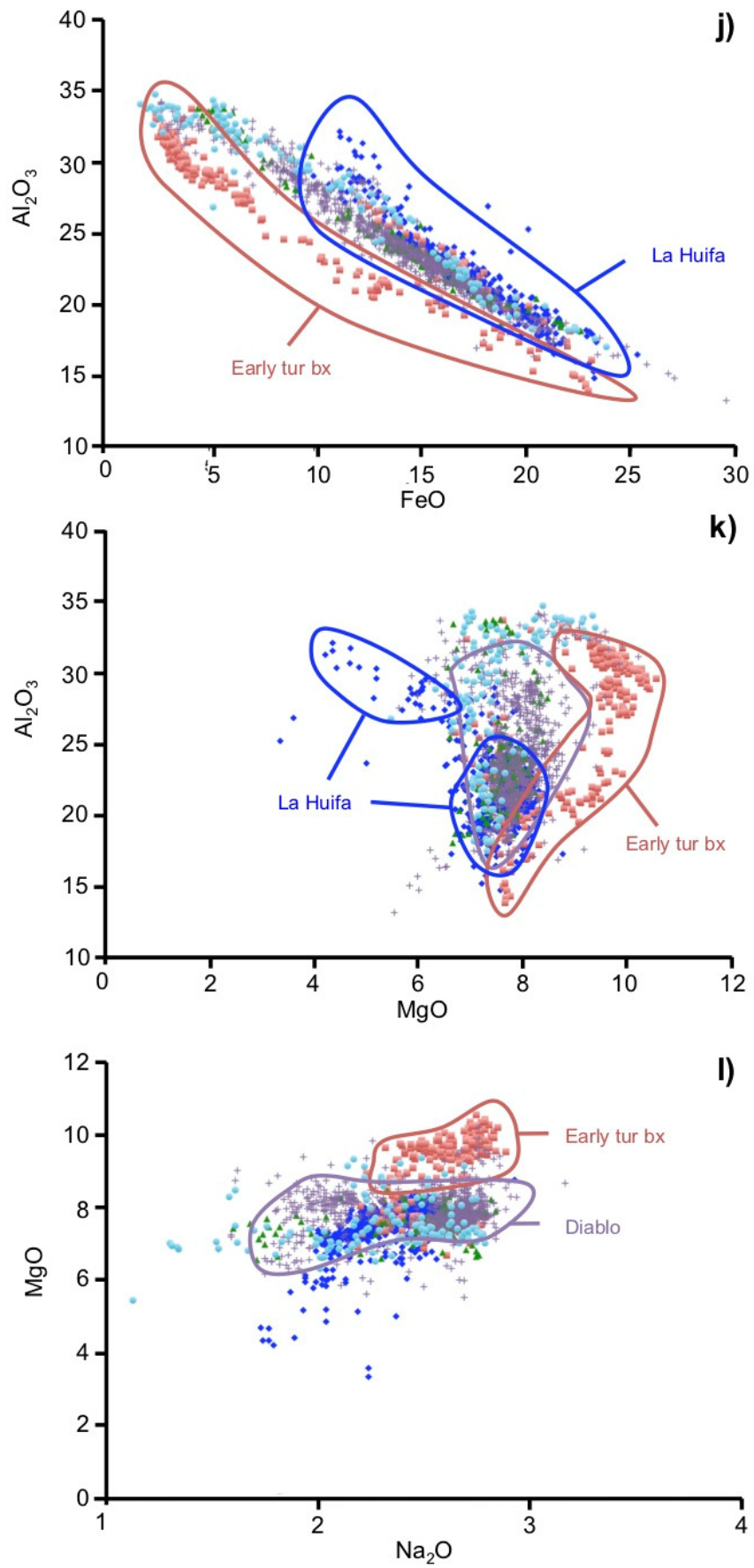


Fig. 4.35 cont. **j)** FeO vs.  $Al_2O_3$ ; **k)** MgO vs.  $Al_2O_3$ ; **l)**  $Na_2O$  vs. MgO.

**Diablo Breccias** - Tourmaline from the Diablo Breccias was sampled at different depths and distances to wall rocks to determine if there is a spatial control on its chemistry (Fig. 4.37). Drill holes sampled and their relative locations are shown in Fig. 4.36. A total of 799 EPMA analyses were undertaken. The data show significant overlaps with all other El Teniente tourmaline breccias (Fig. 4.35). Major element data are plotted in Fig. 4.37 where there appears to be a telescoping (overlap) of compositions. For example, tourmaline at greater depths is mostly classified as schorl ( $\pm$ dravite overgrowths) (e.g., Fig. 4.50). Towards the margins and central areas of the Diablo Breccias, schorl with dravite overgrowths is common and then at shallower levels dravite predominates (Fig. 4.37). Tourmalines from the margins of the Diablo Breccias display larger variations in many elements, such as SiO<sub>2</sub>, CaO and FeO.

Sample ID	Drill hole inclination	Sample depth/m	DDH depth range (Z)	Relative depth	Sample Z depth	Mineralised?	Tourmaline classification
DDH 2136_1	30°	0.90	2160-2175	LI	~2160	Well min. Cu-Mo	Schorl & dravite overgrowths
DDH 1974_1	-80°	214.1	<2160-2200	LI	<2190	Well min. Cu-Mo	Schorl & dravite overgrowths
DDH 2672_1	27.8°	94.9	2235-2255	MM	~2237	Weak Cu	Schorl & dravite overgrowths
DDH 2683_3	42°	151.6	2390-2300	MM	~2295	Mod.-well min. Cu	Schorl & dravite overgrowths
DDH 2679_2	51.65°	110.3	2280-2340	MM	~2285	Well min. Mo-Cu	Schorl & dravite overgrowths
DDH 2677_3	47°	118.0	2265-2315	MI	~2280	Well min. Cu-Mo	Schorl & dravite overgrowths
DDH 1990_6	-72°	181.3	2265-2305	MI	~2270	Weak	Dravite
DDH 2672_9	27.8°	166.6	2390-2400	HI	~2392	Well min. Cu	Dravite

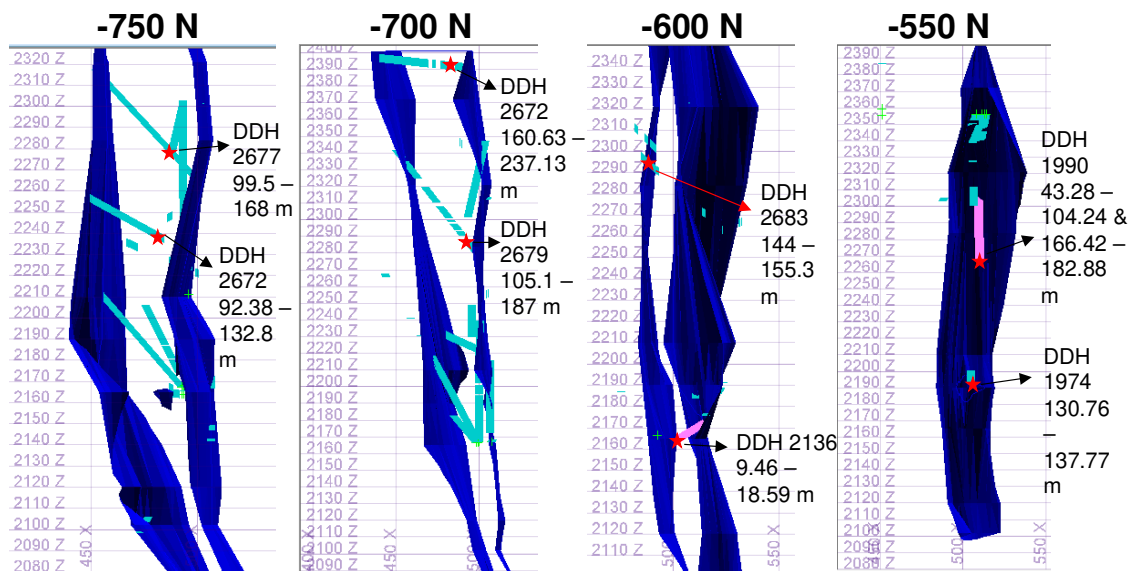


Fig. 4.36 List of Diablo drill holes and sample details with corresponding cross sections showing relative drill hole locations. Intercepts of tourmaline breccia, from which the samples were obtained, are also provided. Sections are courtesy of Codeco. Abbreviations LI= low (deep) inner, MM= middle margin, MI= middle inner and HI= high (shallow) inner. Sample photographs are shown overleaf and sample drill hole depths are shown in Appendix i.

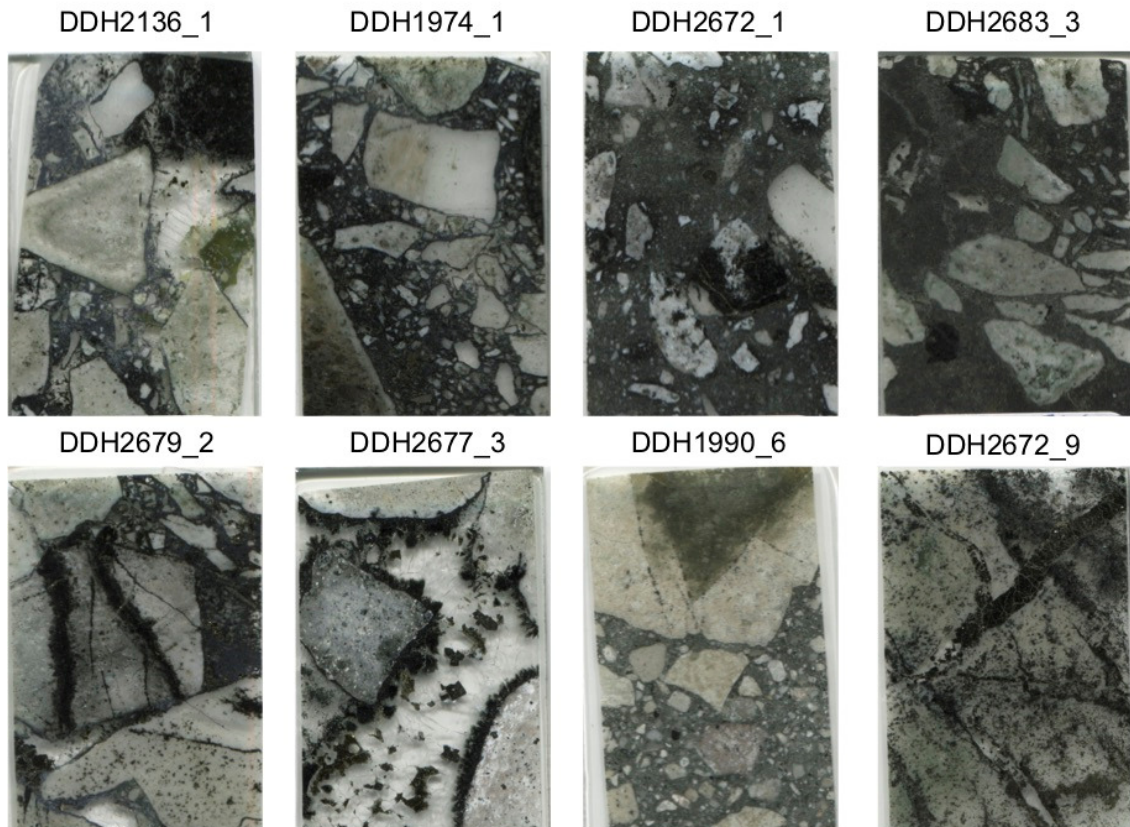


Fig. 4.36 cont. 150  $\mu\text{m}$  thick flatbed scans of the Diablo Breccia polished sections. Samples 2672\_1, 2683\_3 and 1990\_6 are microcrystalline cements compared with the others that are coarser.

From Fig. 4.37a,  $\text{SiO}_2$  and FeO show a negative correlation where  $\text{SiO}_2$  increases as FeO decreases. Tourmalines from the middle inner zone, furthest from the breccia margins, show the lowest values for FeO which range from 2.5 to 6 wt.%. Tourmalines from shallower levels in the breccia also have relatively low FeO between 7 to 11 wt.% which overlap with middle inner and middle margin tourmalines (Fig. 4.37a). Higher FeO concentrations are from tourmalines in the middle and deeper portions of the breccia being between 13 and 22 wt.% FeO, excluding outliers. Broad groupings of data are also delineated based on  $\text{SiO}_2$  contents. Tourmalines from middle inner of the breccia show the highest  $\text{SiO}_2$  values that are generally  $>36.5$  wt.% up to 38.5 wt.%. This, to a degree, overlaps with analyses from shallower levels in the breccia (36.0 to 37.5 wt.%  $\text{SiO}_2$ ). Tourmalines from the margin show the greatest degree of variation in  $\text{SiO}_2$ , ranging from 34.5 to 37.5 wt.%  $\text{SiO}_2$ . Deep-middle level tourmalines have the lowest  $\text{SiO}_2$  relative to the others (34.5 to 36.0 wt.%  $\text{SiO}_2$ ).

MgO from all locations in the breccias shows considerable scatter and no clear trend (Fig. 4.37b). Al<sub>2</sub>O<sub>3</sub> shows a positive correlation with SiO<sub>2</sub>, where middle/inner and shallower level tourmalines are comparatively enriched in Al<sub>2</sub>O<sub>3</sub> (>29 wt.% Al<sub>2</sub>O<sub>3</sub>) and SiO<sub>2</sub> (>36 wt.% SiO<sub>2</sub>) to those deeper in the breccias, which have <25 wt.% Al<sub>2</sub>O<sub>3</sub> and <36 wt.% SiO<sub>2</sub> (Fig. 4.37c). Most MnO is below detection (Fig. 4.37d). Middle, inner and deeper tourmaline analyses have similar CaO (<1.0 wt.% CaO) whereas those from the margin show considerable spread with many tourmalines comparatively CaO-enriched (>1 wt.%) (Fig. 4.37e).

TiO<sub>2</sub> is variable, and deep-middle show the highest concentrations (>1 wt.%) whilst shallower and middle inner are comparatively CaO-depleted (<1 wt.%) (Fig. 4.37e). Tourmalines from higher up in the breccias at shallower levels and on the margin are depleted in Na<sub>2</sub>O (<2.3 wt.%) relative to deeper and middle inner breccia analyses (Fig. 4.37g). The strongest correlation is between FeO and Al<sub>2</sub>O<sub>3</sub> (Fig. 4.37j), which display a negative correlation where increasing FeO is associated to decreasing Al<sub>2</sub>O<sub>3</sub>. Most elemental variability is related a combination of NaFe<sup>2+</sup>(□Al)<sub>-1</sub>, (Fe<sup>2+</sup>Fe<sup>3+</sup>)(MgAl)<sub>-1</sub> and (Fe)(Mg)<sub>-1</sub>.

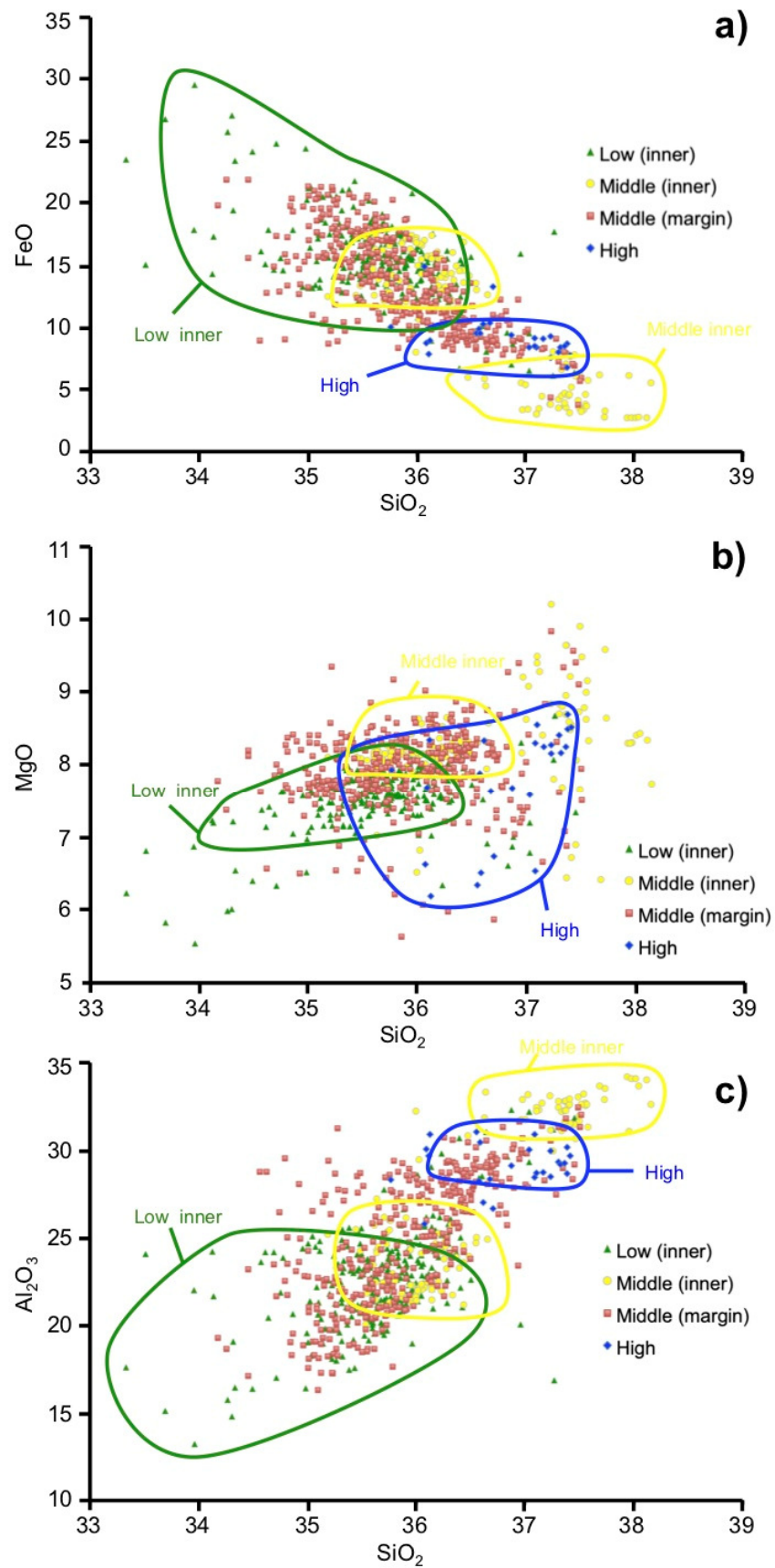


Fig. 4.37 Plots (wt.%) of Diablo Tourmaline Breccia analyses, with groupings, where present, delineated on the graphs. Tourmaline data have been split into their relative depths and positions in the breccia: **a)** SiO<sub>2</sub> vs. FeO; **b)** SiO<sub>2</sub> vs. MgO; **c)** SiO<sub>2</sub> vs. Al<sub>2</sub>O<sub>3</sub>; **d-l)** Overleaf.

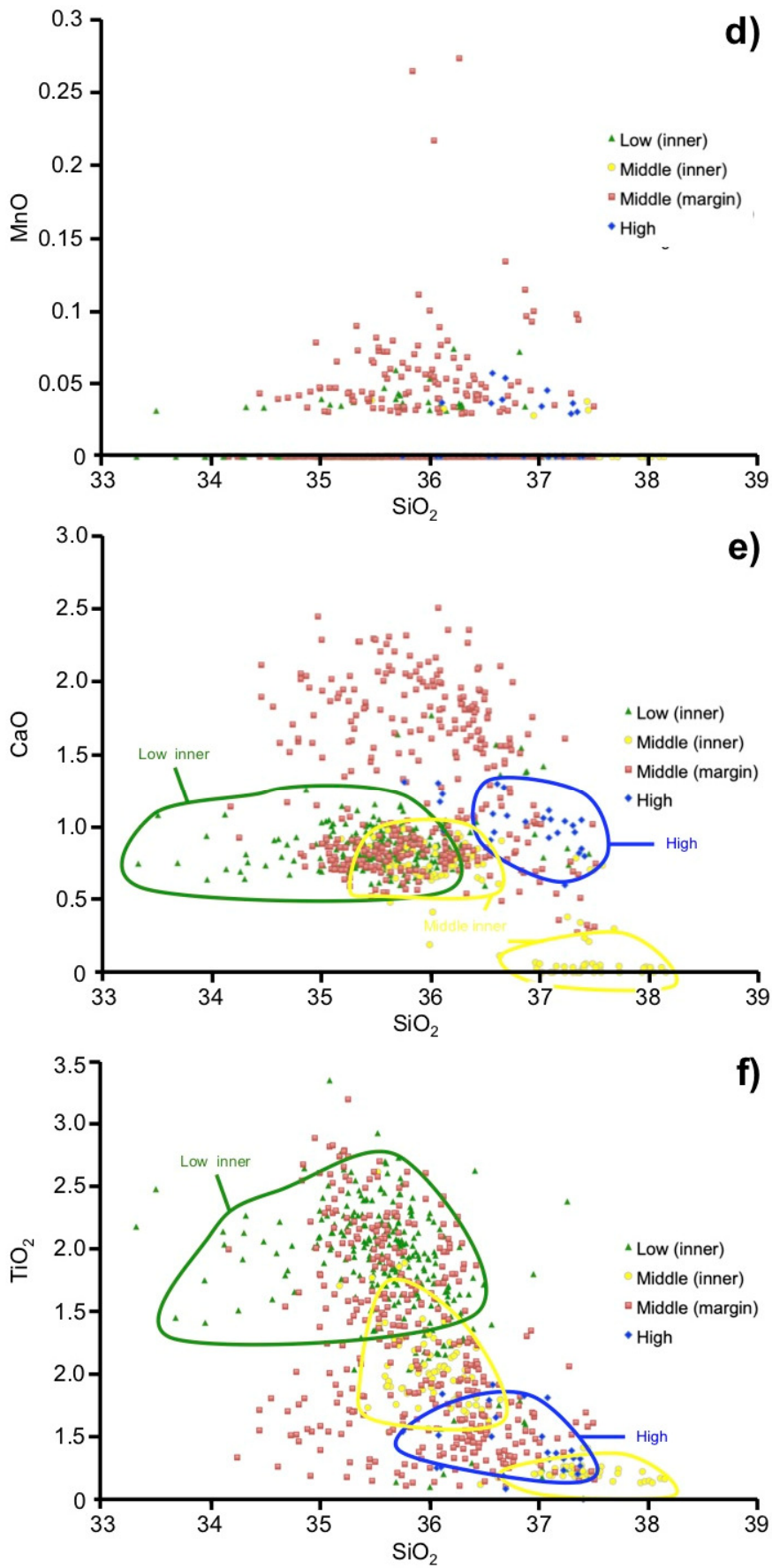


Fig. 4.37 cont. **d)** SiO<sub>2</sub> vs. MnO; **e)** SiO<sub>2</sub> vs. CaO; **f)** SiO<sub>2</sub> vs. TiO<sub>2</sub>.

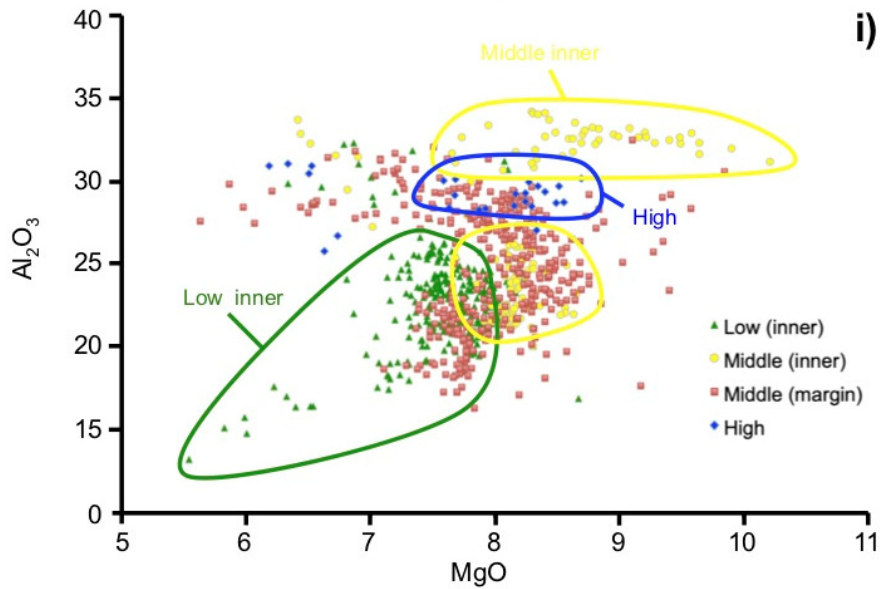
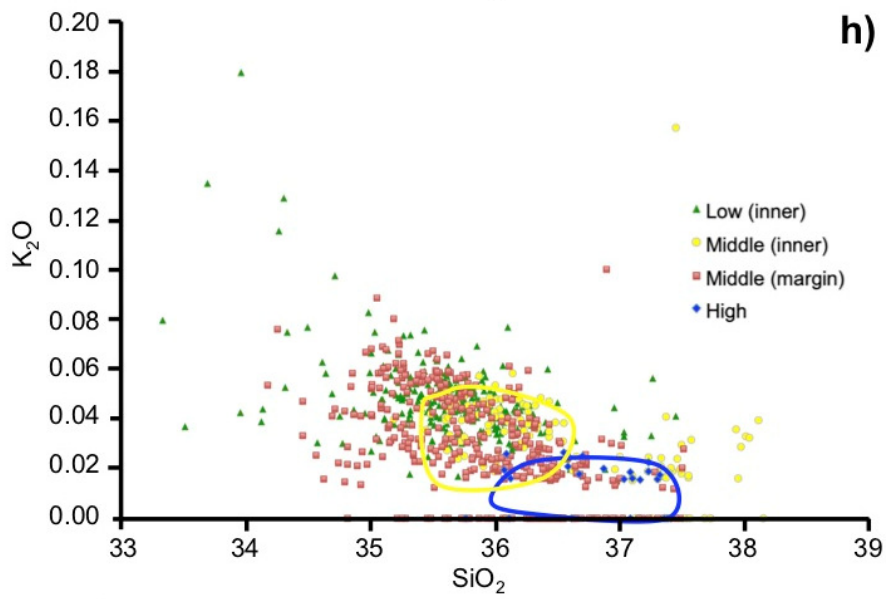
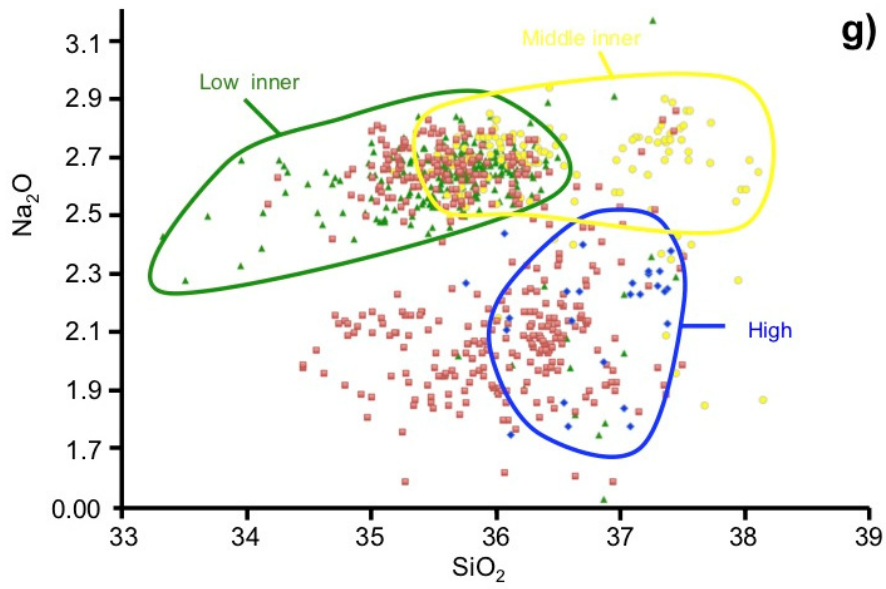


Fig. 4.37 cont. **g)** SiO<sub>2</sub> vs. Na<sub>2</sub>O; **h)** SiO<sub>2</sub> vs. K<sub>2</sub>O; **i)** MgO vs. Al<sub>2</sub>O<sub>3</sub>.

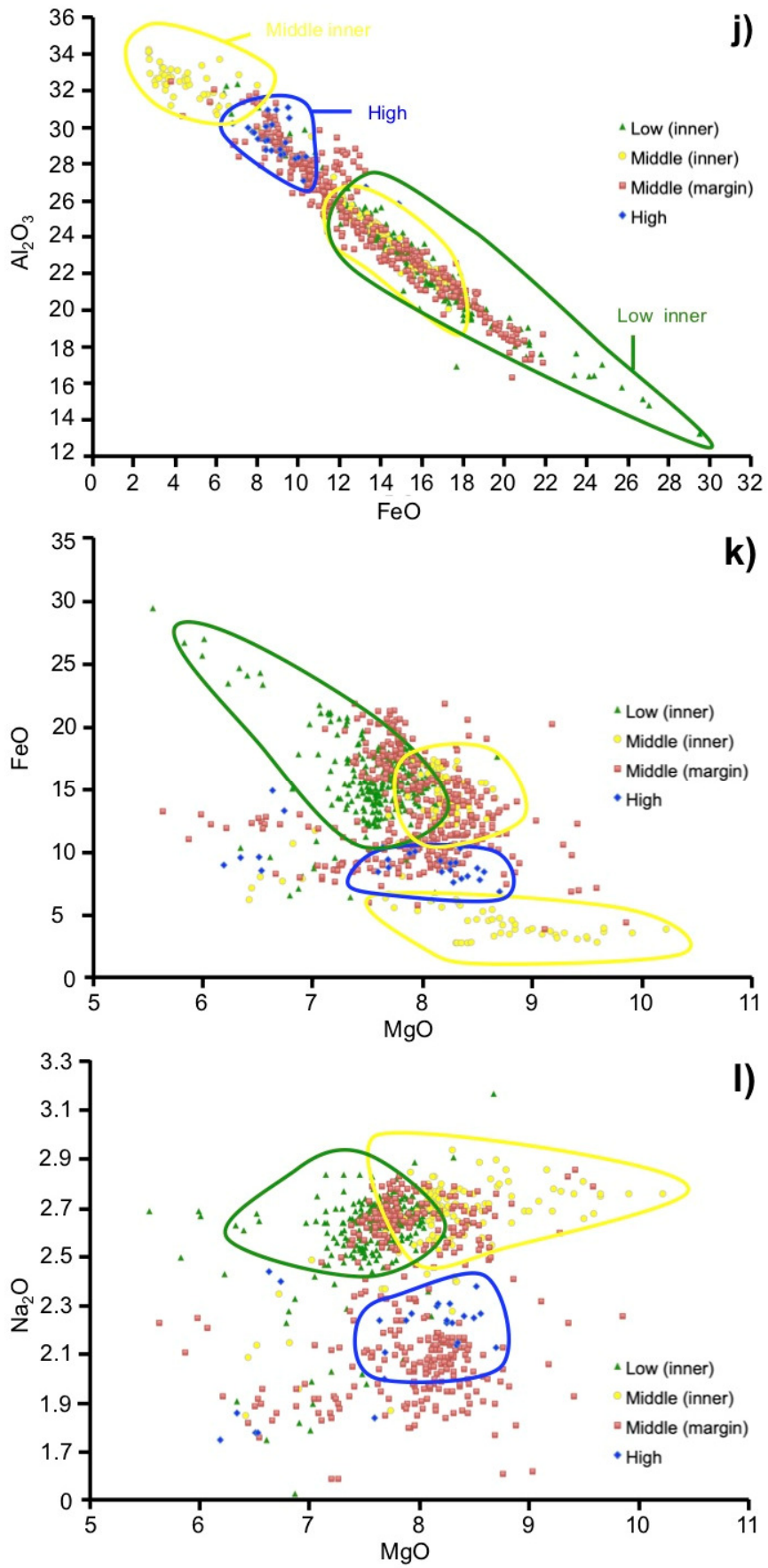


Fig. 4.37 cont. j) FeO vs. Al<sub>2</sub>O<sub>3</sub>; k) MgO vs. FeO; l) MgO vs. Na<sub>2</sub>O.

#### **4.5.2 Trace elements**

Tourmaline from the different breccias at El Teniente show similar ranges in trace element concentrations, with no breccia being particularly distinctive (e.g., Fig. 4.38). Data are shown in Table 4.9. Tourmaline generations within each breccia also, to some degree, show compositional overlaps with one another, however there are some notable exceptions, which are now described with reference to Fig. 4.38.

Table 4.9 LA-ICP-MS data for tourmaline from the five breccias analysed at El Teniente. Abbreviations include: 'Bx'= breccia, 'Tur'= tourmaline,  $\bar{X}$ = mean average of data where n is the number beneath and 'LOD'= limit of detection. Data from the Diablo Breccia have not been divided into sample depths or tourmaline generations, instead all data, termed 'bulk' have been provided.

		LA-ICP-MS data																	
Bx:	Early tur Bx				Marginal Tur Bx		Braden Tur Bx				La Huifa						Diablo		
ppm	Cement		Clast		Cement		Cement core		Overgrowths		Pitted		Non-pitted		Overgrowths		Bulk data		
	Range	$\bar{X}$ (11)	Range	$\bar{X}$ (15)	Range	$\bar{X}$ (20)	Range	$\bar{X}$ (33)	Range	$\bar{X}$ (4)	Range	$\bar{X}$ (4)	Range	$\bar{X}$ (74)	Range	$\bar{X}$ (18)	Range	$\bar{X}$ (169)	
Li	2.15-7.21	4.73	1.85-20.45	6.86	2.36-17.88	5.58	<LOD-42.33	9.15	<LOD-10.76	8.64	<LOD-4.31	4.31	<LOD-7.20	4.08	<LOD-10.22	5.56	1.85-35.81	6.54	
Sc	18.78-341.14	193.05	93.43-571.21	224.07	6.44-106.68	44.70	16.72-67.70	40.07	21.14-75.70	41.00	2.01-20.29	14.40	2.72-103.48	30.61	2.51-46.03	11.33	4.22-425.86	49.25	
V	1064.88-2895.69	1806.00	740.36-3405.28	1516.94	73.70-811.79	434.04	209.74-564.61	434.67	231.66-1742.47	699.48	209.57-381.81	273.44	176.27-613.21	335.01	162.70-372.87	255.21	65.15-2559.95	659.07	
Cr	<LOD-611.76	276.47	33.46-545.20	146.57	<LOD-152.17	46.64	<LOD-414.33	61.75	<LOD-26.90	19.98	<LOD-19.52	12.22	<LOD-194.88	30.27	82.51	22.95	<LOD-343.86	32.12	
Mn	15.20-88.89	34.72	11.38-116.84	42.95	7.33-449.51	160.44	55.72-125.17	75.19	54.97-99.37	84.12	47.46-317.70	124.95	62.05-283.20	90.21	38.63-523.20	111.80	9.80-537.97	125.62	
Co	6.16-21.62	11.05	3.35-19.97	8.93	6.65-26.59	17.40	6.83-25.13	16.66	7.35-20.28	13.05	20.19-28.13	23.64	14.50-34.37	25.63	1.28-45.72	22.08	1.04-43.72	18.86	
Ni	38.70-61.73	51.03	27.41-49.03	38.34	19.28-90.58	41.50	9.66-45.25	34.90	11.40-38.62	25.01	26.22-60.67	37.13	7.92-54.04	31.68	<LOD-50.58	28.01	5.24-59.31	36.72	
Cu	<LOD	<LOD	<LOD	<LOD	<LOD-3.81	3.81	<LOD-26.64	16.95	<LOD-114.91	68.88	<LOD-11.96	11.96	<LOD-15.16	15.16	<LOD-99.70	33.33	<LOD-40.57	17.89	
Zn	<LOD-20.91	13.23	<LOD-22.57	13.91	<LOD-108.63	54.05	<LOD-73.12	27.55	25.81-39.04	33.88	10.05-165.55	68.59	13.72-206.58	39.37	10.29-507.67	80.84	<LOD-199.50	28.56	
Pb	<LOD-1.66	0.87	<LOD-2.10	0.84	<LOD-5.15	2.37	<LOD-7.30	2.08	1.10-2.41	1.89	1.50-8.80	4.80	<LOD-11.91	3.00	0.68-20.34	7.66	<LOD-7.55	1.58	
Mo	<LOD	<LOD	<LOD-0.76	0.60	<LOD-4.33	2.64	<LOD-2.10	1.51	<LOD	<LOD	<LOD	<LOD	<LOD-0.76	0.59	<LOD-2.19	1.93	<LOD-28.01	13.06	
Sn	19.99-70.88	48.82	16.04-201.72	57.04	<LOD-35.65	12.19	<LOD-105.71	20.73	13.24-33.99	23.41	1.55-4.98	2.97	<LOD-32.17	4.96	<LOD-12.48	3.82	<LOD-135.12	22.07	
As	25.84-443.17	171.19	48.94-356.74	161.54	<LOD-498.51	129.77	<LOD-157.51	79.13	12.25-108.51	46.80	<LOD-99.52	99.52	<LOD-762.68	124.42	<LOD-764.45	286.27	<LOD-780.53	182.99	
Rb	<LOD	<LOD	<LOD	<LOD	<LOD-3.71	2.92	<LOD-5.10	4.42	<LOD	<LOD	<LOD	<LOD	<LOD	<LOD	<LOD	<LOD	<LOD-3.31	2.57	
Nb	<LOD-2.25	0.93	<LOD-4.38	1.25	<LOD-3.88	1.09	<LOD-6.90	2.84	<LOD-1.91	1.18	<LOD-0.83	0.45	<LOD-2.60	0.55	<LOD-0.82	0.42	<LOD-6.65	2.12	

		LA-ICP-MS data																	
Bx:	Early tur Bx				Marginal Tur Bx		Braden Tur Bx				La Huifa						Diablo		
ppm	Cement		Clast		Cement		Cement core		Overgrowths		Pitted		Non-pitted		Overgrowths		Bulk data		
	Range	$\bar{X}$ (11)	Range	$\bar{X}$ (15)	Range	$\bar{X}$ (20)	Range	$\bar{X}$ (33)	Range	$\bar{X}$ (4)	Range	$\bar{X}$ (4)	Range	$\bar{X}$ (74)	Range	$\bar{X}$ (18)	Range	$\bar{X}$ (169)	
Y	0.29-5.34	2.20	0.35-50.43	9.99	0.22-140.54	14.19	0.28-124.77	21.11	4.48-53.34	23.02	<LOD-24.69	13.95	<LOD-48.60	8.94	<LOD-38.58	12.06	<LOD-153.28	18.62	
La	1.11-77.13	15.50	1.24-67.15	19.61	<LOD-30.11	4.61	0.31-13.55	5.46	0.98-5.66	3.71	0.70-3.37	1.67	0.83-13.51	2.54	0.53-13.74	5.33	<LOD-25.92	6.83	
Ce	1.55-108.66	22.77	2.28-93.63	27.15	0.14-57.57	6.91	0.38-20.48	8.41	1.27-12.13	6.34	0.92-3.58	1.73	0.55-22.89	2.36	0.69-22.38	8.69	<LOD-41.25	10.17	
Pr	<LOD-8.67	2.11	0.27-7.81	2.20	<LOD-6.30	1.12	<LOD-1.80	0.86	0.24-1.65	0.74	<LOD-0.29	0.29	<LOD-2.46	0.31	<LOD-2.41	1.01	<LOD-3.73	1.14	
Nd	<LOD-21.33	8.89	<LOD-21.50	6.49	<LOD-22.19	5.63	<LOD-6.09	2.87	<LOD-5.74	3.50	<LOD-0.89	0.73	<LOD-8.98	2.58	<LOD-8.71	4.12	<LOD-11.35	3.80	
Sm	<LOD-1.63	1.28	<LOD-1.68	1.21	<LOD-3.30	1.84	<LOD-2.17	1.23	<LOD-1.16	1.16	<LOD	<LOD	<LOD-1.77	0.96	<LOD-1.92	1.18	<LOD-3.30	1.12	
Eu <sup>151</sup>	<LOD-0.40	0.26	<LOD-0.39	0.34	<LOD-0.51	0.34	<LOD-1.53	0.39	<LOD-0.45	0.45	<LOD	<LOD	<LOD-0.29	0.24	<LOD-0.56	0.32	<LOD-0.71	0.30	
Eu <sup>153</sup>	<LOD-0.39	0.39	<LOD-0.38	0.33	<LOD-0.60	0.38	<LOD-0.78	0.33	<LOD	<LOD	<LOD	<LOD	<LOD-0.20	0.17	<LOD-0.30	0.23	<LOD-0.73	0.29	
Gd	<LOD-0.74	0.65	<LOD-1.37	0.87	<LOD-5.87	2.01	<LOD-3.79	1.23	<LOD-3.65	2.41	<LOD	<LOD	<LOD-1.24	0.93	<LOD-1.97	1.16	<LOD-9.46	1.54	
Tb	<LOD	<LOD	<LOD-0.33	0.24	<LOD-1.73	0.58	<LOD-1.08	0.40	<LOD-0.79	0.50	<LOD	<LOD	<LOD-0.36	0.22	<LOD-0.44	0.21	<LOD-2.70	0.34	
Dy	<LOD-0.43	0.42	<LOD-3.41	1.33	<LOD-17.39	4.01	<LOD-10.41	2.23	0.27-7.39	2.75	<LOD-2.27	2.27	<LOD-5.08	2.97	<LOD-4.54	1.91	<LOD-23.04	2.80	
Ho	<LOD-0.18	0.13	<LOD-1.16	0.47	<LOD-4.69	0.97	<LOD-4.78	0.95	<LOD-1.98	1.06	<LOD-0.75	0.75	<LOD-1.72	0.92	<LOD-1.54	0.52	<LOD-5.53	0.94	
Er	<LOD-1.38	0.73	<LOD-6.93	1.79	<LOD-16.82	4.30	<LOD-19.83	3.42	0.78-6.34	3.21	<LOD-3.92	2.27	<LOD-7.20	2.51	<LOD-7.08	2.41	<LOD-18.90	3.90	
Tm	<LOD-0.32	0.19	<LOD-1.54	0.48	<LOD-2.54	0.77	<LOD-4.32	0.93	0.12-0.92	0.56	<LOD-0.64	0.41	<LOD-1.36	0.56	<LOD-1.28	0.50	<LOD-3.20	0.79	
Yb	<LOD-2.80	1.55	<LOD-16.48	5.10	<LOD-15.00	3.92	<LOD-31.67	5.67	1.16-6.66	4.40	<LOD-3.96	2.65	<LOD-10.99	2.39	<LOD-8.80	3.69	<LOD-25.95	5.89	
Lu	<LOD-0.63	0.40	<LOD-3.67	0.88	<LOD-2.27	0.59	<LOD-5.72	1.04	0.37-1.31	0.83	<LOD-0.77	0.52	<LOD-1.49	0.48	<LOD-1.41	0.70	<LOD-4.02	1.01	
Y+REE	5.12-227.20	49.72	4.99-229.24	72.91	1.12-232.20	35.92	1.37-221.62	50.45	9.66-108.94	49.96	1.85-38.37	14.49	1.53-88.90	11.72	2.39-82.38	37.47	0.37-259.77	49.41	

LA-ICP-MS data: Diablo																
Bx	Deep inner				Middle Inner						Middle Margin				Shallow	
ppm	2136_1		1974_1		2677_3		1990_6		2672_1		2683_3		2679_2		2672_9	
	Range	$\bar{X}$ (19)	Range	$\bar{X}$ (22)	Range	$\bar{X}$ (27)	Range	$\bar{X}$ (6)	Range	$\bar{X}$ (40)	Range	$\bar{X}$ (26)	Range	$\bar{X}$ (16)	Range	$\bar{X}$ (13)
Li	2.07-21.03	7.63	1.98-2.45	2.20	1.77-35.81	10.17	3.16-23.45	8.10	3.14-8.73	5.93	3.08-12.00	6.62	2.07-4.13	3.03	2.22-3.26	2.74
Sc	41.29-112.17	70.93	12.11-195.59	45.84	16.46-65.51	32.61	19.96-50.21	30.15	4.22-117.47	32.49	16.88-56.94	33.10	28.88-229.80	96.79	8.67-425.86	77.22
V	284.88-1059.12	784.09	211.48-2559.95	847.98	261.42-1026.77	540.94	65.15-444.14	184.96	297.67-2048.81	586.56	297.99-1818.38	652.85	480.78-1759.20	844.77	333.61-1655.91	557.48
Cr	4.41-53.95	17.04	2.38-19.85	7.32	2.64-72.72	24.26	15.77-27.78	20.04	7.95-105.03	28.32	4.81-93.78	39.39	7.36-193.84	64.48	7.27-343.86	66.94
Mn	51.13-138.60	70.45	53.52-354.63	131.08	33.90-389.85	74.08	9.80-83.84	26.38	48.55-537.97	241.42	63.82-147.74	80.74	45.12-79.33	61.72	44.40-244.91	116.75
Co	4.58-21.00	16.27	13.24-43.72	21.27	5.44-18.17	13.47	1.04-14.59	3.70	8.16-39.82	25.76	8.81-18.40	15.93	10.51-17.02	13.03	11.67-43.57	22.89
Ni	6.54-41.70	32.63	17.43-40.72	31.81	5.24-53.67	37.93	6.35-28.19	11.51	23.74-48.68	34.41	40.62-59.31	51.83	38.13-56.35	45.73	15.38-48.88	27.96
Cu	0	0	2.06-53.13	14.06	0	0	0	0	33.71-33.71	33.71	13.91-13.91	13.91	0	0	0	0
Zn	11.14-72.90	18.39	11.12-70.50	30.06	7.52-28.74	15.44	8.02-19.13	13.57	9.82-199.50	42.74	9.41-27.64	17.31	10.44-56.92	20.13	12.15-138.51	44.71
Pb	0.62-2.04	1.24	0.33-2.82	1.41	0.49-4.08	1.26	0.67-2.67	1.32	0.54-7.55	1.79	0.86-4.86	1.96	0.73-6.44	1.72	0.54-2.83	1.18
Mo	0	0	28.01-28.01	28.01	0	0	0	0	0	0	2.58-6.42	4.50	15.23-15.23	15.23	0	0
Sn	3.83-135.12	42.28	1.71-120.81	30.42	3.46-35.47	13.46	1.38-9.34	4.04	1.50-58.72	12.80	5.38-87.36	20.15	6.60-100.77	27.77	1.52-13.51	5.21
As	21.90-271.41	105.59	8.77-150.93	73.51	24.02-477.99	216.46	17.67-358.88	125.08	40.40-780.53	300.92	28.09-242.63	123.06	114.90-451.35	291.40	13.22-264.94	70.36
Rb	3.31-3.31	3.31	0	0	0	0	0	0	2.14-2.49	2.33	0	0	0	0	0	0
Nb	1.61-6.65	3.18	0.08-3.35	2.42	0.28-3.35	1.84	0.70-0.70	0.70	0.19-2.39	0.69	0.96-4.39	2.92	1.79-3.95	2.68	0.34-3.46	1.90
Y	3.64-122.78	36.06	0.51-50.78	15.13	2.08-153.28	22.93	0.64-1.38	0.86	0.31-32.80	2.55	8.21-119.45	32.39	7.15-44.79	20.59	0.37-64.02	9.61
La	1.78-	9.99	0.20-	6.36	0.74-	9.64	0.36-1.45	0.70	0.20-	2.89	2.65-	8.44	6.26-	14.05	0.19-	2.00

LA-ICP-MS data: Diablo																
Bx	Deep inner				Middle Inner						Middle Margin				Shallow	
ppm	2136_1		1974_1		2677_3		1990_6		2672_1		2683_3		2679_2		2672_9	
	Range	$\bar{X}$ (19)	Range	$\bar{X}$ (22)	Range	$\bar{X}$ (27)	Range	$\bar{X}$ (6)	Range	$\bar{X}$ (40)	Range	$\bar{X}$ (26)	Range	$\bar{X}$ (16)	Range	$\bar{X}$ (13)
	20.26		13.74		20.00				25.92		14.07		22.99		12.70	
Ce	3.03-33.44	14.60	0.56-20.04	9.27	1.66-33.01	15.51	0.65-2.95	1.35	0.20-41.25	3.91	4.05-20.38	12.51	9.13-36.93	22.80	0.24-20.10	3.16
Pr	0.30-3.06	1.18	0.08-1.68	0.98	0.25-3.40	1.48	0.12-0.30	0.21	0.13-3.73	0.59	0.31-2.11	1.14	0.74-3.51	2.12	0.20-1.84	0.80
Nd	0.93-8.82	3.32	0.39-5.08	2.67	0.90-10.81	4.74	0.94-1.37	1.16	0.99-11.06	4.49	0.84-6.30	3.15	2.52-11.35	6.25	0.51-6.94	2.71
Sm	0.42-1.05	0.79	0.46-0.84	0.65	0.63-2.04	1.05	0.46-0.46	0.46	1.19-1.19	1.19	3.30-3.30	3.30	0.62-1.38	1.01	0	0
Eu <sup>151</sup>	0.18-0.42	0.26	0.22-0.39	0.29	0.20-0.71	0.34	0	0	0	0	0-0.41	0.30	0.12-0.42	0.31	0.16-0.29	0.21
Eu <sup>153</sup>	0.15-0.40	0.26	0.20-0.35	0.27	0.19-0.73	0.40	0	0	0	0	0.23-0.37	0.28	0.21-0.38	0.28	0.15-0.37	0.26
Gd	0.36-3.19	1.07	0.31-1.01	0.65	0.54-7.99	1.80	0.35-0.50	0.42	0	0	0.30-9.46	2.46	0.38-1.52	0.92	0.87-2.95	1.91
Tb	0.10-1.05	0.29	0.07-0.37	0.18	0.06-2.30	0.38	0	0	0.19-0.28	0.24	0.06-2.70	0.47	0.11-0.44	0.19	0.14-0.88	0.51
Dy	0.50-11.22	3.12	0.80-3.91	1.65	0.59-23.04	3.02	0.30-0.30	0.30	0.50-2.68	1.07	0.68-21.79	3.52	0.80-4.28	1.88	0.76-8.20	2.75
Ho	0.16-3.85	1.19	0.32-1.68	0.74	0.05-5.53	0.81	0	0	0.13-1.07	0.40	0.35-4.99	1.18	0.22-1.39	0.68	0.14-2.41	0.69
Er	0.71-17.07	5.68	1.88-7.46	3.72	0.48-18.90	3.15	0.29-0.29	0.29	0.70-4.75	1.76	1.35-10.85	4.42	0.84-6.37	3.18	0.28-8.11	2.07
Tm	0.30-3.20	1.33	0.38-1.58	0.84	0.11-2.86	0.59	0.05-0.13	0.09	0.11-0.73	0.25	0.30-1.38	0.82	0.21-1.42	0.63	0.23-1.30	0.57
Yb	0.88-25.95	9.71	0.31-12.89	6.12	0.55-19.28	3.93	0	0	0.41-8.55	2.31	1.67-14.13	6.73	1.47-11.40	5.40	0.34-7.45	2.69
Lu	0.14-4.02	1.67	0.14-2.76	1.15	0.13-2.21	0.62	0.11-0.11	0.11	0.08-1.59	0.54	0.27-2.51	1.03	0.25-2.22	0.96	0.17-1.68	0.62
Y+REE	13.95-225.81	87.90	1.16-95.46	43.36	17.04-259.03	67.34	0-6.84	0.49	1.17-136.60	11.16	23.91-194.81	76.84	42.59-148.11	79.97	0.37-109.98	21.15

The concentrations of different trace and rare earth elements within, and between tourmalines, can vary by several orders of magnitude, with the lowest often being below detection limits. Several elements such as Li, Ni, Pb, Zn and Sn mostly have relatively low concentrations of <100 ppm although a number of tourmalines do have up to 500 and 210 ppm Zn and Sn, respectively. There are higher median concentrations of Sc, Cr, Mn, and As (10 s to several hundred ppm), however V and Ti regularly reach >1,000 ppm (Fig. 4.38c, d). Cu, Mo and Rb are mostly below detection limits in all breccias (Table 4.9). Later generations of tourmaline, described earlier in the petrography section as fibrous overgrowths on coarser tourmaline crystals, are often enriched in many trace and rare earth elements (e.g., Zn, As, Y, Tb, Sm) relative to other tourmaline generations. Some fibrous overgrowths are however depleted in a number of elements (e.g., Ni, Ti, Co).

Mn, Pb and Nb do not show any trends with most analyses from all breccias containing <150 ppm Mn (can be up to 540 ppm) and those above, are linked to specific crystal traverses, or samples with no consistent difference between tourmaline generations present. Pb concentrations in tourmaline from all breccias are similar, with most tourmalines containing <10 ppm Pb although a number of analyses, mostly from La Huifa (some of the later overgrowths) contain up to 21 ppm Pb. Cu, Mo and Rb are mostly below detection in all of the Teniente breccias and analyses above detection are either related to specific traverses, overgrowths or individual points.

Tourmalines from all El Teniente breccias contain <50 ppm Li (and a number below detection), with little variation within or between breccias (Fig. 4.38a). Those from the La Huifa, Diablo and Braden Tourmaline Breccia (BTB) contain <10 ppm Li. In the Early Tourmaline Breccia (ETB), Li concentrations in clast- and cement-hosted tourmaline overlap. In the Marginal Tourmaline Breccia (MTB), they range from below detection to 5 ppm, except sample 1694\_12 which is relatively enriched compared with other MTB samples containing >6 ppm Li. Overgrowths are not consistently enriched relative to earlier generations.

Sc concentrations (Fig. 4.38b) are largely <100 ppm for all breccias except the ETB (both clast and cement tourmalines) which range up to 571 ppm. Little variation between samples is present in the La Huifa, Braden Tourmaline and Diablo Breccias or between clast and cement-hosted tourmalines in the ETB. Overgrowths in La Huifa and the BTB are largely depleted in Sc whilst overgrowths in the Diablo Breccia are neither consistently enriched nor depleted.

Tourmaline Ti concentrations from El Teniente vary from a few hundred up to 22,000 ppm and lower concentrations in the La Huifa, BTB and Diablo (e.g., sample 2677\_3) breccias are largely associated with later stage overgrowths (Fig. 4.38c). Clast and

cement tourmaline from the ETB overlap and both show very high Ti values up to 22,000 ppm, despite no inclusions being observed. Within the BTB, all but one analysis from sample 1754\_15 cluster tightly between 1,500 and 2,500 ppm Ti, whereas most analyses from sample 1754\_13 range between 3,500 and 9,500 ppm Ti. The Diablo Breccias contain Ti-enriched samples such as 2683\_3 (12,250 to 7,000 ppm), 2136\_1 (7,500 to 9,500 ppm) and 2679\_2 (6,250 to 10,250 ppm) compared to Ti-depleted samples 1990\_6 (600 to 1,200 ppm), 2672\_9 (50 to 2,750 ppm) and there is a bimodal distribution of data in sample 1974\_1 (1,000 to 3,000 ppm and to >5,000 ppm). The MTB contains <4,000 ppm Ti, except sample 1694\_20, which is comparatively, enriched containing between 8,000 and 9,500 ppm Ti.

V contents of tourmalines from La Huifa and the BTB have the least variation in V ranging from 160 to 610 ppm and show no disparity between samples or generations (Fig. 4.38d). The ETB tourmalines have the largest range and are relatively V-enriched (~750 to 3,400 ppm) compared to most tourmalines from the other breccias. Tourmalines from the Diablo Breccia mostly contain between 200 and 1,100 ppm V except sample 1990\_6, which is comparatively depleted (<200 ppm V), show inter-sample variation and later overgrowths are neither enriched nor depleted. For example three clusters are present sample 1974\_1 relating to traverse 1 (550 to 2,550 ppm V), traverse 2 (~600 to 900 ppm V) and traverses 3 and 4 (<500 ppm V). The MTB shows minor variation between samples, with sample 1694\_12 depleted (<200 ppm V) compared to the other samples that contain >250 ppm V.

Tourmaline from the Teniente breccias mainly contain <150 ppm Cr except the ETB which is enriched relative to other breccias (up to ~620 ppm Cr; Fig. 4.38e). The BTB and Diablo Breccias display the most inter- and intra-sample variation such as samples 1754\_15 and 1754\_13 of the BTB are enriched (up to 144 ppm) and depleted (<77 ppm) relative to each other, respectively. In the Diablo, samples 2672\_1 (<110 ppm), 2683\_3 (<100 ppm) and 2679\_2 (<200 ppm) have the largest range in Cr. Intra-sample variation is present in samples 2672\_2 and 2677\_3, the latter showing two progressive decreases in Cr from ~60 ppm at the beginning to ~below detection at the end of crystal traverses. Samples from the MTB show different ranges, with sample 1213 of the MTB shows the greatest range (up to 155 ppm Cr) and 1694\_20 having the smallest range (<30 ppm Cr).

Sn concentrations of tourmaline from all El Teniente breccias are <210 ppm (Fig. 4.38f). La Huifa tourmalines have the smallest range (<18 ppm) showing no variation between samples or generations. Tourmaline overgrowths in the other breccias are also not significantly or consistently enriched or depleted relative to the earlier tourmalines. The ETB tourmaline analyses contain between 16 and 85 ppm Sn with

two higher values of ~165 and ~205 ppm Sn, the latter associated with a dravite overgrowth/tip. The BTB samples show distinct differences between samples, with sample 1754\_15 being relatively Sn-depleted (<9.5 ppm) compared with sample 1754\_13 (3 to 34 ppm and up to 105 ppm Sn). Most tourmalines from the Diablo Breccias contain <40 ppm Sn, and sample 1974\_1 has a bimodal distribution reflecting traverses 3 and 4 (<5 ppm) and traverses 1 and 2 (14 to 52 ppm). Samples from the MTB are mostly <20 ppm and Sn levels largely overlap.

The majority of tourmalines from the Teniente breccias analysed in this study contain <100 ppm Zn (Fig. 4.38g). The exception to this are a number of the later stage overgrowths in the La Huifa breccia which contain up to a few hundred ppm Zn and samples 2672\_1 (traverses 1 and 2 contain up to 200 ppm) and 2672\_9 (traverse 2 up to 140 ppm) from the Diablo Breccias.

El Teniente breccia tourmalines contain similar amounts of Ni (mainly <65 ppm; (Fig. 4.38h)). La Huifa tourmalines show intra-sample variation such as sample ES026\_8 contains two groups equating to traverses 1 and 6 (15 to 27 ppm Ni) and traverses 3, 4 and 5 (27 to 50 ppm Ni). These traverses in sample ES026\_8 are associated to same generation/paragenetic period of growth. Some of the higher Ni concentrations (e.g., >45 ppm) at La Huifa, in particular samples ES026\_9 and ES026\_8 correspond with analyses just before and some within overgrowths. But many of the lower Ni concentrations (e.g., <15 ppm) in the La Huifa samples ES026\_8 and ES026\_6 are also related to overgrowths (Fig. 4.38h). Ni-depleted overgrowths are also observed in the BTB (sample 1754\_13) and in some samples of the Diablo Breccias (e.g., 2677\_3). Intra-and inter-sample variation is present within samples from the Diablo Breccias such as the bimodal distribution in sample 1974\_1 where Ni-enriched analyses (35 to 40 ppm) are associated with traverses 1 and 2 and depleted analyses (17 to 25 ppm Ni) are from traverses 3 and 4. Sample 1990\_6 tourmalines are depleted (<10 ppm Ni) compared with other samples from the Diablo Breccias.

Tourmaline Co contents in all El Teniente breccias analysed are <46 ppm (Fig. 4.38i). La Huifa tourmalines contain between 17 and 35 ppm Co with little disparity between samples and overgrowths are neither consistently enriched nor depleted. La Huifa tourmalines are comparatively enriched to the ETB (~4 to 22 ppm) BTB (6 to 25 ppm Co), many tourmalines of the Diablo (4 to 44 ppm) and the MTB (~6 to 26 ppm). Sample 1990\_6 of the Diablo is relatively depleted (1 to 2.7 ppm) and intra-sample variation is present in sample 2677\_3 with each traverse progressively increasing in Co from 11 to 19 ppm. The later overgrowths in these traverses are Co-depleted (<11 ppm).

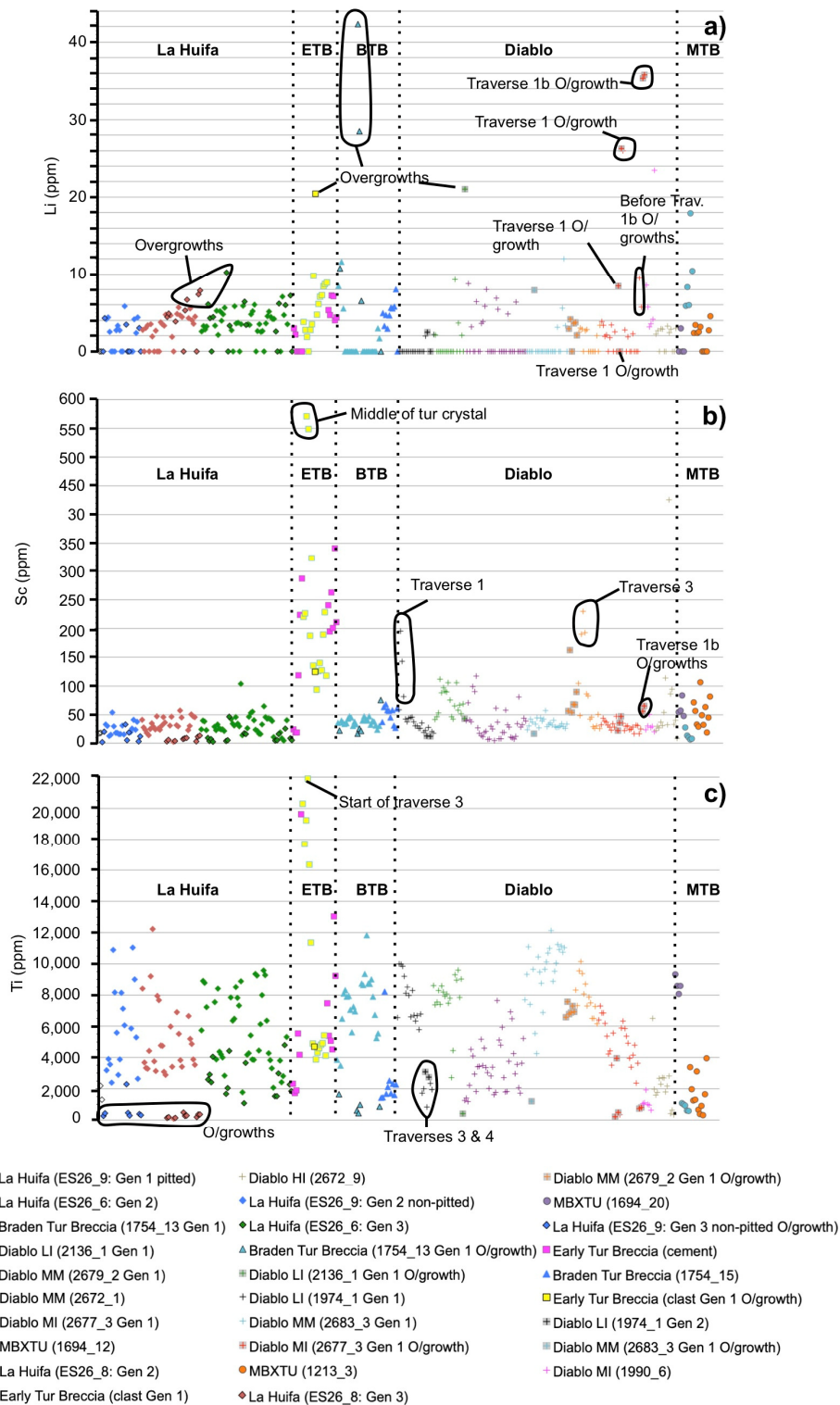


Fig. 4.38 Tourmaline minor and trace element LA-ICP-MS data from the five El Teniente tourmaline breccias selected in this study. Each breccia has been subdivided into samples and, in the case of the Early Tourmaline Breccia (ETB), where only one sample was collected, it has been divided into clast- or cement-hosted tourmaline. Sample details are provided in Appendices i and ii. Abbreviations are as follow: P.T.= Pitted Tourmaline: the first generation of tourmaline at La Huifa which is now pitted and embayed; O/growth= fibrous tourmaline overgrowths, the last generation of tourmaline to form in the breccias. Diablo key abbreviations are as follows: LI= low (deep) inner, MM= middle margin, MI= middle inner, HI= high (shallow) inner: **a)** Li; **b)** Sc; **c)** Ti; **d-f)** Overleaf. Vertical lines separate the five breccias analysed, from left to right as follows: La Huifa, ETB, Braden Tourmaline Breccia (BTB), Diablo breccias and the Marginal Tourmaline Breccia (MTB).



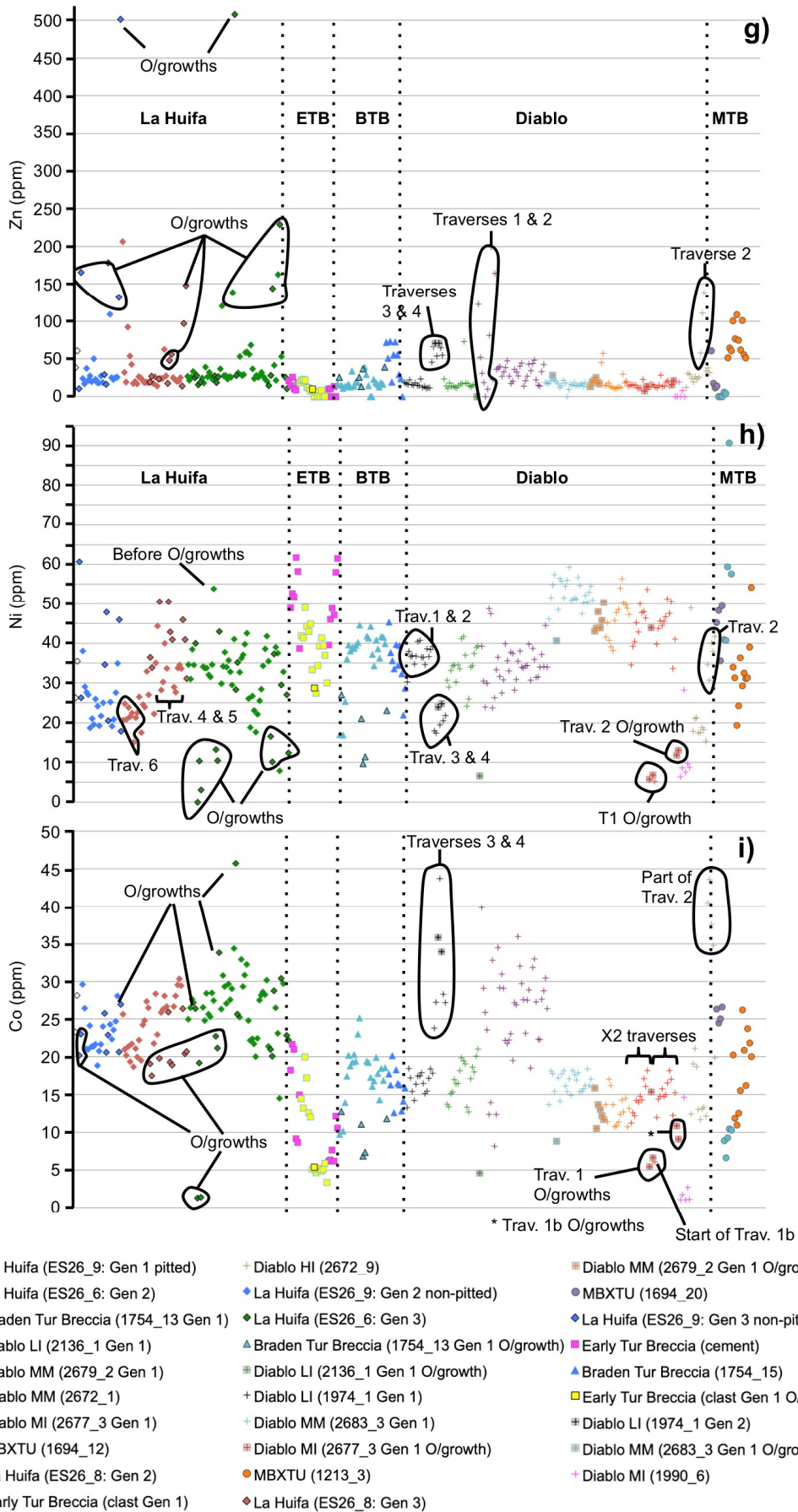


Fig. 4.38 cont. Minor and trace element LA-ICP-MS tourmaline data from the five El Teniente tourmaline breccias selected in this study: **g)** Zn; **h)** Ni; **i)** Co; **j)** Overleaf.

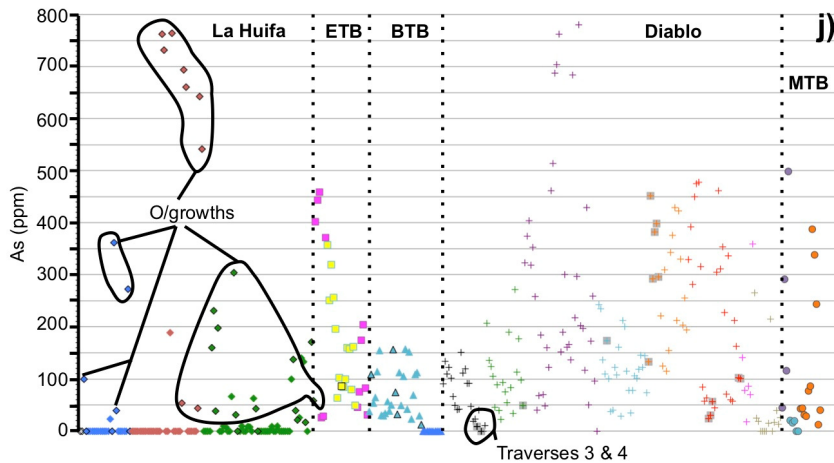


Fig. 4.38 cont. Minor and trace element LA-ICP-MS tourmaline data from the five El Teniente tourmaline breccias selected in this study: j) As.

El Teniente tourmalines contain a wide range of As concentrations between and within breccias from below detection up to ~800 ppm (Fig. 4.38j). La Huifa tourmaline As contents is below detection and where above they are largely associated with overgrowths. The BTB samples show distinct differences between sample 1754\_15, (below the limits of detection), and sample 1754\_13 (12 to 160 ppm As). All Diablo tourmaline breccia samples show significant variation, however samples 1990\_6 (<100 ppm), 2672\_9 (<50 ppm) and 1974\_1 (<150 ppm) are comparatively As-depleted.

### 4.5.3 Tourmaline rare earth element contents

REE concentrations, shown in Fig. 4.39, vary slightly between the Teniente breccias and within samples from each of the breccias. LREE concentrations from all breccias are variable, ranging between <20 and >100 ppm. Of the LREE, La (Fig. 4.39b) and Ce (Fig. 4.39c) have comparatively higher concentrations. La is mostly <25 ppm with some values upwards of 75 ppm, and Ce is mainly <40 ppm, with a small number of points containing up to 110 ppm Ce. Nd shows intermediate concentrations of tens of ppm Nd (Fig. 4.39e), and lower median concentrations <10 ppm are present for Pr, Sm, Eu, Gd. HREE (Fig. 4.39g-o) were mostly below detection in many analyses. Higher median HREE concentrations are presented by Yb (Fig. 4.39n) and Er (Fig. 4.39l). A more detailed description of each elemental variation is provided below.

Most tourmalines from the Teniente breccias contain <70 ppm Y except a number of analyses from the BTB, Diablo and MTB which exceed 120 ppm Y (Fig. 4.39a). Most La Huifa tourmalines contain <5 ppm Y except for some overgrowths which are enriched and contain >5 ppm (see Fig. 4.39a). Unlike many other minor, traces and REEs, tourmalines from the ETB are not enriched in Y (<10 ppm) relative to other breccias. The BTB samples are however distinctly different with sample 1754\_15 being

depleted (<5.5 ppm Y) compared with 1754\_13. Tourmalines from the Diablo Breccias have changeable Y concentrations (below detection to 155 ppm) within and between samples but do not show a clear correlation. Tourmalines from the MTB vary, with sample 1694\_20 Y-enriched (12 to 50 ppm) compared to samples 1213\_3 (<16.5 ppm) and 1694\_12 (<3 ppm).

La (Fig. 4.39b), Ce (Fig. 4.39c), Pr (Fig. 4.39d), and Nd (Fig. 4.39e) show similar trends and most tourmalines contain <25 ppm La, <30 ppm Ce (except a small number of tourmalines from the ETB), <3.5 ppm Pr and <11 ppm Nd. The same samples enriched and depleted in Y and La are also enriched or depleted to varying extents in Ce, Pr and Nd. Higher tourmaline Ce, Pr and Nd concentrations at La Huifa are mostly associated to the overgrowths although this trend is not consistently replicated throughout the Diablo Breccias or others. A number of tourmalines from the ETB are enriched in these elements relative to the other tourmaline breccias. Tourmalines from the Diablo and MTB show relative enrichment and depletion between breccia samples.

Analogous trends are present between Sm, Eu and Gd which where are above detection they do not show consistent trends, and are sometimes associated to overgrowths (e.g., sample 2677\_3, Diablo), individual crystals (e.g., traverse 3 sample 2683\_3, Diablo) or random analyses. Most tourmalines contain <9.5 ppm Gd (Fig. 4.39h), <2.2 ppm Sm (Fig. 4.39f) and <0.5 ppm Eu (Fig. 4.39g). A large number of tourmalines with Gd and Sm above detection at La Huifa are from the fibrous overgrowths.

The remaining tourmaline HREE (Tb, Dy, Ho, Er, Tm, Yb and Lu) data have similar trends and are discussed as a group. Those above detection in La Huifa are primarily associated to the tourmaline overgrowths, which are also below detection. Clast- and cement-hosted tourmalines from the ETB overlap and are neither relatively enriched nor depleted relative to each other or remaining breccias. Tourmalines from the BTB vary between samples, with sample 1754\_13 enriched relative to sample 1754\_15. Large variations between and within samples at the Diablo Breccias are present for all HREE. Samples 1990\_6 and 2672\_1 (except traverses 1 and 2) are consistently depleted compared to other samples. A bimodal distribution is frequently observed in samples 1974\_1 and 2672\_1. The highest HREE concentrations in sample 2677\_3 are associated to points spatially positioned just before the overgrowths. The MTB contains low levels of HREE except sample 1694\_20, which is comparatively enriched to the other two samples and the remaining breccias.

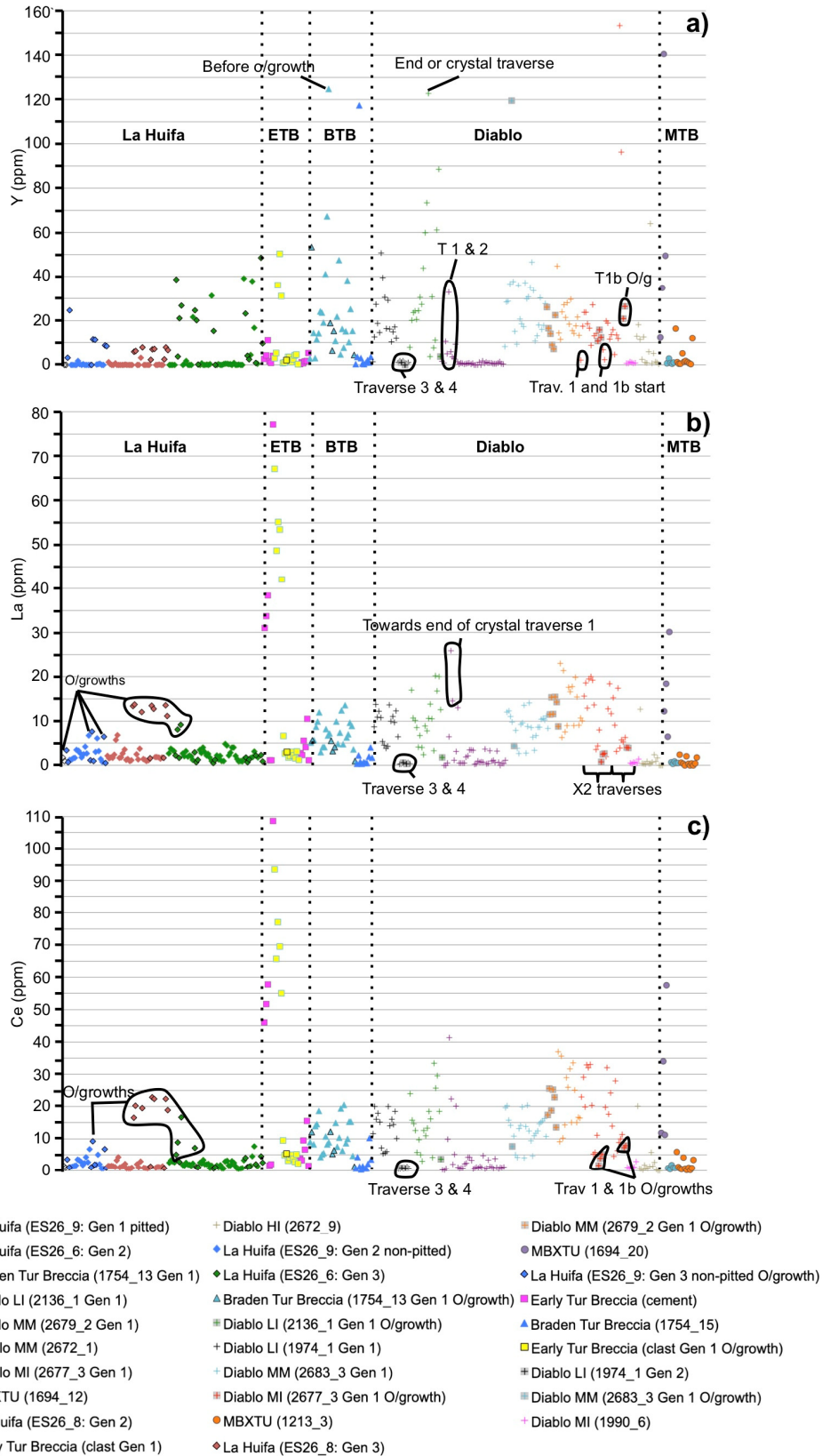


Fig. 4.39 Rare earth LA-ICP-MS tourmaline data from all five breccias selected. Each breccia has been subdivided into samples. In the case of ETB where only one sample was collected, it has been divided into clast or cement tourmaline. Diablo key abbreviations are as follows: LI= low (deep) inner, MM= middle margin, MI= middle inner, HI= high (shallow) inner: **a)** Y; **b)** La; **c)** Ce; **d-p)** Overleaf. Vertical lines separate the five breccias analysed, from left to right as follows: La Huifa, ETB, BTB, Diablo breccias and the MTB.

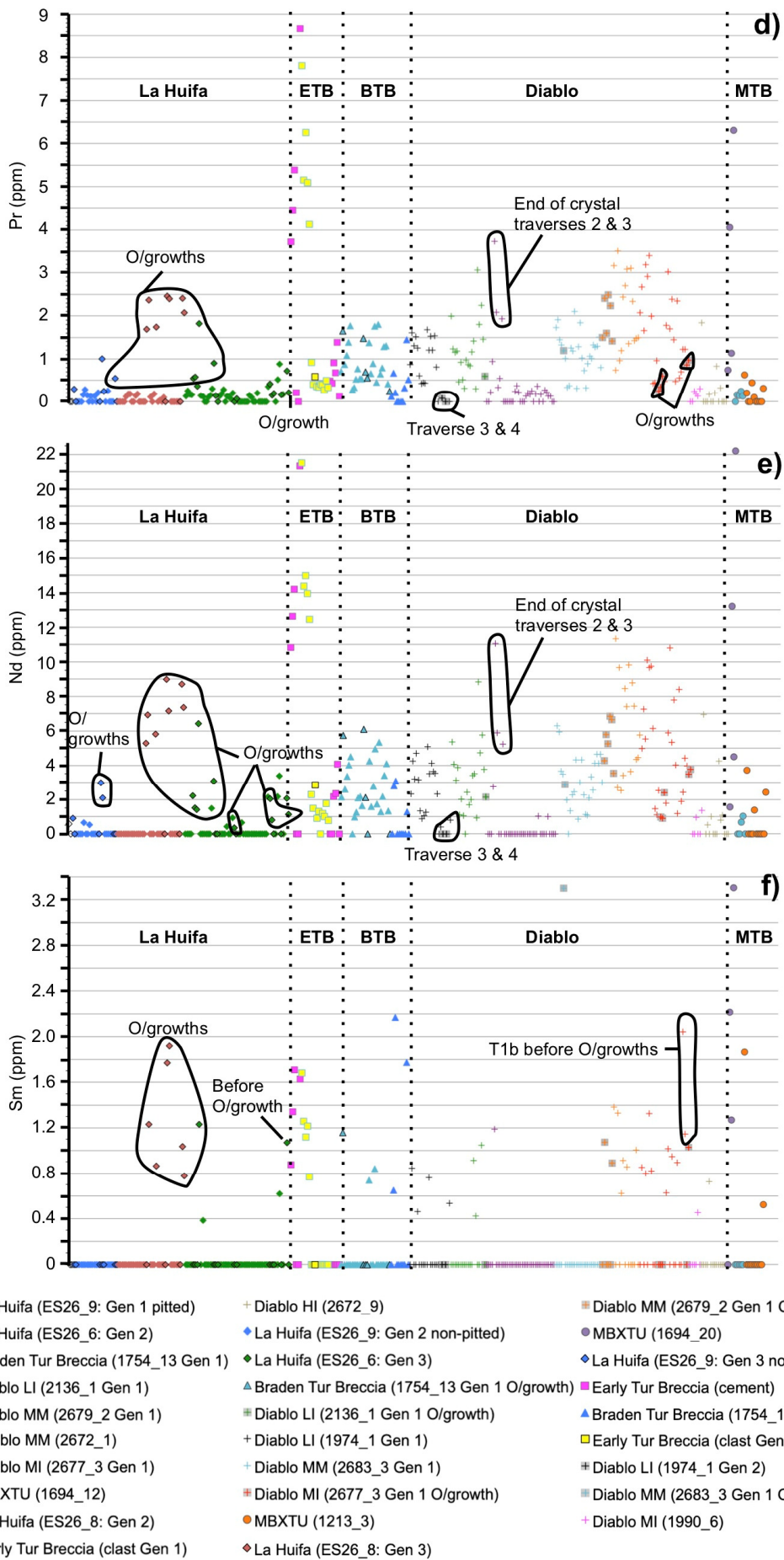


Fig. 4.39 cont. **d)** Pr; **e)** Nd; **f)** Sm; **g-p)** Overleaf.

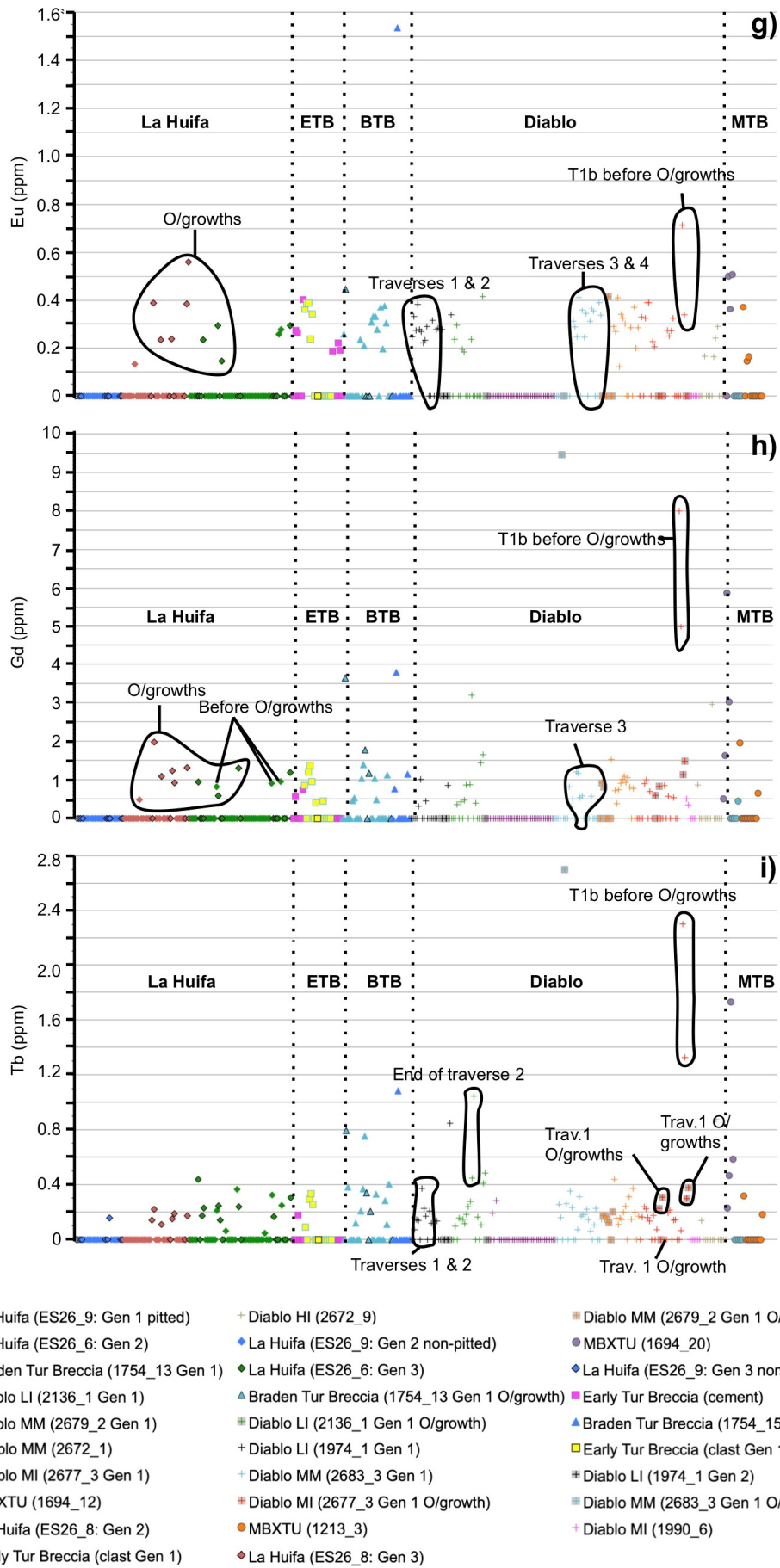


Fig. 4.39 cont. **g)** Eu; **h)** Gd; **i)** Tb; **j-p)** Overleaf.

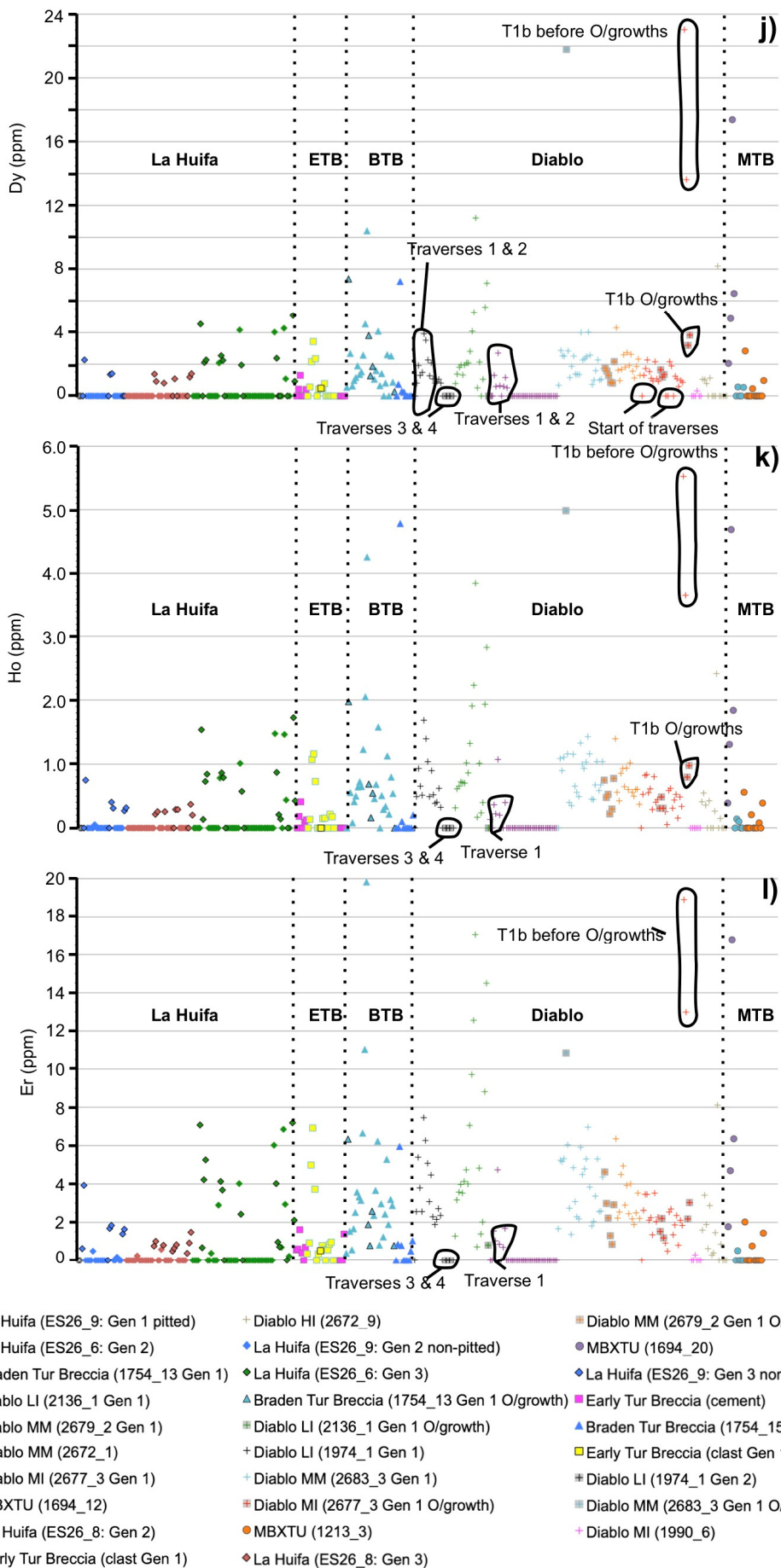


Fig. 4.39 cont. j) Dy; k) Ho; l) Er; m-p) Overleaf.

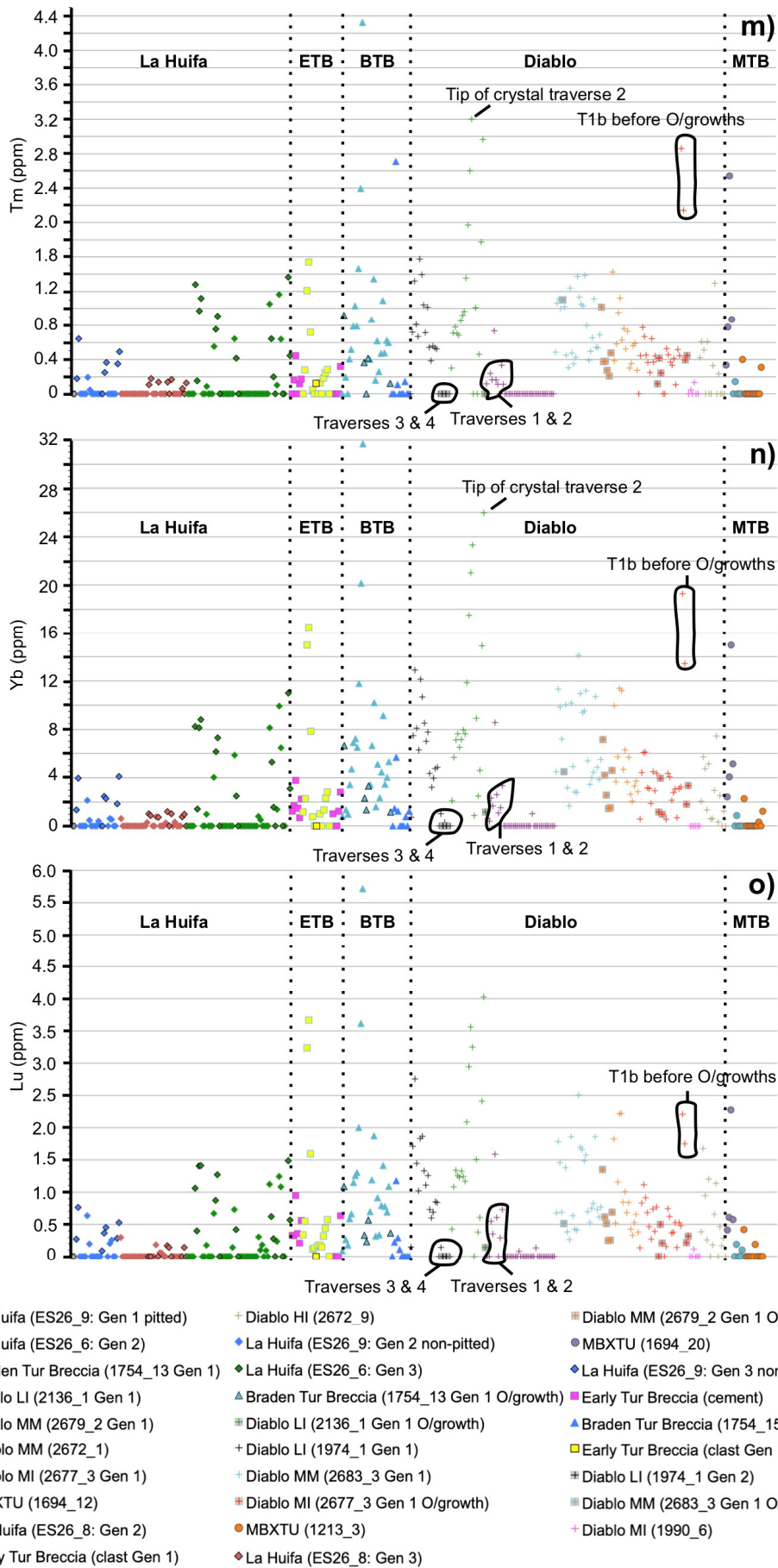


Fig. 4.39 cont. **m)** Tm; **n)** Yb; **o)** Lu; **p)** Overleaf.

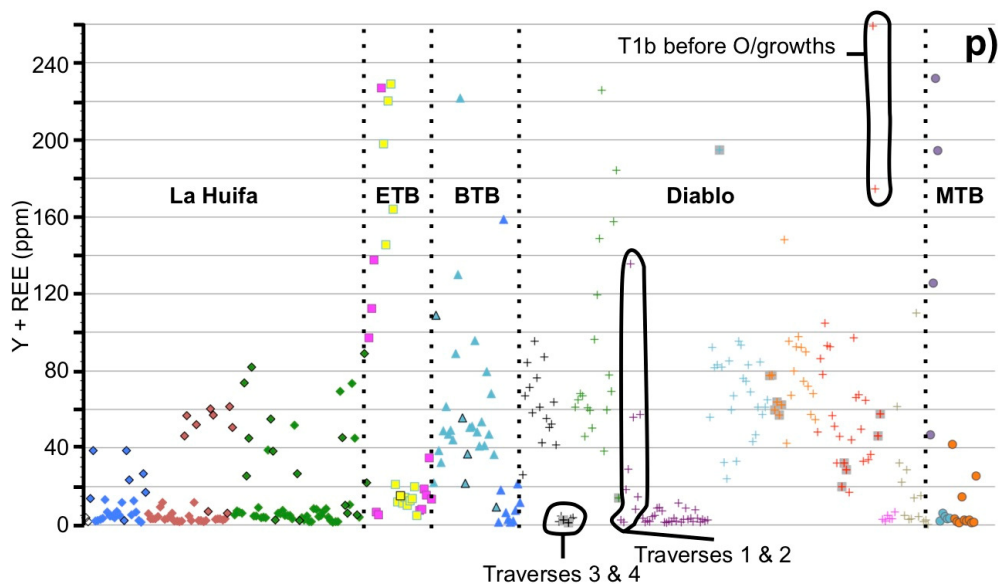


Fig. 4.39 cont. **p)** Y+REE. Key the same as previous.

**Chondrite-normalised REE profiles** - The REE patterns of tourmalines from the Teniente breccias are shown in Fig. 4.40. Tourmalines have asymmetric concave-upward shape patterns with weak Eu-anomalies (where present) and are often incomplete (Fig. 4.40). The REE patterns of tourmaline are highly variable in terms of LREE- and HREE-enrichment. Tourmalines from the BTB generally show minor HREE-enrichment (Fig. 4.40a), no noticeably consistent positive or negative Eu-anomalies and sample 1974\_15 has lower La and Ce than 1754\_13. The REE patterns of tourmalines from the ETB (Fig. 4.40b) are incomplete, concave with weak positive and negative Eu-anomalies. Cement- and clast-hosted tourmaline REE concentrations overlap. Tourmalines from the MTB (Fig. 4.40c) have comparatively flat profiles with no or small negative Eu-anomalies. Sample 1694\_20 has higher LREE and HREE compared to the other samples. Diablo (Fig. 4.40d) and La Huifa (Fig. 4.40e) tourmalines have incomplete concave patterns with weak positive and negative Eu-anomalies. Dividing the Diablo up into respective deposit depth categories (Fig. 4.40f-i) shows tourmalines from different depths contain similar concentrations with most individual samples and tourmaline generations overlapping.

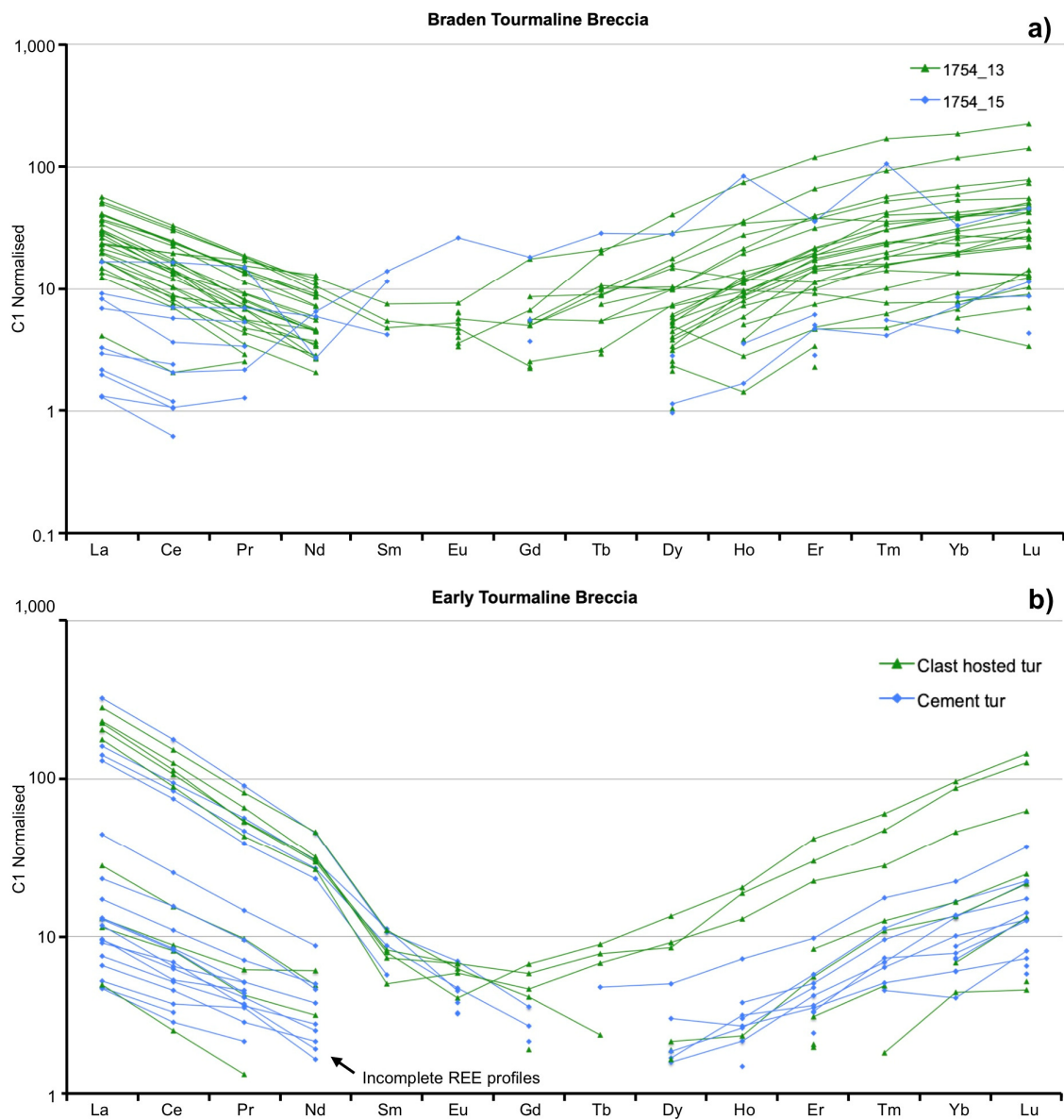


Fig. 4.40 Chondrite-normalised (values from Sun and McDonough, 1989) REE patterns for: **a)** Braden Tourmaline Breccia; **b)** Early Tourmaline Breccia; **c-e)** Overleaf.

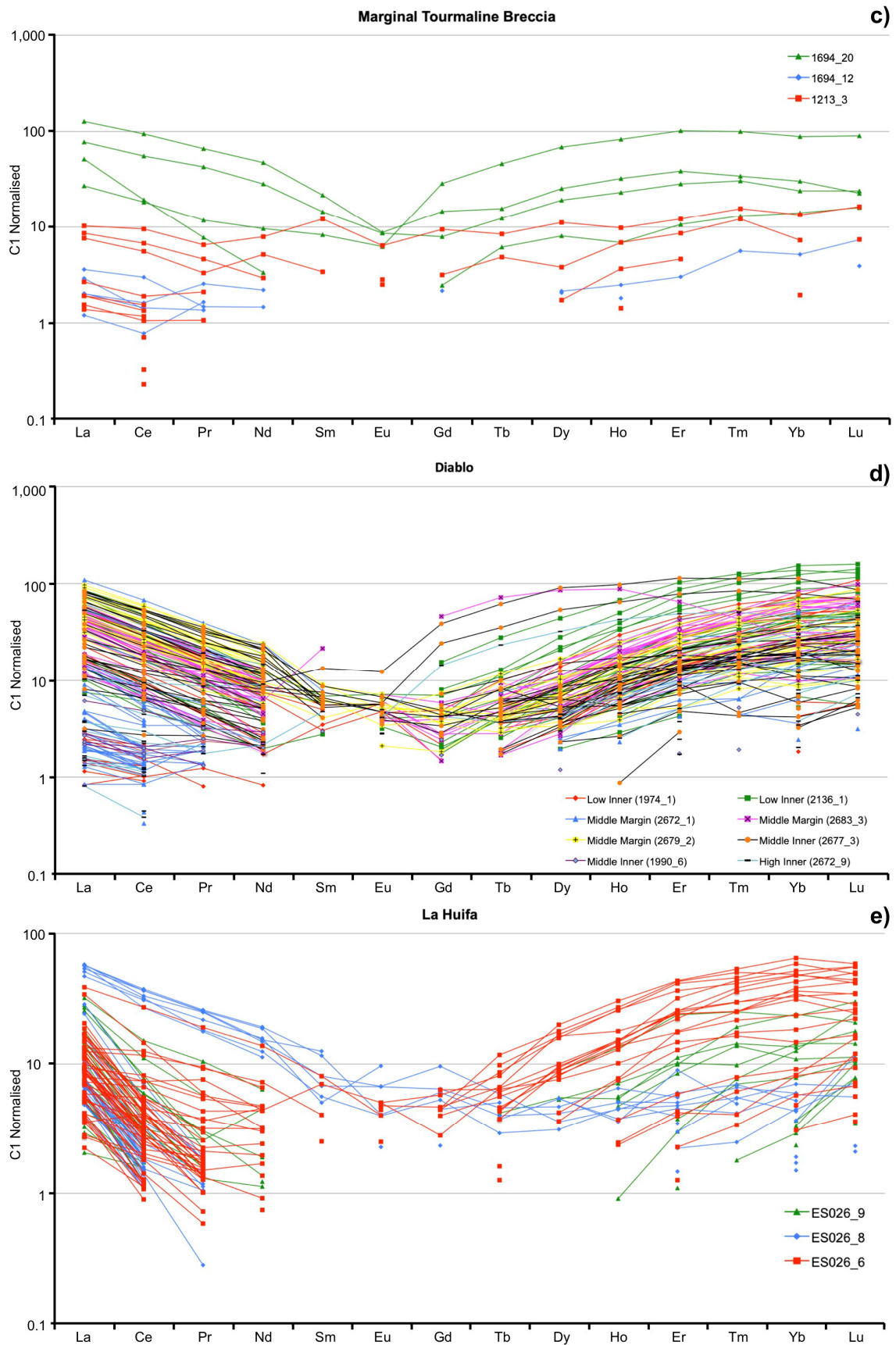


Fig. 4.40 cont. Chondrite-normalised (values from Sun and McDonough, 1989) REE patterns for: **c)** Marginal Tourmaline Breccia; **d)** Diablo Breccias; **e)** La Huifa; **f-i)** Overleaf.

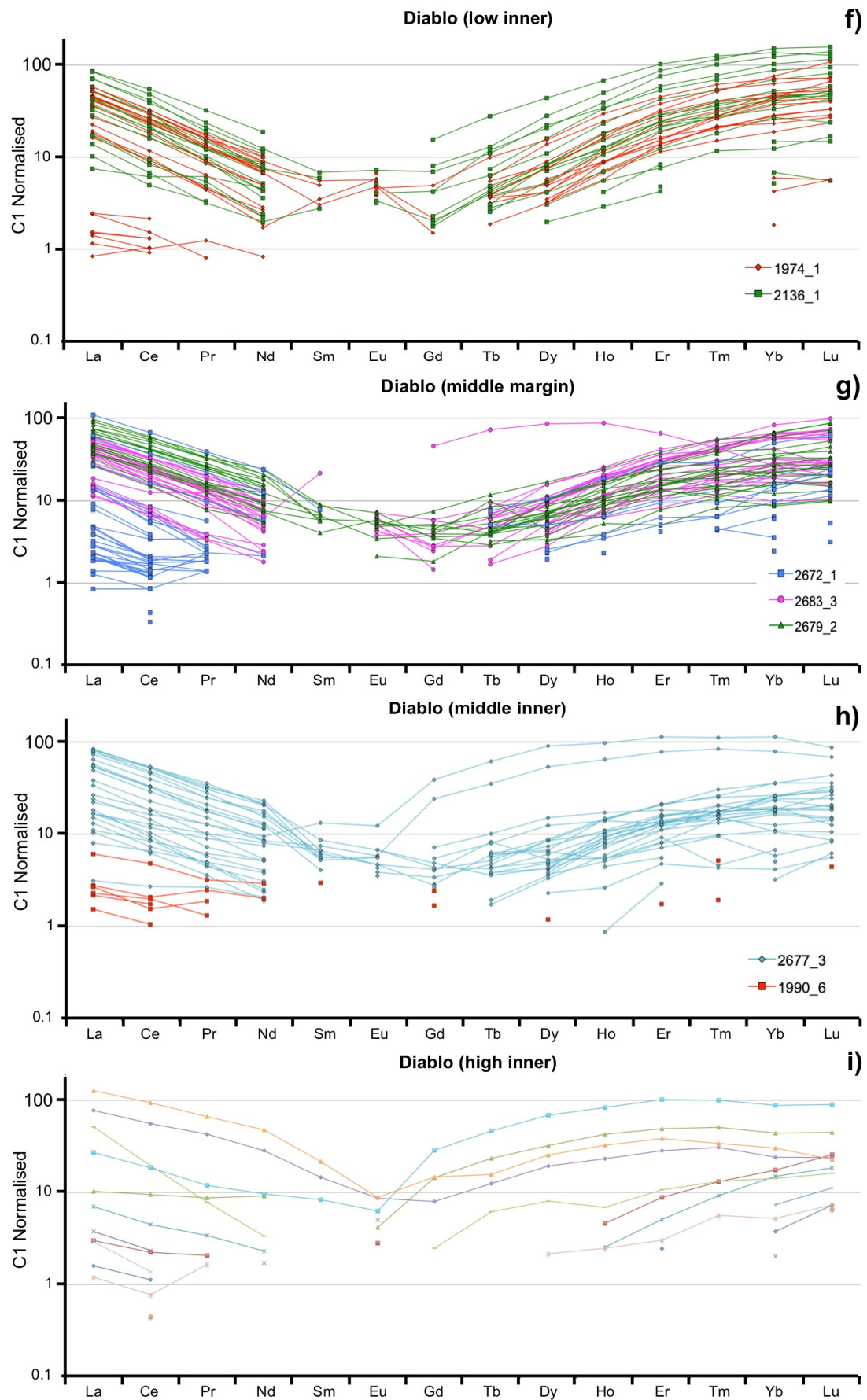


Fig. 4.40 cont. Chondrite-normalised REE data (values from Sun and McDonough, 1989). REE for the Diablo Breccias are separated into different deposit depth intervals and grouped per sample: **f)** Low (deep) inner; **g)** Middle margin; **h)** Middle inner; **i)** High (shallow) inner (sample 2672\_9).

## 4.6 Intra-crystalline tourmaline compositional variations

The above section showed that there are no consistent elemental differences between the five breccias, or between the different tourmaline generations in the breccias. For example, tourmalines that are nearly adjacent (within mm) and associated with the same paragenetic period have variable trace and/or REE profiles, which applies to all breccias. In the following section, only a few representative tourmaline traverses will be described from each breccia to illustrate intra-crystalline major, minor, and trace element variations and inconsistencies in greater detail. Additional traverses are shown in Appendix v. Many of the tourmalines in the breccias show high Si apfu (>6) which given the secondary standard data looks to be analytical artifacts of data processing introduced due to all Fe assumed to be FeO (rather than FeO and Fe<sub>2</sub>O<sub>3</sub>).

### 4.6.1 Early Tourmaline Breccia

Clast- and cement-hosted tourmalines were analysed to determine if any differences exist between them. Identifying additional generations is difficult due to the fine-grained/microcrystalline habit and no clear cross-cutting relationships. In total, 258 EPMA and 26 corresponding LA-ICP-MS analyses were acquired. Two tourmalines from clasts are shown in Fig. 4.41 and Fig. 4.42, and two from the cement are shown in Fig. 4.43 and Fig. 4.44. An additional traverse from the cement is presented in Appendix v. Element concentrations within cement- and clast-hosted tourmalines can vary by a few or several orders of magnitude.

**Cement-hosted tourmaline** - Similar textural and chemical trends are observed in the cement-hosted tourmalines (Fig. 4.41, Fig. 4.42). No tourmaline overgrowths or tourmaline-healed fractures are present. Fractured tourmalines are instead 'healed' by adjacent cementing phases. Major element variability is attributed to (Fe<sup>2+</sup>+Fe<sup>3+</sup>)(MgAl)<sub>-1</sub>, NaFe<sup>2+</sup>(□Al)<sub>-1</sub>, and (Fe)(Mg)<sub>-1</sub> exchanges, which results in the patchy zoning commonly observed in SEM-BSE images and EDS elemental maps (Fig. 4.41a-b, Fig. 4.42a). The scale of zoning is quite often <50 μm and therefore less than the resolution of the laser. The brighter BSE zones contain relatively high FeO, CaO, Na<sub>2</sub>O whilst the darker areas are enriched in Al<sub>2</sub>O<sub>3</sub> and MgO.

Al (4.18 to 6.07 apfu) and Fe (0.43 to 2.90 apfu) show the largest elemental variations in the traverses. There is no significant difference between the concentrations of remaining major constituent elements. Si and Na are near consistent across the traverses from base to tip being between 5.96 to 6.40 apfu and 0.7 to 0.9 apfu, respectively. Mg is also largely constant (1.79 to 2.48 apfu) although does show minor depletion (1.79 to 2.04 apfu) in the schorl domain of Fig. 4.41c.

Ca also increases in the schorl zones of each crystal from <0.1 up to 0.24 apfu (Fig. 4.41d, Fig. 4.42c), due to  $(\text{Ca}(\text{Fe}, \text{Mg}))(\text{Al Na})_{-1}$  exchange. Ti contents vary between traverses (0.025 to 0.16 apfu in Fig. 4.41d and among 0.09 to 0.5 apfu in Fig. 4.42c) and Ti decreases (Fig. 4.41d) and increases (Fig. 4.42c) in the Fe-rich schorl zones.

V, Sn, Sc, and to some extent Cr display similar trends. For example, V, Sn and Sc show increasing concentrations towards the end of both traverses (Fig. 4.41e, Fig. 4.42d). V increases from 1,409 to 2,895 ppm in Fig. 4.41e and from 1,651 to 2,810 ppm in Fig. 4.42d. These increases, however, are not always consistently progressive. Cr increases towards the tips of both tourmalines (from ~1,200 to ~2,050 ppm in Fig. 4.42d and from below detection to ~1,400 ppm in Fig. 4.41e). Both tourmaline traverses however show large differences in Cr concentrations, with Fig. 4.41e largely below detection (up to 32 ppm) compared to the tourmaline in Fig. 4.42d which has between 246 and 612 ppm. Progressive increases in Sc are observed throughout both tourmalines from 100 up to 300 ppm in Fig. 4.41e and from 240 up to 340 ppm in Fig. 4.42d. Sn contents are largely constant throughout both tourmalines although that in Fig. 4.41e has between 60 and 70 ppm Sn compared with Fig. 4.42d which has between 20 and 71 ppm. Both traverses show increases to ~70 ppm Sn at their ends.

The following trace elements are present in both traverses at similar concentrations: Li (below detection to 7 ppm), Sc (118 to 341 ppm), V (1,267 to 2,896 ppm), Mn (15.2 to 89 ppm), Co (6.2 to 15 ppm), Ni (38.7 to 62 ppm), Zn (below detection to 18 ppm), As (26 to 371 ppm), Y (0.3 to 4 ppm) and Nb (below detection to 2.3 ppm). Cu, Mo and Rb are largely below detection in both tourmalines and where above detection are within range of one another.

In both tourmaline traverses, REEs show abrupt increases by a few to several orders of magnitude at the tips (Fig. 4.41f, Fig. 4.42e). A number of differences between the cement-hosted tourmalines are present. Firstly the REE concentrations are by orders of magnitude different for some elements in the traverses. For example, tourmaline in Fig. 4.41f has up to 110 ppm Ce and ~21 ppm Nd, and ~9 ppm Pr at the tip compared to ~16 ppm Ce, ~4 ppm Nd and ~2 ppm Pr in Fig. 4.42e. Secondly, there is a more progressive increase in REE in Fig. 4.42e compared with the large increase seen in Fig. 4.41f. Many REE in Fig 4.42 are below detection and where above are present in similar concentrations in both traverses: La (1.1 to 7.7 ppm), Sm (below detection to 1.6 ppm), Eu (below detection to 0.4 ppm), Gd (below detection to 0.7 ppm), Dy (below detection to 0.4 ppm), Ho (below detection 0.1 ppm), Er (below detection to 0.7 ppm), Tm (below detection to 0.18 ppm), Yb (0.69 to 2.3 ppm) and Lu (0.2 to 0.6 ppm). Tb and Rb are below detection.

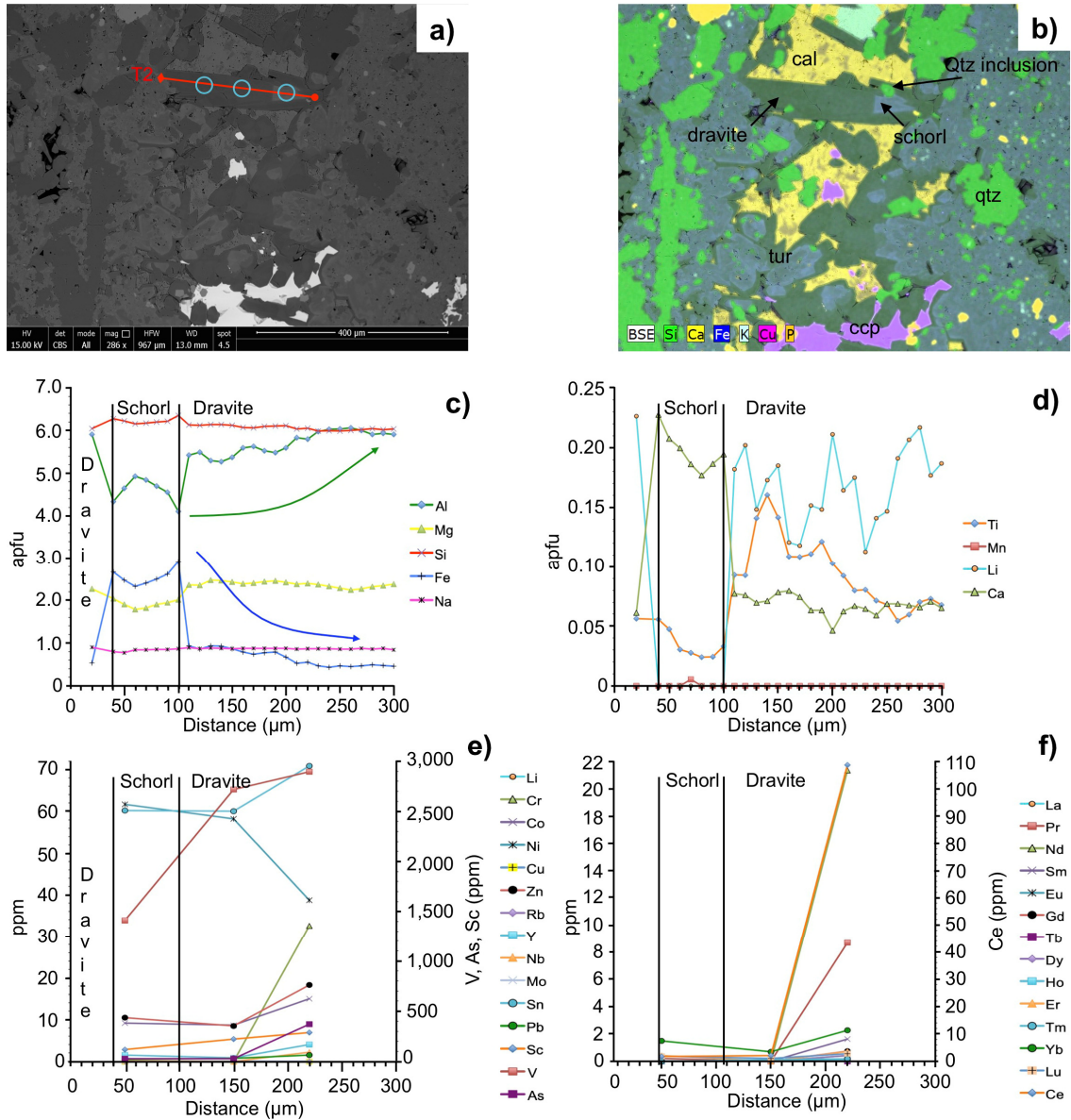


Fig. 4.41 Cement-hosted tourmaline EPMA and LA-ICP-MS data from the ETB: **a-b)** SEM-BSE image and EDS elemental map showing tourmaline-calcite-quartz cement where calcite, quartz and lesser chalcopyrite infill around tourmaline. A Fe-rich (schorl) subdomain is present in the acicular crystal. Blue circles indicate LA-ICP-MS points whilst the red line shows the relative start (circle) and end (diamond) of the EPMA traverse; **c-d)** EPMA data for major and minor element traverse (286  $\mu\text{m}$  long, 10  $\mu\text{m}$  intervals); **e-f)** LA-ICP-MS trace and REE data.

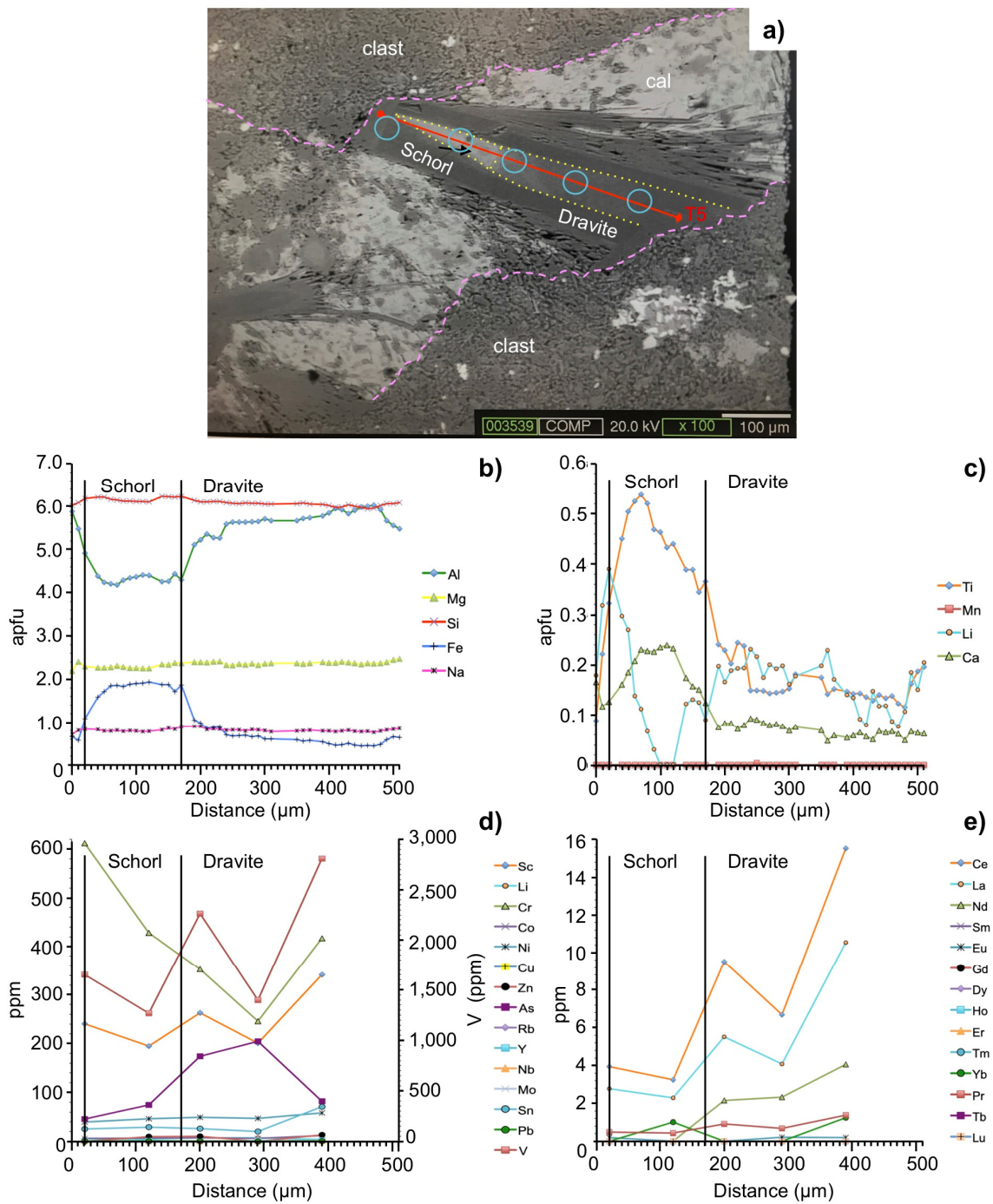


Fig. 4.42 Cement-hosted tourmaline EPMA and LA-ICP-MS data from the ETB: **a)** SEM-BSE image with clast margins outlined in purple. A brighter schorl subdomain is present towards the core/centre of the crystal. Blue circles indicate laser ablation points whilst the red line shows the relative start (circle) and end (diamond) of the EPMA traverse; **b-c)** EPMA data for major and minor element traverses (510 μm long, 10 μm intervals); **d-e)** LA-ICP-MS trace and REE data.

**Clast-hosted tourmaline** - EPMA and LA-ICP-MS data from two separate tourmaline crystals are presented in Fig. 4.43 and Fig. 4.44). Like cement-hosted tourmaline, there are major and minor elemental similarities largely relating to the substitution  $(\text{Fe}^{2+}\text{Fe}^{3+})(\text{MgAl})_{-1}$ . The backscatter images of tourmaline sometimes show irregular/complex patchy zoning where dark zones are enriched in  $\text{Al}_2\text{O}_3 \pm \text{MgO}$  and the lighter zones contain higher  $\text{FeO} \pm \text{Na}_2\text{O} \pm \text{CaO}$  (e.g., Fig. 4.43a). For example, coarse tourmaline shown in Fig. 4.43a has patchy zoning in the schorl with a darker dravite overgrowth. Many elements decrease at the dravite tip on the zoned tourmaline (Fig. 4.43b) such as Si (from  $>6.0$  to  $\sim 5.9$  apfu), Mg (from 2.24 to 1.6 apfu), Na (from 0.8 to 0.6 apfu) and Ti (from 0.12 to 0.012 apfu). These decreases correspond to Al (6 to 6.4 apfu) and Fe (0.4 to 0.76 apfu) increases. Ti also shows a large increase (up to 0.7 apfu) at  $\sim 350 \mu\text{m}$  along the traverse associated with a rise in Ca (from 0.2 to 0.25 apfu) and Fe, and a drop in Al and to a lesser extent Mg. This illustrates Fe and Al are at times substituting for Mg, Ti and Si. Ca shows a progressive decrease in the first zoned crystal from base to tip, decreasing from  $\sim 0.24$  to 0.08 apfu.

Optical or SEM-BSE zoning is not always present in clast-hosted tourmalines. Fig. 4.44a, for example, shows a comparatively homogenous dravite crystal with very limited compositional variation, particularly compared with that in Fig. 4.43a. Most compositional variability in this tourmaline is in Al (5.52 to 6.26 apfu), which shows a degree of substitution for Mg, rather than Fe in cement tourmalines. In this homogenous tourmaline, Mg (2.08 to 2.25 apfu) and Na ( $\sim 0.8$  apfu) are constantly higher than Fe (0.4 to 0.6 apfu). Despite no zoning or major element variations, Ti (0.076 to 0.185 apfu) and Ca (0.05 to 0.08 apfu) are erratic throughout the traverse.

Despite these differences, both crystals show similarities with one another and cement-hosted tourmalines. For example, concentrations of Na (0.8 to 0.9 apfu), Mg (1.9 to 2.5 apfu) and Si (6.3 to 5.0 apfu) are consistent in both clast-hosted crystal traverses showing comparatively restricted chemical ranges. Like the cement-hosted tourmalines clast-hosted crystals show the largest variations in element concentrations of Al (3.3 to 6.3 apfu) and Fe (0.5 to 3.5 apfu).

Trace and REE element trends within individual traverses are highly variable and show significant scatter between crystals. Elemental concentrations also vary between crystals (Fig. 4.43 and Fig. 4.44) but are within the range of the cement-hosted tourmalines from the ETB. Some of the variation may be due to the fibrous and intergrown nature of tourmaline towards the tip of many clast-hosted tourmalines (e.g., Fig. 4.43a) which complicated the acquisition of LA-ICP-MS data. In general, there are increases from the base to the tip of the tourmaline for Cr (33 to 230 ppm) and Ni (29 to 49 ppm), whilst Zn (18.6 to 9.5 ppm), Co (14.5 to 5.4 ppm), and Sc (220 to 125 ppm) show decreases from base to tip (Fig. 4.43). The other trace elements are mostly <7 ppm and show little variation, although As does decrease (from 357 to ~100 ppm). Decreases in REE from the start to the end of the traverse are present for Ce (93 to 4.9 ppm), Nd (21.5 to 1.5 ppm), La (67 to 2.7 ppm) and Pr (7 to 0.5 ppm), and many show elevated concentrations at ~200  $\mu\text{m}$  point (Fig. 4.43e). This could be due to subsurface inclusions, as inclusions on surface, where present, were avoided as best as possible. Remaining REE are present at concentrations of <4 ppm and show little increase or decrease.

In comparison, many trace and rare earth elements in the optically homogenous clast-hosted tourmaline (Fig. 4.44d) do not show the same profiles or progressive decreases as described above in Fig. 4.43d-e. For example V and As concentrations fluctuate throughout the traverse between 740 to 906 ppm and 49 to 161 ppm, respectively, showing neither enrichment or depletion. Sc and Cr are largely between 93 to 228 ppm and 48 to 264 ppm, respectively, for the traverse, with both Sc decreasing from 228 to 118 ppm and Cr increasing to 264 ppm at the last point of the traverse. Ni contents progressively increase from 27 ppm at the base, peaking in the middle of the traverse (41 ppm; 340  $\mu\text{m}$ ) and then decreasing to 30 ppm at the end (Fig. 4.43d). Remaining trace elements are <10 ppm and show minor fluctuations across the traverse. Sn increases from 16 ppm at the start and peaks at 48 ppm at 500  $\mu\text{m}$  on the traverse, and then decreases to 16 ppm at the end. Rb, Cu and Mo are below detection. Similar peaks in La (3.1 ppm), Ce (5.1 ppm), Yb (2.8 ppm), Nd (1.8 ppm), and Er (0.95 ppm) concentrations are present at the 500  $\mu\text{m}$  point (Fig. 4.44e). The largest variations are in Ce (2.8 to 5.1 ppm), La (1.2 to 3.1 ppm) and Yb (below detection to 2.8 ppm). Remaining REE in Fig. 4.44 are <1 ppm and are lower than those from traverse in Fig. 4.43e.

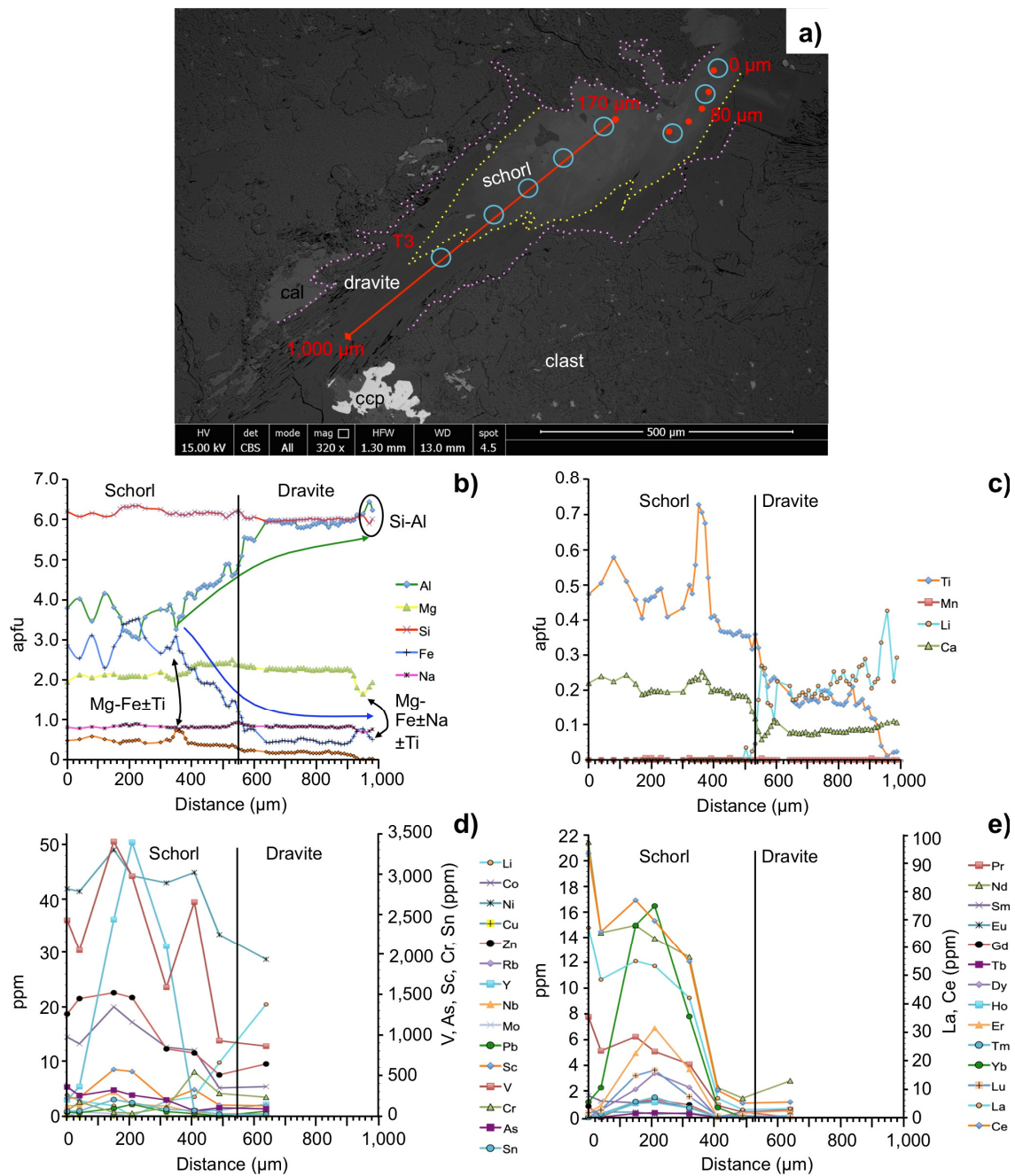


Fig. 4.43 Clast-hosted tourmaline (schorl-dravite) crystal from the ETB: **a)** SEM-BSE image with zones outlined in yellow and the crystal margin in purple. Blue circles indicate laser ablation points whilst the red line shows the relative start (circle) and end (diamond) of the EPMA traverse; **b-c)** EPMA data for major and minor element traverse (traverse 3 (excluding earlier points): 830.85 μm long, 10 μm intervals); **d-e)** LA-ICP-MS trace and REE data.

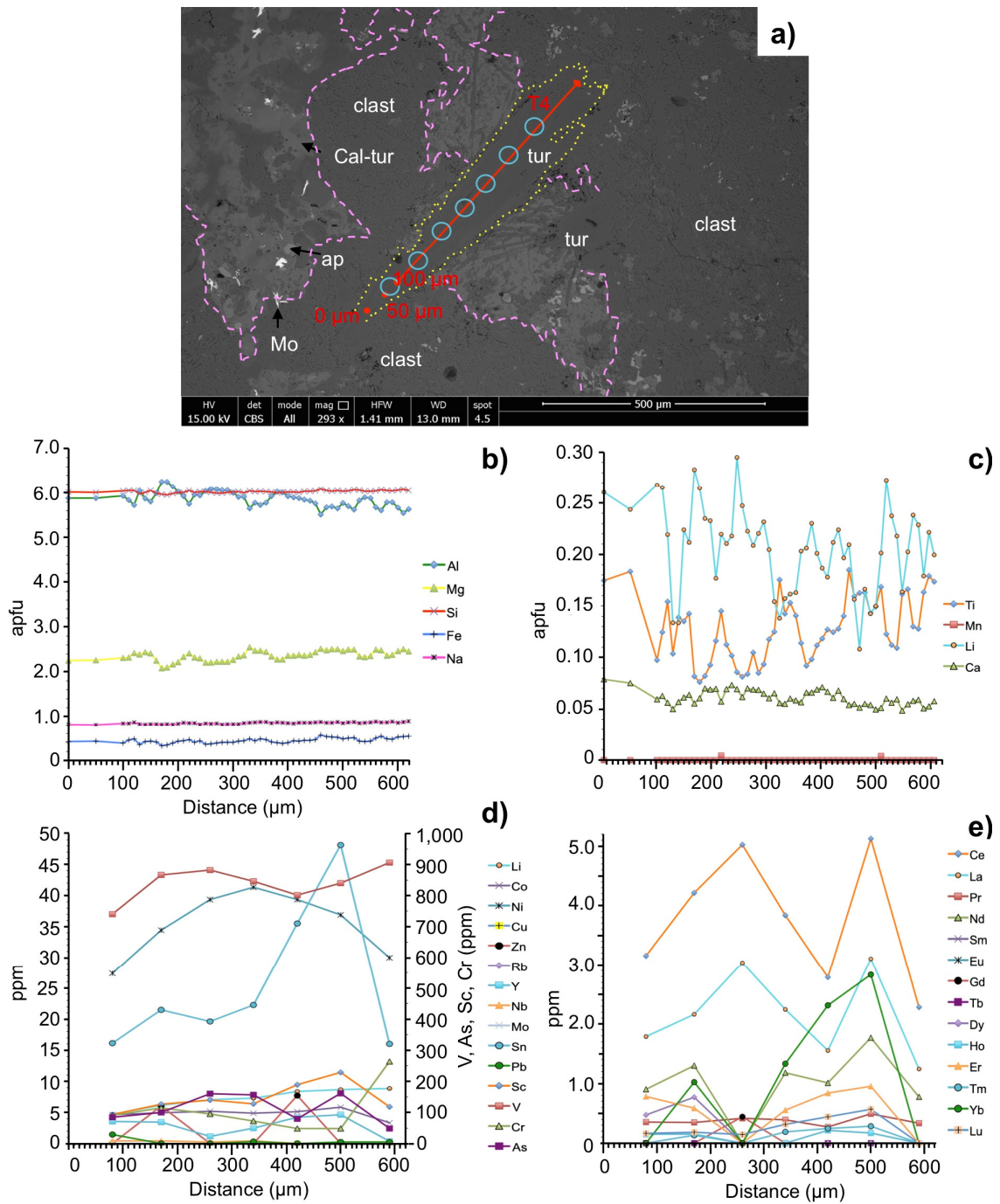


Fig. 4.44 Clast-hosted dravite crystal from the ETB: **a)** SEM-BSE image with clast margins outlined in purple. No zonation is evidence in the BSE image. Blue circles indicate laser ablation points whilst the red line shows the relative start (circle) and end (diamond) of the EPMA traverse; **b-c)** EPMA data for major and minor element traverse (traverse 4 (excluding earlier points): 554.99 μm long, 10 μm intervals); **d-e)** LA-ICP-MS trace and REE data.

## 4.6.2 Marginal Tourmaline Breccia (MTB)

Cement-hosted tourmalines were analysed to compare with those in other breccia types. Acquiring LA-ICP-MS data for the later tourmaline overgrowths, however, proved problematic because they are not as frequently present as in La Huifa or Diablo, and their narrow nature (<50  $\mu\text{m}$  to  $\sim 80 \mu\text{m}$ ) often resulted in mixed ablation signals. In total, approximately 133 EPMA and 20 corresponding LA-ICP-MS analyses were acquired from the MTB. In the following text, two tourmaline crystal traverses are described to illustrate trace and rare earth element variations in tourmalines over short spatial intervals (Fig. 4.45 and Fig. 4.46). The tourmalines described below are mainly schorl which show patchy zoning in SEM-BSE. Due to the complexity and scale (<50  $\mu\text{m}$ ) of the zoning, and the resolution of the laser (50  $\mu\text{m}$  spot), obtaining zone-specific chemistry was near impossible. Composition variations are largely attributed to  $(\text{Fe}^{2+}\text{Fe}^{3+})(\text{MgAl})_{-1}$  (Fig. 4.45b) and  $(\text{Ca}(\text{Fe}, \text{Mg}))(\text{Al}, \text{Na})_{-1}$  (Fig. 4.46b).

Unlike many other tourmalines in the MTB, and other breccias at El Teniente, the tourmaline in Fig. 4.45b has consistent Mg and Fe concentrations (between 1.5 to 2.1 apfu) over the entire traverse. All other major element components (5.8 to 6.2 apfu Si, 4.7 to 6.4 apfu Al and 0.4 to 0.73 apfu Na) show little variation. The second traverse illustrated in Fig. 4.46b-c shows more variable Al-Fe concentrations resulting in a small number of analyses being classified as Mg-foitite and feruvite. Mg-foitite points have high X-site vacancy (see Fig. 4.34c), low  $\text{Fe}_{\text{tot}}/(\text{Fe}_{\text{tot}}+\text{Mg})$  with <1 apfu Fe and <1 apfu Mg. The feruvite analysis has elevated Ca, up to 0.8 apfu.

Trace and REE variability is such that no clear trends across the crystal traverses are present. The following traces are found at similar levels in both tourmalines: Li (below detection to 3.4 ppm), V (367 to 812 ppm), Mn (156 to 450 ppm), Co (11 to 26.2 ppm), Ni (19.2 to 36 ppm), Zn (51 to 109 ppm), Pb (1.1 to 52 ppm), Y (0.5 to 16.3 ppm), Nb (below detection to 1.1 ppm). Cu, Rb and Mo are largely below detection.

Sc concentrations are different between the traverses, lying between 18.6 and 63 ppm in Fig. 4.45d compared with 29 and 107 ppm in Fig. 4.46d. A similar trend is present for Cr which fluctuates from 7.5 to 50 ppm (Fig. 4.45d), and from 44 to 86 ppm (Fig. 4.46d). As ranges from 86 to 387 ppm (Fig. 4.45d) and from 28 to 77 ppm (Fig. 4.46d). Sn shows the same trend ranging from 1.4 to 3.1 ppm in Fig. 4.45d and up to 33 ppm in Fig. 4.46d.

Concentrations of REE are different within both traverses and between them. Tourmaline REE contents in the first traverse, Fig. 4.45e, are <1 ppm, with Nd, Sm, Eu, Gd, Tb, Dy, Ho, Er and Tm below detection. In the second traverse (Fig. 4.46e), all REE except Pr, Eu, Tb, Ho, Tm and Lu are <1 ppm with remaining REE exceeding 2 ppm. No inclusions could be observed to explain this. In the second traverse (Fig.

4.46e), where most REE are <1 ppm, the HREE and LREE are enriched but the MREE relatively depleted.

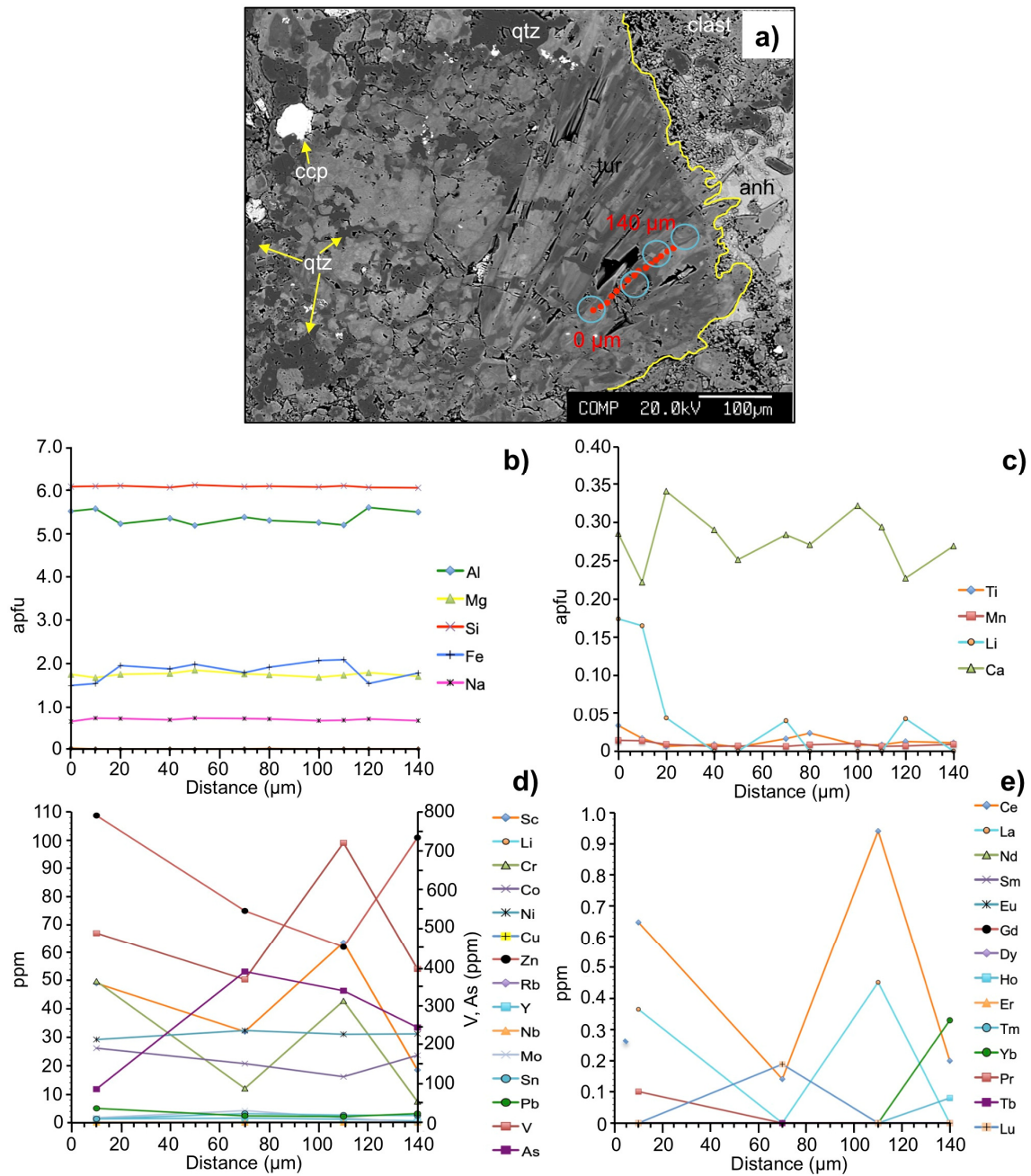


Fig. 4.45 Cement-hosted tourmaline (mostly schorl) crystal from sample DDH1213-38.13 m of the MTB: **a)** SEM-BSE image illustrating zoning throughout the tourmaline. Blue circles indicate laser ablation points whilst the red dots indicate EPMA points; **b-c)** EPMA data for major and minor elements in the traverse; **d-e)** LA-ICP-MS trace and REE data.

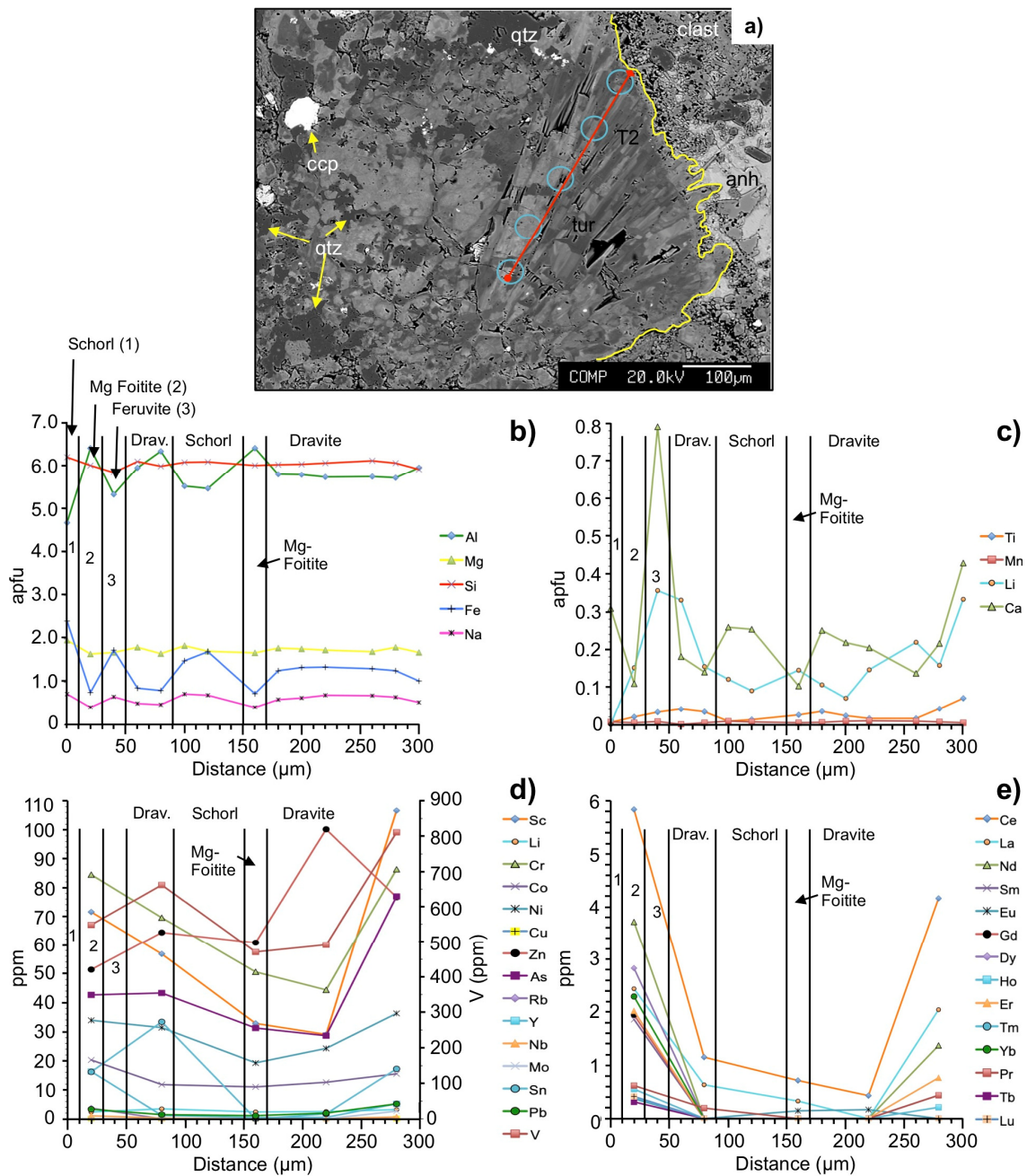


Fig. 4.46 Cement-hosted tourmaline (mostly schorl) crystal from sample DDH1213-38.13 m of the MTB: **a)** SEM-BSE image. Blue circles indicate laser ablation points whilst the red line shows the relative start (circle) and end (diamond) of the EPMA traverse; **b-c)** EPMA data for major and minor element data for traverse 2 (310.54 μm long, 20 μm interval); **d-e)** LA-ICP-MS trace and REE data.

### 4.6.3 Braden Tourmaline Breccia (BTB)

Tourmaline from the BTB occurs as masses of fine interlocking acicular needles alongside end-stage space-filling quartz-calcite ( $\pm$ manganoc calcite) in the cement. The fine acicular nature of tourmaline throughout this breccia body made acquiring reliable LA-ICP-MS data problematic. A number of traverses parallel, or as close to parallel, to the *c*-axis were conducted to assess geochemical changes. In total, 163 EPMA and 37 corresponding LA-ICP-MS analyses were undertaken. Three tourmalines from the cement are shown in Fig. 4.47, Fig. 4.48 and Fig. 4.49. Additional traverses are presented in Appendix v.

Like other breccias, tourmaline within this breccia variably displays major element compositional variability reflected by irregular/complex patchy zoning seen in SEM-BSE images. The scale of zonation is up to  $\sim 80 \mu\text{m}$  although it is quite often  $< 50 \mu\text{m}$  and therefore less than the resolution of LA-ICP-MS. The brighter BSE zones contain high FeO and CaO whilst the darker areas are enriched in  $\text{Al}_2\text{O}_3$  and MgO. Major element variability in the earlier tourmalines is due to the exchange  $(\text{Fe}^{2+}\text{Fe}^{3+})(\text{MgAl})_{-1}$  vector with minor  $(\text{Ca}(\text{Fe Mg}))(\text{Al Na})_{-1}$  (Fig. 4.49a, b).

Like the ETB, Diablo and La Huifa (latter two described later), the traverses shown in Fig. 4.48 and Fig. 4.49 have Al enrichment and associated Fe depletion towards the tips of the earlier tourmaline crystals. Many of these in the BTB are fractured, and have fibrous overgrowths. A significant number of tourmalines within the BTB, including those in Fig. 4.47, Fig. 4.48 and Fig. 4.49 have undergone brittle deformation, causing fracturing. Many of these fractures are 'healed' (e.g., Fig. 4.47a) by up to  $80 \mu\text{m}$  wide darker BSE tourmaline overgrowths and fills (e.g., Fig. 4.48a). Minor elemental variability within the 'healed' fractures and overgrowths is likely due to the exchange  $(\text{Fe}^{2+}\text{Fe}^{3+})(\text{MgAl})_{-1}$ . Chemically, these 'healed' areas and overgrowths are relatively enriched in Al ( $\sim 6$  apfu) and depleted in Fe ( $\sim 1$  apfu) and Ti ( $\sim 0.02$  apfu). They can also either be relatively depleted (Fig. 4.49b) or enriched in Ca (Fig. 4.47c, Fig. 4.48c) and are classified as dravite. Si ( $\sim 6$  apfu) and Na (0.9 to 1.0 apfu) are near consistent throughout the traverses.

BTB tourmaline contains widely varying concentrations of trace and rare earth elements throughout the crystals. For example in the 'healed' fracture zone (darker grey BSE dravite area) in Fig. 4.47, V, Sc and Cr decrease whilst Zn, Ni, Sn and As increase relative to the remainder of the crystal. These enrichments and/or depletions in the 'healed' dravite fractures or overgrowths are not however consistent. In the dravite overgrowths for example, V and Sc either increase (Fig. 4.49) or decrease (Fig. 4.48) towards crystal tips, and Sn decreases (Fig. 4.48). REE follow similar, inconsistent trends in the overgrowths and all REE to varying degrees increase in the 'healed' dravite fracture (Fig. 4.47e).

In the first two traverses, V increases towards crystal tips, (decreasing in the 'healed' dravite fracture in the first figure) and increases in the dravite overgrowth. The largest differences in trace elements between the three traverses are for Li, V, Cr, Cu and Y. Tourmaline Li concentrations in Fig. 4.47d and Fig. 4.48d are <12 ppm and up to 42 ppm in Fig. 4.49a. V is between 210 and 560 ppm in Fig. 4.47d and Fig. 4.49d but is from 399 to 1,742 ppm in Fig. 4.48d. Cr is present in higher concentrations (27 to 77 ppm) in Fig. 4.47d compared with Fig. 4.48d and Fig. 4.49d (<27 ppm). Other traces are present in similar concentrations throughout the traverses: Sc (16.7 to 75.7 ppm), Mn (55 to 125 ppm), Co (6.8 to 25 ppm), Ni (9.7 to 44.6 ppm), Zn (11 to 39 ppm), As (12.2 to 156.6 ppm), Nb (below detection to 5.2 ppm), Sn (3.7 to 106 ppm) and Pb (0.5 to 5.1 ppm). Rb, Cu and Mo are mostly below detection.

REE concentrations largely overlap in all traverses as follows: La (0.98 to 12 ppm), Ce (1.3 to 18.6 ppm), Pr (0.2 to 1.65 ppm), Nd (below detection to 6.1 ppm), Sm (below detection to 1.2 ppm), Eu (below detection to 0.4 ppm), Gd (below detection to 3.6), Tb (below detection to 0.8 ppm), Dy (below detection to 10.4 ppm), Ho (below detection to 4.26 ppm), Er (below detection to 19.8 ppm), Tm (below detection to 4.3 ppm) and Lu (0.08 to 5.7 ppm). The main difference is in Yb which is <9 ppm in Fig. 4.47e and Fig. 4.48e but is present at concentrations up to 32 ppm in Fig. 4.49e.

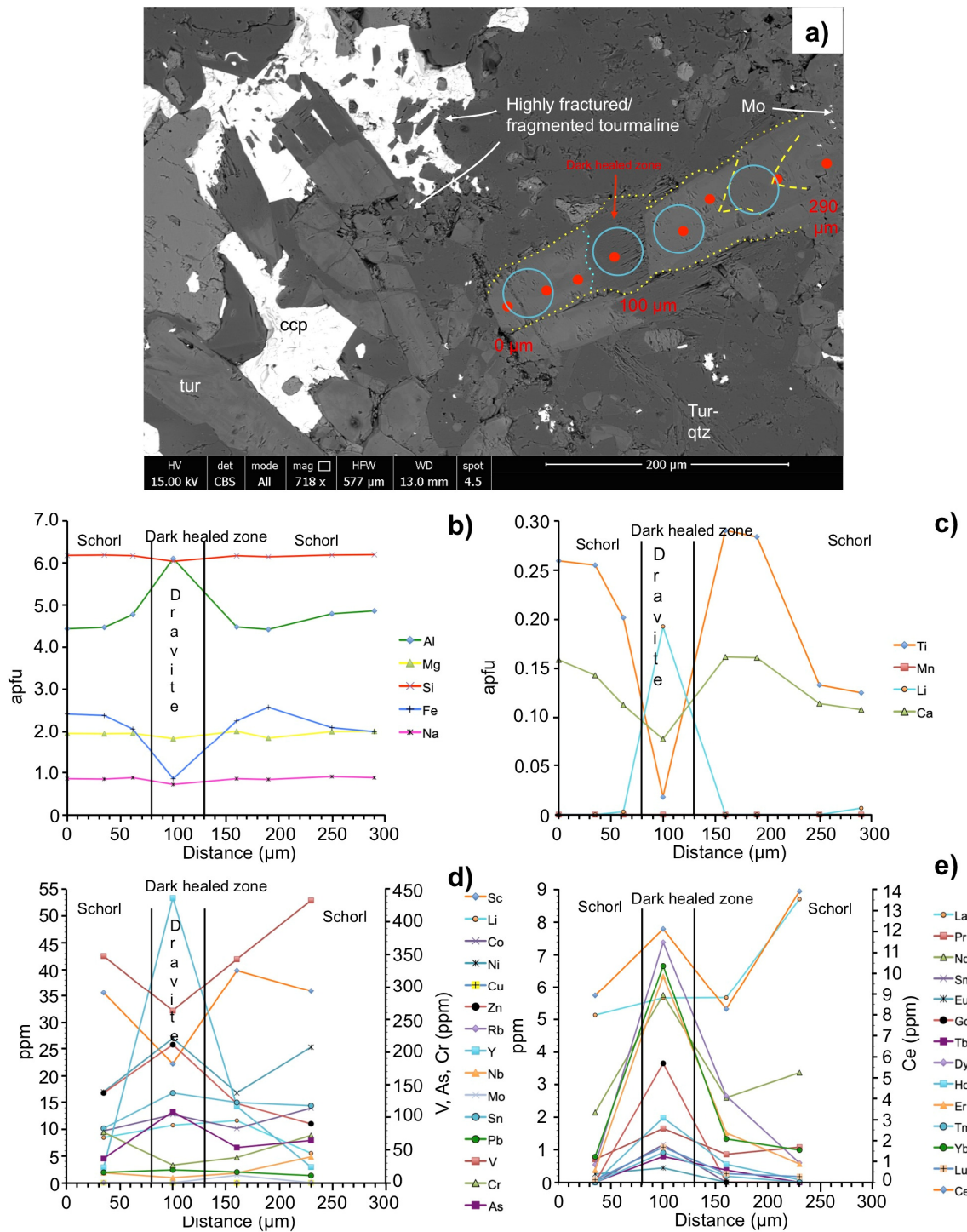


Fig. 4.47 Cement-hosted tourmaline (dravite-schorl) intergrown with tourmaline-quartz and chalcopyrite from sample DDH1754\_13 (5.06 m, BTB): **a)** SEM-BSE image with 'healed' fracture (dravite) present. Blue circles indicate laser ablation points whilst the red dots indicate EPMA points. Note the highly fragmented tourmaline which is largely 'healed' by later dravite; **b-c)** EPMA data for major and minor elements in the traverse; **d-e)** LA-ICP-MS trace and REE data.

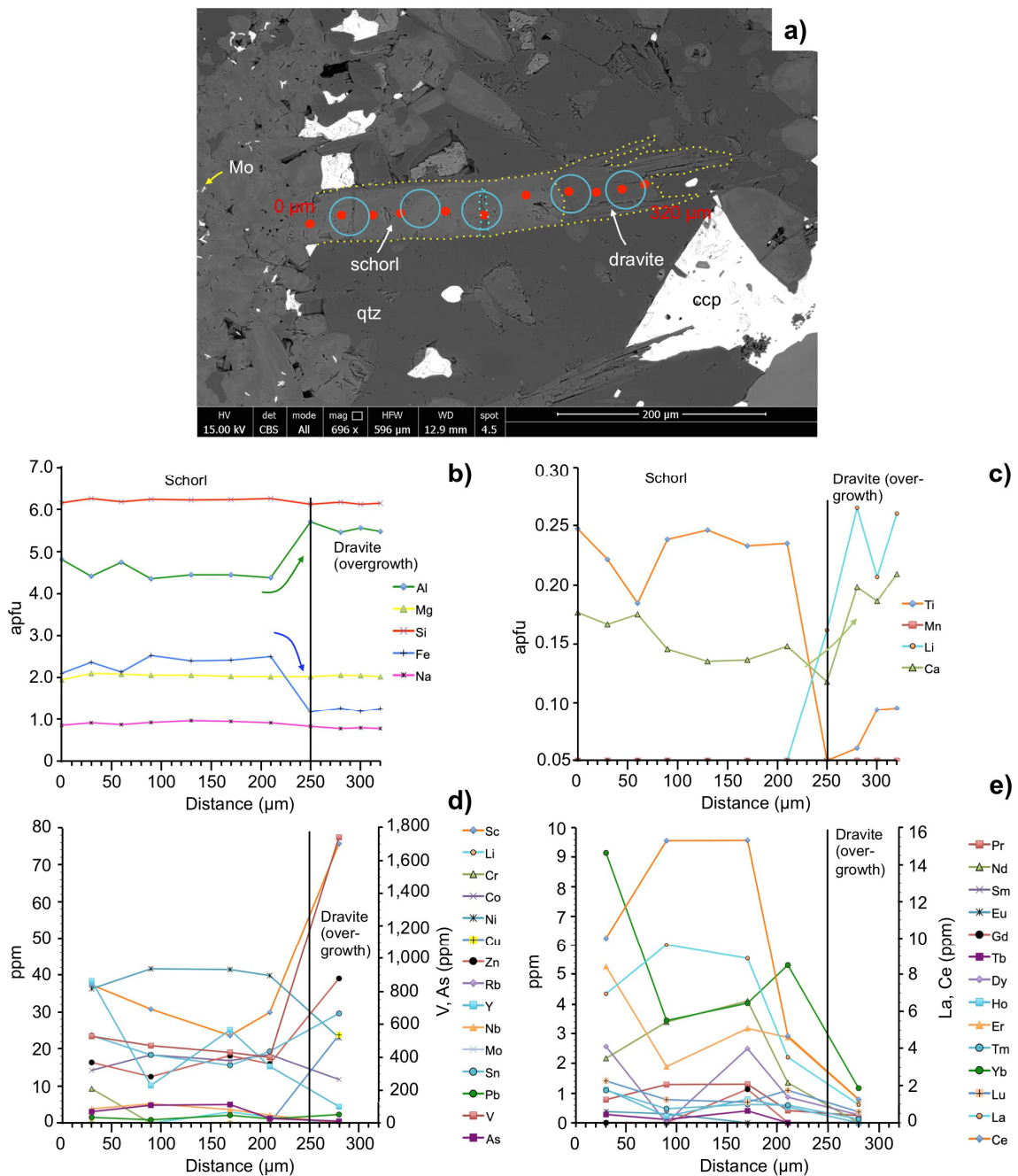


Fig. 4.48 Cement-hosted tourmaline intergrown with quartz and chalcopyrite from sample DDH1754\_13 (BTB): **a)** SEM-BSE image showing schorl crystal with fibrous dravite overgrowths both outlined in yellow. 'Healed' fracture is outlined with a blue dotted line. Blue circles indicate laser ablation points whilst the red dots indicate EPMA points; **b-c)** EPMA data for major and minor elements in the traverse; **d-e)** LA-ICP-MS trace and REE data.

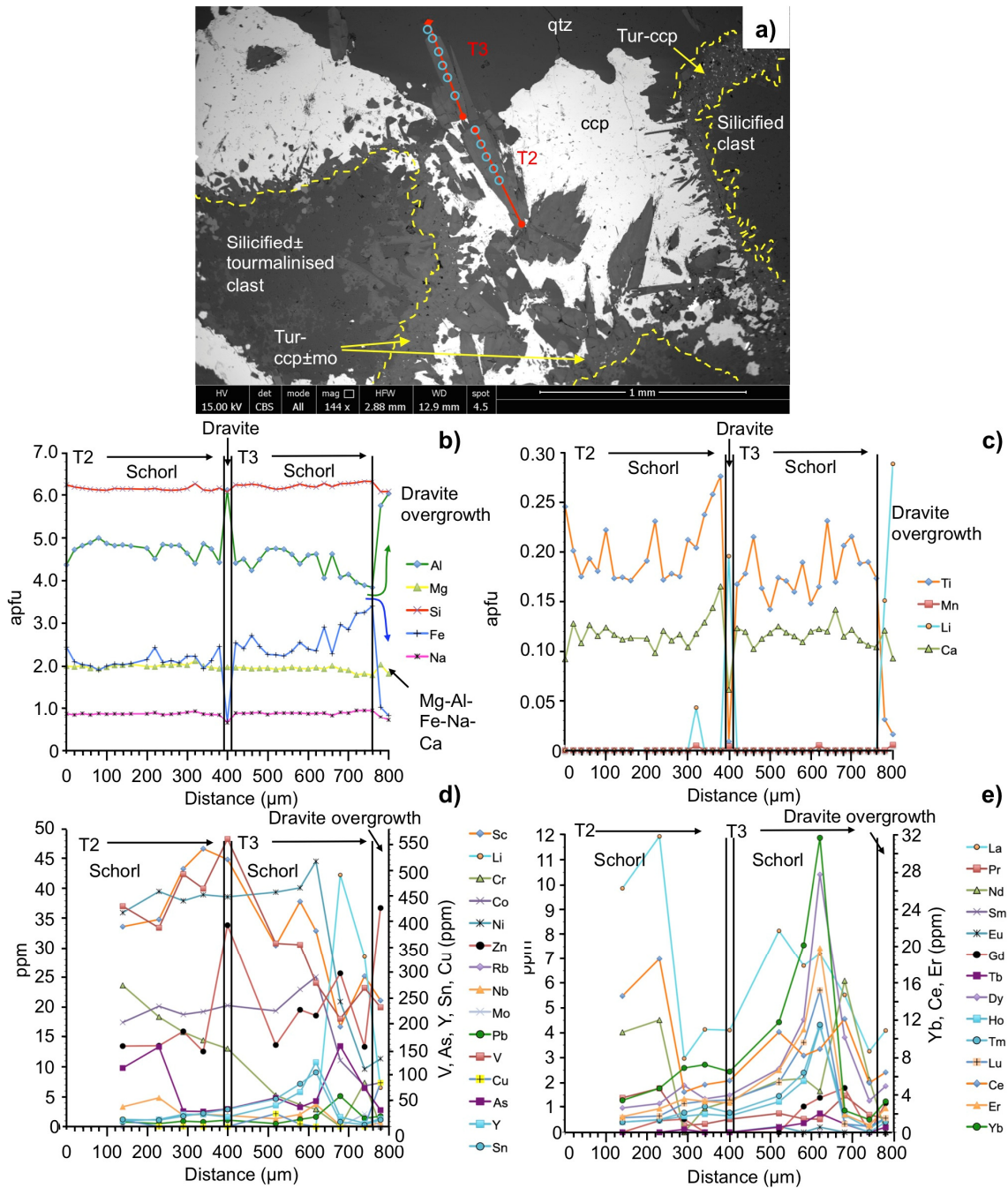


Fig. 4.49 Cement-hosted tourmaline (schorl) intergrown with quartz and chalcopyrite from sample DDH1754\_13 (BTB). A number of tourmaline crystals have been fractured and show weak zoning present in BSE images: **a)** SEM-BSE image. Blue circles indicate laser ablation points whilst the red line shows the relative start (circle) and end (diamond) of the EPMA traverse; **b-c)** EPMA data for major and minor elements in the traverses (traverses 2 and 3 being 400.98 and 416.24 μm long respectively, 20 μm intervals); **d-e)** LA-ICP-MS trace and REE data.

#### 4.6.4 Diablo

Tourmaline from the Diablo Breccias occurs as masses of interlocking acicular needles in the finer-grained areas and as coarser tourmaline crystals and/or rosettes alongside end-stage space-filling quartz-anhydrite ( $\pm$ gypsum) in the cement. A number of traverses parallel, or as close to parallel, with the *c*-axis were conducted to assess elemental variations. Given no large scale repeatable trace or REE trends occur through the individual Diablo traverses, they were compared between tourmalines sampled from the following zones in the breccias:

- **‘Deep inner’**: Two traverses, from the same paragenetic period, illustrating markedly different tourmaline trace and rare earth element trends (schorl $\pm$ dravite overgrowths) associated with the same paragenetic period.
- **‘Middle margin’**: Two schorl cement-hosted rosettes, within a few mm of one another, which show intense irregular/complex patchy zoning and dravite overgrowths. The rosettes are from the same paragenetic stage yet do not have similar trace and REE profiles.
- **‘Shallow inner’**: Weakly zoned dravite (with no schorl).

##### **Deep inner (Fig. 4.50 and Fig. 4.51)**

Both tourmalines in Fig. 4.50 and Fig. 4.51 are related to the same paragenetic period in the Diablo Breccias and are classified as schorl. Both have consistent Si ( $\sim$ 6 apfu), Mg (1.9 to 2.1 apfu) and Na (0.9 to 1.0 apfu) and more erratic Ca (0.1 to 0.2 apfu) and Ti (0.14 to 0.45 apfu) (Fig. 4.50c and Fig. 4.51c). In the SEM-BSE images in Fig. 4.50a and Fig. 4.51a, tourmalines show irregular/complex patchy zoning at a scale of  $\sim$ 100  $\mu$ m. The darker areas are enriched in Al<sub>2</sub>O<sub>3</sub> and MgO and the brighter zones in FeO and CaO. The largest variability in the traverses is in Fe (1.8 to 3.1 apfu) and Al (3.8 to 5.4 apfu). Minor Mg, Ca and Na are also interchanging suggesting the exchange (Ca(Fe Mg))(Al Na)<sub>-1</sub>. Darker grey BSE dravite overgrowths are present in 20 to 60% of tourmalines.

Both tourmaline traverses show compositional differences and internal variations in trace and REE elements. In Fig. 4.50d, for example, V concentrations vary from 668 to 2,560 ppm, whereas in Fig. 4.51d they range from 285 to 1,059 ppm. For As, the traverses contain between 42 and 134 ppm (Fig. 4.50d) and 22 and 206 ppm (Fig. 4.51d). Common trends towards crystal tips are a decrease in V and that Sn shows a large increase at intermittent points. In Fig. 4.50d, Sn increases from 21 ppm at the start to 1,201 ppm (at 120  $\mu$ m), then decreases to 21.6 ppm (at 420  $\mu$ m) and then increases to 40 ppm at the end of the traverse. In comparison, in Fig. 4.51d, Sn increases from 12 ppm at the start of the traverse, progressively increasing to 27 ppm (540  $\mu$ m) and then decreasing to between 19 and 21 ppm over the next 320  $\mu$ m. A

sharp increase to 115 ppm (1020  $\mu\text{m}$ ) is then observed, before decreasing to 50 ppm at the end of the traverse. All REE concentrations in both tourmalines are largely  $<5$  ppm in both traverses except Ce ( $<24$  ppm), La ( $<17$  ppm), Er ( $<17$  ppm) and Yb ( $<23$  ppm), which are also present at similar concentrations. The traverse in Fig. 4.51e shows relatively high REE at its start and end, which is not repeated in Fig. 4.50e.

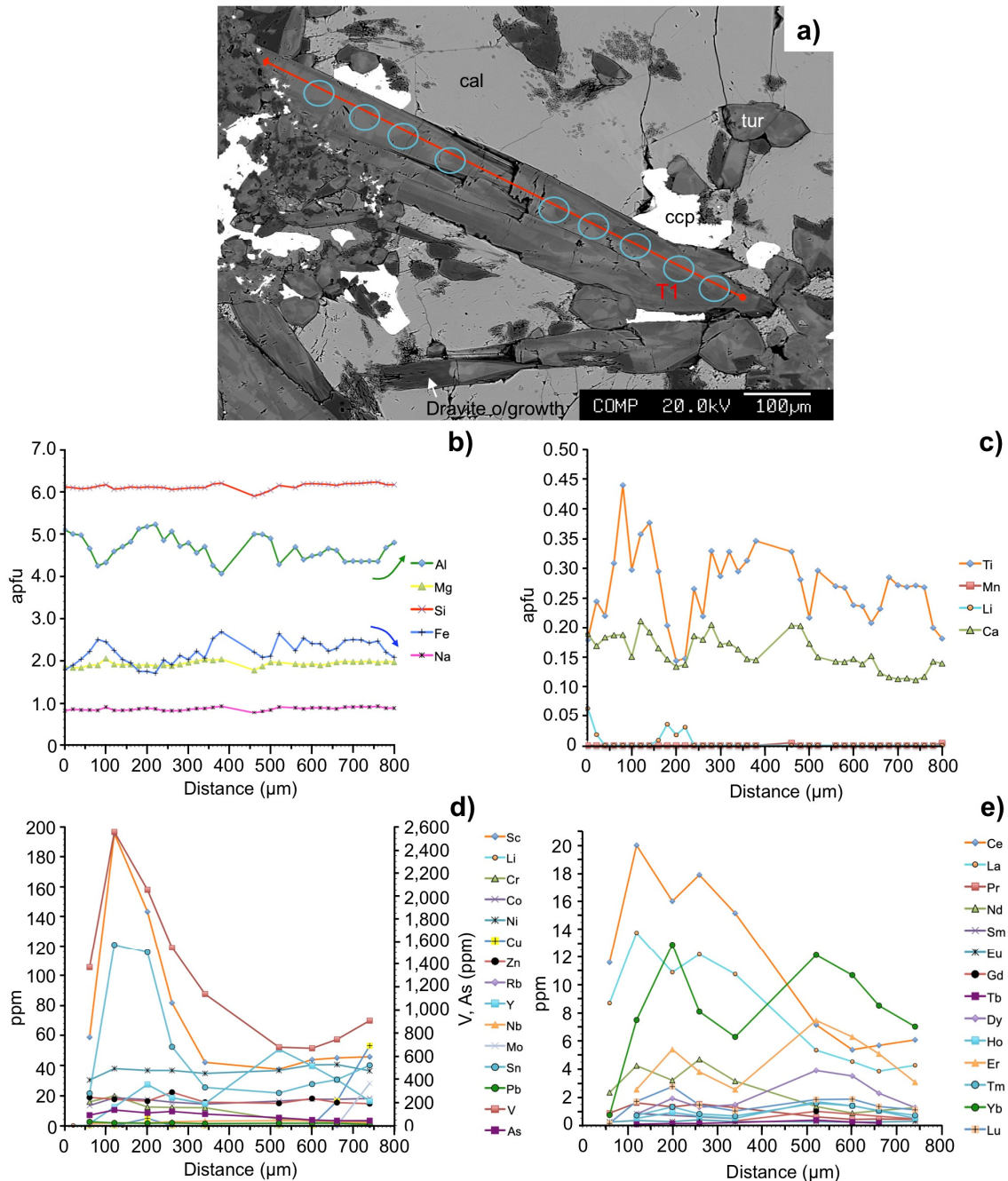


Fig. 4.50 Cement-hosted tourmaline (schorl) intergrown with calcite and chalcopyrite from the deepest part of the Diablo breccia sampled (DDH1974\_1-131.07 m): **a)** SEM-BSE image. Blue circles indicate laser ablation points whilst the red line shows the relative start (circle) and end (diamond) of the EPMA traverse; **b-c)** EPMA data for major and minor elements in the traverse (812.58  $\mu\text{m}$  long, 10  $\mu\text{m}$  intervals); **d-e)** LA-ICP-MS trace and REE data.

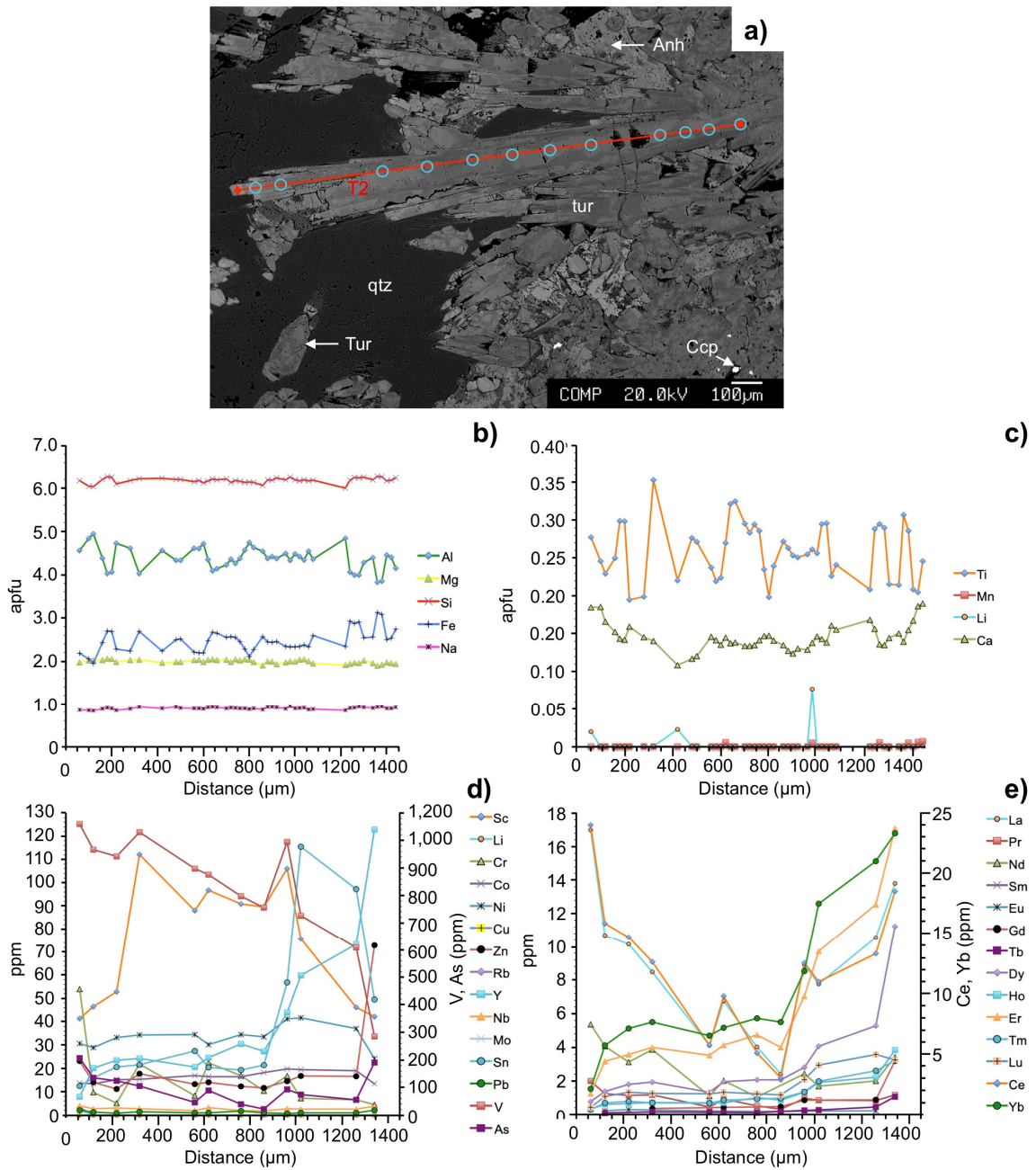


Fig. 4.51 Coarse tourmaline (schorl) with surrounding quartz and lesser anhydrite infill from sample DDH2136\_1 (0.96 m; deep inner): **a)** SEM-BSE image. Blue circles indicate LA-ICP-MS points whilst the red line shows the relative start (circle) and end (diamond) of the EPMA traverse; **b-c)** EPMA data for major and minor elements in the traverse (1,368.99 μm long, 20 μm intervals); **d-e)** LA-ICP-MS trace and REE data.

### **Middle inner (Fig. 4.52 and Fig. 4.53)**

Two coarse (>1 mm) cement-hosted schorl rosettes, shown in Fig. 4.52 and Fig. 4.53 were analysed. Both are overgrown with fibrous dravite that can be up to a few hundred  $\mu\text{m}$  long. These overgrowths are coarse in comparison to those in other breccias such as the BTB, MTB and ETB. This particular sample (2677\_3) and traverses are from one of the coarser cementing sections in the Diablo Breccias so are not wholly representative of the middle portions of the system. Identifying additional generations from the above is difficult due to the absence of clear cross-cutting relationships.

Both cement-hosted tourmalines show similar textural characteristics (Fig. 4.52a and Fig. 4.53a) with irregular/complex patchy zoning, at a scale of <50  $\mu\text{m}$  wide to >100  $\mu\text{m}$  long, being common in SEM-BSE images. The bright zones contain high FeO, CaO, Na<sub>2</sub>O whilst the darker areas are enriched in Al<sub>2</sub>O<sub>3</sub> and MgO. Major element variability is due to (Fe<sup>2+</sup>+Fe<sup>3+</sup>)(MgAl)<sub>-1</sub> exchange (Fig. 4.52b and Fig. 4.53b). Al (4.18 to 6.07 apfu) and Fe (0.43 to 2.90 apfu) show the largest variations, whereas Si (5.96 to 6.40 apfu) and Na (0.7 to 0.9 apfu) are near constant across the traverses. Mg is relatively consistent in both traverses (~2 apfu), with minor depletion (<2 apfu) in the dravite domains at the tips.

Despite being within 1 cm of one another, and related to the same paragenetic stage, the trace and REE traverse profiles within these cement-hosted tourmalines are inconsistent. V (261 to 1,026 ppm), As (24 to 478 ppm), Sc (22 to 66 ppm), Li (below detection to 36 ppm), Cr (below detection to 73 ppm), Co (5.4 to 18.2 ppm), Ni (5.2 to 54 ppm), Zn (7.5 to 29 ppm) and Nb (below detection to 3.4 ppm) are present at similar concentrations in both traverses. Rb and Cu are below detection. In Fig. 4.52d, Y is between 2 and 27 ppm and in Fig. 4.53d it is amid 11.7 and 96 ppm. In Fig. 4.53d, the highest and lowest concentrations of Ni and Zn, respectively, are present just before the later tourmaline overgrowth. This observation does not hold in the other traverse. In both tourmaline traverses, most REEs are erratic throughout and show relative decreases within ~100  $\mu\text{m}$  of the overgrowths and then increase by a few to several ppm into the overgrowths (see Fig. 4.52e and Fig. 4.53e). In the overgrowths, LREE range up to 8 ppm and HREE up to 4 ppm compared with up to 33 and 23 ppm in the earlier coarser tourmaline respectively.

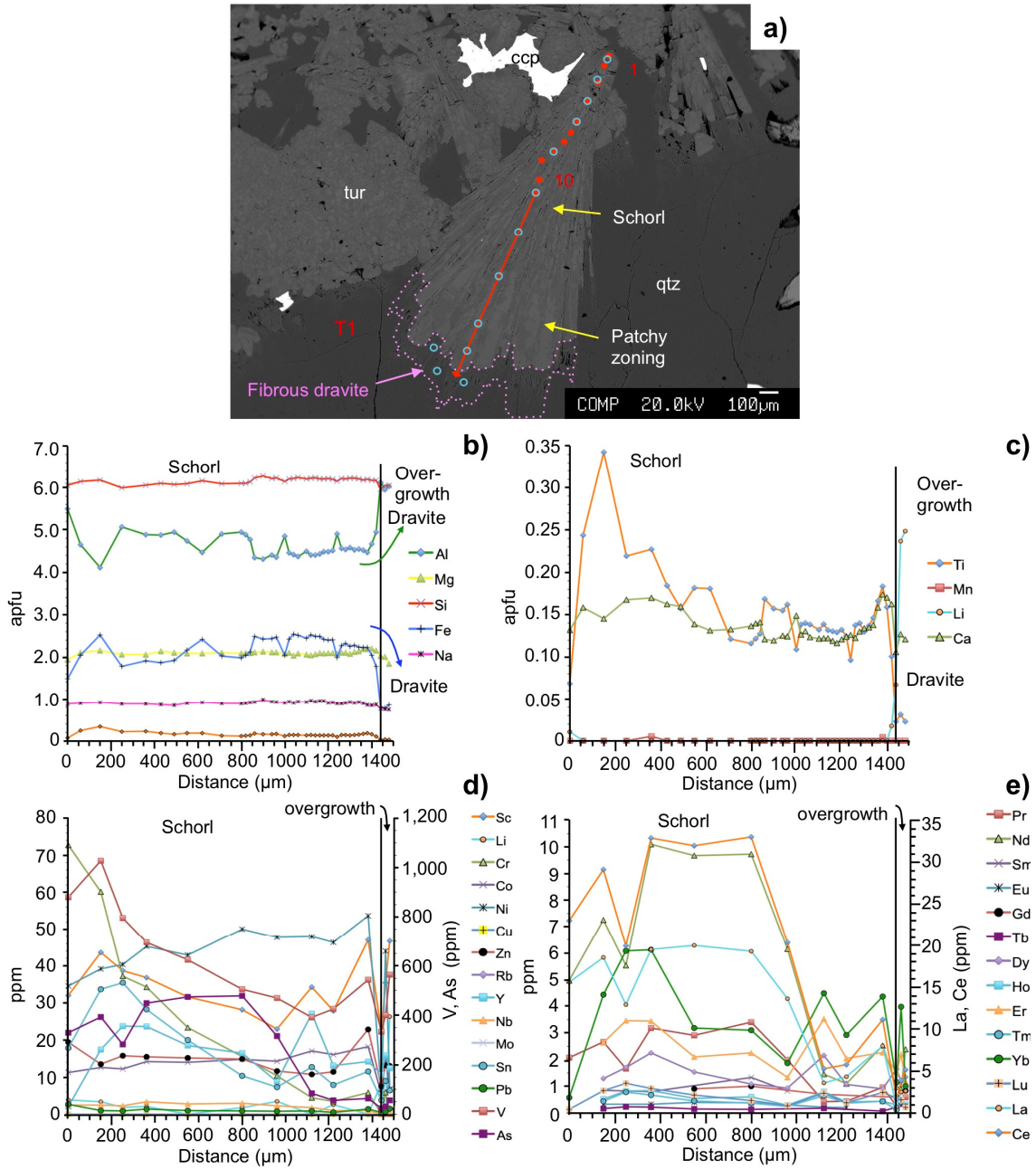


Fig. 4.52 Coarse radiating tourmaline (schorl) rosettes with fibrous dravite tips outlined in pink. Other cementing phases include quartz and chalcopyrite. From DDH2677\_3 (118 m; middle inner): **a)** SEM-BSE image. Blue circles indicate LA-ICP-MS points whilst the red line shows the relative start (circle) and end (diamond) of the EPMA traverse. Red dots signify individual EPMA analyses. Complex patchy zonation is present in the schorl; **b-c)** EPMA data for major and minor elements in the traverse (traverse 1 (excluding earlier individual points 1 to 10): 703.40 μm long, 20 μm intervals); **d-e)** LA-ICP-MS trace and REE data.

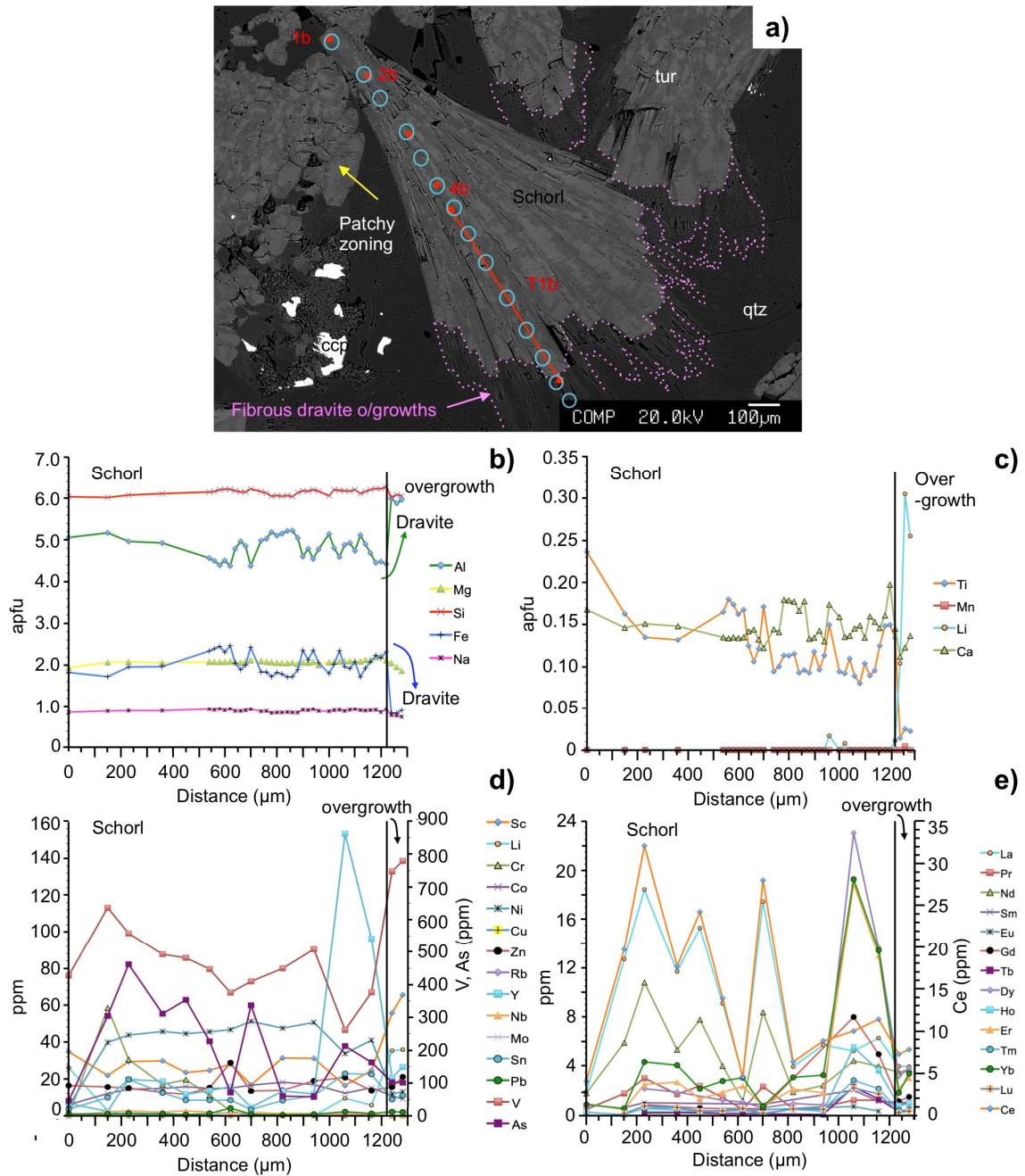


Fig. 4.53 Coarse radiating tourmaline (schorl) rosettes with fibrous dravite tips outlined in pink. Other cementing phases include quartz and chalcopyrite. Schorl displays complex patchy zoning. From 2677\_3 (middle inner): **a)** SEM-BSE image. Blue circles indicate laser ablation points whilst the red line shows the relative start (circle) and end (diamond) of the EPMA traverse. Red dots signify individual EPMA analyses; **b-c)** EPMA data for major and minor elements (traverse 1b (excluding earlier points 1b to 4b): 768.16  $\mu\text{m}$  long, 20  $\mu\text{m}$  intervals); **d-e)** LA-ICP-MS trace and REE data.

### **Shallow inner (Fig. 4.54)**

Tourmalines from the highest/shallowest sample 2672\_9 are largely classified as dravite, with little schorl present. Well-developed zonation is not commonly observed in SEM-BSE images which is reflected in their restricted range in major and minor element concentrations (Fig. 4.54b). Dravite is characterised by relatively high Al:Fe ratios, with Al concentrations of 5.5 to 5.9 apfu which are near similar to Si (~6 apfu). Fe contents range between 1.1 to 1.4 apfu, Na from 0.58 to 0.73 apfu and Mg 1.85 to 2.1 apfu. CaO (0.17 to 0.2 apfu) and Ti (0.04 and 0.1 apfu) are also roughly constant across the traverse (Fig. 4.54b).

Trace element concentrations of V (461 to 576 ppm), As (below detection to 14 ppm), Sc (32 to 114 ppm), Li (below detection to 3.2 ppm), Cr (40 to 78 ppm), Co (11.6 to 13.1 ppm), Ni (17.5 to 18.8 ppm), Zn (23 to 26.4 ppm), Y (0.8 to 5.9 ppm), Pb (below detection to 0.6 ppm), and Sn (3.9 to 5.3 ppm) are present in similar concentrations to other tourmalines in the Diablo Breccias. Cu, Rb, Nb and Mo are below detection. Elemental trends include: trace elements show little variation except As which increases from below detection to 14 ppm at the last point. V increases from 460 to 550 ppm. Cr decreases from 70 ppm at the start to 40 ppm at the end, similar to the traverses from sample 2677\_3 described above. Sn increases from 3.9 at the start to 5 ppm then decreases to 4 ppm at the end (Fig. 4.54d). All REE increase towards the end of the traverse by 0.2 up to a few ppm (Fig. 4.54e).

La (0.3 to 0.7 ppm), Ce (0.7 to 1.4 ppm), and Yb (0.59 to 2.95 ppm) show the most variability, others less so including Pr (below detection to 0.2 ppm), Eu (below detection to 0.16 ppm), Ho (below detection to 0.26 ppm), Lu (below detection to 0.65 ppm). A number are below detection in Fig. 4.54e, including Nd, Sm, Gd, Tb, and Dy.

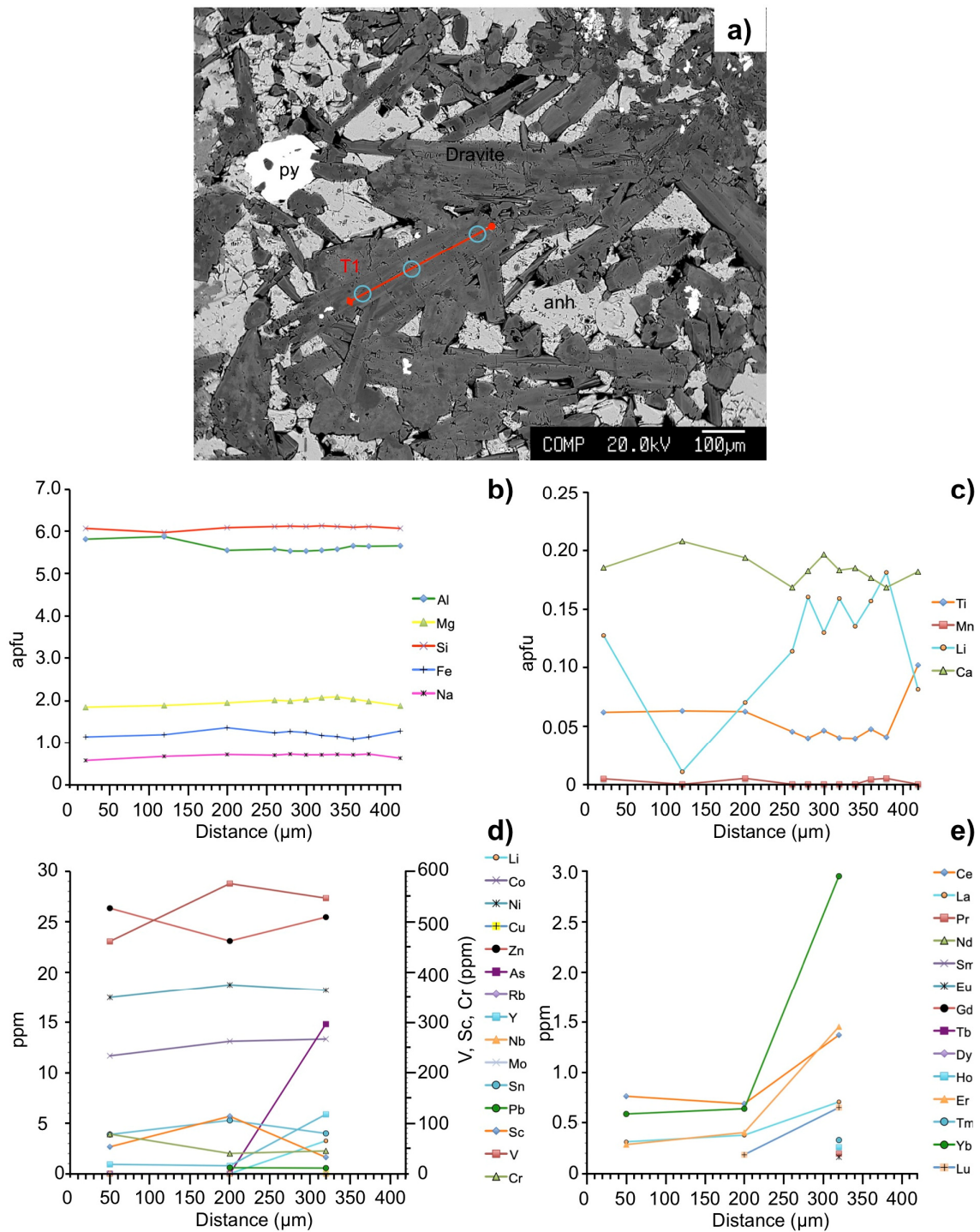


Fig. 4.54 Weakly zoned dravite with end-stage anhydrite-pyrite infill from DDH2672\_9 (166.66 m; high (shallow) inner): **a)** SEM-BSE image. Blue circles indicate laser ablation points whilst the red line shows the relative start (circle) and end (diamond) of the EPMA traverse; **b-c)** EPMA data for major and minor elements in traverse 1 (430  $\mu\text{m}$  long, 20  $\mu\text{m}$  intervals); **d-e)** LA-ICP-MS trace and REE data.

#### 4.6.5 La Huifa

Cement-hosted tourmalines were analysed to compare with those from other breccias. Due to the small size and highly pitted nature of the earliest tourmaline generation (with later anhydrite, rutile and lesser chalcopyrite filling these pits), it was not possible to carry out single point analysis by LA-ICP-MS. As observed in other breccias, the coarser tourmaline (generation 2) has fine fibrous overgrowths (generation 3) on the tips, which are parallel to the *c*-axis. These overgrowths range in size from 100 to several hundred  $\mu\text{m}$ . Data for generation 2 (characterised by euhedral non-pitted tourmaline) and generation 3 (comb-like overgrowths on tourmalines or tourmaline-healed fractures) are shown in Fig. 4.55, Fig. 4.56 and Fig. 4.57. Additional traverses from the cement are presented in Appendix v.

Compared with the other breccias studied, tourmaline from La Huifa shows particularly well-developed zoning in optical and SEM-BSE images. This is mostly oscillatory and patchy zoning. The brighter zones are depleted in Al and enriched in Fe compared with the darker patches. The scale of individual oscillatory zones is often  $<50 \mu\text{m}$ , whilst patchy zones are  $<100 \mu\text{m}$ .

The largest range in compositions is shown by Al (3.2 to 6.2 apfu) and Fe (1.4 to 3.6 apfu). Si (5.9 to 6.34 apfu) shows little variation across either tourmaline in Fig. 4.55b, Fig. 4.56b and Fig. 4.57b, as does Mg ( $\sim 1.16$  to 2.14 apfu), and Na (0.55 to 0.87 apfu). Mn is largely below detection and Ca (0.005 to 0.3 apfu), and Ti (0.005 to 0.48 apfu). Increases in Ca correspond to decreases in Al (and increases in Fe). Zoning identified in the overgrowths by optical and SEM-BSE imaging is attributed to  $(\text{Ca}(\text{Fe Mg}))(\text{Al Na})_{-1}$  exchange. Through the overgrowths, Al increases as Fe decreases, and Na slightly decreases with a reduction in Mg, Si Ca and Ti (see Fig. 4.56b, c). Ti and Ca both show large relative decreases at the start of the overgrowths and then, after  $\sim 100 \mu\text{m}$ , begin to increase.

Li (below detection to 10.2 ppm), Sc (4.1 to 55 ppm), V (162 to 499 ppm), Co (21 to 39 ppm), Ni (10.5 to 54 ppm), Zn (17.8 to 59 ppm), Rb (below detection), Y ( $<39$  ppm) Nb ( $<0.74$  ppm), Mo ( $<1.67$  ppm), Sn (below detection to 32 ppm), and Pb (0.48 to 19 ppm), have similar concentrations across the three traverses in Fig. 4.55d, Fig. 4.56d and Fig. 4.57d. Cr shows a relatively large range up to 61 ppm (Fig. 4.56d). All REE increase in the tourmaline overgrowths, except that in Fig. 4.56e where they spike just before the beginning of the overgrowths, and then rapidly decrease in the overgrowths. All traverses (including overgrowths) have similar levels of REE for the following: La (0.53 to 4 ppm), Ce (0.55 to 4 ppm), Er ( $<7$  ppm) and Yb ( $<8.2$  ppm). The remaining REE are found at lower concentrations with similar ranges in all traverses, with the overgrowths enriched in Pr ( $<0.9$  ppm), Nd ( $<3.1$  ppm), Sm ( $<0.39$  ppm), Eu ( $<0.3$

ppm), Gd (<1.3 ppm), Tb (<0.4 ppm), Dy (<4.5 ppm), Ho (<1.5 ppm), and Tm (<1.3 ppm).

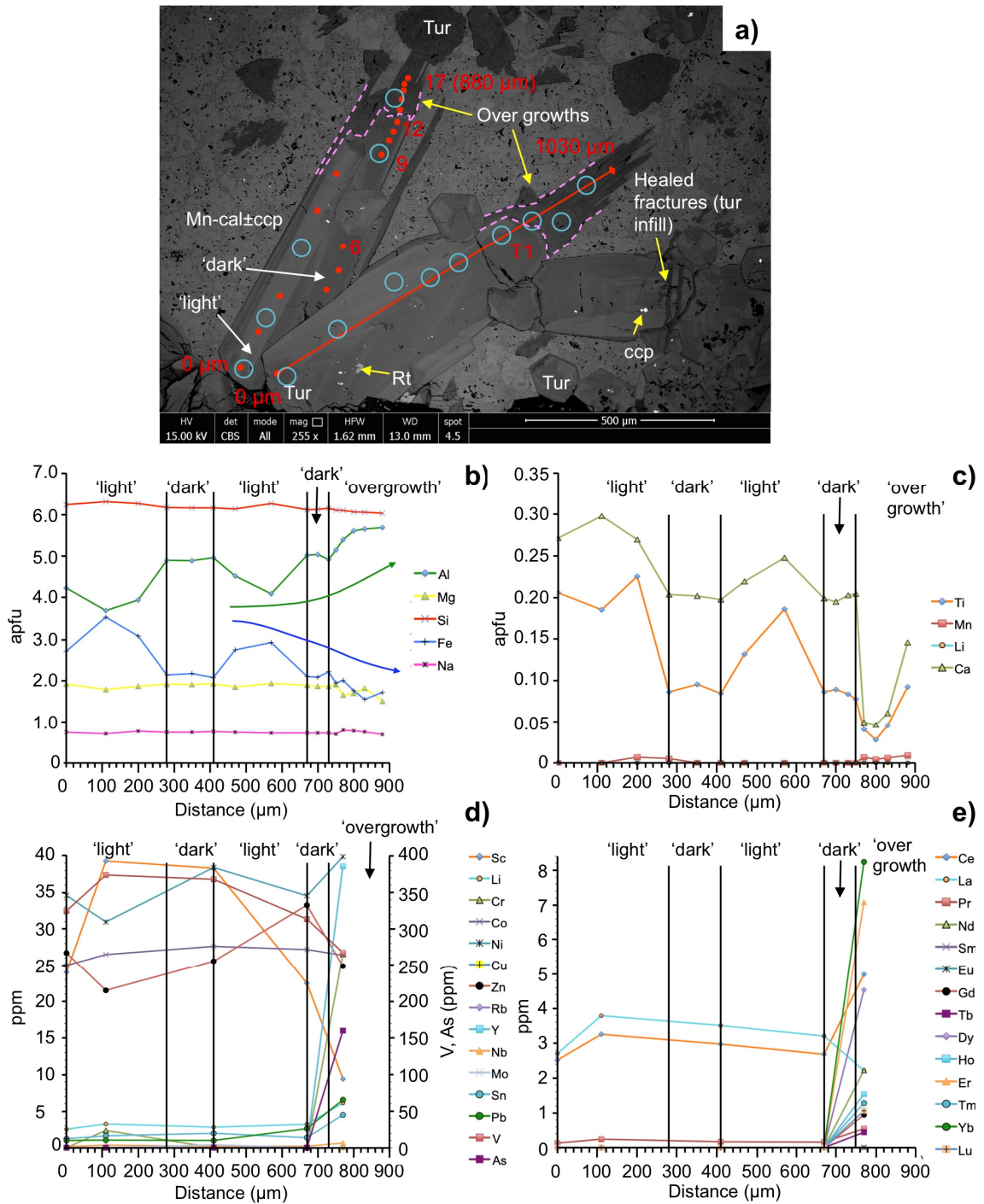


Fig. 4.55 Coarse tourmaline with <10 μm chalcopyrite and rutilite inclusions. Porous manganous calcite (±chalcopyrite inclusions) infills around tourmaline. From La Huifa ES026\_6 (191.74 m): **a)** SEM-BSE image. Blue circles indicate LA-ICP-MS points whilst the red line shows the relative start (circle) and end (diamond) of the EPMA traverse. Red dots signify EPMA point analyses; **b-c)** EPMA data for major and minor elements at points 1 to 17; **d-e)** Corresponding LA-ICP-MS trace and REE data.

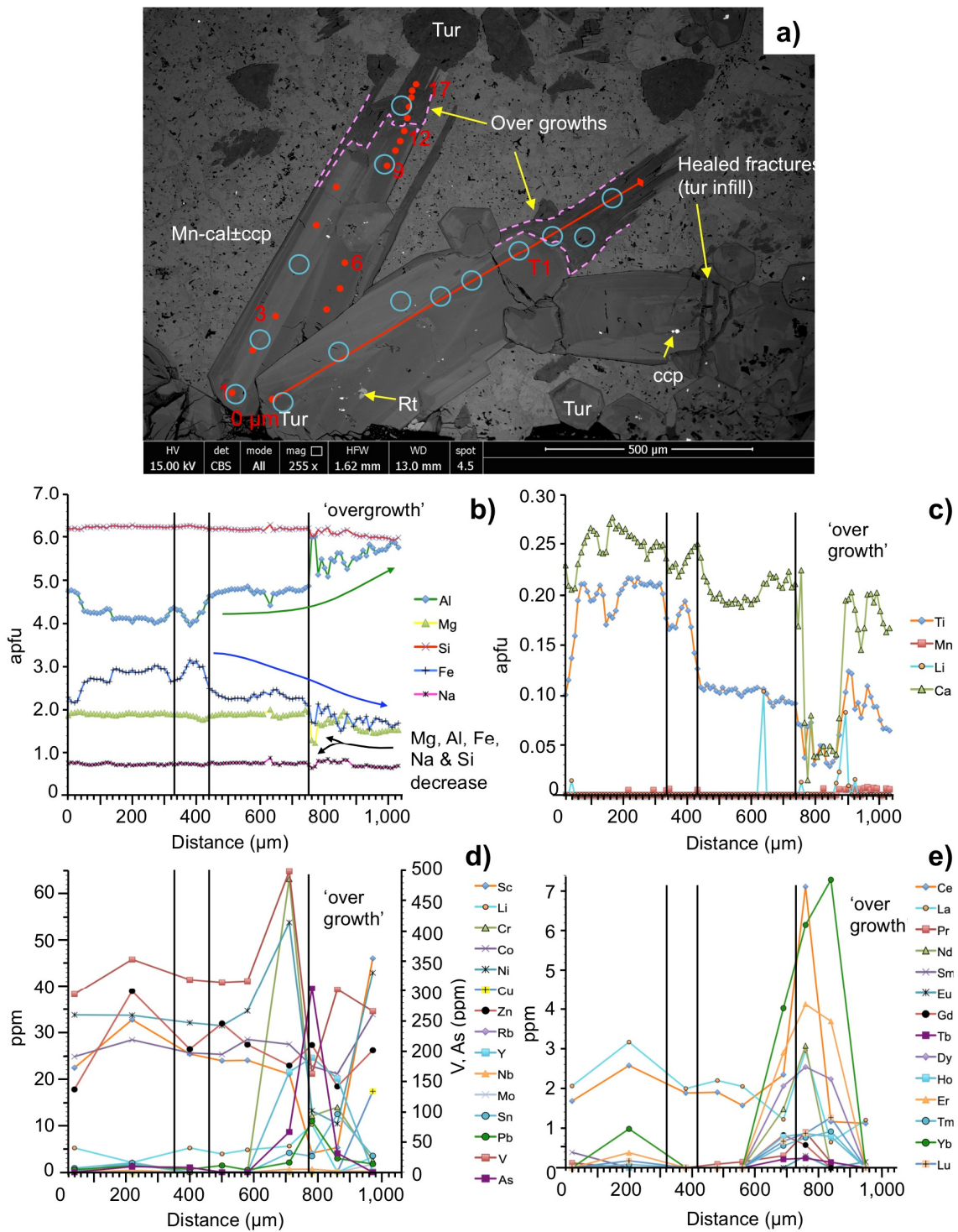


Fig. 4.56 Coarse tourmaline with <math><10\ \mu\text{m}</math> chalcopyrite and rutilite inclusions. Porous manganocalcic ( $\pm$ chalcopyrite inclusions) infills around tourmaline. From La Huifa ES026\_6 (191.74 m): **a)** SEM-BSE image. Blue circles indicate laser ablation points whilst the red line shows the relative start (circle) and end (diamond) of the EPMA traverse. Red dots signify EPMA point analyses; **b-c)** EPMA data for major and minor elements from traverse 1 (1,060.17  $\mu\text{m}$  long, 10  $\mu\text{m}$  intervals); **d-e)** Corresponding LA-ICP-MS trace and REE data.

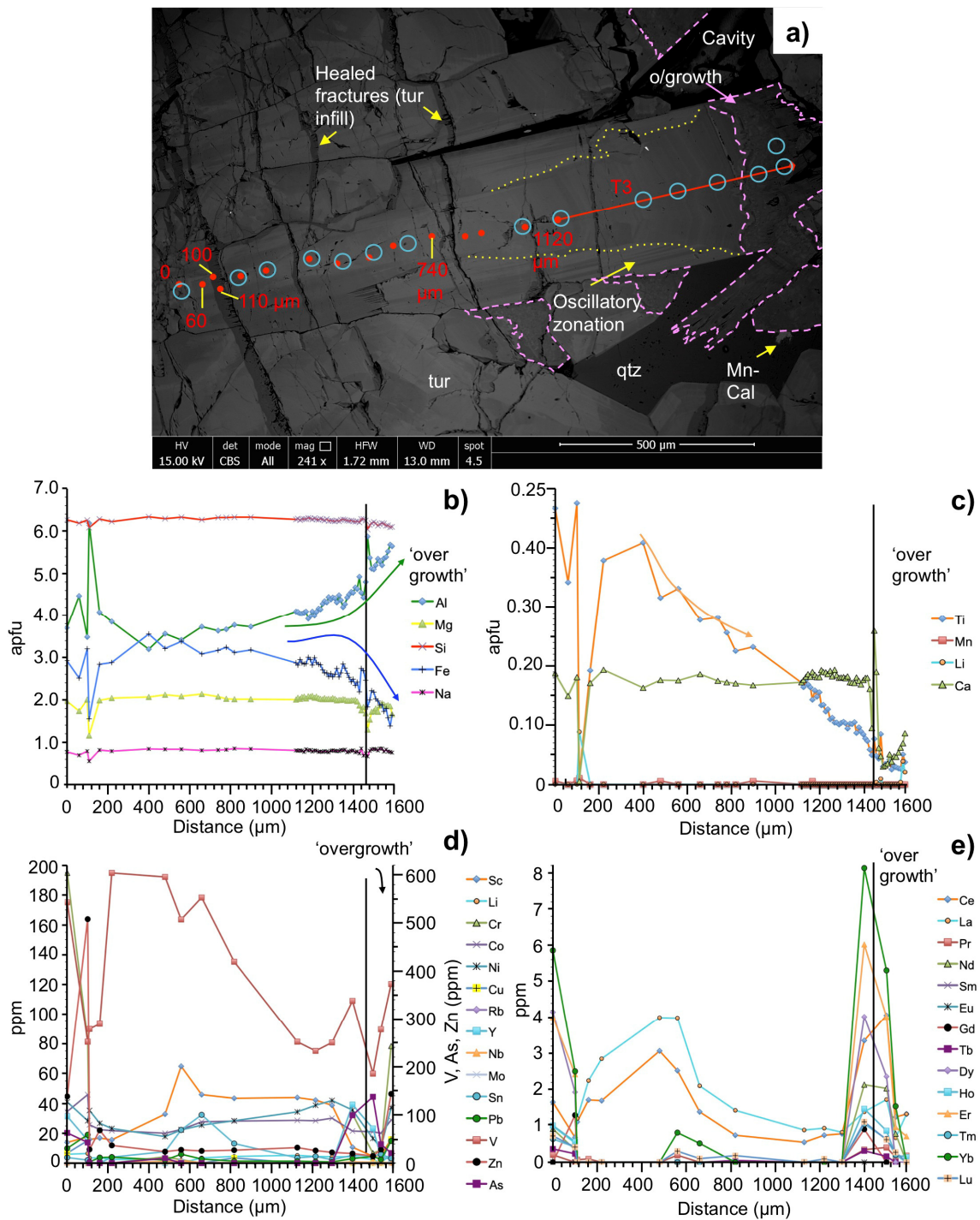


Fig. 4.57 Coarse euhedral blocky tourmaline with oscillatory and patchy zonation. Dravite overgrowths (outlined in pink) and 'healed' fractures (dravite) are common. Additional cementing phases are quartz and manganian calcite. From La Huifa ES026\_6 (191.74 m): **a)** SEM-BSE image. Blue circles indicate laser ablation points whilst the red line shows the relative start (circle) and end (diamond) of the EPMA traverse; **b-c)** EPMA data for major and minor elements in traverse 3 (excluding earlier points: 475.65  $\mu\text{m}$  long, 10  $\mu\text{m}$  intervals); **d-e)** LA-ICP-MS trace and REE data.

#### 4.6.6 Summary

Listed below are the main findings of tourmaline geochemistry from the studied tourmaline breccias in the Teniente district.

- Tourmalines in all of the breccias are members of the schorl-dravite solid solution series. They have fine oscillatory zoning and coarser, often irregular/complex patchy zoning where present.
- Main elemental variability is explained by a combination of  $\text{NaFe}^{2+}(\square\text{Al})_{-1}$ ,  $(\text{Fe}^{2+}\text{Fe}^{3+})(\text{MgAl})_{-1}$ ,  $(\text{Ca}(\text{Fe}, \text{Mg}))(\text{Al Na})_{-1}$ , and  $(\text{Fe})(\text{Mg})_{-1}$  vectors.
- Compositions of tourmalines from all five breccias studied at El Teniente are chemically similar with no distinguishing features between the weakly Cu-Mo mineralised/sub-economic Braden Tourmaline Breccia or Early Tourmaline Breccia to the well-mineralised Diablo, Marginal or La Huifa breccias.
- Tourmalines have asymmetric concave-upward chondrite-normalised REE shape patterns with weak Eu-anomalies (where present).
- All tourmaline breccias show high Si (>6.1 apfu) and  $\Sigma Y$  when all Fe is assumed to be  $\text{Fe}^{2+}$ , thought to be due to the presence of  $\text{Fe}^{3+}$  in addition to  $\text{Fe}^{2+}$ .
- Depth-related trends in the Diablo Breccias were identified including gradual decreases in Na, Ti, Fe and increases of Al upwards.
- Schorl±dravite overgrowths are prevalent at increased depths in the Diablo which compositionally change towards dravite at shallower levels, although there are overlaps to varying degrees in all elements across the different depths.
- Tourmalines closer to the breccia margins in the Diablo mine sector show larger variations in all elements compared with tourmalines towards the centre of the breccias.

## 5 Discussion

Porphyry-breccia-type deposits are becoming increasingly sought after by exploration and mining companies because they can be relatively high-grade and often occur in clusters giving large tonnages (e.g., Río Blanco-Los Bronces district contains >200 Mt of contained Cu; Toro et al., 2012). In addition, breccias often overlie or are adjacent to porphyry-type mineralisation and can therefore act as vectors towards it. Like porphyry intrusions, many breccia pipes are barren (containing no, or subeconomic Cu-Mo) forcing mineral exploration companies to look for new, innovative fertility proxies to help better focus exploration efforts (e.g., Wilkinson et al., 2017, and references therein).

In this chapter, the textural and chemical data presented in Chapter 4 for five tourmaline breccias at El Teniente, weakly mineralised through to high-grade, will be discussed. This is mainly to help determine their internal architecture, whether they were formed by physical (magmatic-hydrothermal intrusion-(±collapse) related or diatreme phreatomagmatic or magmatic) and/or chemical replacement mechanisms, and if tourmaline composition can be used to discriminate barren from mineralised breccias. The results of this are then compared with those from other work on porphyry-breccias (e.g., King et al., 2000, 2003; Skewes et al., 2003; Frikken, 2004; Baksheev et al., 2012; Dill et al., 2012), and granite-related tourmaline breccias from other worldwide systems (e.g., Williamson et al., 2000; Demirel et al., 2009; Duchoslav et al., 2017). Finally, this chapter presents an updated model for the Braden Pipe, which was previously proposed to be a diatreme (e.g., Makshev et al., 2004; Cannell et al., 2005, 2007; Spencer et al., 2015) formed by phreatomagmatic interaction between magmas and groundwaters (as per Sillitoe, 1985), or explosive devolatilisation of the underlying dacite porphyry magmas.

### 5.1 Architecture of El Teniente breccia complexes

Detailed and extensive mapping and logging has identified high-grade (Cu-Mo), vertically zoned breccia complexes located on the apices and flanks of the felsic-intermediate porphyry intrusives at El Teniente (e.g., Codelco Mine Geologists; Skewes et al., 2002; Cannell et al., 2005; Vry et al., 2010; Spencer et al., 2015; this study). Based on available geochronological data (Cannell, 2004; Makshev et al., 2002, 2004; Spencer et al., 2015), the porphyry intrusives and breccias across the Teniente district were not contemporaneous. From this, and cross-cutting relationships, the breccias mostly post-date the crystallisation of the porphyry intrusives, and in many cases their related mineralisation. This is evident from the breccias frequently containing clasts which host porphyry-style veinlet and disseminated Cu-Mo mineralisation. The breccia complexes at El Teniente do however display analogous

temporal evolution paths to one another and with the porphyry intrusives (Vry et al., 2010; this study).

In this section, the architecture/distribution of mineralisation in the different breccia bodies, and how this can help establish the level of exposure/mineralisation in the vertically extensive tourmaline breccia bodies is overviewed.

**Vertical zoning** - The complexes generally contain igneous- as well as biotite- and anhydrite-cemented breccias at depth, with tourmaline-cemented breccias becoming more common towards shallower levels (see Fig. 5.1). Other minor cementing phases at depth include K-feldspar and magnetite. Wall-rock and clast alteration largely reflects the cement composition of the breccias as per the generalised alteration-mineralisation zoning model for telescoped porphyry Cu deposits by Sillitoe (2010), shown earlier in Fig. 2.2. For example, tourmaline breccias are mostly sericite ( $\pm$ quartz)-altered whereas biotite breccias and adjacent host rocks at greater depths are biotite-altered. The exception to this is the La Huifa tourmaline ( $\pm$ anhydrite) breccia where intense calcic-sodic alteration is observed. Given the rarity of this alteration style, and from general models for porphyry systems (with Ca-Na below the potassic zone, e.g., Sillitoe, 2010, and references therein), it is likely that current exposure of La Huifa is at a relatively deep level in a porphyry system. This implies that tourmaline breccias are capable of having much larger vertical extents than other breccias (Fig. 5.1).

Within the extensively zoned larger complexes at El Teniente, the breccias show overlapping and/or transitioning clast and groundmass styles and alteration for between tens of m up to 100 m. Similar vertical trends, possibly reflecting an upward transition from magmatic to hydrothermal conditions, are present at other porphyry Cu deposits in Chile such as Río Blanco-Los Bronces (Warnaars et al., 1985; Skewes et al., 2003), in particular the Sur-Sur breccia (Frikken et al., 2005). It should be noted, however, that the transitional nature of the zoning can easily lead to confusion, or mixed or inconsistent classification, particularly where the cementing phases, on which the classifications are often partly based, e.g. tourmaline or anhydrite, are present in roughly equal proportions (see Fig. 5.1f).

At El Teniente, the tourmaline breccias were some of the last to form, as: a) few structures or later bodies cross-cut or overprint them, except for Cu-mineralised (bornite-chalcopryrite) quartz dykes (>90% quartz; see Fig. 5.8 for example photo) in the Diablo sector, and where Póstuma alteration assemblages infrequently cross-cut the Marginal Tourmaline Breccia; and b) anhydrite-cemented breccias are cross-cut by tourmaline veins $\pm$ crackle breccias. Vry (2010) also suggested that tourmaline breccias 'may not necessarily represent the end-point of localised intrusion breccia-complex

evolution, instead they may form by a separate mechanism to the other breccias based on the occurrence of the late type 9 tourmaline veins and other tourmaline breccias in the district'.

**Horizontal zoning** - Although tourmaline breccias display near vertical continuous cylindrical forms, in plan view they are between circular and ovoid. The long axis of the ovoid shape of the Diablo Breccias, for example, is oriented NNW-SSE, parallel to the dominant structural trend, which likely reflects local stress conditions during breccia emplacement. In addition, its margins are jagged, often displaying m-sized areas which flare outwards and taper inwards; perhaps controlled by wall-rock properties such as jointing. Their ragged outline is significant as the margins, particularly lobate areas, are often sulphide-rich. Surrounding the main breccias are zones of crackle breccias up to several tens of metres wide, which host tourmaline-quartz-sulphide veins (Fig. 5.1d). In places, these developed within reactivated porphyry-style veinlets introducing later breccia cement-phase assemblages.

**Breccia pipe geometry and distribution of Cu-Mo mineralisation** - This study has shown that not only is there significant textural and mineralogical variability throughout the El Teniente breccias, there is also an irregular distribution of Cu-Mo within the breccia columns. This is best illustrated towards the margins of Diablo Breccias where Mo and Cu-sulphides are often the main cementing phases. Although these high-grade zones partially formed from late Cu-Mo-rich fluids, which exploited more permeable corridors, and/or by earlier mineral cements being replaced, pipe geometry may have also influenced permeability throughout the breccias. Increased permeability towards breccia margins could have been generated by poor stacking of large wall-rock fragments, plucking of wall rocks into the breccia, generation of vertically sheeted zones and slightly lower contents of small fragments and rock-flour compared with central portions.

In contrast, the more central parts of the breccias usually have reduced permeability due to increased volumes of fine particles produced through attrition and abrasion during rapid emplacement and comparatively faster central flow. As a consequence of this, the margins of the Diablo Breccias are particularly Cu-Mo-rich, with Cu- and Mo-sulphides filling open-space, which is also observed in other porphyry-related breccias, such as San Francisco De Los Andes Breccia; San Juan, Argentina (Llambias and Malvicini, 1969), the Donoso Breccia; Río Blanco-Los Bronces (Warnaars et al., 1985) and the Ilkwang Breccia; Ilkwang Mine South Korea (Fletcher, 1977). In the San Francisco De Los Andes Breccia, "the bulk of the orebody formed in the rim of the breccia-pipe", which replaced the earlier quartz-tourmaline-pyrite cementing phases by

ore minerals including bismuthinite, chalcopyrite, bornite, digenite and tetrahedrite (Llambias and Malvicini, 1969).

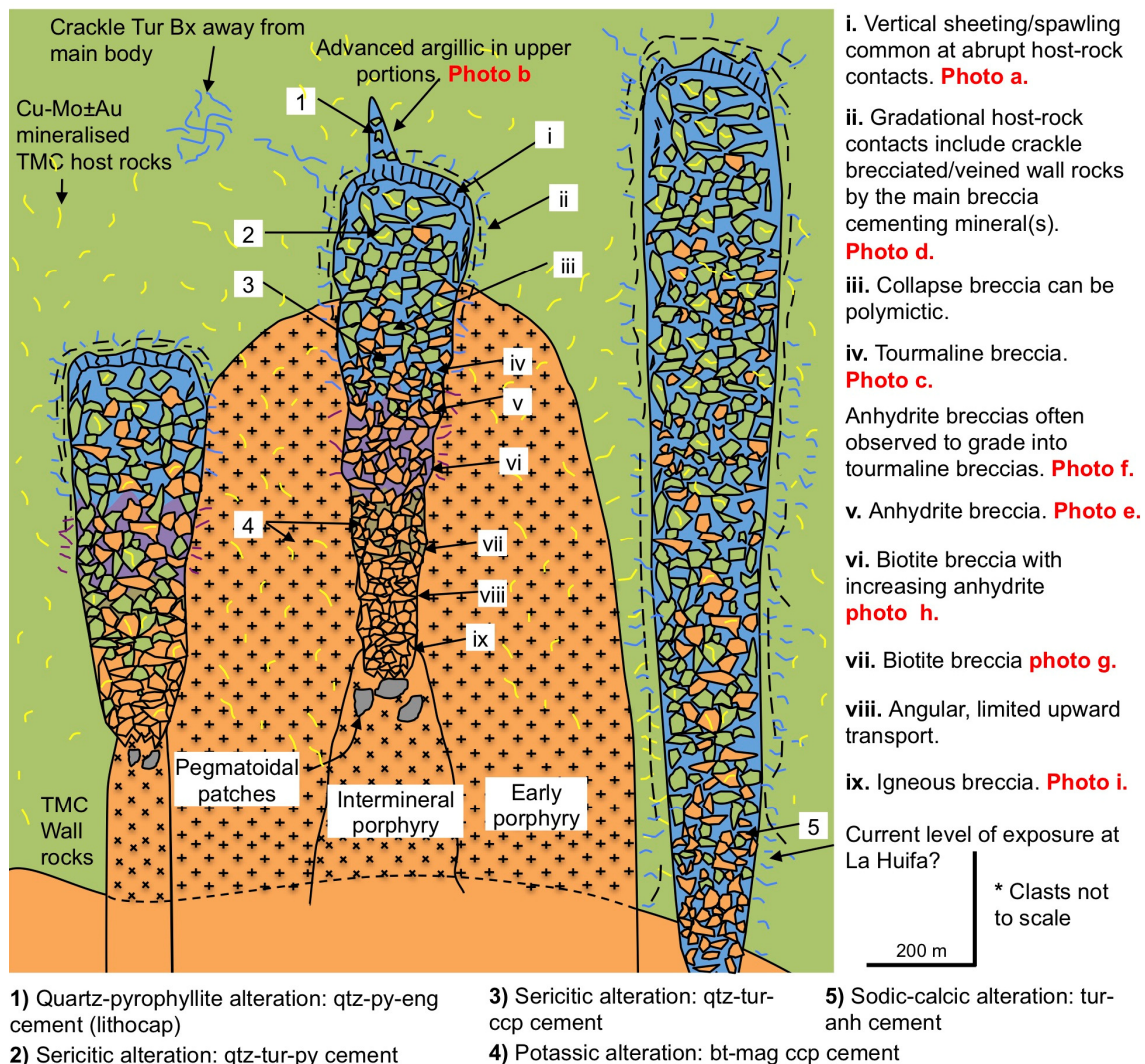
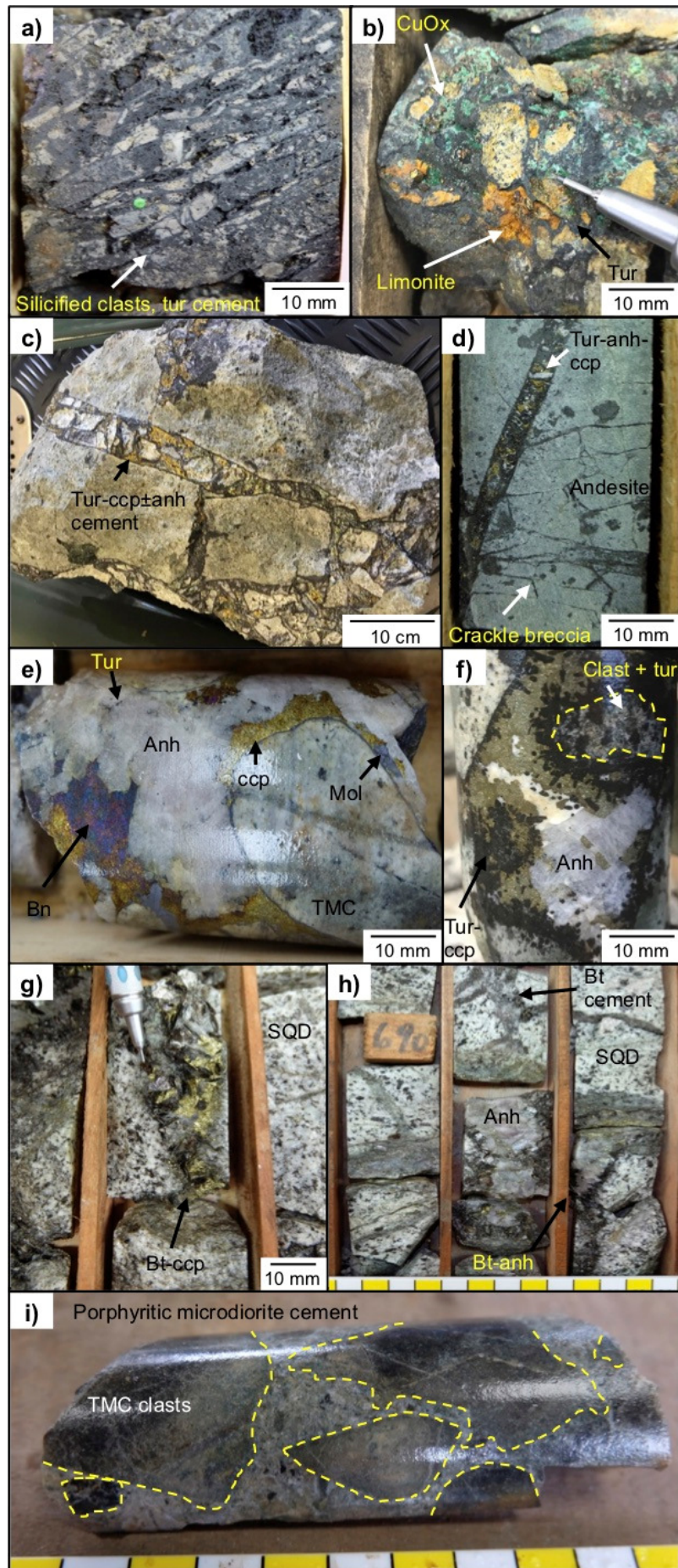


Fig. 5.1 Schematic of vertically zoned magmatic-hydrothermal breccia complexes at El Teniente genetically linked to the apex and/or flanks of intermineral porphyry intrusions such as the Teniente Dacite Porphyry. Also included on the right is a tourmaline breccia independent of these zoned complexes. Figure adapted from Sillitoe (2010) with observations from the current study added. Example photos from El Teniente district are provided below: **a)** Preferentially aligned silicified, bleached clasts with a high aspect ratio, cemented by porous tourmaline. Sample is near the margin of the La Huifa breccia. From ES05-3 m; **b)** La Huifa tourmaline breccia with advanced argillic overprint. CuOx precipitated in fractures and cavities. From ES03-68 m; **c)** La Huifa tourmaline breccia from outcrop. Andesite and diorite clasts are sodic-calcic-altered with a chlorite overprint cemented by tourmaline-chalcopyrite-bornite; **d)** Crackle breccias and veining in propylitic-altered host rocks at La Huifa. From ES026-105 m; **e)** High-grade anhydrite-cemented breccia (Diablo) with a significant portion of chalcopyrite-bornite and little tourmaline. Clasts are well-rounded and contain porphyry-style veinlet mineralisation. From DDH2672-98 m; **f)** La Huifa tourmaline breccia with a significant anhydrite cementing component. These are particularly common near anhydrite breccias at depth, where they can gradually transition between one another. From ES026~180 m; **g)** Biotite-chalcopyrite-cemented breccia from the A-Porphyry with little anhydrite. From DDH1794-215 m; **h)** Biotite-cemented breccia from the A-Porphyry with an increasing anhydrite cement component. From DDH1794-210 m; **i)** Igneous breccia associated with the Southern Diorite (east of the Braden Diatreme) with clasts of the TMC within a porphyritic diorite cement. TMC clasts are often bleached a lighter colour towards their margins whilst smaller clasts are more intensely bleached. Sample from DDH1512-350.52 m.



## **5.2 Models for tourmaline breccia formation at El Teniente**

From the textural observations discussed above, the El Teniente tourmaline breccias were formed by magmatic and magmatic-hydrothermal processes. The two main mechanisms for this were magmatic intrusion, which initiated explosive fluid exsolution, and magmatic-hydrothermal replacement of previous rock flour breccias, the latter confined to the BTB in the Braden Diatreme. Magmatic-hydrothermal intrusion-related breccias are more common and are characterised by angular to subrounded fragments, derived from adjacent TMC wall rocks and the underlying and/or adjacent felsic intrusions. The felsic fragments have a similar mineralogy, alteration, and texture to the adjacent and/or underlying felsic-intermediate intrusive (Vry et al., 2010; this study). Magmatic-hydrothermal intrusion-related breccias show a mixture of mosaic and chaotic textures, and are clast- and cement-supported, grading laterally outwards into in-situ crackle breccias and tourmaline (±other cement phases) veining. The other, less common, variety is magmatic-hydrothermal replacement breccias, which at El Teniente, have the same framework as the Braden Diatreme and unlike magmatic-hydrothermal intrusion breccias are not surrounded by crackle breccias.

### **5.2.1 Magmatic-hydrothermal intrusion breccias**

The formation of tourmaline breccia pipes at El Teniente was likely related to the emplacement of high crustal level, volatile-rich, felsic-intermediate porphyry intrusion(s), ultimately derived from a deep-seated crustal magma chamber, as per the models of Sillitoe (1985, 2010). The main evidence for this is the close spatial association of steep pipe-like breccias on the flanks, apices or above causative intermineral porphyry phases (e.g., Fig. 2.11; Fig. 5.1). Many of the breccias incorporate clasts showing porphyry-style alteration-mineralisation and therefore post-date partial crystallisation of the porphyry phases (e.g., Sillitoe, 2010; this study). Fluid inclusion and stable isotope analyses suggested the Marginal Breccias formed from magmatic fluids (Skewes et al., 2002).

Due to decompression (first-type boiling) and/or the crystallisation of the magma (second-type boiling; Burnham, 1985; Candela, 1997), large volumes of volatiles likely accumulated in the cupola/carapace or apophyses until fluid pressure overcame lithostatic pressure. This resulted in the lifting and fracturing of the overlying rock column, explosive upward release of magmatic-hydrothermal fluids and the generation of a brecciated rock column (see Fig. 5.1i), in accordance with the models proposed by Burnham (1979, 1985).

In the model described above, significant open-space (up to 20% in many pipes; Sillitoe, 1985) would have been present throughout the breccias, in particular before the formation of the hydrothermal cements. The mechanisms to produce the necessary open-space and association between porphyry intrusives, breccias and alteration-mineralisation are still poorly understood, but are likely to have included one of, or a combination of the following:

1. Downward movement of magma, through shrinkage or withdrawal, underlying the current breccia which opened up space (e.g., Perry, 1961; Sillitoe, 1985);
2. Accumulation and explosive release of exsolved magmatic fluids (once hydrostatic pressure exceeds tensile strength of confining units and lithostatic load) in apical portions of magma chambers along with material carried upwards (e.g., Burnham, 1985; Sillitoe, 1985; Frikken et al., 2005). This somewhat overlaps with the mechanism proposed by Kents (1964), whereby accumulated separated magmatic-hydrothermal fluids in the upper portions of magma chambers were, 'hydraulically rammed into the overlying enclosing rocks during magmatic pulses'. This effectively opened existing and new fractures and eventually lead to spalling and further upwards brecciation;
3. Development of a 'bubble'/void in the roof of a porphyry stock and/or pluton through the accumulation of exsolved fluids, followed by fluid release through fractures, buckling of void walls and onset of caving and infiltration of the breccia by magmatic or external fluids (e.g., Norton and Cathles, 1973);
4. Dissolution of roof rocks and collapse (as per Sillitoe and Sawkins, 1971).

Many of the characteristics of the El Teniente tourmaline breccias can be explained by these theories, but there is no evidence of significant downward magma movement or collapse, likely due to the level of erosion at El Teniente. In addition, hydraulic ramming, proposed by Kents (1964), does not explain the large cement-supported areas and the presence of fine particles thought to be derived from attrition and abrasion from minor transport. Options 2 and 4 are considered to be the most likely as hydrothermal fluids can be corrosive (e.g., Sillitoe, 1985; Frikken et al., 2005) and there is evidence for varying degrees of dissolution in the El Teniente breccias, discussed below.

Breccia characteristics such as clast:cement ratio, clast size, rounding, sorting and morphology, and cement descriptions (infill vs. replacement vs. very small clasts) provide insights into some of the brecciation processes. Below are discussions of the textures and inferred brecciation mechanisms (physical vs. chemical) of the magmatic-hydrothermal intrusion-related tourmaline breccias at El Teniente.

**Early Tourmaline Breccia** - These crackle breccias show no evidence of chemical erosion or attrition and abrasion through transportation. The effect of hydrothermal activity is nonetheless evident from the bleached nature of many clasts and drill core intersections. The crackle breccias located on the eastern side of the deposit are termed 'early' by mine geologists and Spencer et al. (2015), although this term is somewhat vague. The crackle breccia fragments contain porphyry-style veinlet Cu-Mo (type 4a, 6a, 6b and 7b) and disseminated Cu mineralisation so post-date porphyry intrusion and related Cu-Mo mineralisation. Given their limited spatial distribution, lack of cross-cutting relationships with other breccias, and that tourmaline veins and crackle brecciation around the larger breccias can extend for several tens of metres, it proved difficult to paragenetically link or separate crackle breccias from larger breccia bodies nearby.

This 'early' tourmaline breccia is somewhat similar to an early, poorly distributed and poorly encountered subeconomic tourmaline breccia at Los Bronces. This is described by Warnars et al. (1985) as consisting of early barren quartz-tourmaline veins 'which developed locally into sulfide-poor breccias which contain intrusive fragments rotated and cemented by quartz and tourmaline'.

**Marginal and La Huifa Breccias** - The Marginal Tourmaline and La Huifa Breccias at El Teniente are both cement- and clast-supported and their textures vary from mosaic to chaotic (as per Woodcock and Mort, 2008). Large (>2 mm) and small (<0.1 to 2 mm) clasts are generally angular to subangular although a number are subrounded to rounded. Towards the central parts of the breccias, a larger percentage of clasts have subrounded to subangular morphologies compared with nearer the margin where clasts are typically more angular. This indicates that there was more transport, and therefore abrasion/attrition, within the central portions of the breccias.

A combination of fluid-assisted brecciation, volume expansion and wear abrasion/impact took place in these breccias, as evident from the presence of mosaic and chaotic textures with large (>2 mm) and small (<0.1 to 2 mm) angular-subangular clasts (Fig. 5.2). A small percentage (<30%) of clasts in the Marginal Tourmaline Breccia, including the wall rocks, show indications of chemical attack from the presence of strongly bleached clasts and anhedral/lobate clast margins. Clasts of the TMC wall-rocks often have complex lobate clast margins (Fig. 5.2), supporting an origin derived from corrosive fluids, rather than a juvenile origin which can also produce vermiform clast morphologies. These complex morphologies (see red arrows in Fig. 5.2) would not be expected from a strictly fluid-assisted physical brecciation and are not considered to be from a juvenile magmatic origin as they are wall-rock clasts.

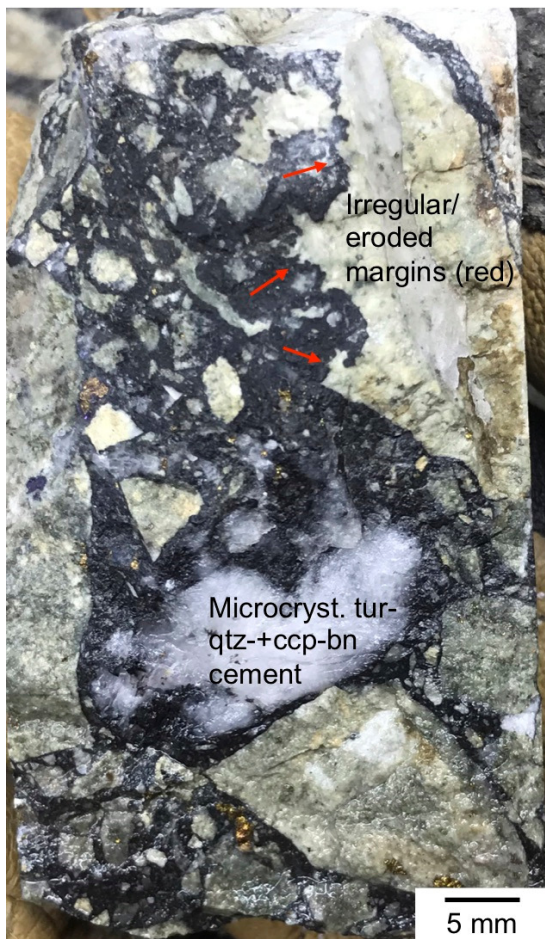


Fig. 5.2 Drill core photograph illustrating complex, wispy-shaped/irregular clast morphologies of the TMC wall-rocks (red arrows) in the MTB from corrosive wear. This sample is 2.5 m from the breccia margin. Chlorite overprint is present. From DDH1213-95.5 m.

Chemical abrasion of the clasts is likely to be intrinsically linked to the acidic to neutral fluids which favour tourmaline crystallisation (e.g., Morgan and London, 1989; Trumbull et al., 2020). The exact timing is difficult to establish, however following the formation of their irregular/eroded margins, the clasts were not transported significantly as this would have resulted in physical abrasion and rounding/removal of irregular margins. Alternatively, chemical corrosion took place after precipitation of the tourmaline-quartz cement. This is deemed unlikely however as there is no evidence of large-scale dissolution and reprecipitation of the tourmaline-quartz cement.

**Diablo Breccias** - Although previously described as a “tourmaline-quartz-chalcopyrite breccia” by Vry et al. (2010), it was clear from drill core observations in this study that it consists of multiple, texturally and mineralogically separate breccias superimposed on one another; they have therefore been termed the Diablo Breccias. They have a similar paragenesis to the La Huifa and Marginal Tourmaline Breccias, where tourmaline was the first cementing phase largely followed by quartz, anhydrite and late Cu-Mo sulphides, often with further quartz and anhydrite, as end-stage space-fill. The presence of fragments of one breccia within another was the best criteria for establishing age relationships between these tourmaline breccias because identifying cross-cutting relationships in drill core was difficult. As an example, Fig. 5.3a shows a clast of weakly mineralised microcrystalline tourmaline breccia within a coarser tourmaline-quartz-anhydrite-sulphide cement, where:

1. The coarser-grained cement phases (anhydrite, quartz, calcite) show well-developed, zoning (up to 1 mm per zone) in hand specimen (Fig. 5.3b) and under CL (Fig. 5.3c). Tourmaline is also comparatively coarser-grained compared with the microcrystalline cements. These indicate slower crystallisation compared with the finer-grained breccias.
2. In the microcrystalline breccias, tourmaline and quartz are the main cementing components, where tourmaline accounts for between 40 and 60 vol.% of the cement. In the later coarser-grained breccias, tourmaline only accounts for 20 and 50 vol.% of the cement, with larger portions of anhydrite and quartz ( $\pm$ Cu-Mo sulphides) present. A smaller tourmaline cementing component in the later coarser breccias could represent a temporal evolution of ever decreasing boron in the accumulating magmatic-hydrothermal fluids.
3. The angularity of clasts and fine-scale zoning (often  $<100 \mu\text{m}$ ) in tourmaline from the microcrystalline tourmaline-quartz breccias, suggests rapid emplacement, cooling of fluids, cementation and minor transport and abrasion compared with the coarser breccias, although clasts in the microcrystalline breccias can also be well-rounded.
4. In the coarser cemented breccias, clasts are more rounded indicating increased transport and/or corrosive wear. Clast margins are highly jagged and irregular on a micron-scale (Fig. 5.3c) supporting a role for corrosive fluids.
5. Smaller clasts ( $<5 \text{ mm}$ ; Fig. 5.3g) in the microcrystalline breccias are more rounded, which was similarly observed in the Donoso breccia by Warnars et al. (1985), signifying that a degree of rounding and transport took place. A large portion of clasts  $<1 \text{ cm}$  in the Diablo Breccias are largely silicified indicating partial replacement associated with fluid ingress (see Fig. 5.3g).
6. In the sulphide-rich portions of the breccia (Fig. 4.27), clasts often do not have coarse tourmaline rims or significant amounts of any of the earlier cementing phases (tourmaline-quartz). Clasts are also relatively well-rounded indicating increased chemical abrasion compared with other breccias. No clasts of coarse-cemented or sulphide-rich breccias were found within one another.

In the areas of superimposed breccias in the Diablo sector, the extent to which earlier breccias facilitated or influenced the emplacement of coarser varieties is unknown. Given the close spatial relations between them, and presence of clasts in one another, the earlier breccias likely provided pre-weakened and increased permeability conduits for later pressurised fluids. Once emplaced, the coarser breccias, with enhanced permeability, provided the main sites for sulphide precipitation. Pore spaces in the finer breccias, largely adjacent to, or within several metres of the coarser breccias were also variably filled by Cu-Mo sulphides. Pervasive infill of all pore spaces in the finer breccias by Cu-Mo sulphides could have occurred, but evidence to indicate this is lacking, such as pore coatings or residual sulphides in the weakly mineralised areas. Some tourmalines with coarse rims have been fractured indicating some degree of reorganisation took place whilst tourmaline rims were forming.

The Diablo Breccias formed through the same physical processes (e.g., fluid-assisted, volume expansion and wear abrasion) as the breccias described above, producing mosaic and chaotic textures. Corrosive wear (partial dissolution) is more widespread in the Diablo Breccias, particularly the sulphide-rich sections, compared to the Marginal Tourmaline and La Huifa Breccias. This produces rounded large and small clasts (comparable to those in the Braden Diatreme) with abraded edges.

The relative timing of the production of porosity, and in particular permeability, in the paragenetic sequence, and therefore the timing of corrosive action/dissolution, is extremely important in understanding the controls on mineralisation in the breccia. Both coarse and microcrystalline breccias have porosity but permeability is likely to be the overriding factor for groundmass deposition in these breccias. From the fine nature of the porosity (<200  $\mu\text{m}$ ) in the microcrystalline breccias, for example, it is probable that a significant portion of the open-space was rapidly filled with early paragenetic phases (tourmaline-quartz), effectively reducing permeability and thereby hindering later precipitation of Cu-Mo-rich sulphides. The later generation of significant interconnected space, through which highly corrosive fluids passed, is likely from a lack of tourmaline rims or other early cementing phases in the sulphide-rich portions. These corrosive fluids removed earlier cements and further rounded the clasts. This late-formed permeability and porosity subsequently filled with Cu-Mo sulphides (Fig. 5.3c, i, j).

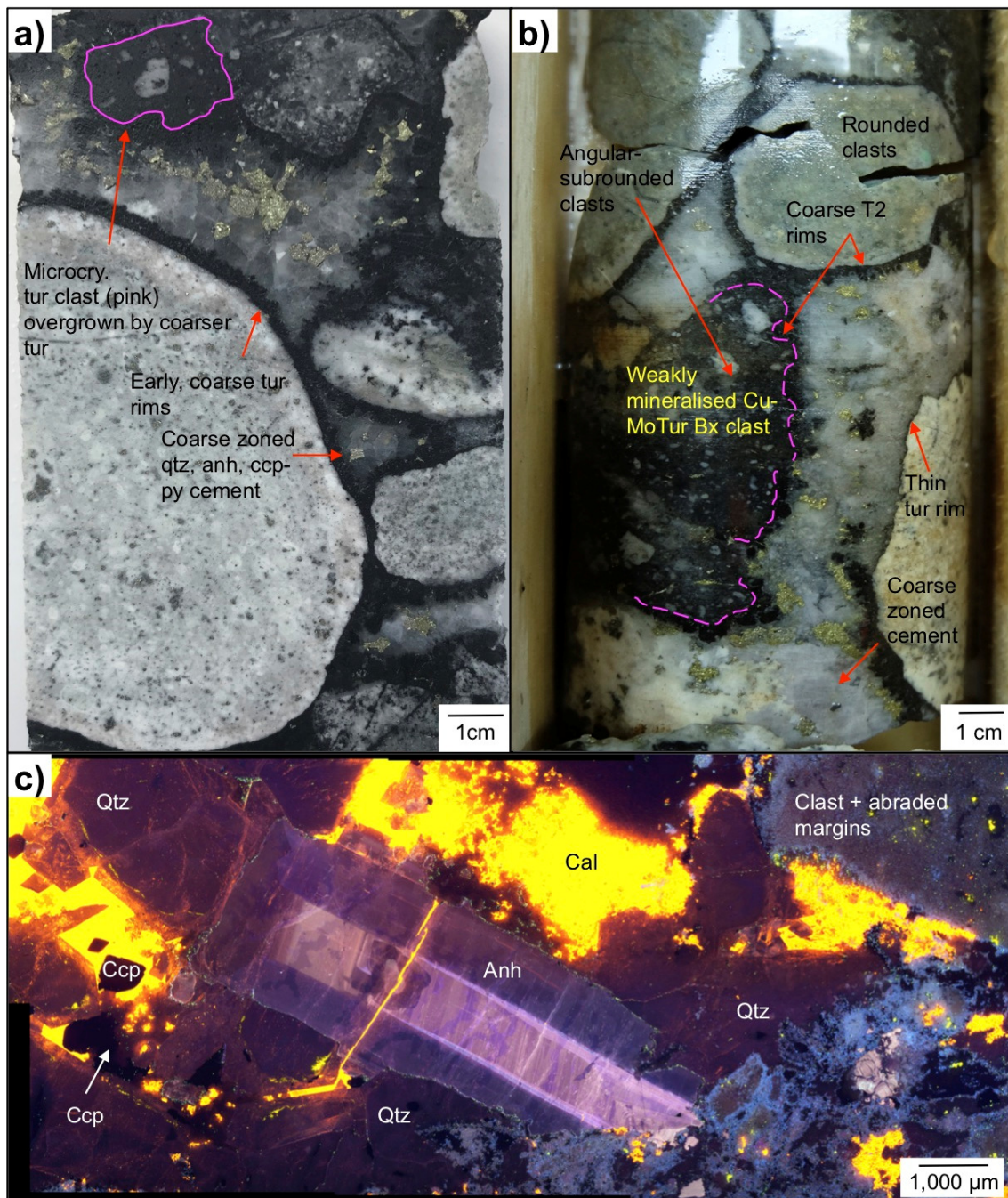


Fig. 5.3 Coarse (a-c) and microcrystalline (d-k) breccias from the Diablo sector: **a-b)** Drill core photographs illustrating coarse tourmaline rims with later quartz-anhydrite-calcite-chalcopyrite-pyrite infill. Clasts of earlier microcrystalline tourmaline breccia are outlined in pink which are rimmed by coarse tourmaline associated with the cement phase. Anhydrite and calcite are zoned. From DDH2677-118 m; **c)** Cold-CL image showing abraded clast margins with coarse euhedral quartz alongside coarse zoned anhydrite cut by calcite. Cu-sulphides are end-stage fill. From DDH2136-0.96 m; **d)** SEM-EDS map of microcrystalline tourmaline cement, with many of the pores partially filled by tourmaline and later anhydrite. Less Cu-Mo mineralisation is present compared with coarser breccias. From DDH1990-181.25 m; **e)** SEM-BSE image of microcrystalline tourmaline cement. Coarser tourmaline rosettes are finely zoned and have rutile inclusions. From DDH1990-181.25 m.

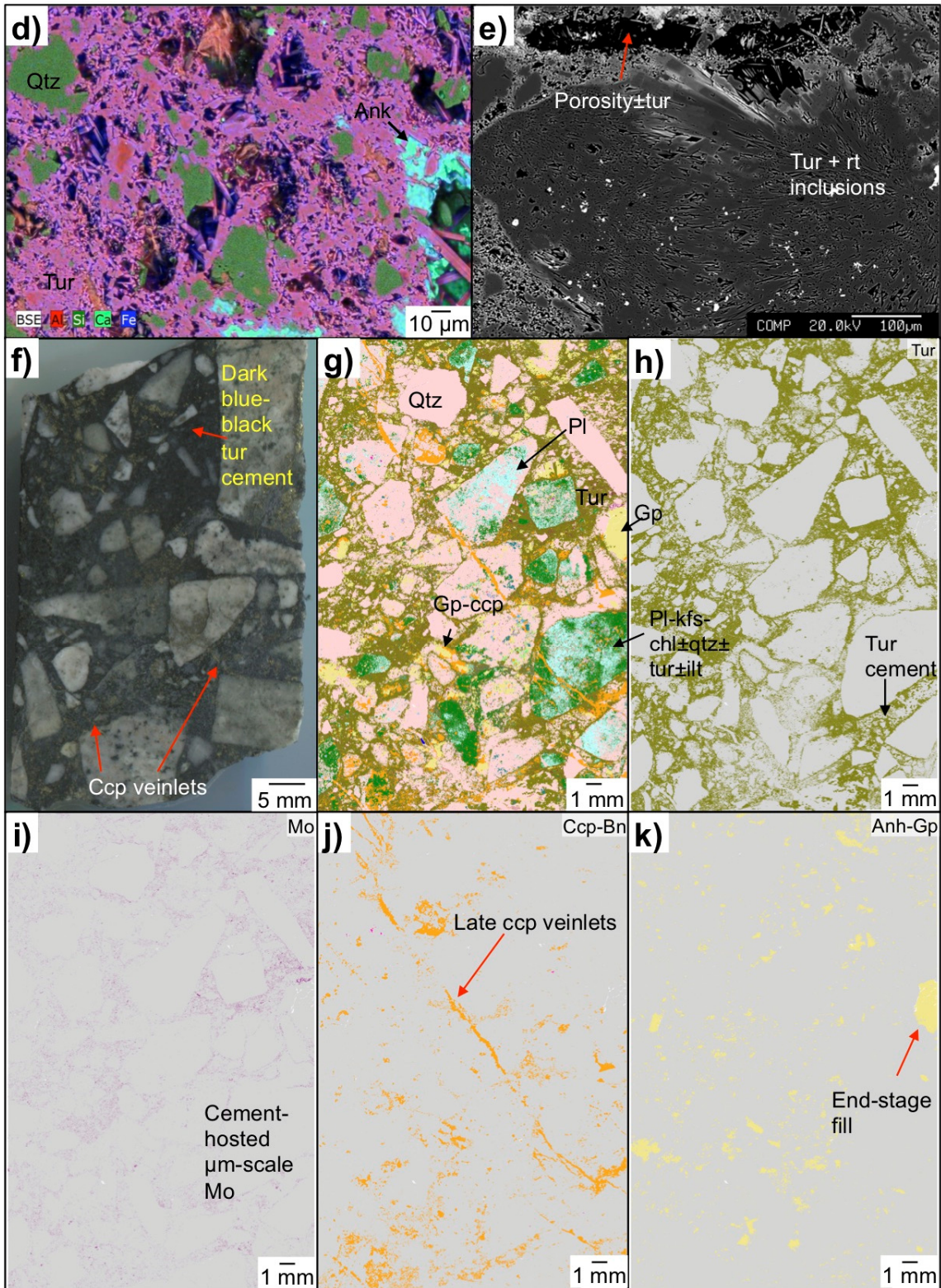


Fig. 5.3 cont. **f-k)** Microcrystalline tourmaline breccia from DDH1990-181.25 m. g-k are 10  $\mu\text{m}$  pixel QEMSCAN<sup>®</sup> mineral maps for all minerals (g), just tourmaline (h), just Mo (i), chalcopyrite-bornite (j) and anhydrite-gypsum (k): **f)** Drill core photo illustrating blue-black microcrystalline tourmaline cement; **g)** 10  $\mu\text{m}$  pixel spaced QEMSCAN<sup>®</sup> mineral map showing silicified clasts and tourmaline-quartz cement. Key is same as all previous maps; **h)** Tourmaline cement; **i)** Molybdenite pervasively throughout the cement; **j)** Chalcopyrite-bornite largely associated with later cross-cutting veinlets and end-stage space-fill; **k)** Anhydrite-gypsum end-stage space-fill.

**Coarse tourmaline vs. microcrystalline tourmaline cements and textures** - There are two end-members of tourmaline cement textures at El Teniente: 1) in coarse cement (Fig. 5.4); and 2) in microcrystalline tourmaline-quartz associations (Fig. 5.5). Fine-scale oscillatory and complex patchy zonation in tourmaline is found in both the coarser and microcrystalline tourmaline-cemented breccias at El Teniente. These fine zoning textures are consistent with rapid growth where homogenous equilibrium could not be maintained under fluctuating (*P-T*-chemistry) conditions (e.g., London and Manning, 1995). The patchy and oscillatory zonation of hydrothermal tourmaline seen in this study has been briefly described at El Teniente (King et al., 2003) and more widely documented and observed in other porphyry-related tourmaline breccia pipes in the central Chilean porphyry Cu belt such as Río Blanco-Los Bronces (Frikken, 2004), or El Salvador (King et al., 2000), and some Canadian deposits (McClenaghan et al., 2017).

Episodes of distinct tourmaline growth followed by dissolution and replacement by tourmaline with a different composition, coupled with fine-scale zonation, suggest that the coarser breccia cements (particularly at La Huifa and Diablo) were likely formed by multiple processes where the paragenetic sequence was repeated several times. These cyclical pulses either variably added to or reworked earlier mineral assemblages. Non-pitted overgrowths on earlier pitted tourmaline in La Huifa for example, are indicative of the action of strongly to weakly acidic fluids (e.g., Morgan and London, 1989). Other cement phases, in particular quartz, also show evidence for changing fluid conditions through patchy zoning, overprinting complex oscillatory growth zones, and with dissolution fronts observable in CL (e.g., Fig. 4.32).

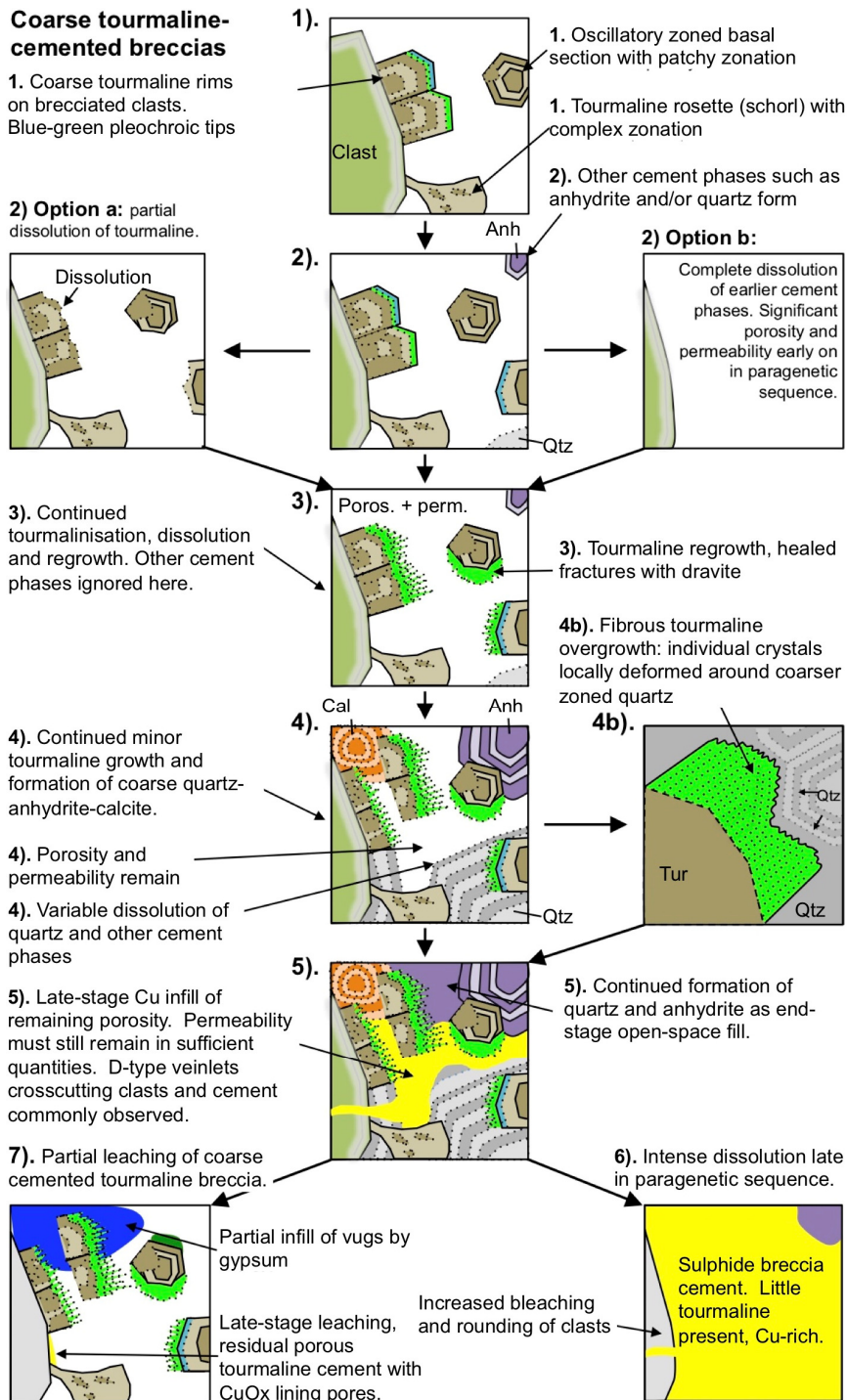


Fig. 5.4 Schematic diagram illustrating the development of coarse tourmaline-cemented breccias. Schematics are an amalgamation of observations from all breccias at El Teniente and are likely repeated several times: **1)** Precipitation of coarse tourmaline rims on brecciated clasts. Tourmalines have variable green/blue pleochroic tips; **2)** Syn- to post-tourmaline formation of other cementing anhydrite and quartz cementing phases; **2a)** Multiple episodes of partial dissolution and regrowth of tourmaline; **2b)** Alternatively complete dissolution and then formation of early phases again leaving no record of earliest phases; **3)** Varying degrees of dissolution, pitting of early tourmaline, re-precipitation of new fibrous overgrowths; **4)** Precipitation of other cementing minerals (quartz, anhydrite, calcite). Fracturing of tourmaline and re-precipitation of fibrous overgrowths on fracture planes; **4b)** During precipitation of tourmaline overgrowth coprecipitating quartz causes individual tourmaline crystals to deform; **5)** Chalcopyrite±quartz infill remaining porosity; **6-7)** Varying degrees of dissolution of earlier cement phases takes place resulting in just leaching of earlier copper sulphides and the formation of CuOx on cavity walls followed by infill of coarse anhydrite (now hydrated to gypsum) or (7) widescale dissolution and the generation of high-grade Cu-Mo cements (6). Alternative to this is microcrystalline-cemented breccias (overleaf).

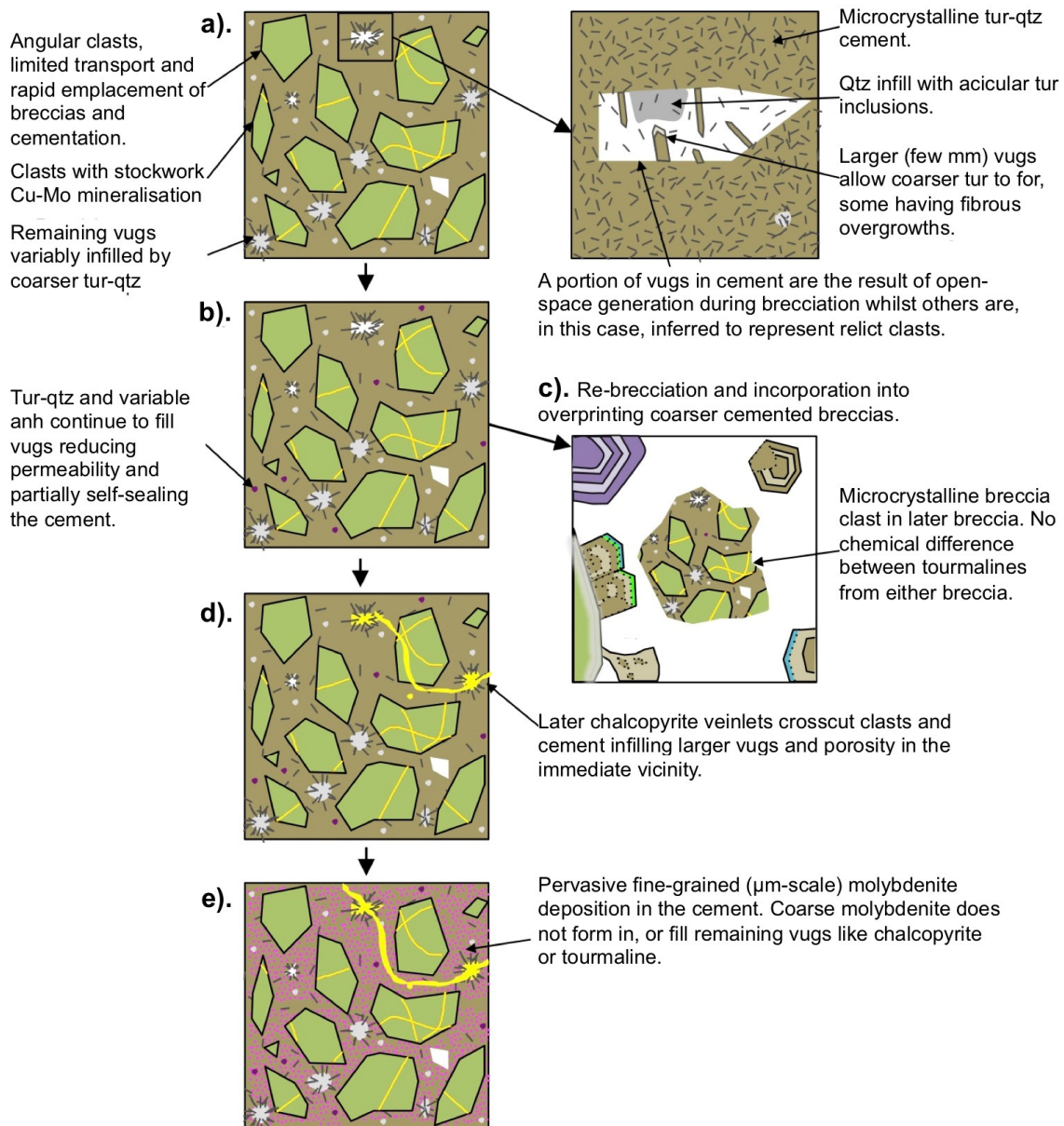


Fig. 5.5 Formation of microcrystalline tourmaline-quartz-cemented breccias: **a)** Rapid precipitation of microcrystalline tourmaline-quartz infilling most of the open-space generated during brecciation. Additional open-space is created through the dissolution of smaller clasts. In these areas of open-space coarser tourmaline with patchy zoning and sometimes overgrowths and quartz with tourmaline inclusions is present; **b)** Continued variable infill of vugs with tourmaline-quartz and anhydrite; **c)** Re-brecciation and incorporation into later breccias; **d)** Later chalcopyrite veinlets cross-cut cement and locally introduce Cu where porosity remains; **e)** Cu-Mo-rich fluids permeate cement and preserve original breccia framework. This is later, rather than simultaneous with d because chalcopyrite veinlets have been observed in areas without pervasive overprint in e (e.g., Fig. 4.27b).

**Source fluids, role of boron and economic concentration of metals** - In magmatic-hydrothermal systems, the widespread presence of large volumes of tourmaline in the breccias and host rocks, such as at El Teniente, indicates the circulation of boron-rich fluids; ultimately derived from boron-rich magmas (e.g., Trumbull et al., 2008; van Hinsberg et al., 2011). From experimental studies (e.g., Pichavant, 1981, 1987), the presence of boron can lower the solidus and increase the solubility of H<sub>2</sub>O in granite melts. This allows them to cool to lower temperatures than would otherwise be expected for magmas, and to be emplaced to higher levels in the crust (e.g., Allman-Ward et al., 1982).

During cooling of the source intrusion(s), boron is thought to become concentrated into the upper portions/apophysis, preferentially partitioning, at low pressures (1 kbar), into the aqueous vapour phase relative to the high-salinity brine (Schatz et al., 2004). These magmatic-hydrothermal aqueous vapours and brines are important carriers of Cu and Au (Heinrich et al., 1999; Pokrovski et al., 2008; Iveson et al., 2019) and coalesce, migrate upwards and accumulate at the tops of intrusions. However, the mechanism to extract these vapours from crystal-rich magma bodies (“mush zones”; e.g., Cashman et al., 2017) remains somewhat enigmatic (e.g., Weinberg and Regenauer-Lieb, 2010; Holtzman et al., 2012; Oppenheimer et al., 2015).

Frikken et al. (2005) invoked that the Sur-Sur Breccia (Río Blanco-Los Bronces) formed from a mixture of low-density magmatic gases (carrying H<sub>2</sub>O, SO<sub>2</sub>, HCl and B<sub>2</sub>O<sub>3</sub>) and dense copper-bearing hypersaline brines, the former being the first to physically separate from the dense copper-bearing brine and to infiltrate the breccia column, “where it condensed into ground waters of uncertain derivation”. Anhydrite, specularite, and tourmaline were deposited. Precipitating from this low-salinity, acidic, oxidised hybrid solution was anhydrite, specularite, and tourmaline. Following this, the upwelling of magmatic-hydrothermal brines resulted in sulphide precipitation. High-grade copper deposition in the Sur-Sur Breccia was interpreted to have occurred “in response to mixing of the oxidized, acidic water with the copper-bearing magmatic-hydrothermal brine”.

This interpretation is supported by fluid inclusion and stable isotope studies at El Teniente (e.g., Skewes et al., 2002; Cannell, 2004; Klemm et al., 2007; Vry et al., 2010; Spencer et al., 2015) which suggested that the tourmaline breccias were formed from magmatic-hydrothermal fluids and that subsequent Cu-Mo mineralisation took place through rapid cooling of the fluids as they ascended upwards and outwards in the system.

**Brecciation, cementation and relative timing of Cu-Mo mineralisation** - The inter-mineral magmatic-hydrothermal tourmaline breccias at El Teniente were generated in close association with the felsic-intermediate intrusions. All of the tourmaline breccias, including the 'early' crackle facies, therefore post-date porphyry stockwork and potassic alteration, but pre-date the draw-down of fluids and onset of sericitic alteration, evidenced by the presence of sericite-altered clasts. For example, porphyry Cu-Mo stockwork  $\pm$  disseminations in brecciated clasts and tourmaline breccias were therefore formed at least after the partial crystallisation and potassic alteration of the intrusions.

From petrographic analysis, the El Teniente tourmaline breccia cements formed from multiphase, repeated fluid pulses. All breccias follow a similar paragenetic evolution where tourmaline was the first mineral to precipitate, often nucleating on fractured clasts in coarser breccias or precipitated alongside quartz in the microcrystalline breccias. This paragenetically early tourmaline cement phase is commonly observed in other Andean porphyry-related tourmaline breccia pipes, such as at Río Blanco-Los Bronces (Skewes et al., 2003; Frikken, 2004) where tourmaline was noted to be the first cementing mineral, followed by quartz. Tourmaline was precipitated co-genetically with sulphide minerals in the Donoso Breccia pipe (Skewes et al., 2003).

After the formation of the initial tourmaline cementing phase ( $\pm$ quartz-anhydrite), as per the models in Fig. 5.4 and Fig. 5.5, a late-stage metal-bearing hydrothermal fluid either partially replaced earlier cementing phases or flooded the remaining interconnected open-space in the cement depositing varying quantities of Cu-Mo sulphides and coeval quartz-anhydrite $\pm$ calcium-bearing phases. This late timing of Cu mineralisation observed in the El Teniente breccias in this study is therefore in line with current porphyry research. An example of this is where Driesner and Heinrich (2019), based on combined observations from Escondida, El Salvador and Erdenet, and earlier studies on Bingham (Rusk and Reed, 2002; Redmond et al., 2004; Porter et al., 2012), Grasberg (Pollard et al., 2002), El Teniente (Vry et al., 2010; Spencer et al., 2015) and Batu Hijau (Zwyer, 2010), suggested that 'no Cu precipitated during high-temperature stockwork veining and potassic alteration'. Instead, they propose that Cu was 'coeval with chloritic to sericitic alteration and sulfide-only veins at temperatures  $<400^{\circ}\text{C}$  with no or minor quartz'. A similarly late paragenesis for porphyry mineralisation was also suggested by Sillitoe (2010), citing Redmond et al. (2001, 2004), from the relatively late generation of Cu-bearing sulphides compared with veinlet quartz.

**Summary and breccia models** - The enhanced open-space initially created during brecciation, and either preservation of some of this and/or the creation of permeability later in the paragenetic sequence, is important for enabling or hindering the ingress of later Cu-Mo-rich fluids, where present. In addition, the availability/location of permeability is important in localising higher-grade areas. Although the microcrystalline-cemented breccias are porous, large volumes of tourmaline-quartz, rapidly precipitating early in the paragenetic sequence, followed by continued infill by quartz and anhydrite, will have reduced the permeability compared with that affecting coarser cements. A number of models are shown in Fig. 5.6 (a below) and Fig. 5.8 (b below) for various scenarios which may influence the location of sulphide-rich portions and pathways for later fluid ingress.

In the first model 'option a' (Fig. 5.6), the margins are comparatively less fluidised than the central portions of the breccia column and therefore have lower portions of smaller (<2 mm) fragments, rock flour and more angular clasts. From observations of core from drill hole 2672, however, which cross-cuts the Diablo Breccias (Fig. 5.7), the variably mineralised microcrystalline tourmaline breccia contains large numbers of rounded to well-rounded clasts within 1 m of the breccia margins. This implies that the margins were equally well fluidised as the central portions, assuming that rounding is entirely a product of physical attrition and abrasion through transport. Nearer the margins, these microcrystalline breccias still contain a large number of small <2 mm fragments in the cement and angular to subrounded larger clasts. In drill hole 2672, the sulphide-rich portions do not always extend up to the breccia margins and can also have a different clast framework to the sulphide-poor areas. This is similar to coarser breccias but different to the microcrystalline breccia, although short intervals of the latter have a sulphide overprint.

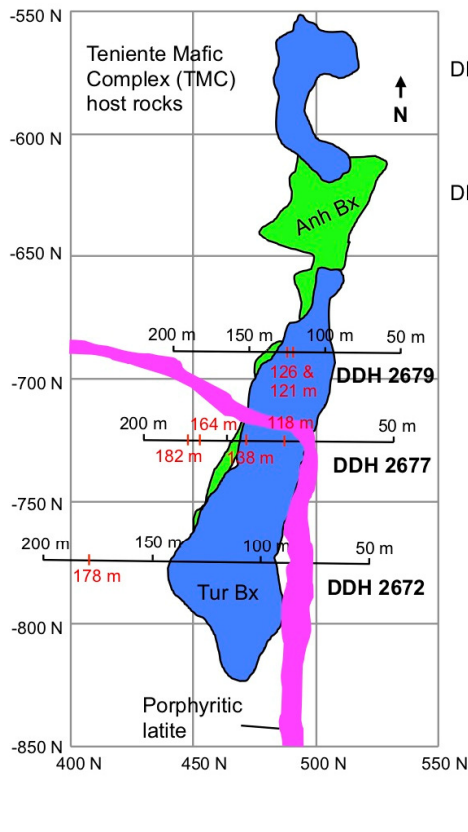
A degree of collapse of surrounding wall rocks and overlying roof packages, typically found in the upper portions of tourmaline breccias (as per the model of Sillitoe, 2010; Fig. 2.4) into the breccia pipes may also generate varying degrees of sheeted zones of high permeability at the margins facilitating fluid flow. Although appreciable collapse has been documented in non-porphyry-related breccias (e.g., Wheal Remfry, Cornwall; Allman-Ward et al., 1982) and some Chilean porphyry-breccias (e.g., 300 m of collapse at the Donoso and Central Breccias at Río Blanco-Los Bronces; Warnaars et al., 1985), the lack of reference stratigraphy at El Teniente makes estimating collapse difficult.

The second model 'option b' (Fig. 5.8) illustrates, in three parts, that the Diablo Breccias are inferred to represent a number of overlapping breccias consisting of later, typically coarser cemented breccias superimposed on one another, and upon earlier microcrystalline breccias (parts one and two). It assumes that all parts of the Diablo Breccias were more or less equally fluidised, and that the emplacement of later, coarser cemented breccias were to some degree influenced by the earlier breccias, which provided pre-weakened, high permeability conduits for later fluids to be focused through. This model also implies the margins were not less fluidised and therefore did not have overly increased permeability, due to less rock flour like material, small clasts and increased poor stacking of angular fragments.

Tourmaline was the first cement phase in both coarse- and fine-cemented breccias to form followed by quartz-anhydrite-calcite and other Ca-bearing phases. During the formation of tourmaline, re-organisation in the breccia took place causing some tourmalines to fracture and become re-healed by later tourmaline. Chalcopyrite-pyrite-molybdenite ( $\pm$ sphalerite-galena) are mainly end-stage open-space fill.

Later-stage Cu-Mo-rich fluids infiltrate the most permeable areas of the Diablo Breccias such as fractured margins, microcrystalline breccias, or in areas particularly amenable to dissolution, such as coarse breccia cements (part 3). In areas of pervasive dissolution and the generation of new late-stage permeability, widespread dissolution of the tourmaline rims is common and the clasts are increasingly rounded where this occurs. In areas of less intense replacement, the original coarse or fine cement breccia framework is preserved, often with a variable Cu-Mo sulphide overprint present instead. For example, areas of the microcrystalline breccia with a sulphide-rich overprint are adjacent at, or near to the coarser breccias which have experienced wider scale dissolution and replacement. The cements are sometimes partially leached leaving residual tourmaline with vugs unevenly infilled by gypsum.

**Plan map: Diablo Breccias, caving level ('TTE6\_Hundimiento')**



**-750 N**

**Comparatively fluidised core**

**Plan view**

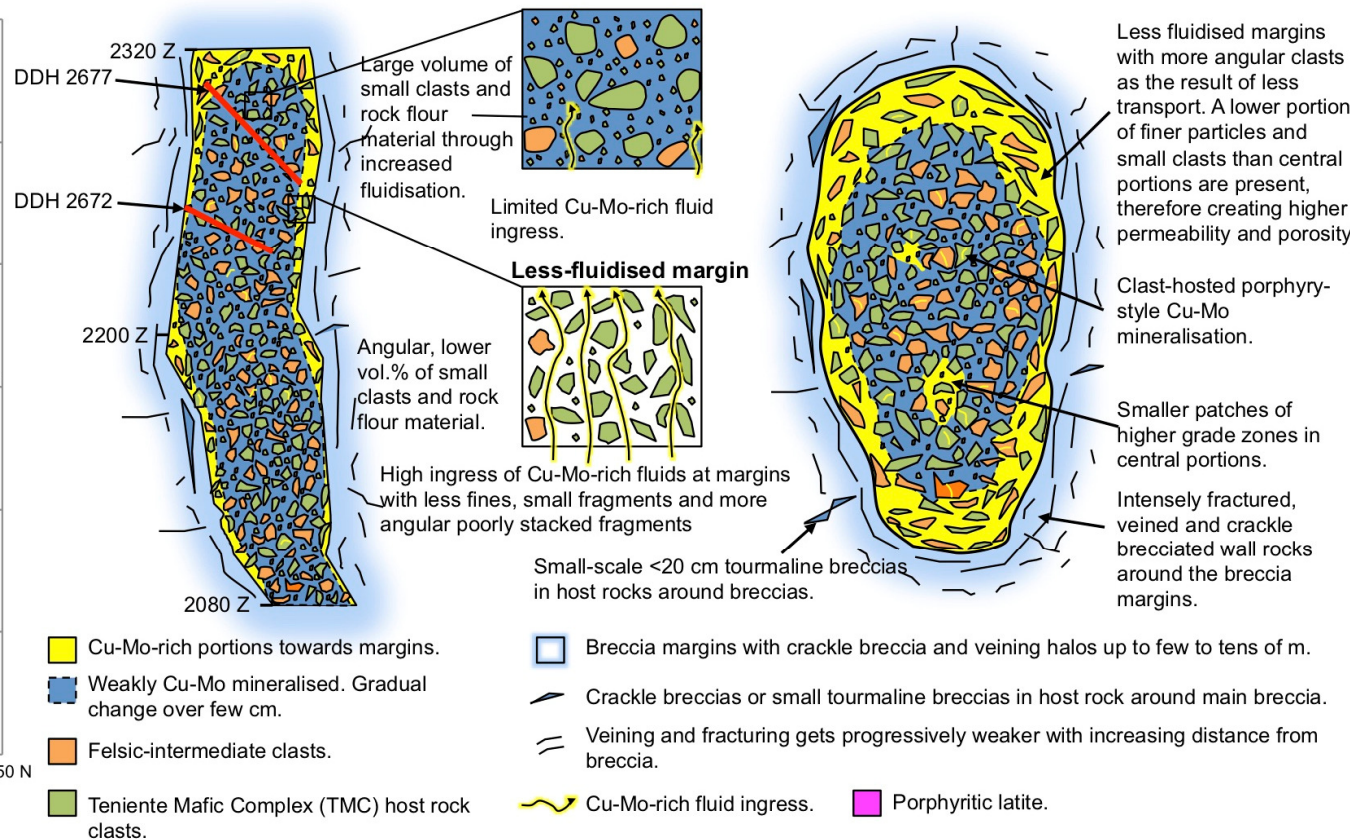
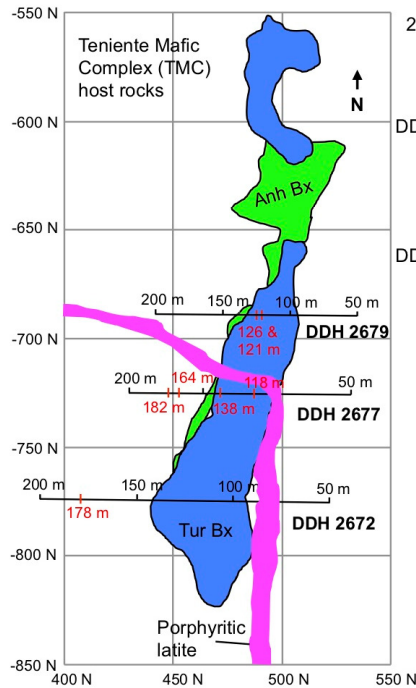


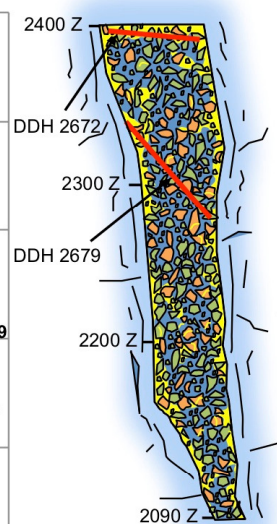
Fig. 5.6 **Option a:** Plan view geological map (left) of the Diablo Breccias, with corresponding cross section (middle) and plan view (right). Geological plan map is of caving level ('TTE6\_Hundimiento'; ~2,165 masl) and is reproduced after Codelco database maps (2017). Drill holes 2679, 2677 and 2672 are shown. Cross section outline (-750 N) of breccia is based on sections provided by Codelco; shown earlier (Fig. 4.36). Schematics show Cu-Mo sulphide-rich margins and weaker mineralised inner portions. This model illustrates less permeability in the central portions compared with the margins for later Cu-Mo-rich fluids to access. Multiple breccias have been ignored; instead just well- and poorly-mineralised portions are shown. The breccia margins are comparatively less fluidised than the central portions of the breccia column and therefore have increased permeability through lower portions of smaller (<2 mm) fragments, rock flour and more angular clasts.



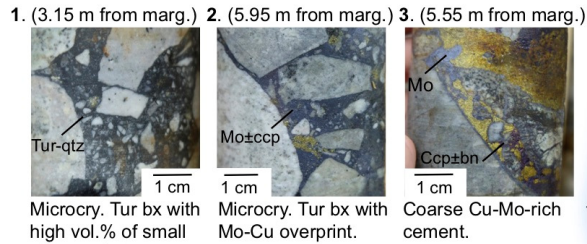
**Plan map: Diablo Breccias, caving level ('TTE6\_Hundimiento')**



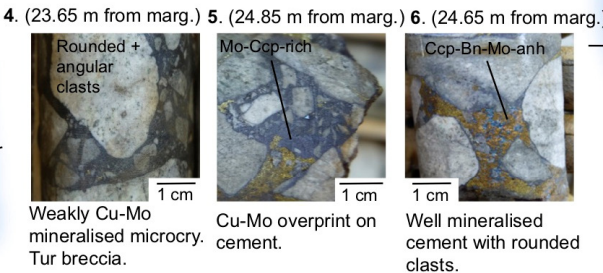
**-700 N**



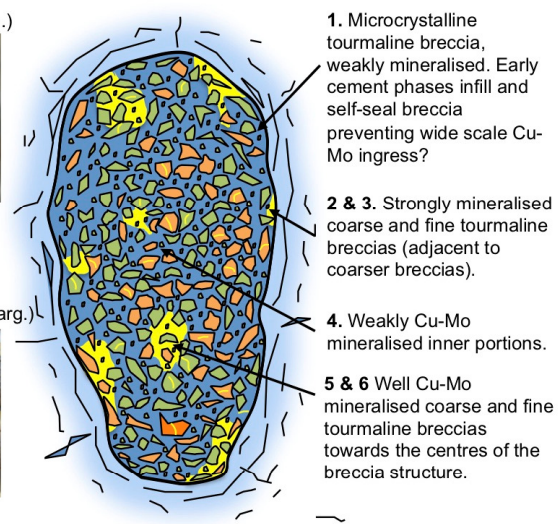
**DDH 2672 margin (1-3)**



**DDH 2672 inner (4-6)**



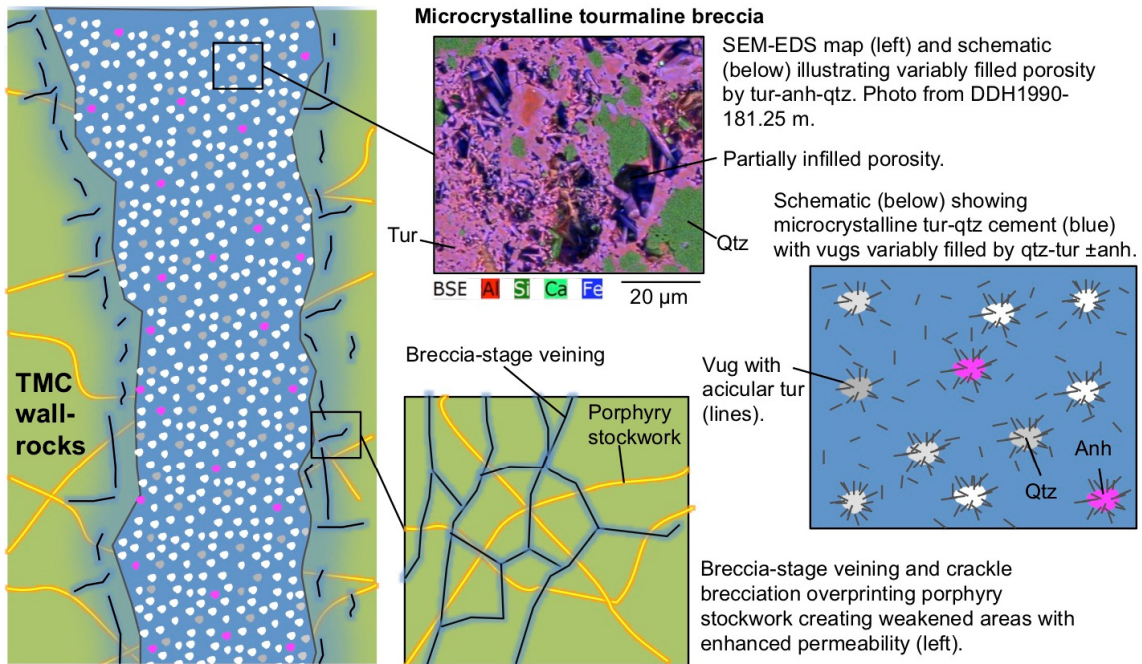
**Plan view**



- Cu-Mo sulphide-rich portions.
- Weakly Cu-Mo mineralised. Gradual change over few cm.
- Felsic-intermediate clasts.
- Teniente Mafic Complex (TMC) host rock clasts.
- Sharp breccia margins with halo several to tens of metres of crackle breccias and veining.
- Crackle breccias or small tourmaline breccias in host rock around main breccia.
- Veining and fracturing progressively getting weaker with increasing distance from breccia.
- Cu-Mo rich fluid ingress.
- Porphyritic latite.

**Fig. 5.8 Option b:** Based on Fig. 5.7, this model considers that all parts of the Diablo Breccias were more or less equally fluidised and takes into account the presence of what have been inferred to represent coarser breccias superimposed on one another and the earlier microcrystalline breccias (parts 1 and 2 overleaf explaining the emplacement of microcrystalline breccias (part 1), subsequent emplacement of coarser breccias containing clasts of earlier breccias (part 2)). The emplacement of later breccias were to some degree influenced by earlier breccias. Later-stage Cu-Mo-rich fluids infiltrate the most permeable areas of the Diablo Breccias such as fractured margins, microcrystalline breccias, or in areas particularly amenable to dissolution, such as coarse breccia cements. Varying degrees of dissolution of the earlier cements, particularly coarse areas, creates new porosity and permeability late in the paragenetic sequence (part 3 overleaf). In areas of intense dissolution, widespread dissolution of the tourmaline rims is common, the clasts are increasingly rounded and higher Cu-Mo grades are common. Within areas of less intense replacement, the original coarse or fine cement breccia framework is preserved, often with a variable Cu-Mo sulphide overprint instead present. Map of caving level ('TTE6\_Hundimiento'; ~2,165 masl).

## 1) Emplacement of microcrystalline tourmaline breccias



## 2) Coarser breccias superimposed on earlier tourmaline breccias

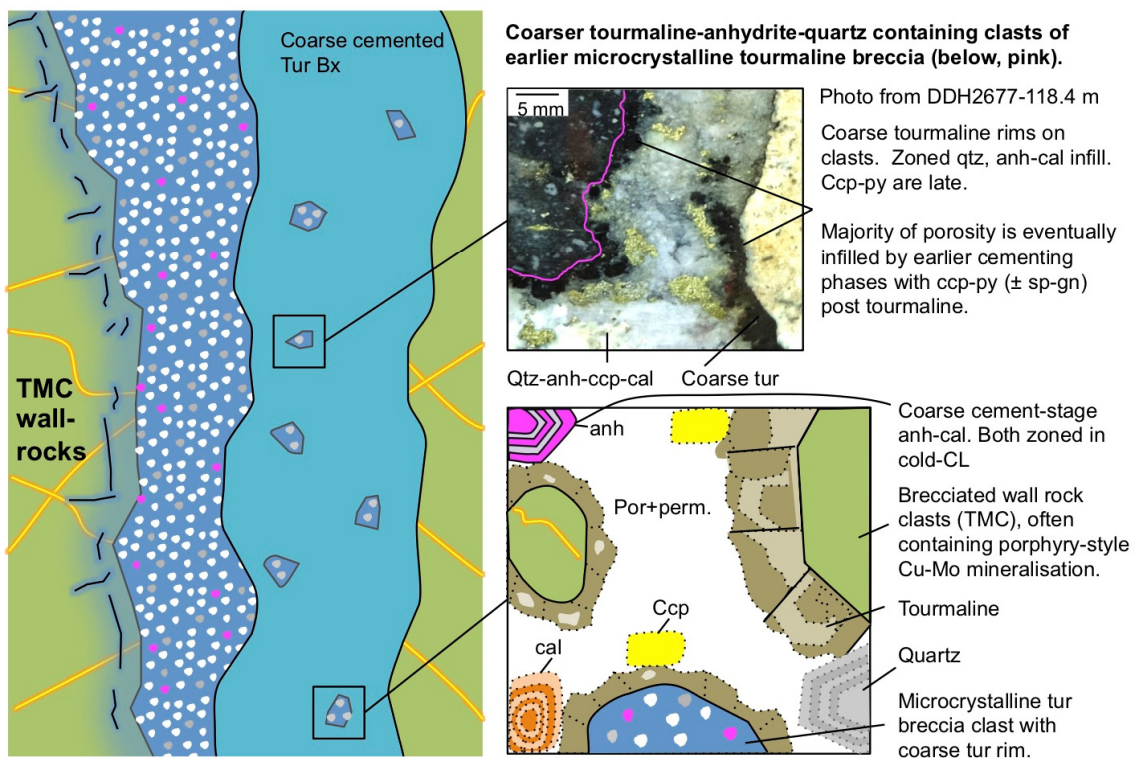


Fig. 5.8: **Part 1)** The emplacement of microcrystalline tourmaline-quartz-cemented breccias created weakened areas of increased permeability which are favourable for the focusing of later fluids that form the coarser cemented breccias. The microcrystalline breccias often incorporate porphyry-style mineralisation in brecciated clasts and the porosity in the cement is often fine to very fine (<100 μm). **Part 2)** Subsequent breccias are emplaced around/within the weakened corridors, incorporating earlier breccias during brecciation. Tourmaline was the first cement phase to form followed by quartz-anhydrite-calcite and other Ca-bearing phases. Chalcopyrite-pyrite (± sphalerite-galena) are end-stage open-space fill. During formation of tourmaline rims, periods of dissolution and growth took place alongside re-organisation in the breccia causing some tourmalines to fracture and become re-healed. Key overleaf.

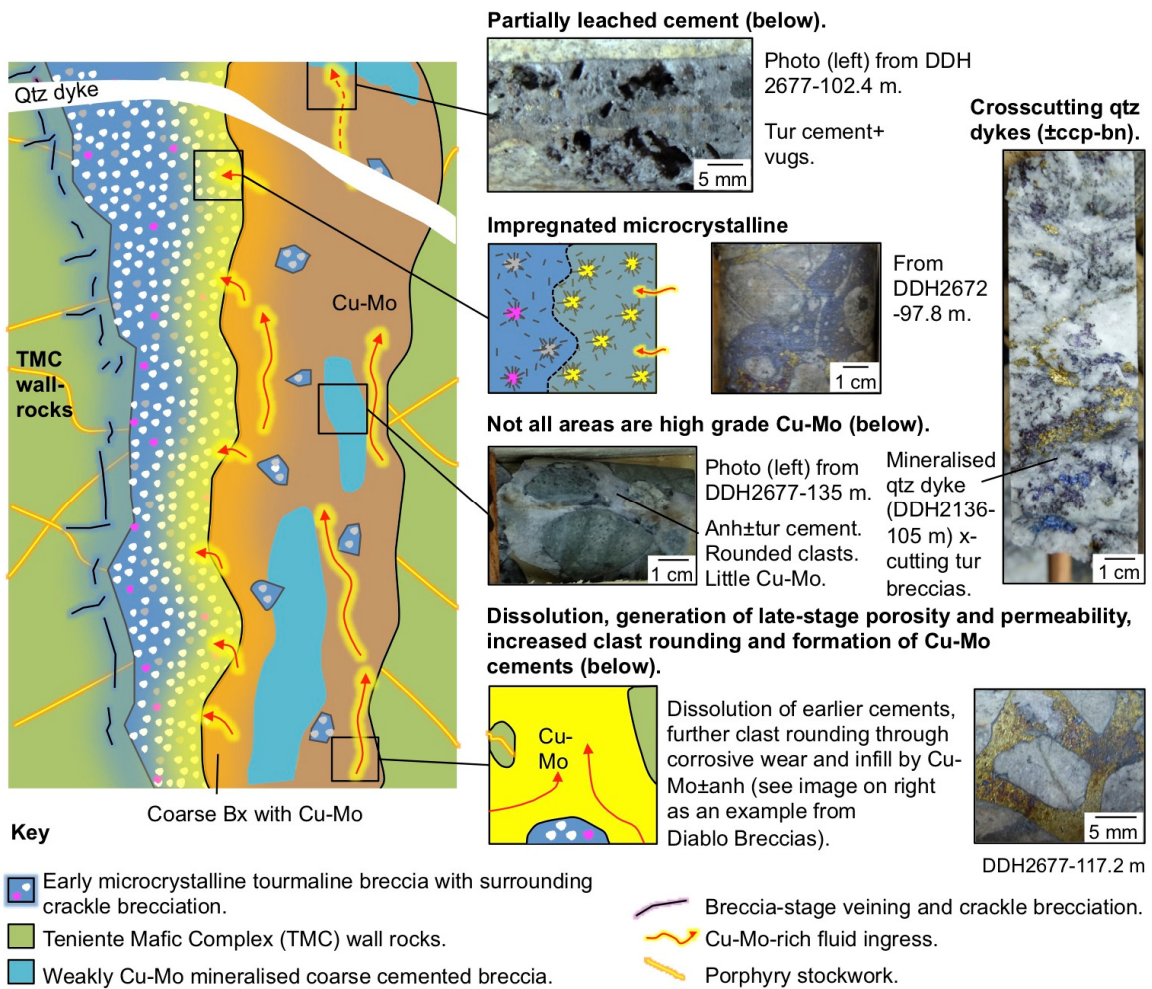


Fig. 5.8 **Part 3)** Later-stage Cu-Mo-rich fluids infiltrate the most permeable areas of the Diablo Breccias including the fractured margins, microcrystalline breccias, and in the coarse cements, in places causing widespread dissolution of the tourmaline rims and reprecipitation of sulphide-rich cements. Clasts are increasingly rounded in higher-grade areas where widespread dissolution has taken place. The generation of permeability late in the paragenetic sequence through dissolution of earlier phases creates a favourable environment for forming high-grade sections. In areas of less intense replacement, the original breccia framework is preserved and often within a few metres surrounding sulphide-cemented portions a sulphide-rich overprint is present (see 'impregnated microcrystalline cement' photos above). In places, partial leaching of the cements can leave residual tourmaline with vugs unevenly infilled by gypsum.

## 5.2.2 Hydrothermal replacement model for the Braden Tourmaline Breccia

Although chemical brecciation (also termed corrosive wear; Jébrak, 1997) is common in natural environments, the concept was initially proposed by Sawkins (1969) based around the mechanism of chemically induced explosions in porphyry deposits. Chemical brecciation can either produce a 'pseudobreccia', retaining the original breccia framework, or 'solution breccias', displaying evidence of dissolution and collapse (Jébrak, 1997, 2010). The mechanisms for this have, however, not been widely discussed in terms of high-grade or poorly mineralised porphyry-related breccias.

From observations in this study, the origin of the Braden Tourmaline Breccia (BTB) is thought to be from progressive replacement of the fine-grained (high reactive surface area) Braden Diatreme rock flour matrix (Braden Sericite Breccia, BSB), i.e. it represents a pseudobreccia, a theory suggested as early as Lindgren and Bastin (1922). Although the presence of paragenetically later BTB and tourmaline veinlets are well documented in the Braden Diatreme (e.g., Floody, 2000; Cannell et al., 2005; Fig. 2.13b), this does not provide direct evidence for progressive replacement. The intense attrition and abrasion produced the fine-grained rock flour, which was highly receptive to corrosive wear given the high volumes of reactive surfaces. Alternatively, the BTB could represent the physical re-brecciation of the rock flour matrix. These options are discussed and a pseudobreccia advocated. The BTB has a number of features that are not seen in other magmatic-hydrothermal intrusion-(±collapse) related tourmaline breccias developed from the explosive expulsion of volatiles from an underlying pluton and emplacement into overlying host rocks at El Teniente, which are listed and then described below:

- Reported transitional/gradational contacts at the margin with the host Braden Diatreme;
- Features consistently present in the Braden Diatreme such as stratification are also found in the BTB and are not truncated at the contacts;
- Both the Braden Diatreme and the BTB have the same clast framework including degrees of clast rounding, similar clast size distributions and polymictic clast population (representing all lithologies at El Teniente, including previous hydrothermal breccias). The BTB therefore has a different clast framework to the other tourmaline breccias;
- Between the clasts in the BTB is a mixture of matrix (rock flour) and hydrothermal cement (tourmaline-quartz±ankerite-anhydrite-gypsum-chalcopyrite). The areas of matrix intermixed with cement are also compositionally the same as the matrix in the BSB.

Stratification in the BTB is easily identified in hand specimen at surface and at different levels throughout the mine (e.g., Fig. 2.23b; Floody, 2000). It is very similar to the stratification observed in the BSB and shows the same orientation at outcrop when adjacent to the BSB (Fig. 2.23; Floody, 2000). Less easily identified is the mm-scale finer banding within the microcrystalline blue-black tourmaline-quartz cement (Fig. 5.9 b-d). This is only visible through optical microscopy because the dark blue to black microcrystalline cement masks it at hand specimen scale (Fig. 5.9b). The banding/stratification is largely down to varying relative proportions of quartz and tourmaline. No appreciable change in the size of brecciation-stage tourmaline, or quartz is observed across these banded zones. Quartz xenocrysts, with similar internal grain textures and CL to those in the BSB, are however coarser ( $>250\ \mu\text{m}$ ), and present in greater volumes (20 to 50 vol.% of cement) in the lighter coloured zones (see Fig. 5.9d).

The chaotic texture of the BTB and abraded edges shown by many of its clasts suggest they have been transported a considerably greater distance from the initial point of fragmentation than the other tourmaline breccias at El Teniente, which display a mosaic ( $\pm$ locally chaotic) texture. The rounded clast morphology, and very similar clast framework and breccia fabric to the adjacent and host diatreme rock flour breccias (Fig. 5.9a), further suggests that the BTB is of replacement origin. Both are polymictic, chaotic and have similar clast:matrix ratios and clast population characteristics (clast type, degree of rounding, size). Unlike other magmatic-hydrothermal intrusion-related breccias at El Teniente, the BTB also has a significant portion of rounded to subrounded clasts, small ( $<2\ \text{mm}$ ) clasts and fines which indicates an appreciable degree of transport, abrasion and attrition (e.g., Jébrak, 1997). At the rock flour-BTB contacts (e.g., Fig. 4.25c-e), clasts in the BTB have not undergone further brecciation-related reorientation or reorganisation, and the BTB contains no clasts of the rock flour breccia.

The presence of rock flour matrix (primarily K-feldspar, Fe-illite/illite, sericite, quartz $\pm$ chlorite) and hydrothermal cementing phases (tourmaline-quartz $\pm$ ankerite-anhydrite-gypsum-chalcopyrite), closely intergrown, was illustrated earlier and in the QEMSCAN<sup>®</sup> mineral maps in Fig. 5.9e-g. This has allowed unprecedented recording of paragenetic detail, on a micron-scale, which indicates that the cement is unevenly distributed and closely intergrown with the rock flour matrix. From this, a more passive, chemical replacement of the rock flour matrix is likely compared with physical re-brecciation of the rock flour diatreme or chemically induced explosions (e.g., Jébrak, 1997), which would ultimately lead to rock flour clasts incorporated into the BTB.

Secondary void space was generated during dissolution of smaller (<2 mm) clasts which were infilled by quartz, anhydrite-gypsum±tourmaline and then rimmed by coarser (>100 μm) acicular tourmaline (Fig. 5.9f, g). The presence of widespread quartz and tourmaline in the BTB cement is indicative of silica and B-rich fluids replacing matrix and a portion of the clast population. Aside from tourmalinisation and silicification, other main alteration processes affecting the Braden Diatreme, and therefore observed to varying extents in the BTB, include chloritisation, illitisation, sericitisation and localised sulphide overprints.

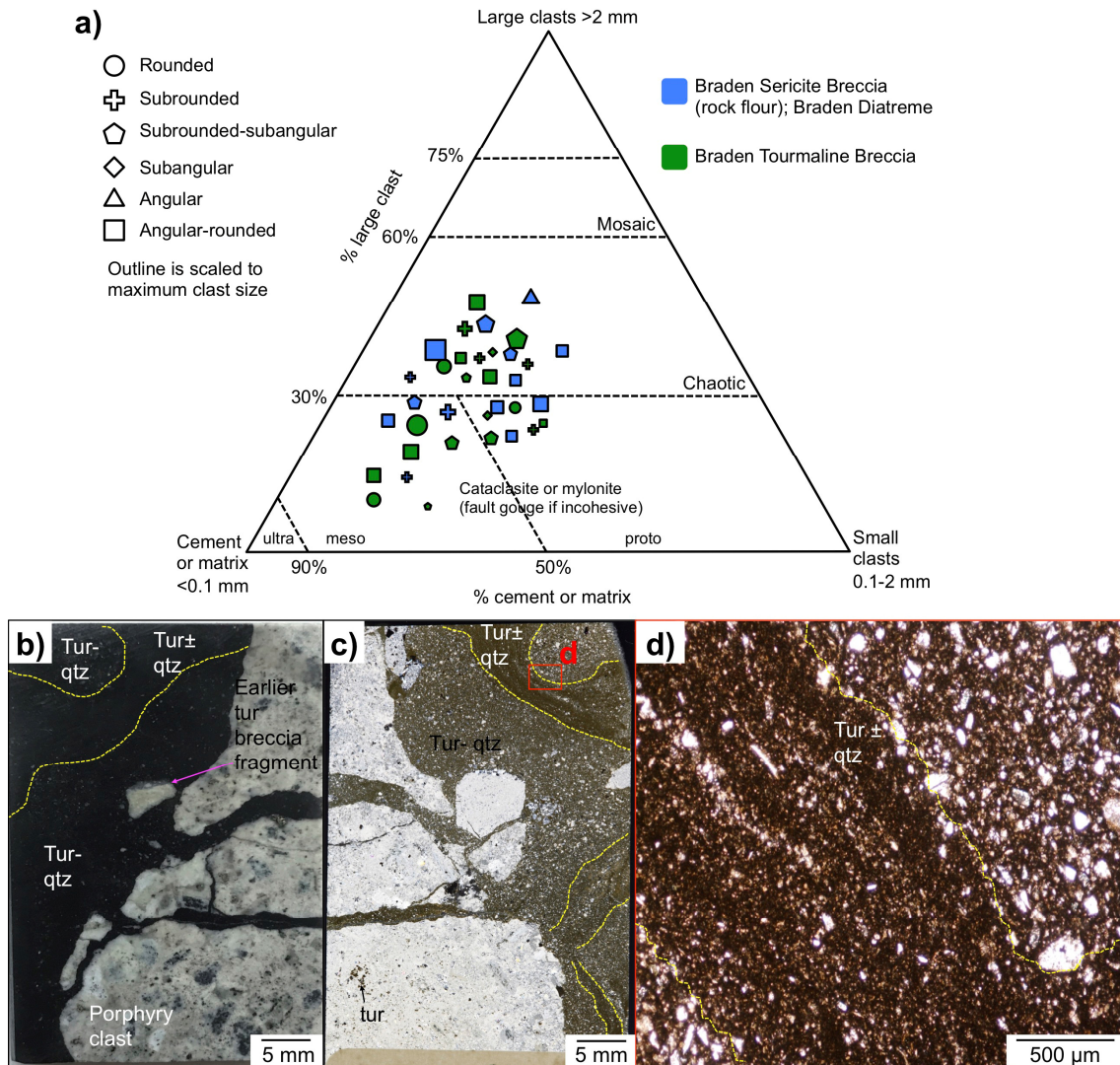
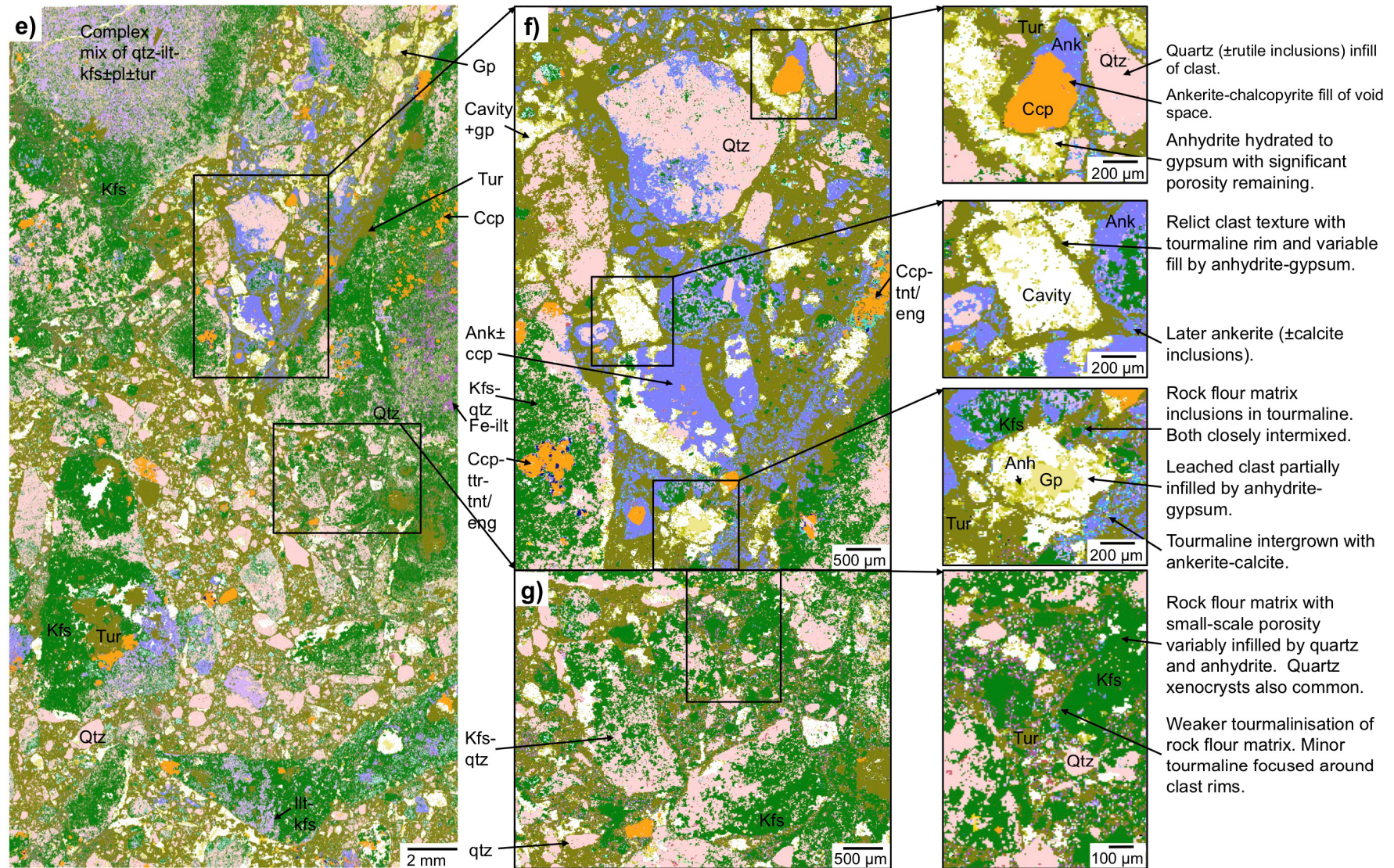


Fig. 5.9 **a)** Textural classification of the Braden Tourmaline and Braden Sericite Breccias at El Teniente from drill core observations in this study. Diagram adapted from Woodcock and Mort (2008); **b-d)** Banding in the BTB cement from DDH1754-9.7 m; **b)** Photograph of a flat cut section showing dark blue-black fine-grained tourmaline-quartz cement with subangular to subrounded porphyry clasts; **c)** XPL thin section photograph of the same area shown to the left (mirror slice), displaying the banding outlined in yellow in the cement; **d)** PPL photomicrograph of the banding which resulted from changes in the ratio of tourmaline:quartz. Breccia-stage tourmaline-quartz are similar throughout but rounded quartz xenocrysts vary; **e)** QEMSCAN® 10 μm pixel mineral map of Braden Tourmaline and Braden Sericite Breccia contact. Relict clast textures characterised by tourmaline rims and later quartz infill are more common in more intensely tourmalinised areas. Tourmaline permeating through K-feldspar-rich matrix is also illustrated; **f-g)** Relict clast textures. From DDH1213-100.07 m.



Mineral Name	Tennantite/Enargite	Molybdenite	Fe-Ox/CO3	Quartz	Biotite/Fe Illite	Calcite	Apatite
Background	Tetrahedrite	Pyrite	Celestine	Plagioclase	Tourmaline	Ankerite	Zircon
Chalcopyrite	Sphalerite	Bismuthinite	Barite	K-feldspar	Chlorite	Gypsum	Monazite
Bornite	Galena	Scheelite	Rutile	Muscovite/Illite	Kaolinite	Anhydrite	Others

**Comparison between the Braden Tourmaline Breccia and other replacement breccias** - Lefebvre and White (2013) suggested that dissolution and replacement took place in the ~300 diatremes ('maar-tuff volcanoes'; Vazquez and Ort, 2006) in the Hopi Buttes volcanic field (Arizona). As observed in the BTB, they found interstitial material, comprising varying proportions of matrix and hydrothermal cement, between the clasts in these diatremes. They identified that wholly-cemented areas show similar breccia frameworks and textural relationships to the matrix-hosted areas. Their evidence for dissolution is similar to observations in this study for the BTB and included:

- "Matrix and cement are unevenly distributed on a mm- to cm-scale, and where matrix is low to absent, the framework clast distribution within the cement remains similar";
- Where the interstitial material is mainly the replacive cement, matrix is locally preserved within clast embayments and around closely packed coarser clasts. In these instances they often observed a gradational contact between the cement and the matrix;
- Ferromagnesian-rich phenocrysts are partially to completely replaced by the cement phases. The process of dissolution also created secondary porosity accompanied by repeated cement precipitation. This is thought to be the case for the BTB where ferromagnesian-rich clasts, such as those from the Teniente Mafic Complex, were progressively replaced by a mixture of phases such as quartz, ankerite and chalcopyrite (Fig. 5.9f, g).

**Whole-rock geochemistry of the Braden Tourmaline breccia vs. Braden Sericite breccia** - Petrographic examination revealed that the mineralogical composition of the BSB has been modified by at least four processes: three are closely associated and include: 1) the replacement of rock flour matrix by hydrothermal cementing minerals, 2) the precipitation of these cementing minerals into leached-out open-spaces, and 3) silicification and tourmalinisation of brecciated clasts. The other process is the widespread sericite-chlorite overprint throughout the Braden Diatreme. These hydrothermal processes have induced mineralogical and chemical changes to the BSB.

To further support the petrological observations, the magmatic-hydrothermal chemical brecciation-alteration thought to form the BTB was additionally evaluated through the method of isocon analysis; a range of other useful methods were recently reviewed by Mathieu (2018). Having been applied to a wide range of geological processes, including hydrothermal alteration, isocon analysis (Grant, 1986, 2005) offers a simple and effective means for quantitatively evaluating chemical losses and gains in mass transfer. It is based on the Gresens' (1967) approach of determining relative changes in immobile element concentrations, as a result of alteration, to calculate volume changes.

The following equation summarises isocon analysis:  $M^O C_i^A = M^A (C_i^O + \Delta C_i)$  where:  $M^O$  = the masses of component i before alteration;  $M^A$  = the masses of component i after alteration;  $C_i^O$  = the concentration of component i before alteration;  $C_i^A$  = the concentration of component i after alteration; and  $\Delta C_i$  = the change in concentration of component i during the alteration process. Elements which plot above the isocon (straight line from the origin with a of  $M^O/M^A$ ) have been gained and those, which plot beneath, have decreased in concentration during the chemical brecciation-alteration process. Unfortunately, due to brecciation and open-space generation, followed by repeated infill of open-space with breccia cement/matrix and veinlet infill of both precursor and altered rock, this method may not accurately represent solely the replacement of the rock flour matrix with hydrothermal cementing phases (tourmaline-quartz±ankerite-anhydrite-gypsum-chalcopyrite).

Breccia samples were classified into 'least altered' and 'altered samples' where the Braden Sericite Breccia is less altered (the precursor) than the Braden Tourmaline Breccia; none of the samples of breccia collected were completely unaltered. The isocon analyses were conducted using the Microsoft Excel spreadsheet program developed by López-Moro (2012). Fig. 5.10 shows the relative enrichment or depletion of elements. In general, there are increases in CaO, MgO (except Fig. 5.10c), P<sub>2</sub>O<sub>5</sub>, S, MnO and TiO<sub>2</sub> (introduction of rutile, commonly as inclusions in tourmaline cement) whilst Al<sub>2</sub>O<sub>3</sub>, Fe<sub>2</sub>O<sub>3</sub>, SiO<sub>2</sub> and As decrease. Decreases in Al<sub>2</sub>O<sub>3</sub> is likely a combination of the replacive tourmaline-quartz-ankerite-anhydrite-gypsum± chalcopyrite cement of the BTB containing overall less Al than the rock flour matrix comprised of K-feldspar intergrown with a combination of fine clays (Fe-illite/illite), sericite, quartz and variable chlorite.

Compared to the precursor Braden Sericite Breccia, there are notable increases in Cu in some BTB samples (Fig. 5.10a, b, d). No other metals such as Mo, Pb and Zn are consistently enriched in the BTB which further supports the interpretation that they are not explicitly associated with tourmalinisation; instead being irregularly introduced later. The results show that REE were immobile or at least less mobile than other elements during the transition from the Braden Sericite Breccia to the Braden Tourmaline Breccia.

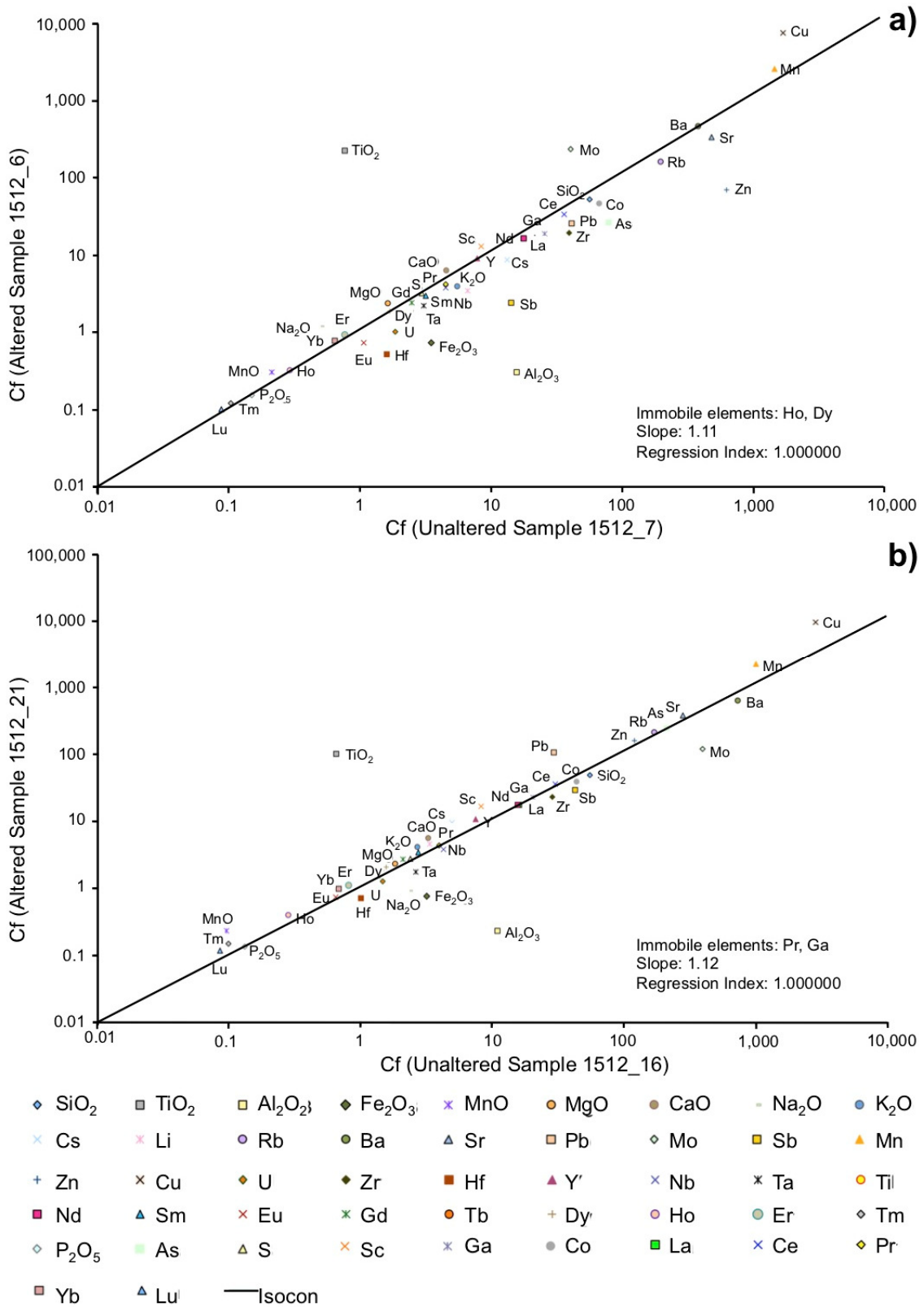


Fig. 5.10 Gresens' isocon analysis for 'unaltered' (actually 'least altered') (Braden Sericite Breccia) vs. altered (Braden Tourmaline Breccia) samples of the Braden Diatreme. The immobile elements are based on their high, >0.9 correlation coefficients to each other and differ in each breccia sample. The reference isocon lines were defined by the line of best fit through the chosen immobile elements: **a)** 1512\_7 vs. 1512\_6; **b)** 1512\_16 vs. 1512\_21; **c)** 1754\_22 vs. 1754\_16; **d)** 1769\_9b vs. 1769\_7.

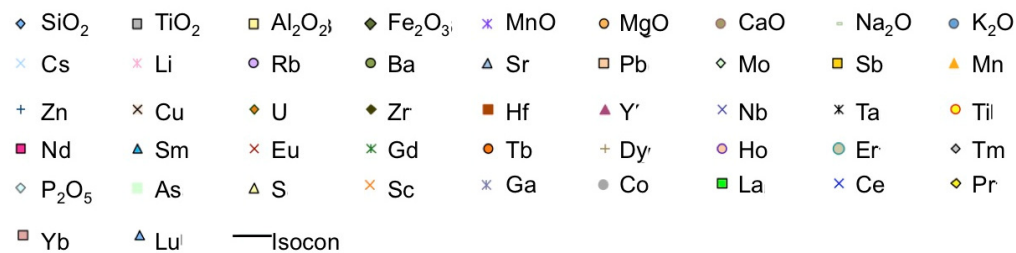
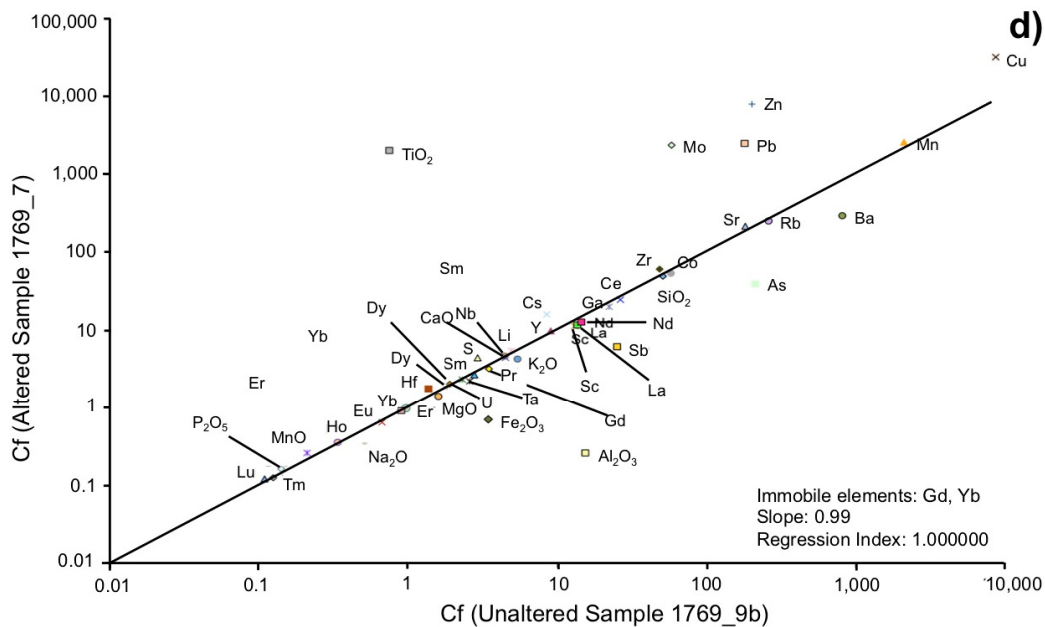
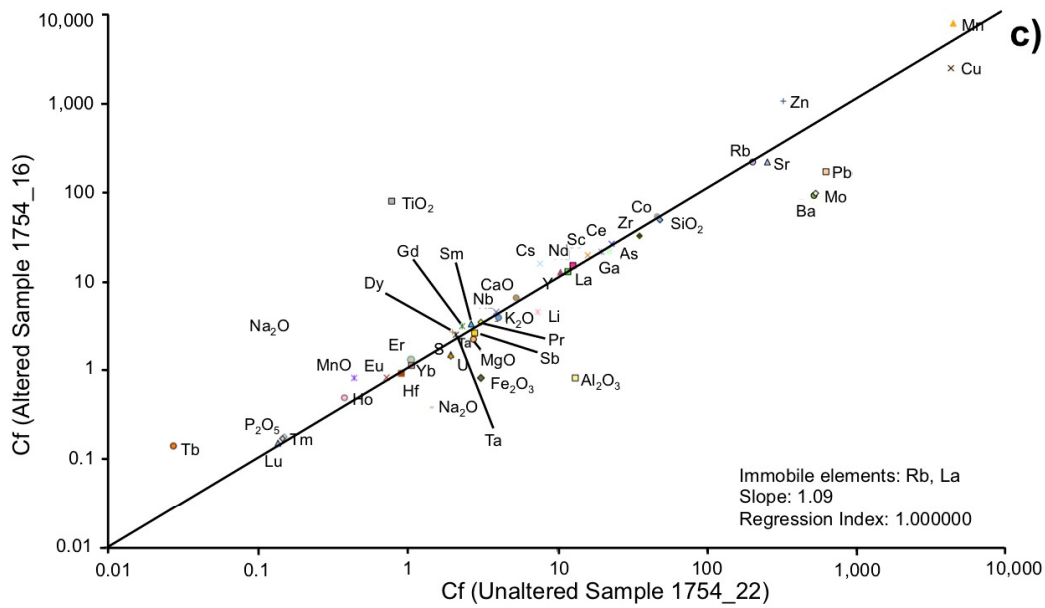


Fig. 5.10 cont.

**Summary and model** - It is interpreted that the Braden Tourmaline Breccia was formed by chemical brecciation (as per Jébrak, 1997), rather than physical intrusion. That said, in this case it is not likely that chemically induced explosions were the major process in forming the BTB. Instead it is proposed that B-rich fluids permeated the porous rock flour, progressively replacing the rock flour matrix and smaller (<2 mm)

clasts with varying proportions of tourmaline-quartz-ankerite-anhydrite-gypsum± chalcopyrite cement, illustrated in the model in Fig. 5.11. This replacement was superimposed on previous anisotropy, such as stratification/bedding, in the diatreme which have, alongside faults and fractures, invariably controlled the infiltration of the fluids. The result is the generation of pseudo-stratification observed in the tourmaline-quartz cement representing previous fabrics associated with diatreme formation. The B-rich fluids also permeated for several metres around the mapped contacts of the BTB forming a chalcopyrite (±tourmaline) halo illustrated in Fig. 5.11.

This progressive replacement method of forming tourmaline breccias, consisting of sub-mm-sized tourmaline, produces the same characteristic grey to black tourmaline cement that is distinctive of many tourmaline breccias associated with porphyry deposits, including the mineralised Marginal Tourmaline Breccia. This poses an interesting question as to whether pre- or inter-mineral diatreme rock flour breccias play a more important role than currently suspected in the formation of some cement-supported tourmaline breccias. Smaller diatremes which formed pre- or syn-porphyry mineralisation may, for example, have actually been completely replaced (clasts and matrix) by tourmaline or have provided highly weakened zones where later porphyry intrusive-related magmatic-hydrothermal breccias formed. There are however no easy ways to identify this in the field if complete replacement has taken place.

Diatremes are also becoming increasingly recognised as providing insights into the formation of porphyry systems, particularly the deeper parts (e.g., Rottier et al., 2018), and as favourable hosts for Au±Cu mineralisation. The Braden Diatreme is estimated to host >5 Mt of Cu at 0.4% (Skewes and Stern, 2007), but is considered uneconomic given the presence of adjacent much larger and higher-grade porphyry deposits. In the Cerro Maricunga gold project, Northern Chile, Au mineralisation is described as being related to a syngenetic diatreme complex (formed through phreatomagmatic and phreatic processes) hosted within “the remnant edifice of the Tertiary Ojo de Maricunga volcano” (Lohmeier et al., 2019).

Although it has a different mode of formation, the BTB has a similar paragenesis to porphyry intrusive-related magmatic-hydrothermal tourmaline breccias, where tourmaline is one of the first cementing phases, followed by a mixture of quartz, anhydrite (hydrated to gypsum) and later Cu-sulphides. It is perhaps the violent brecciation associated with phreatomagmatic or magmatic fragmentation which prevents the accumulation of volatiles inherent in intrusion-related breccias. Instead, phreatomagmatic-magmatic diatreme breccias, following their initial formation, are, under hydrostatic conditions, more likely to be infiltrated passively by B-rich fluids. Whether these reached the diatreme palaeosurface is an interesting question.

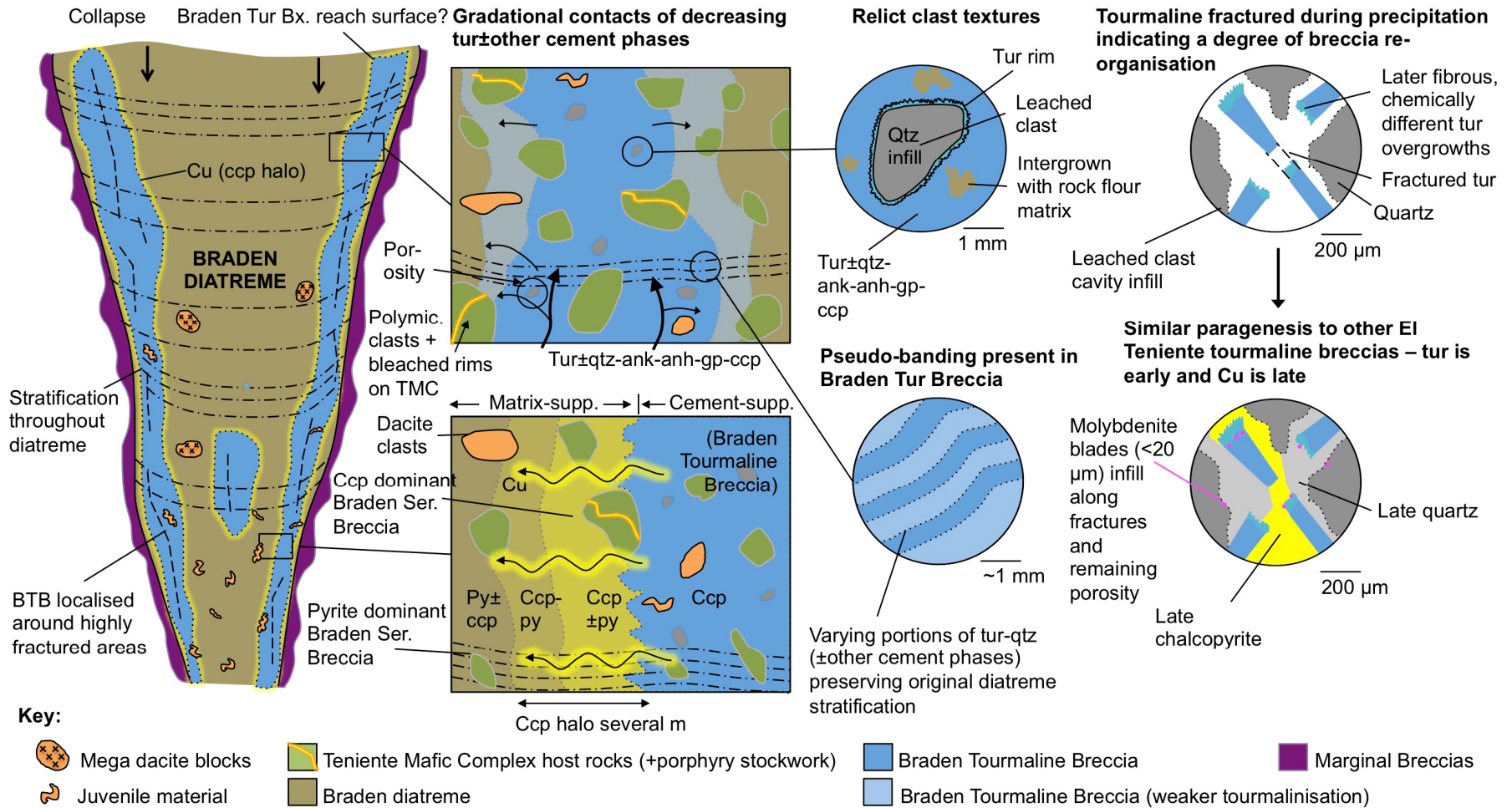


Fig. 5.11 Schematic model for a hydrothermal replacement origin for the Braden Diatreme-hosted Braden Tourmaline Breccia. It is reportedly spatially associated with fractured areas focusing fluids in the diatreme (Floody, 2000). Progressive transitional contacts, characterised by a decreasing tourmaline-quartz-ankerite-gypsum-chalcopyrite cementing component, are common. Small clasts have been leached leaving relict tourmaline rims and later quartz infill. Stratification in the diatreme is also preserved in the BTB cement.

### 5.3 Tourmaline geochemistry and use as an exploration indicator

Tourmaline is associated with a number of diverse ore deposit types, and studies (e.g., Power, 1968; Boyle, 1974; Taylor and Slack, 1984; Slack, 1996; Williamson et al., 2000; Galbraith et al., 2009; Baksheev et al., 2012) have indicated its potential use in mineral exploration. Baksheev et al. (2012) proposed that the tourmaline supergroup can be used as an effective indicator of porphyry-style Cu, Au and Sn mineralisation. It is present as an accessory mineral associated with potassic and phyllic alteration zones, is one of the main cementing components in hydrothermal breccias related to porphyries and is stable over wide pressure and temperature ranges (van Hinsberg et al., 2011; Fig. 1). The lower limits on its stability are not well defined, but could be “as low as, or lower than, 150°C and 100 MPa” (van Hinsberg et al., 2011).

Although tourmaline is abundant in porphyry deposits (Sillitoe, 2010; Baksheev et al., 2012), few studies have in detail characterised the elemental, in particular minor and trace elements, of tourmaline from well-mineralised porphyry deposits and compared these with examples from uneconomic systems. Tourmaline composition is strongly influenced by a combination of fluid phase and host rock chemistry and  $P$ - $T$ - $fO_2$  (Henry and Guidotti, 1985; Slack and Trumbull, 2011; van Hinsberg et al., 2011). In this study, tourmaline, which cemented the magmatic-hydrothermal breccias at El Teniente, precipitated in a high fluid/rock system. Tourmaline chemistry therefore should mostly reflect the composition of the hydrothermal fluid and generally be buffered by the fluid phase (e.g., Slack and Trumbull, 2011). However fluid:wall-rock interaction is known to influence tourmaline chemistry (e.g., Dill et al., 2012; Zhang et al., 2019).

#### 5.3.1 Major and minor element data

Studies such as Pirajno and Smithies (1992) used major element ratios ( $FeO/(FeO+MgO)$ ) as an indicator for the spatial variations in hydrothermal mineral deposits related to granites. This was built upon by Baksheev et al. (2012) who compared tourmaline from several different porphyry types (Cu, Au, Sn) and identified a number of generic yet distinctive features of tourmaline from porphyry deposits, including: 1) oscillatory and patchy zoning throughout multiple generations; 2) Fe-Al coupled substitution; 3) evolution from Fe to Mg-rich varieties resulting from sulphide precipitation at later stages; and 4) Li concentrations ranging from a few ppm up to ~30 ppm.

Additional features specific to porphyry Cu deposits, distinguished by Baksheev et al. (2012), include: 5) ~2 apfu total Mg content; 6) maximum  $Fe_{tot}$  ~3 apfu; 7) maximum F up to 0.1 apfu and 8)  $Fe^{3+}/Fe_{tot}$  between 0.5 and 0.8. The tourmaline data from this study (of porphyry intrusive-related magmatic-hydrothermal and replacement breccias)

corroborate some of these observations, except all breccia tourmaline has from a few ppm up to ~30 ppm Li apart from tourmaline from the BTB which contain up to 42 ppm Li.

Datasets for tourmaline from porphyry-breccias in Chile have been published by King et al. (2000, 2003), Skewes et al. (2003) and Frikken (2004). King et al. (2000) described and chemically analysed (EPMA) tourmaline from three of the giant porphyry-breccia deposits in Chile: El Teniente, Los Pelambres and Río Blanco-Los Bronces (Table 5.1). They also subdivided tourmaline from each deposit, based on its location, into the following categories and found no major compositional differences between: 1) veins, 2) fracture infills, 3) disseminations in alteration haloes across surrounding host rocks, and 4) as a cement phase in breccias. This study, in agreement with King et al. (2000, 2003), Skewes et al. (2003) and Frikken (2004) found that tourmaline has analogous major element compositions and can generally be considered as alkali group with minor X-site vacancy and substitution of Ca for Na (Fig. 5.12).

Table 5.1 Comparative concentrations (in wt.%) of major elements from Andean porphyry tourmaline breccia pipes. King et al. (2000) incorporates data from El Salvador and El Teniente whilst data from King et al. (2003) are from the three breccia-dominated deposits in the central PCD belt of Chile (El Teniente, Río Blanco-Los Bronces and Los Pelambres). Data in Skewes et al. (2003) is for tourmaline from the Donoso Breccia at Río Blanco-Los Bronces and include cement- and clast-hosted tourmalines from near surface, 210 m and 410 m below current day surface. Data from Frikken (2004) is from different elevations (~4,000, 3,520, 3,350, and 2,920 masl) in the Sur-Sur Tourmaline Breccia cement (Río Blanco-Los Bronces). Data from the San Jorge porphyry Cu deposit, Argentina is presented by Dill et al. (2012), which includes that from over ~120 m change in depth. 'BDL' is below detection.

	King et al. (2000)	King et al. (2003)	Skewes et al. (2003)	Frikken (2004)	Dill et al. (2012)	This study
FeO	1.20 – 9.40	5.80 – 17.80	6.76 – 23.95	3.59 – 18.61	1.72 – 18.09	1.76 – 29.51
Al <sub>2</sub> O <sub>3</sub>	27.10 – 35.70	22.79 – 34.31	18.74 – 32.24	21.03 – 34.91	27.15 – 39.02	13.24 – 34.79
MgO	6.30 – 8.80	6.10 – 9.09	5.37 – 6.88	2.25 – 8.59	0.62 – 9.87	3.35 – 10.57
SiO <sub>2</sub>	35.10 – 36.80	34.68 – 36.66	32.60 – 37.16	34.12 – 37.48	27.06 – 37.71	29.67 – 38.54
K <sub>2</sub> O	0.02 – 0.06	0.01 – 0.09	0.02 – 0.08	0.01 – 0.77	BDL – 0.11	0.01 – 1.0
CaO	0.01 – 0.70	0.05 – 1.40	0.03 – 1.10	0.06 – 1.82	0 – 1.91	0.04 – 13.71
Na <sub>2</sub> O	1.50 – 2.80	1.22 – 2.73	1.98 – 2.66	1.84 – 2.71	0.92 – 2.86	1.5 – 3.0
TiO <sub>2</sub>	0.02 – 0.70	0.07 – 1.75	BDL – 0.67	0.14 – 1.81	BDL – 1.29	0.02 – 5.34
MnO	BDL – 0.07	BDL	BDL – 0.08	0 – 0.07	BDL	0.03 – 0.27

Tourmaline from the porphyry intrusive-related magmatic-hydrothermal and replacement (BTB) El Teniente breccias in this study have similar chemical characteristics to those of other porphyry-related tourmaline datasets presented in Table 5.1. Like this study, tourmaline from El Teniente, Río Blanco-Los Bronces, Los Pelambres (King et al., 2000, 2003; Skewes et al., 2003; Frikken, 2004) and El Salvador (King et al., 2000) display the largest compositional variations in FeO, Al<sub>2</sub>O<sub>3</sub>, TiO<sub>2</sub> and moderate variation in SiO<sub>2</sub> and MgO. Smaller variations are present in CaO, Na<sub>2</sub>O whilst K<sub>2</sub>O and MnO.

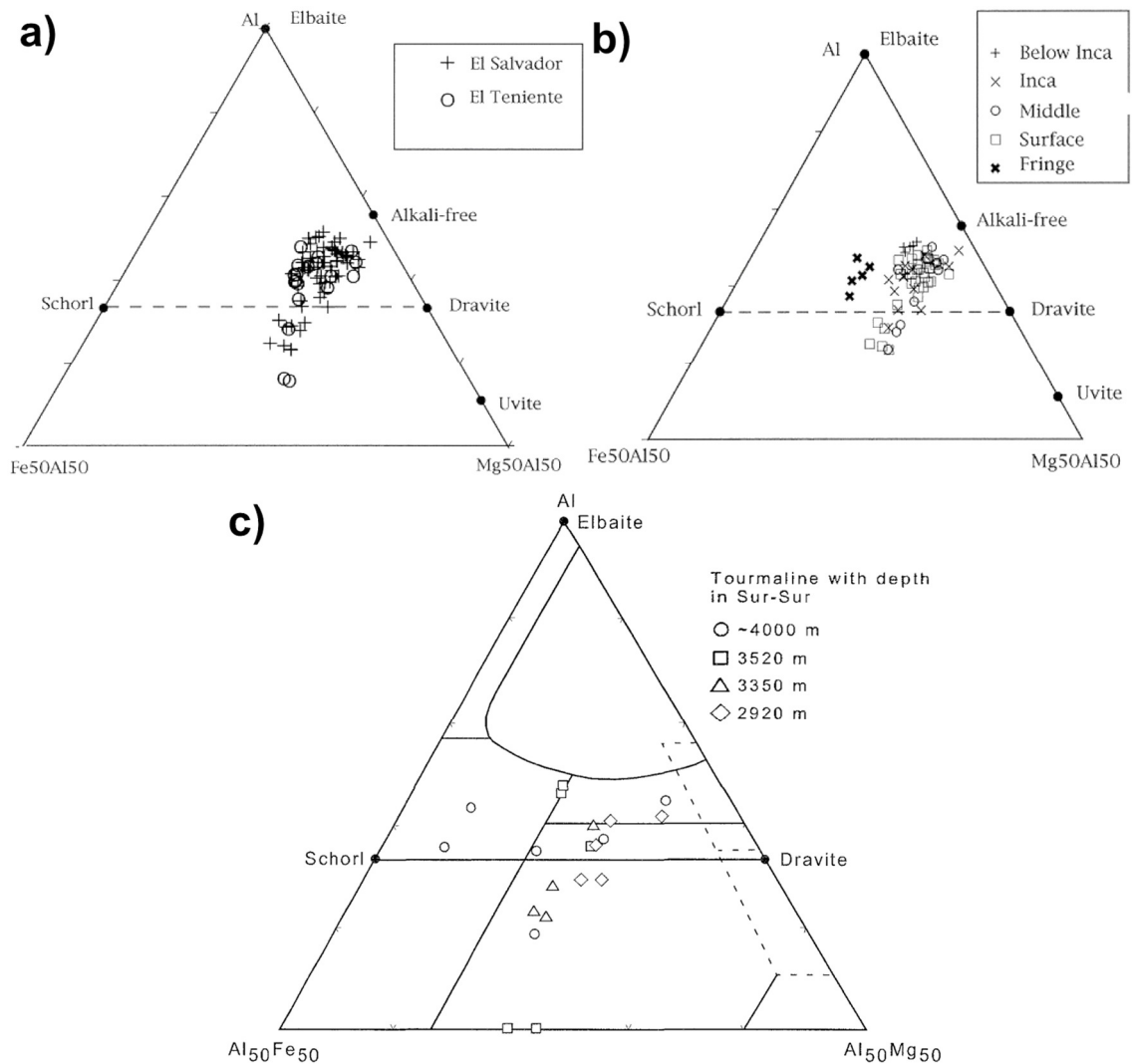


Fig. 5.12 Ternary plots for tourmaline major element data from El Salvador, El Teniente and Río Blanco-Los Bronces porphyry Cu deposits: **a-b)** Data from El Salvador and El Teniente (a) and tourmaline data from different locations within the El Salvador deposit (b) from King et al. (2003); **c)** Tourmaline compositions from different elevations in the Sur-Sur Tourmaline Breccia from Frikken (2004).

Several disparities do however exist between the tourmaline data presented here and those in previous work. Tourmalines from this study have larger ranges in many of the elements, which could be explained by: a) this study has a much larger (>1,500 analyses) EPMA dataset than the others which are mostly <100 analyses each; 2) multiple generations of tourmaline, clast- or cement-hosted and tourmalines from different depths were analysed here. Although previous studies did, where present, differentiate different deposit-scale locations (e.g., King et al., 2003), or depth, it is not clear if any additional generations were analysed in these earlier studies.

Because tourmaline at El Teniente shows little variation in Mg concentration within individual crystals (Chapter 4.6), and Mg is likely the main cation in the Y site, a portion of Fe must occupy both the Y and Z sites, requiring the presence of both Fe<sup>2+</sup> and Fe<sup>3+</sup> (van Hinsberg et al., 2011). The presence of Fe<sup>3+</sup> in the El Teniente breccia tourmalines is therefore likely to indicate relatively oxidising formation conditions (e.g., Zhu et al., 2020), which is consistent with the presence of gypsum after anhydrite in the mineral assemblages (e.g., Su et al., 2019). Oxidising conditions could be produced through the boiling of evolving magmatic-hydrothermal fluids (Drummond and Ohmoto, 1985) and/or mixing between magmatic with more oxidising fluids (e.g., Frikken et al., 2005).

### **5.3.2 Tourmaline trace and REE composition**

At the time of writing there were few trace and REE data in the literature for Chilean porphyry tourmaline breccia pipes. There are, however, data available from other geological environments such as the Cornubian Orefield (Duchoslav et al., 2017), FeOx-apatite (Su et al., 2019), emerald deposits (Baksheev et al., 2017) and the San Rafael Sn (-Cu) deposit (granite-related cassiterite-bearing vein system) in the central Andean tin belt, southeast Peru (Harlaux et al., 2020). These recent papers have proven the utility of trace element and REE data to discriminate between different generations of tourmaline, particularly that of magmatic and hydrothermal origin (e.g., Duchoslav et al., 2017).

Despite a number of magmatic-hydrothermal tourmaline generations identified at El Teniente, many of the later fine/needle-like overgrowths, are neither consistently enriched nor depleted in trace elements, whilst often showing a precipitous increase in REE in a number of crystals. The possibility that their unusual compositions were due to laser ablation signals from other cement phases, contained in the finest intergrowths, was discounted as analysis of these was avoided and the signal was monitored for indications of contamination.

The likely explanation for the large overlap in tourmaline compositions between the five different breccia types and the magmatic-hydrothermal tourmaline generations, was that they were derived from the same, or similarly sourced and evolved fluids. Such a

situation was also proposed for the Berezovskoe gold deposit, Russia (Baksheev and Kudryavtseva, 2004), Jaduguda U (-Cu-Fe) deposit, India (Pal et al., 2010), Xiangshan volcanic–intrusive complex, China (Yang and Jiang, 2012), Variscan Schwarzwald, Germany (Marks et al., 2013), the Cornubian Batholith (Duchoslav et al., 2017) and the Hadamiao porphyry Au deposit, China (Qiao et al., 2019).

In the El Teniente area, the alteration halo is 20×20 km (Cannell, 2004) indicating that fluids circulated for large distances around the porphyry-breccias. In addition, many of the wall rocks, and breccia-wall-rock clasts, are intensely bleached and replaced in many instances. Some of the TMC wall rocks are particularly fine-grained and many contain relatively high-temperature phases, so were particularly susceptible to alteration, especially leaching, by relatively oxidising fluids, and fluid interactions with them therefore likely influenced the compositions of tourmaline in the breccias. Such a mechanism was also suggested to have influenced tourmaline in the Hadamiao porphyry Au deposit where there were overlaps in the relative concentrations of many trace elements in tourmaline. This was attributed to either interaction with country rocks or to a lack of chemical equilibrium (Qiao et al., 2019).

Tourmaline-melt partition coefficients of around one, for most elements (van Hinsberg, 2011), means that tourmaline crystallisation will not cause specific trace elements to be strongly fractionated, and it therefore records changes in melt composition rather than crystallisation of other minerals. In addition, tourmaline preserves its chemical composition as it shows negligible diffusion of major and trace elements (van Hinsberg et al., 2011). An exception to this is that Marks et al. (2013) and Su et al. (2019) identified correlations between major and trace elements (e.g., Ca and Sr) thus questioning the “passive recorder character” of tourmaline (Su et al., 2019). For example, trace element covariations previously identified include Sn vs. Sr, V vs. Sc, Co vs. Ni, Ho vs. Y, La vs. Pr and Yb vs. Lu, which are shown in Fig. 5.13 (Qiao et al., 2019 and references therein). Some of these correlations are observed in the Teniente tourmalines such as Ho vs. Y (Fig. 5.13a), Pr vs. La (Fig. 5.13b), Lu vs. Yb (Fig. 5.13c) and Sc vs. V (Fig. 5.13d) which show positive correlations. Each of the El Teniente tourmaline breccias has a number of analyses which do not follow the general correlations (Fig. 5.13a, b). The lack of correlation in some data analyses could be because either the element contents of the fluids evolved as minerals precipitated, or mixing processes may have locally obscured the partitioning behaviour of that specific tourmaline (e.g., Yang et al., 2015; Baksheev et al., 2017). Tourmalines from the Teniente breccias show fine oscillatory-zoned textures with individual zones being significantly less than the resolution of the laser and therefore correlations between trace elements and major elements in specific zones are not discussed here.

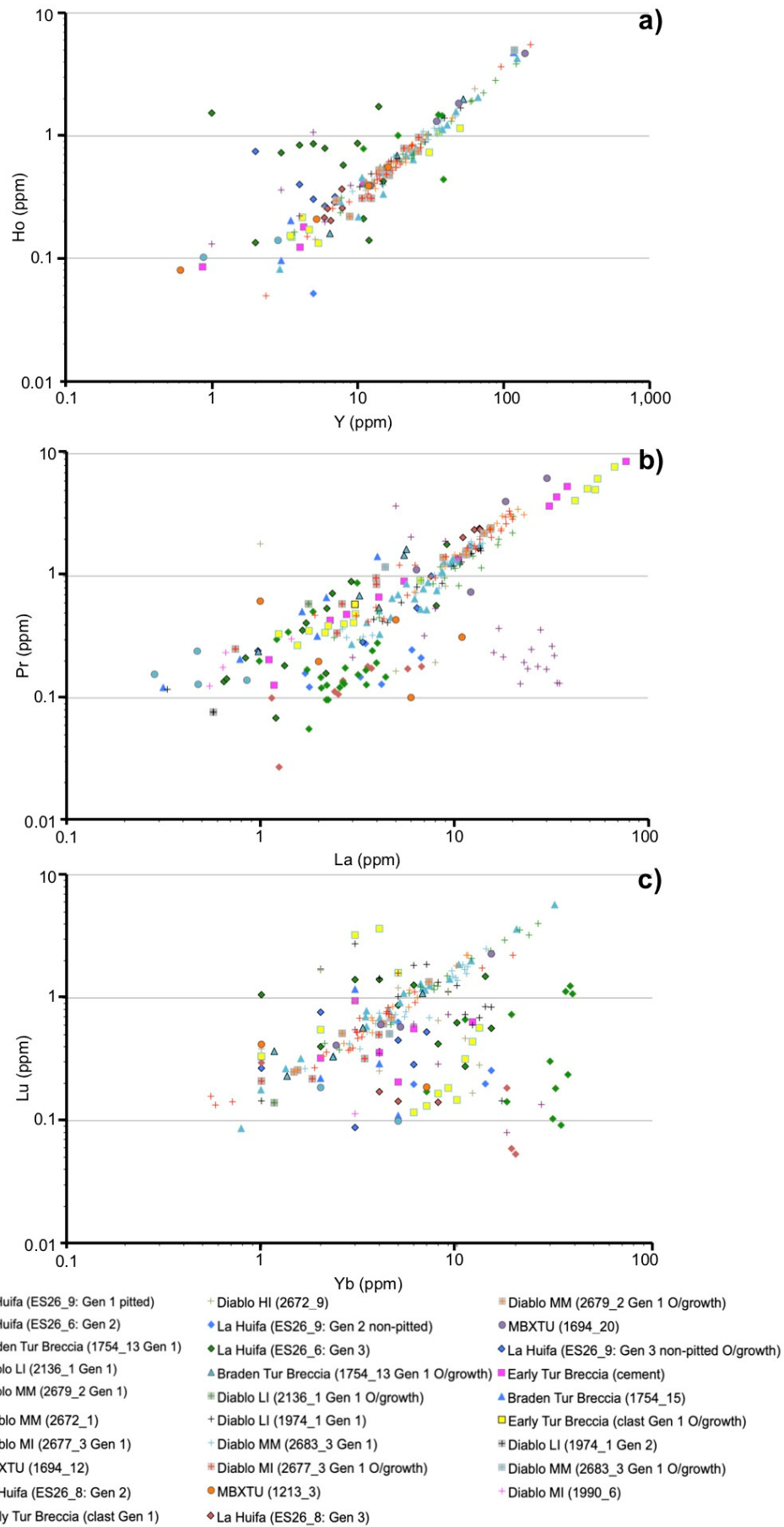


Fig. 5.13 Covariation plots (a-f) for some tourmaline trace elements from El Teniente breccias: **a)** Y vs. Ho; **b)** La vs. Pr; **c)** Yb vs. Lu; **d-f)** Overleaf.

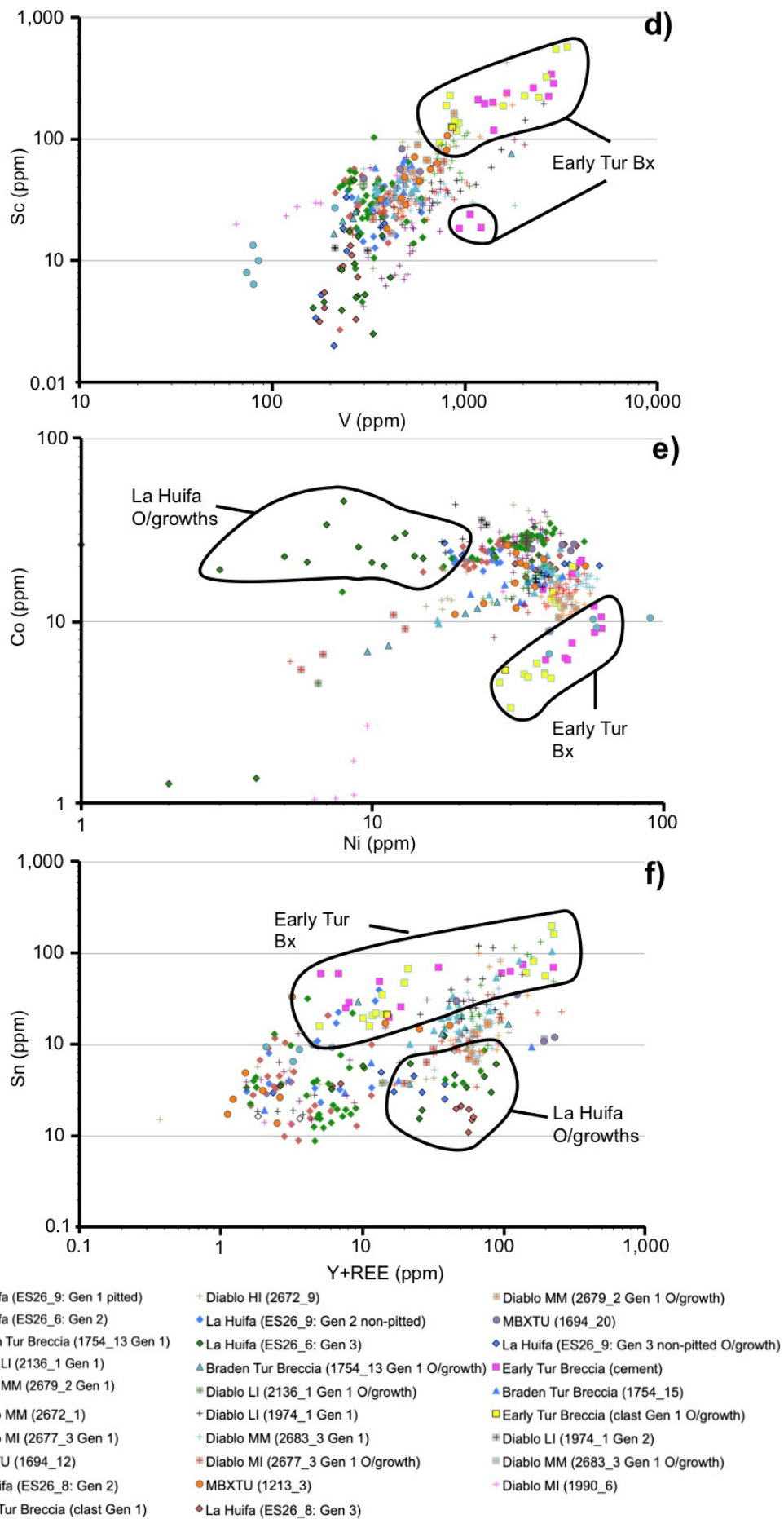


Fig. 5.13 cont. **d)** V vs. Sc; **e)** Ni vs. Co; **f)** Y+REE vs. Sn.

### 5.3.3 Intra-pipe tourmaline compositional variations: Diablo Breccias

There have been few studies on variations in tourmaline chemistry with depth in breccias and therefore this is poorly understood. It was preliminarily tested by Frikken (2004) and Dill et al. (2012) based on the notion that as magmatic-hydrothermal fluids ascend they interact with wall rocks and potentially mix with external fluids, which is reflected in tourmaline chemistry. What is poorly understood is whether samples closer to the wall rocks show noticeable orders of magnitude more variation in their chemistry, compared to those more central to the breccia pipe, and whether this will ultimately introduce false positives or negatives into any trends identified.

Frikken (2004) undertook twenty-one analyses of tourmaline from the Sur-Sur breccia (Río Blanco-Los Bronces) across four thin sections positioned at: the base of the Sur-Sur Tourmaline Breccia (2,920 masl), the biotite-tourmaline transitional zone (3,350 masl), mid-level (3,520 masl) and one from high altitude (~4,000 masl). This showed that as tourmaline shifts from dravite at depth to schorl at higher (shallower) levels. Key elemental trends identified by Frikken (2004) are as follows:

- The highest Al concentrations occurred in the deepest (2,920 masl) and shallowest samples (~4,000 masl), both of which have coarse (up to 2 cm long) tourmaline crystals (e.g., Fig. 3.9b of Frikken, 2004). In contrast tourmaline analysed in the two mid-level samples (3,350 and 3,520 masl) were finer-grained;
- Tourmalines at depth have relatively depleted Fe concentrations which increase at mid to shallow levels;
- The concentration of Na in tourmaline progressively decreases towards surface, from 0.74 cations (2,920 masl), 0.65 cations (3,350 masl), 0.63 cations (3,520 masl) to 0.59 cations at shallow level (~4,000 masl; Fig. 4.2g of Frikken, 2004).

Dill et al. (2012) also conducted a depth study over ~120 m in a tourmaline breccia at the San Jorge porphyry Cu deposit (Argentina) which showed that tourmaline compositions mostly range between the schorl and dravite end-members. They accredited this characteristic to be the result of progressive interaction between a rising magmatic-hydrothermal Fe-B-rich fluid and country rocks. Depth-related trends observed by Dill et al. (2012) include:

- Telescoping of different chemistries into each other;
- Above 90 m depth, Cu-sulphides showed no time or spatial relationship with tourmaline. Instead, tourmaline (schorl-dravite solid solution series (s.s.s.)) at depths of 90 and 155 m were associated with Cu-sulphides;
- The opposite compositional trend to Frikken (2004) regarding the s.s.s., where at shallow levels the tourmaline is largely dravite, at intermediate levels the core

zone is mostly schorl with dravite rims and at depths of 155 m zoned tourmaline is rare; crystals are entirely composed of schorl; only Fe vs. Mg showed a depth-related trend (Fig. 5.14). Tourmaline from Cu-fertile breccias show a better correlation between Mg and Fe ( $R^2 < 0.8$ ) than tourmaline from poorly mineralised breccias which have  $R^2$  of  $< 0.8$  (Fig. 5.14). With this in mind, they suggest that by using the Fe/Mg ratio, tourmaline 'offers a potential tool to discriminate between Cu-bearing and barren breccia pipes'.

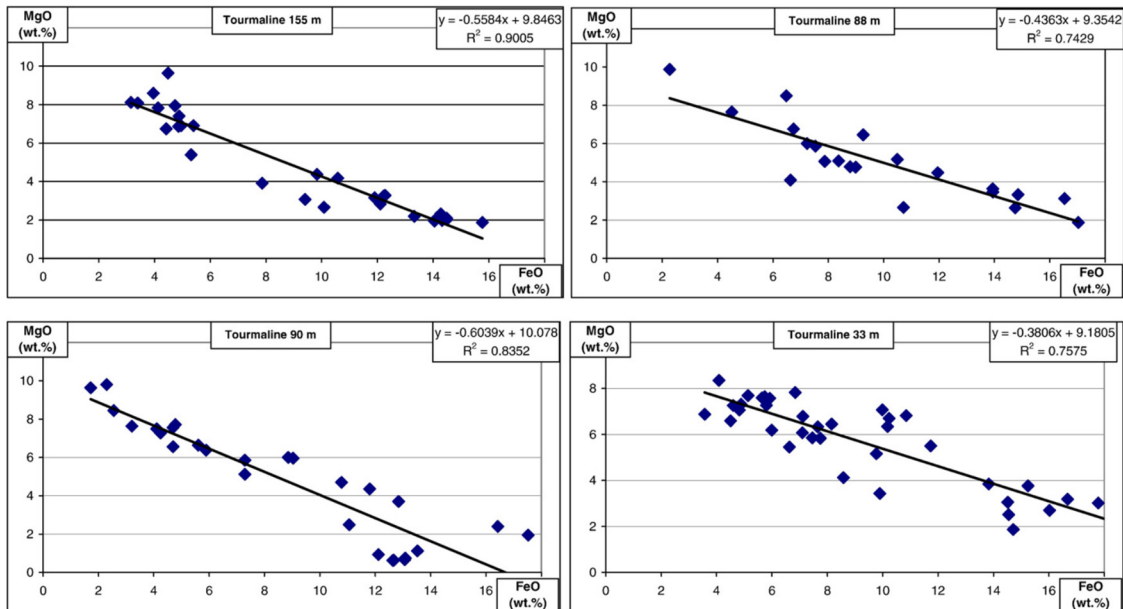


Fig. 5.14 Depth correlation of FeO and MgO from Dill et al. (2012).

Several similarities and disparities exist between the data from the Diablo sector in this study and those presented in previous work. Significant overlap between Diablo samples is observed for  $\text{SiO}_2$ , FeO, MgO,  $\text{Al}_2\text{O}_3$ , CaO,  $\text{TiO}_2$ . Subtle major/minor elemental variability is however present, implying there are a number of depth-related compositional trends. Identified trends in tourmaline composition include:

- 1) Schorl±dravite overgrowths are prevalent at greater depths which compositionally change towards dravite at shallower levels, in accordance with Dill et al. (2012);
- 2) The highest concentrations of Al are at depth which progressively decrease upwards, although there is significant overlap between samples from the middle, upper and marginal parts of the breccias;
- 3) Na decreases towards surface, with deeper tourmaline having  $> 2.3$  wt.%, and those from higher (shallower) levels with  $< 2.3$  wt.%. Samples from the margins contain  $< 1.7$  to  $\sim 2.8$  wt.% so significantly overlap with both of these;
- 4) Fe decreases towards surface with high and middle samples showing similar (3 to 11 wt.%) concentrations of FeO compared with  $> 11$  wt.% for deeper samples;

- 5) Ti moderately decreases upwards where deeper samples contain >1 wt.% Ti and higher up the pipe they contain <1 wt.%;
- 6) Tourmalines from samples from the margin of the breccia show significantly more variation in all elements which overlap with most of the other data. Analyses where MnO is above detection are largely from the margins;
- 7) Diablo shows much weaker  $R^2$  correlations (Fig. 5.15) between FeO and MgO than found by Dill et al. (2012).

Plotting the same cross-plots for tourmaline in the Diablo sector shows that the correlations at all depths are weaker and there is a lot more spread in the data (Fig. 5.15).  $R^2$  correlation coefficients greater than 0.74 were obtained by Dill et al. (2012) and in comparison, the data from the Diablo Breccias (Fig. 5.15) display much less of a correlation  $R^2$  ranging from <0.10 to 0.62. The two best correlations are for the deep inner (Fig. 5.15b) and middle inner (Fig. 5.15g) samples having an  $R^2$  of 0.40 and 0.62, respectively. Splitting the middle zone into individual samples, higher correlation coefficients are shown for finer-grained microcrystalline tourmaline-quartz-cemented samples 1990\_6 (Fig. 5.15g) and 2672\_9 (Fig. 5.15e) which have  $R^2$  values of between 0.62 and 0.14, respectively. Comparing this with the coarser cemented sample 2677\_3 (which contains clasts of microcrystalline breccias, see Fig. 5.3a, b) in Fig. 5.15f, the coarser breccia has a much lower value of <0.01. This relationship between higher correlations and the grain size of the breccia cement is not consistent, because there are other samples with high coefficients, e.g. sample 2136\_1 (Fig. 5.15b;  $R^2= 0.40$ ), which are coarse-grained.

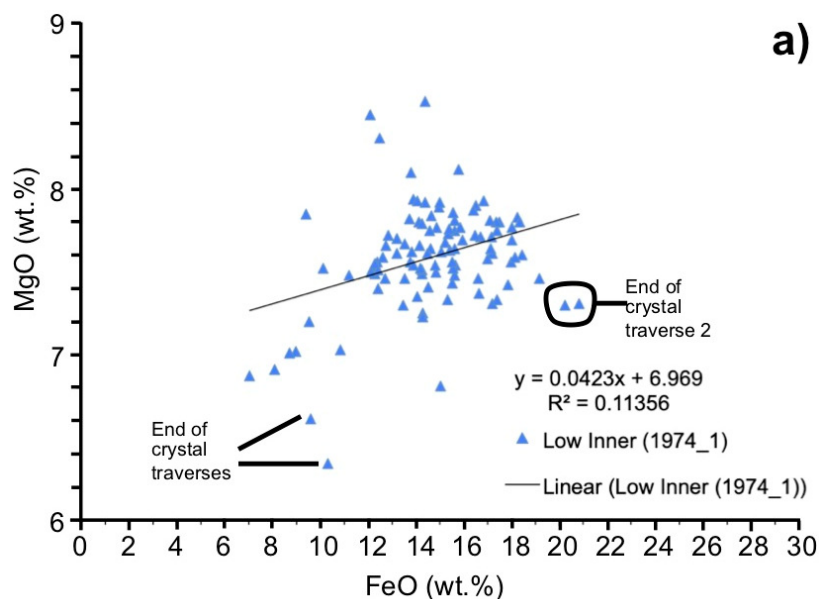


Fig. 5.15 FeO and MgO as a function of depth (generally deep to shallow from diagram a to h) in the Diablo Breccias.  $R^2$  correlation is for all generations of tourmaline. No appreciable difference in the  $R^2$  values is present: **a)** Deep inner sample 1974\_1; **b-h)** Overleaf.

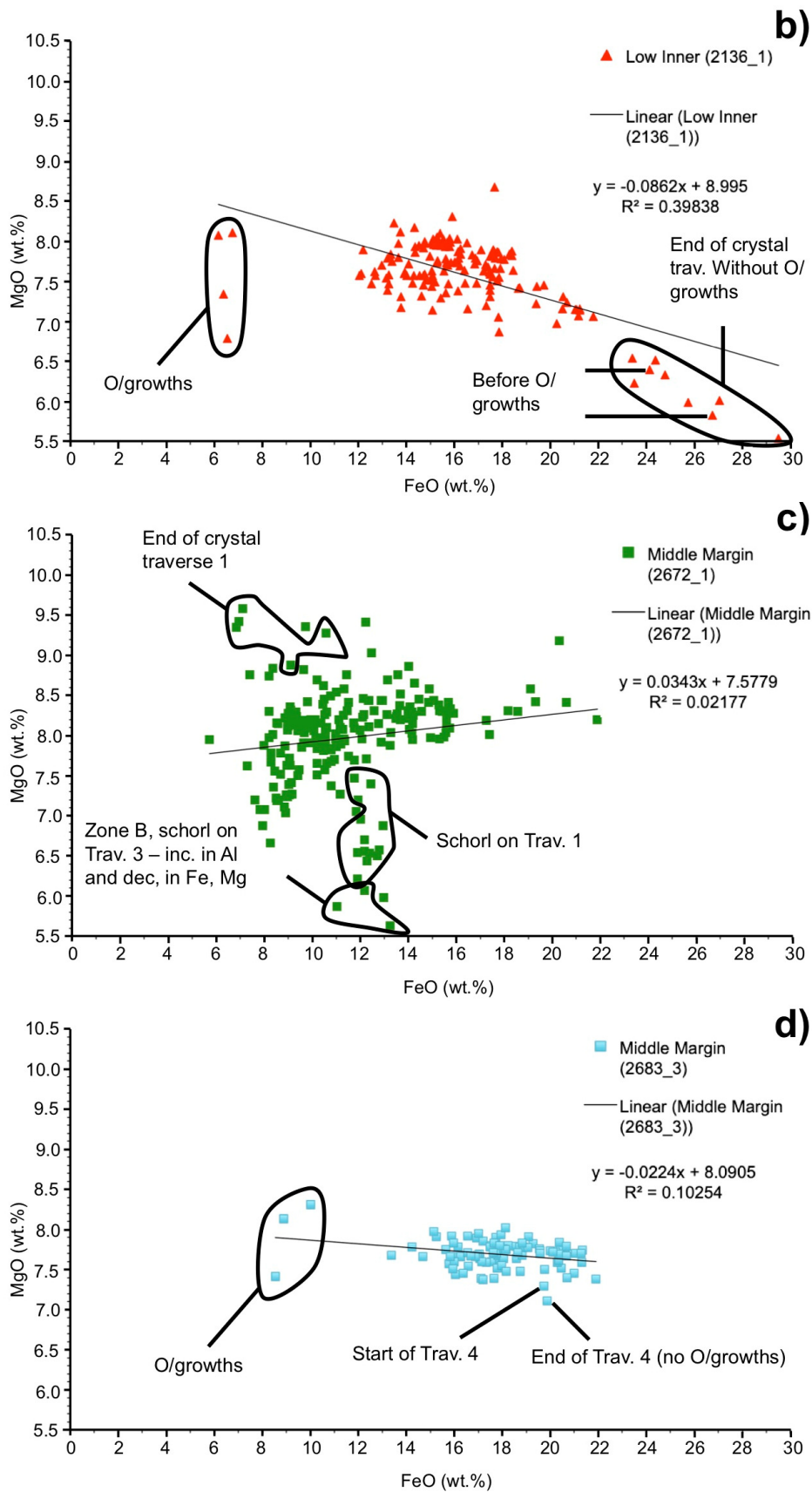


Fig. 5.15 cont. **b)** Deep inner sample 2136\_1; **c)** Middle margin sample 2672\_1; **d)** Middle margin sample 2683\_3.

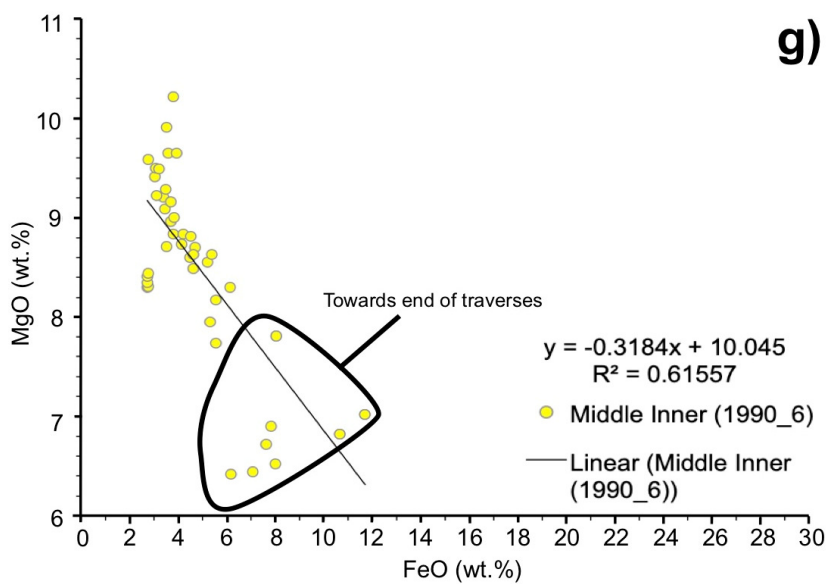
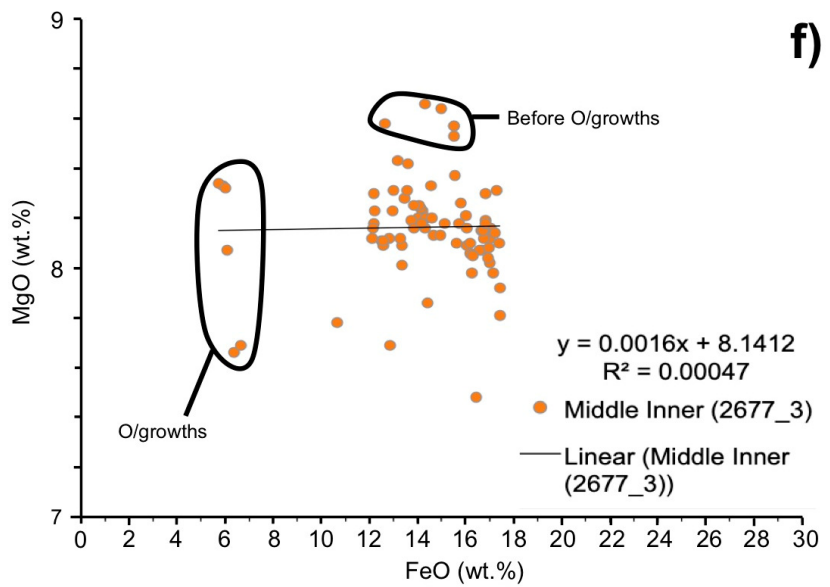
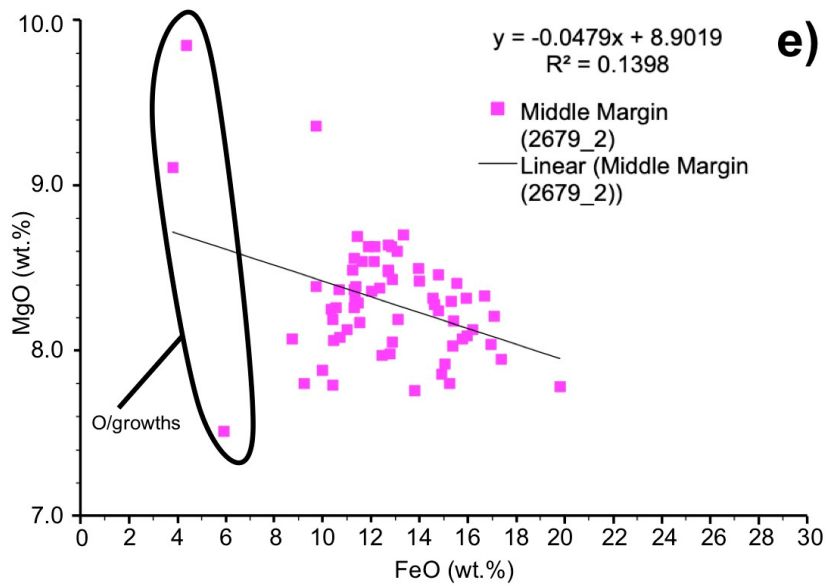


Fig. 5.15 cont. **e)** Middle margin sample 2679\_2; **f)** Middle inner sample 2677\_3; **g)** Middle inner sample 1990\_6.

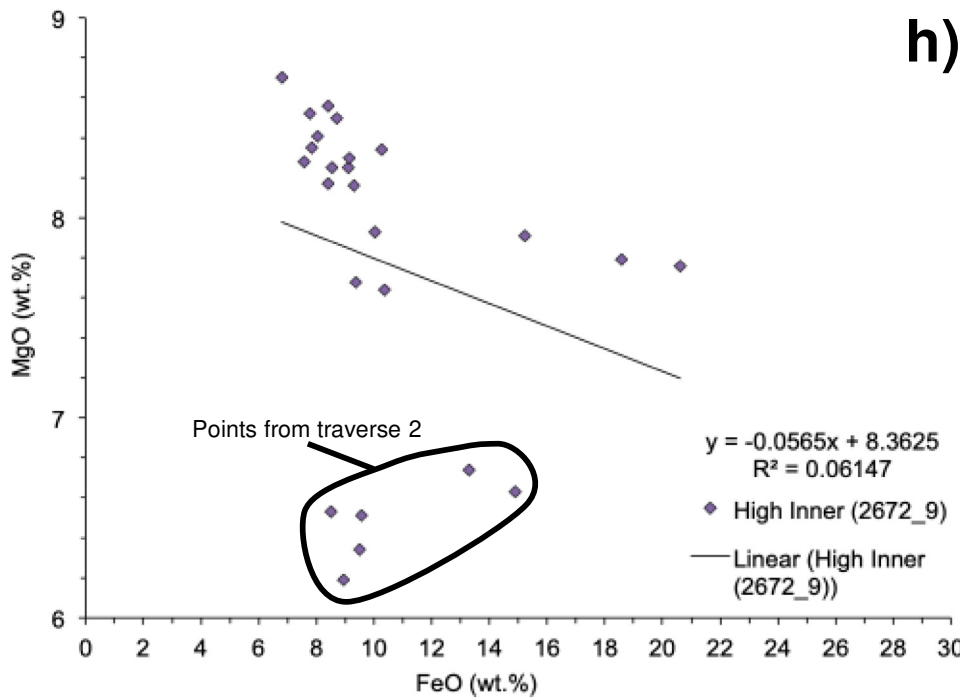


Fig. 5.15 cont. **h)** High (shallow) inner sample 2672\_9.

Data from Río Blanco-Los Bronces breccias (Skewes et al., 2003; Frikken, 2004) also show little correlation between FeO and MgO (Fig. 5.16). That said, these datasets are somewhat more limited than this study or Dill et al. (2012). Plotting the data from Frikken (2004), the opposite trend is identified, where tourmaline from the shallowest levels (Fig. 5.16f) has better correlations (0.71; Fig. 5.16f) than that from deeper in the system (0.61; Fig. 5.16c).

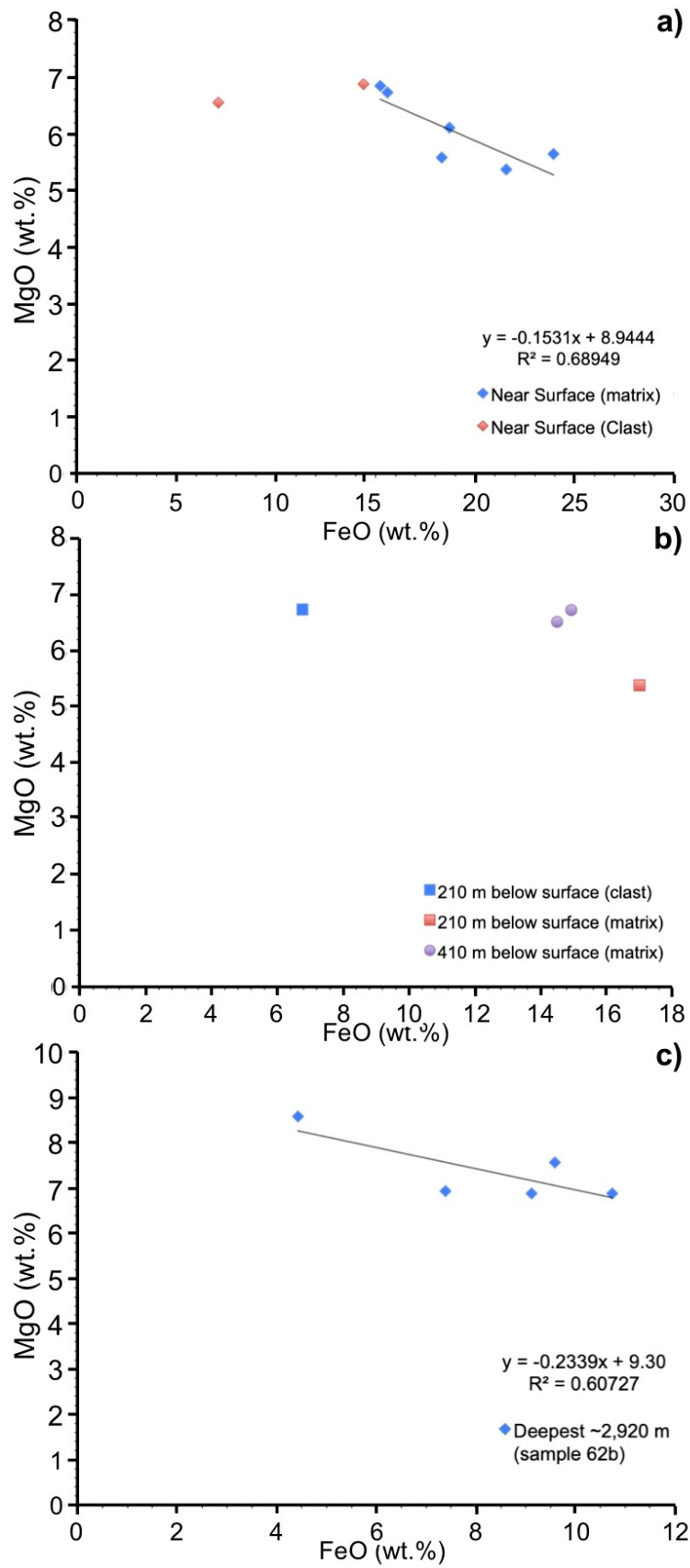


Fig. 5.16 FeO vs. MgO (wt.%) cross plots for tourmaline from Skewes et al. (2003) and Frikken (2004) as a function of depth: **a-b)** Near surface (a) and deeper tourmalines (b) from Skewes et al. (2003); **c-f)** Near surface and deeper tourmalines over ~1000 m (measurements in masl) from Frikken (2004); **d-f)** Overleaf.

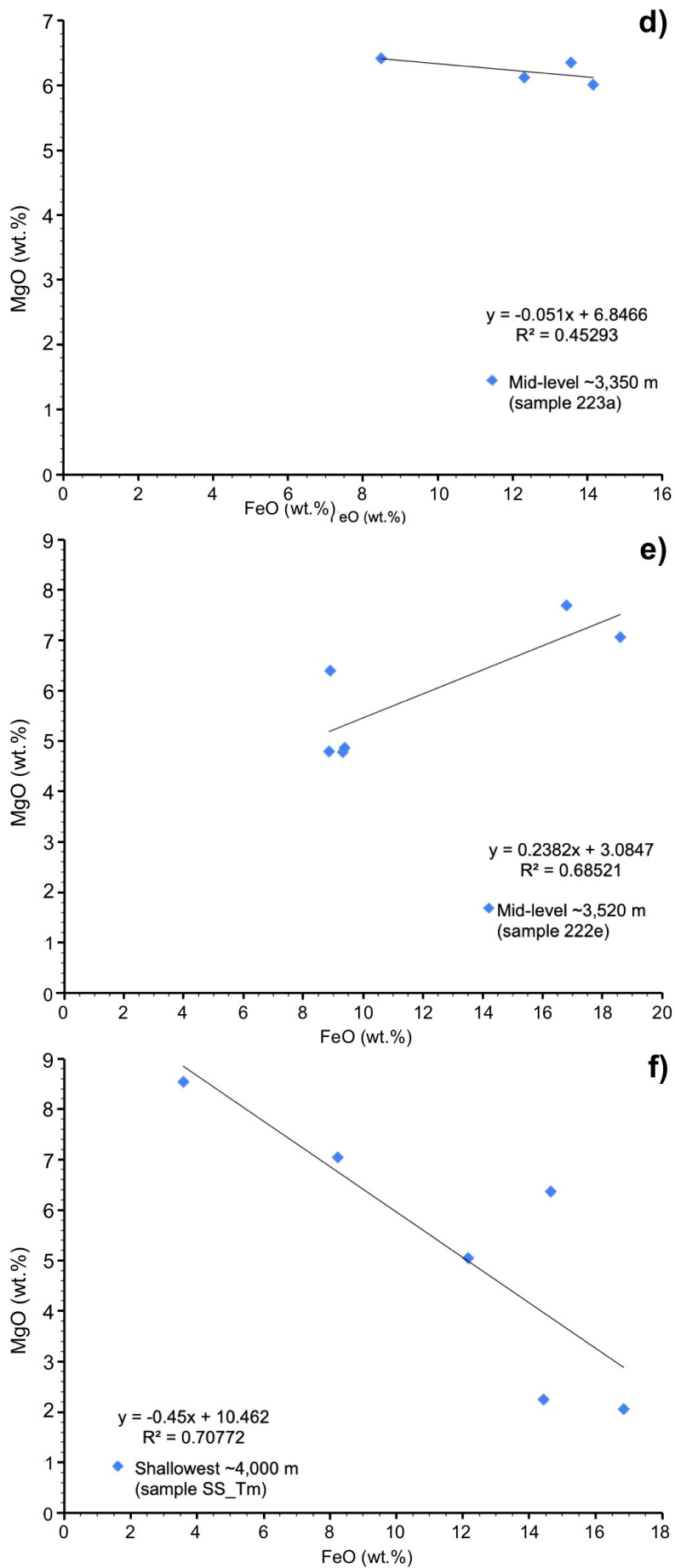


Fig. 5.16 cont. **d)** Mid-level (~3,350 masl); **e)** Mid-level (~3,520 masl); **f)** Shallow (~4,000 masl).

**Depth summary** - The data from the Diablo show significant overlap and telescoping which tracks a gradual change in fluid composition through the breccia columns, both vertically and horizontally. This is likely to have been induced through significant interaction with wall rocks and brecciated fragments throughout the breccia columns. This is also supported by the strong and pervasive bleaching of the clasts, dissolution of smaller fragments in the cement and replacement/infill by cement-stage quartz and carbonate phases.

Further evidence supporting progressive changes to parental fluids throughout the Diablo Breccia columns is the gradual decrease of Na, Ti, and Fe and increase in Al in tourmaline upwards. From the experimental study by Goerne et al. (2001), Na in tourmaline should show a decrease with decreasing fluid temperature. Based on this, tourmalines appear to track decreasing temperature up the Diablo Breccia columns.

Similar Na decreases and increases in Al were observed by Frikken (2004) who attributed decreasing Na in tourmaline up the Sur-Sur breccia column as the result of progressive cooling of fluids which may have allowed the increased precipitation of Na-rich feldspars (e.g., albite). This, in turn, reduced levels of Na in the fluids available to incorporate into tourmaline. Decreasing Ti-in-biotite with increasing elevation was also observed by Frikken (2004) in the Sur-Sur breccia, also interpreted to be due to decreasing temperature towards surface. This coupled with Al-enrichment up the Sur-Sur breccia led them to conclude that temperature decreased and acidity increased. Acidic conditions in the Diablo Breccias and other El Teniente breccias are demonstrated by the spatial correlation of quartz-sericite alteration and tourmaline, particularly the intense alteration ( $\pm$ chemically induced rounding) of brecciated clasts and wall rocks.

#### **5.3.4 Implications for exploration**

Overall, the quantitative results of this study show that tourmaline does record evolving fluid compositions during hydrothermal mineralisation and alteration of breccias (e.g., vertical and horizontal changes in the Diablo Breccias) but cannot effectively and reliably be used to discriminate between well- and poorly-endowed breccia bodies at El Teniente. Trends identified in previous studies (e.g., FeO vs. MgO; Dill et al., 2012) were also not consistently repeated throughout this study or in some of the other datasets (e.g., Skewes et al., 2003; Frikken, 2004). This shows that any compositional trends identified in one study need to be validated across other deposit types to check consistency and repeatability. One problem is finding a truly barren (containing no Cu-Mo) breccia (i.e. a negative control), which has not been mineralised and then leached because if uneconomic Cu-Mo mineralisation is initially intersected during exploration, many prospects are often not drilled further, or to deeper levels which may contain

economic Cu-Mo (e.g., La Huifa). It is also clear that extreme care should be taken when using tourmaline because its composition is strongly influenced by its the mode of formation (clast vs. cement) and proximity to wall rocks (and wall-rock composition).

**Practicality/ease of analysis** - The blocky to acicular habit of tourmaline often closely intergrown with other accessory phases makes obtaining in-situ trace analysis via laser ablation problematic and challenging. It requires a lot of pre-screening and processing to remove unreliable or poor data which is not time or cost-effective. Targeting specific zones in tourmaline to obtain zone-specific chemical data is essentially impossible because of the spatial resolution issues. Specific BSE domains are often sub-beam (<40 µm) width meaning laser ablation sites invariably incorporate a variety of zones and chemistries. The laser spot size could be reduced however detection limits would invariably worsen. Longer ablation times could limit this however the chemical domains also change in 3D depth so deeper ablation pits will also invariably end up incorporating more zones.

## **5.4 Braden Diatreme**

In this section, the links and associations between Mo-Cu-sulphide mineralisation and juvenile dacite clasts, and the origin of the juvenile material, are debated and are incorporated into an updated model of formation for the Braden Diatreme.

### **5.4.1 Juvenile dacite clasts and alternative interpretations**

Owing to the spatial relationship between the Braden Diatreme and underlying large porphyritic dacite intrusion, the diatreme is thought to have spawned from the intrusive. This is supported from observations of deep drill core (Cannel, 2004; this study) where, with increasing depth, dacite clasts become the main clast type and there are megaporphyritic dacite blocks in the diatreme (e.g., Howell and Molloy, 1960). The cause of breccia formation has previously been interpreted to have been explosive phreatomagmatism (e.g., Sillitoe, 1985; Makshev et al., 2004) based on the description by Camus (1975) of tuffaceous material and obsidian within the Braden Diatreme.

Other direct evidence for this explosive process, such as the presence of juvenile material with wispy/vermiform/cuspate clast morphologies (forthwith to be referred to as vermiform clasts) from the parent magma or accretionary lapilli, have not until now been described in the El Teniente breccias. This is because pervasive alteration of the clasts and matrix to “various associations of sericite, chlorite, smectite, calcite, and siderite with subordinate dravite” often makes confidently identifying these features difficult (Makshev et al., 2004). By combining a number of direct and indirect observations in this study, the presence of vermiform clasts was identified and importantly provides direct evidence for breccia formation either by explosive fluid

exsolution from the magma, or phreatomagmatism, the latter in line with the interpretation of Sillitoe (1985). Evidence for the involvement of groundwaters in explosive brecciation, however, as suggested by Sillitoe (1985), remains elusive. Below are the key observations supporting a juvenile origin for the vermiform clasts, together with alternative interpretations.

**Clast morphologies and dacite textures** - The vermiform clasts were visually identified in drill core from their cream-white colour which is easily distinguished from the grey unaltered rock flour matrix or dark grey-blue Mo-Cu-sulphide-rich groundmass. From their morphology, they appear to have been emplaced into the rock flour breccia in a plastic state. Clasts from the wall rocks or other previous hydrothermal breccias do not show these plastic morphologies. Their vermiform appearance suggests they formed by explosive magma fragmentation at depth and entrainment in an upward rising fluidised breccia column. Vermiform fragments with wispy to fluidal morphologies were also described in the diatreme from the Cerro Maricunga gold porphyry-epithermal system in northern Chile (Lohmeier et al., 2019) and in maar-diatremes of the El Guanaco mine volcanic sequence, northern Chile (Páez et al., 2018, Fig. 6). Cannell et al. (2007) also described elongate irregular sericite-altered dacite clasts in a tourmaline-anhydrite breccia which may also have been indicative of a juvenile magmatic origin for those breccias.

The vermiform clasts in the Braden Diatreme mostly occur along its margins suggesting they have poor preservation potential in the central portions of the diatreme. This is attributed to increased attrition and abrasion in the more fluidised portions, as per the modeling by McCallum (1985). It could also be that their presence is masked by destructive sericite-quartz alteration, which overprints large portions of the Braden Diatreme. In areas of intensely altered drill core, where clasts are completely texturally obliterated, clasts can only be identified on the basis of a colour difference with the grey rock flour. Where alteration is less intense, plagioclase and quartz phenocrysts could be identified which confirm a dacite porphyry origin for the vermiform clasts.

**Quartz** - To further explore the origin of the vermiform dacite clasts, they were studied in CL and by determining Ti-in-quartz. Quartz was chosen because it is present in the underlying parental porphyritic dacite, breccia clasts and throughout the rock flour matrix. Its relative durability often allows it to survive brecciation and to potentially retain original textures. Quartz CL imagery may provide information about its formation environment, with an increase in CL intensity (mostly in the blue wavelengths) often correlating with increased Ti concentrations (e.g., Müller et al., 2002, 2010; Kronz et

al., 2012). For example correlations between blue CL emission from magmatic quartz and >70 ppm Ti were described by Müller et al. (2002).

The use of Ti-in-quartz as a geothermometer is based on the substitution of Ti<sup>4+</sup> for Si<sup>4+</sup> being pressure and temperature dependent (e.g., Wark and Watson, 2006; Thomas et al., 2010; Huang and Audétat, 2012). Work by Landtwing and Pettke (2005), Rusk et al. (2006), Müller et al. (2010), Rusk et al. (2011), and Rusk (2012) identified a progressive decrease in Ti concentration and quartz CL intensity from earliest to the latest vein quartz generations in a variety of porphyry-Cu (Mo-Au) deposits (e.g., Butte (Montana), Oyu Tolgoi and Zesen Uul (Mongolia)), interpreted to indicate decreasing fluid temperatures over time.

This study showed that magmatic quartz from the underlying dacite, phenocrysts in the vermiform clasts and xenocrysts in the rock flour matrix all give a strong blue colour in CL, and Ti concentrations >70 up to 200 ppm. Using Ti-in-quartz thermometer of Wark and Watson (2006) ( $T(^{\circ}\text{C}) = (-3765 / (\log \text{Ti} - 5.69)) - 273$ ), temperature estimates in the dacites (and rock flour hosted xenocrysts) are in the range of 900 and 700°C. Other quartz phases are below this (e.g., breccia-stage and quartz associated to molybdenite). Quartz xenocrysts in the breccia rock flour matrix mostly originate from the dacite and therefore have approximately the same grain-internal textures and trace element content as in the dacite.

A large portion of magmatic quartz xenocrysts (slightly more rounded than in the dacite) observed in matrix further supports large degrees of attrition and abrasion of the original dacite in the process forming the fine-grained rock flour. Apart from 'healed' fractures, no internal zoning with strong CL contrasts, skeletal growth, or growth embayments were distinguished within magmatic quartz grains. No widespread dissolution of magmatic quartz was observed implying that subsequent hydrothermal activity was somewhat limited, probably because the formation of the Braden Diatreme depressurised the system.

Breccia-stage quartz in the matrix is largely too fine-grained to be analysed, except for weak blue to purple/pink CL margin/rims on magmatic quartz xenocrysts, which likely formed as a result of brecciation and fluid infiltration (e.g., Fig. 4.17a). These have Ti concentrations below detection (70 ppm) and therefore formation temperatures lower than ~700°C (using the Ti-in-quartz geothermometer). Paragenetically later hydrothermal quartz associated with molybdenite, also has a weak blue to purple/pink CL response and <70 ppm Ti. A similar correlation between low to weak blue CL-intensity veinlet quartz and sulphides was described in the following Cu/Mo porphyry-type deposits: Grasberg, Indonesia (Penniston-Dorland, 2001), Red Hills, USA (Frelinger et al., 2015) and Tongcun, China (Ni et al., 2017). This later hydrothermal

quartz in the Braden Diatreme are, however enriched in Fe ( $\pm$ Al), often containing >300 ppm Fe (up to 1,536 ppm Fe), compared with magmatic and other hydrothermal quartz with <300 ppm Fe. These Fe ( $\pm$ Al) enrichments may be explained by invisible submicroscopic inclusions of matrix minerals (e.g., K-feldspar, illite, Fe-illite). This is supported by larger more easily visible matrix inclusions up to 100  $\mu$ m being sometimes observed (e.g., in Fig. 4.17c, d). Müller et al. (2005) described similar impacts of sub-microscopic inclusions in quartz causing Al-K concentration spikes.

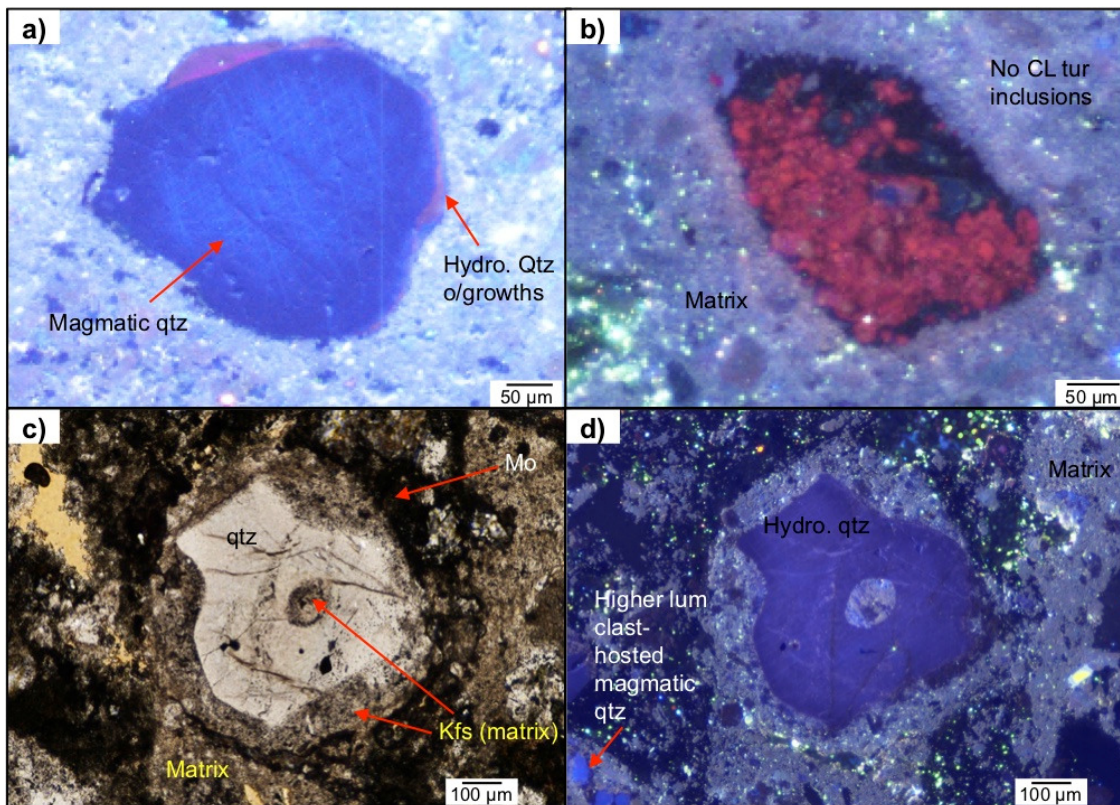


Fig. 5.17 Magmatic and hydrothermal quartz textures in the Braden Diatreme: **a)** Cold-CL image of blue-CL magmatic xenocryst with localised lower luminescence breccia-stage quartz rims/overgrowths. From DDH1196-220.88 m; **b)** Cold-CL image of globular red quartz with non-CL tourmaline inclusions. From DDH1196-242.04 m; **c-d)** PPL photomicrograph (left) and cold-CL (right) of matrix (K-feldspar-illite/Fe-illite) inclusion in weakly luminescing blue quartz. From DDH1196-220.88 m.

Quartz in the rock flour matrix, which has a globular texture and moderate to high red-pink CL response (e.g., Fig. 4.17b), may come from another lithology but without further detailed studies of wall rocks it is difficult to confirm this. For example, Müller et al. (2009) described red-dominant CL emissions from quartz in granite which they associated with “OH- and H<sub>2</sub>O-bearing lattice defects”. It may alternatively be due to the quartz having replaced sulphates (Ramseyer et al., 1988). An increase in Fe<sup>3+</sup> could also cause a red CL response (Müller et al., 2005) which in these quartz grains may be derived through post-crystallisation diffusion of Fe from tourmaline inclusions into the quartz lattice (e.g., vein quartz in the Grasberg Complex; Penniston-Dorland,

2001). Although this quartz does have areas with relatively high Fe (up to 2,700 ppm) they are not consistently enriched.

**CL and Ti-in-quartz summary** - Similar quartz phenocryst internal grain characteristics, CL emissions (bright shades of blue) and Ti concentrations (73 to 298 ppm Ti) between the vermiform clasts and underlying dacite, suggests that they are intrinsically linked, the vermiform clasts probably representing splashes of magma entrained in the upwardly emplacing-fluidised breccia column from the underlying dacite intrusion. The presence of small discontinuous hydrothermal quartz overgrowths on the phenocrysts, with weaker pink-blue CL, and correspondingly lower Ti contents (<73 ppm Ti), implies that breccia-stage quartz formed at lower hydrothermal (opposed to magmatic) temperatures.

**Sulphide mineralisation in the rock flour matrix** - The 10 µm point spacing QEMSCAN® Fieldscan maps of vermiform dacite clasts and rock flour matrix in polished thin-section (Fig. 4.8; Chapter 4.1.5) initially showed that despite the clear colour change in hand specimen there is no major compositional difference between the vermiform dacite clasts and rock flour matrix. Both are primarily composed of K-feldspar intergrown with a combination of fine clays (Fe-illite/illite), sericite, quartz and variable chlorite. Validation of mineral identifications in the QEMSCAN® maps involved checking mineral subcategories and boundary categories (e.g., feldspar) to see if any major mineral phases had been misclassified during database set-up. However this showed nothing untoward.

To compare the vermiform clasts with the rock flour matrix in more detail, selected areas were QEMSCAN® mapped at a much higher (1 µm) pixel spacing (Fig. 5.19). These higher resolution maps corroborated the initial maps, where there is no major elemental difference between the matrix and clasts. This is also supported by separate whole-rock XRD analysis of the rock flour matrix (which was carefully drilled to make sure no clasts were included) and clasts (Fig. 4.6). The close mineralogical similarity between the rock flour matrix and vermiform clasts strongly suggests that the rock flour matrix is a highly fragmented and abraded derivative of the dacite clasts ± a possible small contribution from wall-rock units and other incorporated lithologies evidenced by the presence of these as clasts in the breccia (see Fig. 5.18). The input from wall rocks or other lithologies is likely negligible otherwise there would be a greater contrast between matrix and dacite clast geochemical compositions. The later pervasive overprinting sericite-quartz-chlorite alteration produced the same mineral assemblages in both matrix and clasts.

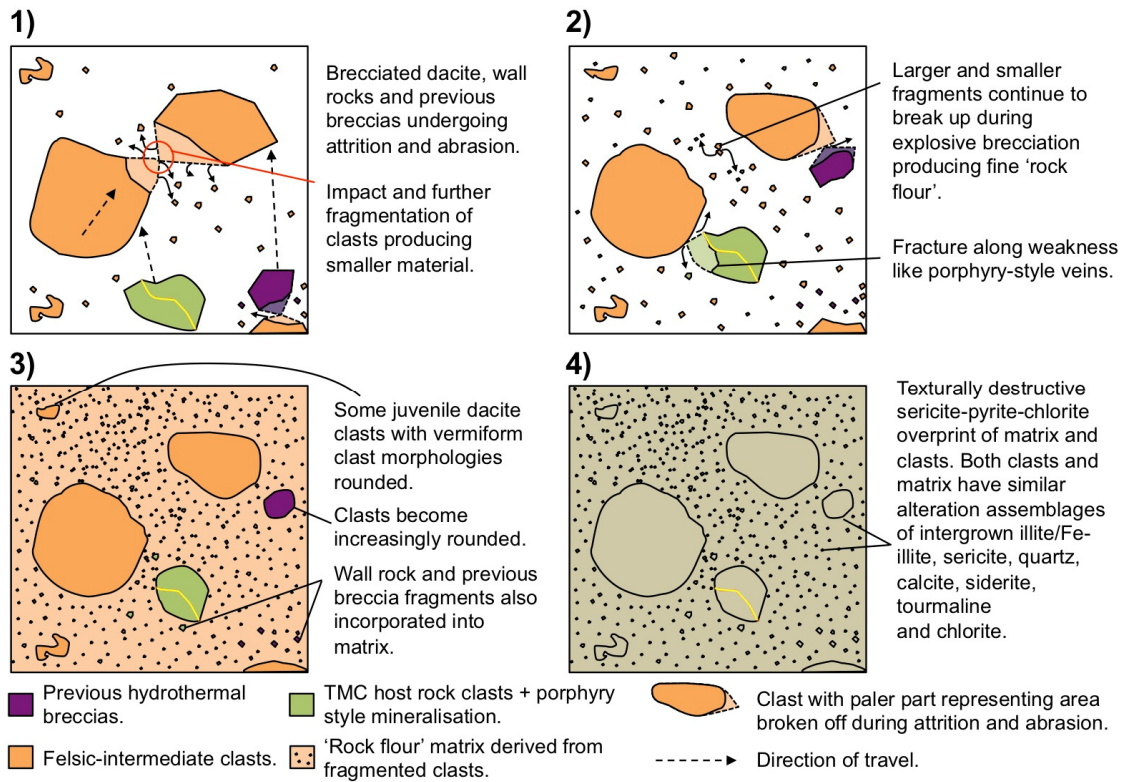


Fig. 5.18 Schematic model illustrating the development of the Braden Diatreme rock flour matrix with exaggerated wall-rock and other lithology components: **1)** Attrition and abrasion of clasts entrained in upwardly rising breccia column breaking clasts up into smaller fragments; **2)** Fragmented particles continue to further abrade each other and larger particles producing smaller particles. Most juvenile clasts are abraded and the complex morphologies obscured/rounded; **3)** Continued violent attrition and abrasion of all sized material further generating fine rock flour; **4)** Texturally destructive sericite-pyrite-quartz±chlorite alteration overprints producing same assemblages in both clasts and matrix.

What these 1 µm maps (Fig. 5.19) did however show is that the contact between the vermiform dacite clasts and rock flour matrix is identifiable due to the presence of very fine-grained individual molybdenite crystals, and 'molybdenite-mixed' sub-categories/boundary categories consisting of: 1) molybdenite, 2) K-feldspar-molybdenite, 3) biotite and/or Fe-illite-molybdenite and 4) chlorite-molybdenite. Molybdenite in the rock flour matrix is micron to sub-micron in size, thus it was difficult to analyse with EDS due to excitation volume issues; most such analyses therefore gave mixed phase spectra.

These sub-category QEMSCAN® maps (e.g., Fig. 5.19c) correlate well with the optical petrography and hand specimen observations in showing the boundary between the vermiform dacite clasts and rock flour matrix. Surrounding the vermiform dacite clasts are molybdenite-quartz zones, a few cm wide, which show outward-declining molybdenite concentrations, suggesting that this stage of Mo-quartz (±Pb-Zn) mineralisation was from fluids exsolved from the vermiform magma splashes as they crystallised. Micron-scale tourmaline is also irregularly present along the vermiform

clast-rock flour boundary (Fig. 5.19l) further suggesting localised exsolution from the vermiform spatters.

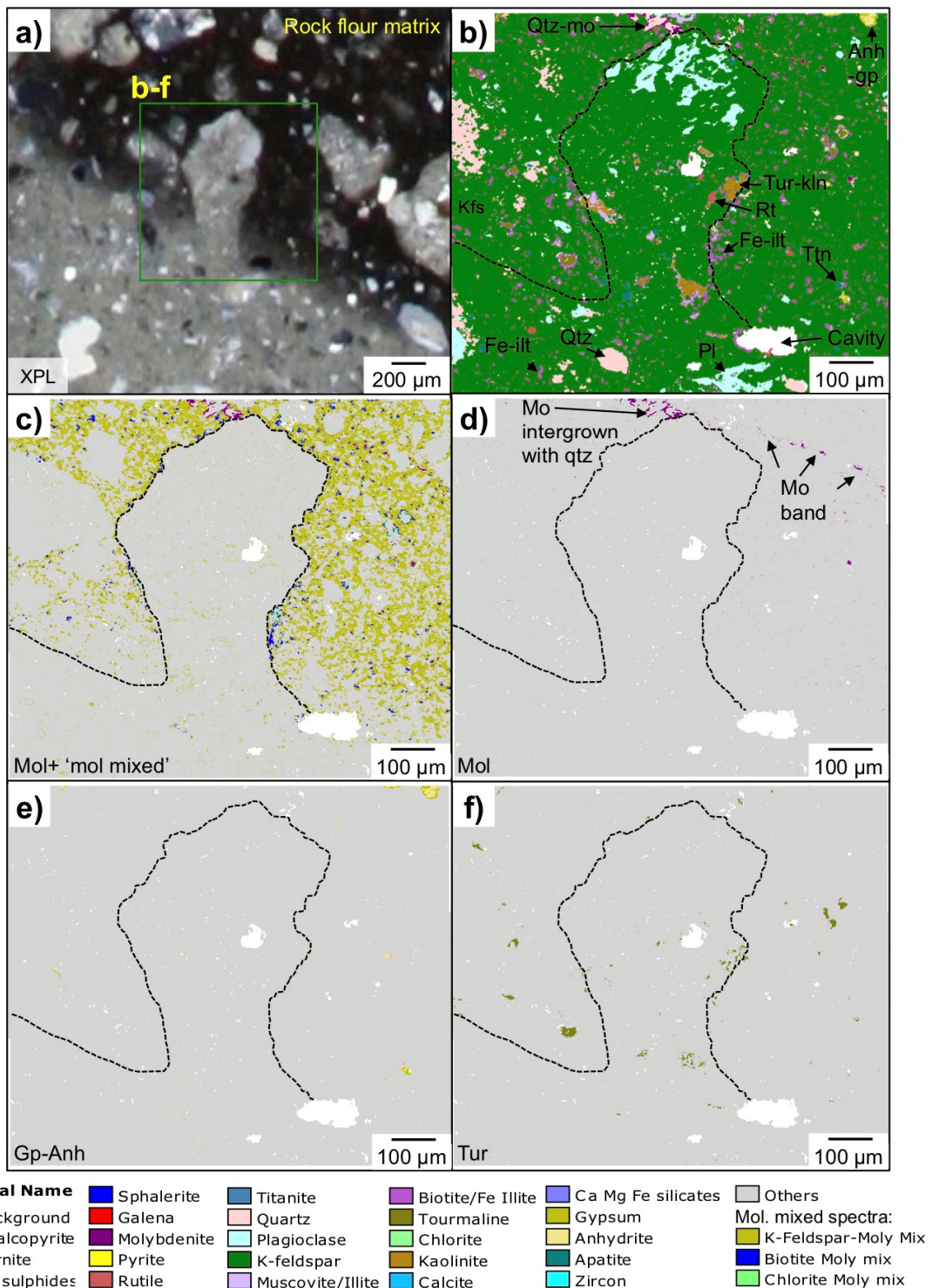


Fig. 5.19 Cross polarised photomicrograph (a) and 1 µm pixel QEMSCAN® maps (b-f) from DDH1196-172.71 m. Molybdenite mixed categories are mixed spectra resulting from the very fine-grained nature of molybdenite: **a)** Dark black rock flour matrix with molybdenite and lighter grey vermiform clast; **b)** QEMSCAN® mineral map showing no mineralogical difference between vermiform clast and rock flour groundmass; **c)** Molybdenite and all the molybdenite mixed categories showing clear change from the comparatively Mo-rich matrix to Mo-poor vermiform dacite clasts which corresponds to the optical image; **d)** Molybdenite map where molybdenite is coarse enough to be categorised on its own. In this case the molybdenite is in a band around the vermiform clast; **e)** Gypsum-anhydrite space-fill in the matrix; **f)** Tourmaline showing only minor tourmaline in the matrix.

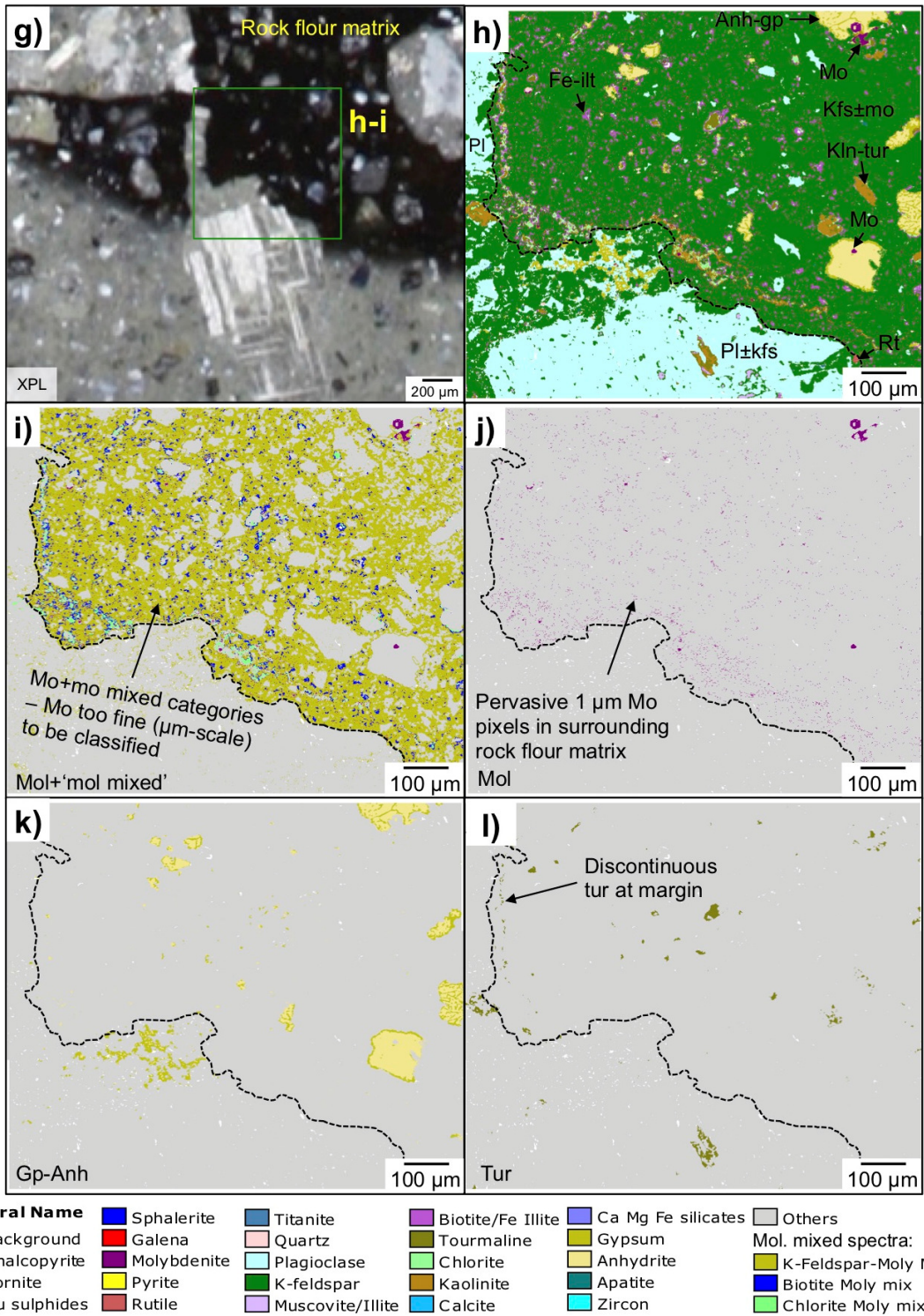


Fig. 5.19 cont. **g)** XPL photomicrograph of clast:matrix boundary distinguished by a sharp colour change; **h)** QEMSCAN<sup>®</sup> mineral map dominated by K-feldspar. In the dacite clasts are coarser phenocrysts (Fig. 5.19h). Vugs in the matrix are mainly infilled by anhydrite-gypsum; **i)** Molybdenite and molybdenite mixed categories which show that the clasts contain relatively low levels of molybdenite; **j)** Molybdenite map; **k)** Gypsum-anhydrite infilling cavities in matrix; **l)** Tourmaline map showing very fine (micron-scale) tourmaline precipitation along the clast margin.

The small-scale Mo-Cu-quartz mineralisation around the vermiform clasts is similar to a larger, near mineralogically identical, more pervasive post-dating mineralisation which further introduced more Mo-Cu-(±Pb-Zn)-quartz-anhydrite, as described in Section 4.1.4, and locally re-brecciated the clasts and rock flour matrix (e.g., Fig. 4.5h, i). This occurred following the formation of the Braden Diatreme whereby the underlying dacite intrusive continued to exsolve fluids which were focused along fractures, particularly at the margins of the Braden Diatreme. These caused the pervasive impregnation of the rock flour matrix with molybdenite (±chalcopyrite)-quartz, supported by what have been interpreted to be fluid/vapour fronts of molybdenite in the rock flour matrix (shown earlier in Fig. 4.9d and Fig. 4.16a in sections 4.1.5 and 4.2.4, respectively).

The following is a list of key supporting evidence for a juvenile origin for the vermiform clasts:

- Their shapes are consistent with formation from a plastic material emplaced within a finely dispersed medium in air (i.e. rock flour within a fluidised breccia column), rather than representing broken/brecciated clasts as for other lithologies in the Braden Diatreme; they are similar to juvenile clasts described in other diatremes (e.g., Páez et al., 2018; Lohmeier et al., 2019);
- The vermiform clasts have the same mineralogy and crystal size as the dacite porphyry which underlies the Braden Diatreme;
- Molybdenite mineralisation decreases with increasing distance from the vermiform clasts;
- Fine (<10 µm) tourmaline has precipitated at the clast margins (e.g., Fig. 5.19l), which is not observed elsewhere in the rock flour matrix;
- In less altered parts of the vermiform clasts, original magmatic textures such as quartz and feldspar phenocrysts are observed (e.g., Fig. 4.7g; Section 4.1.5);
- The vermiform clasts are mainly distributed around diatreme margins where preservation potential was better;
- Quartz phenocryst luminescence and internal grain textures in the vermiform clasts resemble those from the underlying dacite, from which they are thought to have been ejected during magma fragmentation. This magmatic quartz shows more vivid blue CL colours than that of hydrothermal origin in veins and the breccia groundmass.

**Alternative origins for the vermiform dacite clasts** - A number of alternative origins were also considered for the vermiform clasts, which are:

1. The lighter cream-white areas (i.e. the vermiform clasts) represent regions of non-molybdenite-mineralised rock flour, i.e. they are not juvenile clasts. These regions were preserved as the fluids which precipitated the molybdenite were not able (for some reason) to permeate the rock flour.

This option is based on there being no distinct/easily identifiable textural margin between the cream coloured and darker blue-black regions in PPL. Instead, the margin between them is only visible in hand specimen and from the presence of molybdenite or molybdenite mixed spectra in QEMSCAN® mineral maps (e.g., Fig. 5.19). Both regions also share the same whole-rock chemistry (Fig. 4.6, Section 4.1.5) supporting that it might all be the same unit. This possibility has been dismissed, however, as cream-white regions are also observed away from areas of molybdenite overprint of the rock flour (e.g., Fig. 4.7). Many of the cream coloured regions sometimes also host miarolitic cavities (<1 cm) at their centres (e.g., Fig. 4.8b; Fig. 4.12g) which have been variously infilled by later tourmaline and anhydrite-Mo-Cu±Pb-Zn assemblages (e.g., Fig. 5.20d-g) suggesting the vermiform dacite clasts were fluid/volatile-rich. Also, the Mo mineralisation generally is most intense close to the contacts and gradually diminishes away indicating that molybdenite mineralisation is intrinsically linked, and derived from the vermiform dacite clasts. In addition to this, the cream-white regions contain euhedral plagioclase phenocrysts (e.g., Fig. 5.19g), which are not present in the rock flour groundmass, as these are unlikely to have survived the intense brecciation and milling associated with the formation of the fine groundmass - so they are much more likely to represent dacite clasts.

2. The lighter cream-white areas represent late hydrothermal (including Póstuma) stage type 9 (tourmaline-carbonate-anhydrite±chalcopyrite-pyrite-bornite-molybdenite with a sericite-chlorite-quartz halo; Fig. 5.20a) or type 10 (carbonate-anhydrite-gypsum±tennantite-chalcopyrite-pyrite-bornite-molybdenite with a sericite-chlorite-quartz halo; Fig. 5.20b-c) veins, as per the classification schemes used in Vry et al. (2010) and Spencer et al. (2015).

Cannell (2004) describes this late hydrothermal stage (4.85 to 4.40 Ma) as 'a second stage of phyllic alteration and veining, related to intrusion of the Braden Diatreme, and the emplacement of late dacite dykes (4.8 Ma)'. Type 9 and 10 veins formed immediately after the "major release of magmatic volatiles that formed the Braden Diatreme" and the close spatial association between these veins and the margins of the Braden Diatreme suggest they are closely linked (Spencer et al., 2015). But there are generally an 'absence of cross-cutting type 9 and 10 veins in the Braden Breccia'

(Spencer et al., 2015). That said, a small number of type 10 veins were identified in the Braden Sericite (rock flour) Breccia in this study (Fig. 5.20d).

The cream-white regions mainly consist of quartz, K-feldspar and plagioclase, and a mixture of alteration-overprint products including illite/Fe-illite, chlorite, and lesser variable tourmaline, gypsum-anhydrite, ankerite and Cu-sulphides, probably indicating a magmatic precursor, very different to the near monomineralic tourmaline type 9 veins or carbonate-anhydrite type 10 veins which are almost certainly of hydrothermal origin. The vermiform morphologies of the cream-white regions also do not look like veins or vein halos. Many of the type 10 veins observed in the Braden Diatreme do not have distinctive alteration halos and are often present in areas with no molybdenite (Fig. 5.20d). The clast morphologies instead imply the emplacement as semi-solidified blebs into a fluidised rock flour body. In drill core the light cream-white areas do not have large continuity; often ceasing after ~10 cm and are not continuous like veins seen.

Optical and SEM petrography alongside QEMSCAN<sup>®</sup> mapping also did not identify any halos of gypsum, quartz, chlorite or sericite (mapped as illite in QEMSCAN<sup>®</sup>) as has been described for veins (e.g., Vry et al., 2010; Spencer et al., 2015). The quartz textural and trace element study does also not support a late hydrothermal origin either, which would produce low luminescing quartz phases and much lower Ti-in-quartz concentrations than observed (<70 ppm= ~700°C). Finally, if these features were caused by late-stage fluids, related to Póstuma alteration (as per Cannell, 2004), it still does not explain the decreasing Mo with increasing distance from the cream-white clasts, or the quartz-molybdenite-sphalerite-chalcopyrite±tourmaline at the margins, or how there is comparatively very little Cu-Mo-Pb-Zn mineralisation inside the cream coloured areas.

3. The vermiform dacite clasts may have acted as a physical barrier, which caused the pooling of these later Mo-rich mineralising fluids.

This scenario seems highly unlikely as the molybdenite-rich zones occur on all sides of the dacite clasts. In addition to this, other clasts in the diatreme matrix, such as previous hydrothermal breccias or wall-rock fragments do not display concentric zones of gradually decreasing Mo mineralisation in the matrix with increasing distance from the clasts, or host miarolitic cavities (see Fig. 4.8a transmitted light photograph illustrating less molybdenite-sphalerite around clast adjacent to vermiform clast).

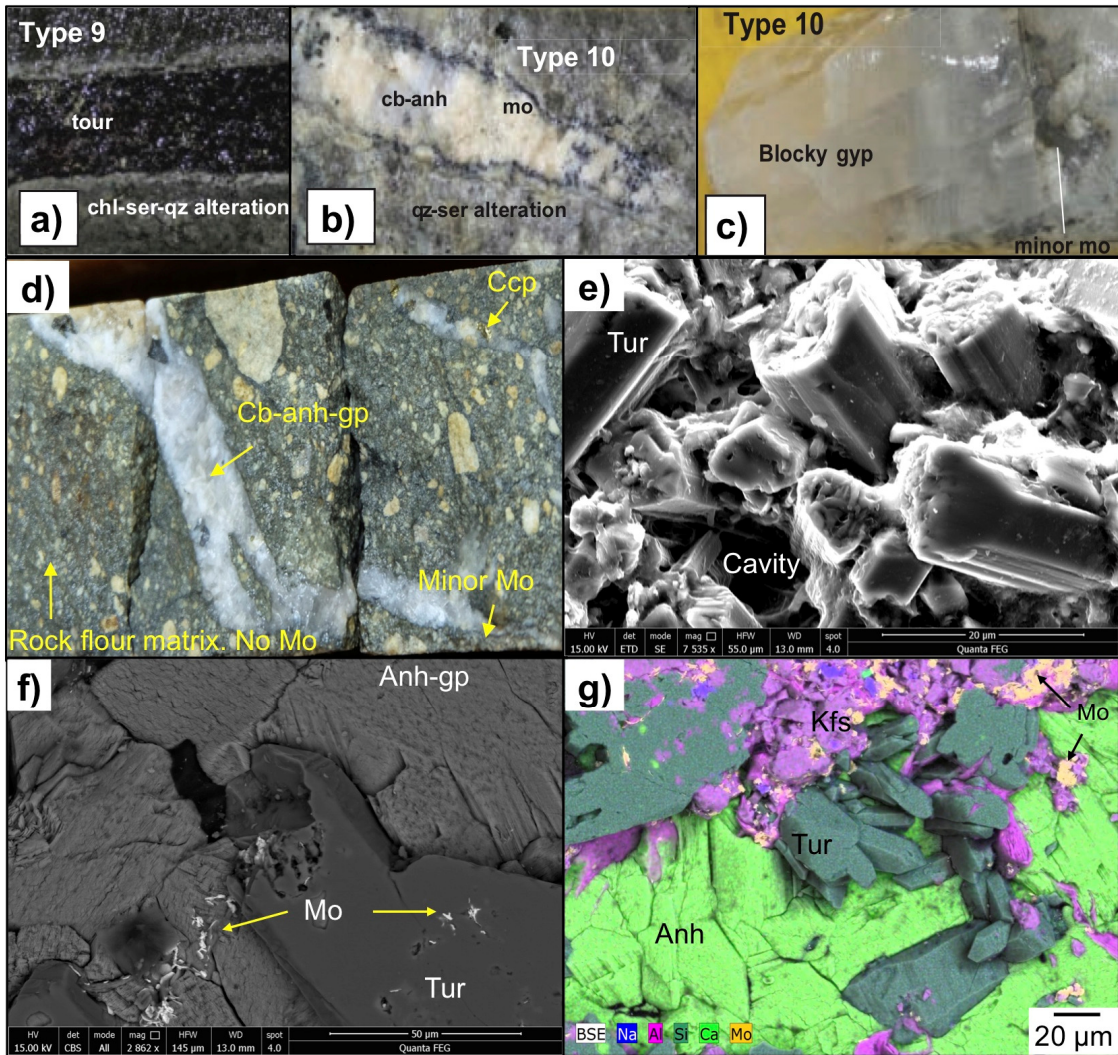


Fig. 5.20 Images (a-c) of type 9 and 10 veins from Spencer et al. (2015) and other late-stage vein cross-cutting the Braden Diatreme: **a)** Type 9 tourmaline vein with minor chalcopyrite-molybdenite in the sericite-altered TDP south of the Braden Diatreme; **b)** Type 10 carbonate-anhydrite vein with a quartz halo from the Southern Diorite; **c)** Type 10 vein with coarse gypsum from proximal to the Southern Diorite; **d)** Type 10 carbonate-anhydrite-gypsum vein cross-cutting the Braden 'rock flour' matrix ~36 m from the diatreme margin (DDH1754-0.61 m). The matrix has contains very little Cu, no molybdenite overprint and no distinctive Mo halo is present around the vein; **e)** SEM-secondary electron image of acicular tourmaline growth in a vermiform clast-hosted miarolitic cavity. From DDH1196-172.93 m; **f)** SEM-BSE image illustrating open-space tourmaline with molybdenite inclusions growing into open-space. Later anhydrite-gypsum are end-stage open-space infill. From DDH1213-157.87 m; **g)** BSE-SEM image with colour EDS map overlaid, demonstrating acicular tourmaline growth from cavity walls and later anhydrite space-fill. Minor molybdenite is localised around the cavity margins. From DDH1213-157.87 m.

#### 5.4.2 Braden Diatreme formation model

The Braden Diatreme was emplaced in a structural corridor between the NE-trending Teniente Fault Zone and NW-orientated Codegua Fault (Garrido, 1995; Cannell et al., 2005). Its evolution was likely the result of highly energetic processes with several key stages discussed below and presented in Fig. 5.21.

**Stage 1: Pre-diatreme formation** - Before the emplacement of the causative intrusion, the withdrawal of magma from the underlying chamber, as per Cannell et al. (2005), led to the development of arcuate faults at/or near the current diatreme walls and the location of the Marginal Tourmaline Breccias. The spatial emplacement of the Braden Diatreme was controlled by pre-existing features. The Marginal Breccias were emplaced prior to the Braden Diatreme and were likely linked to a previous dacite intrusive positioned somewhere in the location of the current diatreme root zone. The presence of the less frequently mentioned Marginal Anhydrite Breccia (e.g., Floody, 2000) further suggests that the Marginal Tourmaline Breccia may once have been part of a vertically zoned breccia complex similar to the others at El Teniente.

**Stage 2: Magma fragmentation** - The cause of the fragmentation which led to the formation of the Braden Diatreme has previously been interpreted as explosive phreatomagmatism (e.g., Sillitoe, 1985; Makshev et al., 2004), based on the description of tuffaceous material and obsidian within the Braden Diatreme by Camus (1975). But, no direct and conclusive evidence for the involvement of groundwaters in the formation of the Braden Diatreme could be found during this study, which leaves open the question as to the role of phreatomagmatism.

If phreatomagmatism is assumed to be the cause, a favourable environment for this at El Teniente was created due to the highly permeable, fractured, veined and brecciated, nature of the TMC host rocks. According to experimental studies (e.g., Lorenz and Kurszlaukis, 1997; Zimanowski and Büttner, 2003 and references therein) the explosive interaction of melt with fluids is thought to not only fragment a certain amount of magma into very fine angular ash grains, but the shock waves released as a result of this are sufficient to further fragment the surrounding country rocks, largely following any pre-existing joint patterns.

The identification of vermiform juvenile dacite clasts with an almost concentric localised distribution (few cm) of molybdenite-quartz zones grading out into ever decreasing molybdenite provides evidence for explosive fragmentation of the magma, likely through explosive volatile exsolution and therefore a magmatic origin (e.g., Cashman and Scheu, 2015; White and Valentine, 2016). This may be by rapid emplacement and decompression of the underlying dacite porphyry, or brittle failure of the magma (e.g., Dürig and Zimanowski, 2012; White and Valentine, 2016), which initiated explosive devolatilisation of the underlying dacite porphyry magma, possibly initiated by faulting and/or extreme overpressures, but again no direct evidence could be found for this. This process of rapid and violent exsolution of volatiles, analogous to releasing the pressure on a fizzy bottle, caused rapid expansion of the volatiles, entrainment and brecciation of clasts and surrounding country rocks. Intense and pervasive sericite

alteration, in particular of the finer matrix material, suggests an explosive-fluidised origin and pervasive interaction with acidic hydrothermal fluids. Further complicating this, is either of these mechanisms are capable of fragmentation and entrainment of juvenile vermiform material (Lorenz and Kurszlaukis, 2007 and references therein) within a fluidised rock flour column creating wispy/vermiform textures, best preserved at greater depths and towards the margins of the Braden Diatreme.

**Stage 2a** - The intrusion of unknown quantities of dacite magma into the heavily veined and brecciated TMC host rocks (associated to previously emplaced Marginal Breccias), coupled with a large heat flux and exsolved volatiles ( $H_2O$  and  $CO_2$ ) from the underlying dacite, decompression, and the presence of unknown quantities of external fluids within the active hydrothermal system, resulted in explosive phreatomagmatic or magmatic brecciation at El Teniente. During this the lithostatic pressure was overcome initiating brecciation. In the case of a phreatomagmatic origin, depending on the volumes of interacting melt and water, the area of phreatomagmatism associated to intense/extreme fragmentation may only be between a few metres and several tens of metres (Lorenz and Kurszlaukis, 2007 and references therein). In this environment, a few hundred to a few thousand individual phreatomagmatic explosions could be expected (Lorenz and Kurszlaukis, 2007). Given the enormous size of the Braden Diatreme, it is likely that shock waves from one explosion generated new explosions in neighbouring magma-water mixtures or volatile-rich magmas creating a self-sustaining system of brecciation (e.g., Lorenz and Kurszlaukis, 2007).

**Stage 2b: Continued fracturing and increasing subsidence** - At a certain point during magma fragmentation and brecciation, a progressively larger area of intensely brecciated rock in both vertical and lateral directions, caused the overlying rocks to become increasingly unstable and collapsed downwards into the site of intense explosive brecciation. In the process this created an upwards-flaring cone of increasingly unstable rock (Fig. 5.21), as per the model of (Lorenz and Kurszlaukis, 2007). This continued to propagate upwards, utilising the pre-existing joint pattern of TMC host rocks and likely along the arcuate ring faults.

**Stage 3: Explosive eruption of the diatreme, and emplacement of juvenile dacite vermiform clasts into a fluidised rock flour column** - Formation of the Braden Diatreme was an extremely energetic and powerful, undoubtedly cataclysmic, process, given its size, and the presence of highly fragmented rock flour and the megadacite blocks described by Floody (2000) and Cannell (2004). An alternative explanation for these large blocks is that they were derived from inward collapse of wall rocks, or more likely were blasted upwards from the underlying parental intrusive.

During formation and evacuation of the Braden Diatreme, the underlying semi-solidified fragmented dacite got emplaced upwards, likely as fluidised slurries (as per Sillitoe, 1985) in a highly dynamic short-term process (e.g., Tămaş and Milési 2002). This resulted in the dispersion of commonly 2 to >10 cm long, fluidal morphologies, blebs and tongues of dacite porphyry (the vermiform clasts) throughout much of the Braden Diatreme. These are relatively uncommon in the central parts of the diatreme is probably because this region was more highly fluidised and fragmented leading to the mechanical destruction of the vermiform clasts. Fluidisation of particulate matter also caused extreme mixing and rounding of clasts of varying origins in a chaotic mélange of matrix (rock flour) and the generation of flow-like fabrics (e.g., Fig. 2.23b).

Whether the Braden Diatreme reached surface is difficult to assess given that the top ~1.5 km of the pipe has been eroded off over the last 5 Ma (Skewes and Holmgren, 1993; Stern et al., 2010). The diatreme does, however, still contain crude inward dipping bedding, which is best developed where either a large void is created, or in this case, where the system likely reached the palaeosurface.

**Stage 4: Surface features, consolidation and preservation of cavities** - During brecciation, the material was, to a limited extent, size-sorted in the fluidised column and then deposited back into the pipe. The large caverns throughout the diatreme have an enigmatic origin, and are only intercepted (often filled with water upon discovery), during mining development (Cannell, 2004). They may represent either small gas pockets (as per Floody, 2000) or self-supported areas of open-space which did not subsequently fill with rock flour. The latter is difficult to envisage given these structures range from a few to several metres “up to 300 cubic metres in volume” (Cannell, 2004), and would likely have quickly filled with fine rock flour material. Similar ‘cave-like openings are present in the diatreme at Dizon’ porphyry Cu-Au deposit, Philippines (Sillitoe, 1985), suggesting that these features may not be just restricted to the Braden Diatreme.

Less powerful brecciation activity at depth, during the waning stages of diatreme formation, likely caused the forceful injection of the Fine Sericite Braden Breccia, which cross-cuts the rock flour facies (see Fig. 4.3c; Section 4.1.2). Alternative explanations for its formation are by attrition and infilling of fractures and voids during breccia collapse and/or by ‘wash down’ of rock flour from above. The tabular, vertically extensive, shapes of the Fine Sericite Braden Breccia bodies (Floody, 2000) somewhat supports the former idea, i.e. that they were injected from depth as a result of weaker brecciation activity.

**Stage 5: Juvenile dacite clast fluid exsolution** - Cooling and solidification of vermiform dacite clasts caused localised exsolution of Mo-rich fluids into the

surrounding rock flour (few cm) and variable infill/replacement by molybdenite-quartz-anhydrite-gypsum-tourmaline ( $\pm$ sphalerite-galena). This resulted in intense precipitation of Mo-Zn $\pm$ Pb at the clast margins which decreases away from the clasts. Molybdenite shows a strong association with quartz, often intergrown.

In a similar fashion, larger volumes of fluids were exsolved from the underlying dacite magma (part 5b), focussed up fractured margins of the Braden Diatreme, which caused wider-scale overprinting of the rock flour matrix by molybdenite, chalcopyrite and a variety of other ore minerals forming the 'Braden Sulphide Breccia'. Subsequent gypsum-anhydrite-ankerite $\pm$ Cu-Mo veining (part 5c) took place and locally brecciated the clasts. Anhydrite-gypsum-ankerite-precipitation was associated with re-brecciation of the Braden Sericite and Braden Sulphide Breccias.

**Stage 6: Formation of the Braden Tourmaline Breccia** - The rock flour matrix was variably tourmaline-quartz-ankerite-anhydrite-gypsum $\pm$ chalcopyrite-altered and mineralised. Diatreme-related textures, including bedding and the vermicular clasts, were preserved. Surrounding the Braden Tourmaline Breccia is a ~10 m halo of Cu enrichment indicating that the fluids permeated outwards. The occurrence of molybdenite in the Braden Tourmaline Breccia shows a strong spatial association with the vermicular dacite clasts (e.g., Fig. 4.26). The relative timing between this unit and other fluid overprints is currently unknown.

**Stage 7: Late-stage 'Póstuma' alteration** - Precipitation of gypsum, carbonates, quartz, tennantite-tetrahedrite, sphalerite and galena throughout the Braden Diatreme caused infill of the cavities, sometimes, in larger examples, with cm- to metre-sized gypsum crystals. These are mineralogically similar to stage 5c (Fig. 5.21) gypsum-anhydrite-ankerite $\pm$ Cu-Mo veins which vein/brecciate the vermicular clasts. Weakly Cu-Mo mineralised gypsum veinlets with variable, minor tetrahedrite-tennantite also cross-cut the rock flour matrix.

**Stage 8: Emplacement of pebble dykes and continued uplift and erosion** - Pebble dykes, which consist of polymictic sericite-altered rounded to subrounded clasts set in a cement of sericite, quartz, tourmaline and variable Cu-sulphides, cross-cut the Braden Diatreme facies. They are also mapped around the diatreme perhaps associated with reactivation of concentric faults and emplaced into dilational cone sheets. They are likely to have formed by late resurgence of deep-seated magma chamber (Floody, 2000) and this implies that minor magmatic activity and fluid exsolution/brecciation continued after the main formation of the Braden Diatreme. Uplift and erosion removed a significant portion of the Braden Diatreme and ingress of meteoric water likely caused reworking, to some degree, of the mineral assemblages.

**Stage 1)**

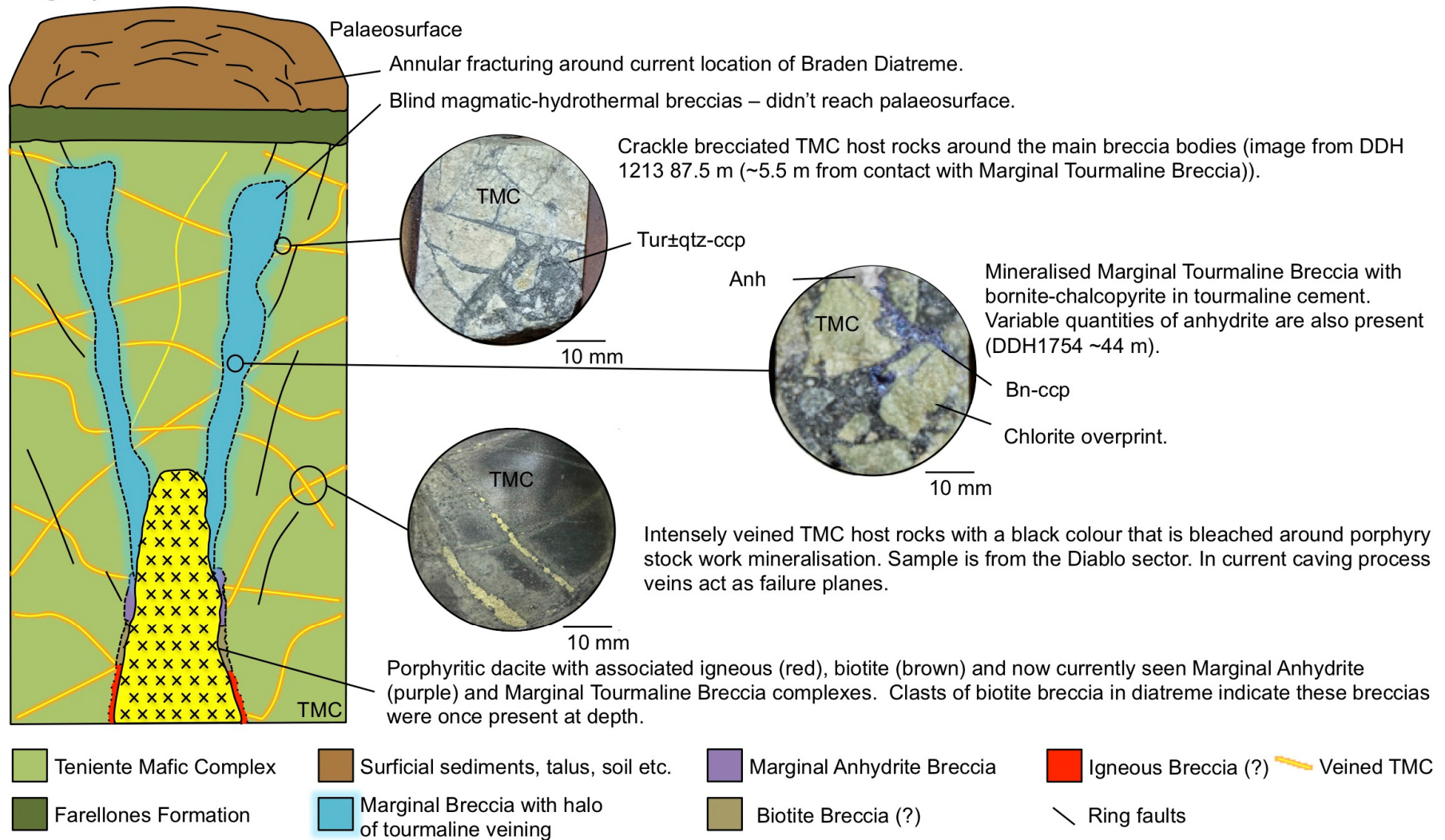
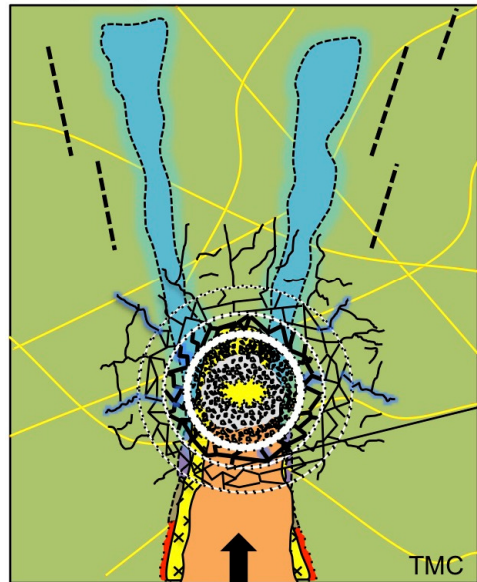


Fig. 5.21. **Stage 1)** Conditions prior to the formation of the Braden Diatreme are speculative, although it is likely that a felsic-intermediate intrusion, with associated flanking breccias (the Marginal Tourmaline Breccia), were likely emplaced along arcuate faults.

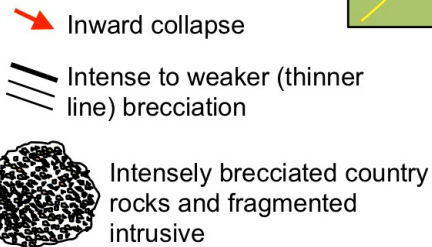
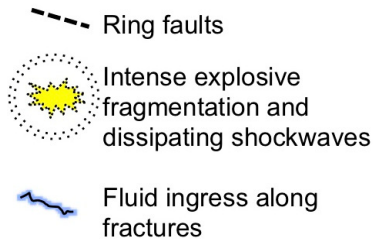
**Stage 2a)**



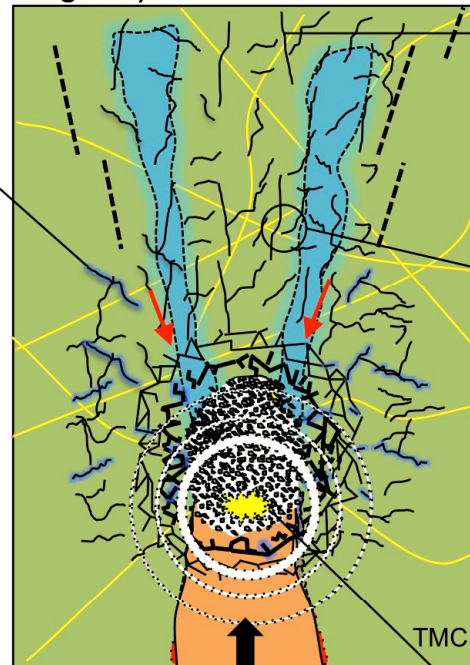
Rapid emplacement.

Increased fracturing and brecciation = increasing fluid ingress.

Parental intrusive for Braden Diatreme emplaced in similar location to earlier porphyry and associated Marginal Breccias. Interaction of melt and external fluids may have caused phreatomagmatism. Alternatively explosive fragmentation through volatile exsolution of magma took place.



**Stage 2b)**

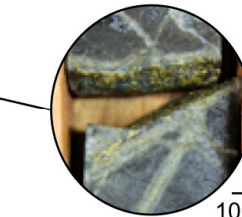


Continued input from deeper magma source.

Late dacite intrusive (presently underneath Braden Diatreme)

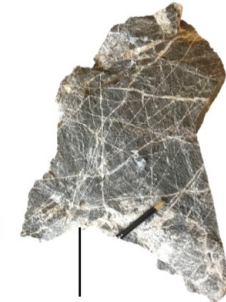
Magnified upwards fracturing.

Failure likely occurred along pre-existing planes of weakness – e.g., mineralised veins.

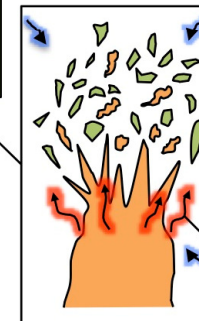


(DDH 1754~318 m).

10 mm



Intense porphyry stockwork veining in TMC. Location unknown. Pencil for scale.



Angular country rock fragments (green) and wispy-shaped juvenile dacite clasts derived from the increasingly fragmented magma (orange).

Explosive volatile exsolution (red arrows) and/or external fluid ingress (phreatomagmatism mechanism; blue arrows).

Fig. 5.21 cont. **Stage 2a)** Emplacement of dacite intrusive and either magma:water interaction initiating phreatomagmatism or explosive fluid exsolution from volatile-rich dacite. Progressive and repeated fragmentation of the magma and the surrounding country rocks continues; **2b)** Increasing fragmentation produces a progressively larger area of intensely brecciated rock in both vertical and lateral directions. The overlying rock becomes progressively unstable, fractured and likely began to collapse inwards and downwards towards the site of explosive brecciation forming a cone of subsidence. Through ongoing explosive magma fragmentation activity at depth and resultant subsidence downwards, the diatreme grows in diameter and depth.

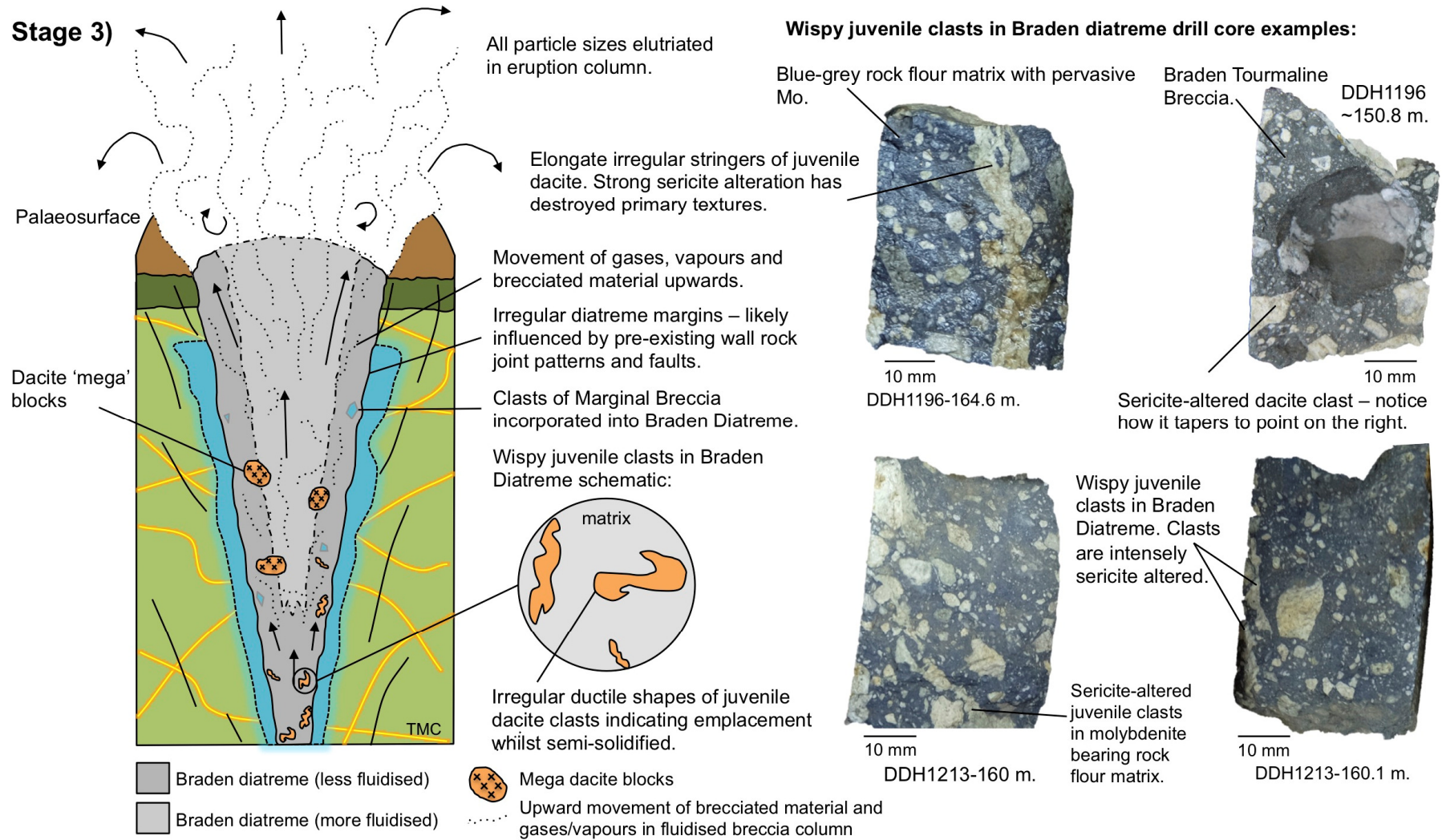
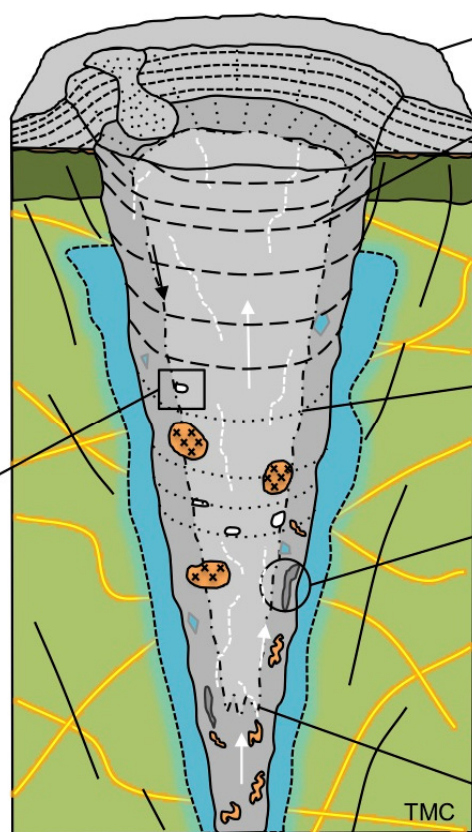
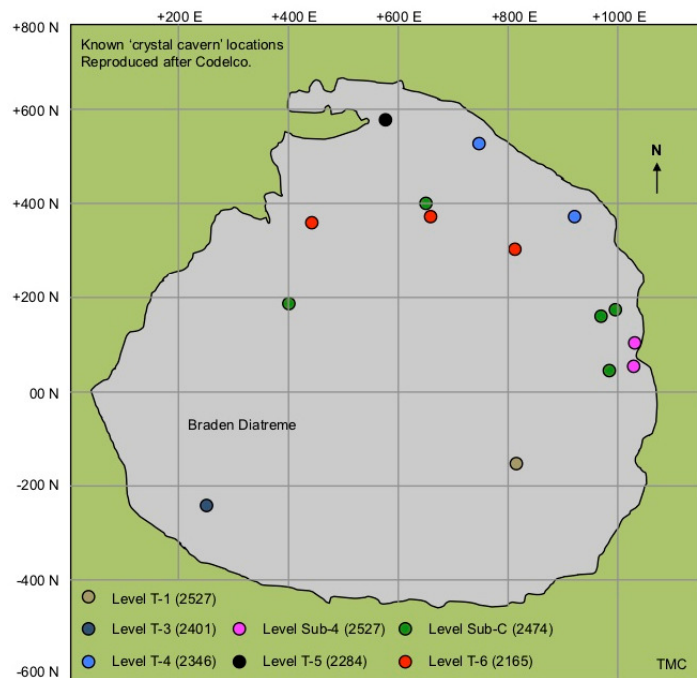


Fig. 5.21 cont. **Stage 3)** Explosive eruption of Braden Diatreme, entrainment of megadacite blocks and smaller juvenile vermiform clasts into the breccia column. The vermiform clasts are best preserved at greater depths and within a few hundred metres of the margin where the Braden Diatreme was likely less fluidised and the delicate wispy/vermiform clast textures preserved.

### Stage 4)

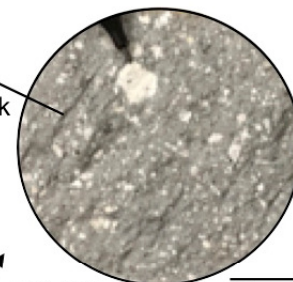
Cavities remain during consolidation and are later filled with fluids (see later stages).



Surface features such as crater and pyroclastic aprons present?

Subsidence and consolidation during waning stages. Formation of bedding/stratification.

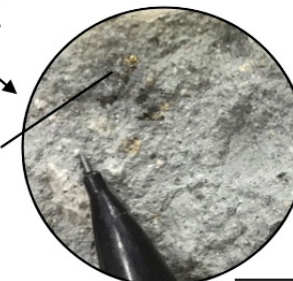
Fragmented sericite altered clasts in fine grained grey rock flour matrix.



Bedding decreases with depth.

Clast volumes in Fine Sericite Breccia vary.

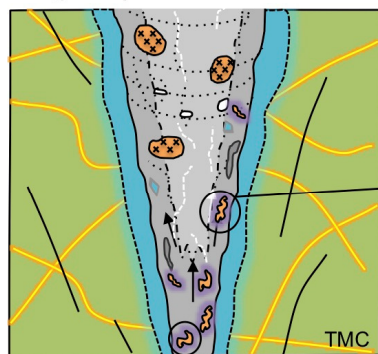
Minor chalcopyrite sometimes present.



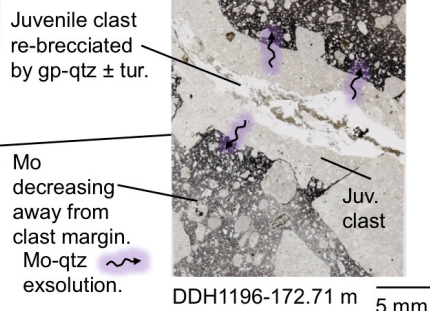
Gasses/vapour rising from depth.

Fig. 5.21 cont. **Stage 4)** During consolidation, the rock flour stratified and the 'caverns' were preserved. Volatiles and gases were likely still rising during this period. Surface features may have formed but given the level of erosion (~1.5 km since 5 Ma when the Braden Diatreme likely had a vertical extent >3.5 km; Skewes and Holmgren, 1993; Stern et al., 2010) none of these have been preserved. Injections of the Fine Sericite Braden Breccia, observed at a variety of levels within the diatreme, were likely the result of continued, but weaker explosive fragmentation at depth. Plan view map on left is reproduced after Floody (2000).

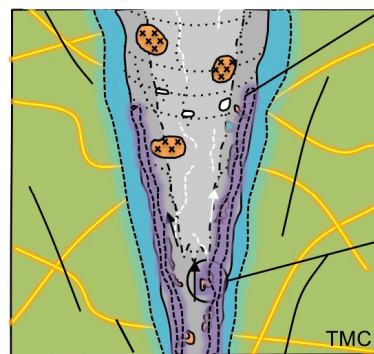
**Stage 5a)**



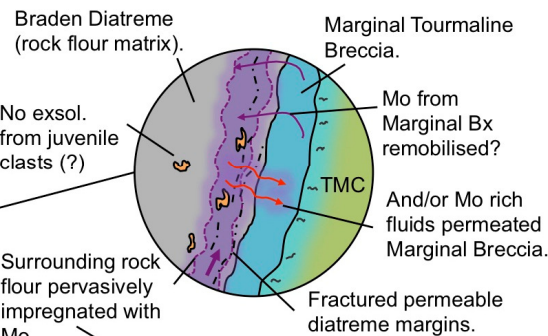
**PPL polished thin section photo (below) including juvenile clast.**



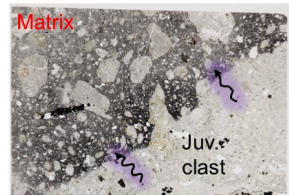
**Stage 5b)**



Mo-rich fluids from parental porphyritic dacite focused up fractured diatreme margin.

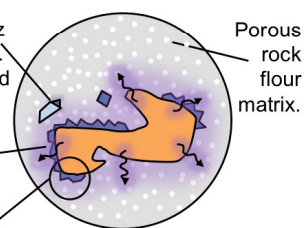


**PPL polished thin section of juvenile clast**



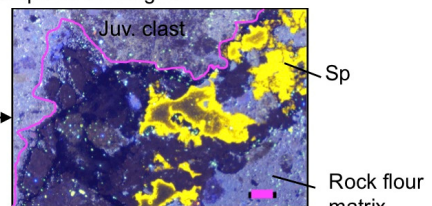
Luminescing magmatic qtz xenocrysts with non-lumin. qtz overgrowths associated to Mo.  
Intense darkening of matrix (with Mo) at clast margins.

**Juvenile clast schematic**



DDH1196-172.93 m. 5 mm

Mo halo + euhedral quartz at margins.



Darker = more intense Mo.

Intense and pervasive Mo (DDH 1196-152.7 m).

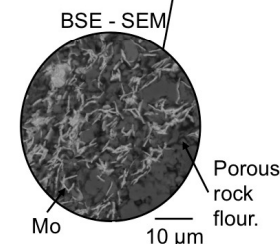
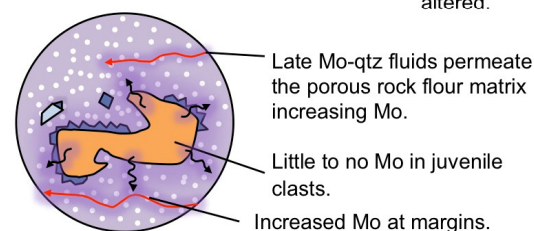


Fig. 5.21 cont. Schematics (a and b) to illustrate the exsolution of Mo-rich fluids from the vermiform clasts. The lower and upper portions of the pipe are omitted from the schematics. **Stage 5a)** Juvenile clasts exsolved Mo-Si-rich fluids shortly after eruption/formation of the diatreme causing intense mineral deposition at and close to the clast margins, decreasing away from the clasts. **Stage 5b)** Shortly after the formation of the Braden Diatreme, late-stage Mo-rich fluids were focused up the comparably more fractured diatreme margins and permeated throughout the rock flour matrix; they little affected the vermiform clasts as these had much lower permeability. In this scenario perhaps a degree of Mo was remobilised from the well-mineralised Marginal Tourmaline Breccia.

**Stage 5c)**

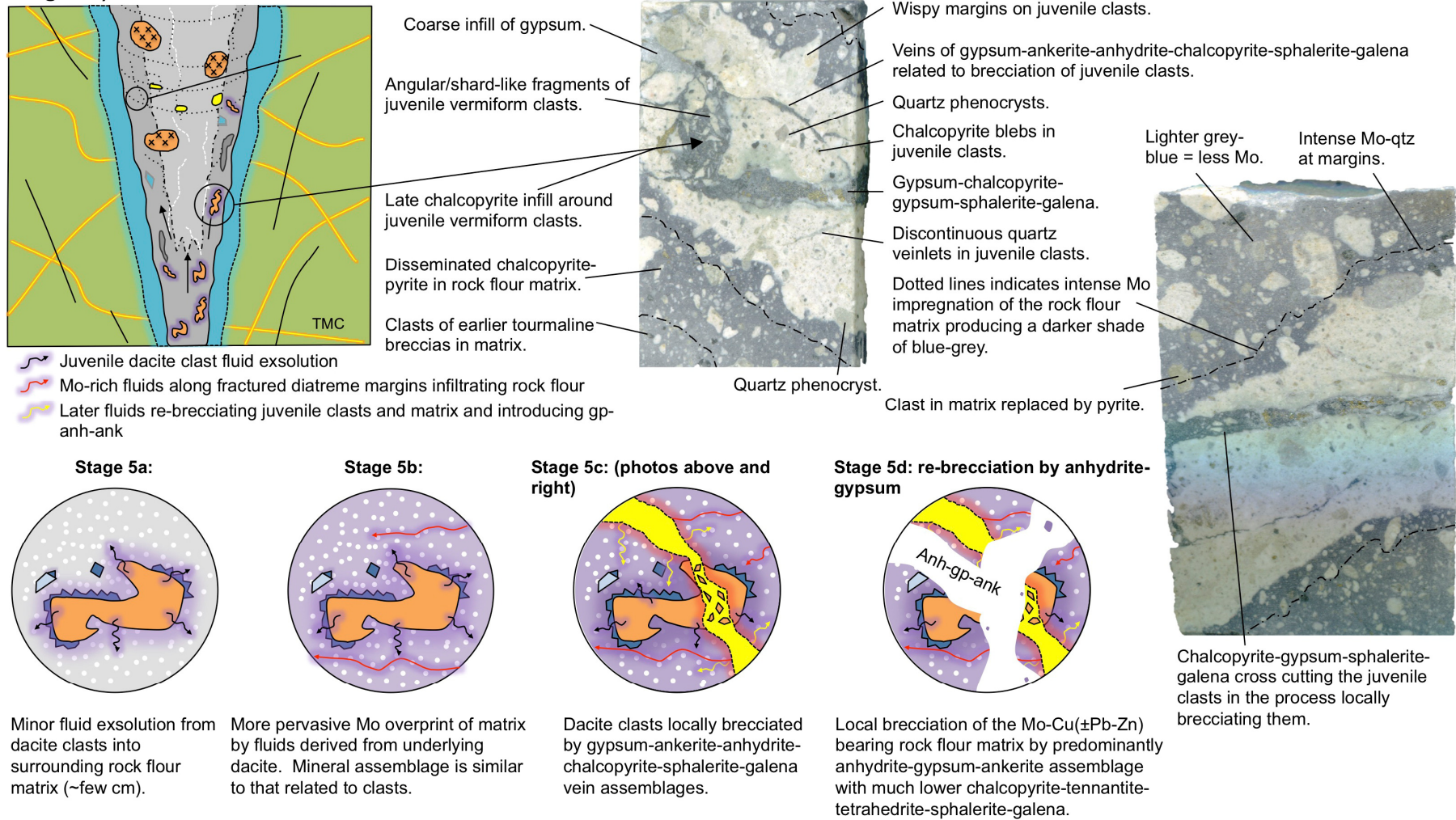


Fig. 5.21 cont. **Stage 5c)** A number of juvenile vermiform clasts were cross-cut by veins consisting of gypsum-anhydrite-chalcopyrite-sphalerite and galena which locally re-brecciated the clasts.

**Stage 6)**

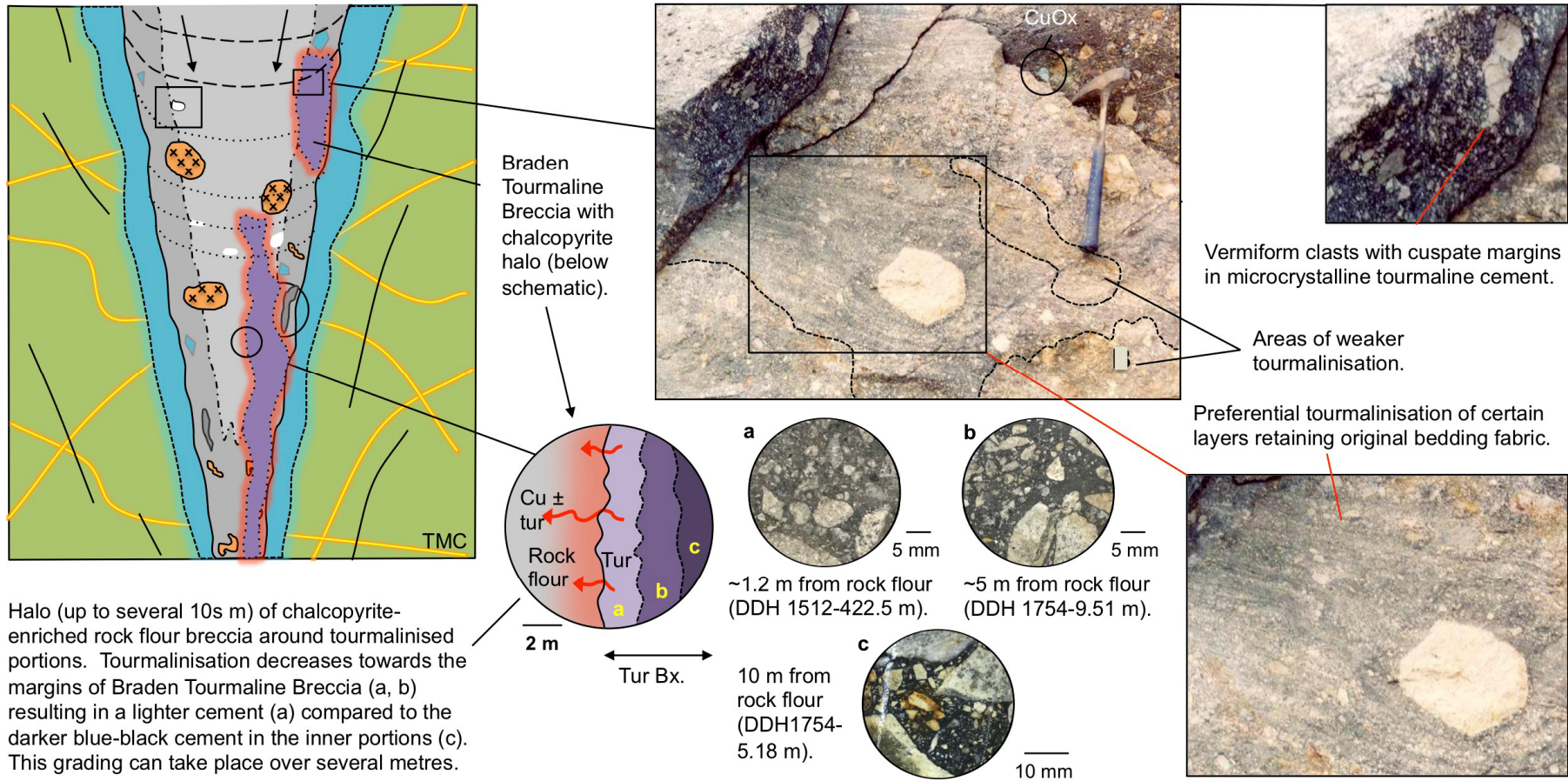
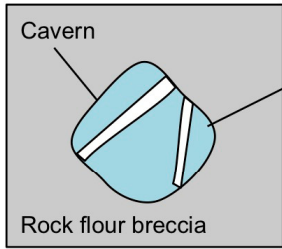


Fig. 5.21 cont. **Stage 6)** Formation of Braden Tourmaline Breccia due to ingress of magmatic, B-rich fluids, focused along pre-existing fractures, which largely replaced the rock flour matrix with dark blue-black tourmaline-quartz. Original fabrics and clast populations remain including the presence juvenile vermicular clasts. During replacement of matrix, B-rich fluids were likely contaminated to some degree.

**Stage 7)**



Large meter-sized gypsum crystals growing from the cavity walls. The walls are also lined with a coarse mixture of quartz, tetrahedrite-tennantite-sphalerite-galena.

At time of discovery caverns still contained fluids.

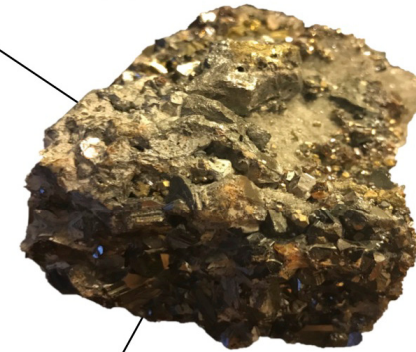
Ten-6 cavern below and to the right. Notice steel I-beam supports and author for scale in foreground. In the background are large gypsum crystals and fragments of the walls supported on wooden blocks.



Part of a gypsum crystal on public display in the Sewell Museum.



Euhedral quartz from 'Ten-6' cavern on public display in the Sewell Museum.



Tetrahedrite-tennantite-chalcopyrite growing on cavern walls.

Fig. 5.21 cont. **Stage 7)** Infill of larger cavities by coarse mixtures of gypsum-quartz-Cu-sulphides-Cu sulfosalts.

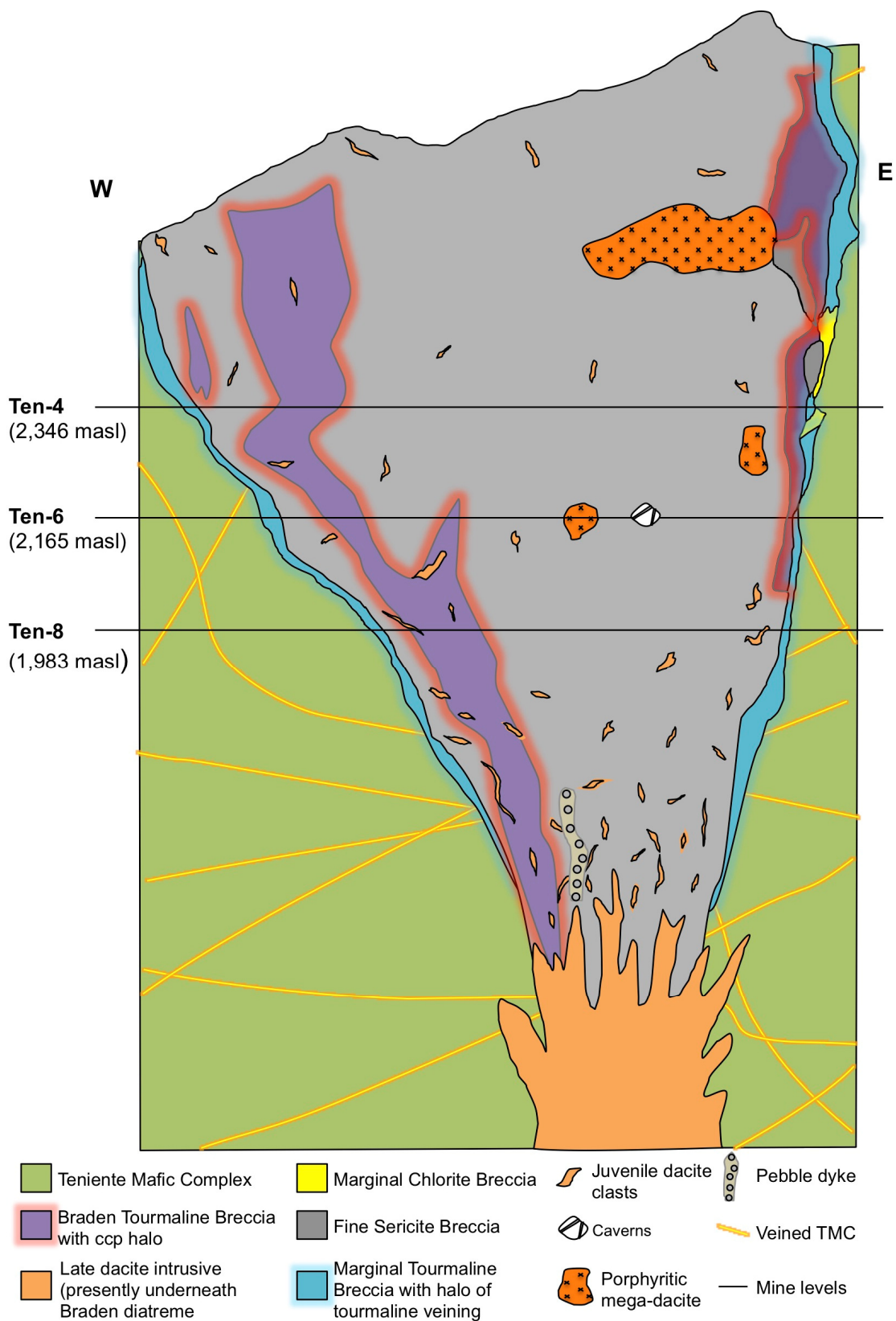


Fig. 5.21 cont. Emplacement of pebble dykes and erosion to current day level: cross section down to Ten-8 (1,983 masl) is reproduced after Floody (2000) at 00 N except the juvenile vermiform material. Beneath Ten-8 is interpretation by the author. The shallower parts of the diatreme were likely ejected into the atmosphere in an eruption column forming a crater at surface among other surficial features.

### 5.4.3 Use of diatreme facies as an exploration indicator

Although diatremes are not typically the primary focus of porphyry-breccia exploration, their use as a vector towards deeper, concealed porphyry-style mineralisation (e.g., Rottier et al., 2018), or potential to host economic ore (e.g., Cerro Maricunga gold project, Northern Chile; Lohmeier et al., 2019) is becoming increasingly recognised. This study has shown that given the large (km-scale) vertical extents of diatremes, determining relative depth in the diatreme system using textural characteristics, or specific breccia facies can be somewhat problematic and challenging.

For example, bedding in the Braden Diatreme occurs at all mapped levels extending hundreds of metres vertically, and an estimated ~1.5 km of the pipe, which also likely had bedding and a similar breccia framework, has been eroded off over the last 5 Ma (Skewes and Holmgren, 1993; Stern et al., 2010). The presence of fluid overprints like the Braden Tourmaline and Braden Sulphide Breccias can also be vertically and horizontally widespread, and it is therefore difficult to estimate the position in a vertical sense, from these breccia facies. The Braden Tourmaline Breccia for example, has been mapped at the deepest mine levels and is present on the surface, having a known vertical extent of at least several hundred metres.

A number of features may, however, indicate the relative position in a diatreme such as juvenile material, and particularly high-grade areas. If juvenile material, with vermiform morphologies is present, then it is likely that the exposure is from the deeper portion of the diatreme due to these features having poor preservation potential. How far this 'deeper' section extends vertically from the causative intrusion until the juvenile component is no longer preserved is not currently known. It likely extends for hundreds of metres though.

If localised fluid exsolution overprints containing economic sulphides are identified to be linked with juvenile vermiform material, such as in the Braden Diatreme (this study), this not only suggests magmatic fragmentation through the explosive exsolution of fluids and volatiles as an initiator for brecciation, but it importantly provides an indication that there was a fluid/volatile-rich porphyry magma at depth. This likely contained the required volatiles to form a porphyry-breccia-type system.

This study has also shown that Diatreme margins are more conducive to later, often ore-bearing fluid overprints. Therefore, any sampling and drilling should look to intersect these marginal areas at varying depths. Given the possibility of vertically continuous facies, vertical drilling is not recommended. Instead, inclined drilling should aim to cut across the pipe in order to see the pipe structure and any lateral and vertical changes in facies and any potential mineralisation.

## 6 Conclusions

A summary of key findings from this study, addressing the six hypotheses proposed in Chapter 1, are provided below.

1. The larger breccia complexes at El Teniente are vertically zoned, generally containing igneous- as well as biotite- and anhydrite-cemented breccias at depth, with tourmaline-cemented breccias more common towards shallower levels. No vertical zoning in terms of clast characteristics (e.g., rounding) were observed in the tourmaline breccias. Within these larger complexes at El Teniente, breccias show overlapping and/or transitioning cement styles and alteration for between tens of m up to 100 m. This easily leads to confusion, or mixed/inconsistent classification, particularly where the cementing phases are present in roughly equal proportions. Breccia margins, particularly lobate areas, are often sulphide-rich (e.g., Diablo Breccias), which is due to increased permeability and enhanced open-space generated during brecciation. Preservation of some of this, and/or the creation of permeability later in the paragenetic sequence, was important for enabling the ingress of Cu-Mo-rich fluids. Permeability was also created subsequently through the emplacement of later breccias or widespread dissolution of earlier paragenetic phases due to continued hydrothermal activity. This again created favourable sites for mineralisation, often in the form of very high-grade sulphide-cemented breccias.
2. Although evidence favours magmatic fragmentation, the role of phreatomagmatism (magma:water interaction) in at least the initiation of brecciation (i.e. by explosive interaction with groundwaters) in the Braden Diatreme cannot be ruled out. In comparison, the BTB originated through chemical replacement where fluids permeated and, to varying extents, replaced the porous rock flour matrix and smaller (< few mm) clasts creating a closely intergrown mixture of matrix (primarily K-feldspar, Fe-illite/illite, sericite, quartz±chlorite) and hydrothermal cement phases (tourmaline-quartz±ankerite-anhydrite-gypsum-chalcopyrite). Replacement was superimposed on previous anisotropy such as stratification/bedding. This progressive replacement produced the same characteristic grey to black tourmaline cement that is distinctive of many well-mineralised tourmaline breccias associated with porphyry deposits, e.g. the mineralised Marginal Tourmaline, Diablo and La Huifa Breccias at El Teniente. These formed from explosive brecciation initiated through volatile-rich porphyry magmas interacting with relatively cool and oxidising groundwaters (the latter supported by higher interpreted levels of Fe<sup>3+</sup> in tourmaline), which caused the rapid precipitation of an early tourmaline-quartz cement. These breccias can be distinguished texturally from the BTB.
3. That the Braden pipe was mainly produced by fragmentation due to explosive exsolution of volatiles from magma beneath the Braden Pipe, opposed to phreatomagmatism, is suggested from the presence of 1 to 5 cm juvenile vermiform dacite clasts (±Mo-Cu±Zn-Pb), sometimes containing miarolitic

cavities, in the Braden Diatreme. Their vermiform morphologies suggest entrainment as viscous bodies in an upward rising fluidised breccia column. Their limited occurrence at greater depths and along diatreme margins implies that they had poor preservation potential in the more fluidised central portions of the Breccia pipe. Surrounding the vermiform dacite clasts, in the rock flour matrix, with an almost concentric distribution (few cm), are molybdenite-quartz ( $\pm\text{Cu-Pb-Zn}$ ) mineralised zones which have gradational contacts with surrounding rocks. This shows that the clasts, and therefore the underlying parental intrusive, exsolved mineralising fluids. In addition to this, the vermiform clasts have very similar compositions to the underlying dacite intrusive and rock flour matrix. This strongly indicates that the rock flour matrix is a highly fragmented and abraded derivative of the dacite clasts, and also, therefore, the underlying dacite intrusion. Relatively resistant minerals present in the underlying dacite, vermiform clasts and rock flour matrix, such as quartz, have the same internal grain characteristics, mainly strong blue CL and Ti contents, further supporting a genetic link. The identification of fluid/volatile-rich juvenile clasts associated with Mo ( $\pm\text{Cu-Pb-Zn}$ ) may be useful in exploration as it may suggest the presence of volatile-rich magmas at depth capable of producing porphyry-breccia-type mineralisation.

4. Overall, tourmaline cannot effectively and reliably be used to discriminate between well- and poorly-endowed breccia bodies at El Teniente. All tourmalines are members of the schorl-dravite solid solution series and share similar, indistinguishable major, minor, trace and REE chemistry. The substitution mechanisms include a combination of  $(\text{Fe}^{2+}\text{Fe}^{3+})(\text{MgAl})_{-1}$ ,  $\text{NaFe}^{2+}(\square\text{Al})_{-1}$ ,  $(\text{Fe})(\text{Mg})_{-1}$  and  $(\text{Ca}(\text{Fe}, \text{Mg}))(\text{Al Na})_{-1}$ .
5. Tourmaline in the Diablo Breccias changes compositionally with depth where schorl ( $\pm\text{dravite}$  overgrowths) is prevalent at greater depths and dravite at shallower levels. The gradual decrease of Na, Ti, Fe and increase of Al upwards are interpreted as the result of progressive cooling towards surface and increasing acidity. Acidic conditions in the Diablo Breccias and other El Teniente breccias are demonstrated by the spatial correlation of intense quartz-sericite-tourmaline alteration within and around the breccias. Trends identified in previous studies (e.g., FeO vs. MgO; Dill et al., 2012) were not consistently seen in this study. This shows that any compositional trends identified in one study need to be validated across other deposit types to check consistency and repeatability.
6. Although geochemical data for tourmaline from the Diablo Breccias track a gradual vertical change in fluid composition through the breccia column, the data show significant overlap vertically. In addition, data from the breccia margins display a much wider range in elemental compositions compared with those from internal zones. Vertical trends in tourmaline composition reflect decreasing temperature and increasing acidity. The likely reason for horizontal variations is significant interaction with the Teniente Mafic Complex wall rocks

and brecciated fragments throughout the breccia column. It is therefore clear that extreme care should be taken when using tourmaline because its composition is strongly influenced by its environment of formation (temperature and pH) and proximity to wall rocks (and wall-rock composition).

## **7 Future work**

There are a number of areas of further work which may enhance the understanding of the Teniente district, and use of tourmaline as a fertility indicator.

### **7.1 La Huifa**

- The Cu-Mo-bearing Na-Ca alteration at La Huifa is particularly interesting given these alteration zones are usually sulphide and metal poor (e.g., Sillitoe, 2010). The fluids involved in Na-Ca alteration are thought to be dominated by inflowing, externally-derived non-magmatic brines, although high-temperature, oxidising, hypersaline magmatic fluids have also been implicated, particularly where these zones are mineralised (Sillitoe, 2010 and references therein). It would therefore be interesting to undertake quantitative micro-analysis (e.g., microthermometry and LA-ICP-MS or proton-induced X-ray emission) of fluid inclusions to determine compositional information, and possible sources. This should be integrated with cathodoluminescence studies to understand, in detail, paragenetic relationships to help constrain fluid evolution and ore genesis at La Huifa.

### **7.2 Tourmaline**

- A similar tourmaline study at another breccia-rich deposit, such as Río Blanco-Los Bronces, should be undertaken to check consistency and repeatability of the depth and lateral (wall-rock induced) trends seen in this study.
- An additional requirement in the development of tourmaline as an exploration indicator is the identification of a truly barren breccia (i.e. a negative control with very little Cu-Mo), i.e. which has not been mineralised and then leached, or contains Cu-Mo at depth.
- The impact of fluid:wall-rock (Teniente Mafic Complex) interaction on tourmaline chemistry should be investigated further, ideally at another deposit with different wall-rock packages.
- Mössbauer to assess the oxidation states of Fe in tourmalines from each of the breccias, and boron isotopes, to determine the sources of hydrothermal fluids and effects of fluid-wall-rock interaction.

### 7.3 Braden Diatreme

- If, as concluded herein, the Braden Diatreme formed through violent exsolution of vast quantities of volatiles from the underlying dacite magma, then this raises the question as to whether these volatiles, potentially carrying Cu and Mo, vented to atmosphere which limited mineralisation within the breccia pipe. Although difficult to prove given ~1.5 km of the Braden Diatreme has been eroded off over the last 5 Ma (Skewes and Holmgren, 1993; Stern et al., 2010), fertility signatures, such as mineral textures or chemistry (e.g., apatite cathodoluminescence, plagioclase chemistry) or whole-rock chemistry (e.g., Sr/Y, and V/Sc; Loucks, 2014) should be evaluated for the underlying parental dacite.
- Ion probe analyses should be carried out on quartz to determine low-level Ti concentrations and oxygen isotope compositions to assess fluid temperatures and possible sources and therefore the relative contributions of magmatic and 'formation' waters in the genesis of the pipe, i.e. whether formed by explosive release of exsolving fluids and/or phreatomagmatism. Oxygen isotope data may also be useful for further determining whether individual quartz clasts/crystals in the rock flour matrix were derived from the dacite intrusion, wall rocks (of various kinds) or crystallised from magmatic-hydrothermal or hydrothermal fluids.

## References

- Abrams, M.J., Brown, D., Lepley, L. and Sadowski, R., 1983. Remote sensing for porphyry copper deposits in southern Arizona. *Economic Geology*, **78**, 591-604.
- Abzalov, M.Z., 2008. Quality Control of Assay Data: A Review of Procedures for Measuring and Monitoring Precision and Accuracy. *Exploration and Mining Geology*, **17**, 131-144.
- Abzalov, M.Z., 2011. Sampling Errors and Control of Assay Data Quality in Exploration and Mining Geology. In Ivanov, O. (ed.). *Applications and Experiences of Quality Control*, 611-644.
- Allman-Ward, P., Halls, C., Rankin, A.H. and Bristow, C.M., 1982. An intrusive hydrothermal breccia body at Wheal Remfry in the western part of the St Austell granite pluton, Cornwall, England. In Evans, A.M. (ed.). *Metallization associated with acid magmatism. John Wiley and Sons Ltd, London*, 1-28.
- Almond, H. and Morris, H.T., 1951. Geochemical techniques as applied in recent investigations in the Tintic District, Utah. *Economic Geology*, **46**, 608-625.
- Annen, C., Blundy, J.D. and Sparks, R.S.J., 2006. The genesis of intermediate and silicic magmas in deep crustal hot zones. *Journal of Petrology*, **47**, 505-539.
- Astudillo, N., Roperch, P., Townley, B., Arriagada, C. and Chauvin, A., 2010. Magnetic polarity zonation within the El Teniente copper–molybdenum porphyry deposit, central Chile. *Mineralium Deposita*, **45**, 23-41.
- Atkinson, W.W. Jr., Souviron, S., Vehrs, T.I. and Faunes, A., 1996. Geology and mineral zoning of the Los Pelambres porphyry copper deposit, Chile. In Camus, F., Sillitoe, R.H. and Petersen, R. (eds.). *Andean Copper Deposits, Society of Economic Geologists Special Publication*, **5**, 131-155.
- Baker, E.M., Kirwin, D.J. and Taylor, R.G., 1986. Hydrothermal breccia pipes. *E.G.R.U. Contribution 12*, James Cook University of North Queensland, Australia, 45 p.
- Baksheev, I.A. and Kudryavtseva, O.E., 2004. Nickeloan tourmaline from the Berezovskoe gold deposit, Middle Urals, Russia. *The Canadian Mineralogist*, **42**, 1065-1078.
- Baksheev, I.A., Yu Prokof'ev, V., Zaraisky, G.P., Chitalin, A.F., Yapaskurt, V.O., Nikolaev, Y.N., Tikhomirov, P.L., Nagornaya, E.V., Rogacheva, L.I., Gorelikova, N.V. and Kononov, O.V., 2012. Tourmaline as a prospecting guide for the porphyry-style deposits. *European Journal of Mineralogy*, **24**, 957-979.
- Baksheev, I.A., Trumbull, R.B., Popov, M.P., Erokhin, Y.V., Kudryavtseva, O.E., Yapaskurt, V.O., Khiller, V.V., Vovna, G.M. and Kiselev, V.I., 2017. Chemical and boron isotopic composition of tourmaline from the Mariinsky emerald deposit, Central Urals, Russia. *Mineralium Deposita*, **53**, 565-583.
- Ballard, J.R., Palin, M.J. and Campbell, I.H., 2002. Relative oxidation states of magmas inferred from Ce (IV)/Ce (III) in zircon: application to porphyry copper deposits of northern Chile. *Contributions to Mineralogy and Petrology*, **144**, 347-364.

- Baros, M.C., 1995. El Teniente, Los Hombres del Mineral. Santiago, Grafica Andes, 500.
- Beane, R.E. and Bodnar, R.J., 1995. Hydrothermal fluids and hydrothermal alteration in porphyry copper deposits. *In* Wahl, P.W. and Bolm, J.G. (eds.). *Porphyry copper deposits of the American Cordillera: Tucson. Arizona Geological Society*, 83-93.
- Behn, G., Camus, F., Carrasco, P. and Ware, H., 2001. Aeromagnetic Signature of Porphyry Copper Systems in Northern Chile and Its Geologic Implications. *Economic Geology*, **96**, 239-248.
- Berger, B.R., King, T.V.V., Morath, L.C. and Phillips, J.D., 2003. Utility of High-Altitude Infrared Spectral Data in Mineral Exploration: Application to Northern Patagonia Mountains, Arizona. *Economic Geology*, **98**, 1003-1018.
- Berger, B.R., Ayuso, R.A., Wynn, J.C. and Seal, R.R., 2008. Preliminary model of porphyry copper deposits. *U.S. Geological Survey Open-File Report 2008-1321*.
- Bertrand, G., Guillou-Frottier, L. and Loiselet, C., 2014. Distribution of porphyry copper deposits along the western Tethyan and Andean subduction zones: Insights from a paleotectonic approach. *Ore Geology Reviews*, **60**, 174-190.
- Blundy, J.D., Mavrogenes, J.A., Tattitch, B., Sparks, R.S.J. and Gilmer, A., 2015. Generation of porphyry copper deposits by gas–brine reaction in volcanic arcs. *Nature Geoscience*, **8**, 235-240.
- Bogie, I., Lawless, J.V., Rychagov, S. and Belousov, V., 2005. Magmatic-related hydrothermal systems: classification of the types of geothermal systems and their ore mineralization. *In* Rychagov, S. (ed.). *Geothermal and Mineral Resources of Modern Volcanism Areas. Proceedings of the International Kuril-Kamchatka field workshop, July 16-August 6, 2005. Moscow: Óottiskô*, 51-73.
- Bouzari, F., Hart, C.J.R., Barker, S. and Bissig, T., 2011. Porphyry Indicator Minerals (PIMs): A new exploration tool for concealed deposits in south-central British Columbia. *Geoscience BC Report 2011-17*.
- Bouzari, F., Hart, C.J.R., Bissig, T. and Barker, S., 2016. Hydrothermal alteration revealed by apatite luminescence and chemistry: A potential indicator mineral for exploring covered porphyry copper deposits. *Economic Geology*, **111**, 1397-1410.
- Boyle, R.W., 1974. Elemental associations in mineral deposits and indicator elements of interest in geochemical prospecting (revised). *Geological Survey of Canada*, 74-75.
- Braxton, D.P., Cooke, D.R., Rye, R.O. and Petersen, E.U., 2008. Geologic and stable isotope evidence for submarine diatreme formation, and emplacement of the Boyongan and Bayugo porphyry copper-gold deposits, Philippines. *Pacrim Congress 2008, Gold Coast, Queensland, 2008, Extended Abstracts: Melbourne. Australasian Institute of Mining and Metallurgy*, 259-265.

- Braxton, D.P., Cooke, D.R., Ignacio, A. and Waters, P., 2018. Geology of the Boyongan and Bayugo Porphyry Cu-Au Deposits: An Emerging Porphyry District in Northeast Mindanao, Philippines. *Economic Geology*, **113**, 83-131.
- Brzovic, A., Beck, D. and Villaescusa, E., 2008. Rock mass disassembly during caving propagation at the El Teniente Mine Chile. In: *MassMin 2008*. [online] 1-2. Available at: [https://www.researchgate.net/publication/269932680\\_Rock\\_mass\\_disassembly\\_during\\_caving\\_propagation\\_at\\_the\\_El\\_Teniente\\_Mine\\_Chile](https://www.researchgate.net/publication/269932680_Rock_mass_disassembly_during_caving_propagation_at_the_El_Teniente_Mine_Chile) [Accessed 19 Dec. 2017].
- Burnham, C.W., 1979. Magmas and hydrothermal fluids. In Barnes, H.L. (ed.). *Geochemistry of hydrothermal ore deposits*. John Wiley and Sons Ltd, London, 71-136.
- Burnham, C.W., 1985. Energy release in subvolcanic environments: Implications for breccia formation. *Economic Geology*, **80**, 1515-1522.
- Burnham, C.W. and Ohmoto, H., 1980. Late-stage processes of felsic magmatism. *Mining Geology Special Issue*, **8**, 1-11.
- Byrne, K. and Tosdal, R.M., 2014. Genesis of the Late Triassic Southwest Zone Breccia-Hosted Alkalic Porphyry Cu-Au Deposit, Galore Creek, British Columbia, Canada. *Economic Geology*, **109**, 915-938.
- Cameron, E.M., Leybourne, M.I. and Kelley, D.L., 2005. Exploring For Deposits Under Deep Cover Using Geochemistry. *SEG Newsletter*, **63**, 9-15.
- Camus, F., 1975. Geology of the El Teniente orebody with emphasis on wall-rock alteration. *Economic Geology*, **70**, 1341-1372.
- Camus, F., 2002. The Andean Porphyry Systems. In Porter, T.M. (ed.). *Super Porphyry Copper and Gold Deposits: A Global Perspective, 1st ed.: Adelaide, PGC Publishing*, **1**, 45-63.
- Camus, F., 2003. Geología de los Systemas Porfíricos en los Andes de Chile. *Santiago, Chile, Servicio Nacional de Geología y Minería*, 267.
- Camus, F., 2005. The Andean Porphyry Systems. In Porter, T.M. (ed.). *Super Porphyry Copper and Gold Deposits: A Global Perspective, PGC Publishing Adelaide*, **1**, 45-63.
- Candela, P.A. and Holland, H.D., 1984. The partitioning of copper and molybdenum between silicate melts and aqueous fluids. *Geochimica et Cosmochimica Acta*, **48**, 373-380.
- Candela, P.A., 1989. Magmatic ore-forming fluids; thermodynamic and mass transfer calculations of metal concentrations. In Whitney, J.A. and Naldrett, A.J. (eds.). *Ore deposition associated with magmas. Reviews in Economic Geology. Society of Economic Geologists*, 203-221
- Candela, P.A., 1997. A review of shallow, ore-related granites: Textures, volatiles and ore minerals. *Journal of Petrology*, **38**, 1619-1633.
- Cannell, J.B., 2004. The El Teniente porphyry copper-molybdenum deposit, central Chile. Unpublished PhD thesis, University of Tasmania.

- Cannell, J.B., Cooke, D.R., Walshe, J.L. and Stein, H., 2005. Geology, mineralization, alteration, and structural evolution of El Teniente porphyry Cu-Mo deposit. *Economic Geology* **100**, 979-1004.
- Cannell, J.B., Cooke, D.R., Walshe, J.L. and Stein, H., 2007. Geology, mineralization, alteration and structural evolution of the El Teniente porphyry Cu-Mo deposit - a reply. *Economic Geology*, **102**, 1165-1180.
- Canil, D., Grondahl, C., Lacourse, T. and Pisiak, L.K., 2016. Trace elements in magnetite from porphyry Cu-Mo-Au deposits in British Columbia, Canada. *Ore Geology Reviews*, **72**, 1116-1128.
- Cashman, K.V. and Scheu, B., 2015. Magmatic fragmentation. In Sigurdsson, H., Houghton, B., McNutt, S.R., Rymer, H. and Stix, J. (eds.). *Encyclopedia of volcanoes*. Elsevier/Academic Press, San Diego, 459-471.
- Cashman, K.V., Sparks, R.S.J. and Blundy, J.D., 2017. Vertically extensive and unstable magmatic systems: A unified view of igneous processes. *Science*, **355**, 1-9.
- Celis, M.A., Bouzari, F., Bissig, T., Hart, C.J.R. and Ferbey, T., 2014. Petrographic characteristics of porphyry indicator minerals from alkalic porphyry copper-gold deposits in south-central British Columbia (NTS 092, 093). *Geoscience BC Summary of Activities 2013, Geoscience BC, Report 2014-1*, 53-62.
- Celis, M.A., 2015. Titanite as an indicator mineral for alkalic porphyry Cu-Au deposits in south-central British Columbia; M.Sc. thesis, University of British Columbia, Vancouver, British Columbia.
- Chang, Z., Hedenquist, J.W., White, N.C., Cooke, D.R., Roach, M., Deyell, C.L., Garcia, J., Gemmell, J.B., McKnight, S. and Cuison, A.L., 2011. Exploration Tools for Linked Porphyry and Epithermal Deposits: Example from the Mankayan Intrusion-Centered Cu-Au District, Luzon, Philippines. *Economic Geology*, **106**, 1365-1398.
- Charrier, R. and Munizaga, F., 1979. Edades K/Ar de volcanitas Cenozóicas del sector cordillerano del Río Cachapoal, Chile (34°15'S). *Revista Geológica de Chile*, **7**, 41-51.
- Charrier, R., Baeza, O., Elgueta, S., Flynn, J.J., Gans, P., Kay, S.M., Muñoz, N., Wyss, A.R. and Zurita, E., 2002. Evidence for Cenozoic extensional basin development and tectonic inversion south of the flat-slab segment, southern central Andes, Chile (33°-36°S). *Journal of South American Earth Sciences*, **15**, 117-139.
- Che, X.D., Linnen, R.L., Wang, R.C., Groat, L.A. and Brand, A.A., 2013. Distribution of trace and rare earth elements in titanite from tungsten and molybdenum deposits in Yukon and British Columbia, Canada. *The Canadian Mineralogist*, **51**, 415-438.
- Chiaradia, M., Ulianov, A., Kouzmanov, K. and Beate, B., 2012. Why large porphyry Cu deposits like high Sr/Y magmas? *Nature*, **2**, 7.
- Chiaradia, M. and Caricchi, L., 2017. Stochastic modelling of deep magmatic controls on porphyry copper deposit endowment. *Nature*, **7**, 1-11.

- CIA, 2017. The World Factbook: Chile. Available at:  
<https://www.cia.gov/library/publications/the-world-factbook/geos/ci.html>
- Clark, A.H., Farrar, E., Camus, F. and Quirt, S., 1983. K-Ar age data for the El Teniente porphyry copper deposit, Central Chile. *Economic Geology*, **78**, 1003-1006.
- Clarke, O.M., 1953. Geochemical prospecting for copper at Ray, Arizona. *Economic Geology*, **48**, 39-45.
- Clarke, D.B., Reardon, N.C., Chatterjee, A.K. and Gregoire, D.C., 1989. Tourmaline composition as a guide to mineral exploration; a reconnaissance study from Nova Scotia using discriminant function analysis. *Economic Geology*, **84**, 1921-1935.
- Cline, J.S. and Bodnar, R.J., 1991. Can economic porphyry copper mineralization be generated by a typical calc-alkaline melt? *Journal of Geophysical Research*, **96**, 8113-8126.
- Cloos, H., 1941. Bau und Tätigkeit von Tuffschloten. Untersuchungen an dem Schwäbischen Vulkan. *Geol. Rundschau*, **32**, 709-800.
- Codelco, 2013. *Resultados exploraciones 2013: Codelco descubre nuevos yacimientos de cobre en Chile*. [online] Available at:  
[https://www.codelco.com/codelco-descubre-nuevos-yacimientos-de-cobre-en-chile/prontus\\_codelco/2014-04-07/175731.html](https://www.codelco.com/codelco-descubre-nuevos-yacimientos-de-cobre-en-chile/prontus_codelco/2014-04-07/175731.html) [Accessed 31 Mar. 2017].
- Codelco, 2014. *Exploraciones*. [online] Available at:  
[https://www.codelco.com/memoria2014/site/artic/20150406/asocfile/20150406150937/memoria\\_2014\\_exploraciones.pdf](https://www.codelco.com/memoria2014/site/artic/20150406/asocfile/20150406150937/memoria_2014_exploraciones.pdf) [Accessed 31 Mar. 2017].
- Codelco, 2015. *Annual Report 2015*. [online] Available at:  
<https://www.codelco.com/memoria2015/pdf/memoria-anual/en/annualreport2015-13-explorations.pdf> [Accessed 31 Mar. 2017].
- Cooke, D.R., Hollings, P. and Walshe, J.L., 2005. Giant porphyry deposits: characteristics, distribution, and tectonic controls. *Economic Geology*, **100**, 801-818.
- Cooke, D.R., Agnew, P., Hollings, P., Baker, M., Chang, Z., Wilkinson, J.J., Ahmed, A., White, N.C., Zhang, L., Thompson, J., Gemell, J.B., Danyushevsky, L. and Chen, H., 2020. Recent advances in the application of mineral chemistry to exploration for porphyry copper–gold–molybdenum deposits: detecting the geochemical fingerprints and footprints of hypogene mineralization and alteration. *Geochemistry: Exploration, Environment, Analysis*, **20**, 176-188.
- Corbett, G.J. and Leach, T.M., 1995. S.W. Pacific Rim Au-Cu Systems: Structure, Alteration and Mineralization. Short Course No. 17, MRDU, University of British Columbia, Vancouver.
- Corbett, G.J. and Leach, T.M., 1998. Southwest Pacific gold-copper systems: Structure, alteration and mineralization. *Society of Economic Geologists, Special Publication* **6**, 238.
- Cuadra, P.C., 1986. Geochronología K-Ar del yacimiento El Teniente y áreas adyacentes. *Revista Geológica de Chile*, **27**, 3-26.

- Cuadra, P.C., 1992. Geocronología del yacimiento El Teniente y áreas adyacentes. Informe de Situación, Superintendencia de Geología, El Teniente, Codelco-Chile.
- Cunningham, C.J., Singer, D.A., Zappettini, E.O., Vivallo, W.S., Celada, C.M., Quispe, J., Briskey, J.A., Sutphin, D.M., Gajardo, M.M., Diaz, A., Portigliati, C., Berger, V.I., Carrasco, R. and Schulz, K.J., 2007. A Preliminary Quantitative Mineral Resource Assessment of Undiscovered Porphyry Copper Resources in the Andes Mountains of South America. *SEG Newsletter*, **71**, 8-13.
- Daubrée, A., 1891. Recherches expérimentales sur le rôle des gaz à hautes températures. *Soc. Géol. France Bull*, **19**, 313-354.
- Davies, A.G.S., Cooke, D.R., Gemmell, J.B., van Leeuwen, T., Cesare, P. and Hartshorn, G., 2008. Hydrothermal Breccias and Veins at the Kelian Gold Mine, Kalimantan, Indonesia: Genesis of a Large Epithermal Gold Deposit. *Economic Geology*, **103**, 717-757.
- Davis, J.D. and Guilbert, J.M., 1973. Distribution of the Radioelements Potassium, Uranium, and Thorium in Selected Porphyry Copper Deposits. *Economic Geology*, **68**, 145-160.
- Demirel, S., Göncüoğlu, M.C., Topuz, G. and Isik, V., 2009. Geology and chemical variations in tourmaline from the quartz-tourmaline breccias within the Kerkenez granite- monzonite massif, Central Anatolian Crystalline Complex, Turkey. *The Canadian Mineralogist*, **47**, 787-799.
- Dill, H.G., Garrido, M.M., Melcher, F., Gomez, M.C. and Luna, L.I., 2012. Depth-related variation of tourmaline in the breccia pipe of the San Jorge porphyry copper deposit, Mendoza, Argentina. *Ore Geology Reviews*, **48**, 271-277.
- Driesner, T. and Heinrich, C.A., 2019. Revised model of porphyry-Cu formation: ore forms at the porphyry to epithermal transition, overprinting barren stockwork veining and potassic alteration. Proceedings of the 15<sup>th</sup> SGA Biennial Meeting, 27-30 August 2019, Glasgow, Scotland, 955-958.
- Drummond, S.E. and Ohmoto, H., 1985. Chemical evolution and mineral deposition in boiling hydrothermal systems. *Economic Geology*, **80**, 126-147.
- Duchoslav, M., Marks, M.A.W., Drost, K., McCammon, C., Marschall, H.R., Wenzel, T. and Markl, G., 2017. Changes in tourmaline composition during magmatic and hydrothermal processes leading to tin-ore deposition: The Cornubian Batholith, SW England. *Ore Geology Reviews*, **83**, 215-234.
- Dürrig, T. and Zimanowski, B., 2012. "Breaking news" on the formation of volcanic ash: Fracture dynamics in silicate glass. *Earth and Planetary Science Letters*, **335-336**, 1-8.
- Edmonds, M., 2008. New geochemical insights into volcanic degassing. *Philosophical Transactions of the Royal Society A. Mathematical, Physical and Engineering Sciences*, **366**, 4559-4579.
- Encinas, A., Makshev, V., Pinto, L., Le Roux, J., Munizaga, F. and Zentilli, M., 2006. Pliocene lahar deposits in the Coastal Cordillera of central Chile: Implications

- for uplift, avalanche deposits, and porphyry copper systems in the Main Andean Cordillera. *Journal of South American Earth Sciences*, **20**, 369-381.
- Ernst, W., 2000. *Earth systems*. 1st ed. Cambridge: Cambridge University Press.
- Farías, M., Charrier, R., Carretier, S., Martinod, J., Fock, A., Campbell, D., Cáceres, J. and Comte, D., 2008. Late Miocene high and rapid surface uplift and its erosional response in the Andes of central Chile (33°-35°S). *Tectonics*, **27**, 1-22.
- Farmin, R., 1934. "Pebble dikes" and associated mineralization at Tintic, Utah. *Economic Geology*, **29**, 356-370.
- Fletcher, C.J.N., 1977. The geology, mineralization, and alteration of Ilkwang Mine, Republic of Korea; a Cu-W-bearing tourmaline breccia pipe. *Economic Geology*, **72**, 753-768.
- Fletcher, W.K., 1981. Analytical methods in geochemical prospecting. *Elsevier, Amsterdam*, 255.
- Floody, R. and Huete, C., 1998. Potencial Distrito Teniente, Superintendencia de Geología, El Teniente, CODELCO-Chile.
- Floody, R., 2000. Estudio de vulnerabilidad geológica-geotécnica de la chimenea de Brecha Braden: Internal report, Superintendencia de Geología, El Teniente, Codelco.
- Floody, R., 2017. *Superintendencia de Geología, El Teniente, Codelco División El Teniente, Rancagua, Chile*.
- Fournier, R.O., 1999. Hydrothermal processes related to movement of fluid from plastic into brittle rock in the magmatic-epithermal environment. *Economic Geology*, **94**, 1193-1211.
- Frelinger, S.N., Ledvina, M.D., Kyle, J.R. and Zhao, D., 2015. Scanning electron microscopy cathodoluminescence of quartz: Principles, techniques and applications in ore geology. *Ore Geology Reviews*, **65**, 840-852.
- Frikken, P.H., 2004. Breccia-hosted copper-molybdenum mineralisation at Río Blanco, Chile. PhD thesis. University of Tasmania. Available at: <http://eprints.utas.edu.au/17677/>.
- Frikken, P.H., Cooke, D.R., Walshe, J.L., Archibald, D., Skarmeta, J., Serrano, L. and Vargas, R., 2005. Mineralogical and Isotopic Zonation in the Sur-Sur Tourmaline Breccia, Río Blanco-Los Bronces Cu-Mo Deposit, Chile: Implications for Ore Genesis. *Economic Geology*, **100**, 935-961.
- Galbraith, C.G., Clarke, D.B., Trumbull, R.B. and Wiedenbeck, M., 2009. Assessment of tourmaline compositions as an indicator of emerald mineralization at the Tsada Glisza Prospect, Yukon Territory, Canada. *Economic Geology*, **104**, 713-731.
- Gandhi, S.M. and Sarkar, B.C., 2016. *Essentials of Mineral Exploration and Evaluation*. 1<sup>st</sup> ed. Elsevier, 2016, 165-170.

- Garrido, I., Riveros, M., Cladouhos, T., Espiñeira, D. and Allmendinger, R., 1994. Modelo geológico-estructural, yacimiento El Teniente. *Actas del VIII Congreso Geológico Chileno Concepción*, **2**, 1553-1558.
- Garrido, I., 1995. Geología estructural del distrito & la mina El Teniente & situación geodinámica regional. Proyecto Geodinámico Mina El Teniente, Proyecto API-1-1689. Reporte interno, **1**, 61. Superintendencia de Geología, Codelco-Chile, División El Teniente.
- Garrido, I., Cembrano, J., Siña, A., Stedman, P. and Yañez, G., 2002. High magma oxidation state and bulk crustal shortening: key factors in the genesis of Andean porphyry copper deposits, central Chile (31-34°S). *Revista Geológica de Chile*, **29**, 43-54.
- Gates, O., 1959. Breccia pipes in the Shoshone Range, Nevada. *Economic Geology*, **54**, 790-815.
- Gilmour, P., 1977. Mineralized intrusive breccias as guides to concealed porphyry copper systems. *Economic Geology*, **72**, 290-298.
- Gil-Rodríguez, J., 2010. Igneous petrology of the Colosa gold-rich porphyry system (Tolima, Colombia). Professional Master of Science. University of Arizona.
- Goerne, G.V., Franz, G. and Heinrich, W., 2001. Synthesis of tourmaline solid solutions in the system Na<sub>2</sub>O–MgO–Al<sub>2</sub>O<sub>3</sub>–SiO<sub>2</sub>–B<sub>2</sub>O<sub>3</sub>–H<sub>2</sub>O–HCl and the distribution of Na between tourmaline and fluid at 300 to 700°C and 200 MPa. *Contributions to Mineralogy and Petrology*, **141**, 160-173.
- Goodall, W.R. and Scales, P.J., 2007. An overview of the advantages and disadvantages of the determination of gold mineralogy by automated mineralogy. *Minerals Engineering*, **20**, 506-517.
- Godoy, E., Yañez, G. and Vera, E., 1999. Inversion of an Oligocene volcano-tectonic basin and uplifting of its superimposed Miocene magmatic arc in the Chilean central Andes: first seismic and gravity evidences. *Tectonophysics*, **306**, 217-236.
- Google Earth., 2020. Available at: [https://www.google.co.uk/intl/en\\_uk/earth/](https://www.google.co.uk/intl/en_uk/earth/)
- Gottlieb, P., Wilkie, G., Sutherland, D., Ho-tun, E., Suthers, S., Perera, K., Jenkins, B., Spencer, S., Butcher, A. and Rayner, J., 2000. Using Quantitative Electron Microscopy for Process Mineralogy Applications. *Minerals Metals & Materials Society, Warrendale PA USA*, **52**, 24-25.
- Grant, J.A., 1986. The isocon diagram; a simple solution to Gresens' equation for metasomatic alteration. *Economic Geology*, **81**, 1976-1982.
- Grant, J.A., 2005. Isocon analysis: A brief review of the method and applications. *Physics and Chemistry of the Earth*, **30**, 997-1004.
- Gresens, R.L., 1967. Composition-volume relationships of metasomatism. *Chemical Geology*, **2**, 47-65.
- Gustafson, L.B. and Hunt, J.P., 1975. The porphyry copper deposit at El Salvador, Chile. *Economic Geology*, **70**, 857-912.

- Gustafson, L.B. and Quiroga, G.J., 1995. Patterns of mineralization and alteration below the porphyry copper orebody at El Salvador, Chile. *Economic Geology*, **90**, 2-16.
- Halls, C., 1994. Energy and mechanism in the magmato-hydrothermal evolution of the Cornubian Batholith: A review. In Seltmann, R., Möller, P. and Kämpf, H. (eds.). Metallogeny of collisional orogens. *Czech Geological Survey Prague*, 275-294.
- Harrison, R.L., Maryono, A., Norris, M.S., Rohrlach, B.D., Cooke, D.R., Thompson, J.M., Creaser, R.A. and Thiede, D.S., 2018. Geochronology of the Tumpangpitu Porphyry Au-Cu-Mo and High-Sulfidation Epithermal Au-Ag-Cu Deposit: Evidence for Pre- and Postmineralization Diatremes in the Tujuh Bukit District, Southeast Java, Indonesia. *Economic Geology*, **113**, 163-192.
- Harlaux, M., Mercadier, J., Marignac, C., Villeneuve, J., Mouthier, B. and Cuney, M., 2019. Origin of the atypical Puy-les-Vignes W breccia pipe (Massif Central, France) constrained by trace element and boron isotopic composition of tourmaline. *Ore Geology Reviews*, **114**, 103-132.
- Harlaux, M., Kouzmanov, K., Gialli, S., Laurent, O., Rielli, A., Dini, A., Chauvet, A., Menzies, A., Kalinaj, M. and Fontboté, L., 2020. Tourmaline as a Tracer of Late-Magmatic to Hydrothermal Fluid Evolution: The World-Class San Rafael Tin (-Copper) Deposit, Peru. *Economic Geology*. doi:10.5382/econgeo.4762; 33 p.
- Hattori, K.H. and Keith, J.D., 2001. Contribution of mafic melt to porphyry copper mineralization: evidence from Mount Pinatubo, Philippines, and Bingham Canyon, Utah, USA. *Mineralium Deposita*, **36**, 799-806.
- Hattori, K.H., Wang, J., Baumgartner, R., Kobylinski, C.H., Morfin, S. and Shen, P., 2017. Zircon composition: indicator of fertile igneous rocks related to porphyry copper deposits; 14th Society for Geology Applied to Mineral Deposits Biennial meeting 2017, Québec, **1**, 295-298.
- Hawthorne, F.C., 1996. Structural mechanisms for light-element variations in tourmaline. *The Canadian Mineralogist*, **34**, 123-132.
- Hawthorne, F.C. and Henry, D.J., 1999. Classification of the minerals of the tourmaline group. *European Journal of Mineralogy*, **11**, 201-216.
- Hawthorne, F.C. and Dirlam, D.M., 2011. Tourmaline the indicator mineral: from atomic arrangement to Viking navigation. *Elements*, **7**, 307-312.
- Hedenquist, J.W. and Lowenstern, J.B., 1994. The role of magmas in the formation of hydrothermal ore deposits. *Nature Geoscience*, **370**, 519-527.
- Heinrich, C.A., Günther, D., Audétat, A., Ulrich, T. and Frischknecht, R., 1999. Metal fractionation between magmatic brine and vapor, determined by microanalysis of fluid inclusions. *Geology*, **27**, 755-758.
- Heinrich, C.A., Driesner, T., Stefánsson, A. and Seward, T.M., 2004. Magmatic vapor contraction and the transport of gold from the porphyry environment to epithermal ore deposits. *Geology*, **32**, 761-764.

- Heinrich, C.A., 2005. The physical and chemical evolution of low-salinity magmatic fluids at the porphyry to epithermal transition: a thermodynamic study. *Mineralium Deposita*, **39**, 864-889.
- Henley, R.W., King, P.L., Wykes, J.L., Renggli, C.J., Brink, F.J., Clark, D.A. and Troitzsch, U., 2015. Porphyry copper deposit formation by sub-volcanic sulphur dioxide flux and chemisorption. *Nature Geoscience*, **8**, 210-215.
- Henry, D.J. and Guidotti, C.V., 1985. Tourmaline as a petrogenetic indicator mineral: an example from the staurolite-grade metapelites of NW Maine. *American mineralogist*, **70**, 1-15.
- Henry, D.J. and Dutrow, B.L., 1996. Metamorphic tourmaline and its petrogenetic applications. In Anovitz, L.M. and Grew, E.S. (eds.). Boron: Mineralogy, Petrology and Geochemistry, **33**, 503-557. *Reviews in Mineralogy, Mineralogical Society of America, Washington, D.C.*
- Hickson, C.J. and Juras, S.J., 1986. Sample contamination by grinding. *The Canadian Mineralogist*, **24**, 585-589.
- Hollings, P., Cooke, D.R. and Clark, A., 2005. Regional geochemistry of Tertiary igneous rocks in central Chile: Implications for the geodynamic environment of giant porphyry copper and epithermal gold mineralization. *Economic Geology*, **100**, 887-904.
- Holtzman, R., Szulczewski, M.L. and Juanes, R., 2012. Capillary fracturing in granular media. *Physical Review Letters*, **108**.
- Howell, F.H. and Molloy, J.S., 1960. Geology of the Braden orebody, Chile, South America. *Economic Geology*, **55**, 863-905.
- Huang, R. and Audétat, A., 2012. The titanium-in-quartz (TitaniQ) thermobarometer: A critical examination and re-calibration. *Geochimica et Cosmochimica Acta*, **84**, 75-89.
- Hustrulid, W.A. and Bullock, R.L., 2001. Underground mining methods: Engineering Fundamentals and International Case Studies. 1st ed. Littleton, Colorado. *Society for Mining, Metallurgy, and Exploration*.
- Irarrazaval, V., Sillitoe, R.H., Wilson, A.J., Toro, J.C., Robles, W. and Lyall, G.D., 2010. Discovery History of a Giant, High-Grade, Hypogene Porphyry Copper-Molybdenum Deposit at Los Sulfatos, Los Bronces-Río Blanco District, Central Chile. *Society of Economic Geologists Special Publication*, **1**, 253-269.
- Ishihara, S., 1981. The granitoid series and mineralization. *Economic Geology 75<sup>th</sup> Anniversary Volume*, 458-484.
- Iveson, A.A., Webster, J.D., Rowe, M.C. and Neill, O.K., 2019. Fluid-melt trace-element partitioning behaviour between evolved melts and aqueous fluids: Experimental constraints on the magmatic-hydrothermal transport of metals. *Chemical Geology*, **516**, 18-41.
- Jébrak, M., 1997. Hydrothermal breccias in vein-type ore deposits; a review of mechanisms, morphology and size distribution. *Ore Geology Reviews*, **12**, 111-134.

- Jébrak, M., 2010. Use of breccias in IOCG(U) exploration. Geol. Assoc. Canada Short Course Notes, **20**, 79-87.
- Jiang, S.-Y., Han, F., Shen, J.-Z. and Palmer, M.R., 1999. Chemical and Rb-Sr, Sm-Nd isotopic systematics of tourmaline from the Dachang Sn-polymetallic ore deposit, Guangxi Province, P.R. China. *Chemical Geology*, **157**, 49-67.
- Jiang, S.-Y., Palmer, M.R. and Yeats, C.J., 2002. Chemical and boron isotope compositions of tourmaline from the Archean Big Bell and Mount Gibson gold deposit, Murchison Province, Yilgarn Craton, Western Australia. *Chemical Geology*, **188**, 229-247.
- Jiang, S.-Y., Yu, J.-M. and Lu, J.-J., 2004. Trace and rare-earth element geochemistry in tourmaline and cassiterite from the Yunlog tin deposit, Yunnan, China: implication for migmatite-hydrothermal fluid evolution and ore genesis. *Chemical Geology*, **209**, 193-213.
- Jochum, K.P., Weis, U., Schwager, B., Stoll, B., Wilson, S.A., Haug, G.H., Andreae, M.O. and Enzweiler, J., 2016. Reference Values Following ISO Guidelines for Frequently Requested Rock Reference Materials. *Geostandards and Geoanalytical Research*, **40**, 333-350.
- Johnson, T.W. and Thompson, T.B., 2006. Breccia- and Carbonate-Hosted Au-Cu-Ag Replacement Mineralization Associated with the Homestake Porphyry Intrusive Complex, New World District, Montana. *Economic Geology*, **101**, 955-980.
- Johnston, W.P. and Lowell, J.D., 1961. Geology and origin of mineralized breccia pipes in Copper Basin, Arizona. *Economic Geology*, **56**, 916-940.
- Kalliomäki, H., Wagner, T., Fusswinkel, T. and Sakellaris, G., 2017. Major and trace element geochemistry of tourmalines from Archean orogenic gold deposits: Proxies for the origin of gold mineralizing fluids? *Ore Geology Reviews*, **91**, 906-927.
- Kay, S.M. and Kurtz, A.C., 1995. Magmatic and tectonic characterization of the El Teniente region: Internal report, *Superintendencia de Geología, El Teniente, Codelco-Chile*, 180.
- Kay, S.M., Mpodozis, C. and Coira, B., 1999. Neogene magmatism, tectonism, and mineral deposits of the central Andes (22° to 33° latitude). In Skinner, B. (ed.). *Geology and ore deposits of the central Andes. Society of Economic Geologists Special Publication*, **7**, 27-59.
- Kelley, D.L., Benn, C., Brock Riedell, K. and Johnson, T., 2009. The Role of Geochemistry in Andean Copper Discoveries. *Society of Economic Geologists, Special Publication*, **15**, 271-281.
- Kents, P., 1961. Brief outline of a possible origin of copper porphyry breccias. *Economic Geology*, **56**, 1465-1469.
- Kents, P., 1964. Special breccias associated with hydrothermal developments in the Andes. *Economic Geology*, **59**, 1551-1563.
- Kerrich, R., Goldfarb, R., Groves, D. and Garwin, S., 2000. The geodynamics of world-class gold deposits: characteristics, space-time distribution, and origins. In

- Hagemann, S.G. and Brown, P.E. (eds.). *Gold in 2000. Reviews in Economic Geology, Society of Economic Geologists*, **13**, 501-551.
- King, R.W., Rabbia, O.M. and French, D.H., 2000. Tourmaline from Andean porphyry copper deposits: its significance in the exploration of Andean mineralization. Conference paper: *Canadian Society of Exploration Geophysicists*.
- King, R.W., Rabbia, O.M., Hernandez, L.B. and Lopez-Escobar, L., 2003. Tourmaline and tourmaline breccia pipes from the supergiant porphyry copper deposits of the El Teniente belt, central Chile. *10° Congreso Geológico Chileno. Special symposium on supergiant Andean Porphyry Copper Deposits*.
- Klemm, L.M., 2006. Cu-Mo-Au ratios in Porphyry-type Ore Deposits: Constraints from Fluid Inclusion Microanalysis. Unpublished PhD thesis, ETH Zurich.
- Klemm, L.M., Pettke, T., Heinrich, C.A. and Campos, E., 2007. Hydrothermal evolution of the El Teniente deposit, Chile: Porphyry Cu-Mo ore deposition from low-salinity magmatic fluids. *Economic Geology*, **102**, 1021-1045.
- Klemme, S., Marschall, H.R., Jacob, D.E., Prowatke, S. and Ludwig, T., 2011. Trace-element partitioning and boron isotope fractionation between white mica and tourmaline. *The Canadian Mineralogist*, **49**, 165-176.
- Kobylnski, C.H., Hatori, K., Smith, S. and Plouffe, A., 2016. Report on the composition and assemblage of minerals associated with the porphyry Cu-Mo mineralization at the Gibraltar deposit, south central British Columbia, Canada. *Geological Survey of Canada*, Open File 8025, 30 p.
- Koeppen, R.P. and Godoy, E., 1994. Volcanic geology of the El Teniente study area, Chile: Internal report, SERNAGEOMIN, Superintendencia de Geología, El Teniente, Codelco-Chile.
- Kronz, A., Van den Kerkhof, A.M. and Müller, A., 2012. Analysis of Low Element Concentrations in Quartz by Electron Microprobe. In Götze J. and Möckel R. (eds). *Quartz: Deposits, Mineralogy and Analytics. Springer Geology. Springer, Berlin, Heidelberg*, **1**, 191-217.
- Kurtz, A.C., Kay, S.M., Charrier, R. and Farrar, E., 1997. Geochronology of Miocene plutons and exhumation history of the El Teniente region, Central Chile (34-35° S). *Revista Geológica de Chile*, **16**, 145-162.
- KPMG, 2014. Chile: Country mining guide. Available at: <https://assets.kpmg.com/content/dam/kpmg/pdf/2014/03/chile-mining-guide.pdf>
- Landes, K.K., 1945. The Mackinac Breccia. *Michigan Geological Survey*, **44**, 123-153.
- Landtwing, M.R., Dillenbeck, E.D., Leake, M.H. and Heinrich, C.A., 2002. Evolution of the Breccia-Hosted Porphyry Cu-Mo-Au Deposit at Agua Rica, Argentina: Progressive Unroofing of a Magmatic Hydrothermal System. *Economic Geology*, **97**, 1273-1292.
- Landtwing, M.R. and Pettke, T., 2005. Relationships between SEM-cathodoluminescence response and trace-element composition of hydrothermal vein quartz. *American Mineralogist*, **90**, 122-131.

- Laznicka, P., 1988. Breccias and Coarse Fragmentites. Petrology, Environments, Associations, Ores. *Elsevier Science Ltd.*
- Lee, C.-T., Luffi, P., Chin, E.J., Bouchet, R., Dasgupta, R., Morton, D.M., Le Roux, V.L., Yin, Q.-Z. and Jin, D., 2012. Copper Systematics in Arc Magmas and Implications for Crust-Mantle Differentiation. *Science*, **336**, 64-68.
- Lee, R.G., Dilles, J.H., Tosdal, R.M., Wooden, J.L. and Mazdab, F.K., 2017. Magmatic evolution of granodiorite intrusions at the El Salvador porphyry copper deposit, Chile, based on trace element composition and U/Pb age of zircons. *Economic Geology*, **112**, 245-273.
- Lefebvre, N. and White, J.D., 2013. Dissolution-replacement textures in Hopi Buttes diatreme deposits indicate that primary deposits had a fine-ash matrix. *American Geophysical Union*. [online] Available at: <https://ui.adsabs.harvard.edu/abs/2013AGUFM.V41D2832L/abstract> [Accessed 3 Feb. 2020].
- Lindgren, W. and Bastin, E.S., 1922. The Geology of the Braden Mine, Rancagua, Chile. *Economic Geology*, **17**, 75-99.
- Llambias, E.J. and Malvicini, L., 1969. The geology and genesis of the Bi-Cu mineralized breccia-pipe, San Francisco de los Andes, San Juan, Argentina. *Economic Geology*, **64**, 271-286.
- Lohmeier, S., Schneider, A., Belyatsky, B. and Lehmann, B., 2019. Magmatic evolution of the Cerro Maricunga gold porphyry-epithermal system, Maricunga belt, N-Chile. *Journal of South American Earth Sciences*, **92**, 374-399.
- London, D. and Manning, D.A.C., 1995. Chemical variation and significance of tourmaline from southwest England. *Economic Geology*, **90**, 495-519.
- Longerich, H.P., Jackson, S.E. and Günther, D., 1996. Inter-laboratory note. Laser ablation inductively coupled plasma mass spectrometric transient signal data acquisition and analyte concentration calculation. *Journal of Analytical Atomic Spectrometry*, **11**, 899-904.
- Longwell, C.R., 1951. Megabreccia developed downslope from large faults. *American Journal of Science*, **249**, 343-355.
- López-Moro, F.J., 2012. EASYGRESGRANT-A Microsoft Excel spreadsheet to quantify volume changes and to perform mass-balance modeling in metasomatic systems. *Computers and Geosciences*, **39**, 191-196.
- Lorenz, V., 1975. Formation of phreatomagmatic maar- diatreme volcanoes and its relevance to kimberlite diatremes. *Physics and Chemistry of the Earth*, **9**, 17-27.
- Lorenz, V., 1986. On the growth of maars and diatremes and its relevance to the formation of tuff rings. *Bulletin of Volcanology*, **48**, 265-274.
- Lorenz, V. and Kurszlaukis S., 2007. Root zone processes in the phreatomagmatic pipe emplacement model and consequences for the evolution of maar-diatreme volcanoes. *Volcanology and Geothermal Research*, **159**, 4-32.

- Loucks, R.R., 2014. Distinctive composition of copper-ore-forming arc magmas. *Australian Journal of Earth Sciences*, **61**, 5-16.
- Lovering, T.S., Sokoloff, V.P. and Morris, H.T., 1948. Heavy metals in altered rock over blind ore bodies, East Tintic District, Utah. *Economic Geology*, **43**, 384-399.
- Lovering, T.S., Huff, L.C. and Almond, H., 1950. Dispersion of copper from the San Manuel copper deposit, Pinal County, Arizona. *Economic Geology*, **45**, 493-514.
- Lowell, J.D. and Guilbert, J.M., 1970. Lateral and vertical alteration-mineralization zoning in porphyry copper deposits. *Economic Geology*, **65**, 363-408.
- Maksaev, V., Munizaga, F., McWilliams, M., Fanning, C.M., Mathur, R., Ruiz, J. and Thiele, K., 2002. El Teniente porphyry copper deposit in the Chilean Andes: new geochronological timeframe and duration of hydrothermal activity - abstract: *GSA, 2002, Denver, USA*.
- Maksaev, V., Munizaga, F., McWilliams, M., Fanning, C.M., Mathur, R., Ruiz, J. and Zentilli, M., 2004. New Chronology for El Teniente, Chilean Andes, from U-Pb,  $^{40}\text{Ar}/^{39}\text{Ar}$ , Re-Os, and Fission-Track dating: Implications for the Evolution of a Supergiant Porphyry Cu-Mo Deposit. *Special Publication of the Society of Economic Geologists*, **11**, 15-54.
- Mao, M., Rukhlov, A.S., Rowins, S.M., Spence, J. and Coogan, L.A., 2016. Apatite Trace Element Compositions: A Robust New Tool for Mineral Exploration. *Economic Geology*, **111**, 1187-1222.
- Marks, M.A.W., Marschall, H.R., Schühle, P., Guth, A., Wenzel, T., Jacob, D.E., Barth, M. and Markl, G., 2013. Trace element systematics of tourmaline in pegmatitic and hydrothermal systems from the Variscan Schwarzwald (Germany): The importance of major element composition, sector zoning, and fluid or melt composition. *Chemical Geology*, **344**, 73-90.
- Marschall, H.R. and Jiang, S.-Y., 2011. Tourmaline Isotopes: No Element Left Behind. *Elements*, **7**, 313-319.
- Mathieu, L., 2018. Quantifying Hydrothermal Alteration: A Review of Methods. *Geosciences*, **8**.
- Mârza, I., Tămaş, C.G. and Ghergari, L., 1997. Low sulfidation epithermal gold deposit from Roşia Montană, Metaliferi Mountains, Romania. *St. Cerc. Geol.*, **42**, 3-12.
- Maughan, D., Keith, J., Christiansen, E., Pulsipher, T., Hattori, K. and Evans, N., 2002. Contributions from mafic alkaline magmas to the Bingham porphyry Cu-Au-Mo deposit, Utah, USA. *Mineralium Deposita*, **37**, 14-37.
- McCallum, M.E., 1985. Experimental evidence for fluidization processes in breccia pipe formation. *Economic Geology*, **80**, 1523-1543.
- McClenaghan, M.B., McDonald, A., Leybourne, M.I., Beckett- Brown, C., Chapman, J.B., Layton-Matthews, D., Lougheed, H.D., Plouffe, A. and Ferbey, T., 2017. Controls on the fertility of porphyry mineralizing systems recorded in indicator minerals. In Rogers, N. (ed.). Targeted Geoscience Initiative-2016 Report of Activities. *Geological Survey of Canada*, Open File 8199, 87-89.

- McClenaghan, M.B., Beckett-Brown, C.E., McCurdy, M.W., McDonald, A.M., Leybourne, M.I., Chapman, J.B., Plouffe, A. and Ferbey, T., 2018. Mineral markers of porphyry copper mineralization: Progress report on the evaluation of tourmaline as an indicator mineral. In Rogers, N. (ed.). Targeted Geoscience Initiative: 2017 Report of Activities, *Geological Survey of Canada*, Open File 8358, 69-77.
- McCuaig, T.C. and Hronsky, J., 2014. The Mineral System Concept: The Key to Exploration Targeting. *Society of Economic Geology, Special Publication*, **18**, 153-176.
- Meyer, C., 1965. An early potassic type of wall rock alteration at Butte, Montana. *American Mineralogist*, **50**, 1717-1722.
- Mining Technology., 2013. *The 10 biggest copper mines in the world*. [online] Available at: <http://www.mining-technology.com/features/feature-the-10-biggest-copper-mines-in-the-world/> [Accessed 27 Apr. 2017].
- Mining Technology., 2015. *El Teniente New Mine Level Project*. [online] Available at: <http://www.mining-technology.com/projects/el-teniente-new-mine-level-project/> [Accessed 20 Feb. 2017].
- Mills, J.W., 1972. Origin of Copper-Bearing Breccia Pipes. *Economic Geology*, **67**, 533-535.
- Mitcham, T.W., 1974. Origin of breccia pipes. *Economic Geology*, **69**, 412-413.
- Moreno, T. and Gibbons, W., 2007. The Geology Of Chile. *Geological Society of London*.
- Morgan, G.B. and London, D., 1989. Experimental reactions of amphibolite with boron-bearing aqueous fluids at 200 MPa: Implications for tourmaline stability and partial melting in mafic rocks. *Contributions to Mineralogy and Petrology*, **102**, 281-297.
- Moxham, R.M., Foote, R.S. and Bunker, C.M., 1965. Gamma-ray spectrometer studies of hydrothermally altered rocks. *Economic Geology*, **60**, 653-671.
- Müller, A., Lennox, P.G. and Trzebski, R., 2002. Cathodoluminescence and microstructural evidence for crystallisation and deformation processes of granites in the Eastern Lachlan Fold Belt (SE Australia). *Contributions to Mineralogy and Petrology*, **143**, 510-524.
- Müller, A., Williamson, B.J. and Smith, M.P., 2005. Origin of quartz cores in tourmaline from Roche Rock, SW England. *Mineralogical Magazine*, **69**, 381-401.
- Müller, A., van den Kerkhof, A.M., Behr, H., Kronz, A. and Koch-Müller, M., 2009. The evolution of late-Hercynian granites and rhyolites documented by quartz – a review. *Earth and Environmental Science Transactions of the Royal Society of Edinburgh*, **100**, 185-204.
- Müller, A., Herrington, R.J., Armstrong, R., Seltmann, R., Kirwin, D.J., Stenina, N.G. and Kronz, A., 2010. Trace elements and cathodoluminescence of quartz in stockwork veins of Mongolian porphyry-style deposits. *Mineralium Deposita*, **45**, 707-727.

- Mungall, J.E., Brenan, J.M., Godel, B., Barnes, S.J. and Gaillard, F., 2015. Transport of metals and sulphur in magmas by flotation of sulphide melt on vapour bubbles. *Nature Geoscience*, **8**, 216-219.
- Muñoz, M., Charrier, R., Fanning, C.M., MaksaeV, V. and Deckart, K., 2012. Zircon trace element and O-Hf isotope analyses of mineralized intrusions from El Teniente ore deposit, Chilean Andes: Constraints on the Source and magmatic evolution of porphyry Cu-Mo related magmas. *Journal of Petrology*, **53**, 1091-1122.
- Ni, P., Pan, J.Y., Wang, G.G., Chi, Z., Qin, H., Ding, J.Y. and Chen, H., 2017. A CO<sub>2</sub>-rich porphyry ore-forming fluid system constrained from a combined cathodoluminescence imaging and fluid inclusion studies of quartz veins from the Tongcun Mo deposit, South China. *Ore Geology Reviews*, **81**, 856-870.
- Norton, D.L. and Cathles, L.M., 1973. Breccia Pipes, Products of Exsolved Vapor from Magmas. *Economic Geology*, **68**, 540-546.
- O'Neill, H.S.C. and Eggins, S.M., 2002. The effect of melt composition on trace element partitioning: an experimental investigation of the activity coefficients of FeO, NiO, CoO, MoO<sub>2</sub> and MoO<sub>3</sub> in silicate melts. *Chemical Geology*, **186**, 151-181.
- Oppenheimer, J., Rust, A.C., Cashman, K.V. and Sandnes, B., 2015. Gas migration regimes and outgassing in particle-rich suspensions. *Frontiers in Physics*, **3**, 60.
- Ossandón, G.C., Fréaut, R.C., Gustafson, L.B., Lindsay, D.D. and Zentilli, M., 2001. Geology of the Chuquicamata mine: A progress report. *Economic Geology*, **96**, 249-270.
- Oyarzun, R., Márquez, A., Lillo, J., López, I. and Rivera, S., 2001. Giant versus small porphyry copper deposits of Cenozoic age in northern Chile: adakitic versus normal calc-alkaline magmatism. *Mineralium Deposita*, **36**, 794-798.
- Páez, G.N., Permuy Vidal, C., Galina, M., López, L., Jovic, S.M. and Guido, D.M., 2018. Intrusive hyaloclastite and peperitic breccias associated to sill and cryptodome emplacement on an Early Paleocene polymagmatic compound cone-dome volcanic complex from El Guanaco mine, Northern Chile. *Journal of Volcanology and Geothermal Research*, **354**, 153-170.
- Pal, D.C., Trumbull, R.B. and Wiedenbeck, M., 2010. Chemical and boron isotope compositions of tourmaline from the Jaduguda U (-Cu-Fe) deposit, Singhbhum shear zone, India: Implications for the sources and evolution of mineralizing fluids. *Chemical Geology*, **277**, 245-260.
- Parada, M.A., López-Escobar, L., Oliveros, V., Fuentes, F., Morata, D., Calderón, M., Aguirre, L., Féraud, G., Espinoza, F., Moreno, H., Figueroa, O., Muñoz Bravo, J., Vásquez, R. and Stern, C.R., 2007. In Moreno, T. and Gibbons, W. (eds.). *The Geology of Chile: Andean Magmatism*, 115-146. *Geological Society of London*.
- Pardo, R., 2015. *Discovery and geology of La Huifa porphyry Cu-Mo deposit, VI Región, Chile*. From Servicio Nacional de Geología y Minería. [online]

Available at:

[http://biblioteca.sernageomin.cl/opac/DataFiles/14905\\_v2\\_pp\\_368.pdf](http://biblioteca.sernageomin.cl/opac/DataFiles/14905_v2_pp_368.pdf)

[Accessed 19 Feb. 2017].

- Pardo, R. and Villarroel, P., no date. Geología y Potencial de Exploración del Distrito El Teniente. Andes Centrales, VI Región del Libertador Bernardo O`Higgins, Chile. From Servicio Nacional de Geología y Minería. [online] Available at [https://biblioteca.sernageomin.cl/opac/DataFiles/14127\\_pp\\_10\\_12.pdf](https://biblioteca.sernageomin.cl/opac/DataFiles/14127_pp_10_12.pdf)
- Parry, W.T., Jasumback, M. and Wilson, P.N., 2002. Clay mineralogy of phyllic and intermediate argillic alteration at Bingham, Utah. *Economic Geology*, **97**, 221-239.
- Paton, C., Hellstrom, J., Paul, B., Woodhead, J. and Hergt, J., 2011. Lolite: Freeware for the visualisation and processing of mass spectrometric data. *Journal of Analytical Atomic Spectrometry*, **26**.
- Penniston-Dorland, S.C., 2001. Illumination of vein quartz textures in a porphyry copper ore deposit using scanned cathodoluminescence: Grasberg Igneous Complex, Irian Jaya, Indonesia. *American Mineralogist*, **86**, 652-666.
- Perelló, J., Sillitoe, R.H., Mpodozis, C., Brockway, H. and Posso, H., 2012. Geologic setting and evolution of the porphyry copper-molybdenum and copper-gold deposits at Los Pelambres, central Chile. *Society of Economic Geologists Special Publication*, **16**, 79-104.
- Perry, V.D., 1961. The significance of mineralized breccia pipes: *Mining Engineering*, **13**, 367-376.
- Pichavant, M., 1981. An experimental study of the effect of boron on a water saturated haplogranite at 1 kbar vapour pressure. *Contributions to Mineralogy and Petrology*, **76**, 430-439, <https://doi.org/10.1007/BF00371485>.
- Pichavant, M., 1987. Effects of B and H<sub>2</sub>O on Liquidus Phase Relations in the Haplogranite System at 1 kbar. *American Mineralogist*, **72**, 1056-1070, <https://doi.org/10.1177/039219218403212602>.
- Piquer, J., Berry, R.F., Scott, R.J. and Cooke, D.R., 2016. Arc-oblique fault systems: their role in the Cenozoic structural evolution and metallogensis of the Andes of central Chile. *Journal of Structural Geology*, **89**, 101-117.
- Piquer, J., Hollings, P., Rivera, O., Cooke, D.R., Baker, M. and Testa, F., 2017. Along-strike segmentation of the Abanico Basin, central Chile: New chronological, geochemical and structural constraints. *Lithos*, **268-271**, 174-197.
- Piquer, J., 2017. Assistant Professor at Universidad Austral de Chile, formerly Exploration greenfield and brownfield exploration geologist at EMSA.
- Piquer, J., Yanez, G., Rivera, O. and Cooke, D.R., 2019. Long-lived crustal damage zones associated with fault intersections in the high Andes of Central Chile. *Andean Geology*, **46**, 223-239.
- Pirajno, F. and Smithies, R.H., 1992. The FeO/(FeO+MgO) ratio of tourmaline: A useful indicator of spatial variations in granite-related hydrothermal mineral deposits. *Journal of Geochemical Exploration*, **42**, 371-381.

- Pirrie, D., Butcher, A.R., Power, M.R., Gottlieb, P. and Miller, G.L., 2004. Rapid quantitative mineral and phase analysis using automated scanning electron microscopy (QemSCAN); potential applications in forensic geoscience. *In* Pye, K. and Croft, D.J. (eds.). *Forensic Geoscience: Principles, Techniques and Applications. Geological Society, London, Special Publications*, **232**, 123-136.
- Pirrie, D. and Rollinson, G.K., 2011. Unlocking the applications of automated mineral analysis. *Geology Today*, **27**, 235-244.
- Pisiak, L.K., Canil, D., Lacourse, T., Plouffe, A. and Ferbey, T., 2017. Magnetite as an indicator mineral in the exploration of porphyry deposits: A case study in till near the Mount Polley Cu-Au deposit, British Columbia, Canada. *Economic Geology*, **112**, 919-940.
- Pizarro, H., Campos, E., Bouzari, F., Rouse, S., Bissig, T., Gregoire, M. and Riquelme, R., in press. Porphyry Indicator Zircons (PIZs): Application to exploration of Porphyry Copper Deposits. *Ore Geology Reviews*.
- Pokrovski, G.S., Borisova, A.Y. and Harrichoury, J-C., 2008. The effect of sulfur on vapour-liquid fractionation of metals in hydrothermal systems. *Earth and Planetary Science Letters*, **266**, 345-362.
- Pollard, P.J. and Taylor, R.G., 2002. Paragenesis of the Grasberg Cu-Au deposit, Irian Jaya, Indonesia: results from logging section 13. *Mineralium Deposita*, **37**, 117-136.
- Porter, J.P., Schroeder, K. and Austin, G., 2012. Geology of the Bingham Canyon Porphyry Cu-Mo-Au Deposit, Utah. *Society of Economic Geologists*, **16**, 127-146.
- Potts, P.J., Webb, P.C. and Thompson, M., 2015. Bias in the Determination of Zr, Y and Rare Earth Element Concentrations in Selected Silicate Rocks by ICP-MS when Using Some Routine Acid Dissolution Procedures: Evidence from the GeoPTProficiency Testing Programme. *Geostandards and Geoanalytical Research*, **39**, 315-327.
- Power, G.M., 1968. Chemical variation in tourmalines from south-west England. *Mineralogical Magazine*, **36**, 1078-1089.
- Qiao, X., Li, W., Zhang, L., White, N.C., Zhang, F. and Yao, Z., 2019. Chemical and boron isotope compositions of tourmaline in the Hadamiao porphyry gold deposit, Inner Mongolia, China. *Chemical Geology*, **519**, 39-55.
- Quirt, G.S., 1972. A potassium-argon geochronological investigation of the Andean mobile belt of north-central Chile. Unpublished Ph.D. thesis, Kingston, Queen's University. Canada.
- Rabbia, O.M., Hernández, L.B., French, D.H., King, R.W. and Ayers, J.C., 2009. The El Teniente porphyry Cu-Mo deposit from a hydrothermal rutile perspective. *Mineralium Deposita*, **44**, 849-866.
- Ramseyer, K., Baumann, J., Matter, A. and Mullis, J., 1988. Cathodoluminescence Colours of  $\alpha$ -Quartz. *Mineralogical Magazine*, **52**, 669-677.
- Redmond, P.B., Landtwing, M.R. and Einaudi, M.T., 2001. Cycles of porphyry dike emplacement, veining, alteration and mineralization in the Bingham porphyry

- Cu-Au-Mo deposit, Utah. In Piestrzynski, A. et al., (eds.). Mineral deposits at the beginning of the 21st century: Joint Biennial SGA-SEG Meeting, 6th, Kraków, Poland, 2001, Proceedings, 473-476.
- Redmond, P.B., Einaudi, M.T., Inan, E.E., Landtwing, M.R. and Heinrich, C.A., 2004. Copper deposition by fluid cooling in intrusion-centered systems: New insights from the Bingham porphyry ore deposits, Utah. *Geology*, **32**, 217-220.
- Reich, M., Parada, M.A., Palacios, C., Dietrich, A., Schultz, F. and Lehmann, B., 2003. Adakite-like signature of Late Miocene intrusions at the Los Pelambres giant porphyry copper deposit in the Andes of central Chile: metallogenic implications. *Mineralium Deposita*, **38**, 876-885.
- Richards, J.P., 2000. Lineaments Revisited. *SEG Newsletter*, **42**, 14-19.
- Richards, J.P. and Tosdal, R.M., 2001. Structural controls on ore genesis. 1st ed. Littleton, Colorado. *Society of Economic Geologists*.
- Richards, J.P., 2003. Tectono-magmatic precursors for porphyry Cu-(Mo-Au) deposit formation. *Economic Geology*, **98**, 1515-1533.
- Richards, J.P. and Kerrich, R., 2007. Special paper: adakite-like rocks: their diverse origins and questionable role in metallogenesis. *Economic Geology*, **102**, 537-576.
- Richards, J.P., 2011a. Magmatic to hydrothermal metal fluxes in convergent and collided margins. *Ore Geology Reviews*, **40**, 1-26.
- Richards, J.P., 2011b. High Sr/Y arc magmas and porphyry Cu±Mo±Au deposits: just add water. *Economic Geology*, **106**, 1075-1081.
- Richards, J.P., 2013. Giant ore deposits formed by optimal alignments and combinations of geological processes. *Nature Geoscience*, **6**, 911-916.
- Richards, J.P., 2016. Economic geology: Clues to hidden copper deposits. *Nature Geoscience*, **9**, 195-196.
- Rinne, M.L., Cooke, D.R., Harris, A.C., Finn, D.J., Allen, C.M., Heizler, M.T. and Creaser, R.A., 2018. Geology and Geochronology of the Golpu Porphyry and Wafi Epithermal Deposit, Morobe Province, Papua New Guinea. *Economic Geology*, **113**, 271-294.
- Rivano, S., Godoy, E., Vergara, M. and Villaroel, R., 1990. Redefinición de la Formación Farellones en la Cordillera de los Andes de Chile central (32°-34°S). *Revista Geológica de Chile*, **17**, 205-214.
- Rivera, O. and Falcón, M.F., 1998. Estudio Geológico distrital de la división El Teniente de Codelco-Chile, Escala 1:25 000: Internal report to Vicepresidencia de Exploraciones y Asociaciones Mineras, Codelco-Chile.
- Rollinson, G.K., Andersen, J.C.Ø., Stickland, R.J., Boni, M. and Fairhurst, R., 2011. Characterisation of non-sulphide zinc deposits using QEMSCAN®. *Minerals Engineering*, **24**, 778-787.
- Rollinson, G.K., 2018. QEMSCAN® Specialist and Facility Manager, CIMF, Camborne School of Mines, University of Exeter, Cornwall.  
<http://emps.exeter.ac.uk/csm/staff/gkr201>

- Ross, P-S., Jébrak, M. and Walker, B.M., 2002. Discharge of Hydrothermal Fluids from a Magma Chamber and Concomitant Formation of a Stratified Breccia Zone at the Questa Porphyry Molybdenum Deposit, New Mexico. *Economic Geology*, **97**, 1679-1699.
- Ross, P-S., Carrasco Núñez, G. and Hayman, P., 2017. Felsic maar-diatreme volcanoes: a review. *Bulletin of Volcanology*, **79**.
- Rosenbaum, G., Giles, D., Saxon, M., Betts, P.G., Weinberg, R.F. and Duboz, C., 2005. Subduction of the Nazca Ridge and the Inca Plateau: Insights into the Formation of ore deposits in Peru. *Earth and Planetary Science Letters*, **239**, 18-22.
- Rottier, B., Kouzmanov, K., Casanova, V., Bouvier, A.-B., Baumgartner, L.P., Wälle, M. and Fontboté, L., 2018. Mineralized breccia clasts: a window into hidden porphyry-type mineralization underlying the epithermal polymetallic deposit of Cerro de Pasco (Peru). *Mineralium Deposita*, **53**, 919-946.
- Rukhlov, A.S., Plouffe, A., Ferbey, T., Mao, M. and Spence, J., 2016. Application of trace-element compositions of detrital apatite to explore for porphyry deposits in central British Columbia. In Geological Fieldwork 2015, British Columbia Ministry of Energy and Mines, British Columbia Geological Survey, Paper 2016-1, 145-179.
- Rusk, B.G. and Reed, M.H., 2002. Scanning electron microscope–cathodoluminescence analysis of quartz reveals complex growth histories in veins from the Butte porphyry copper deposit, Montana. *Geology*, **30**, 727-730.
- Rusk, B.G., Reed, M.H., Dilles, J.H. and Kent, A.J., 2006. Intensity of quartz cathodoluminescence and trace-element content in quartz from the porphyry copper deposit at Butte, Montana. *American Mineralogist*, **91**, 1300-1312.
- Rusk, B.G., Koenig, A. and Lowers, H., 2011. Visualizing trace element distribution in quartz using cathodoluminescence, electron microprobe, and laser ablation-inductively coupled plasma-mass spectrometry. *American Mineralogist*, **96**, 703-708.
- Rusk, B.G., 2012. Cathodoluminescent textures and trace elements in hydrothermal quartz. In Götze, J. and Möckel, R. (eds.). *Quartz: Deposits, Mineralogy and Analytics* (307-329). Berlin, Heidelberg: Springer-Verlag.
- Sawkins, F.J., 1969. Chemical brecciation, an unrecognized mechanism for breccia formation? *Economic Geology*, **64**, 613-617.
- Schatz, O.J., Dolejš, D., Stix, J., Williams-Jones, A.E. and Layne, G.D., 2004. Partitioning of boron among melt, brine and vapor in the system haplogranite–H<sub>2</sub>O–NaCl at 800°C and 100MPa. *Chemical Geology*, **210**, 135-147.
- Scott, P.W. and Rollinson, G.K., 2016. Crushed rock aggregates: their mineralogy and textures using automated scanning electron microscopy. In Hunger, E. and Brown, T.J. (eds.). *Proceedings of the 18th Extractive Industry Geology Conference 2014 and technical meeting 2015, EIG Conferences Ltd*, 49-68.

- Seedorff, E., Dilles, J.H., Proffett, Jr., J.M., Einaudi, M.T., Zurcher, L., Stavast, W.J.A., Johnson, D.A. and Barton, M.D., 2005. Porphyry deposits-characteristics and origin of hypogene features. *Society of Economic Geologists, Economic Geology 100<sup>th</sup> Anniversary Volume*, 251-298.
- Seguel, J., 2017. Geologo Especialista, *Codelco División El Teniente, Rancagua, Chile*.
- Serrano, L., Vargas, R., Stambuk, V., Aguilar, C., Galeb, M., Holmgren, C., Contreras, A., Godoy, S., Vela, I., Skewes, A.M. and Stern, C.R., 1996. The late Miocene to early Pliocene Río Blanco-Los Bronces copper deposit, central Chilean Andes. In Camus, F., Sillitoe, R.H. and Petersen, R. (eds.). *Andean Copper Deposits, Society of Economic Geologist Special Publication*, **5**, 120-129.
- SGL-I-123/03., 2003. Estándares & Metodologías de Trabajo para Geología de Minas Actualización Año 2003. Superintendencia Geología, División El Teniente, Codelco- Chile. Alto Colón, Chile.
- Sillitoe, R.H., 1973. The tops and bottoms of porphyry copper deposits. *Economic Geology*, **68**, 799-815.
- Sillitoe, R.H. and Sawkins, F.J., 1971. Geologic, mineralogic and fluid inclusion studies relating to the origin of copper-bearing tourmaline breccia pipes, Chile. *Economic Geology*, **66**, 1028-1041.
- Sillitoe, R.H., Baker, E.M. and Brook, W.A., 1984. Gold deposits and hydrothermal eruption breccias associated with a maar volcano at Wau, Papua New Guinea. *Economic Geology*, **79**, 638-655.
- Sillitoe, R.H., Grauberg, G.L. and Elliot, J.E., 1985. A diatreme-hosted gold deposit at Montana Tunnels, Montana. *Economic Geology*, **80**, 1707-1721.
- Sillitoe, R.H., 1985. Ore-Related Breccias In Volcanoplutonic Arcs. *Economic Geology*, **80**, 1467-1514.
- Sillitoe, R.H., 1997. Characteristics and Controls of the Largest Porphyry Copper-Gold and Epithermal Gold Deposits in the Circum-Pacific Region. *Australian Journal of Earth Sciences*, **44**, 373-388.
- Sillitoe, R.H. and Perelló, J., 2005. Andean copper province-Tectonomagmatic settings, deposit types, metallogeny, exploration, and discovery. *Society of Economic Geologists, Economic Geology 100<sup>th</sup> Anniversary Volume*, 845-890.
- Sillitoe, R.H., 2000. Gold-rich porphyry deposits; descriptive and genetic models and their role in exploration and discovery. In Hagemann, S.G. and Brown, P.E. (eds.). *Gold in 2000. Reviews in Economic Geology*, **13**, 315-345.
- Sillitoe, R.H., 2010. Porphyry Copper Systems. *Economic Geology*, **105**, 3-41.
- Sillitoe, R.H., Tolman, J. and Van Kerkvoort, G., 2013. Geology of the Caspiche Porphyry Gold-Copper Deposit, Maricunga Belt, Northern Chile. *Economic Geology*, **108**, 585-604.
- Sillitoe, R.H., 2019. Role of breccias in porphyry copper formation. Proceedings of the 15<sup>th</sup> SGA Biennial Meeting, 27-30 August 2019, Glasgow, Scotland, 998-1001.

- Simons, F.S., 1964. Geology of the Klondyke Quadrangle, Graham and Pinal Counties, Arizona. *USGS*.
- Simmons, A.T., Tosdal, R.M., Wooden, J.L., Mattos, R., Concha, O., McCracken, S. and Beale, T., 2013. Punctuated Magmatism Associated with Porphyry Cu-Mo Formation in the Paleocene to Eocene of Southern Peru. *Economic Geology*, **108**, 625-639.
- Sinclair, W., 2007. Porphyry deposits. Mineral deposits of Canada: A synthesis of major deposit-types, district metallogeny, the evolution of geological provinces, and exploration methods. *Geological Association of Canada, Mineral Deposits Division, Special Publication*, **5**, 223-243.
- Singer, D.A., 2017. Future copper resources. *Ore Geology Reviews*, **86**, 271-279.
- Skewes, A.M. and Atkinson, W.W. Jr., 1985. Petrology of the early formed hydrothermal veins within the central potassic alteration zone of Los Pelambres porphyry copper deposit. *Revista Geológica de Chile*, **25**, 39-56.
- Skewes, A.M. and Holmgren, C., 1993. Solevantamiento andino, erosión y emplazamiento de brechas mineralizadas en el depósito de cobre porfídico, Los Bronces, Chile Central (33°S); aplicación de geotermometría de inclusiones fluida. *Revista Geológica de Chile*, **20**, 71-84.
- Skewes, A.M., 1999. Notas petrográficas sobre algunas breccias de El Teniente: Internal report, Superintendencia de Geología, El Teniente, CODELCO-Chile.
- Skewes, A.M., Arévalo, A.G., Floody, R., Zuñiga, P. and Stern, C.R., 2002. The Giant El Teniente Breccia Deposit: Hypogene Copper Distribution and Emplacement. *Society of Economic Geologists, Special Publication*, **9**, 299-332.
- Skewes, A.M., Holmgren, C. and Stern, C.R., 2003. The Donoso copper-rich, tourmaline-bearing breccia pipe in central Chile: petrologic, fluid inclusion and stable isotope evidence for an origin from magmatic fluids. *Mineralium Deposita*, **38**, 2-21.
- Skewes, A.M., Arévalo, A.G., Floody, R., Zuñiga, P. and Stern, C.R., 2005. The El Teniente megabreccia deposit, the world's largest copper deposit. In Porter, T.M. (ed.). *Super Porphyry Copper and Gold Deposits - A Global Perspective: Porter Geoscience Consultancy Publishing, Adelaide, Australia*, **1**, 83-113.
- Skewes, A.M. and Stern, C.R., 1994. Tectonic trigger for the formation of late Miocene Cu-rich breccia pipes in the Andes of central Chile. *Geology*, **22**, 551-554.
- Skewes, A.M. and Stern, C.R., 1995. Genesis of the Giant Late Miocene to Pliocene Copper Deposits of Central Chile in the Context of Andean Magmatic and Tectonic Evolution. *International Geology Review*, **37**, 893-909.
- Skewes, A.M. and Arévalo, A.G., 2000. El complejo de gabros y diabasas que hospeda a las brechas mineralizadas del depósito de cobre El Teniente. *Chile central, IX Congreso Geológico Chileno, Puerto Varas, Actas*, **1**, 380-384.

- Skewes, A.M. and Stern, C.R., 2005. Magmagenesis and mineralization of giant Miocene and Pliocene megabreccia deposits in the Andes of central Chile. *Abstracts with Programs-Geological Society of America*, **37**, 163.
- Skewes, A.M. and Stern, C.R., 2007. Geology, mineralization, alteration and structural evolution of El Teniente porphyry Cu-Mo deposit - a discussion. *Economic Geology*, **102**, 1165-1170.
- Slack, J.F., 1996. Tourmaline associations with hydrothermal ore deposits. *Reviews in Mineralogy*, **33**, 559-643.
- Slack, J.F. and Trumbull, R.B., 2011. Tourmaline as a Recorder of Ore-Forming Processes. *Elements*, **7**, 321-326.
- Sparks, R.S.J. and Marshall, L.A., 1986. Thermal and mechanical constraints on mixing between mafic and silicic magmas. *Journal of Volcanology and Geothermal Research*, **29**, 99-124.
- Spencer, E.T., 2015. *The Transport and Deposition of Molybdenum in Porphyry Ore Systems*. PhD. Imperial College London.
- Spencer, E.T., Wilkinson, J.J., Creaser, R.A. and Seguel, J., 2015. The Distribution and Timing of Molybdenite Mineralization at the El Teniente Cu-Mo Porphyry Deposit, Chile. *Economic Geology*, **110**, 387-421.
- Stanley, C.R., 2003b. THPLOT.M: A MAT-LAB function to implement generalized Thompson-Howarth error analysis using replicate data. *Computers and Geosciences*, **29**, 225-237, [http://dx.doi.org/10.1016/S0098-3004\(02\)00072-9](http://dx.doi.org/10.1016/S0098-3004(02)00072-9).
- Stanley, C.R., 2006. On the special application of Thompson-Howarth error analysis to geochemical variables exhibiting a nugget effect. *Geochemistry, Exploration, Environment, Analysis*, **6**, 357-368.
- Stanley, C.R. and Lawie, D., 2007. Average relative error in geochemical determinations: Clarification, calculation, and a plea for consistency. *Exploration and Mining Geology*, **16**, 267-275.
- Štemprok, M., 1990. Solubility of tin, tungsten and molybdenum oxides in felsic magmas. *Mineralium Deposita*, **25**, 205-212.
- Stern, C.R., 1989. Pliocene to present migration of the volcanic front, Andean Southern Volcanic Zone. *Revista Geológica de Chile*, **16**, 145-162.
- Stern, C.R., 1991. Role of subduction erosion in the generation of Andean magmas. *Geology*, **19**, 78-81.
- Stern, C.R. and Skewes, A.M., 2005. Origin of giant Miocene and Pliocene Cu-Mo deposits in Central Chile: Role of ridge subduction, decreased subduction angle, subduction erosion, crustal thickening and long-lived, batholiths-size, open system magma chambers. In Porter, T.M. (ed.). *Super Porphyry Copper and Gold Deposits - A Global Perspective: Adelaide, Australia*, Porter Geoscience Consultancy Publishing, **1**, 65-82.
- Stern, C.R., Funk, J.A., Skewes, M.A. and Arévalo, A.G., 2007. Magmatic anhydrite in plutonic rocks at the El Teniente Cu-Mo deposit, Chile, and the role of sulfur- and copper-rich magmas in its formation. *Economic Geology*, **102**, 1335-1344.

- Stern, C.R., Skewes, A.M. and Arévalo, A.G., 2010. Magmatic evolution of the giant El Teniente Cu-Mo deposit, central Chile. *Journal of petrology*, **52**, 1591-1617.
- Stern, C.R., Pang, K., Lee, H., Skewes, A.M. and Arévalo, A.G., 2019. Implications of Hf Isotopes for the Evolution of the Mantle Source of Magmas Associated with the Giant El Teniente Cu-Mo Megabreccia Deposit, Central Chile. *Minerals*, **9**, 550.
- C.R. Stern, 2020. The role of subduction erosion in the generation of Andean and other convergent plate boundary arc magmas, the continental crust and mantle. *Gondwana Research*. <https://doi.org/10.1016/j.gr.2020.08.006>.
- Sun, S.-S. and McDonough, W.F., 1989. Chemical and isotopic systematics of oceanic basalts: implications for mantle composition and processes. *Geological Society, London, Special Publications*, **42**, 313-345.
- Su, Z.-K., Zhao, X.-F., Zeng, L.-P., Zhao, K.-D. and Hofstra, A.H., 2019. Tourmaline boron and strontium isotope systematics reveal magmatic fluid pulses and external fluid influx in a giant iron oxide-apatite (IOA) deposit. *Geochimica et Cosmochimica Acta*, **259**, 233-252.
- Sun, W.-D., Huang, R.-F., Liang, H.-Y., Ling, M.-X., Li, C.-Y., Ding, X., Zhang, H., Yang, X.-Y., Ireland, T. and Fan, W.-M., 2014. Magnetite-hematite, oxygen fugacity, adakite and porphyry copper deposits: Reply to Richards. *Geochimica et Cosmochimica Acta*, **126**, 646-649.
- Takamasa, A. and Nakai, S., 2009. Contamination introduced during rock sample powdering: Effects from different mill materials on trace element contamination. *Geochemical Journal*, **43**, 389-394. Available at: <https://www.terrapub.co.jp/journals/GJ/pdf/4305/43050389.pdf>.
- Tămaş, C.G. and Milési, J.P., 2002. Hydrovolcanic Breccia Pipe Structures-General Features and Genetic Criteria. I. Phreatomagmatic Breccias. *Studia UBB Geologia*, **47**, 127-147.
- Tapster, S., Condon, D.J., Naden, J., Noble, S.R., Petterson, M.G., Roberts, N.M.W., Saunders, A.D. and Smith, D.J., 2016. Rapid thermal rejuvenation of high-crystallinity magma linked to porphyry copper deposit formation; evidence from the Koloula Porphyry Prospect, Solomon Islands. *Earth and Planetary Science Letters*, **442**, 206-217.
- Taylor, B.E. and Slack, J.F., 1984. Tourmalines from Appalachian Caledonian massive sulfide deposits: textural, chemical, and isotopic relationships. *Economic Geology*, **79**, 1703-1726.
- Taylor, R.G. and Pollard, P.J., 1993. Mineralized breccia systems: Methods of recognition and interpretation. Contributions of the Economic Geology Research Unit, James Cook University of North Queensland, Townsville.
- Taylor, R.G., 2003a. Ore textures Volume IV. Broken rocks – breccia 1. EGRU, School of Earth Sciences, James Cook University of North Queensland, 52.
- Taylor, R.G., 2003b. Ore textures. Recognition and interpretation. Vol. V. Broken rocks – Breccia 2. (intrusive breccia)., Pollard and Taylor Geological Services Pty in

conjunction with the Economic Geology Research Unit at James Cook University.

- Taylor, R.G., 2009. Ore textures. 1st ed. Berlin: Springer.
- Thomas, J.B., Bruce Watson, E., Spear, F.S., Shemella, P.T., Nayak, S.K. and Lanzirrotti, A., 2010. Titanite under pressure: the effect of pressure and temperature on the solubility of Ti in quartz. *Contributions to Mineralogy and Petrology*, **160**, 743-759.
- Thompson, A.J.B., Hauff, P.L. and Robitaille, A.J., 1999. Alteration Mapping in Exploration: Application of Short-Wave Infrared (SWIR) Spectroscopy. *SEG Newsletter*, **39**, 16-27.
- Thompson, M. and Howarth, R.J., 1973. The rapid estimation and control of precision by duplicate determinations. *Analyst*, **98**, 153-160.
- Thompson, M. and Howarth, R.J., 1978. A new approach to the estimation of analytical precision. *Journal of Geochemical Exploration*, **9**, 23-30.
- Toro, J.C., Ortúzar, J., Zamorano, J., Cuadra, P.C., Hermosilla, J. and Spröhnle, C., 2012. Protracted magmatic-hydrothermal history of the Río Blanco-Los Bronces district, central Chile: Development of the world's greatest known concentration of copper. In Hedenquist, J.W., et al., (eds.). *Geology and Genesis of Major Copper Deposits and Districts of the World: A Tribute to Richard H. Sillitoe. Society of Economic Geologists Special Publication*, **16**, 105-126.
- Tosdal, R.M. and Richards, J.P., 2001. Magmatic and structural controls on the development of porphyry Cu ± Mo ± Au deposits. *Reviews in Economic Geology*, **14**, 157-181.
- Trumbull, R.B., Krienitz, M.S., Gottesmann, B. and Wiedenbeck, M. 2008. Chemical and boron-isotope variations in tourmalines from an S-type granite and its source rocks: the Erongo granite and tourmalinites in the Damara Belt, Namibia. *Contributions to Mineralogy and Petrology*, **155**, 1-18.
- Trumbull, R.B., Codeço, M.S., Jiang, S-Y., Palmer, M.R. and Slack, J.F., 2020. Boron isotope variations in tourmaline from hydrothermal ore deposits: A review of controlling factors and insights for mineralizing systems. *Ore Geology Reviews*, **125**, 103682.
- Un.org., 2010. [online] Available at:  
<https://www.un.org/Depts/Cartographic/map/profile/Chile.pdf> [Accessed 13 Jun. 2019].
- Uribe, F., 2000. Estudio de Vulnerabilidad Geológica-Geotécnica de Chimenea de Brecha Braden (API T99M224). Fase I: Caracterización Geológica y Geotécnica de la Chimenea de Brechas Braden. Superintendencia de Geología. Codelco, El Teniente. Inédito. Nota Interna GL-116/00.
- Uribe, F. and Floody. R., 2003. Geología y vulnerabilidad del Complejo Brechas Braden: nuevos antecedentes, El Teniente, Chile. Superintendencia de Geología. Codelco, El Teniente.

- van Hinsberg, V.J., 2011. Preliminary experimental data on trace-element partitioning between tourmaline and silicate melts. *The Canadian Mineralogist*, **49**, 153-163.
- van Hinsberg, V.J., Henry, D.J. and Marschall, H.R., 2011. Tourmaline: an ideal indicator of its host environment. *The Canadian Mineralogist*, **49**, 1-16.
- Vargas, R., Gustafson, L.B., Vukasovic, M., Tidy, E. and Skewes, A.M., 1999. Ore breccias in the Río Blanco-Los Bronces porphyry copper deposit, Chile. In Skinner, B. (ed.). *Geology and Ore Deposits of the Central Andes. Society of Economic Geologists*.
- Vazquez, J.A. and Ort, M.H., 2006. Facies variation of eruption units produced by the passage of single pyroclastic surge currents, Hopi Buttes volcanic field, USA. *Journal of Volcanology and Geothermal Research*, **154**, 222-236.
- Vega, E. and Maksaev, V., 2003. La Chimenea Braden: nuevos antecedentes geológicos y geocronológicos. *Congreso Geológico Chileno*, 10. Concepción, Chile, Octubre, 2003.
- Vidakovic, J., 2013. *Exploración en Distrito El Teniente La Huifa y Matancillas Alto El Código Minero [online]*. Available at: <http://www.comisionminera.cl/documentacion/category/60-seminario-practicas-internacionales-para-la-estimacion-de-recursos-y-reservas-mineras-7-may-2014?download=421:3-modelos-geologicos-y-de-exploracion-j-camacho-codelco>
- Vignerresse, J.-L., Truche, L. and Richard, A., 2019. How do metals escape from magmas to form porphyry-type ore deposits? *Ore Geology Reviews*, **105**, 310-336.
- Vry, V.H., 2010. Geological and Hydrothermal Fluid Evolution at El Teniente, Chile. Unpublished PhD thesis, Imperial College London, United Kingdom.
- Vry, V.H., Wilkinson, J.J., Seguel, J. and Millan, J., 2010. Multistage Intrusion, Brecciation, and Veining at El Teniente, Chile: Evolution of a Nested Porphyry System. *Economic Geology*, **105**, 119-153.
- Wallier, S., Rey, R., Kouzmanov, K., Pettke, T., Heinrich, C.A., Leary, S., O'Connor, G., Tămaş, C.G., Vennemann, T. and Ullrich, T., 2006. Magmatic Fluids in the Breccia-Hosted Epithermal Au-Ag Deposit of Rosia Montana, Romania. *Economic Geology*, **101**, 923-954.
- Wang, Q., Xu, J.-F., Jian, P., Bao, Z.-W., Zhao, Z.-H., Li, C.-F., Xiong, X.-L. and Ma, J.L., 2006. Petrogenesis of adakitic porphyries in an extensional tectonic setting, Dexing, South China: implications for the genesis of porphyry copper mineralization. *Journal of Petrology*, **47**, 119-144.
- Wark, D.A. and Watson, E.B., 2006. TitanQ: a titanium-in-quartz geothermometer. *Contributions to Mineralogy and Petrology*, **152**, 743-754.
- Warnaars, F.W., Holmgren, C.D. and Barassi, S.F., 1985. Porphyry copper and tourmaline breccias at Los Bronces-Río Blanco, Chile. *Economic Geology*, **80**, 1544-1565.

- Webb P.C., Thompson M., Potts P.J. and Wilson S.A., 2012. GeoPT31 – An international proficiency test for analytical geochemistry laboratories – Report on round 31 (Modified River Sediment, SdAR-1)/July 2012. International Association of Geoanalysts, <http://www.geoanalyst.org/documents/GeoPT31Report.pdf>
- Weinberg, R.F. and Regenauer-Lieb, K., 2010. Ductile fractures and magma migration from source. *Geology*, **38**, 363-366.
- White, J.D.L. and Valentine, G.A., 2016. Magmatic versus phreatomagmatic fragmentation: Absence of evidence is not evidence of absence. *Geosphere*, **12**, 1478-1488.
- Whitney, D.L. and Evans, B.W., 2009. Abbreviations for names of rock-forming minerals. *American Mineralogist*, **95**, 185-187.
- Wilkinson, J.J., 2013. Triggers for the formation of porphyry ore deposits in magmatic arcs. *Nature Geoscience*, **6**, 917-925.
- Wilkinson, J.J., Chang, Z., Cooke, D.R., Baker, M.J., Wilkinson, C.C., Inglis, S., Chen, H. and Gemmell, B.J., 2015. The chlorite proximator: A new tool for detecting porphyry ore deposits. *Journal of Geochemical Exploration*, **152**, 10-26.
- Wilkinson J.J., Cooke, D.R., Baker, M.J., Chang, Z., Wilkinson, C.C., Chen, H., Fox, N., Hollings, P., White, N.C., Gemmell, J.B., Loader, M.A., Pacey, A., Sievwright, R.H., Hart, L.A. and Brugge E.R., 2017. Porphyry indicator minerals and their mineral chemistry as vectoring and fertility tools. In McClenaghan, M.B. and Layton-Matthews, D., (eds.). Application of indicator mineral methods to bedrock and sediments. *Geological Survey of Canada*, 66-77.
- Wilkinson, J.J., Baker, M.J., Cooke, D.R. and Wilkinson, C.C., 2020. Exploration Targeting in Porphyry Cu Systems Using Propylitic Mineral Chemistry: A Case Study of the El Teniente Deposit, Chile. *Economic Geology*, **115**, 771-791.
- Williamson, B.J., Spratt, J., Adams, J.T., Tindle, A.G. and Stanley, C.J., 2000. Geochemical constraints from zoned hydrothermal tourmalines on fluid evolution and Sn mineralization: An example from fault breccias at Roche, SW England. *Journal of Petrology*, **41**, 1439-1453.
- Williamson, B.J., Herrington, R.J. and Morris, A., 2016. Porphyry copper enrichment linked to excess aluminium in plagioclase. *Nature Geoscience*, **9**, 237-241.
- Woodcock, N.H. and Mort, K., 2008. Classification of fault breccias and related fault rocks. *Geological Magazine*, **145**, 435-440.
- Yamazaki, S., 2011. Trace element contamination from tungsten carbide rod mill. Science reports of Niigata University. *Geology*, **26**, 91-99.
- Yang, S.-Y. and Jiang, S.-Y., 2012. Chemical and boron isotopic composition of tourmaline in the Xiangshan volcanic–intrusive complex, Southeast China: Evidence for boron mobilization and infiltration during magmatic–hydrothermal processes. *Chemical Geology*, **312-313**, 177-189.
- Yang, S.-Y., Jiang, S.-Y., Zhao, K.-D., Dai, B.-Z. and Yang, T., 2015. Tourmaline as a recorder of magmatic–hydrothermal evolution: an in situ major and trace

- element analysis of tourmaline from the Qitianling batholith, South China. *Contributions to Mineralogy and Petrology*, **170**, 1-21.
- Yavuz, F., Jiang, S.-Y., Karakaya, N., Karakaya, M.C. and Yavuz, R., 2011. Trace-element, rare-earth element and boron isotopic compositions of tourmaline from a vein-type Pb–Zn–Cu ± U deposit, NE Turkey. *International Geology Review*, **53**, 1-24.
- Zhang, C.-C., Sun, W.-D., Wang, J.-T., Zhang, L.-P., Sun, S.-J. and Wu, K., 2017. Oxygen fugacity and porphyry mineralization: A zircon perspective of Dexing porphyry Cu deposit, China. *Geochimica et Cosmochimica Acta*, **206**, 343-363.
- Zhang, M., Zhang, D., Zhao, B., Wu, M., Bao, B., Liu, Y. and Huang, C., 2019. Petrography and geochemistry of tourmaline breccia in the Longtoushan Au deposit, South China: genesis and its exploration significance. *Geochemistry: Exploration, Environment, Analysis*, **19**, 448-464.
- Zhu, X., Raschke, M.B. and Liu, Y., 2020. Tourmaline as a Recorder of Ore-Forming Processes in the Xuebaoding W-Sn-Be Deposit, Sichuan Province, China: Evidence from the Chemical Composition of Tourmaline. *Minerals*, **10**, 438.
- Zimanowski, B. and Büttner, R., 2003. Phreatomagmatic explosions in subaqueous volcanism. In White, J.D.L., Smellie, J.L. and Clague, D.A. (eds.). *Explosive Subaqueous Volcanism. A.G.U Monograph*, **140**, 51-60.
- Zimanowski, B., Büttner, R., Delino, P., White, J.D.L. and Wohletz, K., 2015. Magma-water interaction and phreatomagmatic fragmentation. In Sigurdsson, H., Houghton, B., McNutt, S.R., Rymer, H. and Stix, J., (eds.). *Encyclopedia of Volcanoes, Second edition. Academic Press, London*, 473-484.
- Zwyer, T., 2010. Temporal and Spatial Evolution of Hydrothermal, Ore-Related Fluids in the Batu Hijau Porphyry Copper-Gold Deposit, Sumbawa (Indonesia). Unpublished MSc Thesis, ETH Zurich.

# Appendices

## i) Drill hole intercepts and locations

List of drill holes intercepts studied and sampled. Drill holes 1068 to 1797 (purple) relate to those around and in the Braden Diatreme. Drill holes with prefix 'ES' (beige) correspond to La Huifa and the remaining are from the Diablo sector. BBS= Braden Sericite Breccia, PLA= Porphyritic Latite, PDA= Porphyritic Dacite, BXPDI= Porphyritic diorite igneous breccia, CBB= Braden Breccia Complex (generic term for all Braden Breccias), TMC= Teniente Mafic Complex, BXTU= Tourmaline Breccia, BBTU= Braden Tourmaline Breccia, BXSU= Braden Sulphide Breccia, BBSF= Fine Sericite Braden Breccia, DQQZ= Quartz Dyke, PDA= Porphyritic Dacite, BXCL= Chlorite Breccia, BXANH= Anhydrite Breccia, TON= Tonalite (SQD), BXBI= Biotite Breccia, BXVOL= Brecciated Volcanics, BHT1= First generation tourmaline breccia, BHT2= Second generation tourmaline breccia. Note: northing uses local El Teniente Mine grid.

Drill Hole ID	Length/m	Easting	Northing	Azimuth	Inclination°	Sector	Level	Intervals studied/m	Lithologies
DDH1068	1013.46	755.10	217.69	91.00	-85.00	Teniente 8	Transport	0-16.76, 424.59-583.39, 939.70-1013.46	BBS, PLA, PDA, BXPDI
DDH1079	819.91	753.75	219.78	332.00	-62.00	Teniente 8		0-32.61, 349-819.91	CBB
DDH1196	257.25	210.85	-326.97	27.00	30.00	Teniente 5		90.20-274.32	TMC, BXTU, BBTU, BXSU, BBS, PLA, BBSF
DDH1213	230.43	146.20	-170.47	85.00	40.00	Teniente 5		0-230.43	TMC, DQQZ, BXANH/TU, BXTU, BBTU, BBS, BXSU
DDH1512	451.10	1381.39	81.11	263.58	-25.00	Teniente 5	Transport	199.03-451.1	PDA, BXPDI, BXCL, BBS, BBTU, BXANH, PDI, TMC
DDH1694	259.08	91.92	324.63	77.00	-29.00	Teniente 5	Transport	0-245.97	TMC, BXANH, BBS, BXTU, BBTU
DDH1754	384.05	933.36	318.66	87.75	-10.00	Teniente 5	Transport	0-307.24	BBTU, BBS, BXCL, BXTU, TMC, BXPDI, PDI, PLA
DDH1769	601.37	857.70	337.21	125.67	10.00	TTE Sub 6	Production	0-48.16, 57.9-230.43, 301.75-323.1	BBS, BBSF, BBTU, BBSB, BXCL, TMC, BXPDI, PDI, PLA
DDH1775	465.13	857.63	337.14	135.00	-15.00	TTE Sub 6	Production	0-152.40	BBS, BBSF, BBTU ±BXANH
DDH1794	307.24	1520.13	97.20	101.67	-25.00	Teniente 5	Transport	54.25-156.67	BXANH, TMC, BXPDI, TON, BXBI, LAM
DDH1797	182.88	843.51	-400.32	115.00	-14.00	TTE 4 Fortuna	UCL Regimiento	0-180.75	BXTU, LAM, PDA, BXANH, PLA, BXSU
ES0003	114.09	1627.60	3282.90	302.62	-48.00	La Huifa		0-114.09	TOB, BXTU (BHT1, BHT2), BXVOL
ES0005	118.90	1649.59	2742.10	21.62	-70.00	La Huifa		0-55.5	BXTU, BXVOL, PDI, TOB, BXANH
ES0026	776.55	1488.09	3161.62	36.69	-50.00	La Huifa		98-276	Andesite, BXANH, BXANH±BXTU, Toba Litica
DDH1974	355.40	505.70	-536.86	180.22	-80.21	TTE 4 Regimiento		123.75-215.19	TMC, BXANH, BXTU, DQQZ, BXSU
DDH1990	201.17	509.59	-545.00	180.00	-72.00	TTE 4 Regimiento		160-184.71	TMC, DQQZ, BXTU
DDH2136	160.02	501.67	-600.33	90.00	30.00	TTE 6	Diablo Regimiento	0-6.1	BXTU, TMC
DDH2138	151.49	507.37	-651.16	90.00	28.50	TTE 6	Diablo Regimiento	0-6.1	BXTU, TMC, DQQZ
DDH2672	190.00	565.30	-775.52	270.67	28.79	Diablo Reg	Production	88-122, 156-190	BXTU, PLA, TMC
DDH2677	240.00	566.05	-725.75	270.28	47.14	Diablo Reg	Production	97.5-170.54	BXTU/ANH
DDH2679	245.00	566.15	-689.59	270.34	51.65	Diablo Reg	Production	117.9-192.4	TMC, BXTU, BXTU/ANH
DDH2683	275.00	599.90	-625.59	270.51	42.07	Diablo Reg	Production	143-162.81	TMC, BXTU
SG0602	150.00	496.00	-755.74	0.00	25.00			45-55, 90-105	BXTU, BXTU/ANH

Lithological maps of different mine levels with studied drill holes shown: **a)** Level TTE\_3 (2,401 masl); **b)** Level TTE\_6 (2,165 masl); **c)** Level TTE\_8 (1,983 masl). All maps are plotted on the local mine grid which is oriented 14.5°E of geographic north. Courtesy of Codelco División El Teniente.

